Lecture Notes in Electrical Engineering 522

SOLUSIBUKUKITA

Mohammed Chadli
Sofiane Bououden · Salim Ziani
Ivan Zelinka
Editors

Advanced Control Engineering Methods in Electrical Engineering Systems

Springer

Lecture Notes in Electrical Engineering

Volume 522

Lecture Notes in Electrical Engineering (LNEE) is a book series which reports the latest research and developments in Electrical Engineering, namely:

- Communication, Networks, and Information Theory
- Computer Engineering
- Signal, Image, Speech and Information Processing
- Circuits and Systems
- Bioengineering
- Engineering.

The audience for the books in LNEE consists of advanced level students, researchers, and industry professionals working at the forefront of their fields. Much like Springer's other Lecture Notes series, LNEE will be distributed through Springer's print and electronic publishing channels.

More information about this series at http://www.springer.com/series/7818

Mohammed Chadli · Sofiane Bououden
Salim Ziani · Ivan Zelinka
Editors

Advanced Control Engineering Methods in Electrical Engineering Systems

Springer

Editors
Mohammed Chadli
MIS (EA 4290)
Université de Picardie Jules Verne
Amiens, France

Salim Ziani
Faculty of Sciences and Technology
University of Constantine
Constantine, Algeria

Sofiane Bououden
Faculty of Sciences and Technology
University Abbes Laghrour Khenchela
Khenchela, Algeria

Ivan Zelinka
Department of Computer Science, Faculty of Electrical Engineering and Computer Science
VŠB-TUO
Ostrava-Poruba, Czech Republic

ISSN 1876-1100 ISSN 1876-1119 (electronic)
Lecture Notes in Electrical Engineering
ISBN 978-3-319-97815-4 ISBN 978-3-319-97816-1 (eBook)
https://doi.org/10.1007/978-3-319-97816-1

Library of Congress Control Number: 2018950463

This Springer imprint is published by the registered company Springer Nature Switzerland AG
The registered company address is: Gewerbestrasse 11, 6330 Cham, Switzerland

Foreword

This proceeding book about the Advanced Control Engineering Methods in Electrical Engineering Systems conference contains accepted papers presenting the most interesting state of the art on this field of research.

Presented topics are focused on classical as well as modern methods for modeling, control, identification, and simulation of complex systems with applications in science and engineering. Topics are (but not limited to): control and systems engineering, renewable energy, faults diagnosis-faults tolerant control, large-scale systems, fractional-order systems, unconventional algorithms in control engineering, signal and communications… and much more.

The control of complex systems dynamics, analysis, and modeling of its behavior and structure is a vitally important problem in engineering, economy, and generally in science today. Examples of such systems can be seen in the world around us and are a part of our everyday life. Application of modern methods for control, electronics, signal processing, and more can be found in our mobile phones, car engines, home devices as for example washing machine is as well as in such advanced devices as space probes and communication with them.

The main aim of the conference is to create periodical possibility for students, academics, and researchers to exchange their ideas and novel methods. This conference will establish a forum for the presentation and discussion of recent trends in the area of applications of various modern as well as classical methods for researchers, students, and academics.

The accepted selection of papers was extremely rigorously reviewed in order to maintain the high quality of the conference that is supported by organizing universities and related research grants. Regular as well as student's papers have been submitted to the conference, and in accordance with review process, has been accepted after a positive review.

We would like to thank the members of the Program Committees and reviewers for their hard work. We believe that this conference represents a high-standard conference in the domain of control, modeling, and analysis of dynamical and electronic systems.

We would like to thank all the contributing authors, as well as the members of the Program Committees and the Local Organizing Committee for their hard and highly valuable work. Their work has definitely contributed to the success of the conference.

Mohammed Chadli
Sofiane Bououden
Salim Ziani
Ivan Zelinka

Organization

Conference

General Chairs

Mohammed Chadli	University of Picardie Jules Verne Amiens, France
Khaled Belarbi	Ecole Nationale Polytechnique de Constantine, Algeria

The International Conference on Electrical Engineering and Control Applications (ICEECA) provides a forum for specialists and practitioners to present and discuss their research results in the several areas of the conference, and also state-of-the-art findings in using the applied electrical engineering and automatic control to solve national problems that face developing countries. The conference ICEECA publishes papers on theoretical analysis, experimental studies, and applications in the domain of automatic control and computer engineering. The objective of the conference is not only the exchange of knowledge and experience, since the conference is an open door to students, but also provides opportunities for researchers to target future collaboration on current issues.

Steering Committee

Sofiane Bououden	University of Khenchela, Algeria
Mohammed Chadli	University of Picardie Jules Verne Amiens, France
Hamid Reza Karimi	Ecole Polytechnique de Milan, Italy
Peng Shi	Victoria University, Australia

Program Chairs

S. Ziani
S. Bououden
I. Zelinka

Local Committee

Abdemalek Zahaf	University of Brothers Mentouri Constantine 1, Algeria
Abdelhamid Bounemeur	University of Brothers Mentouri Constantine 1, Algeria
Samir Teniou	Ecole Nationale Polytechnique de Constantine, Algeria
Kheireddine Lamamra	University of Oum El Bouaghi, Algeria

International Advisory Committee

Khaled Belarbi	Ecole Nationale Polytechnique de Constantine, Algeria
Peng Shi	Victoria University, Australia
Abedlhamid Tayebi	Lakehead University, Canada
Hamid Reza Karimi	Ecole Polytechnique de Milan, Italy
L. X. Zhang	Zhejiang University, China
N. B. Braiek	L'Ecole Polytechnique de Tunisie, Tunisia

Scientific Program Committee

ICEECA established an international committee of selected well-known experts in electrical engineering who are willing to be mentioned in the program and to review a set of papers each year. The list below comprises the Scientific Program Committee members

Aawatif Hayar	University Hassan II Casablanca, Morocco
Abdelaziz Hamzaoui	University of Reims, France
Abdeldjalil Ouahabi	Polytech Tours, France
Abdellah Kouzou	University of Djelfa, Algeria
Ahmed Chemori	University Montpellier 2, France
Ahmed Hafaifa	Université de Djelfa

Amar Djouak	Université Catholique de Lille, France
Ameur Ikhlef	University of Mentouri Constantine, Algeria
Aziz Naamane	Université de Marseille Nord, France
Belkacem Fergani	University of USTHB, Algeria
Bin Haji Hassan Masjuki	University of Malaya, Malaysia
Bhekisipho Twala	Institute for Intelligent Systems, University of Johannesburg, South Africa
Carlos Astorga Zaragoza	CENIDET, Mexico
Chérif Chibane	Massachusetts Institute of Technology, Lincoln Laboratory, Boston, USA
De Lima Neto Fernando	Polytechnic School of Pernambuco, University of Pernambuco, Recife, Brazil
Drai Redouane	Centre de Recherche en Technologies Industrielles CRTI, Algeria
Faouzi Bouani	Ecole Nationale d'Ingénieurs de Tunis, Tunisie
Fella Hachouf	University of the Brothers Mentouri Constantine 1, Algeria
Fernando Tadeo	University of Valladolid, Spain
Fouad Kerrour	University of the Brothers Mentouri Constantine 1, Algeria
Gloria Osorio Gordillo	CENIDET, Mexico
Hervé Coppier	ESIEE, France
Hicham Jamouli	University, Agadir, Morocco
Ilyes Boulkaibet	RSA, Johannesburg, University of Johannesburg, South Africa
J. Amudhavel	University, Andhra Pradesh, India
J. A. T Machado	Institute of Engineering of Coimbra, Portugal
Jean-Jacques Loiseau	IRCyN, France
Kamel Guesmi	University of Djelfa, Algeria
Kheireddine Lamamra	University of Oum Bouaghi, Algeria
Lamir Saidi	University of Batna, Algeria
Maamer Bettayeb	University of Sharjah, UAE
Malika Kandouci	University of Sidi Bel-Abbes, Algeria
Manuel Adam Medina	CENIDET, Mexico
Marouane Alma	Centre de Recherche en Automatique de Nancy, France
Mehadji Abri	University of Tlemcen, Algeria
Mohamed Boutayeb	Centre de Recherche en Automatique de Nancy, France
Mohamed Seghir Boucherit	Ecole Nationale Polytechnique, Algeria
Mohammed Chaabane	University of Sfax, Tunisia
Mostapha Ziad	University of Suffolk, Boston, USA
Mounira Ouarzeddine	Faculty of Electronics and Computer Science of the USTHB University

Najib Essounbouli	University of Reims Champagne-Ardenne, CReSTIC, France
Noureddine Mannamani	University of Reims, France
Ouassila Bourbia	University of Brothers Mentouri Constantine 1, Algeria
Pierre Borne	Ecole Centrale de Lille, France
Rachid Illoul	Ecole Nationale Polytechnique de Alger, Algeria
Reda Boukezzoula	Université de Savoie, France
Roman Senkerik	Tomas Bata University in Zlin, Czech Republic
Said Touati	Centre de recherche Nucléaire de Birine, Ain Oussera, Algeria
Salim Ziani	University of Brothers Mentouri Constantine 1, Algeria
Samir Teniou	Ecole Nationale Polytechnique de Constantine, Algeria
Zoheir Hammoudi	University of Constantine 1, Algeria
Zoubeida Messali	University of BBA, Algeria

Contents

Control and Systems Engineering (CSE)

Backstepping Control of Abnormal Behaviours in DC-DC Boost Converter

Zineb Madni[1(✉)], Kamel Guesmi[1,2], and Atallah Benalia[1]

[1] LACoSERE, University of Amar Telidji, Laghouat, Algeria
madnizineb@gmail.com, guesmi01@univ-reims.fr, a.benalia@lagh-univ.dz
[2] CReSTIC, Reims University, Reims, France

Abstract. The aim of this work is to control the nonlinear phenomena exhibited by the Boost converter. To this end a backstepping controller is synthesised. Simulation results are used to validate the controller and to show its effectiveness in suppressing all nonlinear phenomena and keeping simple the converter behaviour despite the variation of its parameters.

Keywords: Backstepping control · Boost converter · Bifurcation · Chaos Nonlinear phenomena

1 Introduction

The energy conversion is an important step in several industrial applications and the power converters are the main element for energy processing. Indeed, they are used in power distribution systems, flexible alternating current transmission systems, renewable energy systems (photovoltaic, fuel cells and wind), computers, telecommunication equipments, transportation, machines and drivers [1, 2].

The power converters are nonlinear systems that exhibit a variety of complex behaviors like bifurcation, quasi-periodicity and chaos. These phenomena can change the system behaviour; they can affect dramatically the system stability and even damage it. In the literature many works focused on the study of such phenomena in different systems [1, 3–8].

The physical systems change their nominal behaviour and bifurcate to another one when one or more of its parameters are subject to variation [2, 5, 7, 9–13].

To deal with nonlinear phenomena, many approaches are proposed in the literature, like fuzzy controllers [14, 15], sliding mode techniques [16, 17], ramp compensation approach [18], feedback based controllers [19, 20], and resonant parametric perturbation [21] and PD controller [22].

In the literature, there are many goals for nonlinear phenomena control. Indeed, for automatic control engineers some phenomena can be delayed like period doubling, suppressed like chaotic behaviour [23, 24] or changed to another type more safe. In another direction, the researchers are focused on the generation of these nonlinear phenomena for many purposes like “chaotification” [25, 26] for information encryption.

M. Chadli et al. (Eds.): ICEECA 2017, LNEE 522, pp. 3–13, 2019.
https://doi.org/10.1007/978-3-319-97816-1_1

The control of bifurcation had many applications in the world [27], it is also a route to chaos control due to the fact that the chaos is obtained via a series of bifurcation or of period doubling and quasi-periodic behaviours until attaining chaos [28].

The controller design can be done based on indirect or direct Lyapunov methods for stabilisation. The first class of approaches is difficult to use and needs arduous calculations; whereas, the second family, of approaches, had the problem of Lyapunov function choice as drawbacks.

To overcome these problems, the backstepping approach of control can be considered as an issue. It is a recursive method of the second class with a systematic choice of Lyapunov function [30]. This technique of control was reported intensively in the literature [30–32] due to its performances and advantages. One of the most advantages of this control technique is its robustness against the system parameters variation [33] and its remarkable capability to deal with complex nonlinear phenomena. Indeed, in [31, 34] the authors propose an adaptive backstepping scheme to control chaotic behaviours in mechanical and electromechanical systems. However, to attain the desired performance the authors used adaptive schemes that fail in the case of systems with fast dynamics like in power converters. To solve this problem, we propose, in this paper, a simple backstepping control approach to control bifurcation in a DC-DC Boost converter while avoiding the aforementioned problems.

The rest of this paper is organized as follows: the model of Boost converter is presented in Sect. 2 and the Sect. 3 is devoted to the systematic design method of backstepping to stabilise the converter. The obtained results in term of bifurcations and chaos control are presented in Sect. 4.

2 Modelling of Boost Converter

The scheme of Boost converter is given by Fig. 1.

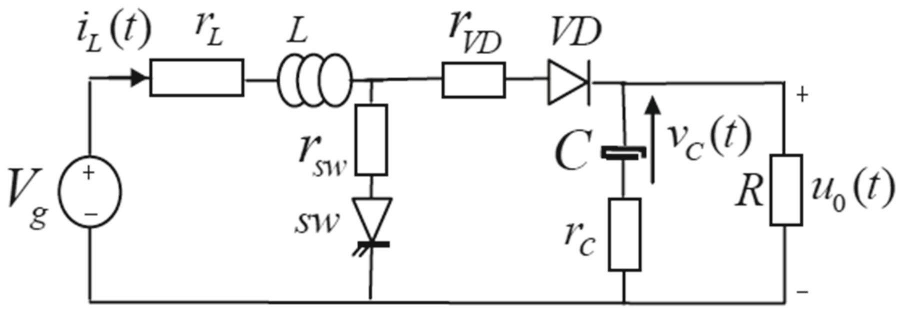

Fig. 1. Boost converter.

The converter functioning principle is related to the state of switch *sw*. Indeed, the energy is accumulated in the inductance, from the supply, in a part of the switching period *T* and transferred, then, to the load during the remaining of the switching period.

When the switch is ON, the system can be described by:

$$L\frac{d}{dt}i_L(t) = V_g - (r_L + r_{sw})i_L(t) \tag{1}$$

$$C\frac{d}{dt}v_c(t) = \frac{v_c(t)}{R + r_c}x_2 \tag{2}$$

and when the switch is OFF, the system is given by:

$$L\frac{d}{dt}i_L(t) = V_g - \left(r_L + r_{VD} + \frac{Rr_c}{R + r_c}\right)i_L(t) - \frac{R}{R + r_c}v_c(t) \tag{3}$$

$$C\frac{d}{dt}v_c(t) = \frac{1}{R + r_c}(Ri_L(t) - v_c(t)) \tag{4}$$

Averaged model of this system can be expressed:

$$\dot{x} = \begin{cases} \dot{x}_1 = \dfrac{V_g}{L} - (1 - d)\dfrac{x_2}{L} \\ \dot{x}_2 = (1 - d)\dfrac{x_1}{C} - \dfrac{x_2}{RC} \end{cases} \tag{5}$$

$$x_1 = i_L$$
$$x_2 = v_c$$

In our case this model will be used to synthesise the control law.

For simulation and validation purposes we use the discrete model. Using the mapping technique, the last model is given by:

$$\begin{aligned} &x((n + 1)T) = \Phi_2(t_2)\Phi_1(t_1)x(nT) \\ &+ \Phi_2(t_2)\int_{nT}^{(n+d)T}\Phi_1((n + d)T - \tau)B_1V_g d\tau + \int_{(n+d)T}^{(n+1)T}\Phi_2((n + 1)T - \tau)B_2V_g d\tau \end{aligned} \tag{6}$$

where

$$t_1 = d_nT$$
$$t_2 = (1 - d_n)T$$

d_n is the duty ratio

T is the switching period

$\Phi_i, i = 1, 2,$ is the transition matrix calculated in [14].

$x = \left[i_L, v_c\right]^T$ is the system state (inductance current and voltage across capacitor respectively).

3 Stabilisation and Control of Boost Converter Using Backstepping Controller

For controller synthesis we have the following steps:

Step1:
We assume

$$z_1 = x_1 - I_{ref} \tag{7}$$

with I_{ref} the reference current.

For a candidate Lyapunov function:

$$V_0 = \frac{1}{2} z_1^2 \tag{8}$$

we have

$$\dot{V}_0 = z_1 \dot{z}_1 \tag{9}$$

$$\dot{z}_1 = \frac{V_g}{L} - (1 - d)\frac{x_2}{L} - \dot{I}_{ref} \tag{10}$$

If one use

$$\dot{z}_1 = -c_1 z_1 \tag{11}$$

with

$$c_1 > 0$$

we obtain

$$\frac{x_2}{L} = (c_1 z_1 + \frac{V_g}{L} - \dot{I}_{ref})/(1 - d) \tag{12}$$

and

$$\dot{V}_0 = -c_1 z_1^2 \tag{13}$$

We denote by:

$$\alpha = \left(c_1 z_1 + \frac{V_g}{L} - \dot{I}_{ref}\right)/(1 - d) \tag{14}$$

The value of $\frac{x_2}{L}$ that ensures the asymptotic stability of z_1.

Step2:
If we assume

$$z_2 = \frac{x_2}{L} - \alpha \tag{15}$$

then

$$\frac{x_2}{L} = z_2 + \alpha \tag{16}$$

using (10), (14) and (16) we obtain:

$$\dot{z}_1 = -c_1 z_1 - (1-d) z_2 \tag{17}$$

$$\dot{z}_2 = (1-d)\frac{x_1}{LC} - \frac{x_2}{RLC} - \frac{(c_1 \dot{z}_1 - \ddot{I}_{ref})}{(1-d)} - \frac{\dot{d}\alpha}{(1-d)} \tag{18}$$

For the Lyapunov function:

$$V = \frac{1}{2} z_1^2 + \frac{1}{2} z_2^2 \tag{19}$$

we have

$$\dot{V} = z_1 \dot{z}_1 + z_2 \dot{z}_2 \tag{20}$$

$$\dot{V} = z_1(-c_1 z_1 - (1-d) z_2) + z_2 \dot{z}_2 \tag{21}$$

$$\dot{V} = -c_1 z_1^2 + z_2(\dot{z}_2 - z_1(1-d)) \tag{22}$$

For stability requirement, we assume

$$\dot{z}_2 - z_1(1-d) = -c_2 z_2 \tag{23}$$

where $c_2 > 0$
and we obtain then,

$$\dot{V} = -c_1 z_1^2 - c_2 z_2^2 \tag{24}$$

and, hence, the system asymptotic stability is ensured.
Using (18) and (23) the law control is given by the following expression:

$$\dot{d} = \frac{1}{\alpha}\Big(\big(c_1^2 - (1-d)^2\big) z_1 + (1-d)\big(c_1 + c_2\big) z_2 + (1-d)^2 \frac{x_1}{LC} - (1-d)\frac{x_2}{RLC} \Big) \tag{25}$$

Generally, this control law is used to regulate the output voltage. In our case, we investigate the effect of this law on the nonlinear behaviours of the converter.

4 Simulation and Results

For simulation purposes we use the enhanced discrete model given in [14] to describe the converter fast and slow behaviours and to describe the nonlinear phenomena exhibited by this last.

The simulation parameters are given by the following Table 1:

Table 1. Boost converter parameters

Bifurcation parameters	Converter parameters				
	Vg(V)	R(Ω)	L(mH)	C(μF)	Iref(A)
Vg(V)	[7,40]	30	20	68	2
R(Ω)	15	[7,50]	20	68	2
L(mH)	15	30	[5, 30]	68	2
Iref(A)	15	30	20	68	[1, 7]
$T = 1/20\,000$ s					

To explore the original nonlinear behaviour of the Boost converter, we use the simplified control law [35]:

$$d_n = \frac{L}{T}\left(\frac{I_{ref} - i_L(n)}{V_g}\right)$$

The backstepping control law is used to control the converter nonlinear dynamics and the obtained results will be compared to the original behaviour of the converter.

The bifurcation diagram and the Lyapunov exponent are used, under MATLAB environment, as analysis tools and to explore the different behaviours of the converter. Using the bifurcation diagram, the converter operates in nominal mode (period one) when its state takes a one value for each value of the bifurcation parameter; and operates in period two when we have two values and so on until it attains the chaotic region characterized by a random set of values for each value of the bifurcation parameter.

The Lyapunov exponent is used to distinguish the chaotic behaviour from the quasi-periodic movements. Indeed, chaotic behaviour is characterized by high sensitivity to initial conditions and hence it leads to a positive Lyapunov exponent.

The bifurcation parameters in this work are the reference current I_{ref}, the input voltage V_g, the load R and the inductance L.

According to Fig. 2a, the variation of the input voltage produces a chaotic behaviour for values less than 14, 5 V, outside this region the system had a period 2T in the interval [14.5, 15] V and a stable period one when the input voltage is higher than 15 V. These statements are confirmed by the corresponding Lyapunov exponent given by Fig. 2b. It had positive values in the region of chaotic behaviour, zero for critical or bifurcation values and negative values in stable regions.

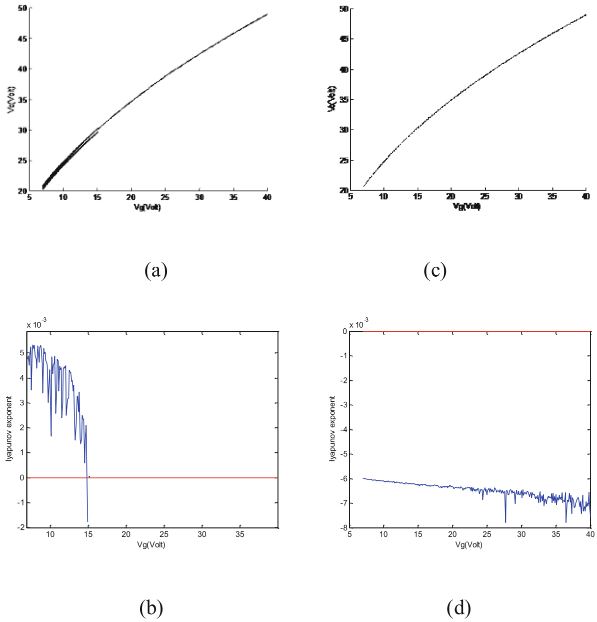

Fig. 2. System response under V_g variation, bifurcation diagram: (a) original behaviour (c) behaviour with backstepping, Lyapunov exponent: (b) original behaviour (d) behaviour with backstepping.

In order to eliminate these behaviours and keep the system operating in period one region, the backstepping controller is used and the obtained results are depicted Figs. 2c and d. It is clear, from these last figures, that the system had a period one behaviour; the bifurcation and the chaos are eliminated from the whole range of input voltage.

In the case of reference current variation, the bifurcation diagram of Fig. 3a depicts a stable period one for values of I_{ref} less than $2A$, a stable period two and chaos when the reference current I_{ref} is increased further. The corresponding Lyapunov exponent is given in the Fig. 3b. Using the backstepping control law, the bifurcation diagrams of Fig. 3c and the lyapunov exponent Fig. 3d shows the total suppression of all undesirable complex behaviours and the extension of the simple period one behaviour on the whole range of reference current.

For the case of load variation, the system operates in period one behaviour until $R = 29\,\Omega$, then the system period is doubled in the interval $[29,\ 30.5]\,\Omega$ and the behaviour becomes chaotic over this interval as shown in Fig. 4a and confirmed by the Lyapunov exponent of Fig. 4b. From the results of Figs. 4c and d, we remark the enhancement introduced by the backstepping controller. Indeed, we remark the abnormal behaviours suppressing and the period one region widening on the whole range of load variation.

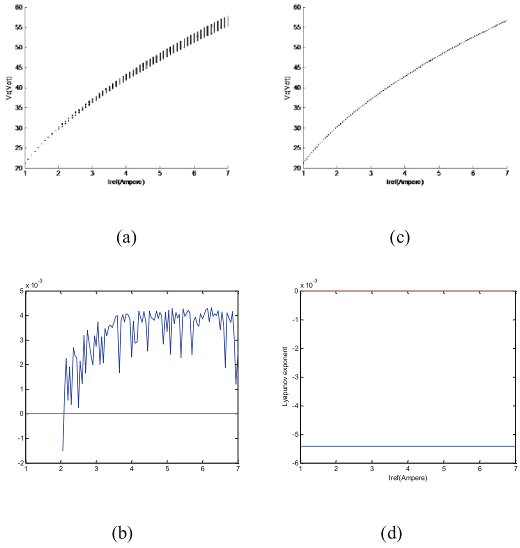

Fig. 3. System response under I_{ref} variation, bifurcation diagram: (a) original behaviour (c) behaviour with backstepping, Lyapunov exponent: (b) original behaviour (d) behaviour with backstepping.

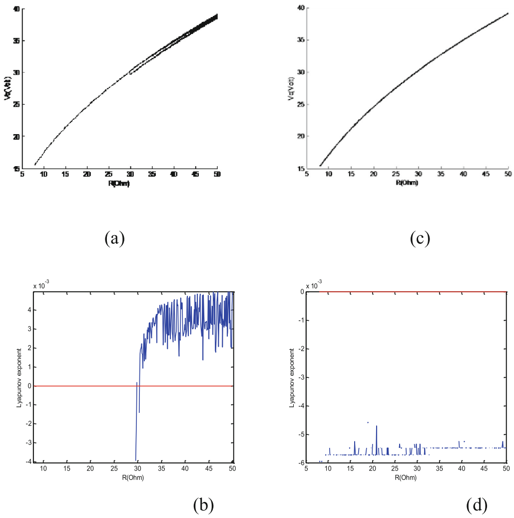

Fig. 4. System response under R variation, bifurcation diagram: (a) original behaviour (c) behaviour with backstepping, Lyapunov exponent: (b) original behaviour (d) behaviour with backstepping.

For the inductance variation, the system has, in its original behaviour, a period doubling bifurcation at the critical value $0.008H$ as shown in the bifurcation diagram of

Fig. 5a. Chaotic behaviour, as shown by the Lyapunov exponent of Fig. 5b, is in the interval [0.036, 0.05]H. In this case also the backstepping controller successes in suppressing abnormal behaviours (bifurcation, chaos) and keeping the system operating in period one behaviour on the whole interval when this is clear in Figs. 5c and d.

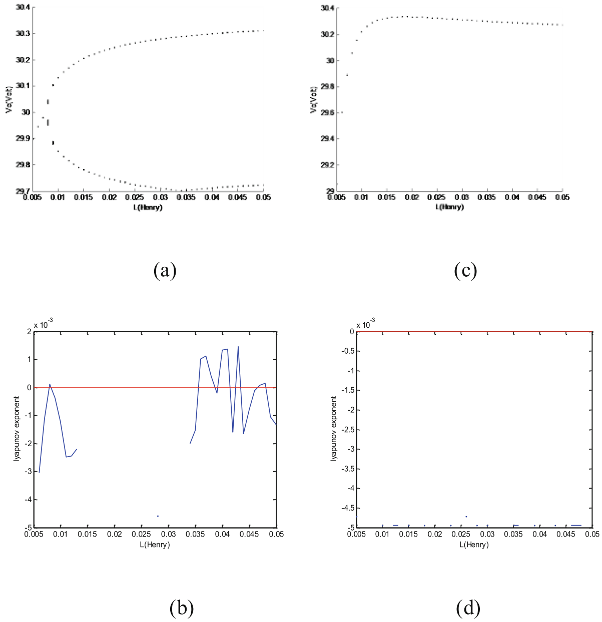

Fig. 5. System response under L variation, bifurcation diagram: (a) original behaviour (c) behaviour with backstepping, Lyapunov exponent: (b) original behaviour (d) behaviour with backstepping.

5 Conclusion

The Boost converter, as dynamical system, exhibits a different complex and undesirable behaviours when its parameters are subject to variation. The use of an appropriate backstepping control law allows us to bypass this drawback and to keep a simple period one behaviour despite the system parameters variation. The simulation results demonstrated the effectiveness of the backstepping controller to eliminate all abnormal behaviours and to ensure a simple behaviour on the whole range of parameters variation.

References

1. Aroudi, A.E., Giaouris, D., Mandal, K., Banerjee, S., Al-Hindawi, M., Abusorrah, A., Al-Turki, Y.: Complex non-linear phenomena and stability analysis of interconnected power converters used in distributed power systems. IET Power Electron. **9**(5), 855–863 (2016)

2. Saublet, L.M., Gavagsaz-Ghoachani, R., Martin, J.P., Nahid-Mobarakeh, B.: Bifurcation analysis and stabilization of DC power systems for electrified transportation systems. IEEE Trans. Transp. Electrification **2**, 86–95 (2016)
3. Banerjee, S., Verghese, G.C.: Nonlinear phenomena in power electronics: attractors, bifurcations, chaos and nonlinear control. Wiley, Hoboken (2001)
4. Fang, C.C., Abed, E.H.: Local bifurcations in PWM DC-DC converters. ISR, 25 January 1999
5. Tse, C.K.: Complex Behavior of Switching Power Converters. CRC Press LLC, Boca Raton (2004)
6. Liao, X., Mu, N.: Hopf bifurcation and chaos in the time-delay Chua's circuit. In: Sixth International Conference on Information Science and Technologie, Dalian, China, 6–8 May 2016
7. Hou, L., Chen, Y., Fu, Y., Li, Z.: Nonlinear response and bifurcation analysis of a Duffing type rotor model under sine maneuver load. Int. J. Non-Linear Mech. **78**, 133–141 (2016)
8. Nikolov, S., Nedev, V.: Bifurcation analysis and dynamic behaviour of an inverted pendulum with bounded control. J. Theor. Appl. Mech. Sofia **46**(1), 17–32 (2016)
9. Zadeh, M.K., Gavagsaz-Ghoachani, R., Pierfederici, S., Nahid-Mobarakeh, B., Molinas, M.: Stability analysis and dynamic performance evaluation of a power electronics-based DC distribution system with active stabilizer. IEEE J. Emerg. Sel. Top. Power Electron. **4**(1), 93–102 (2016)
10. Pikulins, D., Litvinenko, A.: On the effectiveness of application of compensation ramp in switching power converters with delays. In: 26th Conference Radioelektronika, Košice, Slovak Republic, 19–20 April 2016
11. Xie, F., Zhang, B., Qiu, D., Jiang, Y.: Non-linear dynamic behaviours of DC cascaded converters system with multi-load converters. IET Power Electron. **9**(6), 1093–1102 (2016)
12. Cheng, L., Cao, H.: Bifurcation analysis of a discrete-time ratio-dependent predator–prey model with Allee Effect. Commun. Nonlinear Sci. Numer. Simul. **38**, 288–302 (2016)
13. Pandey, V., Singh, S.: A bifurcation analysis of boiling water reactor on large domain of parametric spaces. Commun. Nonlinear Sci. Numer. Simul. **38**, 30–44 (2016)
14. Guesmi, K., Essounbouli, N., Hamzaoui, A.: Systematic design approach of fuzzy PID stabilizer for DC–DC converters. Energy Convers. Manag. **49**, 2880–2889 (2008)
15. Ayati, M., Bakhtiyari, A., Gohari, A.: Chaos control in buck converter using fuzzy delayed-feedback controller. In: 2016 4th International Conference on Control, Instrumentation, and Automation, Qazvin Islamic Azad University, Qazvin, Iran, 27–28 January 2016
16. Biswal, M., Sabyasachi, S.: Bifurcation study in discredited sliding mode controlled DC-DC Buck converter. Int. J. Eng. Res. Technol. **1**(9) (2012). ISSN: 2278-0181
17. Du, W., Zhang, J., Qin, S.: Hopf bifurcation and sliding mode control of chaotic vibrations in a four-dimensional hyperchaotic system. IAENG Int. J. Appl. Math. **46**(2) (2016). IJAM_46_2_15
18. Morcillo, J.D., Burbano, D., Angulo, F.: Adaptive ramp technique for controlling chaos and subharmonic oscillations in DC–DC power converters. IEEE Trans. Power Electron. **31**(7), 5330–5343 (2016)
19. Yfoulis, C., Giaouris, D., Stergiopoulos, F., Ziogou, C., Voutetakis, S., Papadopoulou, S.: Robust constrained stabilization of boost DC–DC converters through bifurcation analysis. Control Eng. Pract. **35**, 67–82 (2015)
20. Tan, W., Gao, J., Fan, W.: Effective control and bifurcation analysis in a chaotic system with distributed delay feedback. Hindawi Publ. Corp. Math. Probl. Eng. **2016**, Article ID 7068479, 14 p. (2016)

21. Deivasundari, P., Geetha, R., Uma, G., Murali, K.: Chaos, bifurcation and intermittent phenomena in DC-DC converters under resonant parametric perturbation. Eur. Phys. J. Spec. Top. **222**, 689–697 (2013)
22. Ding, D., Zhang, X., Cao, J., Wang, N., Liang, D.: Bifurcation control of complex networks model via PD controller. Neurocomputing **175**, 1–9 (2016)
23. Ayati, M., Sharifi, Z.: Analysis and fuzzy control of chaotic behaviors in Buck converter. In: 2016 4th International Conference on Control, Instrumentation, and Automation (ICCIA), Qazvin Islamic Azad University, Qazvin, Iran, 27–28 January 2016
24. Meimei, J.: Suppression of chaos in the Buck converter using a delayed differential feedback with two adjustable parameters. In: Proceedings of the 35th Chinese Control Conference, Chengdu, China, 27–29 July 2016
25. Ben Jemaa-Boujelben, S., Feki, M.: Chaotification of permanent magnet DC motor using discrete nonlinear control. In: 13th International Multi-conference on Systems, Signals and Devices (2016)
26. Göksu, A., Kocamaz, U.E., Uyaroğlu, Y.: Synchronization and control of chaos in supply chain management. Comput. Ind. Eng. **86**, 107–115 (2014)
27. Chen, G., Moiola, J.L., Wang, H.O.: Bifurcation control: theories, methods, and applications. Int. J. Bifurcat. Chaos **10**(3), 511–548 (2000)
28. Varney, P., Green, I.: Nonlinear phenomena, bifurcations, and routes to chaos in an asymmetrically supported rotor–stator contact system. J. Sound Vib. **336**, 207–226 (2015)
29. Krstic, M., Kanellakopoulos, I., Kokotovic, P.V.: Nonlinear and adaptive control design. Willy, New York (1995)
30. El Fadil, H., Giri, F.: Backstepping based control of PWM DC-DC boost power converters. IEEE (2007)
31. Zhonghua, Z.: Chaos control of oscillator circuit based on adaptive backstepping method. In: 2014 26th Chinese Control and Decision Conference (2014)
32. Massaoudi, Y., Damak, T., Ghamgui, M., Mehdi, D.: Comparison between a backstepping mode control and a sliding mode control for a boost DC-DC converter of a photovoltaic panel. In: 2013 10th International Multi-conference on Systems, Signals and Devices (SSD), Hammamet, Tunisia, 18–21 March 2013
33. Roy, T.K., Morshed, M., Tumpa, F.K., Pervej, M.F.: Robust adaptive backstepping speed controller design for a series DC motor. In: 2015 International WIE Conference on Electrical and Computer Engineering (WIECON-ECE), BUET, Dhaka, Bangladesh, 19–20 December 2015
34. Luo, S., Song, Y.: Chaos analysis based adaptive backstepping control of the micro-electro-mechanical resonators with constrained output and uncertain time delay. IEEE Trans. Ind. Electron. **63**, 6217–6225 (2016)
35. Banerjee, S., Chakrabarty, K.: Nonlinear modeling and bifurcations in the boost converter. IEEE Trans. Power Electron. **13**, 252–260 (1998)

Phase-Plane Methods to Analyse Power System Transient Stability

Walid Rahmouni(✉) and Lahouaria Benasla

Faculty of Electrical Engineering, Department of Electrical Engineering, University of Sciences and Technology of Oran Mohammed Boudiaf, USTO, Oran, Algeria
walid.rahmouni@univ-usto.dz, jbenasla@yahoo.fr

Abstract. Phase plane analysis is one of the most important techniques for studying the behavior of dynamic systems, especially in the nonlinear case. Recent research shows that transient stability problem of a power system following a large disturbance such as a fault can be solved with greater efficiency based on phase plane analysis.

In this paper, we will consider the phase plane-analytical method and phase plane-delta method to analyze the transient stability of IEEE 5 bus system with two generators and a three phase fault created at a bus. The classical model representation of power system is used here. To simplify the analysis, all nodes other than the generator internal nodes are eliminated using Kron reduction formula.

Keywords: Transient stability · Kron's reduction · Phase plane Analytical method · Delta méthod · Critical clearing time

1 Introduction

Power system stability has been recognized as an important problem for secure system operation since the 1920s [1]. Transient stability is concerned with the ability of the power system to maintain synchronism when subjected to severe disturbances. These disturbances can be faults such as a short circuit on a transmission line, loss of a generator, loss of a load, gain of load or loss of a portion of transmission network [2].

The study of the stability of power systems under transient conditions is a tedious task because the differential equations describing even the simplest system are nonlinear. Studies of large systems include numerous involved calculations.

This stability can be assessed using several approaches. In this paper phase plane method is used.

Phase plane analysis is one of the most important techniques for studying the behavior of nonlinear systems, since there is usually no analytical solution for a nonlinear system [3, 4]. It is a graphical method for studying the first-order and second-order linear or nonlinear systems, which is firstly introduced by Poincare. H in 1885 [3].

The coordinate plane whose axes correspond to dependent variable $x(t)$ and its first derivative $x'(t)$ is called phase plane. In phase plane plot $x(t)$ and $x'(t)$ are plotted in a

M. Chadli et al. (Eds.): ICEECA 2017, LNEE 522, pp. 14–29, 2019.
https://doi.org/10.1007/978-3-319-97816-1_2

two axes plane. The trace of the phase plane plot as time increases is called trajectory [5].

There are many methods for constructing this trajectory, such as the so called method of Isocllines, Lienard's method, Pell's method, the delta method and analytical method. There are two techniques for generating phase plane portraits analytically [6].

In this paper, the delta method and analytical method for power system transient stability analysis have been reviewed and compared. The proposed methods have been applied to IEEE 5 Bus system with two generators and a three phase fault created at a bus. The system has been simulated with a classical model for the generators and Kron reduction is used to remove all non-generator buses. The results obtained clearly illustrate the effectiveness of the proposed methods.

2 Mathematical Modeling of Power System Transient Stability Analysis

The most elementary representation of the synchronous machine, known as classical model, is considered valid for the transient period in the order of one second or less [7].

This model represents the machine as a constant voltage source behind the transient reactance in the direct axis x'_d [8, 9]. It only includes the swing Eq. (2) of the generator and the active power that is supplied by the generator. For an n-bus system including ng-generators, by the application of the Kron reduction, the system can be reduced to ng internal nodes of each classical machine [10]. All other nodes are eliminated as the result of the Kron reduction. If node k has zero current injection, then we can obtain the reduced admittance matrix $\left[\vec{Y}_{ij\,red}\right]$ by eliminating node k by using the formula:

$$\begin{gathered}\left[\vec{Y}_{ij\,red}\right] = \left[\vec{Y}_{ij}\right] - \left[\vec{Y}_{ik}\right]\left[\vec{Y}_{kk}\right]^{-1}\left[\vec{Y}_{kj}\right] \\ i,j = 1,2,\ldots,ni,j \neq k\end{gathered} \tag{1}$$

The reduced system can be represented as follows:

$$\frac{2H_i}{\omega_s}\frac{d^2\delta_i}{dt^2} = p_{mi} - p_{ei}(\delta_i) \quad i = 1,2,3\ldots,ng \tag{2}$$

$$P_{ei}(t) = \sum\nolimits_{j=1}^{ng} \left|\overrightarrow{E_i}\right|\left|\overrightarrow{E_j}\right|\left|\vec{Y}_{ij\,red}\right| cos\left(\delta_i(t) - \delta_j(t) - \theta_{ij}\right) \tag{3}$$

$$P_{mi} = \sum\nolimits_{j=1}^{ng} \left|\overrightarrow{E_i}\right|\left|\overrightarrow{E_j}\right|\left|\vec{Y}_{ij\,red}\right| cos\left(\delta_{i0} - \delta_{j0} - \theta_{ij}\right) = P_{ei0} \tag{4}$$

p_{mi}: Mechanical power input generator, in pu.
p_{ei}: Electrical power input generator, in pu.
H_i: Inertia constant, in MW.s/MVA.
δ: Rotor angle, in elec. Rad.
t: Time, in s.
$\vec{E}$: Generator internal voltage.

θ_{ij}: Phase angle of the reduced admittance matrix elements.

$\left|\vec{Y}_{ij\,red}\right|$: Modulus of the elements of the reduced bus admittance matrix.

The elements $\vec{Y}_{ij\,red}$ have different values depending upon the fault occurrence and the effect of the resulting circuit breaker operation. In most cases, there are three minimum states of the network: pre-fault state, in-fault and post-fault [11]. In this paper, those three states are denoted by subscripts 1, 2, and 3, respectively.

If ng = 2, the swing equation equivalent to that of a single machine in terms of the relative power angle between the two interconnected synchronous machines $\delta = \delta_1 - \delta_2$, can be written as [9, 12]:

$$\frac{2H}{\omega_s}\frac{d^2\delta}{dt^2} = p_M - p_E(\delta) \tag{5}$$

Where

$$\begin{cases} H = H_1 H_2 \\ p_M = H_2 p_{m1} - H_1 p_{m2} \\ p_E(\delta) = H_2 p_{e1}(\delta_1) - H_1 p_{e2}(\delta_2) \end{cases} \tag{6}$$

Equation (5) is a second order differential equation, which can be written as two first order differential equations as follows:

$$\begin{cases} \frac{2H}{\omega_s}\frac{d\Delta\omega}{dt} = p_M - p_{E(\delta)} \\ \frac{d\delta}{dt} = \omega - \omega_s = \Delta\omega \end{cases} \tag{7}$$

Where $\omega = \omega_1 - \omega_2$.

Here the initial conditions are obtained by a result of a standard load flow [13, 14]. After all the needed values are obtained, we are now ready to solve the transient stability problem. In this paper, this problem is solved by application of the phase-plane methods.

3 Phase Plane Methods

The Phase Plan method is a graphical method for linear and non linear second-order differential equation [15]. It consists of the geometrical picture formed by the solution curves of the system [16].

The coordinates of the plane are $x(t)$ and its first derivative $x'(t)$ which are called the phase variables of the system [17] and the parametric curves traced by the solutions are called trajectories [18].

From a set of different initial conditions, we can plot the trajectories in the phase plane to obtain the phase portrait [17].

There are many techniques for obtaining the phase portrait, the trajectories can be obtained analytically, graphically or experimentally [15].

In this paper, we will focus on the analytical method and the Delta method.

3.1 Analytical Methods

The free motion of any second-order non-linear system can be described by an equation of the form

$$f = \left(\frac{d^2x(t)}{dt^2}, \frac{dx(t)}{dt}, x(t), t\right) \tag{8}$$

This equation can be reduced to a set of two first order differential equations

$$\begin{cases} \frac{dx_1(t)}{dt^2} = f_1(x_1(t); x_2(t)) \\ \frac{dx_2(t)}{dt} = f_2(x_1(t); x_2(t)) \end{cases} \tag{9}$$

There are two techniques for generating phase plane portraits analytically [6].

First Technique
The first technique consists on integrating the equations expressed by (9) analytically or numerically and finding two solutions g_1 and g_2 as a function of the time.

$$\mathrm{x_1(t) = g_1(t)\ and\ x_2(t) = g_2(t)} \tag{10}$$

By eliminating the time, it is possible to establish an implicit representation of the phase portrait in the form:

$$\mathrm{g(x_1(t), x_2(t), c) = 0} \tag{11}$$

Where the constant c depends on the initial conditions.

Second Technique
The second technique consists on eliminating the time variable from the two equations of the system (9) by dividing the equations,

$$\frac{dx_2(t)}{dx_1(t)} = \frac{f_2(x_1(t); x_2(t))}{f_1(x_1(t); x_2(t))} \tag{12}$$

Then, by integration we can establish a relationship between $x_1(t)$ and $x_2(t)$.

3.2 Delta Method

The phase plan delta method is a step by step graphic-numeric technique used for the evaluation of transient response of second order non-linear systems on the usual phase plane [19].

A major class of second-order non-linear systems can be described by the differential equations of the form

$$\ddot{x} + f(x, \dot{x}, t) = 0 \tag{13}$$

Where $\dot{x} = \frac{dx}{dt}$ and $\ddot{x} = \frac{d^2x}{dt^2}$.

The first step consists of rewriting (13) in the standard delta form,

$$\ddot{x} + p^2(\Delta + x) = 0 \tag{14}$$

This is accomplished by adding and subtracting p^2x from (13).

$$\ddot{x} + \left[f(x, \dot{x}, t) - p^2x\right] + p^2x = 0 \tag{15}$$

Then

$$\Delta = \frac{1}{p^2}\left[f(x, \dot{x}, t) - p^2x\right] \tag{16}$$

In this paper x, ẋ and t will represent displacement, velocity and time.
The phase plane coordinates are defined as

$$x = x \, \text{and} \, v = \frac{\dot{x}}{p} \tag{17}$$

Then the following relationships can be developed:

$$\ddot{x} = p\frac{dv}{dt} = p\left(\frac{dv}{dx}\right)\frac{dx}{dt} = p^2v\frac{dv}{dx} \tag{18}$$

By substituting (18) into (14), this second order equation becomes a first order differential equation in x, v and Δ

$$v\frac{dv}{dx} + x + \Delta = 0 \tag{19}$$

This leads to the following relationship:

$$\frac{dx}{dv} = -\frac{v}{x + \Delta} \tag{20}$$

Considering Δ constant over a finite time interval Δt, (18) can be integrated; the result being

$$(x+\Delta)^2 + v^2 = R^2 \tag{21}$$

This is the equation for a circle centered at x = −Δ, v = 0 with radius R.

An expression for time can be obtained from (18) [20]

$$dt = \frac{dx}{pv} \tag{22}$$

A graphical interpretation is given in Fig. 1. At any step for a given initial position P_0, the value of Δ is calculated from the known values of x_0 and v_0, it locates the centre C of the trajectory curve approximated as a circular arc at $-\Delta$.

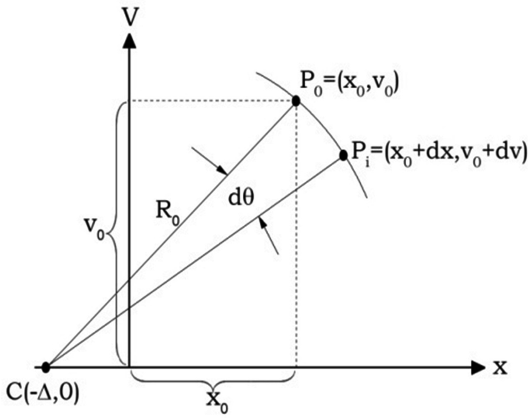

Fig. 1. Construction of the phase portrait using the delta method.

By drawing the circular arc of angle $\Delta\theta$ we obtain the next point P_i on the trajectory, we can again calculate the value of delta and after locating the new centre C draw another circular arc [17, 21].

The angular arc delta theta is proportional to time as shown bellow [20].

$$dt = \frac{1}{p} d\theta \tag{23}$$

The solution at P_i is given by

$$x_i = x_0 + v_0 d\theta \tag{24}$$

$$v_i = v_0 - (x_0 + \Delta) d\theta \tag{25}$$

3.3 Interpretation of Phase Plane

To simplify the interpretation of the phase plane, we considered the second order differential Eq. (5) governing the generator rotor dynamics.

Critical points correspond to solutions of a coupled system given by (7) where the solutions are $\frac{d\Delta\omega}{dt} = 0$ and $\frac{d\delta}{dt} = 0$, simultaneously.

Hence, we obtain

$P_1 = (\delta_0, \Delta\omega_0)$ and $P_2 = (\delta_{max}, \Delta\omega_0)$

The (δ, $\Delta\omega$)-plane with some trajectories is in Fig. 2.

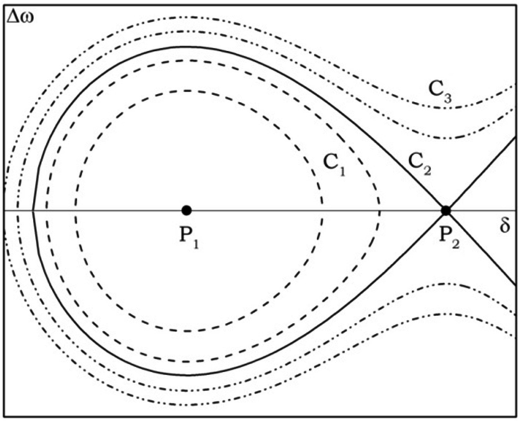

Fig. 2. (δ, $\Delta\omega$)-plane

From the phase portrait it should be clear that even this simple system has fairly complicated behavior. The point P_1 corresponds to a stable center. On the other hand, P_2 is a saddle point, which is an unstable point. Let us concentrate on those points in the phase diagram above where the trajectories seem to start, end, or go around. The trajectories keep oscillating around the origin P_1, and they seem to either go in or out of the point P_2. Those trajectories corresponding to different initial conditions.

If a perturbation is introduced, producing a deviation of the angle δ from its equilibrium point and therefore, a change in the initial values required to solve the swing equation, we may find different trajectories:

In C1, the angle value has been increased in relation to its equilibrium value. As it can be observed, the generator rotor stays indefinitely oscillating round its equilibrium position. It is the stable state.

In C2, the angle has been increased near the point P_2 and the solution corresponds to a homoclinic trajectory. The trajectory corresponding to the critically stable case.

The trajectories C3 shows an oscillation tendency round the equilibrium point P_1 at the beginning. But, nearby the point P_2, the angle and speed start growing indefinitely. Those trajectories corresponding to the unstable case.

4 Applications

To assess the effectiveness of the proposed methods, simulation studies are performed on the IEEE 5 bus system, the data for which is borrowed from [13, 22], and given in Fig. 3. This system has two generators, seven transmission lines and four loads. The loads are modeled as constant impedances and the generators are represented by the classical model.

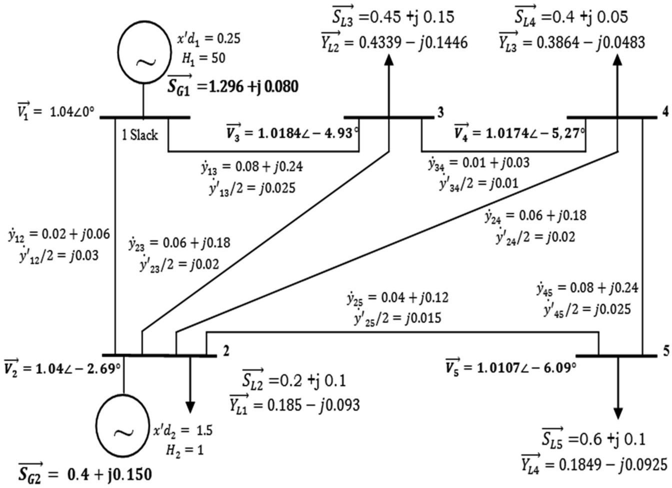

Fig. 3. Single line diagram of the IEEE 5 bus system.

In the performance of a transient stability study, a load-flow study of the pretransient network is needed to determine the mechanical powers p_{mi} of the generators and to calculate the values of $|\overrightarrow{E_i}|$ and δ_{i0} for all the generators.

Gauss-Seidel method is used here for the load flow study of the system. The convergence is achieved in 15 iterations, satisfying a prespecified tolerance of 10-6 for all variables. Prefault bus voltage $\overrightarrow{V_i}$ and powers $\overrightarrow{S_{Gi}}$ obtained from the results of load flow analysis are shown in bold text in Fig. 3.

The equivalent impedances of the loads $\overrightarrow{Y_{Li}}$ are obtained from the load bus data. They are given in p.u in the same figure.

As a disturbance scenario, a three phase fault was applied on bus 4 at 0.1 s and the clearing time of the fault was varied. The fault is cleared without opening the breaker. In this case, the post-fault system is identical to the pre-fault system from.

The reduced admittance matrices $\left[\overrightarrow{Y}_{ij\,red}\right]$ are shown in Table 1 for the prefault network, the faulted network, and the network with the fault cleared respectively.

The Single-line diagram of two machines power system obtained by eliminating load nodes is shown in Fig. 4. This diagram gives the results of the generators internal voltages $|\overrightarrow{E_1}|$ and $|\overrightarrow{E_2}|$ and their initial angles δ_{10} and δ_{20}.

Table 1. Reduced admittance matrices

State	i	j	
		1	2
Pre-fault/post-fault	1	0.893 − j0.957	0.163 + j0.467
	2	0.163 + j0.467	0.037 − j0.574
Faulted	1	0.269 − j2.892	0.026 + j0.103
	2	0.026 + j0.103	0.007 − j0.643

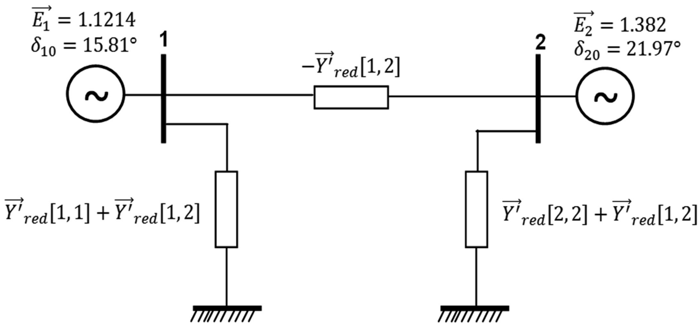

Fig. 4. Single-line diagram of IEEE 5-bus system reduced to generator nodes.

The power system's differential equations before, during and after the fault clearance are given below

Pre-fault:

Before the occurrence of the fault, the system is given by:

$$\begin{cases} \frac{d\Delta\omega}{dt} = \frac{377}{100}(18.70-(2.42 + 12.39cos(\delta) + 37sin(\delta))) \\ \frac{d\delta}{dt} = \omega - 377 \end{cases}$$

The equivalent machine is operating at the initial relative power angle

$$(\delta_0, \Delta\omega_0) = (0.107\,\text{rad}, 0)$$

During fault:

The accelerating power equations are

$$\begin{cases} \frac{d\Delta\omega}{dt} = \frac{377}{100}(18.70-(0.37 + 1.96cos(\delta) + 8.16sin(\delta))) \\ \frac{d\delta}{dt} = \omega - 377 \end{cases}$$

Post-fault:

Since the structure of the network does not change, the power system's differential equations after the fault clearance are same as those before.

The methods described in paragraph III are used for constructing pre-fault, during fault and post-fault system trajectories.

Analytical Method. The two techniques previously described for generating phase plane portraits analytically are used here. Both technique lead to a functional relation between the two phase variables δ and ω.

First Technique

The first technique consists on solving the differential equations numerically and finding two solutions δ(t) and ω(t). The Runge-Kutta fourth-order method with an integration step size of 0.001 s is applied to obtain approximate solutions of those equations. The numerical integration is made for 2.0 s of simulated real time.

Relative rotor angle δ and speed ω responses for different fault clearing time are shown respectively Figs. 5 and 6.

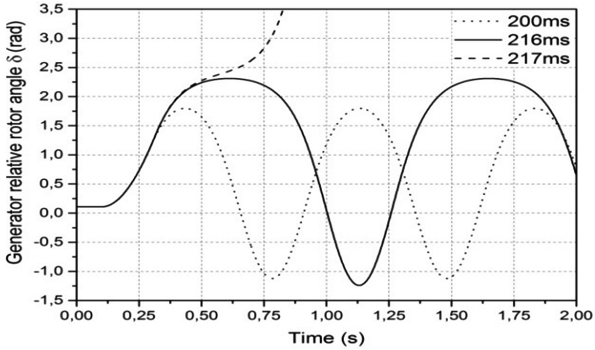

Fig. 5. Generator relative rotor angle response.

By eliminating the time, we establish an implicit representation of the phase portrait. The trajectories are given in Fig. 7.

Second Technique

The second technique involves directly eliminating the time variable by evaluating $\frac{d\Delta\omega}{d\delta}$. We will find the trajectories corresponding to the pre-fault, fault and post-fault intervals.

Pre-fault:

The equilibrium point at pre-fault is given by

$$(\delta_0, \Delta\omega_0) = (0.107\,\text{rad}, 0)$$

The trajectory during pre-fault is the point $(\delta_0, 0)$

During fault:

The motion during the fault starts at $(\delta_{01}, 0)$. The model during the fault is represented by the following equation

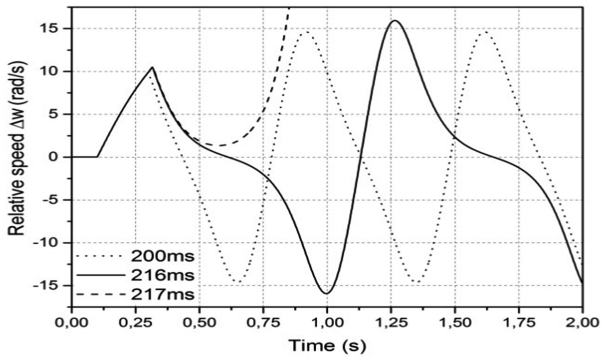

Fig. 6. Generator relative speed response

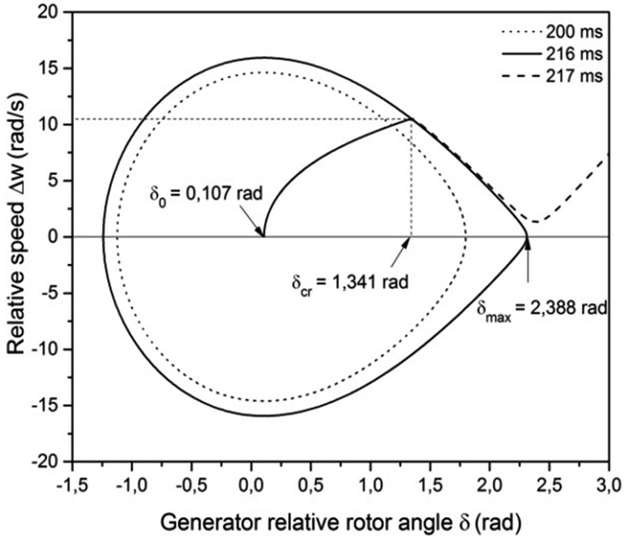

Fig. 7. Phase portrait using the first technique

$$\frac{d\Delta\omega}{d\delta} = \frac{\frac{377}{100}(18.70 - (0.37 + 1.96\,cos\,(\delta) + 8.16\,sin\,(\delta)))}{\omega - 377}$$

By integrating the above equation from δ_0 to δ and from 0 to $\Delta\omega$, we obtain

$$\Delta\omega = +\sqrt{(-74.49 + 138.23\,\delta - 14.79 sin(\delta) + 61.59\,cos(\delta))}$$

The positive radical was taken because we know that the system is accelerating during the fault.

Post-fault:
The equilibrium point is given by

$$(\delta_0, \Delta\omega_0) = (0.107\,\text{rad}, 0\,\text{rad/s})$$

The saddle point is given by

$$(\delta_{max}, \Delta\omega) = (2.388\,\text{rad}, 0\,\text{rad/s})$$

The model after the fault clearance is represented by the following equation

$$\frac{d\Delta\omega}{d\delta} = \frac{\frac{377}{100}(18.70 - (2.42 + 12.39cos(\delta) + 37sin(\delta)))}{\omega - 377}$$

By integrating the above equation from δ to δ_{max} and from $\Delta\omega$ to 0, we obtain

$$\Delta\omega = \pm\sqrt{(-25.85 + 122.79\delta - 93.44sin(\delta) + 278.97cos(\delta))}$$

This equation gives the trajectory after the disturbance.

Figure 8 shows the phase portrait obtained for different fault clearing time using the second technique.

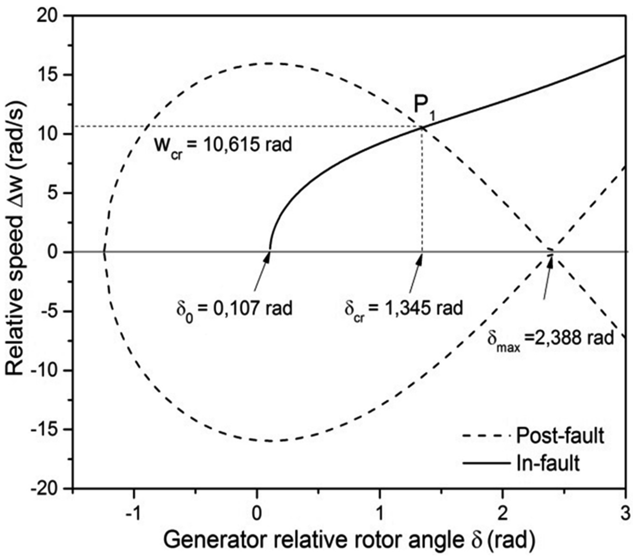

Fig. 8. Phase portrait using the second technique

Delta Method

Delta method with an integration step size of 10^{-4} is applied to obtain approximate solutions of those equations. The numerical integration is made for 2.0 s of simulated real time.

The delta functions of the system according to (14) are:

Pre-fault:

$$\Delta_1(\delta, \Delta\omega, t) = -\left(\pi\frac{60}{50}\right)(18.70 - (2.42 + 12.39\ cos(\delta) + 37\ sin(\delta) - \delta))$$

In-fault:

$$\Delta_2(\delta, \Delta\omega, t) = -\left(\pi\frac{60}{50}\right)(18.70 - (0.37 + 1.96\ cos(\delta) + 8.17\ sin(\delta) - \delta))$$

Post-fault:

$$\Delta_3(\delta, \Delta\omega, t) = \Delta_1(\delta, \Delta\omega, t)$$

Thus the center of the first circular arc is located at point $(-\delta_0, \Delta\omega_0) = (-0.107\,\text{rad}, 0)$ and the radius is $R_0 = 4.66\ 10^{-6}$.

The trajectories obtained for different fault clearing time are shown in Fig. 9.

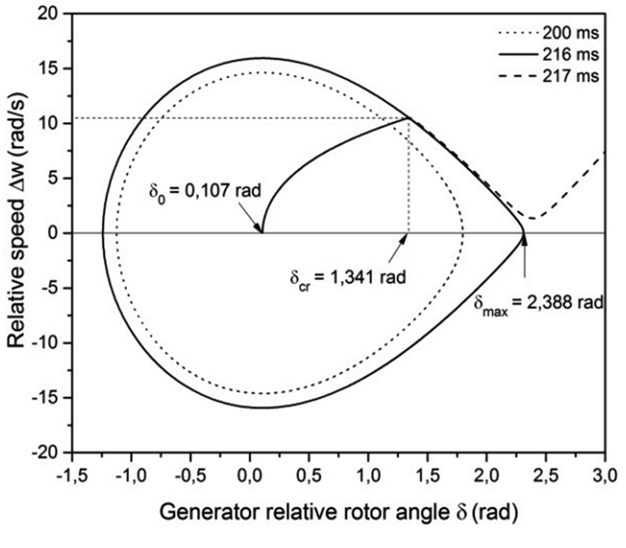

Fig. 9. Phase portrait using Delta method

Figures 5, 6, 7 and 9 show the system response for fault-clearing times 200 ms, 216 ms and 217 ms. For the fault clearing time 200 ms, which is less than the critical clearing time 216 ms, the rotor angle of the generator will remain stable after the fault is cleared. The trajectory is spiral curve converging towards the origin. For the fault clearing time 217 ms, which is greater than the critical clearing time 216 ms, the rotor angle of the generator becomes unstable after the fault is cleared. The trajectory is spiral curve diverging from the origin.

The critical clearing time 216 ms was obtained by progressively increasing the fault time interval until the system loses its stability.

In Fig. 8, the intersection between the trajectories during and after the fault gives the critical clearing angle. The coordinates of the intersection point P_1 are $(\delta_{cr}, \Delta\omega_{cr}) = (1.345\,\text{rad}, 10.615\,\text{rad/s})$.

The critical clearing time obtained by step-by-step method [23] is 0.216 s.

5 Conclusion

This paper presents the transient stability analysis of the IEEE 5-bus 2-machines test system using the analytical method and the Delta method for constructing the phase plane trajectories. Those trajectories allow the visualization in the same graphic of the angle variations and the rotor speed.

The performance and accuracy of the two methods considered are assessed by comparing their results in terms of critical clearing time and angle. It can be found that those results are similar.

The first technique to draw the phase trajectories analytically is very reliable and has been widely used but it requires a trial-and-error scheme for determining the critical clearing time and can be expensive in terms of computational time.

The second technique determines transient stability without solving the differential equations explicitly. This method allows the direct determination of the critical clearing angle avoiding thus the trial and error method, but it does not give the critical clearing time directly which requires the resort to the step-by-step method, nor does it apply to a system of three or more machines which may swing independently.

The delta method is extremely simple to apply. It combines the strength of the conventional numerical-integration methods and the simplicity of graphical methods. However, it is limited to construction of phase trajectories for second-order differential equations only. This method can lead to numerical instability of the solution due to accumulation of errors; therefore, it requires an extremely small interval of time to minimize the cumulative error.

Since there are a many methods for constructing phase plane trajectories, furthermore, future comparison studies with them are necessary so as to identify strengths and weaknesses of analytical method and Delta method.

References

1. IEEE/CIGRE Joint Task Force on Stability Terms and Definitions: Definition and classification of power system stability. IEEE Trans. Power Syst. **19**(3), 1387–1401 (2004)
2. Agber, J.U., Odaba, P.E., Onah, C.O.: Effect of power system parameters on transient stability studies. Am. J. Eng. Res. (AJER) **4**(2), 87–94 (2015)

3. Obeng, C.: Deterministic Sirb cholera model with logistic approach in Dormaa-Ahenkro, Ghana. Master thesis of Science, Department of Mathematics, Kwame Nkrumah University of Science and Technology, October 2015
4. Vathsal, S.: Advanced Control Systems. Lecture Notes, Institute of Aeronautical Engineering Dundigal, Hyderabad, India (2016–2017)
5. Bakshi, U.A., Bakshi, M.V.: Modern Control Theory, 1st edn. Technical Publications, Pune (2013)
6. Nguyen, T.T.: Phase Plane Analysis (2002). http://www4.hcmut.edu.vn/~nttien/Lectures/Applied%20nonlinear%20control/C.2%20Phase%20Plane%20Analysis.pdf. Accessed 11 May 2017
7. Elahi, H.: Transient stability of power systems with non-linear load models using individual machine energy functions. Doctoral thesis, Iowa State Unviersity (1983)
8. Kalyani, S., Prakash, M., Ezhilarasi, G.: Transient stability studies in SMIB system with detailed machine models. In: International Conference on Recent Advancements in Electrical, Electronics and Control Engineering, IConRAEeCE11, Mepco Schlenk Engineering College, Sivakasi, India (2011)
9. Saadat, H.: Power System Analysis, 1st edn. WCB/McGraw-Hill, New York (1999)
10. Evrenosoglu, Y.C., Dag, H.: Detailed model for power system transient stability analysis. In: International Conference on Electrical and Electronics Engineering, ELECO 2001, Bursa, Turkey (2001)
11. Phadke, A.: Handbook of Electrical Engineering Calculations, 1st edn. Marcel Dekker, New York (1999)
12. Van Cutsem, T.: Dynamique des réseaux de transport de l'énergie électrique. Lecutre Notes ELEC 029-0, Université de Liège. http://www.montefiore.ulg.ac.be/~vct/courses.html. Accessed 29 Apr 2016
13. Stagg, G., El-abiad, A.: Computer Methods in Power System Analysis, 1st edn. McGraw-Hill Book Co., New York (1968)
14. Kethavath, P.: Transient Stability Analysis for Power System Networks with Asynchronous Generation. Doctoral thesis, University of Auckland, New Zealand (2015)
15. Yun-Lan, H.: Phase-plane methods. Master of Science in electrical engineering, U.S. Naval Postgraduate School, Monterey, California (1969)
16. Reyn, J.: Phase Portraits of Planar Quadratic Systems, 1st edn. Springer, New York (2007)
17. Sinha, N.: Control Systems, 1st edn. Wiley, New York (1995)
18. Tseng, Z.S.: The Phase Plane (2008). https://sites.psu.edu/s17m250s4n5/files/2017/02/17.Systems.-Stability-and-phase-portraits-2a1wu3c.pdf. Accessed 11 May 2017
19. Prusty, S.: Analysis of power system transient stability problems via computer simulated delta technique. IEE-IERE Proce. India **15**(1), 7 (1977)
20. Simpson, J.: Use of the digital computer with the phase-plane delta method. Master of Science, Oklahoma State University Stillwater, Oklahoma (1963)

21. Rao, J., Gupta, K.: Introductory Course on Theory and Practice of Mechanical Vibrations, 1st edn. Wiley, New York (1985)
22. Arshdeep, K.K., Brar, Y.: FACTS based power system optimization by using newton Raphson technique. Int. J. Emerg. Res. Manag. Technol. **5**(1), 1–7 (2016)
23. Sharma, C.S.: Stability analysis of single machine infinite bus system by numerical methods. Int. J. Electr. Electron. Res. **2**(3), 158–166 (2014)

H_∞ Fuzzy Control for Electrical Power Steering Subject to Actuator Saturation

Mohamed Nasri[1(✉)], Dounia Saifia[1], Mohammed Chadli[2], and Salim Labiod[1]

[1] LAJ, Faculty of Science and Technology, University of Jijel, BP. 98, Ouled Aissa, 18000 Jijel, Algeria
nasrimoh@ymail.com, saifia.dounia@gmail.com, labiod_salim@yahoo.fr

[2] University of Picardie Jules Verne, MIS (EA 4290), 33, rue saint-Leu, 80039 Amiens, France
mchadli@u-picadrie.fr

Abstract. This paper presents a design of H_∞ fuzzy controller for electric power steering (EPS) with actuator saturation. By considering the friction nonlinearity in the steering column, motor column and in the rack, as internal disturbances and using the sector nonlinearity method, a new T-S model is proposed to represent exactly the nonlinear dynamics of an EPS system. To provide a stable driving, an H_∞ nonlinear state feedback is designed to control an EPS system in the presence of actuator saturation and internal disturbances. The robust stabilization results of the closed-loop EPS system are formulated and solved as a linear matrix inequality (LMI) optimization problem. Simulation results validate the effectiveness of the proposed study.

Keywords: Takagi-Sugeno model · Electrical Power Steering (EPS) H_∞ control · Polytopic representation · Saturated control

1 Introduction

The Electrical Power Steering is a system recently used by the automotive industry, it has a very important role in facilitating the maneuvers for the driver, especially in cities where speed is limited, and driving needs a lot of movement. Unlike traditional hydraulic power steering, which uses a hydro system to reduce the physical effort applied by the driver to change the direction, in the EPS system the hydro system is replaced by a brushless DC motor [1].

To improve the performance of an EPS system, many research results have been reported. In the conventional linear control, controllers design is based on a linear model, which does not take into consideration, friction in the steering column, in motor column, and in the rack, such as the LQR control law with Kalman filtering [2], and a force feedback controller with reference model [3]. In order to take into account the nonlinearity of the EPS system, a fuzzy adaptive sliding mode control [4] and a reference model control [5] are applied to an EPS system. In [6] and [7], authors have been reported interesting results of fuzzy control for EPS systems. However, in these

M. Chadli et al. (Eds.): ICEECA 2017, LNEE 522, pp. 30–44, 2019.
https://doi.org/10.1007/978-3-319-97816-1_3

works, reduced T-S model for EPS is used, by considering the movement directions of the steering column, assistant motor and steering rack change in the same way. So this assumption is not generalized for all real EPS systems. In this work, a new nonlinear T-S model of an EPS is given by considering the friction nonlinearities as internal disturbances regardless of the direction of rotation.

In order to be able to eliminate these disturbances, and to guarantee the stability of the system in the presence of saturation, an H_∞ control is proposed. Indeed, The H_∞ approach is used to analyze and to synthesize controllers/observers achieving an optimal level of disturbance attenuation (for example see [8, 9] references therein).

Generally, a brushless DC motor is used at the EPS system, and the current input of this motor is limited. This constraint may degrade the performance of the closed-loop control, and may lead the system to instability [10]. Very few works, especially in EPS control with actuators saturation have reported, see [7], a fuzzy control model considering actuator saturation is designed for EPS system. However, in this work, the results carried out by considering the reduced T-S model. Motivated by this observation, in this paper, H_∞ fuzzy controller for electric power steering (EPS) is investigated.

This paper is organized as follows. Section 2 gives the nonlinear dynamic model of the EPS system. Section 3 gives the TS representation of the EPS system. Section 4 gives the H_∞ stabilization conditions in LMI terms. In Sect. 5, simulation results are provided to show the effectiveness of the proposed method.

2 EPS Dynamic Model

The EPS dynamic system is split into two subsystems; the mechanical subsystem and the vehicle dynamic subsystem.

2.1 Vehicle Dynamic Model

In order to study the dynamic behavior and the lateral stability of the vehicle, the bicycle model of the rigid vehicle is used. This model serves to determine the force f_r generated by the road reaction, see [11].

The bicycle model shown in Fig. 1, is considered with the following assumptions: Longitudinal velocity V is constant, approximation of small angles; the lateral wheel force is proportional to the wheel slip angle [12]. Gives the following lateral vehicle dynamics:

$$\begin{cases} \dot{\varphi}(t) = \frac{1}{MV}\left[-\left(C_f + C_r\right)\varphi(t) - \left(MV - \frac{1}{V}\left(a_f C_f - a_r C_r\right)\gamma(t) + C_f \delta_f\right)\right] \\ \dot{\gamma}(t) = \frac{1}{I_z}\left[-\left(a_f C_f - a_r C_r\right)\varphi(t) - \frac{1}{V}\left(a_f^2 C_f + a_r^2 C_r\right)\gamma(t) + a_f C_f \delta_f\right] \end{cases} \tag{1}$$

where φ is the side slip angle, γ is the yaw rate, C_f is front cornering stiffness, C_r is rear cornering stiffness, a_f is the front chassis length, a_r is the rear chassis length, M is the vehicle mass, and I_z is the inertial moment of the vehicle.

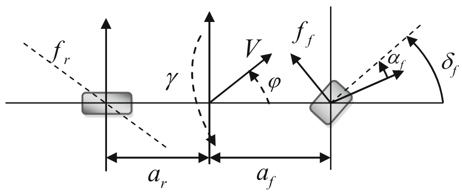

Fig. 1. Vehicle bicycle model

The rack force is given by:

$$f_r(t) = \frac{T_p C_f \left[\delta_f - \left(\varphi(t) + \left(a_f/V\right)\gamma(t)\right)\right]}{r_p} \tag{2}$$

where T_p is the caster trail, and δ_f is the front steering angle, that is given by:

$$\delta_f = \frac{\theta_c}{G_{sc}}$$

where G_{sc} is the ratio of steering system.

Table 1. Parameter values for vehicle bicycle model

Symbols	Values
C_f	126000 N/rad
C_r	126000 N/rad
I_z	4240 kg m^2
T_p	0.033 m
V	20 m/s
a_f	1 m
a_r	1.8 m
M	1814 kg

2.2 Mechanical Steering Model

The mathematical modeling of an EPS system is an unavoidable phase to study and control it. The EPS have three parts: the mechanical part consists of steering wheel, steering column, and the rack. The electric part: consisting of a brushless DC motor. And the electronic part: constitute an electronic control unit with the sensors of different variables to be measured [13], as shown in Fig. 2.

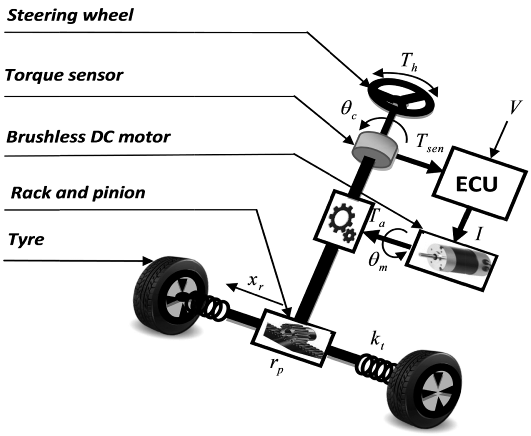

Fig. 2. Electrical Power Steering system

By appealing the Newton laws we have:
The steering column dynamics:

$$J_c \frac{d^2\theta_c}{dt^2} + B_c \frac{d\theta_c}{dt} + Fcsign(\frac{d\theta_c}{dt}) = T_h - T_{sen} \tag{3}$$

The steering rack dynamics:

$$M_r \frac{d^2x_r}{dt^2} = \frac{T_{sen} + GT_a}{r_p} - B_r \frac{dx_r}{dt} - k_r x_r - f_r(t) - F_r sign\left(\frac{dx_r}{dt}\right) \tag{4}$$

The DC motor dynamics:

$$J_m \frac{d^2\theta_m}{dt^2} + B_m \frac{d\theta_m}{dt} + F_m \mathrm{sign}(\frac{d\theta_m}{dt}) = T_m - T_a \tag{5}$$

where J_c is the steering column moment of inertia, B_c is the steering viscous damping, F_c is the steering column friction, J_m is the motor moment of inertia, B_m is the motor damping, F_m is the motor friction, M_r is the assembly mass of the wheel and the rack, G is the motor gear ratio, r_p is the pinion radius, B_r is the damping of the rack, k_r is the tire spring rate, F_r is the rack motor friction and the T_{sen} is steering torque measured by the sensor and is given by:

$$T_{sen} = k_s\left(\theta_c - \frac{x_r}{r_p}\right) \tag{6}$$

where k_s is the steering column stiffness, and the motor torque is given by

$$T_m = k_a I \tag{7}$$

k_a is the torque constant for the motor. The servo force is given by

$$T_a = k_m(\theta_m - G\theta_c) \tag{8}$$

where k_m is the motor torsional stiffness.

Therefore, the nonlinear EPS system can be written as follows:

$$\dot{x}(t) = Ax(t) + B_c u(t) + B_{T_h} T_h(t) + B_w w(t) \tag{9}$$

with

$$A = \begin{bmatrix} 0 & 1 & 0 & 0 & 0 & 0 & 0 & 0 \\ a_{21} & a_{22} & 0 & 0 & a_{25} & 0 & 0 & 0 \\ 0 & 0 & 0 & 1 & 0 & 0 & 0 & 0 \\ 0 & 0 & a_{43} & a_{44} & a_{45} & 0 & 0 & 0 \\ 0 & 0 & 0 & 0 & 0 & 1 & 0 & 0 \\ a_{61} & 0 & a_{63} & 0 & a_{65} & a_{66} & a_{67} & a_{68} \\ a_{71} & 0 & 0 & 0 & 0 & 0 & a_{77} & a_{78} \\ a_{81} & 0 & 0 & 0 & 0 & 0 & a_{87} & a_{88} \end{bmatrix}$$

$$B_w = \begin{bmatrix} 0 & 0 & 0 \\ -sign(\omega_c)/J_c & 0 & 0 \\ 0 & 0 & 0 \\ 0 & -sign(\omega_m)/J_m & 0 \\ 0 & 0 & 0 \\ 0 & 0 & -sign(v_r)/M_r \\ 0 & 0 & 0 \\ 0 & 0 & 0 \end{bmatrix}$$

$$x(t) = [\,\theta_c \quad \omega_c \quad \theta_m \quad \omega_m \quad x_r \quad v_r \quad \varphi \quad \gamma\,]^T, \; u(t) = I(t)$$

$$B_u = [0 \quad 0 \quad 0 \quad k_a/J_m \quad 0 \quad 0 \quad 0 \quad 0]^T$$

$$B_{T_h} = [0 \quad 1/J_c \quad 0 \quad 0 \quad 0 \quad 0 \quad 0 \quad 0]^T$$

$w(t) = [\,F_c \quad F_m \quad F_r\,]^T$, $a_{21} = \frac{-k_c}{J_c}$, $a_{22} = \frac{-B_c}{J_c}$, $a_{25} = \frac{k_c}{J_c r_p}$, $a_{43} = \frac{-k_m}{J_m}$, $a_{44} = \frac{-B_m}{J_m}$, $a_{45} = J\frac{Gk_m}{J_m r_p}$, $a_{61} = \frac{k_c}{M_r r_p} - \frac{T_p C_f}{G_{sc} M_r r_p}$, $a_{63} = \frac{Gk_m}{M_r r_p}$, $a_{65} = -\frac{k_c + k_t + G^2 k_m}{M_r r_p^2}$, $a_{66} = \frac{-B_r}{M_r}$, $a_{67} = \frac{T_p C_f}{M_r r_p}$, $a_{71} = \frac{C_f}{G_{sc}}$, $a_{77} = -\frac{C_f + C_r}{VM}$, $a_{78} = \frac{C_f a_f - C_r a_r - V^2 M}{V^2 M}$, $a_{81} = \frac{C_f a_f}{I_z G_{sc}}$, $a_{87} = \frac{-C_f a_f - C_r a_r}{I_z}$, $a_{88} = -\frac{C_f a_f^2 + C_r a_f^2}{I_z V}$.

Table 2. Parameter values for EPS model

Symbols	Values
G	16.5
G_{sc}	20
M_r	32 kg
r_p	0.007 m
J_c	0.04 kg m^2
B_c	0.072 N m/(rad/s)
K_c	114.6 N m/rad
F_c	0.027 N m
J_m	5×10^{-4} kg m^2
B_m	0.032 N m/(rad/s)
K_m	125 N m
F_m	0.056 N m
B_r	3820
F_r	0.002 N m
K_t	32900 N m
K_a	0.05 N m/A

3 The T-S Fuzzy Model of EPS

In [6, 7], a TS fuzzy model is proposed to represent the dynamics of the EPS system by considering the movement directions of the steering column (ω_c), assistant motor (ω_m) and steering rack (v_r) change in the same way. Consequently, controls based on this simplified model of the EPS, can degrade the performance of the closed-loop real system. In this work, a new T-S model is proposed to represent exactly the nonlinear dynamics of EPS system whatever the direction of rotation.

The fuzzy rules are:

Rule$_i$: if $\varsigma_1(t)$ is about M_{1i} and … and $\varsigma_q(t)$ is about M_{1q}

$$\begin{cases} \dot{x}(t) = A_i x(t) + B_{wi} w(t) + B_{ci}\sigma(t) + B_{T_h} T_h \\ z(t) = C_{1i} x(t) \end{cases}, \quad i \in I_r \tag{10}$$

Let $-1 \leq \mathrm{sign}(\omega_c) \leq 1, -1 \leq \mathrm{sign}(\omega_m) \leq 1, -1 \leq \mathrm{sign}(v_r) \leq 1$ and by using a sector nonlinearity approach, the T-S model of an EPS system can be written as follows:

$$\begin{cases} \dot{x}(t) = \sum_{i=1}^{8} \mu_i(\varsigma(t))(Ax(t) + B_{w_i} w(t) + B_c \sigma(t) + B_{T_h} T_h) \\ z(t) = T_{sen} = C_1 x(t) \end{cases} \tag{11}$$

We have: $\forall(\omega_c, \omega_m, v_r) \in R/\ \{sign(\omega_c), sign(\omega_m), sign(v_r)\} \in [-1, 1]$, then:

$$N_{c1} = \frac{1 - sign(\omega_c)}{2},\ N_{m1} = \frac{1 - sign(\omega_m)}{2},\ N_{v1} = \frac{1 - sign(v_r)}{2}$$
$$N_{c2} = \frac{sign(\omega_c) + 1}{2},\ N_{m2} = \frac{sign(\omega_m) + 1}{2},\ N_{v2} = \frac{sign(v_r) + 1}{2},$$

and

$$\mu_1 = N_{c1}N_{m1}N_{v1},\ \mu_2 = N_{c2}N_{m1}N_{v1},\ \mu_3 = N_{c2}N_{m2}N_{v1}\ , \mu_4 = N_{c2}N_{m1}N_{v2},$$
$$\mu_5 = N_{c2}N_{m2}N_{v2},\ \mu_6 = N_{c1}N_{m2}N_{v1},\ \mu_7 = N_{c1}N_{m2}N_{v2},\ \mu_8 = N_{c1}N_{m1}N_{v2}.$$

$$B_{w_1} = \begin{bmatrix} 0 & 0 & 0 \\ -1/J_c & 0 & 0 \\ 0 & 0 & 0 \\ 0 & -1/J_m & 0 \\ 0 & 0 & 0 \\ 0 & 0 & -1/M_r \\ 0 & 0 & 0 \\ 0 & 0 & 0 \end{bmatrix}, B_{w2} = \begin{bmatrix} 0 & 0 & 0 \\ 1/J_c & 0 & 0 \\ 0 & 0 & 0 \\ 0 & -1/J_m & 0 \\ 0 & 0 & 0 \\ 0 & 0 & -1/M_r \\ 0 & 0 & 0 \\ 0 & 0 & 0 \end{bmatrix},$$

$$B_{w3} = \begin{bmatrix} 0 & 0 & 0 \\ 1/J_c & 0 & 0 \\ 0 & 0 & 0 \\ 0 & 1/J_m & 0 \\ 0 & 0 & 0 \\ 0 & 0 & -1/M_r \\ 0 & 0 & 0 \\ 0 & 0 & 0 \end{bmatrix}, B_{w4} = \begin{bmatrix} 0 & 0 & 0 \\ 1/J_c & 0 & 0 \\ 0 & 0 & 0 \\ 0 & -1/J_m & 0 \\ 0 & 0 & 0 \\ 0 & 0 & 1/M_r \\ 0 & 0 & 0 \\ 0 & 0 & 0 \end{bmatrix},$$

$$B_{w5} = \begin{bmatrix} 0 & 0 & 0 \\ 1/J_c & 0 & 0 \\ 0 & 0 & 0 \\ 0 & 1/J_m & 0 \\ 0 & 0 & 0 \\ 0 & 0 & 1/M_r \\ 0 & 0 & 0 \\ 0 & 0 & 0 \end{bmatrix}, B_{w6} = \begin{bmatrix} 0 & 0 & 0 \\ -1/J_c & 0 & 0 \\ 0 & 0 & 0 \\ 0 & 1/J_m & 0 \\ 0 & 0 & 0 \\ 0 & 0 & -1/M_r \\ 0 & 0 & 0 \\ 0 & 0 & 0 \end{bmatrix},$$

$$B_{w7} = \begin{bmatrix} 0 & 0 & 0 \\ -1/J_c & 0 & 0 \\ 0 & 0 & 0 \\ 0 & 1/J_m & 0 \\ 0 & 0 & 0 \\ 0 & 0 & 1/M_r \\ 0 & 0 & 0 \\ 0 & 0 & 0 \end{bmatrix}, B_{w8} = \begin{bmatrix} 0 & 0 & 0 \\ -1/J_c & 0 & 0 \\ 0 & 0 & 0 \\ 0 & -1/J_m & 0 \\ 0 & 0 & 0 \\ 0 & 0 & 1/M_r \\ 0 & 0 & 0 \\ 0 & 0 & 0 \end{bmatrix}.$$

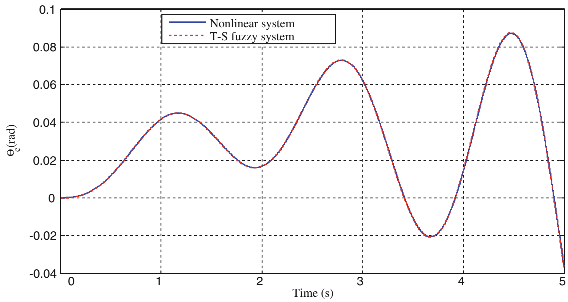

Fig. 3. T-S model validation

4 Fuzzy H∞ Control for EPS System with Actuator Saturation

The subject of this section is to design a nonlinear state feedback control law guaranteeing the performance of EPS in the presence of disturbance, and the actuator saturation. The H∞ criterion makes it possible to give the results attained. It is defined by

$$\int_0^T z^T(\tau)z(\tau)d\tau < \delta^2 \int_0^T w^T(\tau)w(\tau)d\tau \tag{12}$$

It is equivalent to the following optimization problem:

$$\begin{cases} \min \delta \\ \dot{V}(t) + z^T(t)z(t) - \delta^2 w^T(t)w(t) < 0 \end{cases} \tag{13}$$

with $\dot{V}(t)$ is the derivative of the quadratic Lyapunov function, that is defined as follows

$$V(t) = x^T(t)Px(t) \tag{14}$$

where P is a symmetric positive defined matrix.

4.1 Saturating Control

The local i^{th} state feedback control is defined as:

$$u_i(t) = K_i x(t), i = 1\ldots8 \tag{15}$$

So, the global nonlinear state feedback controller is the summation

$$u(t) = \sum_{i=1}^{8} \mu_i(t) K_i x(t) \tag{16}$$

In this section the objective is to calculate a control law which tolerates the saturation in the control signal. Therefore, the actuator output $\sigma(t)$, is a nonlinear function of its input:

$$\sigma(\bullet) = sat(u(\bullet)) \tag{17}$$

Now, let the set $\aleph(H_j)$ be defined as follows:

$$\aleph(H_j) = \left\{x(t) \in \mathbb{R}^n / \left|h_i^j x\right| \leq \bar{u}_i\right\} \tag{18}$$

with, H_j is a matrix $m \times n$, h_i^j is the i^{th} row of the H_j, n is the number of the state variables, m is number of the control inputs and $\bar{u}_i$ is the saturation level of the control signal.

The polytopic representation of the saturation is described as follow [14]:

$$\begin{cases} \sigma(u) = \sum\limits_{s=1}^{2^m} \eta_s (E_s u + \bar{E}_s v) \\ v(t) = \sum\limits_{j=1}^{r} h_i(\varsigma(t)) H_j x(t) \\ \sum\limits_{i=1}^{2^m} \eta_s = 1, \quad 0 \leq \eta_s \leq 1 \end{cases} \tag{19}$$

with, E_s represents all components of E, $\bar{E}_s = I - E_s$ and $E_s \in \{0, 1\}$

In our case, the closed-loop EPS system becomes:

$$\begin{cases} \dot{x}(t) = (A_T + B_{c_T}(E_T K_T + \bar{E}_T H_T))x(t) + B_{w_T} w(t) \\ z(t) = T_{sen} = C_{1_T} x(t) \end{cases} \tag{20}$$

with

$$A_T = \sum_{i=1}^{r} \mu_i(\varsigma(t))A_i, \quad B_{w_T} = \sum_{i=1}^{r} \mu_i(\varsigma(t))B_{w_i}, \; B_{c_T} = \sum_{i=1}^{r} \mu_i(\varsigma(t))B_{c_i}$$
$$C_{1T} = \sum_{i=1}^{r} \mu_i(\varsigma(t))C_{1i}$$

For a constant $\rho > 0$ and a symmetric positive matrix P, define an ellipsoid as $\varepsilon(P,\rho) = \{x \in \Re^n / \; x^T P x \le \rho\}$

Lemma 4.1 [15]: The ellipsoid $\varepsilon(P,\rho)$ is included in the polyhedron $\Theta = \{x/m_i^T x \le \lambda_i\}, \; i \in I_m$ if and only if

$$(m_i)^T \left(\frac{P}{\rho}\right)^{-1} m_i \le \lambda_i^2 \tag{21}$$

Theorem 4.1 [16]: The ellipsoid $\varepsilon(P,\rho)$ is contractively invariant set of the closed-loop system (20) and achieves in a disturbance rejection level δ, if there exist a symmetric positive definite matrix Q and matrices $F_j \in \Re^{m\times n}$, $Z_j \in \Re^{m\times n}$, solutions of following LMI problem:

$$\min{}^{\delta}_{Q,F_j,Z_j}$$

$$\begin{bmatrix} \bar{u}^2 & z_i^j \\ * & Q \end{bmatrix} \ge 0, \quad \forall\, i \in I_m, \, j \in I_r \tag{22}$$

$$\begin{bmatrix} AQ + B_{c_i}E_sF_j + B_{c_i}\bar{E}_sZ_j + (*) & * & * \\ B_{wi}^T & -\delta^2 I & * \\ C_1 Q & 0 & -I \end{bmatrix} < 0, \quad \forall\, i \in I_m, \, j \in I_r \tag{23}$$

with: $C_1 = [\,k_c \quad 0 \quad 0 \quad 0 \quad -k_c/r_p \quad 0 \quad 0 \quad 0\,]$

The control gains in (16) are given by:

$$K_j = F_j Q^{-1}, \quad H_j = Z_j Q^{-1}$$

Proof: Using Lemma 4.1, $\varepsilon(P,\rho) \subset \bigcap_{j}^{r} \aleph(K_j)$ if and only if:

$$\left(h_i^j\right)^T \left(\frac{P}{\rho}\right)^{-1} h_i^j \le \bar{u}_i^2 \tag{24}$$

Introduce the following changes of variables:

$$Q = \left(\frac{P}{\rho}\right)^{-1}, \quad Z_j = H_j Q$$

The (24) inequality can be written as follow

$$\bar{u}_i^2 Q - \left(z_i^j\right)^T z_i^j \geq 0 \tag{25}$$

z_i^j is the i th column of the matrix Z_j. By applying the Schur complement, we arrive at the inequality (22).

For the LMI (23), suppose that there exists a Lyapunov function $V(x(t)) = x^T(t)Px(t)$ satisfying the Hamilton–Jacobi–Bellman (H–J–B) inequality:

$$\dot{V}(t) + z^T(t)z(t) - \delta^2 w^T(t)w(t) < 0 \tag{26}$$

$$\begin{aligned} &= \begin{bmatrix} x(t) \\ w(t) \end{bmatrix}^T \begin{bmatrix} (A_T + B_{c_T}(E_T K_T + \bar{E}_T H_T))^T P + (*) & * \\ B_{w_T}^T & -\delta^2 I \end{bmatrix} \begin{bmatrix} x(t) \\ w(t) \end{bmatrix} + \\ &\begin{bmatrix} x(t) \\ w(t) \end{bmatrix}^T \begin{bmatrix} (C_{1T})^T \\ 0 \end{bmatrix} \begin{bmatrix} (C_{1T})^T \\ 0 \end{bmatrix}^T \begin{bmatrix} x(t) \\ w(t) \end{bmatrix} \end{aligned} \tag{27}$$

Using the Schur complement, we get:

$$\dot{V}(t) + z^T(t)z(t) - \delta^2 w^T(t)w(t) = \begin{bmatrix} x(t) \\ w(t) \end{bmatrix}^T \Delta_T \begin{bmatrix} x(t) \\ w(t) \end{bmatrix} \tag{28}$$

Pre-and post-multiplying Δ_T by $diag(Q, I, I)$, we have

$$\prod\nolimits_T = \begin{bmatrix} A_T Q + B_{c_T} E_T F_T + B_{c_T} \bar{E}_T Z_T & * & * \\ B_{w_T}^T & -\delta^2 I & * \\ C_1 Q & 0 & -I \end{bmatrix} \tag{29}$$

To ensure (23), it suffices to check the following condition:

$$\prod\nolimits_T < 0$$

4.2 Application on EPS System

The control of the EPS consists in controlling the brushless DC motor; the latter has a current limited in its input. This means that, a brushless DC motor is question to input saturation as follows:

$$-\bar{I} \leq I \leq \bar{I} \tag{30}$$

where $\bar{I}$ presents the saturating level. The control law is defined by

$$\sigma(t) = sat(I(t)) \tag{31}$$

Now, assume that saturation level $\bar{I} = 25\,A$, then solving the optimization problem in Theorem 4.1 we obtained the following results (Table 3):

Table 3. Parameter values for saturating control

$$\delta = 0.3732,$$

$$Q = \begin{bmatrix} 3.9165 & -17.1 & 64.2 & -257.2 & 0.0272 & -0.0806 & 0.1218 & 0.7149 \\ -17.1 & 146.6 & -282.6 & 10^3 \times 2.2667 & -0.1196 & 0.7491 & -0.3 & -5.886 \\ 64.2 & -282.6 & 10^2 \times 10.53 & -10^3 \times 4.2770 & 0.4462 & -1.3854 & 2.0 & 11.8 \\ -257.2 & 10^3 \times 2.2667 & -10^3 \times 4.2770 & 10^2 \times 46.496 & -2 & -276.2867 & -3.5873 & -94.5842 \\ 0.0272 & -0.1196 & 0.4462 & -2 & 0.0002 & -0.0006 & 0.0008 & 0.0050 \\ -0.0806 & 0.7491 & -1.3854 & -276.2867 & -0.0006 & 10.8775 & -0.0005 & -0.0363 \\ 0.1218 & -0.3 & 2.0 & -3.5873 & 0.0008 & -0.0005 & 0.0050 & 0.0093 \\ 0.7149 & -5.886 & 11.8 & -94.5842 & 0.0050 & -0.0363 & 0.0093 & 0.2896 \end{bmatrix}$$

$$K_1 = 10^3 \begin{bmatrix} 0.7224 & 0.0036 & -0.0404 & -0.0004 & -2.7010 & -0.0102 & -0.9300 & -0.1217 \end{bmatrix}$$

$$K_2 = 10^3 \begin{bmatrix} 0.8489 & 0.0038 & -0.0480 & -0.0005 & -2.5838 & -0.0123 & -0.9870 & -0.1466 \end{bmatrix}$$

$$K_3 = 10^3 \begin{bmatrix} 0.8574 & 0.0039 & -0.0485 & -0.0005 & -2.5746 & -0.0125 & -0.9961 & -0.1493 \end{bmatrix}$$

$$K_4 = K_6 = K_7 = K_8 = 10^3 \times$$
$$\begin{bmatrix} 0.8900 & 0.0045 & -0.0514 & -0.0006 & -2.5513 & -0.0163 & -0.6865 & -0.1410 \end{bmatrix}$$

$$K_5 = 10^3 \begin{bmatrix} 0.8651 & 0.0040 & -0.0491 & -0.0005 & -2.5668 & -0.0132 & -0.9567 & -0.1493 \end{bmatrix}$$

$$H_1 = H_3 = H_4 = H_6 = H_7 = H_8 = 10^3 \times$$
$$\begin{bmatrix} 0.6224 & 0.0034 & -0.0352 & -0.0004 & -1.6049 & -0.0103 & -0.7599 & -0.1076 \end{bmatrix}$$

$$H_2 = H_5 = 10^3 \begin{bmatrix} 0.6413 & 0.0041 & -0.0366 & -0.0004 & -1.6194 & -0.0113 & -0.6772 & -0.1105 \end{bmatrix}$$

5 Simulation Results

In this part, to illustrate the efficiency of the proposed method, the results obtained previously, are applied to the EPS steering system. The EPS and vehicle parameter models are listed in Tables 1 and 2. Using MATLAB/SIMULINK, LMI control Toolbox, and consider the level of saturation $\bar{I} = 25\,A$, we obtain the followings results (Fig. 3).

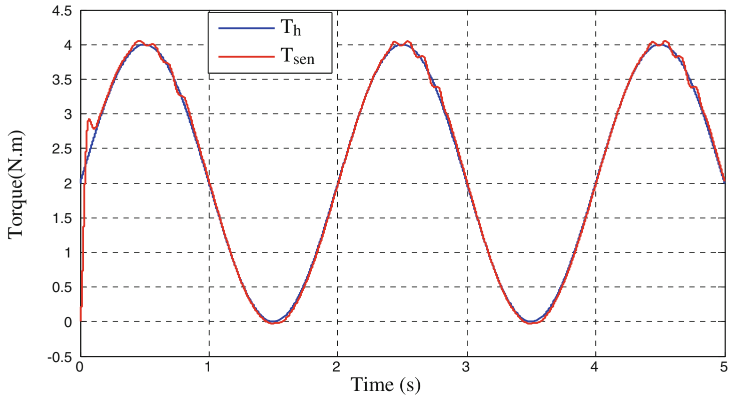

Fig. 4. T_{sen} to T_h at 0.5 Hz and $\bar{I} = 25\,A$

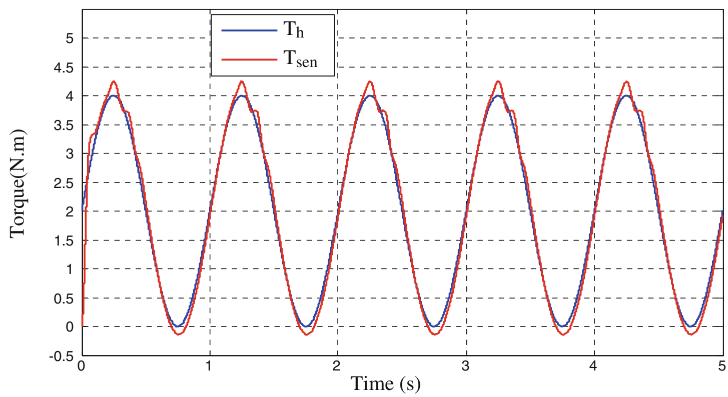

Fig. 5. T_{sen} to T_h at 1 Hz and $\bar{I} = 25\,A$

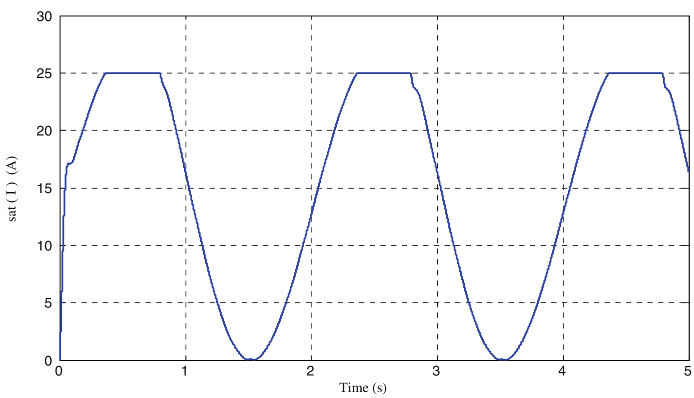

Fig. 6. The Input control I at $\bar{I} = 25\,A$

By choosing the torque applied by the driver in the sinusoidal form which can be similar to the practical form, with two different frequencies (0.5 Hz and 1 Hz respectively), and vehicle speed at 20 m/s. The simulation responses are shown in Figs. 4, 5 and 6. According to these figures, it is noted that in low frequency maneuvers, the saturation control with H_∞ gives good performances, which allows in the presence of saturation and internal disturbances, to give a stable driving. With high frequencies (see Fig. 4), the fuzzy controller improve the vehicle handling and keep the facility of maneuvers and eliminate the great torque ripples.

6 Conclusion

In this work, a new T-S model of an EPS system by considering nonlinearities in the dynamic model that are caused by friction and road reaction as perturbation, and regardless of the direction of rotation. An H_∞ state feedback-controller is designed to control the EPS system. The controller is synthesized to ensure closed-loop system stability in the presence of actuator saturation. Simulation results based on low-high frequencies and with input constraint show the effectiveness of the proposed control approach.

References

1. Rahman, M.F.: Electric power assisted steering system for automobiles. In: Electrical Engineering – Vol. III, ©Encyclopedia of Life Support Systems (EOLSS) (2009)
2. Chitu, C., Lackner, J., Horn, M.: Controller design for an electric power steering system based on LQR techniques. COMPEL **32**(3), 763–775 (2013)
3. Nehaoua, L., Djemaï, M., Pudlo, P.: Rack force feedback for an electrical power steering simulator. In: 20th Mediterranean Conference on Control and Automation (MED), Barcelona, Spain, 3–6 July 2012
4. Lu, Sh, Liau, M., Liu, M., Cho, Ch., Piao, Ch.: An adaptive fuzzy sliding mode control for electric power steering system. J. Mech. Sci. Technol. **31**(6), 2643–2650 (2017)
5. Marouf, A., Sentouh, C., Djemaï, M., Pudlo, P.: Control of an electric power assisted steering system using reference model. In: 50th IEEE Conference on Decision and Control and European Control Conference (CDC-ECC), Orlando, FL, USA, 12–15, December 2011
6. Li, X., Zhao, X.P., Chen, J.: Controller design for electric power steering system using T-S Fuzzy model approach. Int. J. Autom. Comput. **6**(2), 198–203 (2009)
7. Saifia, D., Chadli, M., Karimi, H.R., Labiod, S.: Fuzzy control for electric power steering system with assist motor current input constraints. J. Frankl. Inst. **352**(2), 562–576 (2015)
8. Chabaan, C.: Optimal control and gain scheduling of electrical power steering systems. In: IEEE Conference on Vehicle Power and Propulsion VPPC–09, 7–10 September 2009
9. Dannöhl, C., Müller, S., Ulbrich, H.: H_∞ control of a rack-assisted electric power steering system. Veh. Syst. Dyn. **50**(4), 527–544 (2012)
10. Jungers, M., Tarbouriech, S.: Anti-windup strategies for discrete-time switched systems subject to input saturation. Int. J. Control **89**(5), 919–937 (2016)
11. Tan, H.S., Tomizuka, M.: Discret-time controller design for robust vehicle traction. IEEE Control Syst. Magn. **10**(3), 107–113 (1990)

12. Chadli, M., El Hajjaji, A., Oudghiri, M.: Robust output fuzzy control for vehicle lateral dynamic stability improvement. Int. J. Model. Identif. Control **3**(3), 247–257 (2008)
13. Chun-hua, H.: Modeling and simulation of automotive electric power steering system. In: Second International Symposium on Intelligent Information Technology Application, IITA, Shanghai, China, December 20–22 (2008)
14. Hu, T., Lin, Z.: Control linear systems with actuator saturation. In: Analysis and Design, vol. 16. Birkhause, Boston (2001)
15. Henrion, D., Tarbouriech, S.: LMI relaxations for robust stability of linear systems with saturating. Automatica **35**(9), 1599–1604 (1999)
16. Saifia, D., Chadli, M., Labiod, S., Karimi, H.R.: H_∞ fuzzy control of DC-DC converters with input constraint. In: Mathematical Problems in Engineering, vol. 2012, ID 973082

Power Quality Enhancement with UPQC Systems Based on Multi-level (NPC) Inverters

Chennai Salim(✉)

Electrical Engineering Department, Birine Nuclear Research Center, Djelfa, Algeria
chenaisalimov@yahoo.fr

Abstract. This paper proposes a novel control scheme for Unified Power Quality Conditioner (UPQC) based on five-level (NPC) inverter able to mitigate source current harmonics and compensate all voltage disturbances. The UPQC is designed by the integration of series and shunt active filters (AFs) sharing a common dc bus capacitor. The dc voltage is maintained constant using conventional proportional integral voltage controller. The synchronous reference frame strategy control is used to get the reference signals for shunt APFs and the instantaneous reactive power theory for a series APFs. The reference signals for the shunt and series APFs are derived from the control algorithm and sensed signals are injected in two LS-SPWM controllers to generate switching signals. The performance of proposed UPQC system is evaluated using MATLAB-Simulink program and SimPowerSystem Toolbox for different disturbances condition. The simulation results show that the proposed UPQC system can improve the power quality.

Keywords: Five-level (NPC) inverter · UPQC · Current harmonics mitigation
Voltage disturbances compensation · Shunt active power filter
Series active power filter · Power quality improvement

1 Introduction

There has been a continuous rise of nonlinear loads over the years due to intensive use of power electronic control in industry. The utility supplying these nonlinear loads has to supply large vars. Moreover, the harmonics generated by the nonlinear loads pollute the utility. The basic requirements for compensation process involve precise control with fast dynamic response and on-line elimination of load harmonics. The traditional compensation methods using switched capacitor and thyristor controlled inductor [1] coupled with passive filters are increasingly replaced by active power filters (APFs) [2]. The two types of APFs are shunt and series APF, the shunt APFs are used to mitigate current harmonics and reactive power compensation [3]. The series APFs are used to compensate voltage related problems, such as voltage harmonics, sags, swells, unbalances, flicker [4], etc.

Unified power quality control was widely studied by many researchers as an eventual method to improve power quality of electrical distribution system [5]. The function of unified power quality conditioner is to compensate supply voltage disturbances, reactive

M. Chadli et al. (Eds.): ICEECA 2017, LNEE 522, pp. 45–59, 2019.
https://doi.org/10.1007/978-3-319-97816-1_4

power and harmonics. In other words, the UPQC has the capability of improving power quality at the point of installation on power distribution systems or industrial power systems. Therefore, the Unified Power Quality Conditioner (UPQC) is one of the best solutions to compensate both current- and voltage-related problems simultaneously [6], it is the integration of shunt and series APFs through a common DC link capacitor. Unified Power Quality Conditioner has been widely studied to eliminate or mitigate the disturbances propagated from the source side and the other loads interconnected [7]. The function of the series APF in UPQC is to compensate the all voltage disturbances [8]. The control circuitry of the series APF calculates the reference voltage to be injected by the series APF by comparing the terminal voltage with a reference value of voltage.

This paper presents a 3-phase, 3-wire UPQC configuration based on five-level (NPC) inverter using novel control method. The series AF is controlled to maintain voltage load to the reference level and to eliminate supply voltage sag/swell, harmonics and unbalance from the load terminal voltage. The shunt AF is controlled to mitigate the supply current harmonics. The dc bus voltage is maintained constant by the shunt active filter. The performances of the proposed UPQC system are verified through simulations for transient and steady-state conditions using Matlab-Simulink software and SimPowerSystem Toolbox.

2 UPQC Configuration System

Figure 1 shows the proposed UPQC connected to a power system feeding a nonlinear load. It consists of two five-level (NPC) inverters one for the shunt and the second for a series active filters. The dc link of both active filters is connected to a common dc capacitor. The series filter is connected between the supply and load terminals using three single phase transformers with turn's ratios of 1:1. In addition to injecting the voltage, these transformers are used to filter the switching ripple of the series active filter. A small capacity rated C_{sf} filter [9] is used with inductance to eliminate the high switching ripple content in the series active filter injected voltage. The five-level inverters for both the active filters are designed with IGBTs (Insulated Gate Bipolar Transistors). The three leg shunt active filter is connected ahead of a series filter through a small capacity rated inductive filter. The control algorithm of UPQC is based on synchronous reference frame detection method for the shunt AF and instantaneous reactive power theory for the series [10].

2.1 Five-Level (NPC) Inverter

Multilevel inverters are currently being investigated and used in various industrial applications. Five-level inverter is one of the most converters employed in high power applications. Their advantages include the capability to reduce the harmonic content and decrease the voltage or current ratings of the semiconductors [11]. The disadvantage is that the devices are needed more and the control algorithm gets more complicated with the increasing of levels and the neutral-point potential fluctuates easily. The power circuit of the five-level neutral point clamped inverter is given by Fig. 2.

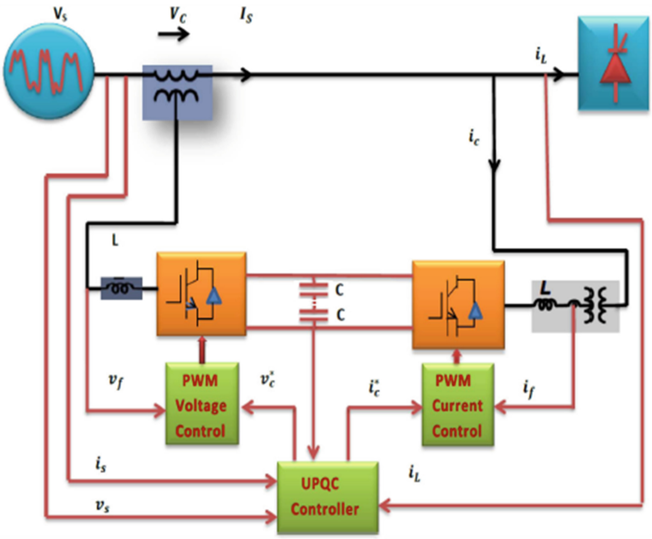

Fig. 1. UPQC configuration system

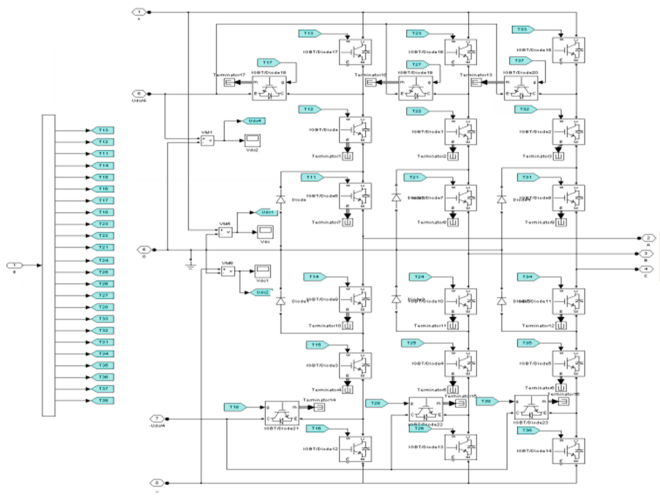

Fig. 2. Five-level (NPC) inverter

The DC bus capacitor is split into four, providing a three neutral-point. Each arm of the inverter is made up of eight IGBTs (Insulated Gate Bipolar Transistor) devices, and six clamping diodes connected to the neutral-point. The diodes are used to create the connection with the point of reference to obtain midpoint voltages. This structure allows the switches to endure larger dc voltage input on the premise that the switches will not raise the level of their withstand voltage. For this structure, five output voltage

Table 1. Five-level (NPC) witching states

Switching symbols	Switching states								Output voltage
	T_{i3}	T_{i2}	T_{i1}	T_{i4}	T_{i5}	T_{i6}	T_{i7}	T_{i8}	
A	ON	ON	ON	OFF	OFF	OFF	OFF	OFF	$U_{dc1} + U_{dc2}$
B	OFF	ON	ON	OFF	OFF	ON	ON	OFF	U_{dc1}
0	OFF	OFF	ON	ON	OFF	ON	OFF	OFF	0
C	ON	OFF	OFF	ON	ON	OFF	OFF	ON	$-U_{dc3}$
D	OFF	OFF	OFF	ON	ON	ON	OFF	OFF	$-U_{dc3\text{-}dc4}$

levels can be obtained, namely, $U_{dc}/2$, $U_{dc}/4$, 0, $-U_{dc}/4$ and $-U_{dc}/2$ corresponding to five switching states A, B, 0, C and D [12]. Table 1 shows the switching states [13].

2.2 Five-Level (NPC) Inverter Logic Control

The neutral-point-clamped (NPC) converter topology has been the centre of research and development effort for numerous applications, including medium- and high-voltage electric motor drives, static compensators (STATCOMs) and other utility type of power electronic systems for almost three decades now. Different modulation schemes have been adapted or developed depending on the application and the converter topology, and each has its unique advantages and disadvantages. The most common modulation method in industry is carrier-based SPWM. The Level Shifted-Sin Pulse Width Modulation (LS-SPWM) method is especially useful for NPC converters [14] (Fig. 3).

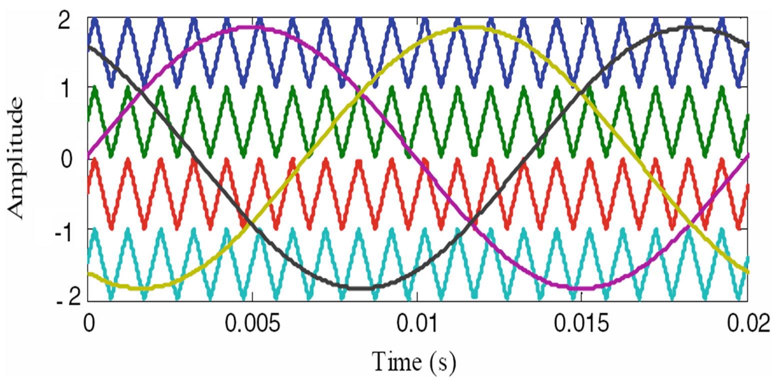

Fig. 3. Four unipolar carriers Uref: 1, 2, 3, 4

The difference between the injected currents (voltages) and the reference currents (voltages) determines the reference signals. These signals are compared with four triangular-carrying identical waves shifted from one to the other by a ($+2U_{pm}$ $+U_{pm}$, $-U_{pm}$ and $-2U_{pm}$) and generating of switching pulses. The control of inverter is summarized in the two following stages:

Determination of the intermediate signals V_{K1} and V_{K0}:

- If error $E_c \geq$ carrying 1 Then $V_{k11} = U_{dc}/4$,
- If error $E_c <$ carrying 1 Then $V_{K11} = 0$,
- If error $E_c \geq$ carrying 2 Then $V_{K12} = U_{dc}/4$,
- If error $E_c <$ carrying 2 Then $V_{K12} = 0$.
- If error $E_c \geq$ carrying 3 Then $V_{K10} = 0$,
- If error $E_c <$ carrying 3 Then $V_{K01} = -U_{dc}/4$,
- If error $E_c \geq$ carrying 4 Then $V_{K02} = 0$,
- If error $E_c <$ carrying 4 Then $V_{K02} = -U_{dc}/4$,

With: $V_{K1} = V_{k11} + V_{K12}$ and $V_{K0} = V_{K01} + V_{K02}$.

Determination of control signals of the switches T_{ij} ($i = 1, 2, 3$; $j = 1, 2, 3$):

- If $(V_{K1} + V_{K0}) = +U_{dc}/2$ Then $T_{i1} = 1$, $T_{i2} = 1$, $T_{i3} = 0$,
- If $(V_{K1} + V_{K0}) = +U_{dc}/4$ Then $T_{i1} = 1$, $T_{i2} = 1$, $T_{i3} = 0$,
- If $(V_{K1} + V_{K0}) = 0$ Then $T_{i1} = 1$, $T_{i2} = 0$, $T_{i3} = 0$,
- If $(V_{K1} + V_{K0}) = -U_{dc}/4$ Then $T_{i1} = 0$, $T_{i2} = 0$, $T_{i3} = 1$,
- If $(V_{K1} + V_{K0}) = -U_{dc}/2$ Then $T_{i1} = 0$, $T_{i2} = 0$, $T_{i3} = 0$,

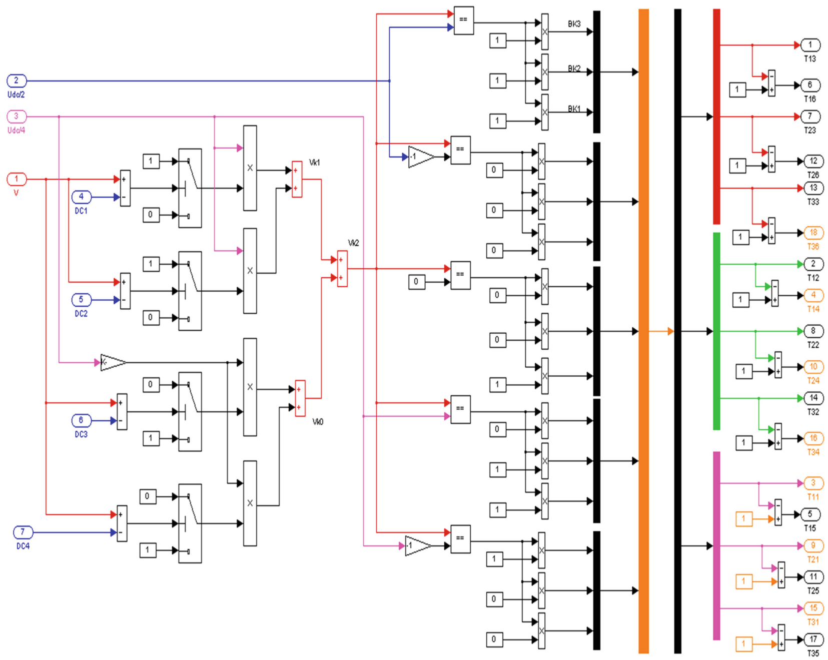

Fig. 4. Five-level (NPC) inverter logic control

The Simulink model of the logic control designed for the five-level (NPC) inverter is shown in Fig. 4.

3 Control Strategies

The control strategy is basically the way to generate reference signals for both shunt and series APFs of UPQC. The compensation effectiveness of the UPQC depends on its ability to follow with a minimum error and time delay to calculate the reference signals to compensate the distortions, unbalanced voltages or currents or any other undesirable condition. The conventional techniques reported in literature give poor results under distorted and/or unbalanced input/utility voltages, and they involve many calculations. The proposed control scheme is a simple scheme to achieve effective compensation for source current harmonics, reactive power compensation and voltage harmonic mitigation under distorted and/or unbalanced input/utility voltages.

3.1 Shunt APF

The shunt APF control strategies adopted in this work use synchronous reference frame method. The principle of this technique is described in [15].

$$\begin{bmatrix} i_\alpha \\ i_\beta \end{bmatrix} = \sqrt{2/3}\begin{bmatrix} 1 & -\frac{1}{2} & \frac{1}{2} \\ 0 & \frac{\sqrt{3}}{2} & -\frac{\sqrt{3}}{2} \end{bmatrix}\begin{bmatrix} i_{La} \\ i_{Lb} \\ i_{Lc} \end{bmatrix} \tag{1}$$

The i_α and i_β currents expression in (d-q) reference frame are given by:

$$\begin{bmatrix} i_d \\ i_q \end{bmatrix} = \begin{bmatrix} \sin(\theta_{est}) & -\cos(\theta_{est}) \\ \cos(\theta_{est}) & \sin(\theta_{est}) \end{bmatrix}\begin{bmatrix} i_\alpha \\ i_\beta \end{bmatrix} \tag{2}$$

The i_d current is transformed to DC and harmonic components using a LPF:

$$\begin{bmatrix} i_d \\ i_q \end{bmatrix} = \begin{bmatrix} \overline{i_d} + \overset{\approx}{i_d} \\ i_q \end{bmatrix} \tag{3}$$

The expression of the reference current $i_{\alpha\text{-ref}}$ and $i_{\beta\text{-ref}}$ are given by:

$$\begin{bmatrix} i_{\alpha-ref} \\ i_{\beta-ref} \end{bmatrix} = \begin{bmatrix} \sin(\theta_{est}) & -\cos(\theta_{est}) \\ \cos(\theta_{est}) & \sin(\theta_{est}) \end{bmatrix}^{-1}\begin{bmatrix} i_d \\ i_q \end{bmatrix} \tag{4}$$

$$\begin{bmatrix} i_{\alpha-ref} \\ i_{\beta-ref} \end{bmatrix} = \begin{bmatrix} \sin(\theta_{est}) & \cos(\theta_{est}) \\ -\cos(\theta_{est}) & \sin(\theta_{est}) \end{bmatrix}\begin{bmatrix} \overline{i_d} + \overset{\approx}{i_d} \\ i_q \end{bmatrix} \tag{5}$$

The reference currents in the (abc) frame are given by:

$$\begin{bmatrix} i_{a-ref} \\ i_{b-ref} \\ i_{c-ref} \end{bmatrix} = \sqrt{2/3} \begin{bmatrix} 1 & 0 \\ -\frac{1}{2} & \frac{\sqrt{3}}{2} \\ \frac{1}{2} & -\frac{\sqrt{3}}{2} \end{bmatrix} \begin{bmatrix} i_{\alpha-ref} \\ i_{\beta-ref} \end{bmatrix} \tag{6}$$

Finally, the compensation currents $i_{comp\text{-}a}$, $i_{comp\text{-}b}$ and $i_{comp\text{-}c}$ are given by:

$$\begin{bmatrix} i_{comp-a} \\ i_{comp-b} \\ i_{comp-c} \end{bmatrix} = \begin{bmatrix} i_{a-ref} \\ i_{b-ref} \\ i_{c-ref} \end{bmatrix} - \begin{bmatrix} i_{La} \\ i_{Lb} \\ i_{Lc} \end{bmatrix} \tag{7}$$

The control scheme principle of the five-level (NPC) shunt active power filter based on the synchronous reference current detection method is given by Fig. 5.

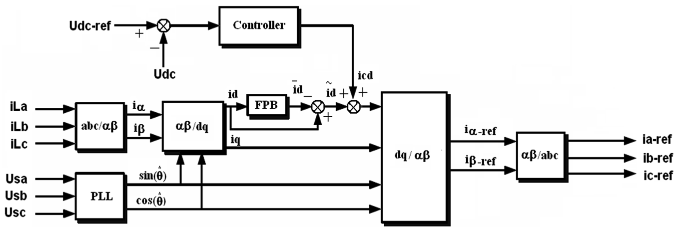

Fig. 5. Shunt APF control strategies

3.2 Series APF

The control strategy used for extracting the reference voltages of series active power filter is based on the p-q theory described in [16]. We assume that the three-phase voltage source in the grid is symmetric and distorted:

$$\begin{bmatrix} U_{sa} \\ U_{sb} \\ U_{sc} \end{bmatrix} = \begin{bmatrix} \sum_{n=1}^{\infty} \sqrt{2} U_n \sin(n\omega t + \theta_n) \\ \sum_{n=1}^{\infty} \sqrt{2} U_n \sin((n\omega t - \frac{2\pi}{3}) + \theta_n) \\ \sum_{n=1}^{\infty} \sqrt{2} U_n \sin((n\omega t + \frac{2\pi}{3}) + \theta_n) \end{bmatrix} \tag{8}$$

U_n and θ_n are respectively the rms voltage and initial phase angle, n is the harmonic order. When n = 1, it means three-phase fundamental voltage source:

$$\begin{bmatrix} U_{sa} \\ U_{sb} \\ U_{sc} \end{bmatrix} = \begin{bmatrix} \sum_{n=1}^{\infty} \sqrt{2}U_1 \sin(n\omega t + \theta_1) \\ \sum_{n=1}^{\infty} \sqrt{2}U_1 \sin((\omega t - \frac{2\pi}{3}) + \theta_1) \\ \sum_{n=1}^{\infty} \sqrt{2}U_1 \sin((n\omega t + \frac{2\pi}{3}) + \theta_1) \end{bmatrix} \tag{9}$$

Equation (9) is transformed into (α–β) reference frame:

$$\begin{bmatrix} U_{s\alpha} \\ U_{s\beta} \end{bmatrix} = C_{32} \begin{bmatrix} U_{sa} \\ U_{sb} \\ U_{sc} \end{bmatrix} = \sqrt{3} \begin{bmatrix} \sum_{n=1}^{\infty} U_n \sin(n\omega t + \theta_n) \\ \sum_{n=1}^{\infty} \mu U_n \sin(n\omega t + \theta_n) \end{bmatrix} \tag{10}$$

$$C_{32} = \sqrt{2/3} \begin{bmatrix} 1 & -1/2 & -1/2 \\ 0 & \sqrt{3}/2 & -\sqrt{3}/2 \end{bmatrix} \tag{11}$$

Three-phase positive fundamental current template is constructed:

$$\begin{bmatrix} i_{sa} \\ i_{sb} \\ i_{sc} \end{bmatrix} = \sqrt{2/3} \begin{bmatrix} \sin(\omega t) \\ \sin(\omega t - \frac{2\pi}{3}) \\ \sin(\omega t + \frac{2\pi}{3}) \end{bmatrix} \tag{12}$$

Equation (18) is transformed to (α–β) reference frame:

$$\begin{bmatrix} i_{s\alpha} \\ i_{s\beta} \end{bmatrix} = C_{32} \begin{bmatrix} i_{sa} \\ i_{sb} \\ i_{sc} \end{bmatrix} = \begin{bmatrix} \sin(\omega t) \\ -\cos(\omega t) \end{bmatrix} \tag{13}$$

According to the instantaneous reactive power theory:

$$\begin{bmatrix} p \\ q \end{bmatrix} = \begin{bmatrix} u_{s\alpha} & u_{s\beta} \\ u_{s\beta} & -u_{s\alpha} \end{bmatrix} \begin{bmatrix} i_{s\alpha} \\ i_{s\beta} \end{bmatrix} \tag{14}$$

Where DC and AC components are included:

$$\begin{bmatrix} p \\ q \end{bmatrix} = \begin{bmatrix} \overline{p} + \overset{\approx}{p} \\ \overline{q} + \overset{\approx}{q} \end{bmatrix} \tag{15}$$

p and q are passed through low pass filter (LPF) and DC component are got:

$$\begin{bmatrix} \overline{p} \\ \overline{q} \end{bmatrix} = \sqrt{3} \begin{bmatrix} U_1 \cos(\theta_1) \\ U_1 \sin(\theta_1) \end{bmatrix} \tag{16}$$

According to (20), transformation is made:

$$\begin{bmatrix} p \\ q \end{bmatrix} = \begin{bmatrix} u_{s\alpha} & u_{s\beta} \\ u_{s\beta} & -u_{s\alpha} \end{bmatrix} \begin{bmatrix} i_{s\alpha} \\ i_{s\beta} \end{bmatrix} = \begin{bmatrix} i_{s\alpha} & i_{s\beta} \\ -i_{s\beta} & i_{s\alpha} \end{bmatrix} \begin{bmatrix} u_{s\alpha} \\ u_{s\beta} \end{bmatrix} \tag{17}$$

As for DC components of p and q:

$$\begin{bmatrix} \overline{p} \\ \overline{q} \end{bmatrix} = \begin{bmatrix} u_{s\alpha f} & u_{s\beta f} \\ u_{s\beta f} & -u_{s\alpha f} \end{bmatrix} \begin{bmatrix} i_{s\alpha} \\ i_{s\beta} \end{bmatrix} = \begin{bmatrix} i_{s\alpha} & i_{s\beta} \\ -i_{s\beta} & i_{s\alpha} \end{bmatrix} \begin{bmatrix} u_{s\alpha f} \\ u_{s\beta f} \end{bmatrix} \tag{18}$$

The fundamental voltages in (α–β) reference frame are:

$$\begin{bmatrix} u_{s\alpha f} \\ u_{s\beta f} \end{bmatrix} = \begin{bmatrix} i_{s\alpha} & i_{s\beta} \\ -i_{s\beta} & i_{s\alpha} \end{bmatrix}^{-1} \begin{bmatrix} \overline{p} \\ \overline{q} \end{bmatrix} = \begin{bmatrix} i_{s\alpha} & -i_{s\beta} \\ i_{s\beta} & i_{s\alpha} \end{bmatrix} \begin{bmatrix} \overline{p} \\ \overline{q} \end{bmatrix} \tag{19}$$

The three-phase fundamental voltages are given by:

$$\begin{bmatrix} U_{saf} \\ U_{sbf} \\ U_{scf} \end{bmatrix} = C_{23} \begin{bmatrix} u_{s\alpha f} \\ u_{s\beta f} \end{bmatrix} = \sqrt{2} U_1 \begin{bmatrix} \sin(\omega t + \theta_1) \\ \sin(\omega t + \theta_1 - \frac{2\pi}{3}) \\ \sin(\omega t + \theta_1 + \frac{2\pi}{3}) \end{bmatrix} \tag{20}$$

Where:

$$C_{23} = \sqrt{2/3} \begin{bmatrix} 1 & -1/2 & -1/2 \\ 0 & \sqrt{3}/2 & \sqrt{3}/2 \end{bmatrix}^T \tag{21}$$

These produced three-phase load reference voltages are compared with load line voltages and errors are then processed by sinusoidal LS-SPWM controller to generate

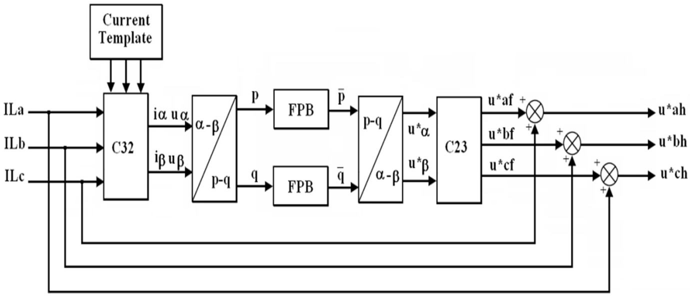

Fig. 6. Series APF control strategies

the required switching signals for series APF switches. The block diagram of the series active filter control is shown in Fig. 6.

4 Simulation Results and Discussions

In this study, a novel control algorithm for the UPQC is evaluated by using simulation results given in Matlab/Simulink software under non-ideal mains voltage conditions. In simulation studies, the results are specified before and after UPQC system are operated. In addition, when the UPQC system is operated, the load has changed and dynamic response of the system is tested. The proposed control method has been examined under all voltage disturbances conditions. The simulated UPQC system parameters are: $V_s = 220$ V, Frequency $F_s = 50$ Hz, Resistor $R_s = 0.1$ mΩ, Inductance $L_s = 0.0002$ mH, Resistor $R_l = 48.6$ Ω, Inductance $L_l = 40$ mH, $C_{dc} = 3000$ μF, Resistor $R_c =$ 0.27 mΩ, $L_c = 0.8$ mH. Figure 7 shows the Matlab-simulink model of the proposed UPQC system.

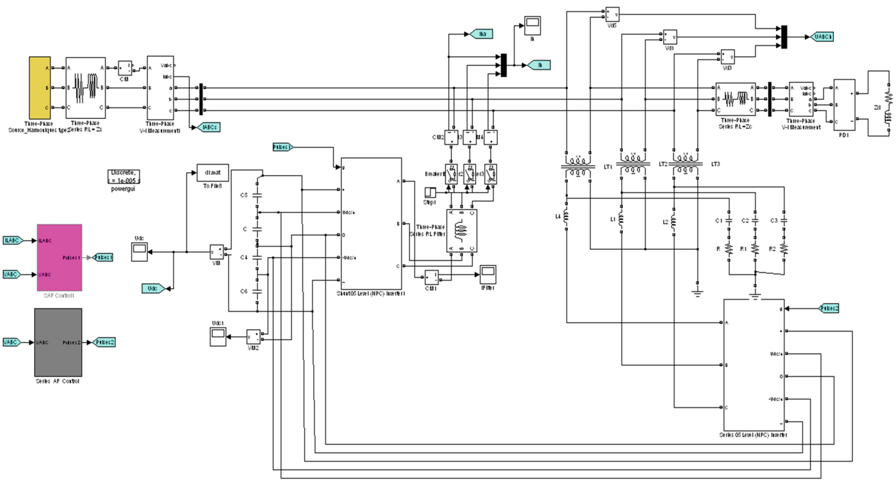

Fig. 7. SimPowerSystem UPQC model based on five-level (NPC) inverter

4.1 Performances of UPQC for All Voltage Disturbances Compensation

The performance of proposed UPQC is tested under all voltage disturbances simultaneously. The simulation results are shown in Fig. 8. The voltage sags (25%) is introduced voluntary between $t_1 = 0.06$ s and $t_2 = 0.12$ s. After that, a voltage swells (35%) is introduced between $t_2 = 0.12$ and $t_3 = 0.18$ s. The voltage harmonics is introduced between $t_3 = 0.18$ s and $t_4 = 0.24$ s. The unbalances is introduced between $t_4 = 0.24$ s and $t_5 = 0.3$ s. After $t_5 = 0.3$ s the system is again at normal working condition. It is illustrated that the proposed UPQC is capable to mitigate all voltage

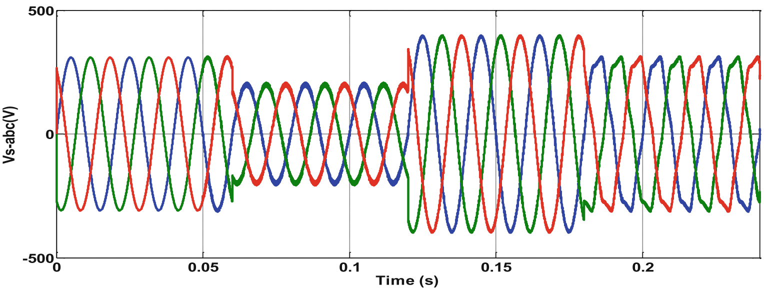

(a) Load voltage before compensation

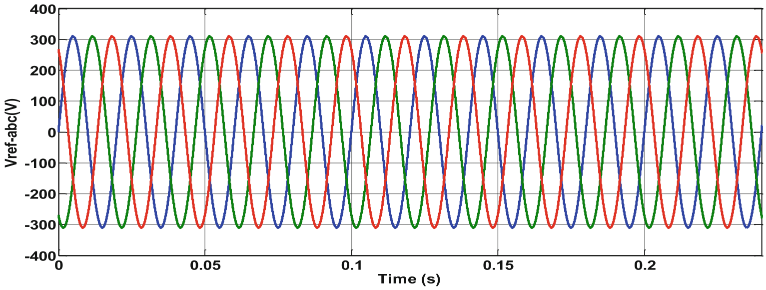

(b) Reference voltages

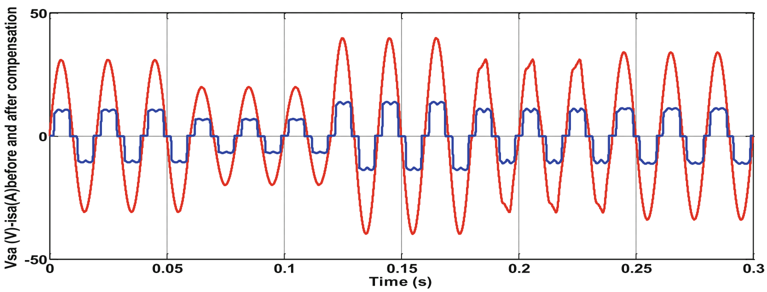

(c) Source current and voltage before compensation

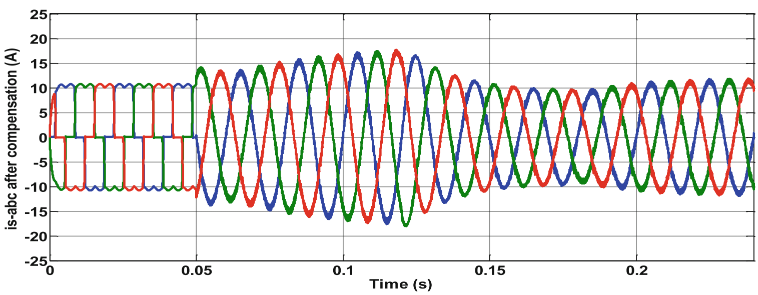

(d) Source current after compensation

Fig. 8. UPQC performances for all voltage disturbances compensation

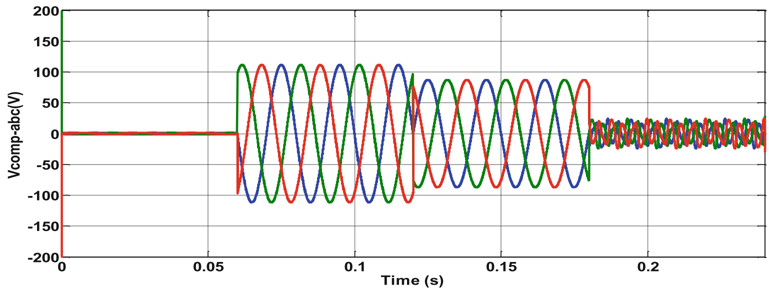

(e) Compensation voltages

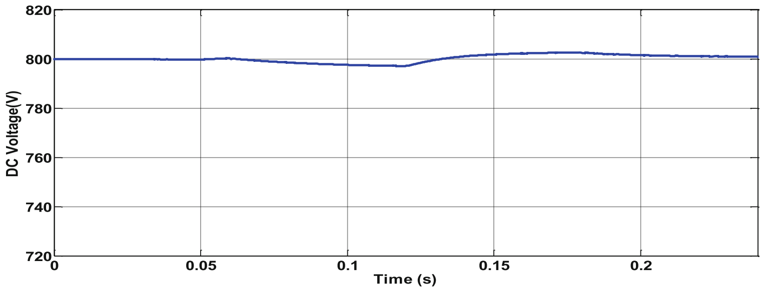

(f) DC link voltage

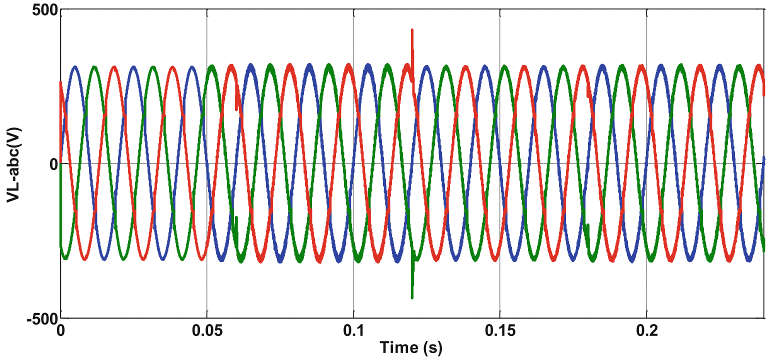

(g) Load voltage after compensation

Fig. 8. (*continued*)

disturbances and does not show any significant effect of disturbance type present in the utility voltages on its compensation capability.

4.2 Dynamic Performances of UPQC for the Sudden Change of Load

In order to evaluate the performance of the proposed UPQC during transient condition, the load on the system is changed suddenly. The simulation results during this condition are shown in the Fig. 9. Before time $t_1 = 0.05$ s, the shunt and series APFs are not working, the source current is highly distorted. After $t_1 = 0.05$ s the shunt active

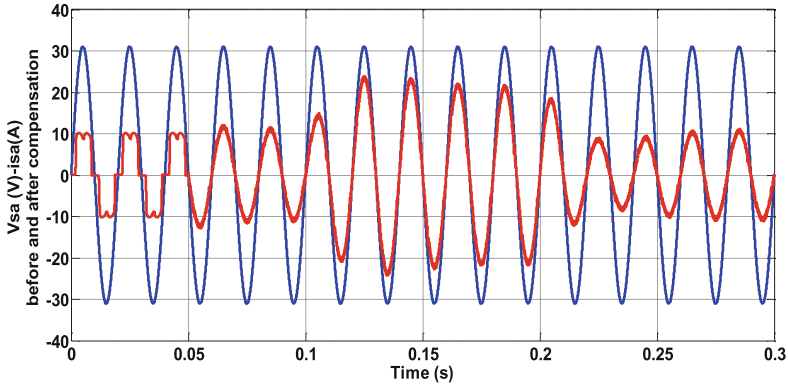

(a) Source current isa(A) and source voltage vsa(V)

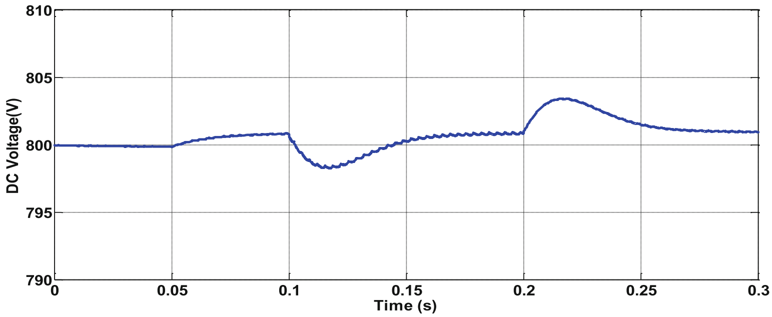

(b) DC link voltage

Fig. 9. UPQC performance in transient condition

filer is only on operation (the source current after compensation is nearly sinusoidal and in phase with the source voltage). When the sudden load current disturbance is introduced voluntary between $t_2 = 0.1$ s and $t_3 = 0.2$ s, the UPQC controller acts immediately without any delay, the shunt APF injects a current equals to sum of harmonic.

In the all dynamic condition the dc voltage is maintained constant and equal to the reference value $U_{dc\text{-}ref} = 800$ V using proportional integral voltage controller. It is observed that the dc voltage passes through a transitional period of 0.02 s before stabilization and reaches its reference with moderate peak voltage approximately equal to 3 V. Before Shunt AF application the source current is distorted with poor power factor, after compensation the source current shown in Fig. 9(a) is sinusoidal and in phase with the source voltage for the all voltage disturbances. The effectiveness of the UPQC in reducing the supply current and load voltage harmonics for all disturbances conditions is proved.

5 Conclusion

To enhance the power quality by reducing the source current harmonics and improve the voltage delivered to sensitive or critical loads, a novel UPQC configuration based on five-level (NPC) inverter topology has been proposed in this paper. The control strategy adopted is based on the instantaneous reactive power method for the series AF and synchronous reference frame detection method for the shunt AF. The developed model is validating through simulation results using Matlab-Simulink software and SimPowerSystem Toolbox. The control algorithm of UPQC has been observed to be satisfactory for various power quality improvements like voltage harmonics mitigation, current harmonic mitigation, voltage sag, swell and unbalance compensation. The UPQC performance during transient conditions has been found satisfactory, the UPQC controller acts immediately without any delay in the operation with fast dynamic response. The result of this study may be useful for potential UPQC applications.

References

1. Mahanty, R.: Large value AC capacitor for harmonic filtering and reactive power compensation. IET Gener. Transm. Distrib. **2**(6), 876–891 (2008)
2. Hirve, S., Chatterjee, K., Fernandes, B.G., Imayavaramban, M., Dwari, S.: PLL-less active power filter based on one-cycle control for compensating unbalanced loads in three-phase four-wire system. IEEE Trans. Power Deliv. **22**(4), 2457–2465 (2007)
3. Chennai, S., Benchouia, M.-T., Goléa, A., Zouzou, S.-E.: Shunt active filter based on three-level NPC inverter using current and DC voltage artificial neural network controllers. Int. Electr. Eng. J. IEEJ **1**(1), 523–528 (2011)
4. Chennai, S., Benchouia, M.-T.: A simplified control scheme for three-phase three-level (NPC) series active filter to compensate all voltage perturbations. Acta Electrotechnica et Informatica, AEI **11**(4), 52–59 (2011)
5. Kesler, M., Ozdemir, E.: A novel control method for unified power quality conditioner (UPQC) under non-ideal mains voltage and unbalanced load condition, pp. 374–379. IEEE (2010)
6. Chennai, S., Benchouia, M.-T.: Simplified control scheme of unified power quality conditioner based on three-phase Three-level (NPC) inverter to mitigate current source harmonics and compensate all voltage disturbances. J. Electr. Eng. Technol. JEET **8**(3), 544–558 (2013)
7. Hideaki, F., Hirofumi, A.: The integration of series and shunt active filters. IEEE Trans. Power Electron. **13**(2), 315–322 (1998)
8. Khadkikar, V., Chandra, A., Barry, A.-O., Nguyen, T.-D.: Application of UPQC to protect a sensitive load at polluted distribution network. IEEE (2006)
9. Moran, L., Pastorini, I., Dixon, J., Wallace, R.: Series active power filter compensates current harmonics and voltage unbalance simultaneously. Proc. IEE Gener. Trans. Distrib. **147**(1), 31–36 (2000)
10. Fujita, H., Akagi, H.: The unified power quality conditioner: The integration of series active filters and shunt active filters. IEEE. Trans. Power Electr. **13**, 315–322 (1998)

11. Chaturvedi, P.K., Shailendra, J., Agrawal, P.: A study of Neutral point potential and common mode voltage control in multilevel SPWM technique. In: Fifteenth National Systems Conference, pp. 518–523 (2008)
12. Chibani, R., Berkouk, E.-M., Boucherit, M.-S.: Five-level NPC VSI: different ways to balance input DC link voltages. Elektrika **11**(1), 19–33 (2009)
13. Ozdemir, S., Ozdemir, E., Leon, M.-T., Surin, K.: Elimination of harmonics in a five-level diode-clamped multilevel inverter using fundamental modulation. In: PEDS, pp. 850–854. IEEE (2007)
14. Krug, D., Bernet, S., Fazel, S., et al.: Comparison of 2.3 kV medium voltage multilevel converters for industrial medium voltage drives. IEEE Trans. Industr. Electron. **54**(6), 2979–2992 (2007)
15. Chennai, S., Benchouia, M.-T.: Three-phase three-level (NPC) shunt active power filter performances based on PWM and ANN's controllers for harmonic current compensation. Int. J. Electr. Eng. Inform. IJEEI **6**(1), 213–234 (2014)
16. Hai, L., Jincheng, L., Weiping, W.: Research of harmonic detection and fuzzy PID control in series active power filter. IEEE, pp. 2957–2962 (2007)

H_∞ Based State Feedback Control of LPV Time-Delay Systems via Parameter-Dependent Lyapunov Krasovskii Functionals

Imen Nejem[1,3(✉)], Mohamed Hechmi Bouazizi[2], and Faouzi Bouani[3]

[1] Tunis University, National Higher Engineering School of Tunis, 1007 Tunis, Tunisia
imen.nejem@yahoo.fr

[2] Tunis El Manar University, Higher Institute of Medical Technologies of Tunis, LR11ES20 Analysis, Conception and Control of Systems Laboratory, 1002 Tunis, Tunisia
hechmi.bouazizi@istmt.utm.tn

[3] Tunis El Manar University, National Engineering School of Tunis, LR11ES20 Analysis, Conception and Control of Systems Laboratory, 1002 Tunis, Tunisia
faouzi.bouani@enit.utm.tn

Abstract. This paper develops the problems of robust stability analysis and H_∞ state feedback control synthesis for Linear Parameter Varying (LPV) Systems with time varying delay, using parameter dependent Lyapunov-Krasovskii functionals. First, we use an integral inequality playing a key role in the derivation of such criterion and allow reducing the H_∞ cost in comparison to other results. Secondly, the LMI dilatation approach presented in this paper can express the original non convex problem in terms of convex linear matrix inequality and reduce consequently the conservatism of LMI synthesis without dilation. Both, analysis and synthesis conditions are formulated in terms of linear matrix inequalities (LMIs). Finally, a numerical example is given to illustrate the effectiveness of the proposed result.

Keywords: Linear parameter-varying systems · Linear matrix inequalities
Time-delay systems · Parameter dependent Lyapunov functional
State feedback · H_∞ performance

1 Introduction

The problem of delayed systems has been investigated over the years because a time delay appears in many dynamical systems such as chemical process, nuclear reactors, and biological systems. Frequently, the presence of delay in state-space model system is a source of instability and poor performance. Hence, the stability analysis and control synthesis problems of time delay system have been examined in the control literature [1, 2]. Existing criteria for stability condition can be classified into two types: delay independent criteria [3, 4] and delay dependent criteria [5, 6]. The relevance of the obtained conditions depends on the type of systems. It is well known that delay independent criteria tend to be more conservative then delay dependent ones.

M. Chadli et al. (Eds.): ICEECA 2017, LNEE 522, pp. 60–71, 2019.
https://doi.org/10.1007/978-3-319-97816-1_5

In other fields of research, Linear Parameter Varying LPV systems have been intensively studied [7, 8] since they provide a general approach to control complex systems such as nonlinear systems, LTV systems, and multimodal systems. Therefore, a control strategy has been developed for these systems based on classical gain scheduled adaptive methodology [9, 10]. This approach, well suitable for slowly varying parameter systems, can be problematic during the real implementation of the controller, especially regarding stability in the switching zones. To overcome these problems, an interesting answer is given by linear parameter dependent controller [11, 12]. These controllers can improve the closed loop characteristic such as the stability and H_∞ performance.

Recently, stability analysis and control of LPV time delay systems have been attracting a lot of attention. Main papers and special publications concerning the stability analysis problem of LPV time delay systems have appeared in [13–15] but it is still an open problem. Motivated by the LPV control theory, in this work, delay-dependent analysis and control for LPV systems with time delays has been studied. The main contribution of this paper is to develop a new H_∞ state feedback control for LPV time-delay systems by means of the Parameter Dependent Lyapunov-Krasovskii functional approach. This approach can reduce the conservatism compared with other methods.

The paper is organized as follows. In Sect. 2, preliminaries used in this paper are defined. In Sect. 3, the stability analysis problem of time-delayed LPV systems is considered using parameter-dependent Lyapunov-Krasovskii functionals. Then, we deal with the problem of H_∞ state-feedback control of time-delayed LPV systems. A numerical example is given.

2 Preliminary

Consider the following state-space model of an LPV system with varying state delay:

$$\begin{cases} \dot{x}(t) = A(\theta(t))x(t) + A_d(\theta(t))x(t-\tau(t)) + B_1(\theta(t))w(t) + B_2(\theta(t))u(t) \\ z(t) = C(\theta(t))x(t) + C_d(\theta(t))x(t-\tau(t)) + D_1(\theta(t))w(t) + D_2(\theta(t))u(t) \\ x(t) = \eta(t), \forall t \in [-\tau, 0] \end{cases} \quad (1)$$

Where $\boldsymbol{x(t)} \in \boldsymbol{R^n}, \boldsymbol{x(t-\tau(t))} \in \boldsymbol{R^n}, \boldsymbol{w(t)} \in \boldsymbol{R^p}, \boldsymbol{u(t)} \in \boldsymbol{R^m}$, $z(t) \in \mathcal{R}^p$ and η are respectively the system state, the delayed state, the external disturbance, the control input, the controlled output and the functional initial condition.

$\tau(t)$ is a time varying delay satisfying $0 < \tau(t) < \tau_{max}$, $0 < \dot{\tau}(t) < \mu < 1$.

The real parameters $\theta(t) = [\theta_1(t), \theta_2(t), \ldots, \theta_r(t)]^T$ that can be known by on line measurement values vary in a polytope Θ as:

$$\theta(t) \in \Theta = \left\{ \sum_{i=1}^{N} \alpha_i(t)\theta_i,\ \alpha_i(t) \geq 0,\ \sum_{i=1}^{N} \alpha_i(t) = 1,\ N = 2^r \right\} \tag{2}$$

and the rate of variation $\dot{\theta}(t)$ are well defined at all times and vary in a polytope Θ_υ as:

$$\dot{\theta}(t) \in \Theta_\upsilon = \left\{ \sum_{j=1}^{N} \beta_j(t)\upsilon_j,\ \beta_j(t) \geq 0,\ \sum_{j=1}^{N} \beta_j(t) = 1,\ N = 2^r \right\} \tag{3}$$

It is assumed that the state-space matrices $A(\theta)$, $A_d(\theta)$, $B_1(\theta)$, $B_2(\theta)$, $C(\theta)$, $C_d(\theta)$, $D_1(\theta)\,and\,D_2(\theta)$ are continuous and bounded functions and depend linearly on $\theta(t)$, so that the LPV system is described through a polytopic model. Let:

$$\begin{pmatrix} A(\theta) & A_d(\theta) & B_1(\theta) & B_2(\theta) \\ C(\theta) & C_d(\theta) & D_1(\theta) & D_2(\theta) \end{pmatrix} = \sum_{i=1}^{N} \alpha_i \begin{pmatrix} A_i & A_{di} & B_{1i} & B_{2i} \\ C_i & C_{di} & D_{1i} & D_{2i} \end{pmatrix} \tag{4}$$

With $i = 1, \ldots, N, \alpha_i \geq 1, \sum_{i=1}^{N} \alpha_i = 1$.

Lemma 1.1 [16]. Let $x(t) \in \mathcal{R}^n$ be a vector-valued function with first-order continuous-derivative entries. Then, the following integral inequality holds for any matrices $M_1(\theta), M_2(\theta) \in \Re^{n\times n}$, $R(\theta) = R(\theta)^T > 0 \in \Re^{n\times n}, \Gamma \in \Re^{2n\times 2n}$ and a scalar function $\tau := \tau(t) \geq 0$:

$$-\int_{t-\tau}^{t} \dot{x}^T(\omega)R(\theta)\dot{x}(\omega)d\omega \leq \xi^T(t)\Upsilon\xi(t) + \tau\xi^T(t)\Gamma^T R^{-1}(\theta)\Gamma\xi(t) \tag{5}$$

Where

$$\Upsilon = \begin{pmatrix} M_1^T(\theta) + M_1(\theta) & -M_1^T(\theta) + M_2(\theta) \\ (*) & -M_2^T(\theta) - M_2(\theta) \end{pmatrix}$$
$$\Gamma^T := \begin{pmatrix} M_1^T(\theta) \\ M_2^T(\theta) \end{pmatrix}, \quad \xi(t) := \begin{pmatrix} x(t) \\ x(t-\tau) \end{pmatrix}$$

3 Stability Analysis of Time-Delayed LPV Systems

We first present delay-dependent conditions for the stability and $\boldsymbol{H}_\infty$ performance analysis of system (1), which are provided in the following theorem:

Theorem 3.1. System (1) with no control input $(u(t) = 0)$ is robustly asymptotically stable for any dependent time delay $\tau(t)$ satisfying both $0 < \tau(t) \leq \tau_{max}\,and\,\frac{\|z\|_2}{\|w\|_2} < \gamma$ if there exist positive-definite matrices $P(\theta) \in \Re^{n\times n}$, $Q(\theta) \in \Re^{n\times n}, R(\theta) \in \Re^{n\times n}$, and matrices $M_1(\theta)$, $M_2(\theta) \in \Re^{n\times n}$, such that for all $\theta(t) \in \Theta$:

$$\begin{pmatrix} \phi_{11}(\theta) & \phi_{12}(\theta) & P(\theta)B_1(\theta) & C^T(\theta) & \tau_{\max}A^T(\theta)R(\theta) & \tau_{\max}M_1^T(\theta) \\ (*) & \phi_{22}(\theta) & 0 & 0 & \tau_{\max}A_d^T(\theta)R(\theta) & \tau_{\max}M_2^T(\theta) \\ (*) & (*) & -\gamma I & D_1^T(\theta) & \tau_{\max}B_1^T(\theta)R(\theta) & 0 \\ (*) & (*) & (*) & -\gamma I & 0 & 0 \\ (*) & (*) & (*) & (*) & -\tau_{\max}R(\theta) & 0 \\ (*) & (*) & (*) & (*) & (*) & -\tau_{\max}R(\theta) \end{pmatrix} < 0 \tag{6}$$

With

$$\begin{aligned} &\phi_{11}(\theta) = A^T(\theta)P(\theta) + P(\theta)A(\theta) + Q(\theta) + M_1^T(\theta) + M_1(\theta), \\ &\phi_{12}(\theta) = P(\theta)A_d(\theta) - M_1^T(\theta) + M_2(\theta), \text{ and} \\ &\phi_{22}(\theta) = -(1-\mu)Q(\theta) - M_2^T(\theta) - M_2(\theta), \end{aligned}$$

Where, μ is an upper bound of the delay derivative $|\dot{\tau}| \le \mu, \forall t \ge 0$.

The parameter-dependent $P(\theta)$ matrix also has equivalently affine formulation as:

$$P(\theta) = P_0 + \theta_1 P_1 + \ldots + \theta_r P_r$$

And the derivation of $P(\theta)$ can be derived as:

$$\frac{dP(\theta)}{dt} = \dot{\theta}_1 P_1 + \ldots + \dot{\theta}_r P_r$$

Proof of Theorem 3.1

The main result of the stability analysis of LPV time delay systems is based on the use of the following parameter dependent Lyapunov-Krasovskii functional

$$V(t) = x^T(t)P(\theta)x(t) + \int_{t-\tau(t)}^{t} x^T(\omega)Q(\theta)x(\omega)d\omega + \int_{-\tau_{max}}^{0}\int_{t+\omega}^{t} \dot{x}(s)R(\theta)\dot{x}(s)dsd\omega \tag{7}$$

Calculating the derivative of $V(t)$ along the trajectories solutions of system (1) leads to:

$$\begin{aligned} \dot{V}(t) = {} & x^T(t)[A^T(\theta)P(\theta) + P(\theta)A^T(\theta) + Q(\theta)]x(t) + 2x^T(t-\tau(t))A_d^T(\theta)P(\theta)x(t) \\ & + 2w^T(t)B_1(\theta)P(\theta)x(t) - (1-\dot{\tau})x^T(t-\tau(t))Q(\theta)x(t-\tau(t)) + \tau_{\max}\dot{x}^T(t)R(\theta)\dot{x}(t) + I \end{aligned} \tag{8}$$

With $I = -\int_{t-\tau_{\max}}^{t} \dot{x}^T(\omega)R(\theta)\dot{x}(\omega)d\omega$
Note that $-(1-\dot{\tau}) \leq -(1-\mu)$
Using lemma 1 we have:

$$\dot{V}(t) \leq X^T(t)\Phi(\theta)X(t) \leq 0 \tag{9}$$

With

$$\Phi(\theta) = \begin{pmatrix} \phi_{11}(\theta) & \phi_{12}(\theta) & P(\theta)B_1(\theta) \\ (*) & \phi_{22}(\theta) & 0 \\ (*) & (*) & 0 \end{pmatrix} + \tau_{\max} Z^T(\theta)R(\theta)Z(\theta) + \Gamma^T R^{-1}(\theta)\Gamma^T,$$

$$X(t) = \begin{pmatrix} x(t) \\ x(t-\tau(t)) \\ w(t) \end{pmatrix}, Z(\theta) = \begin{pmatrix} A(\theta) & A_d(\theta) & B_1(\theta) \end{pmatrix}$$

The criterion J_{zw} to be minimized is considered as:

$$J_{zw} = \int_0^t [-z^T(t)z(t) + \gamma^2 w^T(t)w(t)]dt \tag{10}$$

Define the function H to be

$$H = V - \int_0^t [-z^T(t)z(t) + \gamma^2 w^T(t)w(t)]dt \tag{11}$$

The derivative of the function can be bounded from above by

$$\dot{H} \leq \dot{V} + z^T(t)z(t) - \gamma^2 w^T(t)w(t)dt \tag{12}$$

Then expanding the expression of $z(t)$ into the expression of $\dot{H}$ and affecting the Schur complement obtain LMI (6).

Unfortunately, the representation (6) is not linear in the terms $P(\theta)A^T(\theta)$, $P(\theta)A_d(\theta)$, $A^T(\theta)R(\theta)\, and\, A_d^T(\theta)R(\theta)$. Generally, we solve this problem by using a constant Lyapunov matrix function. However, this method is very conservative. That's why LMI dilation approach can be used to reduce this conservatism.

Theorem 3.2. System (1) with no control input $(u(t) = 0)$ is robustly asymptotically stable for any dependent time delay $\tau(t)$ satisfying both $0 < \tau(t) \leq \tau_{max}\, and\, \frac{\|z\|_2}{\|w\|_2} < \gamma$ if there exist positive-definite matrices $P(\theta) \in \Re^{n\times n}, Q(\theta) \in \Re^{n\times n}, R(\theta) \in \Re^{n\times n}$, matrices $M_1(\theta), M_2(\theta) \in \Re^{n\times n}$ and $X \in \Re^{n\times n}$ such that for all $\theta(t) \in \Theta$:

$$\begin{pmatrix} -X-X^T & \Phi_{12}(\theta) & \Phi_{13}(\theta) & \Phi_{14(\theta)} & 0 & X^T & \tau_{\max}R(\theta) & 0 \\ (*) & \Phi_{22}(\theta) & -M_1(\theta)^T+M_2(\theta)^T & 0 & C(\theta)^T & 0 & 0 & \tau_{\max}M_1(\theta)^T \\ (*) & (*) & \Phi_{33}(\theta) & 0 & 0 & 0 & 0 & \tau_{\max}M_2(\theta)^T \\ (*) & (*) & (*) & -\gamma I & D_1(\theta)^T & 0 & 0 & 0 \\ (*) & (*) & (*) & (*) & -\gamma I & 0 & 0 & 0 \\ (*) & (*) & (*) & (*) & (*) & -P(\theta) & -\tau_{\max}R(\theta) & 0 \\ (*) & (*) & (*) & (*) & (*) & (*) & -\tau_{\max}R(\theta) & 0 \\ (*) & (*) & (*) & (*) & (*) & (*) & (*) & -\tau_{\max}R(\theta) \end{pmatrix} < 0 \quad (13)$$

With

$$\begin{aligned} \Phi_{22}(\theta) &= -P(\theta)+Q(\theta)+M_1(\theta)^T+M_1(\theta), \\ \Phi_{12}(\theta) &= P(\theta)+X^TA(\theta), \\ \Phi_{13}(\theta) &= X^TA_d(\theta), \\ \Phi_{14}(\theta) &= X^TB_1(\theta), \\ \Phi_{33}(\theta) &= -(1-\mu)Q(\theta)-M_2(\theta)^T-M_2(\theta) \end{aligned}$$

Proof of Theorem 3.2. The proof is inspired from [17]. Let's rewrite (13) as:

$$\Psi(\theta)+\mathcal{P}^T(\theta)\mathcal{X}^T\mathcal{Q}+\mathcal{Q}^T\mathcal{X}\mathcal{P}(\theta)<0 \quad (14)$$

With

$$\Psi(\theta) = \begin{pmatrix} 0 & P(\theta) & 0 & 0 & 0 & 0 & \tau_{\max}R(\theta) & 0 \\ (*) & \psi_{22}(\theta) & \psi_{23}(\theta) & 0 & C^T(\theta) & 0 & 0 & \tau_{\max}M_1^T(\theta) \\ (*) & (*) & \psi_{33}(\theta) & 0 & C_{1d}^T(\theta) & 0 & 0 & \tau_{\max}M_2^T(\theta) \\ (*) & (*) & (*) & -\gamma I & D_1^T(\theta) & 0 & 0 & 0 \\ (*) & (*) & (*) & (*) & -\gamma I & 0 & 0 & 0 \\ (*) & (*) & (*) & (*) & (*) & -P(\theta) & -\tau_{\max}R(\theta) & 0 \\ (*) & (*) & (*) & (*) & (*) & (*) & -\tau_{\max}R(\theta) & 0 \\ (*) & (*) & (*) & (*) & (*) & (*) & (*) & -\tau_{\max}R(\theta) \end{pmatrix}$$

$$\begin{aligned} \psi_{22}(\theta) &= \frac{dP(\theta)}{dt}-P(\theta)+Q(\theta)+M_1^T(\theta)+M_1(\theta) \\ \psi_{23}(\theta) &= -M_1^T(\theta)+M_2^T(\theta) \\ \psi_{33}(\theta) &= -(1-\mu)Q(\theta)-M_2^T(\theta)-M_2(\theta) \\ \mathcal{P}(\theta) &= \begin{pmatrix} -I & A(\theta) & A_d(\theta) & B_1(\theta) & 0 & I & 0 & 0 \end{pmatrix} \\ \mathcal{Q} &= \begin{pmatrix} I & 0 & 0 & 0 & 0 & 0 & 0 & 0 \\ 0 & I & 0 & 0 & 0 & 0 & 0 & 0 \\ 0 & 0 & I & 0 & 0 & 0 & 0 & 0 \\ 0 & 0 & 0 & I & 0 & 0 & 0 & 0 \end{pmatrix}, \ \mathcal{X} = \begin{pmatrix} X^T & 0 & 0 & 0 \end{pmatrix}^T \end{aligned}$$

Noting that explicit basis of the null-spaces of $\mathcal{P}$ and are given by

$$\ker(\mathcal{P}) = \begin{pmatrix} A(\theta) & A_d(\theta) & B_1(\theta) & I & 0 & 0 & 0 \\ I & 0 & 0 & 0 & 0 & 0 & 0 \\ 0 & I & 0 & 0 & 0 & 0 & 0 \\ 0 & 0 & I & 0 & 0 & 0 & 0 \\ 0 & 0 & 0 & 0 & I & 0 & 0 \\ 0 & 0 & 0 & I & 0 & 0 & 0 \\ 0 & 0 & 0 & 0 & 0 & I & 0 \\ 0 & 0 & 0 & 0 & 0 & 0 & I \end{pmatrix}, \ \ker(\mathcal{Q}) = \begin{pmatrix} 0 & 0 & 0 \\ 0 & 0 & 0 \\ 0 & 0 & 0 \\ 0 & 0 & 0 \\ I & 0 & 0 \\ 0 & 0 & 0 \\ 0 & I & 0 \\ 0 & 0 & I \end{pmatrix}$$

and applying the projection lemma of [18], the feasibility of LMI (14) implies the feasibility of the tow underlying LMIs:

$$\begin{cases} \ker(P(\theta))^T \Psi(\theta) \ker(\mathcal{P}(\theta)) < 0 \\ \ker(Q(\theta))^T \Psi(\theta) \ker(\mathcal{Q}(\theta)) < 0 \end{cases} \tag{15}$$

After some manipulations, it is possible to show that first LMI (15) is equivalent to LMI (13) whereas the second one is the LMI given by:

$$\begin{pmatrix} -\gamma I & 0 & 0 \\ 0 & -R(\theta) & 0 \\ 0 & 0 & -R(\theta) \end{pmatrix} < 0$$

This LMI is a relaxed form of the right bottom 3 $\times$ 3 block of the inequality (13) and it is satisfied for all positive definite matrix $R(\theta)$.

Hence this shows that feasibility of (6) implies the feasibility of (15).

4 H_∞ State-Feedback Control for Time-Delayed LPV System

In this section, the analysis results developed in the previous section are used for the synthesis of a state-feedback parameter-varying controller for LPV systems with time varying state delay.

The problem addressed is to seek a parameter-dependent state-feedback controller of the form

$$u(t) = K(\theta)x(t) + K_d(\theta)x(t - \tau(t)) \tag{16}$$

Such that the closed loop system, over all trajectories $\theta(t) \in \Theta$, is

- Asymptotically stable.
- Provides a guaranteed L_2 performance attenuation gain from w to z satisfying $\|z\|_2 < \gamma \|w\|_2$ with $x(\eta) = 0, \ \eta \in [-\tau_{max}, 0]$ *and* $w(t) \neq 0$.

Then, the corresponding closed-loop system can be denoted by

$$\begin{cases} \dot{x}(t) = A_{cl}(\theta)x(t) + A_{cld}(\theta)x(t-\tau(t)) + B_1(\theta)w(t) \\ z(t) = C_{cl}(\theta)x(t) + C_{cld}(\theta)x(t-\tau(t)) + D_1(\theta)w(t) \end{cases} \tag{17}$$

Where

$$\begin{aligned} A_{cl}(\theta) &= A(\theta) + B_2(\theta)K(\theta) \\ A_{cld}(\theta) &= A_d(\theta) + B_2(\theta)K_d(\theta) \\ C_{cl}(\theta) &= C(\theta) + D_2(\theta)K(\theta) \\ C_{cld}(\theta) &= C_d(\theta) + D_2(\theta)K_d(\theta) \end{aligned}$$

Clearly these matrices are bilinear with respect to the parameters of the controller $K(\theta)$ and $K_d(\theta)$. To avoid this bilinearity, we can assume that input and output matrices are invariant. That is: $B_2(\theta) = B_2$ and $D_2(\theta) = D_2$.

The following Theorem provides the synthesis condition for such a state-feedback H_∞ controller.

Theorem 4.1. Consider the time-delayed LPV system (1). There exist a parameter-dependent controller such that the closed-loop system (17) is robustly asymptotically stable for any dependent time delay $\tau(t)$ satisfying both $0 < \tau(t) \le \tau_{max}$ and $\frac{\|z\|_2}{\|w\|_2} < \gamma$ if there exist positive-definite matrices $\hat{P}(\theta)$, $\hat{Q}(\theta)$, $\hat{R}(\theta), \hat{M}_1(\theta), \hat{M}_2(\theta) \in \Re^{n\times n}$, matrix $V \in \Re^{n\times n}$, and matrices $Y(\theta)$, $Y_h(\theta) \in \Re^{m\times n}$ such that for all $\theta(t) \in \Theta$:

$$\begin{pmatrix} \Theta_{11}(\theta) & \Theta_{12}(\theta) & \Theta_{13}(\theta) & B_1(\theta) & 0 & V^T & \tau_{\max}\hat{R}(\theta) & 0 \\ (*) & \Theta_{22}(\theta) & \Theta_{23}(\theta) & 0 & \Theta_{25}(\theta) & 0 & 0 & \tau_{\max}\hat{M}_1^T(\theta) \\ (*) & (*) & \Theta_{33}(\theta) & 0 & \Theta_{35}(\theta) & 0 & 0 & \tau_{\max}\hat{M}_2^T(\theta) \\ (*) & (*) & (*) & -\gamma I & D_1^T(\theta) & 0 & 0 & 0 \\ (*) & (*) & (*) & (*) & -\gamma I & 0 & 0 & 0 \\ (*) & (*) & (*) & (*) & (*) & -\hat{P}(\theta) & -\tau_{\max}\hat{R}(\theta) & 0 \\ (*) & (*) & (*) & (*) & (*) & (*) & -\tau_{\max}\hat{R}(\theta) & 0 \\ (*) & (*) & (*) & (*) & (*) & (*) & (*) & -\tau_{\max}\hat{R}(\theta) \end{pmatrix} < 0 \tag{18}$$

With

$$\begin{aligned} \Theta_{11}(\theta) &= -V - V^T \\ \Theta_{12}(\theta) &= \hat{P}(\theta) + A(\theta)V + B_2 Y(\theta) \\ \Theta_{13}(\theta) &= \hat{P}(\theta) + A_d(\theta)V + B_2 Y_d(\theta) \\ \Theta_{22}(\theta) &= \tfrac{dP(\theta)}{dt} - P(\theta) + Q(\theta) + \hat{M}_1^T(\theta)\hat{M}_1(\theta) \\ \Theta_{23}(\theta) &= -\hat{M}_1^T(\theta) + \hat{M}_2^T(\theta) \\ \Theta_{25}(\theta) &= [C(\theta)V + D_2 Y(\theta)]^T \\ \Theta_{33}(\theta) &= -(1-\mu)\hat{Q}(\theta) - \hat{M}_2^T(\theta) - \hat{M}_2(\theta) \\ \Theta_{35}(\theta) &= [C_d(\theta)V + D_2 Y_d(\theta)]^T \end{aligned}$$

The state-feedback control law providing guaranteed L_2 norm performance γ is given as: $K(\theta) = Y(\theta)V^{-1}\, and\, K_d(\theta) = Y_d(\theta)V^{-1}$.

Proof: Apply the LMI (6) of Theorem 1 to the closed loop system (17) and made the congruence by the matrix $diag(V, V, V, I, I, V, V, V)$.

Defining the new variables

$$\begin{aligned} &V = X^{-1},\ \hat{P}(\theta) = V^T P(\theta)V,\ \hat{Q}(\theta) = V^T Q(\theta)V \\ &\hat{R}(\theta) = V^T R(\theta)V,\ \hat{M}_1(\theta) = V^T M_1(\theta)V\, and\, \hat{M}_2(\theta) = V^T M_2(\theta)V \end{aligned}$$

5 Numerical Example

We consider the LPV time-delay system

$$\begin{aligned} \dot{x}(t) &= \begin{pmatrix} -1 & \theta_1 \\ 1 & 1+\theta_2 \end{pmatrix} x(t) + \begin{pmatrix} 1+\theta_2 & -1 \\ \theta_1 & -1 \end{pmatrix} x(t-\tau(t)) + \begin{pmatrix} 1 \\ 0 \end{pmatrix} w(t) + \begin{pmatrix} 1 \\ 0 \end{pmatrix} u(t) \\ z(t) &= \begin{pmatrix} 0 & 1 \\ 0 & 0 \end{pmatrix} x(t) + \begin{pmatrix} 0 & 1 \end{pmatrix} u(t) \end{aligned} \tag{19}$$

Where θ_1 and θ_2 are varying parameters in the following uncertainty range: $\theta_1 \in [-0.5\ \ 0.5], \theta_2 \in [-0.4\ \ 0.4]$.

The control objective is to minimize γ performance bound and maintain a reasonable control effort. We use the Theorem 4.1 to derive an H_∞ state feedback problem.

Table 1 present a comparison of the H_∞ norms obtained, using the results of this paper with the results in [14]. It is evident from the Table 1 that the controller design method proposed in this paper provides a lower and better H_∞ performance level.

Table 1. The minimized γ performance bound when τ_{max}

	$\mu = 0$	$\mu = 0.5$	$\mu = 0.7$	$\mu = 0.99$
[16]	3.136	3.527	3.694	6.766
Theorem 4.1	1.028	1.455	2.102	6.233

Table 2 show that the maximum time-delay allowing the controller synthesis as obtained in this paper is much larger than the results in both [14]. This shows that the method in this paper would be less conservative and allow for a larger delay range.

Table 2. The maximum time-delay

	$\mu = 0$	$\mu = 0.5$	$\mu = 0.7$	$\mu = 0.99$
[16]	0.7	0.62	0.53	0.5
Theorem 4.1	0.78	0.65	0.55	0.52

For simulation purposes let $\tau(t) = 0.3|sin(t)|$ *and* $\theta(t) = sin(t)$.

The external disturbance is a rectangular.

The closed loop behavior of the system using the LPV state-feedback control laws designed using the results in this paper and the results in [14] are simulated, respectively. The states are shown in Fig. 1 and the control input is shown in Fig. 2.

The dashed lines are obtained using the controller designed using the result in [14] and the solid lines are obtained using the controller designed using the results in the present paper.

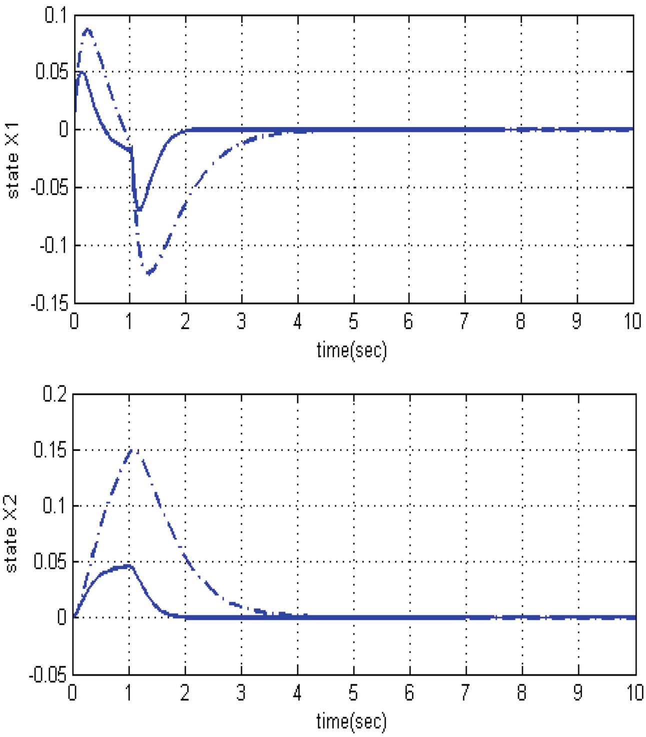

Fig. 1. States evolution (Time delay $\tau(t) = 0.3|sin(t)|$).

Clearly, with our method, the states x_1 and x_2 converge to zero more rapidly than with the method of [14].

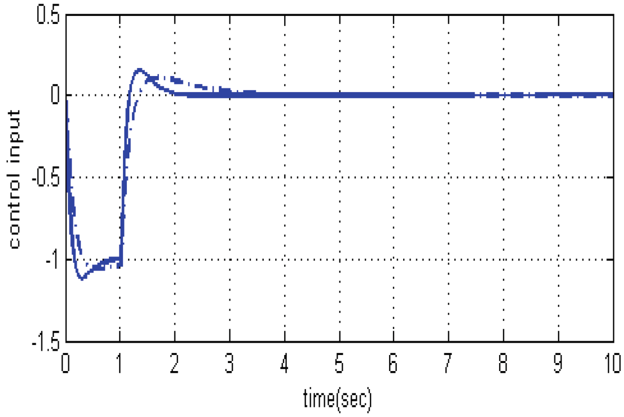

Fig. 2. Control input States evolution (Time delay $\tau(t) = 0.3|sin(t)|$).

6 Conclusion

In this paper, the robust stability analysis and H_∞ state-feedback control synthesis problem of LPV systems with time varying state delay are addressed. Based in the parameter dependent Lyapunov-Krasovskii functional approach, the delay-dependent stability and induced L_2 norm performance are explored. New H_∞ performance approach and state-feedback controller are derived and the corresponding conditions are given in terms of LMIs. This approach eliminated the product of the Lyapunov matrices and the system matrices in the derivative of the Lyapunov functional. Finally, we show the effectiveness of our approach compared to other one trough an example.

References

1. Man, S., Jia, Y., Du, J., Yu, F.: Robust H_2/H_∞ control for time-delay systems with polytopic uncertainty. Asian J. Control **11**(1), 11–20 (2009)
2. Zhang, O.: H_2/H_∞ control for stochastic systems with delay. Asian J. Control **88**(12), 2554–2562 (2015)
3. Xie, W.: Improved delay independent H_2 performance analysis and memoryless state feedback for linear delay systems with polytopic uncertainties. Int. J. Control Autom. Syst. **6** (2), 263–268 (2008)
4. Olgac, N., Sipahi, R.: An exact method for the stability analysis of time-delayed linear time-invariant (LTI) systems. IEEE Trans. Autom. Control **47**(5), 793–797 (2002)
5. Moon, Y.S., Park, P.G., Kwon, W.H., Lee, Y.S.: Delay-dependent robust stabilization of uncertain state-delayed systems. Int. J. Control **74**(14), 1447–1455 (2001)
6. Xia, Y., Jia, Y.: Robust control of state delayed systems with polytopic type uncertainties via parameter-dependent Lyapunov functional. Syst. Control Lett. **50**(3), 183–193 (2003)
7. Syng, W.Y., Chol, Y.J., Park, P.: State feedback disturbance attenuation for polytopic LPV systems with input saturation. Asian J. Control **20**(8), 899–922 (2010)

8. Seron, M.M., De Doná, J.A.: Robust fault estimation and compensation for LPV systems under actuator and sensor faults. Automatica **52**, 294–301 (2015)
9. Rugh, W.J., Shamma, J.S.: Research on gain scheduling. Automatica **36**, 1401–1425 (2000)
10. De Caigny, J., Camino, J.F., Oliviera, R.C.L.F., Peres, P.L.D., Swevers, J.: Gain-scheduled dynamic output feedback control for discrete time LPV systems. Asian J. Control **22**(5), 535–558 (2012)
11. Daafouz, J., Bernussou, J., Geromel, J.C.: On inexact LPV control design of continuous-time polytopic systems. IEEE Trans. Autom. Control **53**(7), 1674–1678 (2008)
12. Xie, W., Eisaka, T.: Design of LPV control systems based on Youla parameterization. IEEE Proc. Control Theory Appl. **151**, 465–472 (2004)
13. Zhang, X., Tsiotras, P., Knospe, C.: Stability analysis of LPV time-delayed systems. Int. J. Control **75**, 538–558 (2002)
14. Briat, C., Sename, O., Lafay, J.: Memory resilient gain-scheduled state-feedback control of uncertain LTI/LPV systems with time-varying delays. Syst. Control Lett. **59**(8), 451–459 (2013)
15. Zhang, F., Grigoriadis, K.M.: Delay-dependent stability analysis and H_∞ control for state-delayed LPV system. In: Proceedings of the IEEE International Symposium on Intelligent Control, pp. 1532–1537 (2005)
16. Zhang, X.M., Wu, M., She, J.H., He, Y.: Delay depended stabilization of linear systems with time-varying state and input delays. Automatica **41**(8), 1405–1412 (2005)
17. Tuan, H., Apkarian, P., Nguyen, T.: Robust filtering for uncertain non linearly parameterized plants. IEEE Trans. Signal Process. **51**(7), 1806–1815 (2003)
18. Gahinet, P., Apkarian, P.: A linear matrix inequality approach to H_∞ controls. Int. J. Robust. Non linear Control **4**(4), 421–448 (1994)

Iterative Learning Control of a Parallel Delta Robot

Chems Eddine Boudjedir[1(✉)], Djamel Boukhetala[1], and Mohamed Bouri[2]

[1] Ecole Nationale Polytechnique (ENP), 10 Rue des Freres OUDEK, El-Harrach, 16200 Algiers, Algeria
{chemseddine.boudjedir,djamel.boukhetala}@g.enp.edu.dz
[2] Ecole Polytechnique Fédérale de Lausanne (EPFL), Station 9, 1015 Lausanne, Switzerland
Mohamed.bouri@epfl.ch

Abstract. In this work, an iterative learning control (ILC) is applied to a Delta robot in order to improve the tracking precision at high dynamic movement. Delta robot is a parallel manipulator designed for high-speed pick and place operations. Since the dynamic of Delta robot is highly coupled and nonlinear, the conventional controller like the proportional derivative (PD) failed to satisfy the required performances. To solve this problem a suitable controller for repetitive pick and place operations represents in the ILC has been introduced. The learning controller is combined with a PD controller to improve the tracking error through the iterations. Numerous simulations and robustness tests are carried out to demonstrate the effectiveness of the proposed scheme.

Keywords: Iterative learning control · Delta robot · High dynamic movement PD control

1 Introduction

The architecture design of Parallel Kinematic Manipulators (PKM) knew a huge progress over the years, starting from the 5 degrees of freedom (dof) of Pollard [1] to the 6 dof of Stewart platform [2] up to the 4 dof of Delta robot [3]. PKM plays a very important role in the industry due to the advantage they present compared to the serial arms, such as higher load capacity and more rigidity and accuracy.

The Delta robot was invented by Reymond. Clavel in 1985 [4] from the EPFL (Ecole Polytechnique Fédérale de Lausanne), where it dedicates to execute pick and place operations at a high dynamic movement. The first prototype has three dof for translation and one dof for rotation, after that, various designs with Delta link architecture were developed, for instance, the Linear Delta [5] and the Inverted Delta [6]. For more designs of the Delta robot the reader may refer to the survey [7].

The traditional controllers like PD/PID are usually used to control the robot manipulators due to its easy synthesis and implementation. However, PD/PID failed to track the desired trajectory for high-speed pick and place tasks, because the gains of the controller are selected without considering the coupling effects. To overcome this

M. Chadli et al. (Eds.): ICEECA 2017, LNEE 522, pp. 72–83, 2019.
https://doi.org/10.1007/978-3-319-97816-1_6

problem many advanced control strategies have been proposed, for instance, decentralized variable structure control [8], robust linear H-infinity control [9] and hybrid PD sliding mode control [10].

Robot manipulators are usually used for repetitive tasks, this repetitive nature makes it logical to try exploiting the information of the previous cycles in order to improve the tracking performance of the actual cycle, which is the main idea of ILC. ILC introduced as a formal theory by Arimoto in 1984 [11], where he proposes several control schemes like PD-type and PID-type. Over the years, many interesting works concern ILC have been developed, for instance, adaptive ILC [12] [13], robust ILC [14], fuzzy logic ILC [15] and velocity observer of actuated joint [16].

The main advantage of ILC is its ability to benefit from the system repeatability contrary the most well-known controllers, also, ILC characterizes by its easy implementation and its practicability, where, as it has shown by Arimoto [17] that the tracking trajectory can improve from iteration to iteration using only the tracking position error information and its derivative. It is noted that ILC has been applied in many areas, such as the serial robot, the chemical process [18], and the laser cutting [19]. The successful implementation of ILC is summarized in the survey [20].

Only a few works concerned the application of the ILC on PKM such as [21], where the author applied ILC on the PaLiDA robot to decrease the remaining errors at high-speed motions.

To the best knowledge of the authors, this is the first application of the ILC on the Delta robot, where a PD-type ILC is combined with a PD feedback controller to improve the tracking error through the iterations. To illustrate the efficacy and the feasibility of this approach simulation are carried out and followed by a comparative study with the conventional PD controller. In order to test the robustness of the proposed controller, a payload mass is added to the travelling plate.

The rest of this paper is organized as follows: In Sect. 2 general description and dynamic model of the Delta robot are presented. Section 3 the PD plus ILC controller is proposed. Section 4 presents simulation results which are discussed at the final Sect. 5.

2 Dynamic Modeling

The Delta robot described in Fig. 1, composes of a fixed base, travelling plate and three identical and symmetrical kinematic chains plus a fourth inner leg connects between the fixed base and the travelling plate which is actually the robot's end effector. Each kinematic chain consists of servo motors and reducers with a gear ratio equal 12, they are arranged on the base platform with 120° to each other. The actuating arm (upper arm) is connected with the reducer and the forearm, while the forearm, which is made up of a parallelogram is connected with the actuating arm and the travelling platform. The travelling platform is kept parallel to the base platform due to the characteristic of the parallelogram.

The dynamic model of the Delta robot is derived based upon the principle of virtual work developed in [21]. It is given by:

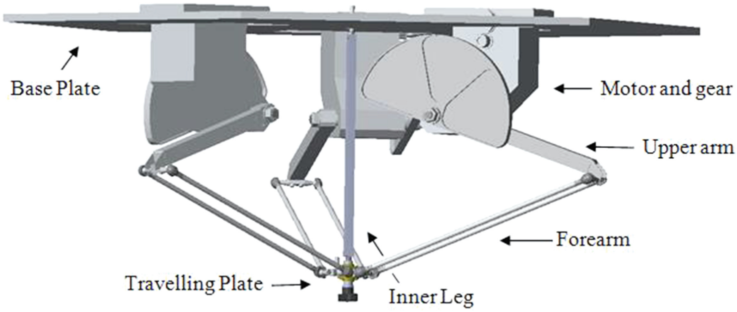

Fig. 1. The delta robot

$$M(q)\ddot{q} + C(q,\dot{q})\dot{q} + G(q) = \tau \tag{1}$$

where:

$M(q) = I_b + m_{nt}J^T J$
$C(q,\dot{q}) = J^T m_{nt}\dot{J}$
$G(q) = -\tau_{Gn} - \tau_{Gb}$

and $q = [q_1, q_2, q_3]^T$ is the generalized joint vector, $M(q) \in \mathrm{R}^{3\times3}$ is the inertia matrix, $C(q,\dot{q})\dot{q} \in \mathrm{R}^{3\times3}$ is a vector resulting from Coriolis and centrifugal forces, $G(q) \in \mathrm{R}^{3\times1}$ represents the vector resulting from the gravitational forces, τ is the control input vector containing the torques to be applied at each joint, τ_{Gn} is the torque produced by the inertial force, τ_{Gb} is the torque produced by the gravitational force of the arms, J represents the Jacobian matrix and $\dot{J}$ is its derivative respect to time, m_{nt} represents the total mass which is the sum of the travelling plate mass m_n, the mass of the payload $m_{payload}$, and the 3 reported masses contributed each of the 3 forearms.

$$m_{nt} = m_n + m_{payload} + 3(1 - r)m_{ab}$$

r is the ratio of the mass of the forearms that is located at their upper extremities. r is chosen to be equal to 2/3. At the arm level, the position of the center of mass of the arm is calculated as:

$$r_{Gb} = L_A \frac{\frac{1}{2}m_{br} + m_c + m_{fb}}{m_b} \tag{2}$$

with

$$m_b = m_{br} + m_c + rm_{fb}$$

Where the geometrical and Dynamic parameters of the manipulator are described in Table 1.

Table 1. Geometric and dynamic parameters

Parameter	Description	Value
L_A	Length of upper arm	0.380 m
L_B	Length of forearm	0.205 m
m_n	Mass of the travelling plate	0.042 kg
m_{br}	Mass of the upper arm	0.098 kg
m_{fb}	Masses of the forearms	0.028 kg
m_c	Mass of the elbow	0.015 kg

I_b is a diagonal matrix represents the inertia of the arms in joint space, where is the sum of the inertia created by the upper arm and inertia created from the contact with the forearm and the inertia created by the motor I_m multiplied with the quadratic of the gear ratio r_g.

$$I_b = I_m r_g^2 + L_A^2\left(\frac{m_{br}}{3} + m_c + r m_{fb}\right) \tag{3}$$

The expression of τ_{Gn} and τ_{Gb} is given by:

$$\tau_{Gn} = J^T m_{nt} \begin{bmatrix} 0 & 0 & -g \end{bmatrix}^T \tag{4}$$

$$\tau_{Gb} = m_b r_{Gb} g \begin{bmatrix} cosq_1 & cosq_2 & cosq_3 \end{bmatrix}^T \tag{5}$$

For the detailed expressions of the Jacobian please refer to [22].

3 Controller Design

In this section, we present the proposed torque control for the parallel Delta robot.

The controller is implemented in joint space and its expression is given by:

$$\tau_k = K_p \tilde{q}_k + K_d \dot{\tilde{q}}_k + u_k \tag{6}$$

While the PD-ILC algorithm can be expressed by:

$$u_{k+1} = u_k + \Lambda \tilde{q}_k + \Gamma \dot{\tilde{q}}_k \tag{7}$$

The terms $\tilde{q}_k$ and $\dot{\tilde{q}}_k$ are given as follows:

$$\tilde{q}_k = q_d - q_k, \dot{\tilde{q}}_k = \dot{q}_d - \dot{q}_k$$

The index k denotes the iteration number, q_d and $\dot{q}_d$ represent the desired joint position and the desired joint velocity respectively, since K_p, K_d, Γ, and Λ are diagonal gains matrices.

The scheme of the proposed controller is illustrated in Fig. 2, where x_d represents the desired trajectory in the task space and IGM indicates the inverse geometric model.

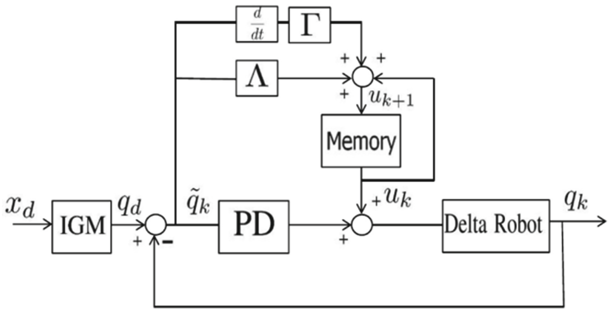

Fig. 2. The proposed control schema

As it can be seen from the scheme of the controller, a very important aspect of the ILC reside in its easy implementation and integration in the industrial robots, where it needs only to use and to store the error information and its derivative to pursue the desired trajectory.

4 Simulation

The desired pick and place trajectory is used along the x-axis and the z-axis, where it is a polynomial of degree five with initial and final velocity and acceleration equal to zero. An important characteristic of this trajectory is its continuity of the movement, in position, velocity, and acceleration.

The desired trajectory used along the x-axis and the z-axis is given as follows:

$$\begin{aligned}
x(t) &= -0.20 + 0.40(6\frac{t}{t_f}^5 - 15\frac{t}{t_f}^4 + 10\frac{t}{t_f}^3) \quad 0 \le t \le t_f \\
z(t) &= -0.40 + 0.05(6\frac{t}{t_f}^5 - 15\frac{t}{t_f}^4 + 10\frac{t}{t_f}^3) \quad 0 \le t \le \frac{t_f}{2} \\
z(t) &= -0.35 - 0.05(6\frac{t}{t_f}^5 - 15\frac{t}{t_f}^4 + 10\frac{t}{t_f}^3) \quad \frac{t_f}{2} \le t \le t_f
\end{aligned} \tag{8}$$

Where t_f is the duration of the movement.

Therefore the desired trajectory starts from $(-0.2, 0, -0.4)$ m *to* $(0.2, 0, -0.4)$ m *then* $(-0.2, 0, -0.4)$m with a height of transit 0.05 m. All this movement was performed in 0.5 s without payload as shown in Fig. 3 To judge the performance, quality of the controller, the Maximum Absolute Error (MaxAE) and the Root Mean Square Error (RMSE) criteria have been utilised, their expressions are given by:

$$MaxAE_x = max(|x_i - x_{d_i}|) \tag{9}$$

$$RMSE_x = \sqrt{\frac{1}{n}\sum_{i=1}^{n}(x_i - x_{d_i})^2} \tag{10}$$

where x_d is the desired trajectory, x_i is the actual response, and n is the total number of samples in one iteration. The MaxAE and the RMSE expression when considered all the three axes is given as follows:

$$MaxAE = \max(MaxAE_x, MaxAE_y, MaxAE_z) \tag{11}$$

$$RMSE = \sqrt{RMSE_x^2 + RMSE_y^2 + RMSE_z^2} \tag{12}$$

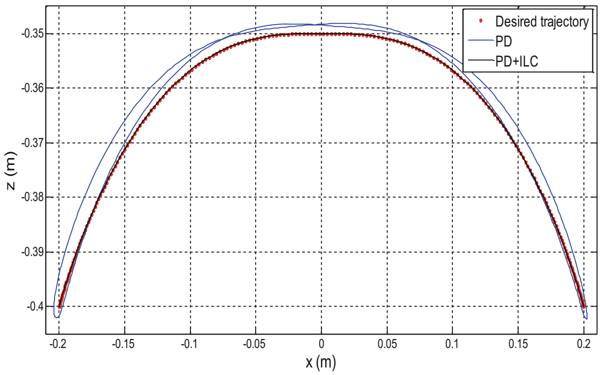

Fig. 3. The trajectory tracking under the proposed controller.

The controller gains were selected so that the minimum performance criteria specified by the MaxAE and the RMSE is obtained after 80 iterations:

$$K_p = diag\{6.00\}, K_d = diag\{0.0625\}\Lambda = diag\{0.34\}, \Gamma = diag\{0.06\}$$

Figure 3 indicates the trajectory tracking performance after 80 iterations under the PD controller and the PD plus ILC controller. Figures 4, 5, 6 and 7 show the progress through the iteration of the RMSE, the MAXE, the tracking error for joint 1 and the tracking error for joint 2 respectively, (the tracking error of joint 3 is similar to the joint 2 due to the nature of the trajectory). It is observed that with the combination of the ILC and the conventional PD controller the tracking error can improve from iteration to iteration where it can tend to zero when the number of iterations tends to infinity. Figures 8 and 9 represent the control torque for joint 1 and joint 2 respectively. As it can be seen the proposed controller has the same variation with low amplitude compared to the PD controller, which provide a very important advantage of the controller, where it can enhance the tracking error with less energy.

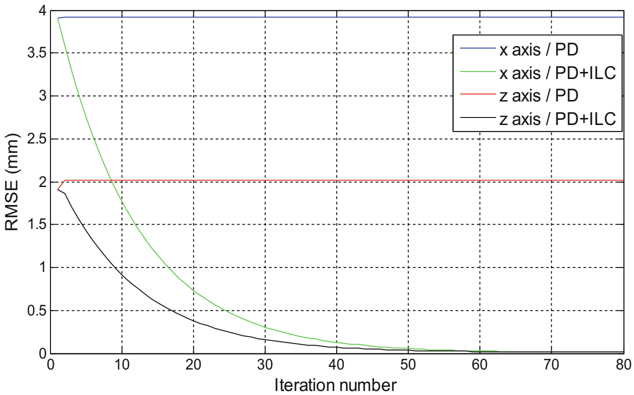

Fig. 4. The RMSE along the iteration axis.

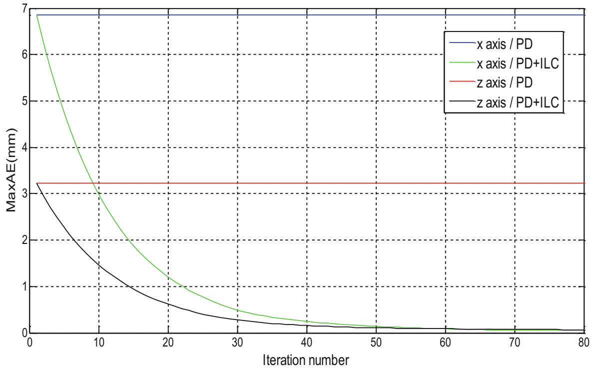

Fig. 5. The MaxAE along the iteration axis.

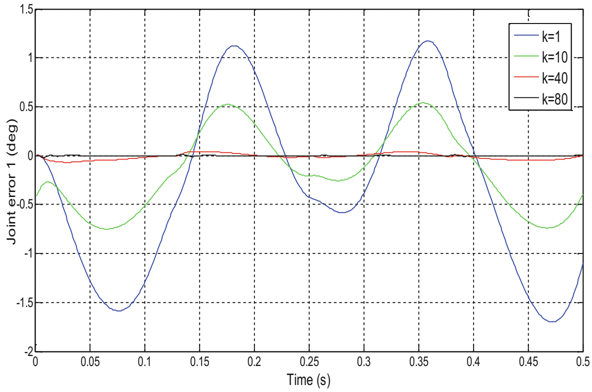

Fig. 6. Tracking error of joint 1 for iteration k = 1, 10, 40, 80.

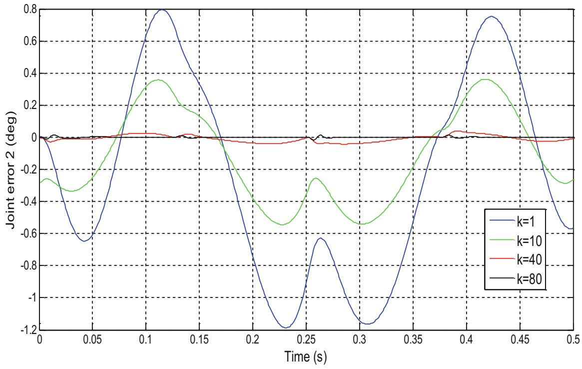

Fig. 7. Tracking error of joint 2 for iteration k = 1, 10, 40, 80.

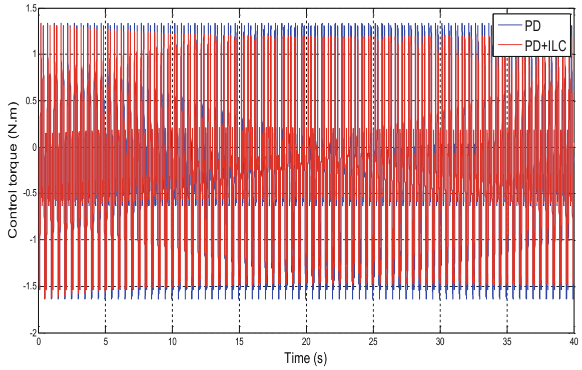

Fig. 8. Control torque of joint 1.

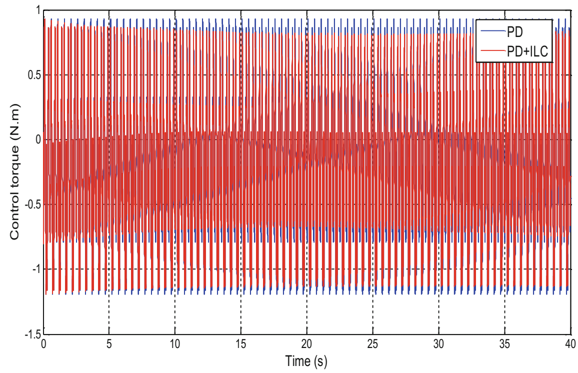

Fig. 9. Control torque of joint 2

Test of Robustness
In order to test the ability to track the desired trajectory in the presence of parametric disturbances, an additional load of 50 g is introduced on the travelling plate of the Delta robot, from the 30 iterations to the 80 iterations.

The simulation results are shown from Figs. 10, 11, 12, 13, 14 and 15. It is observed that the ILC still able to provide better performances with less energy compared to the PD controller, where it can guarantee the robustness against variation parametric, for instance, the RMSE increases along the x-axis from 0.16 mm to 0.39 mm then decrease to 0.02 mm, contrary the PD where it increases from 2.16 mm to 2.35 mm. Table 2 given a detailed performance of the control law. It can be clearly seen that the combination of the PD feedback control with the PD-type ILC present superior performance compared to the conventional PD controller.

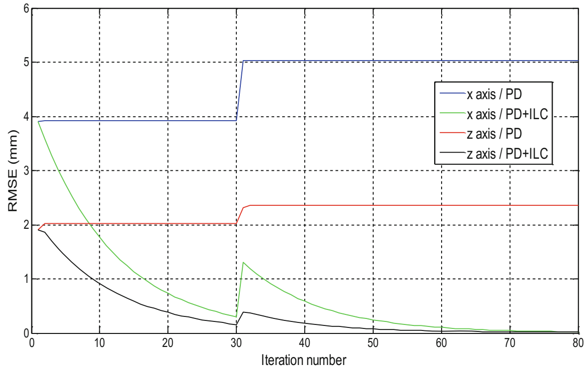

Fig. 10. The RMSE through the iteration in the presence of disturbance.

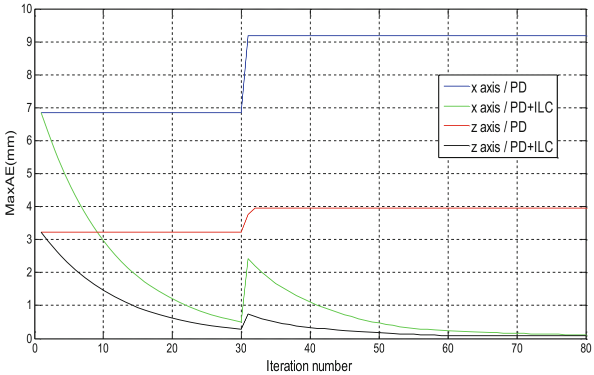

Fig. 11. The MaxAE through the iteration in the presence of disturbance.

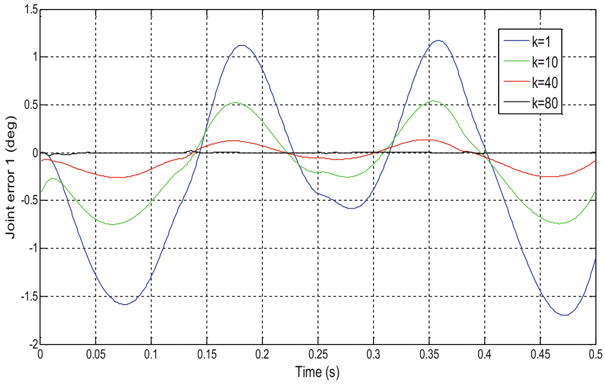

Fig. 12. Tracking error of joint 1 in the presence of disturbance

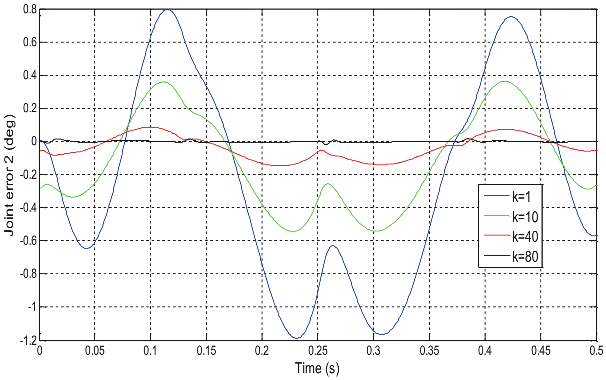

Fig. 13. Tracking error of joint 2 in the presence of disturbance

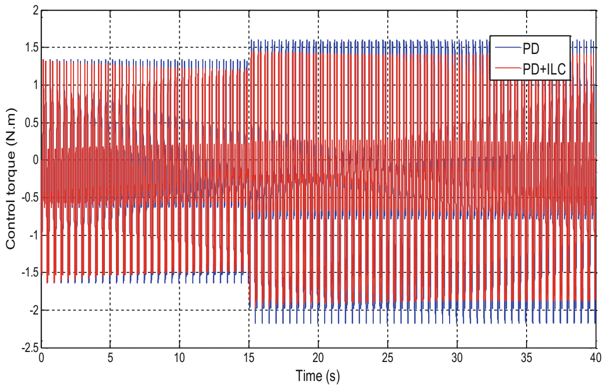

Fig. 14. Control torque of joint 1 in the presence of disturbance.

Table 2. The tracking performances

	Iterations		1	10	40	80
Without disturbances	PD	RMSE (mm)	4.34	4.40	4.40	4.40
		MaxAE (mm)	6.85	6.85	6.85	6.85
	PD + ILC	RMSE (mm)	4.34	1.99	0.15	0.02
		MaxAE (mm)	6.85	2.98	0.25	0.06
With disturbances	PD	RMSE (mm)	4.43	4.40	5.54	5.54
		MaxAE (mm)	6.85	6.85	9.18	9.18
	PD + ILC	RMSE (mm)	4.43	1.99	0.62	0.22
		MaxAE (mm)	6.85	2.98	1.10	0.08

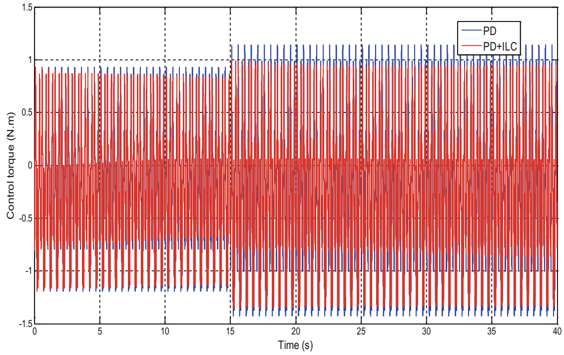

Fig. 15. Control torque of joint 2 in the presence of disturbance.

5 Conclusion

In this paper, a new approach to control the parallel Delta robot has been proposed. The control law scheme consists of a combination of the ILC and the PD feedback control for the purpose to enhance the tracking error from iteration to iteration. A very important advantage of this method is its simple implementation and practicability in the industry. The control algorithm is applied successfully, where a pick and place trajectory has been tested for a travel time equal 0.5 s. Simulation results show better performances and robustness against variation of the loads compared to the traditional PD control. The tracking error converges to zero through the iteration with nearly the same control torque, which means that we can enhance the tracking error without requiring more energy.

References

1. Pollard, W.L.V.: Position controlling apparatus. US Patent No. 2,286,571, 16 June (1942)
2. Stewart, D.: A platform with six degrees of freedom. In: Proceedings of the IMechE, vol. 180, pt. 1, no. 15, pp. 371–385 (1966)
3. Clavel, R.: Device for movement and displacing of an element in space. US Patent n: 4976582, date of patent: 11 December 1990 (1990)

4. Clavel, R.: Conception d'un robot parallèle rapide à 4 degré de liberté [Doctoral Thesis]. Swiss Federal Institute of Technology Lausanne (EPFL) (1991)
5. Bouri, M., Clavel, R.: The linear delta: developments and applications. In: International Symposium on Robotics, Munich, June 2010 (2010)
6. Bouri, M., Clavel, R., Zerrouki, M.Y., Maeder, W.: Towards a new delta robot: an inverted delta. In: Proceedings of the International Symposium of Robotics, Paris (2004)
7. Brinker, J., Covers, B.: A survey on parallel robots with delta-like architecture. In: The 14th IFToMM World Congress, Taipei, Taiwan, October 2015 (2015)
8. Boukhetala, D., Boudjema, F., Madani, T., Boucherit, M.S., M'Sirdi, N.K.: A new decentralized variable structure control for robot manipulators. Int. J. Robot. Autom. **18**(1), 28–40 (2003)
9. Rachedi, M., Hemici, B., Bouri, M.: Design of an H1 controller for the delta robot: experimental results. In: Advanced Robotics, vol. 29, no. 18, pp. 1165–1181, July 2015 (2015)
10. Ouyang, P.R., Acob, J., Pano, V.: PD with sliding mode control for trajectory tracking of robotic system. Robot. Comput. Integr. Manuf. **30**, 189–200 (2014)
11. Arimoto, S., Kawamura, S., Miyazaki, F.: Bettering operation of robots by learning. J. Robot. Syst. **1**(2), 123–140 (1984)
12. Tayebi, A.: Adaptive iterative learning control for robot manipulators. Automatica **40**, 1195–1203 (2004)
13. Zhang, L., Chen, W., Liu, J., Wen, C.: A robust adaptive iterative learning control for trajectory tracking of permanent-magnet spherical actuator. IEEE Trans. Industr. Electron. **63**(1), 291–301 (2016)
14. Li, X., Huang, D., Chu, B., Xu, J.-X.: Robust iterative learning control for systems with norm-bounded uncertainties. Int. J. Robust Nonlinear Control **26**(4), 697–718 (2015)
15. Boudjedir, C.E., Boukhetala, D., Bouri, M.: Fuzzy logic iterative learning control for trajectory tracking of parallel kinematic manipulators. In: 2017 5th International Conference on Electrical Engineering - Boumerdes (ICEE-B), Boumerdes, pp. 1–6 (2017). https://doi.org/10.1109/icee-b.2017.8192041
16. Bouakrif, F., Boukhetala, D., Boudjema, F.: Velocity observer-based iterative learning control for robot manipulators. Int. J. Syst. Sci. **44**(2), 214–222 (2013)
17. Arimoto, S.: Robustness of learning control for robot manipulators. In: IEEE International Conference on Robotics and Automation (1990)
18. Lee, K.S., Bang, S.H., Yi, S., Son, J.S., Yoon, S.C.: Iterative learning control of heat up phase for a batch polymerization reactor. J. Process. Control **6**(4), 255–262 (1996)
19. Tsai, C.H., Chen, C.J.: Application of iterative path revision technique for laser cutting with controlled fracture. Opt. Laser Eng. **41**(1), 189–204 (2004)
20. Ahn, H.S., Chen, Y., Moore, K.L.: Iterative learning control: brief survey and categorization. IEEE Trans. Syst. Man Cybern. C Appl. Rev. **37**(6), 1099–1121 (2007)
21. Abdellatif, H., Feldt, M., Heimann, B.: Application study on iterative learning control of high speed motions for parallel robotic manipulator. In: Proceedings of IEEE International Conference on Control Applications, Germany, October 2006 (2006)
22. Codourey, A.: Dynamic modelling and mass matrix evaluation of the delta parallel robot for axes decoupling control. In: The International Conference on Intelligent Robots and Systems, vol. 3, pp. 1211–1218 (1996)

Boundary Control of Burgers' Equation by Input-Output Linearization

Dyhia Hamdadou[1(✉)], Ahmed Maidi[1], and Jean-Pierre Corriou[2]

[1] Laboratoire de Conception et Conduite des Systèmes de Production (L2CSP), Université Mouloud MAMMERI de Tizi-Ouzou, Tizi-Ouzou, Algeria
hamdadoudyhia@gmail.com, ahmed.maidi@gmail.com

[2] Reaction and Process Engineering Laboratory (LRGP), UMR 7274-CNRS, Lorraine University, ENSIC, 1, rue Grandville, BP 20451 54001 Nancy Cedex, France
jean-pierre.corriou@univ-lorraine.fr

Abstract. This paper addresses the boundary control law of a viscous Burgers' equation with a Dirichlet actuation. The control objective consists in achieving a desired set point for a punctual output defined at a given spatial position. This control problem is characterized by an infinite characteristic index. To tackle this problem in the framework of geometric control, a design approach based on the concept of the characteristic index is proposed. First, it is proposed to convert the boundary control problem to an equivalent punctual control problem based both on the linearization of the equation and the Laplace transform in space domain. Then, to have a finite characteristic index, an auxiliary controlled output is defined and a control law that achieves a global linearization between an external variable (desired set point) and this auxiliary output is derived. To enforce set point tracking of the original punctual output, a control strategy is proposed based on the steady state relation between the punctual and the auxiliary outputs. The performance of the proposed control strategy is evaluated via numerical simulation runs.

Keywords: Boundary control · Burgers' equation · Characteristic index
Distributed parameter systems · Geometric control
Partial differential equations

1 Introduction

Many physical systems exhibit complex dynamics and their characteristic variables (state, controls and outputs) are often inhomogeneous [4, 23]. The modeling of this kind of systems based on first principles leads to partial differential equations [14]. This class of systems is termed distributed parameters systems [23] or also infinite dimensional systems [7].

Basically, the control design problem for a distributed parameter system can be tackled according to two distinguished approaches: early and late lumping [4, 23]. A review of the different control techniques for distributed parameter systems can be found in [19].

The first approach termed early lumping consists in reducing the distributed parameter system to a finite dimensional system, that is, a lumped parameter system. The model reduction is achieved either by approximating the partial differential equations or their

M. Chadli et al. (Eds.): ICEECA 2017, LNEE 522, pp. 84–96, 2019.
https://doi.org/10.1007/978-3-319-97816-1_7

solutions [5, 14, 23]. The early lumping approach allows to take advantage from the well developed and well established control theory of lumped parameter systems. Nevertheless, it is well known that the reduction process often masks the infinite dimensional nature of the distributed parameter system [6, 23, 25] and the design based on the reduced model leads to a controller that achieves poor performance [6]. For these reasons, the second approach, termed late lumping, constitutes an interesting alternative design approach.

The principle of the late lumping approach consists in designing the controller using directly the partial differential equations model [4, 6]. This allows to keep the distributed nature of the system and yields controllers with acceptable quality control [8, 11, 16, 17, 24]. In the case of linear distributed parameter systems, the early lumping approach has been successfully applied using the semigroup theory [7, 10] that extends the finite dimensional control theory to linear distributed parameter systems [7]. On the other hand, the control design of nonlinear distributed parameters based on the late lumping systems is a difficult task and remains an active research area [2, 3]. It might be noted that the development of a unified control theory for nonlinear distributed parameter systems is almost impossible. This research field is investigated case-by-case by assuming the important particular classes of partial differential equations (e.g. first-order hyperbolic equation, quasilinear and nonlinear parabolic equations) [6, 8, 17].

Among important nonlinear partial differential equation, Burgers' equation has attracted considerable attention. This nonlinear second-order partial differential equation describes a flow phenomenon that exhibits both convective and viscous forces [28]. The control of Burgers' equation, which presents a challenging problem, has been addressed by the control community. However, it is worth noting that most contributions are based on the early lumping approach [1, 13, 20, 21, 26]. The control design based on the late lumping approach remains less explored and few contributions are reported in the literature [12, 15].

In this paper, following the late lumping approach, a control strategy that enforces set point tracking for Burger's equation is developed in the framework of the geometric control.

The rest of the paper is structured as follows. The boundary control problem of Burger's equation is formulated in Sect. 2. In Sect. 3, for the controller design purpose, the formulated boundary control problem is converted to a punctual control one. Section 4 is devoted to the controller design. The global strategy that enforces the set point tracking for a given punctual output is presented in Sect. 5. In Sect. 6, the performance of the proposed strategy is demonstrated by simulation. The paper ends with a conclusion.

2 Control Problem Formulation

The control problem addressed in this paper is formulated as follows. Let us consider the following dimensionless viscous Burgers' equation that describes the fluid dynamic behavior [28]:

$$\frac{\partial x(z,t)}{\partial t} = -x(z,t)\frac{\partial x(z,t)}{\partial z} + \nu\frac{\partial^2 x(z,t)}{\partial z^2}, \quad z \in \Omega \tag{1}$$

with the following Dirichlet boundary conditions

$$x(0, t) = 0 \tag{2}$$

$$x(1, t) = u(t) \tag{3}$$

and the initial condition

$$x(z, 0) = x_0(z) \tag{4}$$

with $\Omega = [0, 1]$.

Assume a punctual output variable defined as follows

$$y(t) = x\left(z_i, t\right) \tag{5}$$

where z_i is a given spatial position, that is, $z_i \in \Omega$.

The objective consists in designing a control law $u(t)$ that forces the output variable to track a desired set point reference $y^d(t)$.

In the formulated control problem, z and t are independent space and time variables, respectively. Ω is the spatial domain and $\partial\Omega = \{0, 1\}$ are the boundaries of Ω. $x(z, t)$ is the state (the fluid velocity), $u(t)$ is the manipulated variable (actuation) applied at $z = 1$ and $x_0(z)$ is the initial spatial profile. $v > 0$ is the fluid viscosity coefficient.

The aim of the present work is to tackle the boundary control problem in the framework of geometric control. The idea is to achieve a global linearization using the characteristic index concept [6]. Nevertheless, by calculating the successive temporal derivatives of the output variable (5), one concludes that the formulated control problem is characterized by an infinite characteristic index. To overcome this difficulty, it is proposed to convert the boundary control problem to a new one with a punctual actuation and an auxiliary output defined as the spatial weighted average of the state $x(z, t)$ according to [18]. Note that the formulated boundary control problem is characterized by an unbounded control operator that introduces technical complexities, which makes the design problem, based on state theory, difficult [7, 9].

3 Punctual Control Equivalent Form

To derive the punctual control equivalent form of the formulated boundary control problem, the Laplace transform in the spatial domain is used [16]. To exploit this Laplace transform property, let us introduce the following change of variables

$$\xi = 1 - z \tag{6}$$

$$x(z, t) = x(1 - \xi, t) \tag{7}$$

$$= w(\xi, t) \tag{8}$$

hence, Burgers' Eq. (1) is transformed as

$$\frac{\partial w(\xi,t)}{\partial t} = w(\xi,t)\,\frac{\partial w(\xi,t)}{\partial \xi} + \nu\,\frac{\partial^2 w(\xi,t)}{\partial \xi^2}, \quad \xi \in \Omega \tag{9}$$

with the following boundary conditions

$$w(0,t) = u(t) \tag{10}$$

$$w(1,t) = 0 \tag{11}$$

and the output variable (5) takes the following form

$$y(t) = w\left(\xi_i, t\right), \quad \xi_i \in \Omega \tag{12}$$

The next step consists in performing a linearization of the resulting Burgers' Eq. (9) around the steady state profiles w_s for a given u_s. For this purpose, the technique of small perturbations is used. Assume that the control $u(t)$ is perturbed by a small amount $\varepsilon\, U(t)$ that results in a small variation $\varepsilon\, W(\xi,t)$ of the state $W(\xi,t)$, that is,

$$u(t) = u_s + \varepsilon\, U(t) \tag{13}$$

$$w(\xi,t) = w_s + \varepsilon\, W(\xi,t) \tag{14}$$

where ε is a small positive number.

Then by substituting the variables $w(\xi,t)$ and $u(t)$ by their expressions given by (14) and (13) in Eqs. (9), (10) and (11), we obtain

$$\varepsilon\,\frac{\partial W(\xi,t)}{\partial t} = \varepsilon^2\, W(\xi,t)\frac{\partial W(\xi,t)}{\partial \xi} + \varepsilon\; w_s\,\frac{\partial W(\xi,t)}{\partial \xi} + \varepsilon\;\nu\,\frac{\partial^2 W(\xi,t)}{\partial \xi^2} \tag{15}$$

$$w_s + \varepsilon\, W(0,t) = u_s + \varepsilon\, U(t) \tag{16}$$

$$w_s + \varepsilon\, W(1,t) = 0 \tag{17}$$

Neglecting the first term of the right-hand side (the second order term $O\left(\varepsilon^2\right)$) of Eq. (15) and dividing by ε, the following linearized equation results

$$\frac{\partial W(\xi,t)}{\partial t} = w_s\,\frac{\partial W(\xi,t)}{\partial \xi} + \nu\,\frac{\partial^2 W(\xi,t)}{\partial \xi^2} \tag{18}$$

In addition, at steady state, from the boundary conditions (10) and (11), it follows that $w_s = u_s$ and $w_s = 0$, therefore Eqs. (16) and (17) yield the following boundary conditions

$$W(0,t) = U(t) \tag{19}$$

$$W(1,t) = 0 \tag{20}$$

for the linearized Eq. (18).

Hence, the Laplace transform in the space domain of Eq. (18) gives

$$\frac{d\overline{W}(s,\,t)}{dt} = w_s\left(s\,\overline{W}(s,\,t) - W(0,\,t)\right) + v\left(s^2\overline{W}(s,\,t) - \left.\frac{\partial W(\xi,t)}{\partial \xi}\right|_{\xi=0} - s\,W(0,\,t)\right) \tag{21}$$

where $\overline{W}(s,\,t)$ is the Laplace transform in the space domain of $W(\xi,\,t)$. Then, taking into account the boundary condition (19), Eq. (21) can be written

$$\frac{d\overline{W}(s,\,t)}{dt} = w_s\left(s\,\overline{W}(s,\,t) - U(t)\right) + v\left(s^2\overline{W}(s,\,t) - \left.\frac{\partial W(\xi,t)}{\partial \xi}\right|_{\xi=0} - s\,U(t)\right) \tag{22}$$

or equivalently as follows

$$\frac{d\overline{W}(s,\,t)}{dt} = w_s\left(s\,\overline{W}(s,\,t) - \mathrm{W(0,t)} - U(t)\right) + v\left(s^2\overline{W}(s,\,t) - \left.\frac{\partial W(\xi,t)}{\partial \xi}\right|_{\xi=0} - s\,W(0,t)\right) - vsU(t) \tag{23}$$

with

$$W(0,\,t) = 0 \tag{24}$$

Applying the inverse Laplace transform in (23), we get

$$\frac{\partial W(\xi,t)}{\partial t} = w_s\frac{\partial W(\xi,\,t)}{\partial \xi} + v\frac{\partial^2 W(\xi,\,t)}{\partial \xi^2} - \left(w_s\,\delta(\xi) + v\,\frac{d\delta(\xi)}{d\xi}\right)U(t) \tag{25}$$

with the following boundary conditions

$$W(0,\,t) = 0 \tag{26}$$

$$W(1,\,t) = 0 \tag{27}$$

where $\delta(\xi)$ is Dirac delta-function [22].

Equations (25), (26) and (27) represent the equivalent punctual control form of the linearized boundary control Eq. (18) with boundary conditions (19) and (20). Clearly, for any steady state profile w_s, the boundary condition (26) is homogeneous and the control variable $U(t)$ appears in state-space Eq. (25). Consequently, the certainty equivalence principle yields the following nonlinear punctual control form

$$\frac{\partial w(\xi,t)}{\partial t} = w(\xi,\,t)\frac{\partial w(\xi,\,t)}{\partial \xi} + v\frac{\partial^2 w(\xi,\,t)}{\partial \xi^2} - \left(w_s\,\delta(\xi) + v\,\frac{d\delta(\xi)}{d\xi}\right)u(t) \tag{28}$$

$$w(0,\,t) = 0 \tag{29}$$

$$w(1,\,t) = 0 \tag{30}$$

of the boundary control form given by Eqs. (1), (2) and (3).

Figure 1 illustrates the physical meaning of the transformation of the boundary actuation to a punctual actuation. In the equivalent punctual problem, the actuation is applied inside the space domain Ω whereas in the boundary case, the actuation is applied through the boundary condition $\partial\Omega$ at $z = 1$.

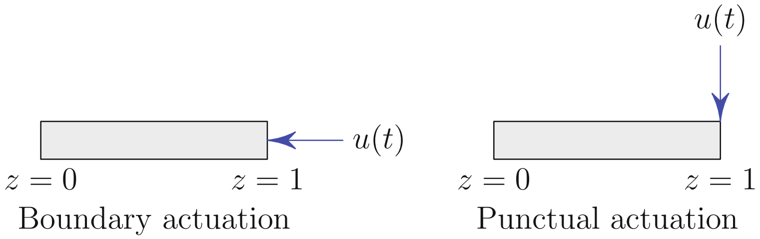

Fig. 1. Equivalence between boundary and punctual actuations.

Note that, in the obtained equivalent punctual control, the control $u(t)$ appears in the state Eq. (28), that allows to take advantage from the state control theory, which is done in this work in the framework of geometric control.

Now, it is easy to verify that this punctual boundary control with the output (12) is also characterized with an infinite characteristic index. Thus, to have a finite characteristic index, the approach proposed by [18] is used. Instead of controlling the punctual output (12), the following auxiliary output is considered

$$y_m(t) = \int_0^1 \xi\, w(\xi, t)\, d\xi \tag{31}$$

which is the spatial weighted average of the state $w(\xi, t)$.

Remark 1. *Notice that Eq.* (31) *with respect to the space variable z yields*

$$y_m(t) = \int_0^1 (1 - z)\, x(z, t)\, dz \tag{32}$$

4 Input-Output Linearization

In this section, a control law $u(t)$ that forces the auxiliary output (31) to track a desired set point reference $y_m^d(t)$ is derived using the notion of the characteristic index from the geometric control theory. Thus, the first time derivative of (31) yields

$$\begin{aligned} \frac{dy_m(t)}{dt} &= \int_0^1 \xi \frac{\partial w(\xi, t)}{\partial t}\, d\xi \\ &= \underbrace{\int_0^1 \xi \left(w(\xi, t) \frac{\partial w(\xi, t)}{\partial \xi} + \nu \frac{\partial^2 w(\xi, t)}{\partial \xi^2} \right) d\xi}_{I_1} \end{aligned} \tag{33}$$

$$\underbrace{-\left[\int_0^1 \xi \left(w_s\, \delta(\xi) + v\, \frac{d\delta(\xi)}{d\xi}\right) d\xi\right] u(t)}_{I_2} \tag{34}$$

Then, by taking into account the properties of the Dirac delta-function [22], the integration by parts of the second integral term of the right-hand side of Eq. (34) gives

$$I_2 = -v \neq 0 \tag{35}$$

which implies that the characteristic index $\sigma = 1$ since the viscosity coefficient $v > 0$.

Remark 2. *From Eq.* (35)*, it may be concluded that the integral term I_2 is actually independent of the steady-state profile w_s.*

Now, having a characteristic index $\sigma = 1$ implies that there exists a control law $u(t)$ that enforces a dynamic behavior of a first-order linear system between the set point reference $y_m^d(t)$ and the auxiliary output $y_m(t)$, that is,

$$\tau\, \frac{dy_m(t)}{dt} + y_m(t) = y_m^d(t) \tag{36}$$

where the time constant τ is the controller tuning parameter used to achieve a desired dynamics of the controlled output $y_m(t)$.

The control law $u(t)$ is obtained easily by substituting $y_m(t)$ and its first derivative $dy_m(t)/dt$ by their expressions given by Eqs. (31) and (34), respectively, into Eq. (36), and solving the resulting algebraic equation with respect to $u(t)$, which leads to the following control law

$$u(t) = \frac{1}{\tau\, v}\left[y_m^d(t) - y_m(t) - \tau \int_0^1 \xi \left(w(\xi, t)\frac{\partial w(\xi, t)}{\partial \xi} + v\frac{\partial^2 w(\xi, t)}{\partial \xi^2}\right) d\xi\right] \tag{37}$$

which can be written under the following form

$$u(t) = \frac{1}{\tau\, v}\left[y_m^d(t) - y_m(t) - \tau \int_0^1 \xi\, w(\xi, t)\frac{\partial w(\xi, t)}{\partial \xi}\, d\xi - v\, \tau \int_0^1 \xi \frac{\partial^2 w(\xi, t)}{\partial \xi^2} d\xi\right] \tag{38}$$

and the integration by parts of the second integral yields

$$u(t) = \frac{1}{\tau\, v}\left[y_m^d(t) - y_m(t) - \tau \int_0^1 \xi\, w(\xi, t)\frac{\partial w(\xi, t)}{\partial \xi}\, d\xi - v\, \tau \left(\xi\, \frac{\partial w(\xi, t)}{\partial \xi} - w(\xi, t)\right)\Bigg|_{\xi=0}^{\xi=1}\right] \tag{39}$$

Hence, by assuming the boundary conditions (29) and (30), the control law (39) results

$$u(t) = \frac{1}{\tau\, v}\left[y_m^d(t) - y_m(t) - v\, \tau\, \frac{\partial w(\xi, t)}{\partial \xi}\bigg|_{\xi=1} - \tau \int_0^1 \xi\, w(\xi, t)\frac{\partial w(\xi, t)}{\partial \xi}\, d\xi\right] \tag{40}$$

Then, by taking into account the change of variables (6) and (8), the obtained control law (40) can be expressed with respect to the original space variable z as follows

$$u(t) = \frac{1}{\tau\,\nu}\left[y_m^d(t) - y_m(t) + \nu\,\tau\,\frac{\partial x(z,\,t)}{\partial z}\bigg|_{z=0} + \tau\int_0^1 (1-z)\,x(z,\,t)\frac{\partial x(z,\,t)}{\partial z}\,dz\right] \tag{41}$$

5 Global Control Strategy

As explained above, the auxiliary output (31) is introduced only to ensure the existence of a finite characteristic index. But recall that the main objective is to control the punctual output (5). Note that the designed control law (41) forces the auxiliary output $y_m(t)$ to track its desired set point reference $y_m^d(t)$. In this section, a control strategy is proposed to force the punctual output (12), that is, the punctual output (5) to track its set point reference $y^d(t)$.

At steady state, a relation between y_{m_s} and y_s can be found by simulation runs by assuming several values of the desired output $y_m^d(t)$. It is worth noting that this relation cannot be carried out analytically due to the nonlinear nature of Burgers' equation. Let us denote the mapping, at steady-state between y_{m_s} and y_s, by f, that is,

$$y_{m_s} = f\left(y_s\right) \tag{42}$$

Now, as

$$y_{m_s} = \lim_{t\to\infty} y_m(t) \tag{43}$$

the desired set point reference $y_m^d(t)$ can be defined with respect to $y^d(t)$ using Eq. (42). Therefore, the control law (41) takes the following form

$$u(t) = \frac{1}{\tau\,\nu}\left[f\left(y^d(t)\right) - y_m(t) + \nu\,\tau\,\frac{\partial x(z,\,t)}{\partial z}\bigg|_{z=0} + \tau\int_0^1 (1-z)\,x(z,\,t)\frac{\partial x(z,\,t)}{\partial z}\,dz\right] \tag{44}$$

and the structure of the proposed control strategy is given by Fig. 2.

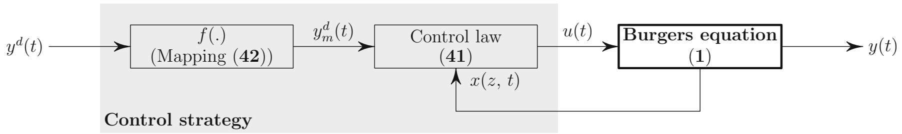

Fig. 2. Structure of the proposed control strategy.

6 Evaluation of the Control Strategy Performance

In this section, the performance of the proposed control strategy is evaluated by means of numerical simulation using the method of lines [27] with 200 spatial discretization points. The integral term of the control law is evaluated using the trapezoidal quadrature. The values used for the parameters are: $\nu = 0.1$ and $\tau = 1$. The initial space profile $x(z, 0) = 0$.

To get a smooth control variation, the desired set point $y^d(t)$ is filtered by a first order system, that is,

$$\tau_f \frac{dy_f^d(t)}{dt} + y_f^d(t) = y^d(t) \tag{45}$$

The first simulation run concerns the tracking capability of the control law (41). Thus a desired set point step $y_m^d(t) = 0.05$ is specified at $t = 1$. Figure 3 shows that the auxiliary output $y_m(t)$ tracks perfectly its reference with a first order dynamics (Eq. 36). The moves of the control law (41) are depicted in Fig. 4.

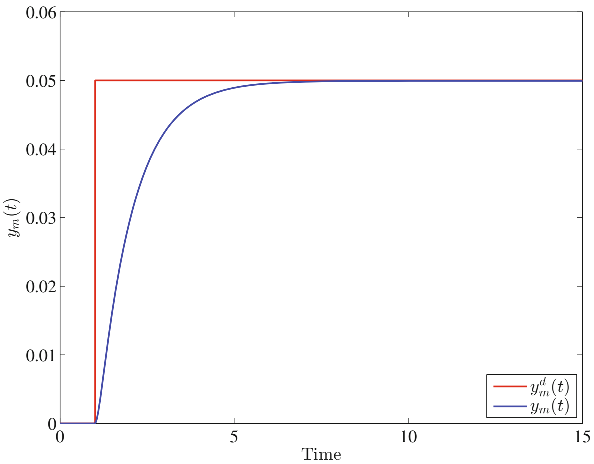

Fig. 3. Evolution of the auxiliary output $y_m(t)$.

The second simulation run deals with the tracking capabilities of the proposed control strategy (see Fig. 2). The objective is to force the state $x(z, t)$ at the position $z_i = 0.5$, that is, the punctual output

$$y(t) = x(0.5, t) \tag{46}$$

to track a specified reference $y^d(t)$.

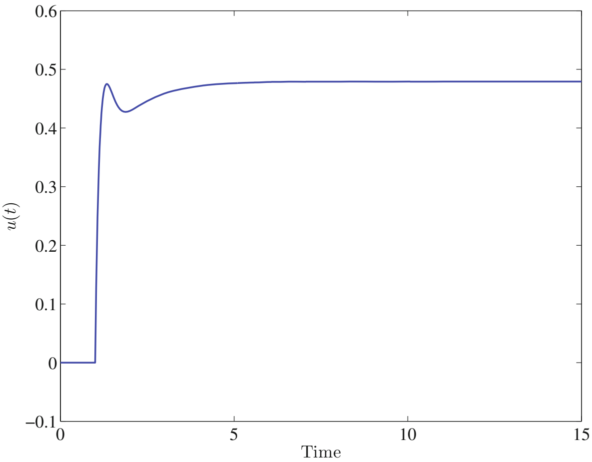

Fig. 4. Evolution of the control $u(t)$.

Let us identify the mapping (42), that is, the function $f(.)$. This is achieved by considering several values of $y_m^d(t)$. Then, the corresponding values of both y_{m_s} and y_s, at steady-state, are collected and fitted (Fig. 5) by the following third-order polynomial

$$y_{m_s} = 0.7971y_s^3 - 0.0514y_s^2 + 0.3402y_s \tag{47}$$

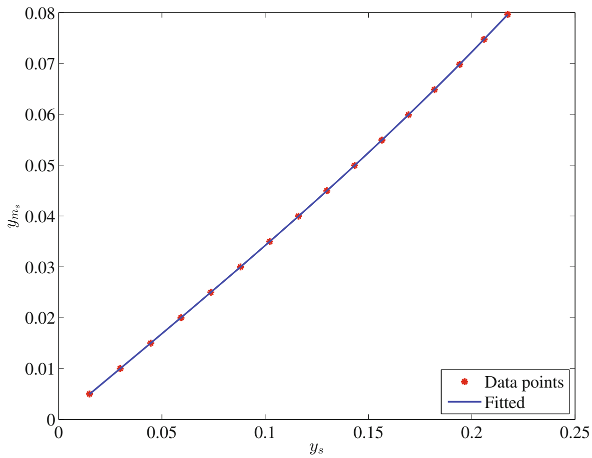

Fig. 5. Data points and best fit.

The mapping (47) allows to define the set point $y_m^d(t)$, used in the control law (41), directly by specifying the desired set point reference $y^d(t)$. In the performed simulation run, two step changes $y^d(t) = 0.1$ and $y^d(t) = 0.2$ are specified at $t = 1$ and $t = 15$, respectively. Figure 6 shows clearly that the tracking of the specified references is achieved with a smooth evolution of the control law $u(t)$ (Fig. 7).

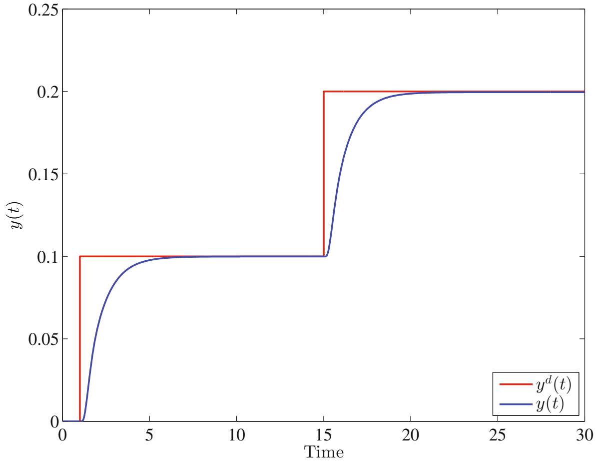

Fig. 6. Evolution of the punctual output $y(t)$.

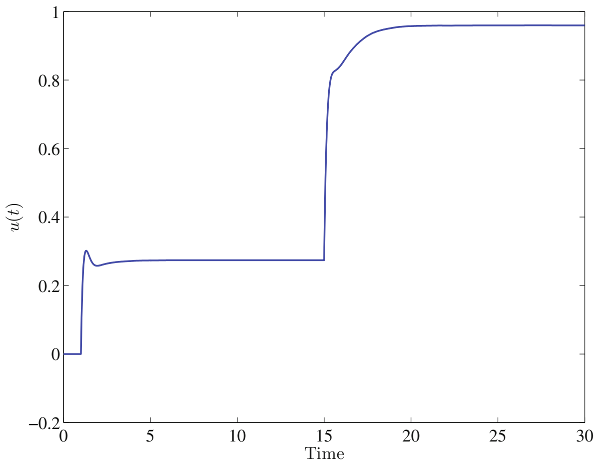

Fig. 7. Evolution of the control $u(t)$.

7 Conclusion

In this paper, a boundary control strategy for a viscous Burgers' equation, with a Dirichlet actuation and punctual output, is proposed. The proposed control strategy involves a state feedback that forces an auxiliary output (the spatial weighted average of the state) to track a set point reference, which is defined as the image of the punctual output set point reference. This image is obtained by means of the steady-state between the two outputs.

To design the state feedback and at the same time overcome the problem of the nonexistence of a characteristic index for the boundary control, an equivalent punctual control problem is derived based on the local linearization (around a steady state profile) and the Laplace transform in the space domain. Thereafter, to make the equivalent punctual problem tractable in the framework of geometric control, an auxiliary output is introduced. Then, based on the notion of the characteristic index, a control law that achieves the set point tracking for the auxiliary output is determined. To solve the original control problem, that is, to control the punctual output, it is proposed to define the set point reference of the auxiliary output from that of the punctual output. This is accomplished by fitting several steady state values of the auxiliary and punctual outputs.

Simulation runs are performed to evaluate the performance of the proposed control strategy and the reported results show clearly its set point tracking capabilities.

References

1. Abbasi, F., Mohammadpour, J.: Reduced order model-based sliding mode control of dynamic systems governed by Burgers' equation. In: 2015 IEEE 54th Annual Conference on Decision and Control (CDC), Osaka, Japan, 15–18 December 2015, pp. 1917–1922 (2015)
2. Chen, G., Lascieka, I., Zhou, J.: Control of Nonlinear Distributed Parameter System. CRC Press, Boca Raton (2001)
3. Christofides, P.D.: Control of nonlinear distributed process systems: recent developments and challenges. AIChE J. **47**(3), 514–518 (2001)
4. Christofides, P.D.: Nonlinear and Robust Control of PDE Systems: Methods and Applications to Transport-Reaction Processes. Birkhaüser, Boston (2001)
5. Christofides, P.D., Baker, J.: Robust output feedback control of quasi-linear parabolic PDE systems. Syst. Control Lett. **36**(5), 307–316 (1999)
6. Christofides, P.D., Daoutidis, P.: Feedback control of hyperbolic PDE systems. AIChE J. **42**(11), 3063–3086 (1996)
7. Curtain, R., Zwart, H.: An Introduction to Infinite-Dimensional Linear Systems Theory. Springer, New York (1995)
8. Dubljevic, S., Christofides, P.D., Kevrekidis, I.G.: Distributed nonlinear control of diffusion-reaction processes. Int. J. Robust Nonlinear Control **14**(2), 133–156 (2004)
9. Emirsjlow, Z., Townley, S.: From PDEs with boundary control to the abstract state equation with an unbounded input operator: a tutorial. Eur. J. Control **6**(1), 27–49 (2000)
10. Engel, K.J., Nagel, R.: A Short Course on Operator Semigroups. Springer, New York (2006)
11. Gundepudi, P.K., Friedly, J.C.: Velocity control of hyperbolic partial differential equation systems with single characteristic variable. Chem. Eng. Sci. **53**(24), 4055–4072 (1998)
12. Krstic, M.: On global stabilization of Burgers' equation by boundary control. Syst. Control Lett. **37**(3), 123–141 (1999)
13. Kucuk, I., Sadek, I.: A numerical approach to an optimal boundary control of the viscous Burgers' equation. Appl. Math. Comput. **210**(1), 126–135 (2009)
14. Li, H.X., Qi, C.: Modeling of distributed parameter systems for applications-a synthesized review from time-space separation. J. Process Control **20**(8), 891–901 (2010)

15. Liu, W.J., Krstic, M.: Backstepping boundary control of Burgers' equation with actuator dynamics. Syst. Control Lett. **41**(4), 291–303 (2000)
16. Maidi, A., Corriou, J.P.: Boundary control of nonlinear distributed parameter systems by input-output linearization. In: 18th IFAC World Congress, Milan, Italy, pp. 10910–10915 (2011)
17. Maidi, A., Corriou, J.P.: Distributed control of nonlinear diffusion systems by input-output linearization. Int. J. Robust Nonlinear Control **24**(3), 386–405 (2014)
18. Maidi, A., Diaf, M., Corriou, J.P.: Boundary geometric control of a heat equation. In: European Control Conference (ECC 2009), Budapest, Hungary, 23–26 August 2009, pp. 4677–4682 (2009)
19. Padhi, R., Faruque Ali, S.: An account of chronological developments in control of distributed parameter systems. Ann. Rev. Control **33**(1), 59–68 (2009)
20. Park, H.M., Jang, Y.D.: Control of Burgers equation by means of mode reduction. Int. J. Eng. Sci. **38**(7), 785–805 (2000)
21. Park, H.M., Lee, M.W., Jang, Y.D.: An efficient computational method of boundary optimal control problems for the Burgers equation. Comput. Methods Appl. Mech. Eng. **166**(3–4), 289–308 (1998)
22. Poularikas, A.D.: The Transforms and Applications Handbook, 2nd edn. CRC Press, Boca Raton (2000)
23. Ray, W.: Advanced Process Control. Butterworths, Boston (1989)
24. Shang, H., Forbes, J.F., Guay, M.: Feedback control of hyperbolic distributed parameter systems. Chem. Eng. Sci. **60**(4), 969–980 (2005)
25. Singh, A., Hahn, J.: Effect of finite-dimensional approximation on observability analysis of distributed parameter models. In: Proceedings of the 8th IFAC Symposium on Dynamics and Control of Processes Systems, Cancun, Mexico, 6–8 June 2007, pp. 199–204 (2007)
26. Smaoui, N.: Boundary and distributed control of the viscous Burgers equation. J. Comput. Appl. Math. **182**(1), 91–104 (2005)
27. Van de Wouwer, A., Saucez, P., Schiesser, W.E.: Adaptive Method of Lines. CRC Press, Boca Raton (2001)
28. Witelski, T., Bowen, M.: Methods of Mathematical Modelling. Continuous Systems and Differential Equations. Springer, Switzerland (2015)

Visual SVSF-SLAM Algorithm Based on Adaptive Boundary Layer Width

Fethi Demim[1(✉)], Abdelkrim Nemra[1], Kahina Louadj[2], Abdelghani Boucheloukh[3], Elhaouari Kobzili[3], Ahmed Allam[3], Mustapha Hamerlain[4], and Abdelouahab Bazoula[1]

[1] Ecole Militaire Polytechnique, EMP, Bordj El Bahri, Algiers, Algeria
demifethi@gmail.com, abdelouahab.bazoula@gmail.com, karim_nemra@yahoo.fr

[2] LIMPAF, Université de Bouira, Bouira, Algeria
louadj_kahina@yahoo.fr

[3] National Polytechnic School, ENP, El Harrach, Algiers, Algeria
abdelghanibouch@gmail.com, ahmedallam900@gmail.com, elhaouari.kobzili@g.enp.edu.dz

[4] Center for Development of Advanced Technologies, CDTA, Baba Hassen, Algiers, Algeria
mhamerlain@cdta.dz

Abstract. This work presents a solution to the Simultaneous Localization and Mapping (SLAM) problem of Unmanned Ground Vehicle (UGV) supported by a stereovision camera. There are many ways to approach this problem, mostly based on the sequential probabilistic process. The EKF-SLAM algorithm is one popular solution based on Extended Kalman Filter (EKF) to solve this problem that struggles with Jacobians' calculation. FAST-SLAM is another popular algorithm based on the Rao-Blackwellized particle filter that has issues with real-time implementation. As a means to ameliorate the SLAM solution limitations, especially when the process and observation models contain uncertain parameters, a new adaptive Boundary Layer With algorithm based on the Smooth Variable Structure Filter (ASVSF) is proposed to solve the UGV visual SLAM problem. Hence, the adaptive SVSF-SLAM algorithm is proposed with an original formulation. This algorithm was implemented on Pioneer 3-AT mobile robot, using a stereo vision sensor in 3D. Simulation results show efficiency and give an advantage face modeling uncertainties and noises and it has significantly improved the performance of the estimation process.

Keywords: Localization · Map building · Autonomous navigation Odomter/Vision sensor fusion · Mobile robot

1 Introduction

Mobile robots are finding a way more and more in our daily life from many applications such as vacuum cleaners to autonomous driving vehicles. Many algorithms exist today to solve SLAM problems for the single mobile robot. Many studies, experiments and research were made covering this topic. For instance, Sty in [1] talks about the

M. Chadli et al. (Eds.): ICEECA 2017, LNEE 522, pp. 97–112, 2019.
https://doi.org/10.1007/978-3-319-97816-1_8

solution to the SLAM problem which is indispensable for making robots fully autonomous. In [2], research treats the problem of SLAM with the growing uncertainties supported by simulation and experimental validation. The famous popular SLAM solution was provided by Smith and Cheeseman in a seminar paper in 1986; and it was developed as a carried out systematically by Moutarlier and Chatila [3]. In [4, 19], we find the Extended Kalman Filter (EKF) based solution specifically for visual SLAM.

The EkF approximates the SLAM posterior as high-dimensional Gaussian overall features in the map and the robot pose. Another type of filter started to appear, it uses the principle of the Unscented Kalman Filter (UKF) that consists of a Gaussian random variable in N dimensions using 2N + 1 samples, in a unique dimension known as sigma points [10]. Though the UKF is not exempt, it suffers less from linearization and also of poor landmarks as in the EKF. However, in [5, 6] the Visual SLAM treated based on Fast-SLAM. This algorithm uses Rao-Blackwellised particle filter estimation scheme which utilizes the multi-hypothesis data association and logarithmic complexity instead of quadratic one [5]. The work presented in [7, 8] is a part of research work done on autonomous navigation for Unmanned Ground Vehicle (UGV), using the Smooth Variable Structure Filter which is based on sliding mode control and estimation concepts and don't require covariance derivation.

In this paper, we presented the development of an adaptive version of the Smooth Variable Structure Filter (ASVSF) based on sliding model theory, using covariance matrices to evaluate the uncertainty of the estimation with optimal adaptive smoothing boundary layer vector to solve the visual SLAM problem. This filter presents a stability and robustness faculties in modeling uncertainties [9, 10], which is capable of being done for the localization and mapping problem of UGV. The paper opens up a new field of a robust recursive estimation adaptive SVSF that deals efficiently with initial conditions and modeling errors of odometer/stereo vision system. Previous studies utilized a stereo vision camera as the best solution for SLAM problem, using an adaptive SVSF filter. The success of this application depends highly on the accuracy and robustness of the strategy for the adaptive Smooth Variable Structure Filter SLAM implementation. The work presented in this paper is organized as follows: Sect. 2 illustrates the process models of UGV and stereo vision sensor. Section 3 describes the SVSF-SLAM algorithm. Section 4 represents the adaptive SVSF-SLAM algorithm in details. Simulation and discussion are presented in Sect. 5 and concluding in Sect. 6.

2 Process Models of UGV and Stereo Vision Sensor

2.1 Process Model

The UGV which is used in this work is the Pioneer P3-AT (see Fig. 1). The P3-AT is a non-holonymic robot with four wheels. We assume that the robot is operating in planar environments. The state vector considered is $[X_r; Y_r; \theta_r]$ with (X_r, Y_r) presents the coordinates of the robot in the global coordinate and θ_r describes its orientation. We note that the robot is controlled by two velocities at sample k: $v(k)$ and $\omega(k)$ that are presented a translational velocity and rotational velocity respectively. The control input

Fig. 1. Pioneer 3-AT robot equipped with a camera stereo vision

at sample k by $U(k) = [v(k), \omega(k)]^T$, According to [13], we can estimate the robot's current location by

$$\begin{pmatrix} X_r(k+1) \\ Y_r(k+1) \\ \theta_r(k+1) \end{pmatrix} = \begin{pmatrix} X_r(k) + \Delta T v(k)\cos(\theta_r(k)) \\ Y_r(k) + \Delta T v(k)\sin(\theta_r(k)) \\ \theta_r(k) + \Delta T \omega(k) \end{pmatrix} + \begin{pmatrix} \varepsilon_{x_r} \\ \varepsilon_{y_r} \\ \varepsilon_{\theta_r} \end{pmatrix} \tag{1}$$

The robot evolution model reflects the relationship between the robot previous states $X_R(k)$ and its current state $X_R(k+1)$. In SLAM, the system state vector has a position of the UGV which is defined as X_R. It is represented by $X_R = [X_r, Y_r, \theta_r]^T \in R^3$, and we call a collection of M features a map such that $L = [L_1 \ldots L_M]^T$, ΔT is the sample period, $\varepsilon_{x_r, y_r, \theta_r}$ are the noises that arise from the encoder and wheels slipping, etc. In this paper, we will use a point feature such that for the i^th landmark: $L_i = [x_i, y_i, z_i]^T$. Where x, y and z are the coordinates of the point in a global frame of reference. We can write the Eq. (1) as follows

$$X_R(k+1) = f(X_R(k), U(k)) + \varepsilon_{x_r, y_r, \theta_r} \tag{2}$$

2.2 Stereo Vision Sensor Model

The perspective camera model comprehends intrinsic and extrinsic parameters. This model makes sure the geometric transformation between camera/image and world/camera reference frames respectively [15] (see Fig. 2).

- **Intrinsic Parameters**

Intrinsic parameters of a camera are defined by the horizontal and vertical scale factor K_v and K_u, the image center coordinates u_0 and v_0 given in the image frame and the focal distance f as (transformation camera/image).

$$I_c = \begin{bmatrix} \alpha_u & 0 & u_0 & 0 \\ 0 & \alpha_v & v_0 & 0 \\ 0 & 0 & 1 & 0 \end{bmatrix}, \text{ with } \begin{cases} \alpha_u = -fxK_u \\ \alpha_v = -fxK_v \end{cases}$$

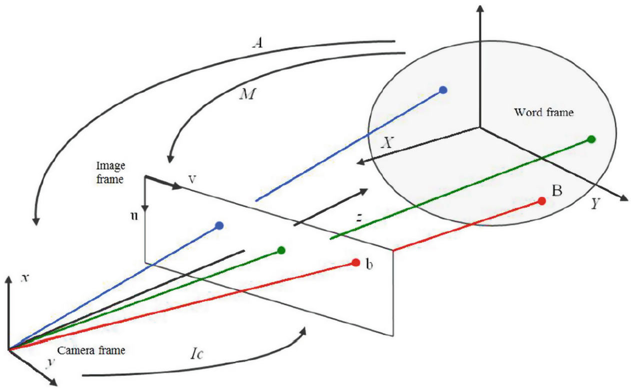

Fig. 2. Camera model

- **Extrinsic Parameters**

These parameters describe the transformation of the world to camera frame contributed by the homogeneity matrix A(transformation world/camera). The matrix A is a combination of a rotation matrix R and a translation matrix t from the world frame to the camera frame and obviously, the matrix A changes with the camera UGV displacement:

$$A = \begin{bmatrix} r_{11} & r_{12} & r_{13} & t_x \\ r_{21} & r_{22} & r_{23} & t_y \\ r_{31} & r_{32} & r_{33} & t_z \\ 0 & 0 & 0 & 1 \end{bmatrix} = \begin{bmatrix} R & t \\ 0 & 1 \end{bmatrix}$$

- **Observation Point Based Model**

In order to perform the SLAM, the robot which must be filled to select and tracks the landmarks in its environment to localize itself. In this paper, we opt for a point landmark in 3D. To compute relative measurement of the landmarks obtained from the images acquired from the stereo vision sensor. For the simulation of the SVSF visual SLAM algorithm, we use theoretical data sets (a set of 3D points) early produced instead of using real data. During the robot motion, the point landmarks included in the vision sensor field (Fig. 3) are detected in 3D space [14].

As said previously, the stereo vision sensor provides relative measurement $Z = \left[L_x^r, L_y^r, L_z^r\right]^T$ of the landmarks with respect to the robot frame, this measurement (observation) will be noted Z. The model representing the robot frame coordinates of an individual landmark, according to its global frame coordinates $L^g = \left[L_x^g, L_y^g, L_z^g\right]^T$

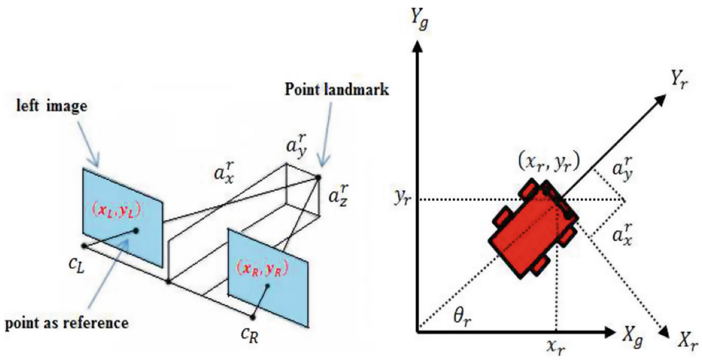

Fig. 3. Observation system geometry

and the robot configuration $R = [x_r, y_r, 0]^T$ is called the direct model observation and will be noted [13, 24] (Fig. 4).

$$Z = h(R, L^g) + \varepsilon_{x,y,z} \tag{3}$$

$$Z = M_{GR} \begin{bmatrix} L_x^g - x_r \\ L_y^g - y_r \\ L_z^g - 0 \end{bmatrix} + \begin{bmatrix} \varepsilon_x \\ \varepsilon_y \\ \varepsilon_z \end{bmatrix} \tag{4}$$

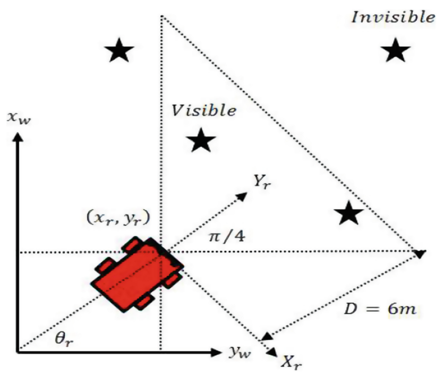

Fig. 4. Sensor vision field of UGV

where $\varepsilon_{x,y,z}$ presents the measurement noises and the global to robot projection matrix M_{GR} is denoted by

$$M_{GR} = \begin{bmatrix} \cos(\theta_r) & \sin(\theta_r) & 0 \\ -\sin(\theta_r) & \cos(\theta_r) & 0 \\ 0 & 0 & 1 \end{bmatrix} \tag{5}$$

- **Inverse Observation Point Based Model**

The new observed landmark must be initialized previously to be added to the state vector [14]. The initialization process is in fact the best estimation of the landmark position, and it is a fundamental point to SLAM implementation. The observation model stated in (4) gives three equations for three dimension variable L^g. The 3D coordinates of a new landmark $\left[L_x^g, L_y^g, L_z^g\right]^T$ with respect to the global framework are initialized by solving (3) as follows

$$L^g = h^{-1}(R, Z) \tag{6}$$

$$L^g = (M_{GR})^{-1} Z + R \tag{7}$$

3 SVSF-SLAM Algorithm

The smooth variable structure filter was introduced in 2007 by Saeid R. Habibi. This filter is based on the sliding mode control and estimation techniques, and is formulated in a predictor-corrector fashion. As shown in the following (Fig. 5), the SVSF utilizes a switching gain to converge the estimates to within a boundary of the true state values (i.e., existence subspace), this creates a robust and stable estimation strategy [8, 12]. The SVSF has been shown to be stable and robust to modeling uncertainties and noise, when given an upper bound on the level of unmodeled dynamics and noise [16].

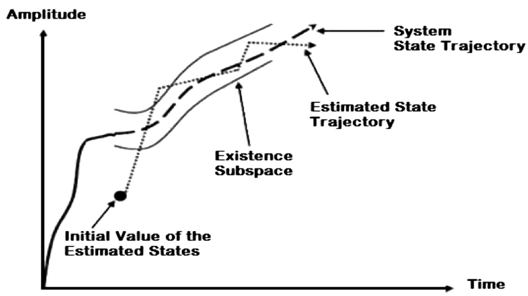

Fig. 5. SVSF estimation concept

In the following section we investigate the ASVSF proposed as an alternative solution to solve the SLAM algorithm problem. We begin by considering the form of SVSF to nonlinear systems, which is necessary to solve our Unmanned Ground Vehicle SLAM problem. The estimation process may be summarized by (8) to (15), and is repeated iteratively. An a priori state estimate is calculated using an estimated model of the system [8, 25]. This a priori value is then used to calculate an a priori

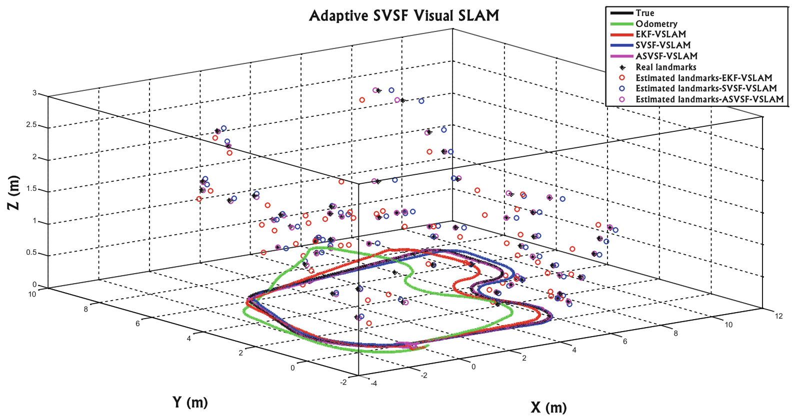

Fig. 6. Simulation results with adaptive SVSF-VSLAM

estimate of the measurement, defined by (13). A corrective term, referred to as the SVSF gain, is calculated as a function of the error in the predicted output, as well as a gain matrix and the smoothing boundary layer width. The correct term calculated in (10) is then used in (15) to find the posteriori state estimate. Two critical variables in this process are the priori and a posteriori output error estimate, defined by (13) and (14) respectively [17, 22]. Note that (13) is the output error estimate from the previous time step, and is used only in the gain calculation.

$$\hat{X}(k+1) = f\left(\hat{X}(k), U(k)\right) \tag{8}$$

$$\hat{Z}(k+1) = h\left(\hat{X}(k)\right) \tag{9}$$

$U(k)$ represents the input control vector. The SVSF guarantees bounded-input bounded-output stability and the convergence of the estimation process by using the Lyapunov stability condition [17]. The derivation of the SVSF gain and its stability conditions can be found in [11]. The gain is computed using the priori, the posteriori measurement error, the smoothing boundary layer widths ϕ, convergence rate γ and measurement matrix $H(k+1)$ [17, 23] as follows

$$K_{k+1}^{SVSF} = \left(\hat{H}(k+1)\right)^{+} diag\left[\left(\left|e_{z(k+1/k)}\right|_{Abs} + \gamma\left|e_{z(k+1/k+1)}\right|_{Abs}\right)^{o} Sat\left(\overline{\varphi}^{-1} e_{z(k+1/k)}\right)\right] \left[diag\left(e_{z(k+1/k)}\right)\right]^{-1} \tag{10}$$

where

- ^{o} represents “Schur” multiplication element-by-element;
- $^+$ refers to the pseudo inverse of a matrix;
- $H(k+1,j) = h(k+1,j)F_{X,i}$ is the derivative of h with respect to the state vector $X(k+1)$, we note that h depends only of the robot pose $R(k+1)$ and the location of the i^{th} landmark, where i is the index of the observed landmark at time k and j is the index of an individual landmark observation in $h(k+1,j)$. $F_{X,i}$ is calculated as follows

$$F_{X,i} = \begin{bmatrix} 1 & 0 & 0 & 0 & \dots & 0 & 0 & 0 & 0 & 0 & \dots & 0 \\ 0 & 1 & 0 & 0 & \dots & 0 & 0 & 0 & 0 & 0 & \dots & 0 \\ 0 & 0 & 1 & 0 & \dots & 0 & 0 & 0 & 0 & 0 & \dots & 0 \\ 0 & 0 & 0 & 0 & \dots & 0 & 1 & 0 & 0 & 0 & \dots & 0 \\ 0 & 0 & 0 & 0 & \dots & 0 & 0 & 1 & 0 & 0 & \dots & 0 \\ 0 & 0 & 0 & 0 & \dots & 0 & 0 & 0 & 1 & 0 & \dots & 0 \end{bmatrix} \tag{11}$$

We can write $\left(\hat{H}(k+1)\right)^+$ as follows

$(H(k+1))^+ = \left(F_{X,i}\right)^T (h(k+1,j))^+$, with knowing that:
$h(k+1,j) = [u_i; v_i] = h\left(X\left(k+1, L_i^{f,k+1}\right)\right)$ represents the observation model of the SVSF-SLAM algorithm.

- $\overline{\varphi}^{-1}$ is a diagonal matrix constructed from the smoothing boundary layer vector φ, such that
$\overline{\varphi}^{-1} = [diag(\varphi)]^{-1} = \begin{bmatrix} \frac{1}{\varphi_1} & 0 & 0 \\ 0 & \ddots & 0 \\ 0 & 0 & \frac{1}{\varphi_{M_i}} \end{bmatrix}$, with M_i represents the number of measurements.
- $Sat\left(\overline{\varphi}^{-1} e_{z(k+1)}\right)$ represents the saturation function:

$$Sat\left(\overline{\varphi}^{-1} e_{z(k+1,i)}\right) = \begin{cases} +1, & \frac{e_{z(k+1,i)}}{\varphi_i} \geq 1 \\ \frac{e_{z(k+1/k,i)}}{\varphi_i}, & -1 < \frac{e_{z(k+1,i)}}{\varphi_i} < 1 \\ -1, & \frac{e_{z(k+1,i)}}{\varphi_i} \leq -1 \end{cases} \tag{12}$$

$$e_{z(k+1/k)} = Z(k+1) - \hat{Z}(k+1/k) \tag{13}$$

$$e_{z(k+1/k+1)} = Z(k+1) - \hat{Z}(k+1/k+1) \tag{14}$$

The update of the state estimates can be calculated as follows

$$\hat{X}(k+1/k+1) = \hat{X}(k+1/k) + K_{k+1}^{SVSF} e_{z(k+1/k)} \tag{15}$$

SLAM is the problem of constructing a model of the environment being traversed with on board sensors, while at the same time maintaining an estimate of the vehicle location within the model. The SVSF filter provides a robust and stable estimate to modeling uncertainties and errors [11, 17]. There are two main SVSF design parameters. The first parameter γ which control the speed of convergence, where the second φ refers to the boundary layer width which is used to smooth out the switching action. These parameters should be chosen carefully. γ is a diagonal matrix with elements were set to the following:

$$0 < \gamma_i \leq 1 \tag{16}$$

According to [10], the estimation process is stable and converges to the existence subspace if the following condition is satisfied

$$\left|e_{z(k)}\right|_{Abs} > \left|e_{z(k+1)}\right|_{Abs} \tag{17}$$

In this section, a framework for feature map SLAM based point on the SVSF is presented. Like EKF-SLAM, SVSF-SLAM is a kind of stochastic SLAM algorithm, which is performed by storing the vehicle pose and map features in a single state vector. It consists of following stages: initialization, prediction, data association and update, finally the management of the map [8, 12].

4 Adaptive SVSF-SLAM Algorithm

As an alternative approach, there is a novel filter, known as the Adaptive smooth variable structure filter (ASVSF). This research focused on advancing the development and implementation of the Adaptive SVSF-VSLAM algorithm using matrix covariance to evaluate the uncertainty of estimating with optimal smoothing boundary layer vector. In this section, we investigate the ASVSF-VSLAM proposed algorithm as a novel approach. We will show the nonlinear ASVSF which is necessary to solve our Unmanned Ground Vehicle SLAM problem [7, 8]. The initial conditions used by the ASVSF-VSLAM algorithm were the same as those used by the EKF/SVSF-SLAM algorithm. The Adaptive SVSF-VSLAM algorithm can be described as follows [20]:

- **Initialization**

The process estimation needs the initialization of the original pose $\hat{X}_0$ of the coordinate system and covariance matrix P_0. The posteriori measurement error vector e_0^z can be is initialized arbitrary in the ASVSF-VSLAM algorithm.

$$\overline{X}_0 = [\overline{R}_0, \overline{L}_1^{f,0}, \ldots, \overline{L}_{M_0}^{f,0}]^T,\ P_0 = \begin{bmatrix} 0 & 0 & 0 & 0 & \ldots & 0 \\ 0 & 0 & 0 & 0 & \ldots & 0 \\ 0 & 0 & 0 & 0 & \ldots & 0 \\ 0 & 0 & 0 & \sigma_m^2 & \ldots & 0 \\ \vdots & \vdots & \vdots & \vdots & \ddots & \vdots \\ 0 & 0 & 0 & 0 & \ldots & \sigma_{m_M}^2 \end{bmatrix},\ e_{0/0}^z = [e_0^{z_1}, \ldots, e_0^{z_{M_0}}]^T$$

where $\hat{X}_0 = [0, 0, 0]^T$ is the initial pose of the UGV, P_0 is the covariance matrix and M_0 is the number of initial feature. $Z_k = [Z_1, \ldots Z_M]^T$ be a set of system measurements.

- **Prediction**

The prediction stage is a process, which deals with vehicle motion based on incremental dead reckoning estimates and increases the uncertainty of the vehicle pose estimate [8]. First, the state vector is augmented with a control input $U(k)$. We consider the following process for the ASVSF estimation strategy, as applied to a nonlinear system. The predicted state estimates $X(k+1/k)$ and the predicted covariance matrix $P(k+1/k)$ are first calculated as follows [20, 21]:

1- $X(k+1) = f\left(\hat{X}(k), \hat{U}(k)\right) = f\left(R(k+1), L_i^{f,k+1}\right)$
2- $P(k+1/k) = \nabla F_X P(k/k) \nabla F_X^T + \nabla F_U Q(k) \nabla F_U^T$
where ∇F_X and ∇F_U be the Jacobian matrices of $f(.)$ with respect to $X(k+1)$ evaluated at an elsewhere specified point, denoted by

$$\nabla F_X = \begin{bmatrix} J_1 & 0 & \cdots & 0 \\ 0 & 1 & \cdots & 0 \\ \vdots & \vdots & \ddots & \vdots \\ 0 & 0 & \cdots & 1 \end{bmatrix} \text{ and } \nabla F_U = \begin{bmatrix} J2 \\ 0 \\ \vdots \\ 0 \end{bmatrix}$$

where $$J_1 = \left[\frac{\partial f(.)}{\partial x_r}; \frac{\partial f(.)}{\partial y_r}; \frac{\partial f(.)}{\partial \theta_r}\right] = \begin{bmatrix} 1 & 0 & -v\sin(\theta_r)\Delta T \\ 0 & 1 & v\cos(\theta_r)\Delta T \\ 0 & 0 & 1 \end{bmatrix},$$

$$J_2 = \left[\frac{\partial f(.)}{\partial v}; \frac{\partial f(.)}{\partial \omega}\right] = \begin{bmatrix} \cos(\theta_r)\Delta T & 0 \\ \sin(\theta_r)\Delta T & 0 \\ 0 & \Delta T \end{bmatrix}$$

- **Data association and control update**
  The feature already stored in the map is observed by a vision sensor with the measurement $Z(k+1)$.

3- **For** all features observations $Z(k+1, j)$
4- $\hat{Z}(k+1, i) = h\left(\hat{X}(k+1)\right) = h\left(\hat{R}(k+1), L_i^{f,k+1}\right)$
5- **If** the landmark j is seen before (correspondence is founded)

The posteriori measurements error vector $e_{z(k+1,i)} \in R^{3\times 1}$ may be calculated by

6- $e_{z(k+1,i)} = \hat{Z}(k+1,j) - Z(k+1,i)$

$P^{\overline{\varphi}}_{k+1/k} \in R^{6\times 6}$ is the matrix that is extracted from $P(k+1/k)$ is calculated by

7- $P^{\overline{\varphi}}_{k+1/k} = \begin{bmatrix} P_R & P_{L_i^{f,k+1},R} \\ P_{R,L_i^{f,k+1}} & P_{L_i^{f,k+1}} \end{bmatrix}$, where $P_R \in R^{3\times 3}, P_{L_i^{f,k+1},R} \in 0^{3\times 3}$ and $P_{L_i^{f,k+1}} \in R^{3\times 3}$. The array width of the boundary layer $\overline{\varphi}^{opt}_{k+1} \in R^{2\times 2}$ may be calculated by

8- $$\overline{\varphi}^{opt}_{k+1} = \left(\nabla h(k+1)P^{\overline{\varphi}}_{k+1/k}\nabla h(k+1)^T + R(k)\right)\left(\nabla h(k+1)P^{\overline{\varphi}}_{k+1/k}\nabla h(k+1)^T\right)^{-1} \left[diag\left(\left|e_{z(k+1,i)}\right|_{Abs} + \gamma\left|e_{z(k+1,i)}\right|_{Abs}\right)\right]$$

where $\nabla h(k+1) \in R^{3\times 6} = \left[\frac{\partial h\left(\hat{X}(k+1/k)\right)}{\partial X_R}, \frac{\partial h\left(\hat{X}(k+1/k)\right)}{\partial L_i^{f,k+1}}\right]$

Use the $\overline{\varphi}^{opt}$ to calculate SVSF gain $K^{ASVSF}_{k+1} \in R^{6\times 3}$

9- $$K^{ASVSF}_{k+1} = (H(k+1,j))^+ diag\left[\left(\left|e_{z(k+1,i)}\right|_{Abs} + \gamma\left|e_{z(k+1,i)}\right|_{Abs}\right)^o Sat\left(\left(\overline{\varphi}^{opt}_{k+1}\right)^{-1} e_{z(k+1,i)}\right)\right] \left[diag\left(e_{z(k+1,i)}\right)\right]^{-1}$$

$(H(k+1,j))^+ = F^T_{X,i}(h(k+1,j))^+$ used (21) to calculate $(H(k+1,j))^+$. Note that the matrix $h(k+1,j) = \frac{\partial h\left(\hat{X}(k+1/k)\right)}{X(k+1)}$ is the Jacobian of with respect to $R(k+1)$ and $L_i^{f,k+1}$.

$$h(k+1,j) = \begin{bmatrix} -\cos(\theta_r) & -\sin(\theta_r) & -\alpha_1\sin(\theta_r) + \alpha_2\cos(\theta_r) & \cos(\theta_r) & \sin(\theta_r) & 0 \\ \sin(\theta_r) & -\cos(\theta_r) & -\alpha_1\cos(\theta_r) - \alpha_2\sin(\theta_r) & -\sin(\theta_r) & \cos(\theta_r) & 0 \\ 0 & 0 & 0 & 0 & 0 & 0 \end{bmatrix}$$

where $\alpha_1 = L^{f,k+1}_{x,i} - x_r$ and $\alpha_2 = L^{f,k+1}_{y,i} - y_r$

The gain vector K^{ASVSF}_{k+1} is used to formulate an a posteriori state estimate and the update of the state estimate can be calculated as follows

10- $\hat{X}(k+1/k+1) = \hat{X}(k+1/k) + K^{ASVSF}_{k+1}e_{z(k+1,i)}$

Update $P(k+1/k+1) \in R^{6\times 6}$

11- $$P(k+1/k+1) = \left(I_{6\times 6} - K^{ASVSF}_{k+1}\nabla h(k+1)\right)P^{\overline{\varphi}}_{k+1/k}\left(I_{6\times 6} - K^{ASVSF}_{k+1}\nabla h(k+1)\right)^T + K^{ASVSF}_{k+1}R(k)\left(K^{ASVSF}_{k+1}\right)^T$$

The priori measurements error vector $e_{z(k+1/k)} \in R^{3\times 1}$ may be calculated by

12- $e_{z(k+1,i)} = Z(k+1,j) - h\left(\hat{R}(k+1), L_i^{f,k+1}\right)$

13- **End If**

14**- End For**

15- $\hat{X}(k+1/k+1) = \hat{X}(k+1/k), P(k+1/k+1) = P(k+1/k)$

- **Map management**

  As the environment is explored, new features are observed and should be added to the stored map. In this case, the state vector and the output error estimate matrix are calculated of the new observation.

16- **For** all non-associated features, initialization of the new landmark a_{new}.

17- $a_{new} = h^{-1}\left(\hat{X}(k+1/k+1), Z(k+1/k)\right)$

18- Add a_{new} to the state vector $\hat{X}(k+1/k+1)$

Initialization the covariance matrix $P_{new} \in R^{3\times 3}$ of a_{new}.

19- $P_{new} = \nabla h_R^{-1} P_R \left(\nabla h_R^{-1}\right)^T + \nabla h_z^{-1} R(k) \left(\nabla h_z^{-1}\right)^T$

The measurements of Z_j environment are referenced by relative to the position of the robot, where $Z_j = \left[Z_{x,j}, Z_{y,j}, Z_{z,j}\right]^T, j \in 1, \ldots, M$. ∇h_R^{-1} and ∇h_z^{-1} are the jacobian matrices, denoted by

$$\nabla h_R^{-1} = \begin{bmatrix} 1 & 0 & -Z_{x,j}\sin(\theta_r) - Z_{y,j}\cos(\theta_r) \\ 0 & 1 & -Z_{x,j}\cos(\theta_r) - Z_{y,j}\sin(\theta_r) \\ 0 & 0 & 1 \end{bmatrix} \text{ and}$$

$$\nabla h_z^{-1} = \begin{bmatrix} \cos(\theta_r) & -\sin(\theta_r) & 0 \\ \sin(\theta_r) & \cos(\theta_r) & 0 \\ 0 & 0 & 1 \end{bmatrix}$$

Initialization the inter-covariance matrix $P_{new,x} \in R^{3\times 3M}$ of a_{new}.

20- $P_{new,x} = \nabla h_R^{-1} P_{R,x}$

Use (24) to initialize the posteriori measurement error $e_{z(k+1,new)}$ of the new landmark a_{new}.

21- $e_{z(k+1,new)} = Z(k+1) - h\left(\hat{X}(k+1/k+1), a_{new}\right)$

22- Add $e_{z(k+1,new)}$ to the posteriori measurement error vector $e_{z(k+1,i)}$.

Increment the state vector $\hat{X}_{Incremt}$.

23- $\hat{X}_{Incremt} = \left[\hat{X}(k+1); a_{new}\right]$

Increment the covariance matrix $P_{Incremt}$.

24- $P_{Incremt} = \begin{bmatrix} P & P_{x,new} \\ P_{new,x} & P_{new} \end{bmatrix}$

25- $M = M+1$ is the total number of current landmarks.

26- **End For**

5 Simulation and Discussion

We present the simulation results to validate UGV Visual SLAM algorithm for Unmanned Ground Vehicle localization problem. The sampling rates used for each filter and sensors deals in this study are as follows:

$$f_{Odom} = f_{Camera} = f_{EKF} = f_{SVSF} = f_{ASVSF} = 10\,\text{Hz}$$

We suppose that the observation noise obeys the mixture Gauss distribution as [14] $\varepsilon_{x_r,y_r,\theta_r} \approx 0.5N(0,R_1) + 0.5N(0,R_2)$:

$$R_1 = \begin{bmatrix} 0.010 & 0.001 & 0.002 \\ 0.001 & 0.010 & 0.001 \\ 0.002 & 0.001 & 0.010 \end{bmatrix} \text{ and } R_2 = \begin{bmatrix} 0.002 & 0.010 & 0.020 \\ 0.005 & 0.002 & 0.010 \\ 0.010 & 0.005 & 0.002 \end{bmatrix}$$

The motion noise obeys the Gauss distribution as $N(0, Q(k)), Q(k) = \begin{bmatrix} 0.020 & 0.001 \\ 0.001 & 0010 \end{bmatrix}$

The convergence rate matrix is described by $\gamma = diag(0.8, 0.8, 0.8)$, and the width of the smoothing boundary layer vector used is $\varphi = [21; 21; 21]$.

The visual SLAM (VSLAM) algorithm builds a map consisting of the point landmarks. The adaptive SVSF provides a more accurate estimate than the EKF/SVSF-SLAM as shown in the Fig. 6. It is clear that the ASVSF-VSLAM corrected path is consistently following the reference path better than that of the EKF/SVSF-VSLAM. The good results show the robustness of the adaptive SVSF/SLAM algorithm than EKF/SVSF-SLAM especially when the system or observation models are not accurate enough.

As can be seen in Fig. 7, this figure shows the pose estimation $RMSE_{x_r,y_r,\theta_r}$. From Fig. 8, we can see the convergence of Root Mean Square Error (RMSE) map values. It is clear that the *RMSE* values of the ASVSF-VSLAM algorithm is smaller than that offered by the EKF/SVSF-VSLAM. So we can note that the adaptive SVSF-VSLAM algorithm accuracy is better than that of the EKF/SVSF-VSLAM algorithms. It is worth mentioning that, the estimated uncertainty is very small of ASVSF-SLAM in comparison to the true uncertainty of the other algorithm. When the robot closes the loop at the end, revisiting old landmarks should affect the positions of landmarks all around the loop, which reduces the uncertainty in robot and landmark estimates and become almost fully correlated. The ASVSF-SLAM algorithm provides more an accurate position and the better result than EKF/SVSF-SLAM algorithms. The Table 1 confirms and shows the UGV $RMSE_{x_r,y_r,\theta_r}$ and the consumed time by each algorithm used in the simulation results. The *RMSE* of the EKF-SLAM algorithm increases proportionally with the size of the state vector which is quadratic in the number of the current landmarks on the map. It becomes computationally intractable for large maps. The ASVSF-SLAM algorithm increases slightly by increasing number of measurements. On the other hand, the SVSF-SLAM algorithm uses only the UGV state and the corresponding landmark position to update for each measurement (Table 1).

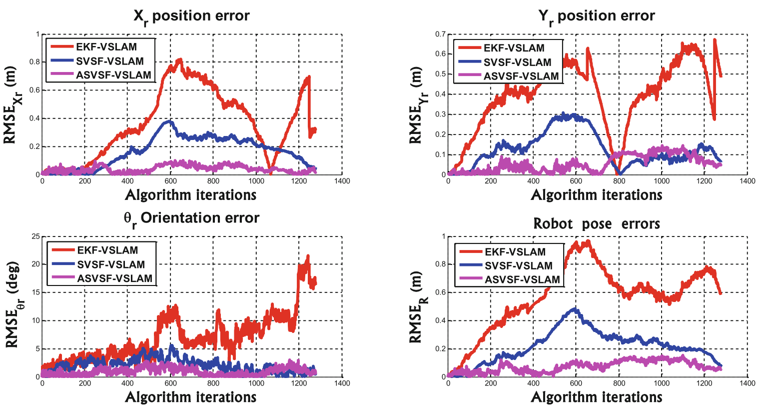

Fig. 7. Position error of adaptive SVSF-VSLAM algorithm

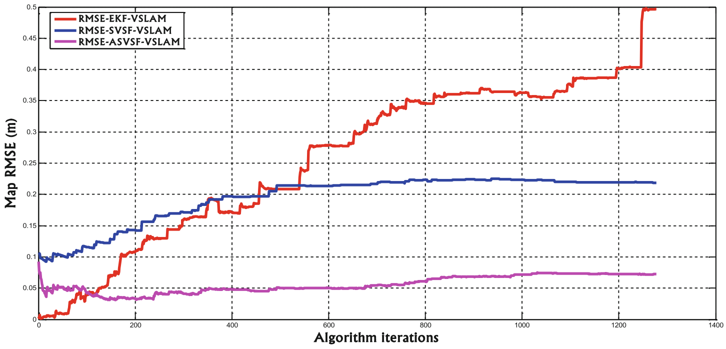

Fig. 8. RMSE for adaptive SVSF-VSLAM algorithm

Table 1. Consumed time and *RMSE* of the UGV by each.

	EKF	SVSF	ASVSF
E[*RMSExr*] (m)	0.29	0.20	0.042
E[*RMSEyr*] (m)	0.4	0.092	0.082
E[*RMSE*θ*r*] (deg)	5.06	2.58	2.16
Prediction time (ms)	1.55	0.2	1.53
Data association time and update (ms)	5.15	1.17	1.86
Map management time (ms)	1.45	0.17	1.62

6 Conclusion

The main goal of the paper is to come up with tools capable of producing an accurate automatic localization that could be used in an accurate map management. This paper offers a new algorithm based on adaptive SVSF for UGV localization and mapping problem using stereo vision sensor. The proposed adaptive SVSF-SLAM algorithm is validated and compared to the EKF/SVSF-SLAM algorithms. The new algorithm was proposed in order to solve the problem of the unknown noise statistic characteristics of the system in the real world and to deal with the parameters uncertainties and linearization errors. After validation of the proposed algorithms with simulation on Pioneer-3AT mobile robot, satisfactory results, good accuracy and robustness were obtained with adaptive SVSF without any assumption on the process and/or observation model accuracy.

References

1. Leonard, J., Tardos, J.D., Thrun, S., Choset, H.: Workshop Notes of the ICRA Workshop on Concurrent Mapping and Localization for Autonomous Mobile Robots. ICRA Conference, Washington (2002)

2. Thorpe, C., Durrant-Whyte, H.: Field robots. In: Springer Tracts in Advanced Robotics, vol. 6, pp. 329–340 (2003)
3. Moutarlier, P., Chatila, R.: An experimental system for incremental environment modeling by an autonomous mobile robot. In: 1st International Symposium On Experimental Robotics, Montreal (1989)
4. Brink, W., van Daalen, C., Brink, W.: Stereo vision as a sensor for EKF SLAM. In: 22nd Annual Symposium of the Pattern Recognition Association of South Africa, New York, pp. 19–24 (2011)
5. Montemerlo, M., Thrun, S., Koller, D., Wegbreit, B.: FastSLAM: a factored solution to the simultaneous localization and mapping problem. In: AAAI National Conference on Artificial Intelligence (2002)
6. Yan, X., Zhao, C., Xiao, J.: A novel FastSlam algorithm based on iterated unscented Kalman filter. In: IEEE International Conference on Robotics and Biomimetics, pp. 1906–1911. IEEE Press, New York (2011)
7. Demim, F., Nemra, A., Louadj, K.: Robust SVSF-SLAM for unmanned vehicle in unknown environment. J. IFAC-Papers OnLine **49**, 386–394 (2016)
8. Demim, F., Nemra, A., Louadj, K., Zakaria, M., Hamelain, M., Bazoula, A.: Simultaneous localization and mapping algorithm for unmanned ground vehicle with SVSF filter. In: 8th IEEE International Conference on Modelling, Identification and Control, pp. 155–162. IEEE Press, New York (2016)
9. Andersson, L.A.A., Nygards, J.: C-SAM, Multi-Robot SLAM using square root information smoothing. In: IEEE International Conference on Robotics and Automation, pp. 2798–2805. IEEE Press, New York (2008)
10. Gadsden, S.A., Dunne, D., Habibi, S.R., Kirubara jan, T.: Comparison of extended and unscented Kalman, particle, and smooth variable structure filters on a bearing-only target tracking problem. In: SPIE, p. 74450B-1 (2013)
11. Al-Shabi, M.: The General Toeplitz/Observability SVSF, Department of Mechanical Engineering, Mc Master University, Hamilton, Ontario (2011)
12. Demim, F., Nemra, A., Louadj, K., Hamelain, M., Bazoula, A.: A new approach to improve the success and solving the UGVs Cooperation for SLAM Problem, using a SVSF Filter. In: ACM Mediterranean Conference on Pattern Recognition and Artificial Intelligence, pp. 56–63. ACM Press, New York (2016)
13. Sfeir, J.: Navigation d'un Robot Mobile en Environnement Inconnu Utilisant les Champs de Potentiels Artificiels, Maïtrise en génie de la production automatisée, Ecole de Technologie Superieure, Montriall, Canada (2009)
14. Allam, A., Nemra, A., Hamerlain, M.: Smooth variable filter VSLAM. J. ScienceDirect (2016). https://doi.org/10.1016/j.ifacol.2016.07.733
15. Nemra, A., Aouf, N.: Robust airborne 3d visual simultaneous localization and mapping with observability and consistency analysis. J. Intell. Robot. Syst. **55**, 4–5 (2009)
16. Habibi, S.R., Burton, R.: The variable structure filter, dynamic systems. J. Measur. Control **125**, 287–293 (2003)
17. Habibi, S.R.: The smooth variable structure filter. In: Proceedings of IEEE, vol. 95, pp. 1026–1059. IEEE Press, New York (2007)
18. Niehsen, W.: Information fusion based on fast covariance intersection filtering. In: International Conference on Information Fusion (FUSION 2002), pp. 901–905 (2002)
19. Davison, A.J., Reid, I.D., Molton, N.D., Stasse, O.: MonoSLAM: real-time single camera SLAM. In: Conference on Pattern Analysis and Machine Intelligence, vol. 29 (2007)

20. Demim, F., Boucheloukh, A., Nemra, A., Louadj, K., Hamerlain, M., Bazoula, A., Mehal, M.: A new adaptive smooth variable structure filter SLAM algorithm for unmanned vehicle. In: 6th IEEE International Conference on Systems and Control, pp. 6–13. IEEE Press, New York (2017)
21. Demim, F., Nemra, A., Louadj, K., Hamelain, M., Bazoula, A.: Cooperative SLAM for multiple UGVs navigation using SVSF filter. J. Control Measur. Electron. Comput. Commun. (Automatika) **58**, 119–129 (2017)
22. Demim, F., Nemra, A., Louadj, K., Hamerlain, M., Bazoula, A.: An adaptive SVSF-SLAM algorithm to improve the success and solving the UGVs cooperation problem. J. Exp. Theor. Artif. Intell. (TETA) **10**, 1–26 (2017)
23. Demim, F., Nemra, A., Louadj, K., Hamerlain, M.: Simultaneous localization, mapping, and path planning for unmanned vehicle using optimal control. J. Adv. Mech. Eng. (SAGE) **10**, 1–25 (2018)
24. Allam, A., Tadjine, M., Nemra, A., Kobzili, E.: Stereo vision as a sensor for SLAM based Smooth Variable Structure Filter with an adaptive Boundary Layer Width. In: 6th IEEE International Conference on Systems and Control (ICSC), pp. 14–20. IEEE Press, New York (2017)
25. Kobzili, E., Larbes, C., Allam, A.: Multi-rate robust scale estimation of monocular SLAM. In: 6th IEEE International Conference on Systems and Control (ICSC), pp. 1–5. IEEE Press, New York (2017)

Projective Lag-Synchronization of Unknown Chaotic Systems with Input Nonlinearities

Sarah Hamel(✉) and Abdesselem Boulkroune

LAJ, University of Jijel, Ouled-Aissa, BP. 98 18000 Jijel, Algeria
m.sarahamel@gmail.com, boulkroune2002@yahoo.fr

Abstract. This paper solves the problem of projective lag-synchronization based on output feedback control for chaotic drive-response systems with input dead-zone and sector nonlinearities. This class of the drive-response systems is assumed in Brunovsky form but with unavailable states and unknown dynamics. To effectively deal with both dead-zone and sector nonlinearities, the proposed controller is designed in a variable structure frame-work. To online learn the uncertain dynamics, adaptive fuzzy systems are used. And to estimate the unavailable states, a simple synchronization-error is constructed. To prove the stability of the overall closed-loop system (controller, observer and drive-response system) and to design the adaptive laws, a Lyapunov theory and strictly positive real (SPR) approach are exploited.

Keywords: Fuzzy control · Projective lag-synchronization
Output-feedback control · Input nonlinearities · Chaotic drive-response systems

1 Introduction

The chaos synchronization has attracted great attention and has been extensively studied [1–14], since it was suggested originally by Pecora and Caroll in [15]. The basic configuration of chaos synchronization consists of two chaotic systems: a drive (master) system and a response (slave) system. It is worth mentioning that the drive and response systems can be identical but with different initial conditions (IC) or quite different. The response system is drived via some transmitted (drive) signals so that the trajectories of the response system synchronize with that of the drive system.

In the literature, there are many types of the chaos synchronization such as complete synchronization (CS) [1, 2], generalized synchronization (GS) [3, 4], projective synchronization (PS) [5, 6], lag synchronization (LS) [7], and so on. In PS, the state vectors of two synchronized systems evolve in a proportional scale. In LS, due to signal propagation delays in the environment, it is reasonable to require the response system at time (t) to synchronize the drive one at time ($t - \tau$), where τ is the propagation delay (lag) [16]. In recent years, lag synchronization has attracted a great deal of attention. Some results have been reported about LS [8–14, 16–18]. Besides, over the past 25 years, a variety of methods have been proposed for chaos synchronization, such as sliding mode control [19, 20], active control [21, 22], adaptive control [23, 24] and fuzzy control [25–27] which are designed via the universal approximation theorem [28].

M. Chadli et al. (Eds.): ICEECA 2017, LNEE 522, pp. 113–127, 2019.
https://doi.org/10.1007/978-3-319-97816-1_9

In real applications of chaos synchronization, the state vectors of drive-response systems are not available for measurement, except the outputs of drive-response systems. Thus, designing a synchronization scheme based on an output-feedback controller (i.e. an observer-based controller) is required. Based on state observer, some adaptive control systems were designed in [29–32]. These systems involve strictly positive real (SPR) concept on the observation-error dynamics. The dynamics of the observation- errors, which are originally not SPR, are augmented by an appropriate low-pass filter designed to meet the SPR concept.

On the other hand, the most of the above works are only valid for chaotic systems without (uncertain) dynamical disturbances and input nonlinearity. However, in the practice, the chaotic systems are inevitably affected by uncertain dynamical disturbances. The existence of these disturbances can generally lead to the synchronization failure and cause undesirable results. How to enhance the disturbance compensation or attenuation is of great significance [33, 34]. Besides, owing to the physical limitations, the practical implementations of the control systems are frequently exposed to input nonlinearities (backlash, dead-zone, saturation). It has been shown that these input nonlinearities can cause a serious degradation of the system performances and in a worst-case system failure. So, the design of a controller for chaos synchronization by considering of the external disturbances and input nonlinearities is of significant importance [31–39]. To effectively deal with these problems, the control schemes have been generally designed in a variable-structure control frame-work.

Motivated by the above discussions, in this paper, we aim at addressing the problem of projective lag-synchronization for a class of uncertain chaotic systems subject to uncertain external dynamical disturbances and input nonlinearities (sector nonlinearities with dead-zone). This synchronization can be practically realized through an appropriate fuzzy adaptive variable-structure controller based on a state observer. Compared with the previous works on the chaos synchronization and control [8–14, 16–20, 31–39], the main contributions of this study are:

- A novel projective lag-synchronization system based on fuzzy adaptive variable-structure output-feedback control is designed for unknown perturbed chaotic systems containing dead-zone nonlinearity.
- Unlike in [40–46], by using the SPR property together with Lyapunov theory, the stability of the resultant closed-loop system is carefully established. Recall that many previous works requiring the SPR property, e.g. [40–46], have not been derived rigorously, as stated in [47].
- By designing a linear observer to estimate the lag-synchronization errors, only the outputs of the response-drive system are assumed to be measurable and required in this synchronization scheme.

2 Problem Formulation

Consider the following class of drive-response chaotic systems:

$$\begin{cases} y_x^{(n)} = F_d(x) + D_d(t, x) \\ y_z^{(n)} = F_r(z) + u + D_r(t, z) \end{cases} \tag{1}$$

Or equivalently of the form

$$\begin{cases} \dot{x} = Ax + B\left[F_d(x) + D_d(t, x)\right] \\ \dot{z} = Az + B\left[F_r(z) + u + D_r(t, z)\right] \end{cases} \tag{2}$$

with

$$A = \begin{bmatrix} 0 & 1 & 0 & \dots & 0 \\ 0 & 0 & 1 & \dots & 0 \\ \dots & \dots & \dots & \dots & \dots \\ 0 & 0 & 0 & \dots & 1 \\ 0 & 0 & 0 & \dots & 0 \end{bmatrix} B = \begin{bmatrix} 0 \\ \vdots \\ 0 \\ 1 \end{bmatrix}$$

where $x = [x_1, \dots, x_n]^T \in R^n$ and $z = [z_1, \dots, z_n]^T \in R^n$ are the state vectors of the drive and response systems respectively. $F_d(x)$ and $F_r(z)$ are unknown nonlinear smooth functions and $u = \varphi(v)$ is the input nonlinearity, and v is the control input.

The input nonlinearity $u = \varphi(v)$ under consideration is [48, 49]:

$$\varphi(v) = \begin{cases} \varphi_+(v)\left(v - v_+\right), & v > v_+ \\ 0, & -v_- \le v \le v_+ \\ \varphi_-(v)\left(v + v_-\right), & v < -v_- \end{cases} \tag{3}$$

with $\varphi_+(v) > 0$ and $\varphi_-(v) > 0$ are nonlinear smooth functions of v, $v_+ > 0$ and $v_- > 0$. Note that this model contains both sector nonlinearity and dead-zone. The nonlinearity $\varphi(v)$ also has the following features:

$$\left(v - v_+\right)\varphi(v) \ge m_+^*\left(v - v_+\right)^2, v > v_+ \tag{4}$$

$$\left(v + v_-\right)\varphi(v) \ge m_-^*\left(v + v_-\right)^2,\ v < -v_-, \tag{5}$$

with m_+^* and m_-^* being so-called "*the gain reduction tolerances*" [48, 49].

Design Objective: Determine an output-feedback control law v to achieve a practical projective lag-synchronization between the drive system and the response one, while ensuring that all involved signals in the closed-loop system remain bounded.

To facilitate the control system design, the following usual assumptions are considered and will be used in the subsequent developments.

Assumption 2.1: The state vectors of the drive and response systems are not measurable, except the system outputs (i.e. except x_1 and z_1).

Assumption 2.2

- The nonlinear functions $\varphi_+(v)$ and $\varphi_-(v)$ are unknown.
- But, the constants v_+, v_-, m_+^* and m_-^* are assumed to be known.

Assumption 2.3: The external disturbances, $D_d(t,x)$ and $D_r(t,z)$, are bounded re*spectively by:*

$$\begin{cases} \left|D_d(t,x)\right| \le c_d \\ \left|D_r(t,z)\right| \le c_r \end{cases} \tag{6}$$

where c_d and c_r are some unknown positive constants.

Definition 2.1: The drive and response systems (2) are projective lag-synchronized if there exists a scaling factor λ such that: $e = z - \lambda x(t-\tau) \to 0$ *as* $t \to \infty$, where $\tau > 0$ is a constant propagation delay or transmission delay. This means that the transmitted signal is received τ time late after it was sent. The value of τ depends on the channel or the distance between drive and response system.

From Eq. (2) and Definition 2.1, one can write the dynamics of the lag-synchronization error as:

$$\begin{aligned} \dot{e} &= \dot{z} - \lambda\dot{x}(t-\tau) \\ &= Ae + B\left[-\lambda F_d\left(x_\tau\right) - \lambda D_d\left(t,x_\tau\right) + F_r(z) + u + D_r(t,z)\right] \\ &= Ae + B\left[F_r(z) + u + P_1\right] \end{aligned} \tag{7}$$

where $x_\tau = x(t-\tau)$ and

$$P_1 = D_r(t,z) - \lambda F_d\left(x_\tau\right) - \lambda D_d\left(t,x_\tau\right). \tag{8}$$

Note that one can easily show the existence of a constant $c_1 > 0$ such as $\left|P_1\right| \le c_1$, for the following reasons: x evolves in a compact set (an intrinsic property of the (non-controlled) chaotic systems), also the delayed state x_τ is bounded and the external disturbances, $D_d(t,x)$ and $D_r(t,z)$, are already assumed to be bounded and finally the function $F_d\left(x_\tau\right)$ is smooth and with a bounded argument.

Since $F_r(z)$ is unknown and the vector e is immeasurable, in this paper, one will use:

(1) A fuzzy adaptive system to approximate the uncertain functions.
(2) An observer to estimate the projective lag-synchronization error e.

3 Controller Design for Projective Lag-Synchronization

This section proposes a fuzzy adaptive output-feedback controller for lag-projective synchronization of the drive-response system (2) using Lyapunov stability theory. The proposed synchronization scheme is shown in Fig. 1. One can rewrite the dynamics of the lag-synchronization errors as follows

$$\begin{cases} \dot{e} = Ae + B\left[F_r(e + \lambda x(t-\tau)) + u + P_1\right] \\ e_1 = Ce \end{cases} \tag{9}$$

where $C = [10\ldots0]$. Note that the pair (C, A) is observable.

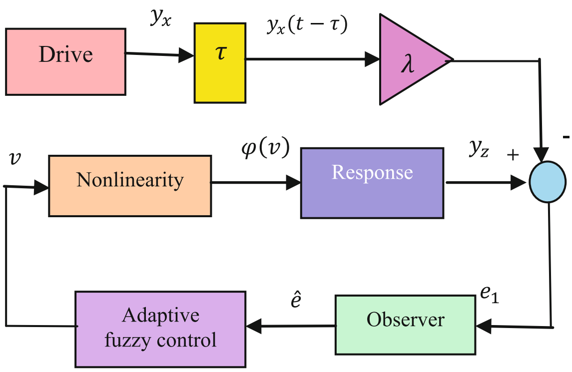

Fig. 1. Projective lag-synchronization scheme.

Using the universal approximations theorem [28], one obtains:

$$F_r(e + \lambda x(t-\tau)) = \theta^{*T}\psi(e) + \varepsilon(e, x(t-\tau)) \tag{10}$$

with $\psi(e)$ being the vector of FBFs (which are assumed to be designed a priori), $\varepsilon(e, x(t-\tau))$ is the fuzzy approximation error and θ^* is the optimal value of the adjustable parameter vector of the fuzzy system which is defined as:

$$\theta^* = \operatorname{argmin}_\theta\left[\sup_{e\in\Omega_e}\left|F_r(e + \lambda x(t-\tau)) - \theta^T\psi(e)\right|\right] \tag{11}$$

Then, (9) becomes:

$$\begin{cases} \dot{e} = Ae + B\left[\theta^{*T}\psi(e) + u + P_2\right] \\ e_1 = Ce \end{cases} \tag{12}$$

where $P_2 = P_1 + \varepsilon(e, x(t-\tau))$.

Since the lag-synchronization error vector e is not available for measurement, one designs the following linear observer to estimate it:

$$\begin{cases} \dot{\hat{e}} = A_c\hat{e} + K_o\tilde{e}_1 \\ \hat{e}_1 = C\hat{e} \end{cases} \tag{13}$$

where $\hat{e}$ is the estimate of e, $K_o = \left[k_{o1}, \ldots, k_{on}\right]^T \in R^n$ is the gains vector of observer, $A_c = A - BK_c^T$ and $K_c = \left[k_{c1}, \ldots, k_{cn}\right]^T \in R^n$ is the feedback gain vector.

Now, one defines the observation error vector as $\hat{e} = \left[\hat{e}_1, \ldots, \hat{e}_n\right]^T = e - \hat{e}$. From (12) and (13), the dynamics of this observation error can be obtained as follows:

$$\begin{cases} \dot{\tilde{e}} = A_o \tilde{e} + B\left[\theta^{*T}\psi(e) + \varphi(v) + P_3\right] \\ \tilde{e}_1 = C\tilde{e} \end{cases} \tag{14}$$

with $A_o = A - K_o C$, and

$$P_3 = P_2 + K_c^T \hat{e} \tag{15}$$

Then, we can rewrite (14) using the time-frequency (mixed) notation as follow [50]:

$$\tilde{e}_1 = H(s)\left[\theta^{*T}\psi(e) + \varphi(v) + P_3\right] \tag{16}$$

where s is the Laplace variable and $H(s) = C\left(SI - A_o\right)^{-1}B$ is the stable transfer function of (14). It is worth noting that this mixed notation is very valuable in the adaptive control literature [50]. It is also refers to the convolution between the inverse Laplace transform $H(s)$ and the term $\theta^{*T}\psi(e) + \varphi(v) + P_3$.

Since $H(s)$ is not SPR, one introduces a low pass filter $T(s)$ such that $\bar{H}(s) = H(s)T^{-1}(s)$ becomes SPR:

$$\begin{aligned} \tilde{e}_1 &= \bar{H}(s)\left[\theta^{*T}T(s)[\psi(e)] + T(s)[\varphi(v)] + T(s)\left[P_3\right]\right] \\ &= \bar{H}(s)\left[\theta^{*T}\psi(\hat{e}) + \varphi(v) + P_4\right] \end{aligned} \tag{17}$$

with

$$P_4 = \theta^{*T}T(s)[\psi(e)] + T(s)[\varphi(v)] + T(s)\left[P_3\right] - \theta^{*T}\psi(\hat{e}) - \varphi(v) \tag{18}$$

Assumption 3.1: One assumes that $\left|P_4\right| \le k_{p0}^* + k_{p1}^*|v| + k_{p2}^*|T(s)[v]| + k_{p3}^*\left|T(s)\left[K_c^T\hat{e}\right]\right| = K_p^{*T}W$, with $K_p^{*T} = \left[k_{p0}^*, k_{p1}^*, k_{p2}^*, k_{p3}^*\right]$ is an unknown positive vector, and $W^T = \left[\,1,\ |v|,\ |T(s)[v]|,\ \left|T(s)\left[K_c^T\hat{e}\right]\right|\,\right]$.

Let us define a novel error e_{m1}, called *the modified error* as follows:

$$e_{m1} = \tilde{e}_1 + e_{a1} \tag{19}$$

with e_{a1} is *the auxiliary error*. Its dynamics are given by:

$$e_{a1} = \bar{H}(s)\left[-K_p^T W\, Tanh\left(K_p^T W e_{m1}/\varepsilon\right)\right] \tag{20}$$

where K_p is the estimate of the unknown vector K_p^* and $\varepsilon > 0$ is a small design constant. $Tanh(.)$ designates the usual hyperbolic tangent function.

From (17), (19) and (20), one can obtain:

$$e_{m1} = \bar{H}(s)\left[\theta^{*T}\psi(\hat{e}) + \varphi(v) + P_4 - K_p^T W\, Tanh\left(K_p^T W e_{m1}/\varepsilon\right)\right] \tag{21}$$

The state-space presentation of (21) can be given by:

$$\begin{cases} \dot{e}_m = \bar{A}_o e_m + \bar{B}\left[\theta^{*T}\psi(\hat{e}) + \varphi(v) + P_4 - K_p^T W\, Tanh\left(K_p^T W e_{m1}/\varepsilon\right)\right] \\ e_{m1} = \bar{C} e_m \end{cases} \tag{22}$$

where $e_m = \left[e_{m1}, \ldots, e_{mn}\right]^T$ and $\left(\bar{A}_o \in R^{n\times n}, \bar{B} \in R^{n\times 1}, \bar{C} \in R^{1\times n}\right)$ is a minimal state realization of $\bar{H}(s) = H(s)T^{-1}(s) = \bar{C}^T\left(SI - \bar{A}_o\right)^{-1}\bar{B}$ and $\bar{C} = [1, 0, \ldots, 0]$.

Since $\bar{H}(s)$ is SPR, the following relation holds:

$$\begin{cases} \bar{A}_o P + P\bar{A}_o = -Q < 0 \\ P\bar{B} = \bar{C}^T \end{cases} \tag{23}$$

where $P = P^T > 0$ and $Q = Q^T > 0$. Later, the expressions (22) and (23) will be exploited in the stability analysis.

To achieve our objective, the control input can be determined as:

$$v = \begin{cases} -\xi\rho sign\left(e_{m1}\right) - v_-, & e_{m1} > 0 \\ 0, & e_{m1} = 0 \\ -\xi\rho sign\left(e_{m1}\right) + v_+, & e_{m1} < 0 \end{cases} \tag{24}$$

with $\xi > \frac{1}{\eta}$, and $\eta = \min\left\{m_-^*, m_+^*\right\}$, where

$$\rho = w_2\|\psi(\hat{e})\| + w_1 \tag{25}$$

where w_1 is a design positive constant and w_2 is an adaptive parameter estimating the upper bound of $\|\theta^*\|$, i.e. $w_2^* \geq \|\theta^*\|$.

The adaptive laws for the control law (24) are defined as:

$$\begin{cases} \dot{w}_2 = -\gamma_w\sigma_w w_2 + \gamma_w\left|e_{m1}\right|\|\psi(\hat{e})\|, & with \quad w_2(0) > 0 \\ \dot{K}_p = -\gamma_K\sigma_K K_p + \gamma_K\left|e_{m1}\right| W, & with \quad K_p(0) > 0 \end{cases} \tag{26}$$

where $\gamma_K, \sigma_K, \gamma_w$ and σ_w are strictly positive design parameters.

Theorem 3.1: Consider the drive and response systems given by Eq. (2) (or (1)) under Assumptions 2.1–2.3 and 3.1. Then, the projective lag-synchronization is practically realized by using the fuzzy adaptive output-feedback controller (24)–(26) and the observer (13).

Proof of Theorem 3.1: Consider the following Lyapunov function:

$$V = \frac{1}{2}e_m^T P e_m + \frac{1}{2\gamma_K}\tilde{K}_p^T \tilde{K}_p + \frac{1}{2\gamma_w}\tilde{w}_2^2 \tag{27}$$

where $\tilde{K}_p = K_p - K_p^*$ *and* $\tilde{w}_2 = w_2 - w_2^*$.

The time derivative of V is:

$$\dot{V} = \frac{1}{2}e_m^T P \dot{e}_m + \frac{1}{2}\dot{e}_m^T P e_m + \frac{1}{\gamma_K}\tilde{K}_p^T \dot{K}_p + \frac{1}{\gamma_w}\tilde{w}_2 \dot{w}_2 \tag{28}$$

As in [48, 49], by using (24)–(26) and (22), one can obtain:

$$\dot{V} \leq -\mu V + \pi \tag{29}$$

with $\pi = \bar{\varepsilon} + \frac{\sigma_K}{2}\left\|K_p^*\right\|^2 + \frac{\sigma_w}{2}w_2^{*2}$ and $\mu = min\{\lambda_{min}(Q)/\lambda_{max}(P), \gamma_w\sigma_w, \gamma_K\sigma_K\}$. Where $\lambda_{min}(X)$ *and* $\lambda_{max}(X)$ are the smallest and largest eigenvalues of the matrix X, respectively.

(29) can be expressed as follows:

$$\frac{d(Ve^{\mu t})}{dt} \leq \pi e^{\mu t} \tag{30}$$

And integrating (30) over $[0, t]$ yields:

$$0 \leq V(t) \leq \frac{\pi}{\mu} + \left(V(0) - \frac{\pi}{\mu}\right)e^{-\mu t} \tag{31}$$

Therefore all signals of the closed-loop system are bounded.

From (27) and (31), one has:

$$\|e_m\| \leq \left(\frac{2}{\lambda_{min}(P)}\left(\frac{\pi}{\mu} + \left(V(0) - \frac{\pi}{\mu}\right)e^{-\mu t}\right)\right)^{1/2} \tag{32}$$

where: $V(0) = \frac{1}{2}e_m^T(0)Pe_m(0) + \frac{1}{2\gamma_K}\tilde{K}_p^T(0)\tilde{K}_p(0) + \frac{1}{2\gamma_w}w_2^2(0)$.

From (32), one can conclude on the asymptotic convergence of the solution e_m to the following bounded region:

$$\Omega_{e_m} = \left\{ e_m \middle| \|e_m\| \leq \left(\frac{2}{\lambda_{min}(P)}\frac{\pi}{\mu}\right)^{1/2} \right\} \tag{33}$$

From (19), (20) and (33), one can establish easily the practical convergence and the boundedness of e_{a1} and $\tilde{e}_1$.

Remark 3.1: If $v_+ = v_- = v_0$, the expression (24) can be simply rewritten as:

$$v = -\left(\xi w_2 \|\psi(\hat{e})\| + \xi w_1 + v_0\right) Sign\left(e_{m1}\right) \tag{34}$$

In (45), the sign function, i.e. $Sign\left(e_{m1}\right)$, can cause the undesirable chattering phenomenon. In the practice, the latter is generally replaced by an equivalent and smooth function (e.g. $Tanh\left(k_{s1} e_{m1}\right)$), as follows:

$$v = -\left(\xi w_2 \|\psi(\hat{e})\| + \xi w_1 + v_0\right) Tanh\left(k_{s1} e_{m1}\right) \tag{35}$$

with $k_{s1} > 0$ is a high constant value.

4 Illustrative Simulation Example

Consider the practical projective lag-synchronization between chaotic Gyros system and Duffing oscillator.

The drive system (chaotic Gyros system)

$$\begin{cases} \dot{x}_1 = x_2 \\ \dot{x}_2 = -\alpha^2 \dfrac{\left(1 - \cos\left(x_1\right)\right)^2}{\sin^3\left(x_1\right)} - c_1 x_2 - c_2 x_2^2 + \left(\beta + f sin\left(\omega_x t\right)\right) \sin\left(x_1\right) + D_d(t, x) \end{cases}$$

where $x = [x_1 x_2]^T$, $\alpha^2 = 100$, $c_1 = 0.5$, $c_2 = 0.05$, $\beta = 1$, $\omega_x = 2$, $f = 35.5$ and $D_d(t, x) = 0.2 \sin(2t)$.

The response system (Duffing oscillator)

$$\begin{cases} \dot{z}_1 = z_2 \\ \dot{z}_2 = -p_1 z_2 - p_2 z_1 - p_3 z_1^3 + q sin\left(\omega_z t\right) + u + D_r(t, z) \end{cases}$$

where $z = [z_1\ z_2]^T, p_1 = 0.4,$ $p_2 = -1.1, p_3 = 1,$ $q = 2.1,$ $\omega_z = 1.8$ and $D_r(t, z) = 0.1 \sin(6t)$.

Then, this chaotic drive-response system can be rewritten as follows:

$$\begin{aligned} &\dot{x} = Ax + B(F_d(x) + D_d(t, x)), \quad y_x = x_1 = C, \\ &\dot{z} = Az + B(F_r(z) + u + D_r(t, z), \quad y_z = z_1 = Cz, \end{aligned}$$

where $A = \begin{bmatrix} 0 & 1 \\ 0 & 0 \end{bmatrix}$, $B = \begin{bmatrix} 0 \\ 1 \end{bmatrix}$ and $C^T = \begin{bmatrix} 1 \\ 0 \end{bmatrix}$. $u = \varphi(v)$ is the input nonlinearity which is defined below, and v is the control input to be designed.

The input nonlinearities $\varphi(v)$ is assumed to be described by:

$$\varphi(v) = \begin{cases} (v - 0.5)\left(1.5 - 0.3e^{0.3|\sin(v)|}\right) & v > 0.5 \\ 0 & -0.5 \le v \le 0.5 \\ (v + 0.5)\left(1.5 - 0.3e^{0.3|\sin(v)|}\right) & v < -0.5 \end{cases}$$

To estimate the synchronization error, the following linear observer is designed:

$$\begin{cases} \dot{\hat{e}} = A_c\hat{e} + K_o\left(y_x(t - \tau) - y_z - \hat{e}_1\right) \\ \hat{e}_1 = C\hat{e} \end{cases}$$

with $\hat{e} = \left[\hat{e}_1, \hat{e}_2\right]^T$ is the estimate of $e = \left[e_1, e_2\right]^T$, $K_o = \left[2\alpha, \alpha^2\right]^T$ is the observer gain vector with $\alpha = 80$, $A_c = A - BK_c^T$ and $K_c = [90, 60]^T$.

Based on Theorem 3.1 and Remark 3.1, the controller for this system can be designed as (34) or (35) with adaptive laws (26). Its associated design parameters are chosen as: $\tau = 0.5$ sec, $\lambda = 1$, $w_1 = 100$, $\varepsilon = 0.2$, $\gamma_w = 100$, $\sigma_w = 0.001$, $\gamma_k = 100$ and $\sigma_k = 0.001$.

For each variable of the entries of the designed fuzzy system, as in [47], one defines three membership functions (one triangular and two trapezoidal) uniformly distributed on the following intervals: $[-2\ 2]$ for $\hat{e}_1$ and $[-2\ 2]$ for $\hat{e}_2$.

One selects the SPR filter $T(s)$ so that $\bar{H}(s) = H(s)T^{-1}(s) = \dfrac{1}{s^2 + 160s + 6400}T^{-1}(s)$ is SPR, as follows:

$$T(s) = \frac{1}{0.3906s + 11.7721}$$

From the expression of $\bar{H}(s)$, one can find that $\bar{A} = \begin{bmatrix} -2\alpha & 1 \\ -\alpha^2 & 0 \end{bmatrix}$, $\bar{B}^T = \begin{bmatrix} 0.3906 & 11.7721 \end{bmatrix}$ and $\bar{C}^T = \begin{bmatrix} 1 & 0 \end{bmatrix}$.

By choosing $Q_1 = \begin{bmatrix} 30 & 3 \\ 3 & 0.5 \end{bmatrix}$ and solving (23), one gets:

$$P_1 = \begin{bmatrix} 10.0937 & -0.2500 \\ -0.2500 & 0.0083 \end{bmatrix}$$

The initial conditions are chosen as $x(0) = \left[x_1(0), x_2(0)\right]^T = [-1, 1]^T$, $z(0) = \left[z_1(0), z_2(0)\right]^T = [0.5, 2]^T$, $w_2(0) = 10$ and $K_p(0) = [0.01, 0.01, 0.01, 0.01]^T$.

Note that, because $v_+ = v_- = v_0 = 0.5$, the variable-structure controller (24) can be directly replaced by (34). Two cases are considered to show the validity of the proposed controller.

1) Simulation by Using the Discontinuous Controller (34)

Figure 2 shows that the proposed controller performs well. In fact, one can see from Fig. 2a, b that the states of response system (z_1, z_2) effectively track that of the drive system $\left(\lambda x_1(t-\tau), \lambda x_2(t-\tau)\right)$, despite the presence of the immeasurable states, uncertain dynamics, dead-zone at the input and external disturbances. From Fig. 2c, it is clear also that the estimates of the synchronization errors are bounded and asymptotically converge towards small values. The corresponding control signal is bounded and not smooth in Fig. 2d.

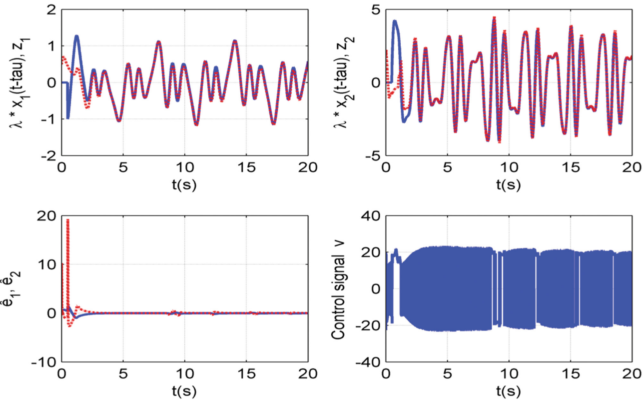

Fig. 2. Simulation results (case 1): **(a)** States: $\lambda x_1(t-\tau)$ (solid line) and z_1 (dashdot line). **(b)** States: $\lambda x_2(t-\tau)$ (solid line) and z_2 (dashdot line). **(c)** Estimates of the synchronization errors $\hat{e}_1$ (solid line) and $\hat{e}_2$ (dashdot line). **(d)** Control signal v.

2) Simulation by Using the Smooth Controller (35)

Figure 3 provides the simulation results. From Fig. 3a, b, one can observe that the states of the response system (z_1, z_2) effectively follow the corresponding desired trajectories $\left(\lambda x_1(t-\tau), \lambda x_2(t-\tau)\right)$. From Fig. 3c, one can see that the estimates of the synchronization errors are well-bounded and converge to a small value. In Fig. 3d, the control signal is smooth, bounded and admissible.

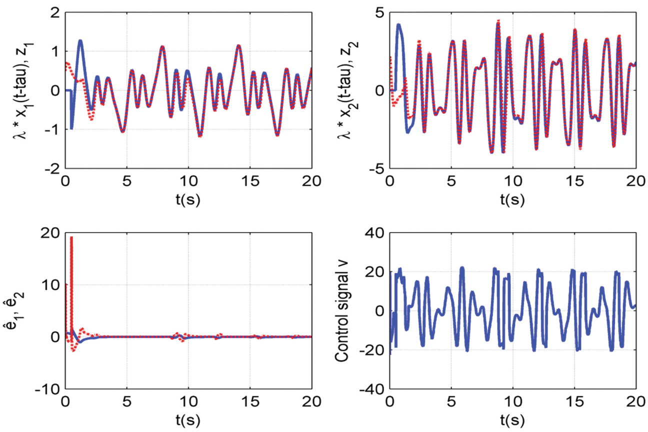

Fig. 3. Simulation results (case 2): **(a)** States: $\lambda x_1(t-\tau)$ (solid line) and z_1 (dashdot line). **(b)** States: $\lambda x_2(t-\tau)$ (solid line) and z_2 (dashdot line). **(c)** Estimates of the synchronization errors $\hat{e}_1$ (solid line) and $\hat{e}_2$ (dashdot line). **(d)** Control signal v.

5 Conclusion

The problem of adaptive fuzzy output-feedback control-based projective lag-synchronization for unknown drive-response chaotic systems has been investigated in this paper. In the design process, the input nonlinearities (dead-zone together with sector nonlinearities) have been considered. To effectively handle the unknown functions in the drive-response system, fuzzy adaptive systems have been incorporated in the control system. To deal with the input nonlinearities, the proposed controller has been designed in a variable structure frame-work. And to estimate the synchronization-error states, a simple linear observer has been constructed.

References

1. Bowonga, S., Kakmenib, M., Koinac, R.: Chaos synchronization and duration time of a class of uncertain systems. Math. Comput. Simul. **71**, 212–228 (2006)
2. Chunni, W., Yujun, H., Jun, M., Long, H.: Parameters estimation, mixed synchronization, and anti-synchronization in chaotic systems. Complexity **20**(1), 64–73 (2014)
3. Wang, Y.W., Guan, Z.H.: Generalized synchronization of continuous chaotic systems. Chaos, Solitons Fractals **27**, 97–101 (2006)
4. Jianping, Y., Changpin, L.: Generalized projective synchronization of a unified chaotic system. Chaos, Solitons Fractals **26**, 1119–1124 (2005)
5. Li, G.: Projective synchronization of chaotic system using backstepping control. Chaos, Solitons Fractals **29**, 490–598 (2006)
6. Li, G.H.: Generalized projective synchronization between Lorenz system and Chen's system. Chaos, Solitons Fractals **32**, 1454–1458 (2007)
7. Cailian, C., Gang, F., Xinping, G.: An adaptive lag-synchronization method for time-delay chaotic systems. In: Proceedings of the American Control Conference, pp. 4277–4282 (2005)

8. Pourdehi, S., Karimipour, D., Karimaghaee, P.: Output-feedback lag-synchronization of time-delayed chaotic systems in the presence of external disturbances subjected to input nonlinearity. Chaos **21**, 043128 (2011)
9. Shahverdiev, E.M., Sivaprakasam, S., Shore, K.A.: Lag synchronization in time-delayed systems. Phys. Lett. A **292**(6), 320–324 (2002)
10. Chen, C., Feng, G., Guan, X.: An adaptive lag-synchronization method for time-delay chaotic systems. In: American Control Conference, Portland, OR (2005)
11. Chen, Y., Chen, X., Gu, S.: Lag synchronization of structurally nonequivalent chaotic systems with time delays. Nonlinear Anal. **66**(9), 1929–1937 (2007)
12. Li, C., Liao, X., Wong, K.W.: Lag synchronization of hyperchaos with application to secure communications. Chaos, Solitons Fractals **23**(1), 183–193 (2005)
13. Wang, L., Yuan, Z., Chen, X., Zhou, Z.: Lag synchronization of chaotic systems with parameter mismatches. Commun. Nonlinear Sci. Numer. Simul. **16**(2), 987–992 (2011)
14. Xu, Y., Zhou, W., Fang, J.A., Sun, W.: Adaptive lag synchronization and parameters adaptive lag identification of chaotic systems. Phys. Lett. A **374**(34), 3441–3446 (2010)
15. Pecora, L.M., Carroll, T.L.: Synchronization in chaotic systems. Phys. Rev. Lett. **64**, 821–824 (1990)
16. Zhao, M., Liu, R., Gao, Y.: Dissipative lag synchronization of chaotic Lur'e systems with unknown disturbances. IMA J. Math. Control Inf. **34**(1), 123–138 (2015)
17. Gu, W.-D., Sun, Z.-Y., Wu, X.-M., Yu, C.-B.: Adaptive lag synchronization of uncertain dynamical systems with time delays via simple transmission lag feedback. Chin. Phys. B **22**(8), 080507 (2013)
18. Sun, Z.: Lag projective synchronization of two chaotic systems with different fractional orders. J. Korean Phys. Soc. **66**(8), 1192–1199 (2015)
19. Khan, A., Shahzad, M.: Synchronization of circular restricted three body problem with Lorenz hyper chaotic system using a robust adaptive sliding mode controller. Complexity **18**, 58–64 (2013)
20. Roopaei, M., Sahraei, B.R., Lin, T.-C.: Adaptive sliding mode control in a novel class of chaotic systems. Commun. Nonlinear Sci. Numer. Simul. **15**, 4158–4170 (2010)
21. Ahmad, I., Saaban, A., Ibrahim, A., Shahzad, M.: Global chaos synchronization of new chaotic system using linear active control. Complexity **21**(1), 379–386 (2015)
22. Ahmad, I., Saaban, A., Ibrahim, A., Shahzad, M.: Research on the synchronization of two novel chaotic systems based on a nonlinear active control algorithm, engineering. Technol. Appl. Sci. Res. **5**(1), 739–747 (2015)
23. Vargas, J., Grzeidak, E., Hemerly, E.: Robust adaptive synchronization of a hyperchaotic finance system. Nonlinear Dyn. **80**(1–2), 239–248 (2015)
24. Ahmad, I., Saaban, A., Ibrahim, A., Al-Hadhrami, S., Shahzad, M., Al-Mahrouqi, S.: A research on adaptive control to stabilize and synchronize a hyperchaotic system with uncertain parameters. Int. J. Optim. Control Theor. Appl. **5**(2), 51–62 (2015)
25. Lin, T., Lee, T., Balas, V.: Adaptive fuzzy sliding mode control for synchronization of uncertain fractional order chaotic systems. Chaos, Solitons Fractals **44**(10), 791–801 (2011)
26. Hwang, E., Hyun, C., Kim, E., Park, M.: Fuzzy model based adaptive synchronization of uncertain chaotic systems: Robust tracking control approach. Phys. Lett. A **373**, 1935–1939 (2009)
27. Wang, J., Chen, L., Deng, B.: Synchronization of Ghostburster neuron in external electrical stimulation via H∞ variable universe fuzzy adaptive control. Chaos, Solitons Fractals **39**(5), 2076–2085 (2009)
28. Wang, L.: Adaptive Fuzzy Systems and Control: Design and Stability Analysis. Prentice-Hall, Englewood Cliffs (1994)

29. Boulkroune, A., Chekireb, H., Tadjine, M., Bouatmane, S.: Observer-based adaptive feedback controller of a class of chaotic systems. Int. J. Bifurc. Chaos **16**(11), 3411–3419 (2006)
30. Boulkroune, A., Chekireb, H., Tadjine, M., Bouatmane, S.: An adaptive feedback controller with observer for linearizable chaotic systems. Control Intell. Syst. **35**(2), 162–168 (2007)
31. Boulkroune, A., M'saad, M.: A practical projective synchronization approach for uncertain chaotic systems with dead-zone input. Commun. Nonlinear Sci. Numer. Simul. **6**, 4487–4500 (2011)
32. Boulkroune, A., M'saad, M.: Fuzzy adaptive observer-based projective synchronization for nonlinear systems with input nonlinearity. J. Vib. Control **18**(3), 437–450 (2012)
33. Hamel, S., Boulkroune, A.: A generalized function projective synchronization scheme for uncertain chaotic systems subject to input nonlinearities. Int. J. Gen. Syst. **45**(6), 689–710 (2016)
34. Hamel, S., Boulkroune, A., Bouzeriba, A.: Function vector synchronization based on fuzzy control for uncertain chaotic systems with dead-zone nonlinearities. Complexity **21**(S1), 234–249 (2016)
35. Boulkroune, A., M'Saad, M.: A fuzzy adaptive variable-structure control scheme for uncertain chaotic MIMO systems with sector nonlinearities and dead-zones. Expert Syst. Appl. **38**(12), 14744–14750 (2011)
36. Pourdehi, S., Karimaghaee, P.: Simple adaptive output-feedback lag-synchronization of multiple time-delayed chaotic systems. Chaos **22**(2), 023145 (2012)
37. Bessa, W., Paula, A., Savi, M.: Sliding mode control with adaptive fuzzy dead-zone compensation for uncertain chaotic systems. Nonlinear Dyn. **70**(3), 1989–2001 (2012)
38. Aghababa, M., Aghababa, H.: A novel finite-time sliding mode controller for synchronization of chaotic systems with input nonlinearity. Arab. J. Sci. Eng. **38**(11), 3221–3232 (2013)
39. Zhang, Z., Lu, J., Gao, L., Shao, H.: Exponential synchronization of Genesio–Tesi chaotic systems with partially known uncertainties and completely unknown dead-zone nonlinearity. J. Frankl. Inst. **350**(2), 347–357 (2013)
40. Leu, Y., Lee, T., Wang, W.: Observer-based adaptive fuzzy-neural control for unknown nonlinear dynamical systems. IEEE Trans. Syst. Man Cybern. Part B Cybern. **29**, 583–591 (1999)
41. Leu, Y., Wang, W., Lee, T.: Observer-based direct adaptive fuzzy-neural control for nonaffine nonlinear systems. IEEE Trans. Neural Netw. **16**(4), 853–861 (2005)
42. Li, H., Tong, S.: A hybrid fuzzy adaptive control for a class of nonlinear MIMO systems. IEEE Trans. Fuzzy Syst. **11**(1), 24–34 (2003)
43. Tong, S., Li, H.X., Wang, W.: Observer-based adaptive fuzzy control for SISO nonlinear systems. Fuzzy Sets Syst. **148**, 355–376 (2004)
44. Wang, W., Leu, Y., Lee, T.: Output-feedback control of nonlinear systems using direct adaptive fuzzy-neural controller. Fuzzy Sets Syst. **140**, 341–358 (2003)
45. Liu, Y., Tong, S., Wang, W., Li, Y.M.: Observer-based direct adaptive fuzzy control of uncertain nonlinear systems and its applications. Int. J. Control Autom. Syst. **7**(4), 681–690 (2009)
46. Ho, H.F., Wong, Y.K., Rad, A.B., Lo, W.L.: State observer based indirect adaptive fuzzy tracking control. Simul. Modell. Pract. Theory **13**, 646–663 (2005)
47. Boulkroune, A., Tadjine, M., M'Saad, M., Farza, M.: How to design a fuzzy adaptive control based on observers for uncertain affine nonlinear systems. Fuzzy Sets Syst. **159**, 926–948 (2008)

48. Boulkroune, A., M'Saad, M., Farza, M.: Adaptive fuzzy controller for multivariable nonlinear state time-varying delay systems subject to input nonlinearities. Fuzzy Sets Syst. **164**, 45–65 (2011)
49. Boulkroune, A., M'Saad, M., Farza, M.: State and output feedback fuzzy variable structure controllers for multivariable nonlinear systems subject to input nonlinearities. Int. J. Adv. Manuf. Technol. **71**(1–4), 539–556 (2014)
50. Boulkroune, A., Bounar, N., M'Saad, M., Farza, M.: Indirect adaptive fuzzy control scheme based on observer for nonlinear systems: a novel SPR-filter approach. Neurocomputing **135**, 378–387 (2014)

Check for updates

Synchronization of Incommensurate Fractional-Order Chaotic Systems with Input Nonlinearities Using a Fuzzy Variable-Structure Control

Amina Boubellouta and Abdesselem Boulkroune(✉)

LAJ, University of Jijel, BP. 98, Ouled-Aissa, 18000 Jijel, Algeria
aminaunivl8@gmail.com, boulkroune2002@yahoo.fr

Abstract. This research work addresses the fuzzy adaptive controller design for a generalized projective synchronization (GPS) of incommensurate fractional-order chaotic systems with input nonlinearities. The considered *master-slave* systems are with different fractional-orders, uncertain models, unknown bounded disturbances and non-identical form. The suggested controller includes two main terms, namely, a fuzzy adaptive control and a fractional-order variable structure control. The fuzzy logic systems are exploited for approximating the system uncertainties. A Lyapunov approach is employed for determining the parameter adaptation laws and proving the stability of the closed-loop system. At last, simulation results are given to demonstrate the validity of the proposed GPS approach.

Keywords: Generalized projective synchronization · Fuzzy adaptive control
Fractional-order variable-structure control
Incommensurate fractional-order chaotic systems

1 Introduction

Throughout the last decades, ***fractional-order*** plants (i.e. the systems with fractional integrals or derivatives) have been studied by several works in many branches of engineering and sciences [1, 2]. It turned out that several plants, in interdisciplinary research areas, may present fractional-order dynamics including: fluid mechanics, spectral densities of music, transmission lines, cardiac rhythm, electromagnetic waves, viscoelastic systems, dielectric polarization, heat diffusion systems, electrode-electrolyte polarization, and many others [3–6].

Chaotic systems are deterministic and nonlinear dynamical plants. They are also characterized by the self similarity of the strange attractor and extreme sensitivity to initial conditions (IC) quantified respectively by fractal dimension and the existence of a positive Lyapunov exponent [5, 6]. In recent works, it was made known that several fractional-order systems may perform chaotically, e.g. fractional-order Lü system [7], fractional-order Arneodo system [8], fractional-order Lorenz system [9], fractional-order Rössler system [10], and so on.

M. Chadli et al. (Eds.): ICEECA 2017, LNEE 522, pp. 128–142, 2019.
https://doi.org/10.1007/978-3-319-97816-1_10

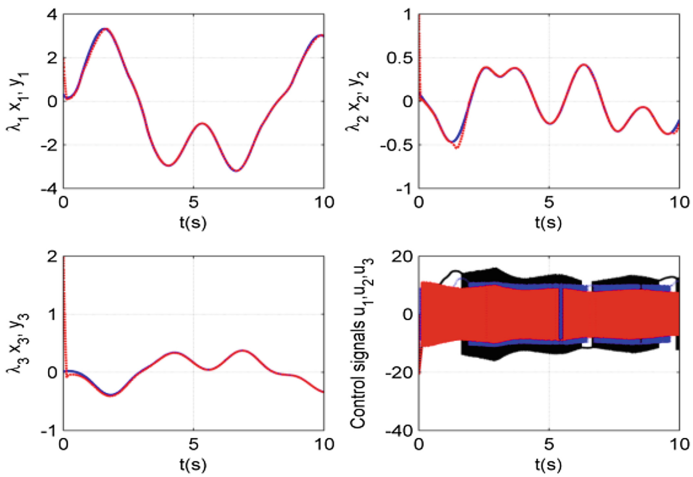

Fig. 1. Simulation results with SIGNfunction ($\lambda_1 = 1, \lambda_2 = -1, \lambda_3 = 0.1$): (a)$\lambda_1 x_1$ (solid line) and y_1 (dashed line). (b) $\lambda_2 x_2$(solid line) and y_2 (dashed line). (c)$\lambda_3 x_3$ (solid line) and y_3 (dashed line). (d) u_1 (solid line), u_2 (dotted line) and u_3 (dashed line).

The sliding mode control technique is an effective tool to *construct* robust controllers for nonlinear systems with bounded external disturbances and uncertainties. The later has several attractive features, including finite-time and fast convergence, strong robustness with respect to unmodeled dynamics, parameters variations and external disturbances. The purpose of the sliding mode is extremely simple: *it consists to oblige the system states to arrive at a suitably sliding surface based on a discontinuous control*. Recently, the fractional-order calculus is employed within the sliding mode control methodologies, in order to seek better performances. Many works have coped with control problems of nonlinear systems with fractional-orders [11–14]. It is worthy to note that the selection of the sliding surface for this class of systems is not an easy task in general. In numerous recent researches, the fuzzy logic system is combined with the sliding mode control in order to remove the main issues of the sliding mode control, including the high-gain authority and chattering in the system. This hybridization can smoothen the sliding mode control in diverse ways, and can also successfully approximate online the model, uncertainties and disturbances present in the system [5, 6].

In recent years, ***the synchronization and control*** of the fractional-order systems is also one of the most attractive topics. Various researcher works have made great contributions in this research topic [5, 6, 15–23]. In [15], a modified projective synchronization of different fractional-order systems has been developed through active sliding mode control. By using a fuzzy adaptive sliding mode control strategy, a generalized projective synchronization (GPS) of fractional order chaotic systems has been proposed in [16]. Chaos synchronization between two different uncertain fractional order chaotic systems has been studied based on a fuzzy adaptive sliding mode control in [17]. In [18], a fuzzy adaptive control has been proposed for the synchronization of uncertain fractional-order chaotic delayed systems involving time delays.

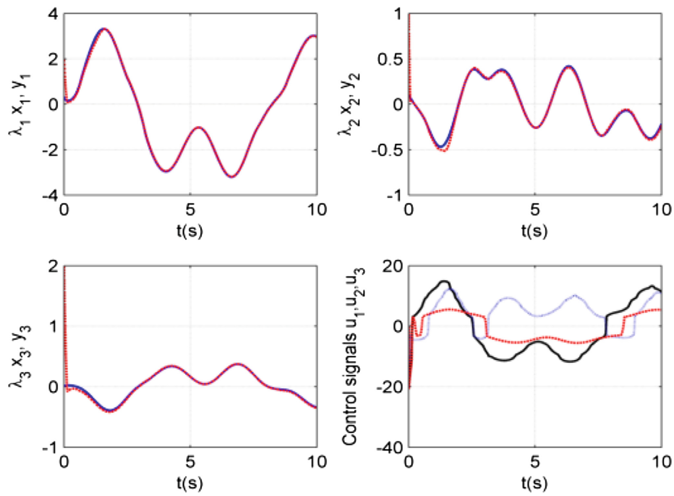

Fig. 2. Simulation results with TANH function ($\lambda_1 = 1, \lambda_2 = -1, \lambda_3 = 0.1$): (a)$\lambda_1 x_1$ (solid line) and y_1 (dashed line). (b) $\lambda_2 x_2$(solid line) and y_2 (dashed line). (c)$\lambda_3 x_3$ (solid line) and y_3 (dashed line). (d) u_1 (solid line), u_2 (dotted line) and u_3 (dashed line).

In [19], a fuzzy adaptive controller has been constructed to realize an H_∞ synchronizing for uncertain fractional-order chaotic systems. Nevertheless, the fundamental results of [17–19] are already questionable, because the stability analysis has not been derived rigorously in mathematics, as stated in [20, 21]. In [5, 6, 22, 23], some adaptive fuzzy controllers have been designed in a sliding mode frame-work for realizing an appropriate synchronization of fractional-order chaotic master-slave systems. In these synchronization approaches, the fuzzy systems have been employed to online estimate the unknown nonlinear functions. Although these schemes can guarantee the satisfactory performances, the issue of the input dead-zone (input nonlinearities) has not yet been considered in the synchronization control design of the fractional-order chaotic systems. This is by no means the case in the real world life as the physical systems commonly involve quantization, dead-zone, input saturations, backlash, and so on. It is worth pointing out that the input nonlinearities can guide to poor performances or even instability of the synchronization control system, if they are not taken into account into the control design. It is thereby more advisable to consider the effects of these input nonlinearities in one way or another when implementing and designing a synchronization control system.

In this research, a fuzzy adaptive variable-structure controller is constructed to correctly realize a GPS of incommensurate fractional-order chaotic systems in which external disturbances and input nonlinearities are present. A fuzzy system is incorporate to estimate the uncertain dynamics and a fractional-order sliding surface is designed. The Lyapunov stability theorem is employed to determine the associated adaptive laws and to bear out the stability of the corresponding closed-loop system. The validity of the proposed GPS scheme is confirmed by means of simulation results.

Compared to the closely-related previous works [5–8, 13–23], the main contributions of this work lie in the following:

(1) The design of a novel adaptive fuzzy variable-structure control-based chaos synchronization of fractional-order chaotic systems with uncertain model, input dead-zone, distinct incommensurate fractional-orders, unknown dynamical disturbances and non-identical structures. To the best of our knowledge, the problem of the input dead-zone (input nonlinearities) has been seldom considered in the synchronization control design of the incommensurate fractional-order chaotic systems.
(2) Unlike the previous literatures [7, 8, 13–15], the synchronization control system does not depend on the master-slave model. In fact, the adaptive fuzzy systems are adopted to handle the dynamical disturbances and model uncertainties.
(3) Compared with the recent researches in [17–19], the stability analysis of the closed-loop system is rigorously established in this work.

2 Basic Concepts

There are several definitions for fractional derivatives, namely: Riemann-Liouville, Grünwald-Letnikov, and Caputo definitions, etc. [1]. Because the meaning of the initial conditions (IC) for the systems described using the Caputo fractional operator is the same as for integer-order systems [1, 24], we will use this operator in the rest of this paper. In addition, a modification version of Adams-Bashforth-Moulton algorithm [25, 26] will be employed for numerical simulation of the Caputo fractional-order differential equations.

The Caputo fractional derivative of order α of a function $x(t)$ with respect to time is defined as [1]:

$$D_t^{\alpha}x(t) = \frac{1}{\Gamma(m-\alpha)}\int_{t}^{t}(t-\tau)^{-\alpha+m-1}x^{(m)}(\tau)d\tau \tag{1}$$

where $m = [\alpha] + 1$, $[\alpha]$ is the integer part of α, D_t^{α} is called the α-*order* Caputo differential operator, and $\Gamma(.)$ is the well-known gamma function which is given by:

$$\Gamma(P) = \int_{0}^{\infty} t^{P-1}e^{-t}dt \tag{2}$$

The following properties of the Caputo fractional-order derivative will be needed later [1]:

Property 1: Let $0 < q < 1$, then

$$Dx(t) = D_t^{1-q}D_t^{q}x(t), \quad \text{where } D = \frac{d}{dt} \tag{3}$$

Property 2: The Caputo fractional derivative operator is linear, i.e.:

$$D_t^q(vx(t) + \mu y(t)) = vD_t^q x(t) + \mu D_t^q y(t) \tag{4}$$

where v and μ are real constants. Especially, we have

$$D_t^q x(t) = D_t^q(x(t) + 0) = D_t^q x(t) + D_t^q 0, \text{ then } D_t^q 0 = 0.$$

3 Problem Statement and Fuzzy Approximation

3.1 Problem Statement

Consider a class of uncertain fractional-order chaotic ***master system*** described by

$$D_t^{\alpha_i} x_i = f_{mi}(x) \text{ for } i = 1, \ldots, n \tag{5}$$

where $D_t^{\alpha_i} = \frac{d^{\alpha_i}}{dt^{\alpha_i}}, 0 < \alpha_i < 1$ is the fractional-order of the system, $x = [x_1, \ldots, x_n]^T \in R^n$ is the measurable pseudo-state vector, and $f_{mi}(x)$ is an unknown continuous function.

Its slave system with input nonlinearity is given by

$$D_t^{\beta_i} y_i = f_{si}(y) + \varphi_i(u_i) + d_i(t, y), \text{ for } i = 1, \ldots, n \tag{6}$$

where $0 < \beta_i < 1$ is the fractional-order of the slave system, $f_{si}(y)$ is an unknown continuous function, $y = [y_1, \ldots, y_n]^T \in R^n$ is its measurable pseudo-state vector. u_i is the control input to be designed later, $\varphi_i(u_i)$ is the input nonlinearity (i.e. dead-zone with sector nonlinearities) and $d_i(t, y)$ represents the external disturbances.

Remark 1: *Several fractional-order chaotic systems can be modeled as (5) or (6), such as: fractional-order Chen system, fractional-order Lorenz system, fractional-order Lu system, fractional-order unified chaotic system, and so on.*

Our objective is to design an appropriate fuzzy adaptive variable-structure control law u_i (for all $i = 1, \ldots, n$) such that a GPS between the master system (5) and the slave system (6) is practically realized, while ensuring the boundedness of all closed-loop signals and despite the presence of uncertainties, dynamical external disturbances, together with input nonlinearities.

The synchronization error variables between the systems (5) and (6) are defined as follows:

$$e_i = y_i - \lambda_i x_i, \text{ for } i = 1, \ldots, n \tag{7}$$

where λ_i is the scaling factor that defines a proportional relation between the synchronized systems.

Now, we introduce a fractional-order sliding surface as

$$S_i = D_t^{\beta_i - 1} e_i + k_{0i} \int_0^t e_i d\tau, \text{ for } i = 1, 2, \ldots, n \tag{8}$$

where $k_{0i} > 0$ is a stable feedback gain, which will be designed later. When the system operates in the sliding mode, we have the following equation $S_i = \dot{S}_i = 0$. Therefore, the equivalent fractional-order sliding mode dynamics can be obtained from $\dot{S}_i = 0$ as follows:

$$D_t^{\beta_i} e_i + k_{0i} e_i = 0, \text{ for } i = 1, 2, \ldots, n \tag{9}$$

Because k_{0i} is positive and $0 < \beta_i < 1$, it is clear that the sliding-mode dynamics (9) are always stable [1, 6]. In other words, the following stability condition is always verified.

$$|Arg(-k_{0i})| > \beta_i \pi/2, \text{ for } i = 1, \ldots, n \tag{10}$$

From (5)-(8), we can determine the dynamics of the fractional-order sliding mode surface as follows:

$$\dot{S}_i = D_t^{\beta_i} e_i + k_{0i} e_i = k_{0i} e_i + f_{si}(y) + \varphi_i(u_i) - \lambda_i D_t^{\beta_i} x_i + d_i(t, y). \tag{11}$$

or equivalently

$$\dot{S}_i = H_i(x, y, d_i) + \varphi_i(u_i), \tag{12}$$

with

$$H_i(x, y, d_i) = k_{0i} e_i + f_{si}(y) - \lambda_i D_t^{\beta_i} x_i + d_i(t, y) \tag{13}$$

3.2 Input Nonlinearity

The input nonlinearity considered in this work is a dead-zone with sector nonlinearities [27, 28]:

$$\varphi_i(u_i) = \begin{cases} \varphi_{i+}(u_i)(u_i - u_{i+}), & u_i > u_{i+} \\ 0, & -u_{i-} \le u_i \le u_{i+} \\ \varphi_{i-}(u_i)(u_i + u_{i-}), & u_i < -u_{i-} \end{cases} \tag{14}$$

where $\varphi_{i+}(u_i) > 0$ and $\varphi_{i-}(u_i) > 0$ are nonlinear functions of u_i, and $u_{i+} > 0$ and $u_{i-} > 0.7$.

The nonlinearity $\varphi_i(u_i)$ satisfies the following properties:

$$(u_i - u_{i+})\varphi_i(u_i) \ge m_{i+}^* (u_i - u_{i+})^2, \textit{for } u_i > u_{i+}$$

$$(u_i + u_{i-})\varphi_i(u_i) \ge m_{i-}^* (u_i + u_{i-})^2, \textit{for } u_i < -u_{i-}, \tag{15}$$

where m_{i+}^* and m_{i-}^* are strictly positive constants which are generally called gain reduction tolerances [27, 28].

Assumption 1: Functions $\varphi_{i+}(u_i)$ and $\varphi_{i-}(u_i)$ and the constants m^*_{i+} and m^*_{i-} are unknown. But, the constants u_{i+} and u_{i-} are known and strictly positive.

3.3 Fuzzy Approximation

The configuration of a fuzzy logic system basically consists of a fuzzifier, some fuzzy IF–THEN rules, a fuzzy inference engine and a defuzzifier.

The fuzzy inference engine is used to represent a non-linear relationship between an input vector $\underline{x}^T = [x_1, \ldots, x_n] \in R^n$ and an output $\hat{f} \in R$, this relationship is described by a set of fuzzy rules of the form:

$$\textbf{if } x_1 \text{ is } A_1^i \textbf{ and} \ldots \textbf{and } x_n \text{ is } A_n^i \textbf{ then } \hat{f} \text{ is } f^i \tag{16}$$

where $A_1^i, A_2^i, \ldots, A_n^i$ are fuzzy sets and f^i is the fuzzy singleton for the output in the ith rule.

By using the singleton fuzzifier, product inference, and center-average defuzzifier, the output of the fuzzy system can be simply expressed as follows:

$$\hat{f}(\underline{x}) = \frac{\sum_{i=1}^m f^i \left(\prod_{j=1}^n \mu_{A_j^i}(x_j)\right)}{\sum_{i=1}^m \left(\prod_{j=1}^n \mu_{A_j^i}(x_j)\right)} = \theta^T \psi(\underline{x}) \tag{17}$$

where $\mu_{A_j^i}(x_j)$ is the degree of membership of x_j to A_j^i, m is the number of fuzzy rules, $\theta^T = [f^1, f^2, \ldots, f^m]$ is the adjustable parameter vector (which are the consequent parameters), and $\psi^T = [\psi^1 \psi^2 \ldots \psi^m]$ with

$$\psi^i(\underline{x}) = \frac{\prod_{j=1}^n \mu_{A_j^i}(x_j)}{\sum_{i=1}^m \left(\prod_{j=1}^n \mu_{A_j^i}(x_j)\right)} \tag{18}$$

which is the fuzzy basis function (FBF).

Following the universal approximation results [29], the fuzzy system (17) can approximate any smooth function $f(\underline{x})$ defined on a compact operating space to a given accuracy. It should be noted that the structure of the fuzzy system and the membership function parameters are properly specified beforehand by designer. But, the vector of consequent parameters θ will be estimated online by using some appropriate adaptations laws which will be designed later.

4 Design of Fuzzy Adaptive Controller

In the sequel, the following mild assumptions are required:

Assumption 2: The disturbance $d_i(t, y)$ satisfies:

$$|d_i(t, y)| \le \bar{d}_i(y), \tag{19}$$

where $\bar{d}_i(y)$ is an unknown continuous positive function.

Assumption 3: There exists an unknown continuous positive function $\bar{h}_i(y)$ such that:

$$|H_i(x, y, d_i))| \leq \eta \bar{h}_i(y), \quad \text{for} \;\; i = 1, \ldots, n \tag{20}$$

with $\eta = min_i\{m^*_{i+}, m^*_{i-}\}$, for $i = 1, \ldots, n$.

Remark 2: Assumptions 2 and 3 are not strong, because the bounds $\bar{h}_i(y)$ and $\bar{d}_i(y)$ are unknown and the state vector of the master system is always bounded (for a non-controlled chaotic system). These assumptions are frequently used in the literature, e.g. [5, 6].

The unknown function $\bar{h}_i(y)$ can be approximated, on a compact set Ω_y, by the linearly parameterized fuzzy systems (17) as follows:

$$\hat{\bar{h}}_i(y, \theta_i) = \theta_i^T \psi_i(y), \; i = 1, \ldots, n \tag{21}$$

where $\psi_i(y)$ is the FBF vector, which is determined a priori by the designer, and θ_i is the vector of the adjustable parameters of this fuzzy system.

Without loss of generality, we assume that there exists an optimal fuzzy approximator with m fuzzy rules that can identify the nonlinear function $\bar{h}_i(y)$ with an minimal approximation error, i.e.

$$\bar{h}_i(y) = \hat{\bar{h}}_i\left(y, \theta_i^*\right) + \delta_i(y) = \theta_i^{*T} \psi_i(y) + \delta_i(y) \tag{22}$$

where $\delta_i(y)$ is the minimal approximation error being usually assumed to be bounded for all $y \epsilon \Omega_y$, i.e. $|\delta_i(y)| \leq \bar{\delta}_i$, with $\bar{\delta}_i$ is an unknown constant [29–36], and

$$\theta_i^* = \arg\min_{\theta_i}\left[\sup_{y \epsilon \Omega_y}\left|\bar{h}_i(y) - \hat{\bar{h}}_i(y, \theta_i)\right|\right] \tag{23}$$

Notice that θ_i^* is the optimal value of θ_i [29–36] and mainly introduced for analysis purposes (i.e. its value is not needed when implementing the control system). From the previous analysis, we have:

$$\begin{aligned} \hat{\bar{h}}_i(y, \theta_i) - \bar{h}_i(y) &= \hat{\bar{h}}_i(y, \theta_i) - \hat{\bar{h}}_i\left(y, \theta_i^*\right) + \hat{\bar{h}}_i\left(y, \theta_i^*\right)\bar{h}_i(y), \\ &= \theta_i^T \psi_i(y) - \theta_i^{*T} \psi_i(y) - \delta_i(y), \\ &= \tilde{\theta}_i^T \psi_i(y) - \delta_i(y). \end{aligned} \tag{24}$$

with $\tilde{\theta}_i = \theta_i - \theta_i^*$, for $i = 1, \ldots, n$.

To achieve our objective, we can design the following adaptive fuzzy variable-structure controller:

$$u_i = \begin{cases} -\rho_i(t) sign(S_i) - u_{i-}, & S_i > 0 \\ 0, & S_i = 0 \\ -\rho_i(t) sign(S_i) + u_{i+}, & S_i < 0 \end{cases} \tag{25}$$

with

$$\rho_i(t) = k_{1i} + k_{2i} + k_{3i}|S_i| + \tilde{\theta}_i^T \psi_i(y), \quad i = 1, \ldots, n \tag{26}$$

Adaptation laws associated to the proposed controller (25) can be designed as follows:

$$\dot{\theta}_i = \gamma_{\theta i}(|S_i|\psi_i(y) - \sigma_{\theta i}|S_i|\theta_i), \quad \text{with} \quad \theta_{ij}(0) > 0 \tag{27}$$

$$\dot{k}_{1i} = \gamma_{ki}(|S_i| - \sigma_{ki}|S_i|k_{1i}), \text{ with } k_{1i}(0) > 0 \tag{28}$$

where $\gamma_{\theta i}, \sigma_{\theta i}$, σ_{ki}, γ_{ki}, k_{2i} and k_{3i} are strictly positive design parameters.

From (12), we have

$$\frac{1}{\eta} S_i \dot{S}_i = \frac{1}{\eta} S_i H_i(x, y, d_i) + \frac{1}{\eta} S_i \varphi_i(u_i) \leq |S_i| \bar{h}_i(y) + \frac{1}{\eta} S_i \varphi_i(u_i) + \rho_i |S_i| - \rho_i |S_i| \tag{29}$$

Using (24) and substituting the control law (26) into (29) yields

$$\frac{1}{\eta} S_i \dot{S}_i \leq \frac{1}{\eta} S_i \varphi_i(u_i) + \rho_i |S_i| - \left(k_{1i} + k_{2i} + k_{3i}|S_i| \tilde{\theta}_i^T \psi_i(y)\right) |S_i| + \delta_i(y) S_i \tag{30}$$

From (15) and (25), we get

$$u_i < -u_{i-} \text{ for } S_i > 0 \Rightarrow (u_i + u_{i-})\varphi_i(u_i) \geq m_{i-}^* (u_i + u_{i-})^2 \geq \eta (u_i + u_{i-})^2 \tag{31}$$

$$u_i > u_{i+} \text{ for } S_i < 0 \Rightarrow (u_i - u_{i+})\varphi_i(u_i) \geq m_{i+}^* (u_i - u_{i+})^2 \geq \eta (u_i - u_{i+})^2 \tag{32}$$

Considering (25) again, we can establish

$$S_i > 0 \Rightarrow (u_i + u_{i-})\varphi_i(u_i) = -\rho_i(t) sign(S_i) \varphi_i(u_i) \geq m_{i-}^* \rho_i^2(t) [sign(S_i)]^2 \geq \eta \rho_i^2(t) \tag{33}$$

$$S_i < 0 \Rightarrow (u_i - u_{i+})\varphi_i(u_i) = -\rho_i(t) sign(S_i) \varphi_i(u_i) \geq m_{i+}^* \rho_i^2(t) [sign(S_i)]^2 \geq \eta \rho_i^2(t) \tag{34}$$

Then, for $S_i > 0$ and $S_i < 0$, we have

$$-\rho_i(t) sign(S_i) \varphi_i(u_i) \geq \eta \rho_i^2(t) \tag{35}$$

Using the fact that $S_i sign(S_i) = |S_i|$, (35) can be rewritten as

$$-\rho_i(t)S_i^2 sign(S_i)\varphi_i(u_i) \geq \eta\rho_i^2(t)S_i^2 = \eta\rho_i^2(t)|S_i|^2 \tag{36}$$

Finally, because $\rho_i(t) > 0$, for all S_i, we have

$$\frac{S_i\varphi_i(u_i)}{\eta} \leq -\rho_i(t)|S_i| \tag{37}$$

By considering (37), Eq. (30) can be rewritten as:

$$\frac{1}{\eta}S_i\dot{S}_i \leq -\Big(k_{1i} + k_{2i} + k_{3i}|S_i| + \tilde{\theta}_i^T\psi_i(y)\Big)|S_i| + \delta_i(y)S_i \tag{38}$$

Now, we are in a position to present our main result.

Theorem 1: *For the master-slave system (5) and (6), if Assumptions 1-3 are valid, the control law (25) together with its adaptation laws (27) and (28) can ensure the following properties:*

(a) *All the signals in the closed-loop system are bounded.*
(b) *Signals S_i asymptotically converge to zero.*

Proof. Consider the following Lyapunov function candidate for a subsystem i:

$$V_i = \frac{1}{2}S_i^2 + \frac{1}{2\gamma_{\theta i}}\left\|\tilde{\theta}_i^2\right\| + \frac{1}{2\gamma_{ki}}\tilde{k}_{1i}^2. \quad \text{for } i = 1, \ldots, n \tag{39}$$

with $\tilde{k}_{1i} = k_{1i} - k_{1i}^*$, where $k_{1i}^* = \bar{\delta}_i + \frac{\sigma_{\theta_i}}{2}\left\|\theta_i^{*2}\right\|$.
Differentiating V_i with respect to time yields

$$\dot{V}_i = S_i\dot{S}_i + \frac{1}{\gamma_{\theta i}}\tilde{\theta}_i^T\dot{\theta}_i + \frac{1}{\gamma_{ki}}\dot{k}_{1i}\tilde{k}_{1i} \tag{40}$$

Using (25)-(27), $\dot{V}_i$ becomes

$$\dot{V}_i \leq -k_{3i}S_i^2 - k_{2i}|S_i| + \bar{\delta}_i|S_i| - \sigma_{\theta_i}|S_i|\tilde{\theta}_i^T\theta_i + \frac{1}{\gamma_{ki}}\dot{k}_{1i}\tilde{k}_{1i}. \tag{41}$$

It is clear that

$$-\sigma_{\theta_i}|S_i|\tilde{\theta}_i^T\theta_i \leq -\frac{\sigma_{\theta_i}}{2}|S_i|\left\|\tilde{\theta}_i\right\|^2 + \frac{\sigma_{\theta_i}}{2}|S_i|\left\|\theta_i^*\right\|^2 \tag{42}$$

$$-\sigma_{k_i}|S_i|k_{1i}\tilde{k}_{1i} \leq -\frac{\sigma_{k_i}}{2}|S_i|k_{1i}^2 + \frac{\sigma_{k_i}}{2}|S_i|k_{1i}^{*2} \tag{43}$$

Substituting (42) and (43) into (41), we obtain

$$\dot{V}_i \leq -k_{3i} S_i^2 \tag{44}$$

where k_{2i} should be selected as $k_{2i} \geq \frac{\sigma_{k_i}}{2} k_{1i}^{*2}$.

Let $V(t) = \sum_1^n V_i(t)$ be the Lyapunov candidate function of the all subsystems. Differentiating $V(t)$ with respect to time yields

$$\dot{V} = \sum_1^n \dot{V}_i \leq -\sum_1^n k_{3i} S_i^2 \tag{45}$$

Therefore, all signals in the closed-loop control system remain bounded. And hence the input u_i is bounded. By using the Barbalat's lemma, one can conclude about the asymptotic convergence of the signal S_i towards zero.

Remark 3: *In the case where $u_{i+} = u_{i-} = u_{i0}$, (25) can be simplified to the following:*

$$u_i = -(\rho_i(t) + u_{i0}) Sign(S_i) \tag{46}$$

with $\rho_i(t) = k_{1i} + k_{2i} + k_{3i}|S_i| + \theta_i^T \psi_i(y), \ \forall i = 1, \ldots, n$.

By replacing the Sign function by tangent hyperbolic function (Tanh; an equivalent smooth function) to deal with the chattering effects, the expression (46) becomes:

$$u_i = -(\rho_i(t) + u_{i0}) Tanh(S_i/\varepsilon_i) \tag{47}$$

where ε_i is a small positive constant.

5 Simulation Results

To show the effectiveness and applicability of the proposed synchronization scheme, the following simulation example is presented.

The master system is a fractional-order Chua's oscillator system [37]:

$$\begin{cases} D_t^{\alpha_1} x_1 = a(x_2 - x_1 - f(x_1)), \\ D_t^{\alpha_2} x_2 = x_1 - x_2 + x_3, \\ D_t^{\alpha_3} x_3 = -bx_2 - cx_3, \end{cases} \tag{48}$$

with $f(x_1) = m_1 x_1 + \frac{1}{2}(m_0 - m_1)(|x_1 + 1| - |x_1 - 1|)$, $m_0 = -1.1726, m_1 = -0.7872, a = 10, 725, b = 10.593, \ c = 0.268$.

According to [37], the system (48) can behave chaotically for $\alpha_1 = 0.93, \ \alpha_2 = 0.99$ and $\alpha_3 = 0.92$.

The slave system is a controlled fractional-order financial system [38], which is described by:

$$\begin{cases} D_t^{\beta_1} y_1 = y_3 + (y_2 - a_1)y_1 + \varphi_1(u_1) + d_1 \\ D_t^{\beta_2} y_2 = 1 - b_1 y_2 - y_1^2 + \varphi_2(u_2) + d_2 \\ D_t^{\beta_3} y_3 = -y_1 - c_1 y_3 + \varphi_3(u_3) + d_3 \end{cases} \tag{49}$$

where $a_1 = 3$ is the saving amount, $b_1 = 0.1$ is the cost per investment and $c_1 = 1$ is the elasticity of demand of commercial markets [38].

For $u_i = 0$ and $d_i(.) = 0$, the system (49) can behave chaotically for $\beta_1 = 0.97$, $\beta_2 = 0.90$ and $\beta_3 = 0.96$. The disturbances are chosen as: $d_1(t) = d_2(t) = d_3(t) = 0.2\sin(3t) + 0.2\cos(3t)$. The initial conditions are:$x(0) = [0.2, -0.1, 0.1]^T$ and $y(0) = [2, 1, 2]^T$.

The input nonlinearities $\varphi_i(u_i)$ for $i = 1, 2, 3$ are selected as:

$$\varphi_i(u_i) = \begin{cases} (u_i - 3)\left(1.5 - 0.3e^{0.3|\sin(u_i)|}\right), & u_i > 3 \\ 0, & -3 \le u_i \le 3 \\ (u_i + 3)\left(1.5 - 0.3e^{0.3|\sin(u_i)|}\right), & u_i < -3 \end{cases}$$

The used fuzzy systems, $\theta_i^T \psi_i(y)$, with i = 1, 2, 3, have the vector $y = [y_1, y_2, y_3]^T$ as input. For each input variable of these fuzzy systems, as in [36], one defines three (one triangular and two trapezoidal) membership functions uniformly distributed on the intervals [− 2, 2].

The design parameters are chosen as follows: $k_{21} = k_{22} = k_{23} = 2, k_{31} = k_{32} = k_{33} = 10, \gamma_{\theta 1} = \gamma_{\theta 2} = \gamma_{\theta 3} = 5, \lambda_1 = 1, \lambda_2 = -1,$ and $\lambda_3 = 0.1, \sigma_{\theta 1} = \sigma_{\theta 2} = \sigma_{\theta 3} = 0.001$, $\gamma_{k1} = \gamma_{k2} = \gamma_{k3} = 5, \sigma_{k1} = \sigma_{k2} = \sigma_{k3} = 0.005$.

The initial conditions for the adaptive parameters are selected as: $\theta_{1j}(0) = \theta_{2j}(0) = \theta_{3j}(0) = 0.001$ and $k_{11}(0) = k_{12}(0) = k_{13}(0) = 0.1$.

According to the used controller (smooth controller or no-smooth controller), we can distinguish two simulation cases:

Case 1. (by applying the no-smooth controller (46)): The obtained simulation results for this GPS are depicted in Fig. 1. It is clear from this figure that the trajectories of slave system (y_1, y_2, y_3) effectively track to that of the master system $(\lambda_1 x_1, \lambda_2 x_2, \lambda_3 x_3)$. The corresponding control signals are also bounded and admissible but with chattering.

Case 2. (by applying the smooth controller (47)): The simulation results, obtained when the smooth controller (47) is used, are presented in Fig. 2 In this case, we can clearly see that the chattering phenomenon is mitigated in the control signals.

6 Conclusion

The problem of GPS of incommensurate fractional-order chaotic systems with dead-zone input has been investigated in this work. This GPS has been successfully accomplished by the conception of an adaptive fuzzy variable-structure controller.

Of fundamental interest, a Lyapunov based analysis has been carried out to conclude about the asymptotical stability as well as the convergence of the fractional-order sliding surfaces towards zero. Computer simulation results have been provided to confirm the validity of the proposed GPS system based on adaptive fuzzy control for the synchronization of incommensurate fractional-order chaotic systems with unknown bounded disturbances, uncertain dynamics, and input nonlinearities.

References

1. Podlubny, I.: Fractional Differential Equations. Academic, New York (1999)
2. Hilfer, R.: Applications of Fractional Calculus in Physics. World Scientific Publishing, Singapore (2000)
3. Baleanu, D., Güvenç, Z.B., Tenreiro Machado, J.A.: New Trends in Nanotechnology and Fractional Calculus Applications. Springer, New York (2010)
4. Sabatier, J., Agrawal, O.P., Machado, J.A.T.: Advances in Fractional Calculus. Springer, London (2007)
5. Bouzeriba, A., Boulkroune, A., Bouden, T., Vaidyanathan, S.: Fuzzy adaptive synchronization of incommensurate fractional-order chaotic systems. In: Vaidyanathan, S., Volos, C. (eds.) Advances and Applications in Chaotic Systems, pp. 363–378. Springer, Cham (2016)
6. Boulkroune, A., Bouzeriba, A., Bouden, T.: Fuzzy generalized projective synchronization of incommensurate fractional-order chaotic systems. Neurocomputing **173**, 606–614 (2016)
7. Deng, W., Li, C.: Chaos synchronization of the fractional Lü system. Phys. A Stat. Mech. Appl. **353**, 61–72 (2005)
8. Lu, J.: Chaotic dynamics and synchronization of fractional-order Arneodo's systems. Chaos, Solitons Fractals **26**(4), 1125–1133 (2005)
9. Grigorenko, I., Grigorenko, E.: Chaotic dynamics of the fractional Lorenz system. Phys. Rev. Lett. **91**(3), 034101 (2003)
10. Li, C., Chen, G.: Chaos and hyperchaos in the fractional-order Rössler equations. Phys. A **341**, 55–61 (2004)
11. Calderón, A., Vinagre, B., Feliu, V.: Fractional order control strategies for power electronic buck converters. Signal Process. **86**(10), 2803–2819 (2006)
12. Efe, M.: Kasnakog̃lu, C.: A fractional adaptation law for sliding mode control. Int. J. Adapt. Control. Signal Process. **22**(10), 968–986 (2008)
13. Si-Ammour, A., Djennoune, S., Bettayeb, M.: A sliding mode control for linear fractional systems with input and state delays. Commun. Nonlinear Sci. Numer. Simul. **14**(5), 2310–2318 (2009)
14. Pisano, A., Rapaić, M., Jeličić, Z., Usai, E.: Sliding mode control approaches to the robust regulation of linear multivariable fractional-order dynamics. Int. J. Robust Nonlinear Control **20**(18), 2045–2056 (2010)
15. Wang, X., Zhang, X., Ma, C.: Modified projective synchronization of fractional-order chaotic systems via active sliding mode control. Nonlinear Dyn. **69**(1–2), 511–517 (2012)
16. Wang, L., Tang, Y., Chai, Y., Wu, F.: Generalized projective synchronization of the fractional-order chaotic system using adaptive fuzzy sliding mode control. Chin. Phys. B **23** (10), 100501 (2014)

17. Lin, T., Lee, T., Balas, V.: Adaptive fuzzy sliding mode control for synchronization of uncertain fractional order chaotic systems. Chaos, Solitons Fractals **44**(10), 791–801 (2011)
18. Lin, T.C., Lee, T.Y.: Chaos synchronization of uncertain fractional-order chaotic systems with time delay based on adaptive fuzzy sliding mode control. IEEE Trans. Fuzzy Syst. **19** (4), 623–635 (2011)
19. Lin, T., Kuo, C.: Synchronization of uncertain fractional order chaotic systems: adaptive fuzzy approach. ISA Trans. **50**(4), 548–556 (2011)
20. Tavazoei, M.S.: Comments on: Chaos synchronization of uncertain fractional-order chaotic systems with time delay based on adaptive fuzzy sliding mode control. IEEE Trans. Fuzzy Syst. **20**(5), 993–995 (2012)
21. Aghababa, M.: Comments on: synchronization of uncertain fractional order chaotic systems: adaptive fuzzy approach. ISA Trans. **51**(1), 11–12 (2012)
22. Bouzeriba, A., Boulkroune, A., Bouden, T.: Fuzzy adaptive synchronization of uncertain fractional-order chaotic systems. Int. J. Mach. Learn. Cybern. **7**(5), 893–908 (2015)
23. Bouzeriba, A., Boulkroune, A., Bouden, T.: Projective synchronization of two different fractional-order chaotic systems via adaptive fuzzy control. Neural Comput. Appl. **27**(5), 1349–1360 (2016)
24. Li, Y., Chen, Y., Podlubny, I.: Stability of fractional-order nonlinear dynamic systems, "Lyapunov direct method and generalized Mittag-Leffler stability. Comput. Math Appl. **59** (5), 1810–1821 (2010)
25. Diethelm, K., Ford, N.J., Freed, A.D.: A predictor-corrector approach for the numerical solution of fractional differential equations. Nonlinear Dyn. **29**, 3–22 (2002)
26. Diethelm, K., Ford, N.: Analysis of fractional differential equations. J. Math. Anal. Appl. **265** (2), 229–248 (2002)
27. Shyu, K., Liu, W., Hsu, K.: Design of large-scale time-delayed systems with dead-zone input via variable structure control. Automatica **41**(7), 1239–1246 (2005)
28. Boulkroune, A., M'Saad, M., Farza, M.: Adaptive fuzzy controller for multivariable nonlinear state time-varying delay systems subject to input nonlinearities. Fuzzy Sets Syst. **164**(1), 45–65 (2011)
29. Wang, L.X.: Adaptive Fuzzy Systems and Control Design and Stability Analysis. Prentice-Hall, Englewood Cliffs (1994)
30. Benzaoui, M., Chekireb, H., Tadjine, M., Boulkroune, A.: Trajectory tracking with obstacle avoidance of redundant manipulator based on fuzzy inference systems. Neurocomputing **196**, 23–30 (2016)
31. Hamel, S., Boulkroune, A.: A generalized function projective synchronization scheme for uncertain chaotic systems subject to input nonlinearities. Int. J. Gen Syst **45**(6), 689–710 (2016)
32. Zouari, F., et al.: Observer-based adaptive neural network control for a class of MIMO uncertain nonlinear time-delay non-integer-order systems with asymmetric actuator saturation. Neural Comput. Appl. **28**(1), 993–1010 (2017)
33. Rigatos, G., Zhu, G., Yousef, H., Boulkroune, A.: Flatness-based adaptive fuzzy control of electrostatically actuated MEMS using output feedback. Fuzzy Sets Syst. **290**, 138–157 (2016)
34. Boulkroune, A.: A fuzzy adaptive control approach for nonlinear systems with unknown control gain sign. Neurocomputing **179**, 318–325 (2016)
35. Boulkroune, A., Bouzeriba, A., Hamel, S., Bouden, T.: Adaptive fuzzy control-based projective synchronization of uncertain nonaffine chaotic systems. Complexity **21**(2), 180–192 (2015)

36. Boulkroune, A., Tadjine, M., M'Saad, M., Farza, M.: How to design a fuzzy adaptive controller based on observers for uncertain affine nonlinear systems. Fuzzy Sets Syst. **159**(8), 926–948 (2008)
37. Zhu, H., Zhou, S., Zhang, J.: Chaos and synchronization of the fractional-order Chua's system. Chaos, Solitons Fractals **39**(4), 1595–1603 (2009)
38. Chen, W.: Nonlinear dynamics and chaos in a fractional-order financial system. Chaos, Solitons Fractals **36**(5), 1305–1314 (2008)

Cement Water Treatment Process Modeling Hybrid Bond Graph

Modeling and Experimental Validation

Eya Fathallah[1(✉)] and Nadia Zanzouri[2]

[1] Université de Tunis El Manar, Ecole Nationale d'Ingénieurs de Tunis, Laboratoire d'Analyse, de Conception et de Commande des Systèmes, LR11ES20, Tunis, Tunisia
fathallah.eya@gmail.com

[2] Université de Tunis, Institut Preparatoire aux Etudes d'Ingénieurs de Tunis, Laboratoire d'Analyse, de Conception et de Commande des Systèmes, LR11ES20, Tunis, Tunisia
Nadia.Zanzouri@enit.rnu.tn

Abstract. This paper propose an Hybrid Bond Graph modeling of the cement water treatment process. The description of this complex process highlights the diversity of physical phenomena which leads to the interaction between several domains such as hydraulic, chemical, electrical, etc. An experimental characterization of the system is performed in order to assess the validated bond graph model of the studied process. The simulation results obtained from this elaborated model reveal a significant conformity compared to the experimental results.

Keywords: Modelling of cement water treatment process · Hybrid bond graph Experimental validation

1 Introduction

The water treatment system is considered as one of the complicate industrial systems due to its large number of components. Closely, it's the result of many interacting domains such as hydraulic, electrical, mechanical and chemical domains. Such system diversity of integrating several kinds of energy behavior makes the modeling process of these multidisciplinary systems difficult due to the fact that the most current software tools can only operate in a single domain. Hence, the Hybrid Bond Graph (HBG) formalism can be seen as powerful tool that is well adapted for dynamic modeling of such a multi-physical system [1]. Nowadays, the modeling community is interested in the hybrid dynamic system (HDS) thanks to its ability to represent the industrial systems in a more real way than any other dynamics. In the latter of 1990s, many suggestions of modeling the (HDS) were presented in the literature. The most interesting of these is the hybrid bond graph. In reality, researchers classify the hybrid bond graph models into two categories. The first one is called the fixed causality approach where the switching elements preserve the causality of these systems and

M. Chadli et al. (Eds.): ICEECA 2017, LNEE 522, pp. 143–154, 2019.
https://doi.org/10.1007/978-3-319-97816-1_11

only the varying parameters at the switching instants. Many models were developed to express this technique. For example, the model in [2] uses the modulated resistor as a switching element. It accords an important value to the resistor to express the ON state then it decreases this value to have the OFF state. Another model is proposed by [3] where the switching element is represented by combining a transformer, which commands the switching process, with a fixed resistor. In a similar vein, the authors in [4] propose the modulated transformer. Later in [5], the model develops bonds modulated by a zero or one signal. When the signal is zero, the bond must disappear; and when it is one, the system considers the presence of this bond. This approach is more developed in [6]. The second category of the hybrid bond graph model focuses on systems where their causalities vary after switching. Many works has dealt with this topic such as the switched source where the switch is modeled as a source of commutation between the source of the null flow and the null effort, imposing a zero flow/effort at the connecting junction when OFF [7]. Based on the switched source, the authors in [8] present the switched storage element as a compound element, acting as a regular storage element when ON and a switched source (null source) when OFF. Shortly afterwards, the work in [9] presented the controlled junction which is a regular 0- or 1-junction when ON and a null source on each bond when OFF. This paper presents a modeling of a real process of water treatment of the Djbel Rassas's cement plant. This modeling is based on a hybrid bond graph approach. Accordingly, the first section includes a detailed description of the cement water treatment process. In Sect. 2, a hybrid bond graph model of whole system is proposed with the aim of imitating the real behavior of the system. Section 3 is dedicated to the experimental background of this system which is then compared to the simulation results developed from the model. The final section presents the conclusion.

2 Cement Water Treatment Process

2.1 The Description of the Process

The water treatment process is a sequence of operations required to reach the anticipated quality. To detail the functioning of the process is described in the next part. The raw water tank (761.TK100) is the storage of the incoming raw water from the source. During the treatment process, the water flow is pumped with two raw water pumps (761.WP110 & 761.WP111). During the normal operation, only one raw water pump is running and is able to feed both filters (761.FU120 and 761.FU121) with a total flow of 72 m^3/h each of the two parallel filters (known as sand filters) feeds one reverse osmosis unit. The capacity of each filter is 36 m^3/h and is fed by the raw water pumps. This sand filtration operation removes the suspended solids and particles from the raw water which can deteriorate the performance of the reverse osmosis membranes. Pressure filters are also intended to protect the subsequent RO process during abrupt situations when the best water quality changes. After that, the two parallel reverse osmosis units (line 1 and 2) are installed. The reverse osmosis is the finest filtration used to purify water and remove salts and other impurities in order to improve the properties of the water. The reverse osmosis uses a semipermeable membrane allowing the water to pass through while rejecting the remaining contaminants. The process of the reverse osmosis requires a driving force to push the pure water through the membrane, typically a high pressure pump. All water cannot be filtered through the membrane; hence the need for the reject of about 25–50% of feed flow. The capacity of one reverse osmosis unit at “maximum” raw water parameters is 21 m^3/h, while the total capacity is 42 m^3/h. As for the water distribution system, the raw water system is supplies water to the cooling water tank (762TK100) which is subdivided into a cold tank and a hot tank when the level indicators (762.TK100N01762.TK100N01) in the cooling water tank indicate a low level. In fact, this level governs the functioning of the RO and the raw water treatment in the following way: when the level of the cooling water reservoir lowers, it will give a “run signal” to the raw water treatment process. The tank level shall determine if one or two RO units are operating. Several levels can be set to the reservoir as follows: Low level 1 < 2.5 m: Start one RO unit. Low level 2: 2.50 m: Start both RO units. High level 1: 4.70 m: Stop RO unit. High level 2: 5 m: Stop the second RO unit (both stopped). When the water flow runs to the cooling water tank, the inhibitor dosing adds a corrosion inhibitor to the water supply pipeline. When it arrives at the cooling water tank with an appropriate level, the cooling water pumps (762WP110 or 762WP111) will circulate the water flow to the cooling towers (762CL120 & 762CL121) and the flow outlet fills the cold tank of the whole cooling water tank (Fig. 1).

Fig. 1. The cement water treatment process.

2.2 Hybrid Bond Graph Model of the Cement Water Treatment Process

Accordingly, the bond graph is used to model our described system. Initially, the whole process detailed in the previous section is modeled by a word bond graph represented in Fig. 2. In this scheme, the main parts which compose the real systems are schematized and will be well detailed in the following sections. The model involves two physical domains, namely (1) the mechanical rotation and (2) the hydraulic domain.

(1) Tank model: The water treatment process contains three tanks namely, raw water storage, cooling water storage and cooling tower storage. In addition, each tank is defined as the hydraulic capacity derived from the equation in [10, 11]. Then, all these tanks are modeled in bond graph’s languages as C-element with (C_{Tank})

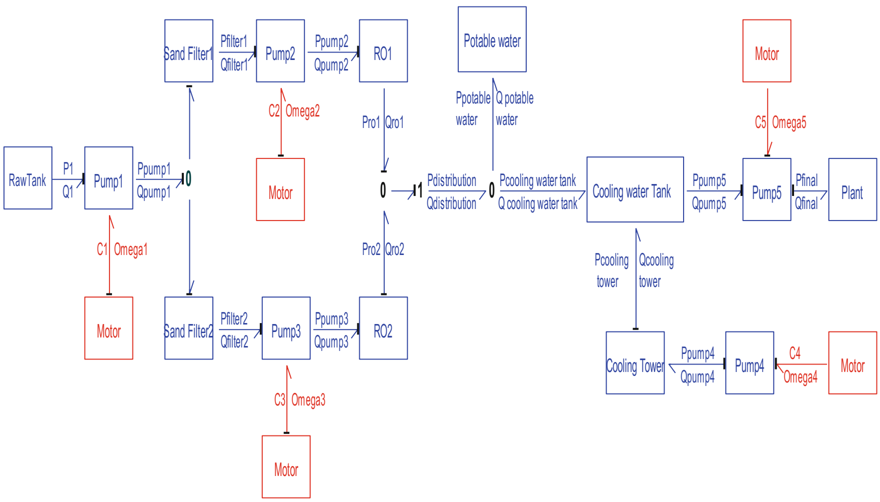

Fig. 2. The bond graph's word

expressing hydraulic capacity, (P_{Tank}) is the pressure and (Q_{Tank}) is the water flow stored in the tank, such that:

$$P_{\text{Tank}} = \frac{1}{C_{Tank}} \int Q_{Tank} dt \quad (1)$$

$$C_{Tank} = \frac{A}{\rho g} \quad (2)$$

Where (A) is the section, (g) is the constant of gravity; g = 9.81 m/s^2 and (ρ) is the density of water.

(2) Pump model: The process disposes of five pumps with different parameters as follows:

- Centrifugal Moto-pump of raw water: This pump is Grundfos (NB50-160/167), it permits pumping the raw water to treatment process with a maximum flow of 72 m^3/h. This one is driven by a three-phase asynchronous motor with 11 kW of the rated power.
- Two centrifugal Moto-pump of RO: each pump of the RO unit is Grundfos (CRN45-11), it allows pumping the filtered raw water to the reverse osmosis with a maximum flow product of 36 m^3/h. Each pump is driven by a three-phase asynchronous motor with 22 kW of the rated power.
- Moto-pump of cooling tower: this centrifugal pump is Grundfos (NK125-500/548), it permits pumping the flow of water from the hot tank to the cooling tower with a maximum flow product of 300 m^3/h. This pump is driven by a three-phase Asynchronous Motor with 55 kW of the rated power.
- Moto-pump of distribution: this centrifugal pump is Grundfos (NB50-200/219), it permits pumping the flow coming from the cooling water tank to the plant

with a maximum flow product of 350 m^3/h. It is driven by a three phase Asynchronous Motor with 22 kW of the rated power. In general, the design of the pump is based on methods using empirical and semi-empirical equations which allow for obtaining the geometry of the hydraulic surfaces insuring a maximum efficiency. In another way, as said in [12], the amount of flow moved by the pump on the total area of its veins, (a), minus the effective loss in the moved flow due to the curvature of veins, (b). In bond graph language, the mechanical–hydraulic power conversion is modeled in many ways [10]. A non-linear gyrator with (a) and (b) coefficients model is chosen in Fig. 3 to suit the actual system's behavior [13].

$$P_P = (a \times \Omega + b \times Q_P) \times \Omega - \mathrm{c} \times Q_P^2 \tag{3}$$

$$T_m = (a \times \Omega + b \times Q_P) \times Q_P + \left(f_m + f_p\right) \times \Omega \tag{4}$$

Where (T_m) is the load torque of the motor of pump, (P_P) is the pressure of the fluid, (Q_P) is the pump's flow, (Ω) is the rotation speed of the motor, (a, b) are the pump parameters; and (c) is a parameter presenting the losses in the pump. The losses in the pump's model are identified as follow: where (c) is the hydraulic friction, ($J_{pm} = J_m + J_p$) is the motor-pump mechanical inertia and ($f_{pm} = f_m + f_p$) is the motor-pump mechanical losses [14]. These pump parameters (a, b, c and fpm) are extracted from experiments. The final resulting motor pump model can be expressed as follows in Fig. 3 after neglecting the equivalent inertia effect (Jpm = Jp + Jm) [15]:

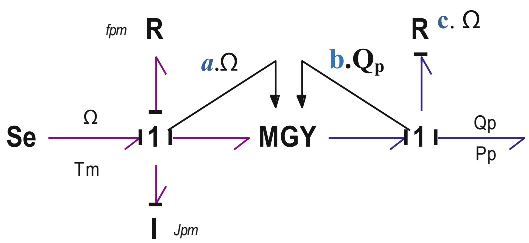

Fig. 3. The pump's bond graph model.

(3) Pipe model: The hydraulic dissipation in the pipes is modeled by an R-element, then the pressure (P_{Pipe}) is computed according to the Bernoulli law [10, 16] as follows:

$$\mathrm{P}_{Pipe} = R_{Pipe} Q_{Pipe}^2 \tag{5}$$

Where (P_{Pipe}) is the pressure, (Q_{Pipe}) is the water flow passing through the pipe and (R_{Pipe}) is the debit coefficients.

(4) Reverse osmosis model: The Reverse Osmosis device is the finest filter. By applying an external pressure, which must be superior to the osmosis pressure, the flow direction will be reversed. To summarize, two types of water will be obtained from the water feed. The first one is the permeate which is the good water that comes out of an RO system and has the majority of removed contaminants. The reject, is the second type of water that contains all of the contaminants that are unable to pass through the RO membrane. To model the RO, only the hydraulic domain is taken into account in this paper. The RO bond graph model is composed of several elements which will be individually detailed [14, 17]. In reality, the plant is equipped with two identical reverse osmosis RO units. Each RO contains nine vessel pipes and every vessel pipe incorporates three membranes of eight inches. These membranes are EUROWATER series 03-27 which is designed with a flow rate from 5 to 30 m^3/h. The important element in RO is the membrane which is modeled as a C-element corresponding to an hydraulic capacity. To characterize the membrane's permeability, the mechanism of mass transport across the membrane, commonly known as the "solution diffusion" model, is considered. The solution-diffusion transport equation for the reverse osmosis can be derived as follows:

$$J = L_m(\Delta P - \Delta\Pi) \tag{6}$$

Where (J) is the water flux through the membrane, (ΔP) is the transmembrane pressure difference, ($\Delta\Pi$) is the difference in osmotic pressure between the feed and the permeate and (L_m) is the permeability coefficient of the membrane. In fact, the pressure needed to force a solvent (water), to leave a solution (seawater, waste water, etc.) and to oblige permeates to pass through the membrane. For an ideal solution with a complete dissociation of salt ions, the osmotic pressure is defined as:

$$\Pi = iCRT \tag{7}$$

Where (Π) is the osmotic pressure, (C) is the salt ion concentration, (R) is the ideal gas constant, (T) is the solution temperature and (i) is the number of the ions in solution. The losses in the RO are also modeled as R-elements. They are subdivided into losses in pipes, also known as a loss of pressure between the input and rejection sides, and a loss at the output of the rejected water through the control valve (Fig. 4).

(5) Cooling tower model: The cooling tower phenomenon consists of the evaporation of the falling water film on the fill packing due to its interaction with the rising air stream which results in the cooling of the water stream as well as the heating and

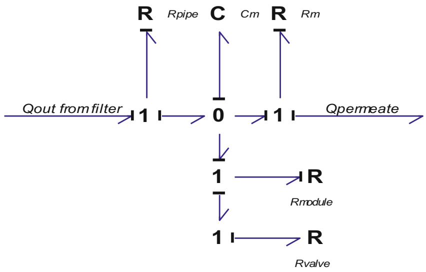

Fig. 4. RO's bond graph model

humidification of the outlet air [18]. Due to the complexity of the thermal phenomenon in the cooling tower, only the hydraulic part is studied in this model. Furthermore, the equations of the mass conservation of the two phases which are available in the cooling towers derived two forms as shown in Eqs. (8) and (9) below. The first one is the mass conservation for the dry air and the second is the mass conservation for water.

$$m_{air,in} = m_{air,out} \tag{8}$$

$$\dot{m}_{water,in} + w_{air,in}\dot{m}_{air,in} = \dot{m}_{water,out} + w_{air,out}\dot{m}_{air,out} \tag{9}$$

With ($\dot{m}_{air,in}$) and ($\dot{m}_{air,out}$) are the mass flow inlet and outlet of air and ($\dot{m}_{water,in}$) and ($\dot{m}_{water,out}$) are the mass flow inlet and outlet of water and (w) is the humidity ratio. The last equations allow approaching the model of the cooling towers.

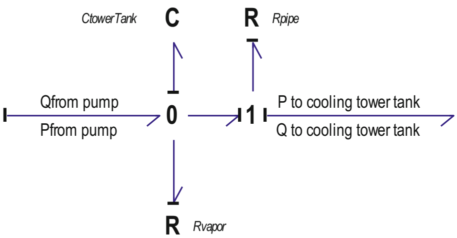

Fig. 5. Cooling tower's bond graph model

Indeed, the cooling towers are modeled as an R-element which represents the flow of water lost in the vapor transformation. Then, the tank storage of the cool water in the cooling tower is seen as a hydraulic capacity (Fig. 5).

3 Experimental Validation of the Process

Aim to model the real behavior of the cement water treatment process; the bond graph model must consider the hybrid character of this system. To detail, the cooling water tank level able to give order to start run the both lines of the RO or stop one and let just one line in function. This was described in the Sect. 2. Closely, in this model we just reveal the significant modes which affect directly the functioning of the process. The first mode is defined when the level in cooling water tank reaches about 2.50 m: this level let start the run of the two RO units. Similarly for the second mode, the level is the only responsible on the control of ON and OFF of the osmosis lines. So for a level of 4.70 m, the cooling water tank let work only one RO unit and stop the second. We refer to the hybrid bond graph and especially to the controlled junction which behaves as a normal 1- or 0-junction when ON and a source of zero flow or effort (respectively) when OFF. The controlled 1-junction is therefore used to break or inhibit flow and a controlled 0-junction is used to inhibit effort. The commonly accepted notation for controlled junctions is X1 and X0. In our model, we deal with autonomous switching when the convenient level is reached the junction commutates. So, we browse a logical function for decision which able to determine the suitable level for switching. To recapitulate, the bond graph model of whole process is shown in appendix.

The simulations of the BG model of the cement water treatment process are achieved by the 20-Sim© software, especially adapted for dynamic modeling of multidisciplinary energy systems. Then, we compare these elaborated simulations with the experimental results. Concerning the experimental results, the water treatment process is exploitable via a specific graphical interface developed by the plant constructor. This interface has the favor to allow the follow of the evolution of the process in real time and have access to any measurable data at any time. A series of illustrations is presented that demonstrate the accuracy of the proposed bond graph model. In reality, the Figs. 7 and 8 show the first mode of the system when the two lines operate together. As said before, the level of cooling water tank determines the operating mode of the treatment process. Consequently, the Figs. 6 and 9 imply the autonomous

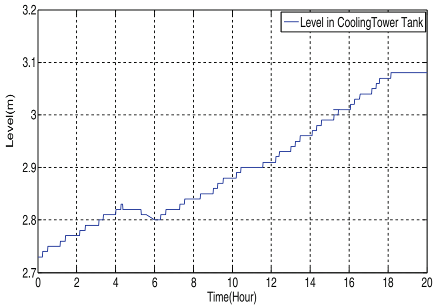

Fig. 6. The cooling water level controlling the first mode.

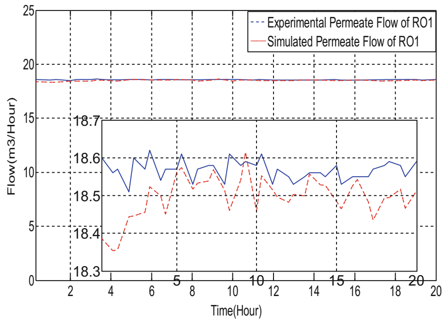

Fig. 7. The behavior of the permeate flow of RO 1 in the first mode.

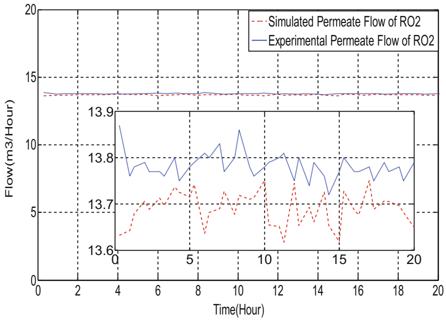

Fig. 8. The behavior of the permeate flow of RO 2 in the first mode

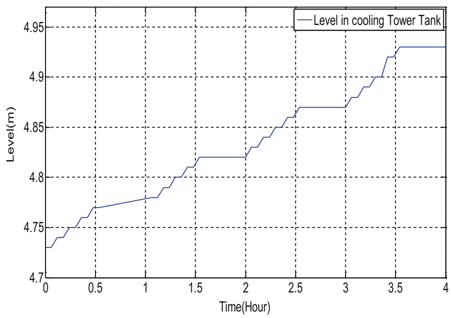

Fig. 9. The cooling water level controlling the second mode.

character of the switching. Indeed the Fig. 6 demonstrates that the chosen range of level from 2.7 to 3.06 m is corresponded to the right condition for establishing the first mode which illustrated respectively in the curve of Figs. 7 and 8. In fact, Fig. 7 show that the real permeate flow of the first osmosis isn't far from the same flow obtained by the hybrid bond graph model. Similarly, the curve drawn in Fig. 8 shows that, despite

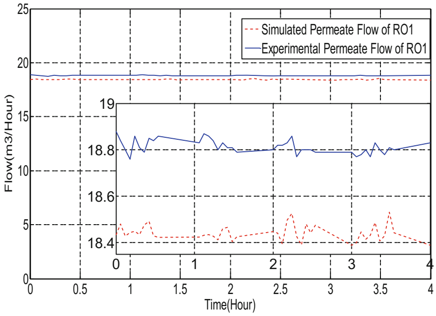

Fig. 10. The behavior of the permeate flow of RO 1 in the second mode.

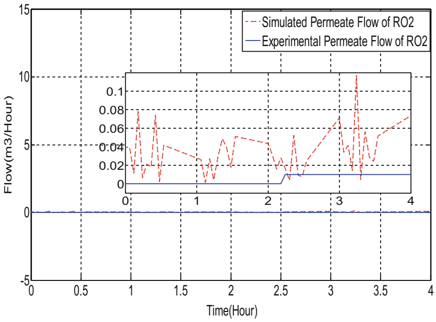

Fig. 11. The behavior of the permeate flow of RO 2 in the second mode.

some errors, simulation results of the second RO in the first mode process model are adequately conform to experimental results.

Practically, for the range of level from 4.74 m to 4.92 m which is illustrated in Fig. 9, our model switches as the real process to the second mode. So the curves respectively in Figs. 8 and 9 demonstrate well this mode. They explain that the behaviors of the simulated and the experimental permeate flow of the first osmosis in this current mode are conform. By the same way, in the second osmosis, the simulated and experimental permeate flow of this osmosis in this current mode reflect that only one osmosis is ON state (Figs. 10 and 11).

4 Conclusion

In this paper, the modeling of cement water process is considered. We develop a model of a real industrial process that takes into consideration many physical fields and presents a hybrid dynamic behavior. Consequently, we used the formalism of the hybrid bond graph because it is considered as a suitable tool to model the multidisciplinary process. In fact, the hydraulic equivalent sub-models of each process's element are deduced from its real hydraulic behaviors which are then integrated into the whole bond graph model of the cement water treatment process. The experimental and simulation results showed the efficiency of the implemented model using hybrid bond graph formalism. Practically, the elaborated model has proved its coherence in case of an autonomous switching between modes and permits the studied flows of each reverse osmosis to reach the experimental ones.

Appendix

Variables	Description	Value	Unit
$A_{Raw\ Tank}$	Surface of Raw Tank	100	$[m^2]$
$A_{Cooling\ Water\ Tank}$	Surface of Cooling Water Tank	42	$[m^2]$
$A_{Cooling\ Tower}$	Surface of Cooling Tower	12.5	$[m^2]$
Q_{Bf}	Flux of first filter before filtering	36	$[m^3/h]$
	Flux of second filter before filtering	36	$[m^3/h]$
Q_{Af}	Flux of first filter after filtering	30.1	$[m^3/h]$
	Flux of second after filtering	35.3	$[m^3/h]$
Pump of raw water 761.WP110			
P_p	Pressure of pump	3	Bar
Ω	Rotation speed of pump	1863	rpm
Moto-pump of RO 761WP151			
P_p	Pressure of pump	23	Bar
Ω	Rotation speed of pump	2950	rpm
Pump of cooling Tower 762WP110			
P_p	Pressure of pump	1.9	Bar
Ω	Rotation speed of pump	966	rpm
Moto-pump of distribution (762WP210)			
Pressure of pump	Pressure of pump	6	Bar
Ω	Rotation speed of pump	2955	rpm
Cooling Tower			
Q_{fout}	Water flow out of cooling Tower	265	$[m^3/h]$
T_{in}	Water inlet temperature	50	°C
T_{out}	Water outlet temperature	35	°C
$Q_{evaporation}$	Evaporation flow	6.4	$[m^3/h]$

References

1. Medjaher, K.: Contribution de l'Outil Bond Graph pour la Conception de Systèmes de Supervision des Processus Industriels. Thèse de doctorat, 2005, USTLille1-ECLille
2. Dauphin-Tanguy, G., Rombaut, C.: Why a unique causality in the elementary commutation cell bond graph model of a power electronics converter. In: IEEE International Conference on Systems, Man and Cybernetics, vol. 1, pp. 257–263 (1993)
3. Canstelain, A.: Modelling and analysis of power electronic networks by bond graph. In: Proceedings of 3rd International Conference Modelling and Simulation of Electrical Machines and Static Converters, IMACS-TCI 1990, Nancy, France, pp. 405–416 (1990)
4. Delgado, M., Sira-Ramirez, H.: Modelling and simulation of switch regulated dc-to-dc power converters of boost type. In: Proceedings of 1995 IEEE 1st International Caracas Conference on Devices Circuits and Systems, Caracas, pp. 84–88 (1995)
5. Broenink, J.F., Wijbrans, C.J.: Describing discontinuities in bond graphs. In: Proceedings 1993 Western Simulation Multiconference—International Conference on Bond Graph Modeling ICBGM–1993, La Jolla, CA, pp. 120–125 (1993)
6. Nacusse, A., Junco, S.: Switchable structured bond: a bond graph device for modeling power coupling/decoupling of physical systems. J. Comput. Sci. **5**, 450–462 (2013)
7. Umarikar, A.C., Umanand, L.: Modelling of switching systems in bond graphs using the concept of switched power junctions. J. Frankl. Inst. **342**(2), 131–147 (2005)
8. Gawthrop, P.J.: Hybrid bond Graphs Using Switched I and C Components. Centre for Systems and Control, University of Glasgow, Glasgow, UK. CSC Report 97005 (1997)
9. Mosterman, P.J., Biswas, G.: Modeling discontinuous behavior with hybrid bond graphs. In: 9th International Workshop on Qualitative Reasoning about Physical Systems, Amsterdam, Netherlands, pp. 139–147 (1995)
10. OuldBouamama, B., Samantaray, A.K.: Model-Based Process Supervision A Bond Graph Approach. Springer, Berlin (2006)
11. Brotusky, W.: Bond Graph Methodology—Development and Analysis of Multidisciplinay Dynamic System Models. Springer, London (2010)
12. Mosterman, P.J.: Hybrid dynamic system: a hybrid bond graph modeling paradigm and its application in diagnosis. Doctoral Thesis, Nashville Tennessee (1997)
13. Turki, M., Belhadj, J., Roboam, X.: Control strategy of an autonomous desalination unit fed by PV-Wind hybrid system without battery storage. J. Electr. Syst. (JES) **4**(2), 1–12 (2008)
14. Ben Ali, I., Turki, M., Belhadj, J., Roboam, X.: Systemic design of a reverse osmosis desalination process powered by hybrid energy system. In: 2014 International Conference on Electrical Sciences and Technologies in Maghreb (CISTEM), pp. 1–6 (2014)
15. Gülich, J.F.: Centrifugal Pumps, vol. 964. Springer, Berlin (2008)
16. Aridhi, E., Abbes, M., Mami, A.: Pseudo bond graph model of a thermohydraulic system. In: International Conference on Modeling, Simulation and Applied Optimization, Tunis, Tunisia, April 2013
17. Sellami, A.: Supervision des systèmes dynamiques Modélisés par approche bond de graph diagnostic et reconfiguration. Thèse de doctorat, école national des ingénieurs de Tunis (2014)
18. Papaefthimiou, V.D., Zannis, T.C., Rogdakis, E.D.: Thermodynamic study of wet cooling tower performance. Int. J. Energy Res. **30**, 411–426 (2006)

Adaptive Neural Control Design of MIMO Nonaffine Nonlinear Systems with Input Saturation

Zerari Nassira[1(✉)], Chemachema Mohamed[1], and Najib Essounbouli[2]

[1] Department Electronics, Faculty of Sciences of Technology, Constantine 1 University, Constantine, Algeria
zer.napg2010@gmail.com, m_chemachema@yahoo.fr
[2] CReSTIC Laboratory, University of Reims Champagne Ardennes, Reims, France
najib.essounbouli@univ-reims.fr

Abstract. In this paper, an adaptive neural networks control approach is proposed for a class of multi-input multi-output (MIMO) non-affine nonlinear dynamic systems in the presence of input saturation. The difficulty in controlling the saturated non-affine system is overcome by introducing a system transformation, so as the system can be reformulated as an affine of a canonical system. In the control design, neural networks are used in the online learning of the unknown dynamics and the input saturation is approximated to reduce the influence caused by the nonlinearities, and a robustifying control term is used to compensate for the approximation errors. Compared to the literature, in the proposed approach, the structure of the designed controller is much simpler since the causes for the problem of complexity growing in existing methods are eliminated. The stability analysis of the closed-loop system is investigated by using Lyapunov theory. Numerical simulation illustrated the proposed control scheme with satisfactory results.

Keywords: Adaptive control · Neural network
Multi-input multi-output (MIMO) nonlinear non-affine systems
Input saturation

1 Introduction

The design of robust adaptive controllers for multivariable unknown non-linear systems remains one of the most challenging tasks in the area of control systems. The principal difficulty for the control of non affine-in-control nonlinear systems resides in the fact that the control signals can not be explicitly obtained although the dynamics of the system is well known. In the literature, some significant results for non-affine MIMO systems for the fuzzy logic control have been obtained (Liu and Wang 2007; Wang et al. 2007; Boulkroune et al. 2012).

M. Chadli et al. (Eds.): ICEECA 2017, LNEE 522, pp. 155–167, 2019.
https://doi.org/10.1007/978-3-319-97816-1_12

Interesting works dealing with non-affine problem by using Taylor series expansion in order to obtain an affine system is addressed in Boulkroune et al. (2012). In Doudou and Khaber (2012), the implicit function theorem is used to demonstrate the existence of an ideal controller that can achieve control objective. In Boulkroune et al. (2012), Wang et al. (2007) the authors developed an adaptive fuzzy control scheme to stabilize a class of MIMO non-affine nonlinear systems where the mean value theorem is first used to transform unknown non-affine functions into an equivalent affine form. Then, by introducing some special type of Lyapunov functions, and using the approximation property of the RBF systems and backstepping method (Min et al. 2009; Wang et al. 2009), the control scheme is achieved. In the above works, the stability analysis of the closed-loop system is performed by using a Lyapunov approach.

In real world, input nonlinearities exist widely in physical systems such as mechanical, hydraulic, magnetic, and other types of systems components, so dealing with these nonlinearities in controller design is an important research field. Dead-zone in Boulkroune and M'Saad (2011), Tong and Li (2013), backlash and hysteresis in Shahnazi (2015), Su et al. (2003), and saturation nonlinearities in Esfandiari et al. (2015), He and Jagannathan (2005) are common non-smooth nonlinear characteristics dealt with in the literature. Input saturation is one of the most important non-smooth nonlinearities in many practical systems, which can hard limit system performance. Therefore, the effect of input saturation should be taken into consideration in the design and analysis of control systems. If the input saturation is ignored in the control design, the closed-loop control performance will be severely degraded, and instability may occur. Many significant results on control design of systems with input saturation have been obtained (Chen et al. 2010; Yang et al. 2015; Shahnazi 2016).

Motivated by the above observations, in this paper, we investigated a direct adaptive neural network control scheme for a class of MIMO non-affine nonlinear systems in the presence of input saturation. The basic idea is to use a function transformation in order to reformulate the non-affine system into an affine in Brunovsky form. The neural network systems are used to approximate the unknown nonlinear function and the nonlinear term arising from the input saturation. To compensate for the approximation errors and external disturbances, a robustifying control term is employed in addition to the σ-modification in the adaptation laws (Ioannou 1984).

Compared to the literature (Shenglin and Ye 2014; Chen 2009), the MIMO affined nonlinear systems, in normal form, are usually used without input saturation, in this paper the more complicated nested non-affine nonlinear systems are considered with input saturation. Therefore, the control design problem of this paper cannot be solved by employing the previous works directly. Furthermore, the considered class of MIMO nonlinear systems. The proposed control scheme can not only guarantee the boundedness of all the signals in the closed loop system and the tracking performance, but also provide a simple and effective way for controlling input saturated non-affine systems with mild assumptions. Simulation experiments are used to verify the effectiveness of the developed approach.

2 Problem Formulation

Consider the MIMO nonlinear non-affine system described by the following normal form:

$$\begin{cases} y^{n_1} = f_1(x, u(v(t)) + d_1(t, x) \\ \quad\vdots \\ y^{n_p} = f_p(x, u(v(t)) + d_p(t, x) \end{cases} \tag{1}$$

where $x = \left[x_1, .., x_p\right]^T \in R^n$ is the system state vector, which is assumed available for measurement, with $x_i^T = \left[y_i, \dot{y}, \ldots, y^{(n_i-1)}\right] \in R^{n_i}, \forall i = 1, \ldots, p$ and $y = \left[y_1, \ldots, y_p\right]^T \in R^p$ are the system output vector, respectively, and $f_i(x, u(v(t))), i = 1, .., p$ are smooth unknown non-affine functions and $d_i(t, x), i = 1, .., p$ are unknown external disturbances. Moreover, $v = \left[v_1, \ldots, v_p\right]^T \in R^p$ denotes the actual control input and $u(v(t)) = \left[u_1(v(t)), \ldots, u_p(v(t))\right]^T \in R^p$ are the input saturation types of the nonlinearity. To Wen et al. (2011), input saturation u(v(t)) can be described by

$$u(v(t)) = sat(v) = \begin{cases} sign(v(t))u_m & |v(t)| \geq u_m \\ v(t) & |v(t)| \leq u_m \end{cases} \tag{2}$$

where $u_m = \left[u_{m1}, \ldots., u_{mp}\right]^T$ are a known bound on u(t). The relationship between the applied control $u(t)$ and the control input $v(t)$ has a sharp corner when $|v(t)| = u_m$. This saturation description cannot be applied directly. According to Wen et al. (2011), the saturation can be approximated by the following smooth function

$$g(v) = {u_m}^* \tanh(\frac{v}{u_m}) = u_m \frac{e^{(v/u_m)} - e^{-(v/u_m)}}{e^{(v/u_m)} + e^{-(v/u_m)}} \tag{3}$$

Then, sat(v(t)) in (2) can be expressed as

$$sat(v) = g(v) + d(v) = {u_m}^* \tanh(\frac{v}{u_m}) + d(v) \tag{4}$$

where $d(v) = sat(v(t)) - g(v)$ is bounded as proved in Wen et al. (2011).

The control objective is to design an adaptive neural network controller $u(t)$ for system (1) such that the system output $y(t)$ follows a desired trajectory $y_{d_i}(t)$, while all the signals of the closed-loop system are bounded.

In order to get explicit control variable, one can transform the non-affine system (1) into an affine system by performing the Mean Value Theorem (Du and Chen 2009) as follows:

$$\begin{aligned} f_1(x,u(v)) &= f_1(x) + g_1(x,u^*)u_1(v) \\ &\vdots \\ f_p(x,u(v)) &= f_p(x) + g_p(x,u^*)u_p(v) \end{aligned} \tag{5}$$

where u^* is a point between zero and $u(v)$.

Throughout this paper we make the following assumption:

Assumption 1: The desired trajectory vector $y_d = \left[y_{d_1}^T, \ldots, y_{d_p}^T, y_{d_p}^{n_p}, \ldots, y_{d_p}^{n_p}\right]^T$ where $y_{d_i} = \left[y_{d_i}, \dot{y}_{d_i}, \ldots, y_{d_i}^{(n_i-1)}\right]$, is continuous and bounded.

Assumption 2: The unknown disturbances $\overline{D}(t)$ are bounded by unknown constants $\overline{D}$ such that: $\left|\overline{D}(t,x)\right| \leq \overline{D}$

Let define the tracking errors as

$$\begin{aligned} e_1(t) &= y_{d_1}(t) - y_1(t) \\ &\vdots \\ e_p(t) &= y_{d_p} - y_p(t) \end{aligned} \tag{6}$$

Then, using (5) we get

$$\begin{aligned} e_1^{n_1} &= y_{d_1}^{n_1} - f_1(x) - g_1(x,u^*)u_1(v) - d_1(x,t) \\ &\vdots \\ e_p^{n_p} &= y_{d_p}^{n_p} - f_p(x) - g_p(x,u^*)u_p(v) - dp(x,t) \end{aligned} \tag{7}$$

Let us define:

$$F(x) = \begin{bmatrix} f_1(x) \\ \vdots \\ f_p(x) \end{bmatrix}, g(x,u^*) = \begin{bmatrix} g_{11}(x,u^*) & \ldots & g_{1p}(x,u^*) \\ \vdots & \ddots & \vdots \\ g_{p1}(x,u^*) & \cdots & g_{pp}(x,u^*) \end{bmatrix} \quad A = diag\left[A_1, \ldots, A_p\right], B = diag\left[b_1, \ldots, b_p\right]$$

with $A_i = \begin{bmatrix} 0 & 1 & \ldots & 0 & 0 \\ 0 & 0 & 1 & \cdots & 0 \\ \vdots & \vdots & \vdots & \ddots & \vdots \\ 0 & 0 & 0 & \vdots & 1 \\ 0 & 0 & 0 & \ldots & 0 \end{bmatrix}, b_i = \begin{bmatrix} 0 \\ 0 \\ 0 \\ \vdots \\ 1 \end{bmatrix} \quad D(x,t) = \begin{bmatrix} d_1(x,t) \\ \vdots \\ dp(x,t) \end{bmatrix}$

which can be written in matrix form as

$$\dot{e} = Ae + B\left[-F(x) - g(x,u^*)u(v) + y_d^{(n)} - D(x,t)\right] \tag{8}$$

Based on (4), the system (1) can be rewritten in the following form:

$$\begin{aligned}\dot{e} &= Ae + B\left[-F(x) - g(x,u^*)(g(v) + d(v)) + y_d^{(n)} - D(x,t)\right]\\ &= Ae + B\left[-F(x) - g(x,u^*)g(v) + y_d^{(n)} - \overline{D}(t,x)\right]\\ &= Ae + B\left[-F(x) - g(x,u^*)v - \Delta u + y_d^{(n)} - \overline{D}(t,x)\right]\end{aligned} \tag{9}$$

where $\Delta u = g(x,u^*)(g(v) - v)$, and where $\overline{D}(t,x) = g(x,u^*)d(v) - D(x,t)$.

Suppose $F(x)$ and $g(x,u^*)$ are known, $\overline{D}(t,x) = 0$, then from (9) the ideal controller can be chosen as.

Thus, the nonlinear system (9) can be written as

$$v^* = g(x,u^*)^{-1}\left[F(\bar{x}) + y_d^{(n)} - \underline{k}^T e + \Delta u\right] \tag{10}$$

where $e = \left[e_1^T, \ldots, e_p^T\right]^T$ with $e_i = \left[e_i, \dot{e}_i \ldots, e_p^{(n_i-1)}\right]^T$, and feedback gain vector $k^T = \left[k_{1c}^T, \ldots, k_{2c}^T\right]$. Inserting Eq. (10) into (9) and after simple manipulations, we have

$$\begin{bmatrix} e_1^{(n_1)} + k_{1n_1} e_1^{(n_1-1)} + \ldots + k_{11} e_1 \\ \vdots \\ e_p^{n_p} + k_{pnp} e_p^{(n_p-1)} + \ldots + k_{p1} e_p \end{bmatrix} = \begin{bmatrix} 0 \\ \vdots \\ 0 \end{bmatrix} \tag{11}$$

If the all coefficients k_{ij} are chosen such that all polynomials in Eq. (11) are Hurwitz, which implies that $\lim_{t\to\infty} e(t) = 0$, the main control objective is achieved.

Nevertheless, $F(\bar{x})$ and $g(x,u^*)$ are unknown, so the controller v^* cannot be realized. A comprehensive solution is to employ NNs to approximate unknown functions and design. It is shown that the nonlinear continuous functions can be approximated by NNs with an arbitrary accuracy.

3 HONN and Function Approximation

The structure of HONN is expressed as the following (Shuzhi et al. 2008):

$$\phi(W,Z) = W^T S(Z) W, S(Z) \in R^l \tag{12}$$

$$S(Z) = [s_1(Z), \ldots, s_l(Z)]^T \tag{13}$$

$$s_i(Z) = \prod_{j \in I_i} \left[s(z_j)\right]^{d_j(i)}, i = 1, \ldots, l \tag{14}$$

where $Z \in \Omega_z \in R^m$ is the input to HONN, l is a positive integer and denotes the NN node number, $\{I_1, \ldots, I_l\}$ is a collection of l unordered subsets of $\{1, \ldots, m\}$, specified by the designer, d_{ij} are non-negative integers, W is an adjustable synaptic weight vector, $s(z_j)$ is chosen as a hyperbolic tangent function

$$s(z_j) = (e^{z_j} - e^{-z_j})/(e^{z_j} + e^{-z_j}) \tag{15}$$

For a smooth function $f(z)$ over a compact set $\Omega_{\underline{z}} \in R^m$, given a small constant real number $\bar{\varepsilon} > 0$, if l insufficiently large, there exists a set of ideal bounded weights W^* such that

$$\sup_{z \in \Omega_z} |f(Z) - \phi(W, Z)| \tag{16}$$

From the universal approximation results for neural networks (Gupta and Rao 1994), it is known that the constant $\bar{\varepsilon}$ can be made arbitrarily small by increasing the NN nodes number l.

4 Control Design and Stability Analysis

To facilitate the controller design, and according to the fact that a neural network system is a universal approximator, we use a HONN in the form of (12) to approximate each component of the ideal input control vector $v^* = \left[v_1^*, \ldots, v_p^*\right]^T$ as follows:

$$v_i^* = W_i^{*T} S_i(Z) + \varepsilon_i(Z), i = 1, \ldots, p \tag{17}$$

where $Z = [x^T, v, u(v), \varphi]^T Z \in \Omega_z$ is the input vector, as Ω_z is a compact set, where $\varphi = \left[\varphi_1, \ldots, \varphi_p\right]^T$ are given as follows:

$$\begin{aligned} \varphi_1 &= y_{d_1}^{(n_1)} + k_{1,n_1} e_1^{(n_1 - 1)} + \ldots + k_{1,1} e_1 \\ &\vdots \\ \varphi_p &= y_{dp}^{(np)} + k_{1,n_p} e_1^{(np-1)} + \ldots + k_{p,1} e_p \end{aligned} \tag{18}$$

$\varepsilon_i(Z)$ is the neural network approximation error considered arbitrarily small and bounded from the theory of the approximation, and W_i^* is ideal parameter vector which minimize the function $|\varepsilon_i(Z)|$. These optimal parameters satisfy:

$$W_i^* = \arg\min_{w_i \in \Omega_w} \left\{ \sup_{z \in \Omega_z} \left| v_i^*(Z) - v_i(Z) \right| \right\} \tag{19}$$

Let us denote

$$W^{*}=\left[W_{1}^{*T},\ldots,W_{p}^{*T}\right]^{T},S(Z)=diag\left[S_{1}(Z),\ldots,S_{p}(Z)\right]\varepsilon(\underline{z})=\left[\varepsilon_{1}(\underline{z}),\ldots,\varepsilon_{p}(\underline{z})\right]^{T}$$

Therefore, we can write

$$v^{*}(\underline{z})=W^{*T}S(Z)+\varepsilon(Z) \tag{20}$$

Since the ideal parameter vector W^{*} is unknown, it should be estimated by a suitable adaptation law. Let W be an estimate of the ideal vector and define the control law as the adaptive neural network approximation of the ideal controller (10), i.e. the control law for system (9) is chosen as

$$v=\hat{W}^{T}S(Z)+u_{s} \tag{21}$$

$$u_{s}=\hat{\rho}\tanh(e^{T}PB/\in) \tag{22}$$

where $u_{s}=\left[u_{s1},\ldots,u_{sp}\right]^{T}$ is a vector of supplementary signal which guarantees the stability of the closed-loop system, is $\in$ a small positive constant, and tanh(.) is the hyperbolic tangent function. To achieve the control objectives, we define the parameter adaption laws as follows:

$$\dot{\hat{W}}=\Gamma(e^{T}PBS(Z)-\sigma_{1}\hat{W}) \tag{23}$$

$$\dot{\hat{\rho}}=\gamma(e^{T}PB\tanh(\frac{e^{T}PB}{\in})-\sigma_{2}\hat{\rho}) \tag{24}$$

where Γ, γ, σ_1 and σ_2 are positive constants.

Assumption 3: The approximation errors $\varepsilon(Z)$ is bounded, i.e., $\|\varepsilon(Z)\|\leq\bar{\varepsilon}$ where $\bar{\varepsilon}$ is unknown constant.

By substituting (10) and (20) into the (9), we get

$$\dot{e}=(A-Bk)e-B\left[W^{*T}S(Z)+\varepsilon(Z)-v-\overline{D}(t,x)\right] \tag{25}$$

Using (21), the error dynamic (25) of the MIMO nonlinear system can be expressed as

$$\dot{e}=(A-Bk)e+B[\widetilde{W}^{T}S(Z)+\varepsilon(Z)-u_{s}-\overline{D}(t,x)] \tag{26}$$

where $\widetilde{W}=W^{*}-\hat{W}$ is the parameter estimation error vector.

Let $\underline{k}^T = \left[\underline{k}_{1c}^T, \ldots, \underline{k}_{2c}^T\right]$, with $\underline{k}_{ic}^T = [k_{i1}, \ldots, k_{in_i}]$ be a feedback gain vector selected such that the matrix $A_k = (A - Bk)$ is stable. Thus, for any given positive definite symmetric matrix, there exists a unique positive definite symmetric solution P to the following Lyapunov algebraic equation:

$$A_k^T P + A_K P = -Q$$

$$(A - Bk)^T P + (A - Bk)P = -Q \tag{27}$$

Therefore, from preceding consideration, we obtain the following theorem.

Theorem: Consider the system (1) with Assumptions 1–3. Then, the control law defined by (21–22) and the adaptation law (23–24). Then, it can be guaranteed that all the signals of the closed-loop system are bounded, and the tracking errors converge to a small neighborhood of origin.

Proof: Let us consider the following Lyapunov function candidate

$$V = \frac{1}{2}(e^T P e + \widetilde{W}^T \Gamma^{-1} \widetilde{W} + \frac{1}{\gamma}\tilde{\rho}^2) \tag{28}$$

Using (26) and the fact that $\tilde{\rho} = \bar{\rho} - \hat{\rho} = \bar{\varepsilon} + \overline{D} - \hat{\rho}$, ($\hat{\rho}$ the estimates of the unknown parameter $\bar{\rho}$), the time derivative of (28) can be written

$$\begin{aligned} \dot{V} &= \tfrac{1}{2}\dot{e}^T P e + \tfrac{1}{2} e^T P \dot{e} - \widetilde{W}^T \Gamma^{-1} \dot{\hat{W}} - \tfrac{1}{\gamma}\tilde{\rho}\dot{\hat{\rho}} \\ &= \tfrac{1}{2} e^T (A_k^T P + A_K P) e + e^T P B [\widetilde{W}^T S(Z) + \varepsilon(z) - \overline{D}(t,x) - u_s] \\ &\qquad - \widetilde{W}^T \Gamma^{-1} \dot{\hat{W}} - \tfrac{1}{\gamma}\tilde{\rho}\dot{\hat{\rho}} \end{aligned} \tag{29}$$

with (27), and the fact that $\left|\overline{D}(t,x)\right| \le \overline{D}$ and $\|\varepsilon(Z)\| \le \bar{\varepsilon}$ from Assumptions 2 and 3, (29) becomes

$$\begin{aligned} \dot{V} \le & -\tfrac{1}{2} e^T Q e + e^T P B [\hat{\rho} \tanh(\tfrac{e^T P B}{\in}) - u_s] + |e^T P B|(\bar{\varepsilon} + \overline{D}) \\ & - e^T P B \bar{\rho} \tanh(\tfrac{e^T P B}{\in}) + \widetilde{W}^T [e^T P B S(Z) - \Gamma^{-1} \dot{\hat{W}}] \\ & + \tfrac{1}{\gamma}\tilde{\rho}[e^T P B \tanh(\tfrac{e^T P B}{\in}) - \dot{\hat{\rho}}] \end{aligned} \tag{30}$$

Note that for any $\in \ \ge 0$, and using the following inequality (Ioannou 1984), $-x\tanh(x/\in) - |x| \le \kappa \in$, with $\kappa = 0.2785$.

According to the parameter adaptation law (23) and (24), then (30) can be reduced to

$$\dot{V} \le -\frac{1}{2} e^T Q e + \sigma_1 \widetilde{W}^T \hat{W} + \sigma_2 \tilde{\rho}\hat{\rho} + \bar{\rho}\kappa \in \tag{31}$$

By completion of squares, we have

$$\sigma_1 \widetilde{W}^T \hat{W} \leq \frac{\sigma_1}{2} \|W^*\|^2 - \frac{\sigma_1}{2} \left\| \widetilde{W} \right\|^2 \tag{32}$$

$$\sigma_2 \tilde{\rho} \hat{\rho} \leq \frac{\sigma_2}{2} \bar{\rho}^2 - \frac{\sigma_2}{2} \tilde{\rho}^2 \tag{33}$$

(31) can be rewritten as follows:

$$\begin{aligned} \dot{V} \leq & -\tfrac{1}{2} e^T Q e - \tfrac{\sigma_1}{2} \left\| \widetilde{W} \right\|^2 - \tfrac{\sigma_2}{2} \tilde{\rho}^2 + \bar{\rho} \kappa \in + \tfrac{\sigma_1}{2} \|W^*\|^2 + \tfrac{\sigma_2}{2} \bar{\rho} \\ & \leq \alpha V + \beta \end{aligned} \tag{34}$$

where $\beta = \bar{\rho}\kappa \in + \frac{\sigma_1}{2} \|W^*\|^2 + \frac{\sigma_2}{2} \bar{\rho}^2$.

let $\alpha = \min\left\{ \frac{\lambda_{\min}(Q)}{\lambda_{\max}(P)}, \frac{\sigma_1}{2\lambda_{\max}(\Gamma^{-1})}, \frac{\sigma_2}{2\gamma} \right\}$, where $\lambda_{\min}(Q)$ denotes the minimum eigenvalue of the matrix Q, and $\lambda_{\max}(\Gamma^{-1})$ and $\lambda_{\max}(P)$ denotes the maximum eigen values of Γ^{-1} and P, respectively.

Multiplying both sides by $e^{-\alpha t}$, (34) can be expressed as

$$\frac{d}{dt}\left(V(t) e^{-\alpha t}\right) \leq \beta e^{-\alpha t} \tag{35}$$

Integrating (35) over [0, t], finally, we arrive at

$$0 \leq V(t) \leq \frac{\beta}{\alpha} + \left[V(0) - \frac{\beta}{\alpha} \right] e^{-\alpha t} \tag{36}$$

It can be shown from (36) that V is bounded. Then, all the variables in V are also bounded, thus e, $\tilde{W}$ and $\tilde{\rho}$ are bounded. From the definitions of $\tilde{W} = W^* - \hat{W}$ and $\tilde{\rho} = \bar{\rho} - \hat{\rho}$ it is easy to show that $\hat{W}$ and $\hat{\rho}$ also bounded. Each actual controller v_i in (21) can be considered as a function of e, $\hat{W}$ and $\hat{\rho}$, thus v_i remains also bounded. Accordingly, we conclude that all the signals in the closed loop system are bounded. From (28) and (36), it follows that

$$|e| \leq \left(\frac{1}{\lambda_{\min}(P)} \left(\frac{\beta}{\alpha} + \left[V(0) - \frac{\beta}{\alpha} \right] e^{-\alpha t} \right) \right)^{\frac{1}{2}} \tag{37}$$

If $V(0) = \frac{\beta}{\alpha}$, e can converge to $\left(\frac{1}{\lambda_{\min}(P)} \frac{\beta}{\alpha} \right)^{\frac{1}{2}}$, i.e., $\lim_{t \to \infty} |e| = \left(\frac{1}{\lambda_{\min}(P)} \frac{\beta}{\alpha} \right)^{\frac{1}{2}}$, $\Omega_e = \left\{ e \middle| \|e\| \leq \left(\frac{1}{\lambda_{\min}(P)} \frac{\beta}{\alpha} \right)^{\frac{1}{2}} \right\}$.

This implies the tracking errors can converge to a bounded compact zero. This completes the proof.

5 Simulation Results

Consider the following nonlinear system (Boulkroune et al. 2012):

$$\begin{cases} \dot{x}_{11} = x_{12} \\ \dot{x}_{12} = x_{11}^2 + x_{12}^2 + 0.15u_1^3(v) + (2 + \cos(x_{11}))u_1(v) - u_2(v) + d_1 \\ \dot{x}_{21} = x_{22} \\ \dot{x}_{22} = x_{22}^2 + x_{11} + x_{12}^2 - 0.5u_1(v) + (1 + x_{21}^2)u_2^3(v) + 2(\sin(x_{21}))u_2(v) + d_2 \\ y_1 = x_{11} \\ y_2 = x_{21} \end{cases} \tag{38}$$

where $x = [x_{11}, x_{12}, x_{21}, x_{22}]^T$ is the state of the system, u_1 and u_2 are the control inputs, y_1 and y_2 are the system outputs, and the input saturation *u(v(t))* are determined by (2) with the parameter u_m = [0.8, 0.8]. The control objective is to force the system output y_1 and y_2 to track the desired trajectories $y_{d1}(t) = \sin(t)$ and $y_{d2}(t) = \sin(t)$. Two HONN systems in the form of (12) are used to generate the unknown controller u_1 and u_2. Each HONN system has $z = \left[z_1^T, z_2^T, z_3^T, z_4^T\right]^T$ as input, where $z_1^T = [x_{11}, x_{12}, x_{21}, x_{22}]$, $z_2^T = [v_1, v_2]$, $z_3^T = [u_1(v), u_2(v)]$ and $z_3^T = [\ddot{y}_{d1} + k_{12}\dot{e}_1 + k_{11}e_1, \ddot{y}_{d2} + k_{21}\dot{e}_1 + k_{22}e_2]$, and the NN is constructed according to (14) and (15) with $l = 60$ neurons. The initial state $x(0) = [0.1, 0, 0.1, 0]^T$ is and the initial values of the parameters estimates $W(0)$ are set equal to zero. The design parameters used in this simulation are chosen as follows: $\Gamma = 12$, $\in\, = 0.01$, $\sigma_1 = 0.1$, $\sigma_1 = 0.01$, $\gamma = 10$ $Q = Diag\,[5.5\ \ 5.5\ 5\ 5]$,

$$d_1 = 5x_{11}^2 - 2x_{22} \quad \text{and} \quad d_2 = 5x_{21}^3 - 2x_{12}, \quad P = \begin{bmatrix} 8.125 & 0 & 2.75 & 0 \\ 0 & 8.125 & 0 & 2.75 \\ 2.75 & 0 & 2.625 & 0 \\ 0 & 2.75 & 0 & 2.625 \end{bmatrix}$$

$$k^T = \begin{bmatrix} 1 & 0 & -2 & 0 \\ 0 & -1 & 0 & -2 \end{bmatrix}.$$

The simulation results for both subsystems are shown in Figs. 1 and 2 illustrate the boundedness and convergence of the tracking curves for both subsystems. The control signals $u_1(t)$ and $sat(u_1(t))$ and the control signals $u_2(t)$ and $sat(u_2(t))$ can be observed in Figs. 3 and 4, respectively. So, clearly, these simulation results verify our theoretical results. Further, the proposed control strategy is compared with Boulkroune et al. (2012), the control input $u_1(t)$ and $u_2(t)$, whose performance is presented in Figs. 3 and 4, it illustrates that the proposed strategy performed better than in the Boulkroune et al. (2012). In contrast, the control low in Boulkroune et al. (2012) does not have any saturation compensation, and then the actuator might operate at the upper/lower saturation region within longer period or suffer more abrupt change, which may result in the wear failure in engineering applications.

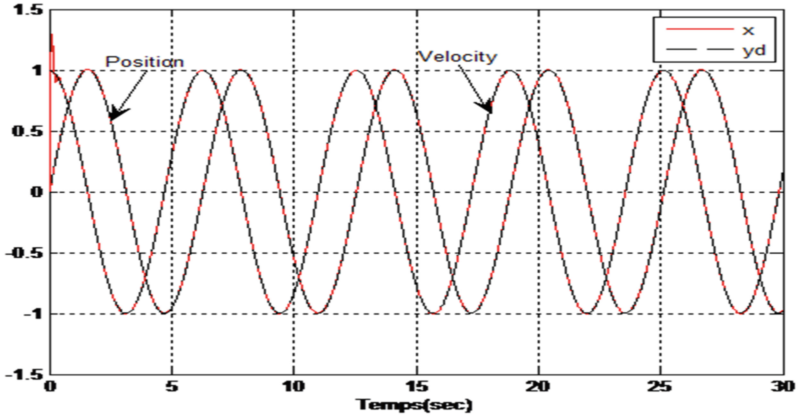

Fig. 1. Tracking curves of subsystem 1: actual; desired

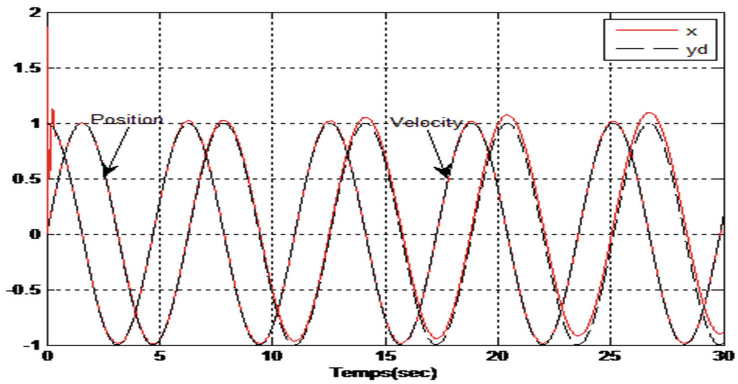

Fig. 2. Tracking curves of subsystem 1: actual; desired

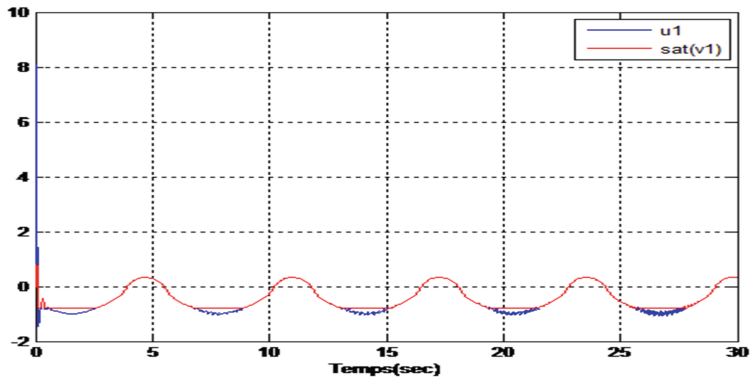

Fig. 3. Trajectory of u_1 and $sat(v_1)$.

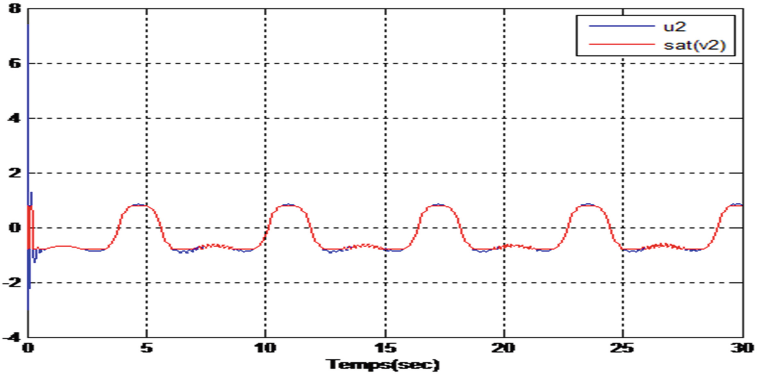

Fig. 4. Trajectory of u_2 and $sat(v_2)$.

6 Conclusions

In this paper, a direct adaptive controller for a class of MIMO non-affine nonlinear systems using neural network systems in the presence of input saturation has been developed. In this approach, a robustifying control term was added to deal with approximation errors and the nonlinear term arising from the input saturation. Thanks to function transformation, non-affine nonlinear systems can be transformed into affine form where an ideal controller was developed. An adaptive HONN was used for approximating the unknown controller to attain the desired performances, where the adaptive laws were deduced from the stability analysis in the sense of Lyapunov. Simulation results obtained showed the effectiveness of this technique.

References

Boulkroune, A., M'Saad, M.: A fuzzy adaptive variable-structure control scheme for uncertain chaotic MIMO systems with sector nonlinearities and dead-zones. Expert Syst. Appl. **38**(12), 1447–14750 (2011)

Boulkroune, A., Tadjine, M., M'Saad, M., Farza, M.: Fuzzy approximation based indirect adaptive controller for multi-input multi-output Non-affine systems with unknown control direction. IET Control Theory Appl. **6**(17), 2619–2629 (2012)

Wen, C., Zhou, J., Liu, Z., Su, H.: Robust adaptive control of uncertain nonlinear systems in the presence of input saturation and external disturbance. Autom. Control IEEE Trans. **56**(7), 1672–1678 (2011)

Chen, C.-S.: Dynamic structure adaptive neural fuzzy control for MIMO uncertain nonlinear systems. Inf. Sci. **179**(15), 2676–2688 (2009)

Su, C.-Y., Oya, M., Hong, H.: Stable adaptive fuzzy control of nonlinear systems preceded by unknown backlash-like hysteresis. IEEE Trans. Fuzzy Syst. **11**(1), 1–8 (2003)

Doudou, S., Khaber, F.: Direct adaptive fuzzy control of a class of MIMO non- affine nonlinear systems. Int. J. Syst. Sci. **43**(6), 1029–1038 (2012)

Du, H., Chen, X.: NN-based output feedback adaptive variable structure control for a class of non-affine nonlinear systems: a nonseparation principle design. Neurocomputing **72**(7–9), 2009–2016 (2009)

Esfandiari, K., Abdollahi, F., Talebi, H.A.: Adaptive control of uncertain nonaffine nonlinear systems with input saturation using neural networks. IEEE Trans. Neural Netw. Learn. Syst. **26**(10), 2311–2322 (2015)

Liu, Y., Wang, W.: Adaptive fuzzy control for a class of uncertain non-affine nonlinear systems. Inf. Sci. **177**, 3901–3917 (2007)

Chen, M., Zou, J., Feng, X., Jiang, C.: Approximation-based tracking control of uncertain MIMO nonlinear systems with input saturation. In: Proceedings of the 29th Chinese Control Conference, pp. 6155–6160 (2010)

Gupta, M.M., Rao, D.H.: Neuro-Control Systems: Theory and Applications. IEEE Press, New York (1994)

Min, W., Cong, W., Siying, Z.: direct adaptive neural control of completely non-affine pure-feedback nonlinear systems with small-gain approach. In: Chinese Control and Decision Conference (CCDC) (2009)

Ioannou, P.A.: Robust Adaptive Control. Prentice-Hall, Upper Saddle River (1984)

He, P., Jagannathan, S.: Reinforcement learning-based output feedback control of nonlinear systems with input constraints. IEEE Trans. Syst. Man Cybern. Part B Cybern. **35**(1), 150–154 (2005)

Shahnazi, R.: Observer-based adaptive interval type-2 fuzzy control of uncertain MIMO nonlinear systems with unknown asymmetric saturation actuators. Neurocomputing **171**, 1053–1065 (2016)

Shahnazi, R.: Output feedback adaptive fuzzy control of uncertain MIMO nonlinear systems with unknown input nonlinearities. ISA Trans. **54**, 39–51 (2015)

Shuzhi, S.G., Chenguang, Y., Tong, H.: Adaptive predictive control using neural network for a class of pure-feedback systems in discrete time. IEEE Trans. Neural Netw. **19**(9), 1599–1614 (2008)

Tong, S., Li, Y.: Adaptive fuzzy output feedback control of MIMO nonlinear systems with unknown dead-zone inputs. IEEE Trans. Fuzzy Syst. **21**(1), 134–146 (2013)

Shenglin, W., Ye, Y.: Adaptive fuzzy neural network control for a class of uncertain MIMO nonlinear systems via sliding-mode design. In: Sixth International Conference on Intelligent Human-Machine Systems and Cybernetics (IHMSC), vol. 2 (2014)

Wang, W., Chien, L., Li, I., Su, S.: MIMO Robust control via T-S fuzzy models for non-affine nonlinear systems. In: Proceedings of IEEE International Conference on Fuzzy Systems, pp. 1–6 (2007)

Wang, W.-J., Hong, C.-M., Kuo, M.-F., Leu, Y.-G., Lee, T.-T.: RBF neural network adaptive backstepping controllers for MIMO nonaffine nonlinear systems. In: Proceedings of the IEEE International Conference on Systems, Man, and Cybernetics, USA, October 2009

Yang, Y., Yue, D., Xue, Y.: Decentralized adaptive neural output feedback control of a class of large-scale time-delay systems with input saturation. J. Frankl. Inst. **352**(5), 2129–2151 (2015)

High Gain Observer Optimization Techniques-Based Synchronization for Nonlinear Chaotic Systems

Ines Daldoul(✉) and Ali Sghaier Tlili

Laboratory of Advanced Systems, Polytechnic School of Tunisia, BP. 743 2078 La Marsa, Tunis, Tunisia
ines.daldoul@gmail.com, ali.tlili@ept.rnu.tn

Abstract. The focus of this paper is on the design of high gain observer optimization techniques for the state synchronization of nonlinear perturbed chaotic systems. The main objective of the developed approaches concerns the state observer optimization design methods using proposed algorithms relevant to the optimal control synthesis. As a matter of fact, two extensive optimization criteria are proposed to calculate the observation gain and especially the setting parameter $\boldsymbol{\theta}$. Thereby, the developed criteria achieve a compromise between the correction term of the state observer and the observation error in the first one and the minimization of a cost functions, dealing with square errors between the master and the slave systems, in the second one. Numerical simulations on the unified perturbed chaotic system demonstrate the performances of the designed optimization approaches.

Keywords: Nonlinear perturbed chaotic systems · High gain observer Optimization · Synchronization

1 Introduction

Chaotic systems are considered as nonlinear bounded unstable systems with high sensitivity to initial conditions, and including infinite unstable periodic orbits in their strange attractors [1]. Synchronization in chaotic dynamic systems reaches a terrific agreement of interest among scientists in several fields [2, 3]. Chaotic systems synchronization are highly applied in various nonlinear domains such as chemical reaction synchronization and secret communication [4, 5].

Synchronization of two identical chaotic systems with different initial conditions was initially considered by Pecora and Carroll. Different methods based on master–slave pattern have been considered to synchronize chaotic systems [6]. The well-known methods in this area are the adaptive control [7, 8], the sliding mode control [9], the polytopic observer-based control [10], the gravitational search algorithm filter [11], etc. Additionally, through [12], it is proven that estimating chaotic systems using nonlinear state observer approach is achievable. Thus, the nonlinear estimation theory can be used to design a receiver, which synchronizes with the driving system [13].

M. Chadli et al. (Eds.): ICEECA 2017, LNEE 522, pp. 168–181, 2019.
https://doi.org/10.1007/978-3-319-97816-1_13

Indeed, depending on the interest of the synchronization between the transmitter and the receiver systems, controllers based on high gain observers might be arranged for chaos synchronization. The characteristics of this observer are highly profitable in secure communications because the signals delivered by systems are broadband, noise-like and difficult to predict [14, 15]. The secure communication system implicates the development of a signal that involve a secret information that persisted indistinguishable inside of a carrier signal [16, 17]. The security of this information can be established by implanting it within a chaotic signal that can be transferred to a recommended receiver, which must be able to detect and recover the information from the chaotic signal [18].

In the last years, numerous works are concentrated in optimizing state observers in order to obtain improved state synchronization results of nonlinear systems. Thereby, in [19, 20], a $H\infty$ nonlinear observer for synchronizing the transmitter-receiver of chaotic systems is dealt with, while the particle swarm optimization in chaos synchronization is considered in [21, 22]. Besides, the Kalman filter in [23], the interval observer in [24], the high-gain proportional integral observer in [25] and the adaptive controller in [26] have been optimized within many observer approaches. Furthermore, various widespread global optimization methods like genetic algorithms (GA) [27], ant colony optimization (ACO) [28], gravitational search algorithms (GSA) [29] and particle swarm optimization (PSO) [30] are extensively used to solve system identification.

In this work, the design of a robust synchronization scheme for nonlinear perturbed chaotic systems based on an optimal high gain observer is achieved. The designed optimization method used both the optimal control theory and also the Tabu algorithm. For this aim, a quadratic optimization criterion is proposed to determine the optimal value of the observation regulation parameter θ. Such a criterion may lead to the minimal value of the cost function by attaining an arrangement between the correction term of the state observer and its observation error. The efficiency of the proposed robust optimization design of the high gain observer is tested through comparisons between an innovative proposed cost function relevant to the optimal control criterion and another one dealing with square error between the master and the slave systems. The effectiveness of the designed approaches is highlighted by numerical simulation on an extensive application example of the unified disturbed nonlinear chaotic systems.

The remainder of this paper is organized as follows. In Sect. 2, the nonlinear perturbed chaotic systems and the high gain observer technique are presented. Section 3 introduces not only the proposed optimization algorithm but also an innovative cost function to synthetize the optimal high gain observer. In Sect. 4, simulation results of the proposed optimal state observer-based synchronization design techniques are provided for the unified perturbed chaotic system. Finally, some concluding remarks are given in Sect. 5.

2 High Gain Observer Design Method

After the ingenious paper of Gauthier et al. [31], which presents a high gain observer for nonlinear uniformly observable systems, the high gain observer framework has been used for several classes of nonlinear systems. In this work, we aim to involve this kind of observer for the state synchronization of nonlinear disturbed chaotic systems given by the following state representation:

$$\begin{cases} \dot{x}(t) = Ax(t) + f(x(t)) + h(s, x(t)) + dt \\ y(t) = Cx(t) \end{cases} \tag{1}$$

where $x(t) \in \mathcal{R}^n$ is the state vector, $y(t) \in \mathcal{R}^m$ is the output vector, $A \in \mathcal{R}^{n\times n}$ and $C \in \mathcal{R}^{m\times n}$ are constant matrices, $s \in \mathcal{R}^q$ is a known signal, $d(t) \in \mathcal{R}^n$ represents the external disturbance vector affecting the system, $f(.)\colon\mathcal{R}^n \to \mathcal{R}^n$ and $h(.)\colon\mathcal{R}^n \to \mathcal{R}^{p\times q}$ are nonlinear functions.

To implement the high gain observer, the chaotic system (1) should be written in the following condensed form:

$$\begin{cases} \dot{x}(t) = F(x(t))x(t) + G(s, x(t)) + d(t) \\ y(t) = Cx(t) \end{cases} \tag{2}$$

where $F(x(t)) = \begin{bmatrix} 0 & F_1(x_1) & 0 & \dots & 0 \\ 0 & 0 & F_2(x_1, x_2) & \dots & 0 \\ \vdots & \vdots & 0 & \ddots & \vdots \\ 0 & 0 & 0 & \dots & F_{n-1}(x) \\ 0 & 0 & 0 & \dots & 0 \end{bmatrix}$,

$$G(s, x(t)) = \begin{bmatrix} G_1(s, x_1) \\ G_2(s, x_2, x_1) \\ \vdots \\ G_n(s, x) \end{bmatrix} \text{ and } C = \begin{bmatrix} I_{n-1} & 0 & \dots & 0 \end{bmatrix}.$$

Consider (1) as the drive system, the response system is then expressed by the high gain observer given by the following state representation:

$$\begin{cases} \dot{\hat{x}}(t) = A\hat{x}(t) + f(\hat{x}(t)) + h(s, \hat{x}(t)) - \theta\Lambda^+(\hat{x}(t))\Delta_\theta^{-1}S^{-1}C^T(C\hat{x}(t) - y(t)) \\ \hat{y}(t) = C\hat{x}(t) \end{cases} \tag{3}$$

where θ is the observer regulating parameter, which is a strictly positive real number, and S is the unique solution of the algebraic Lyapunov equation given by

$$S + \mathcal{A}^T S + S\mathcal{A} - C^T C = 0 \tag{4}$$

with $\mathcal{A}$ the anti-shift matrix and C is the system output matrix expressed respectively as follows

$$\mathcal{A} = \begin{bmatrix} 0 & 1 & \dots & 0 \\ 0 & 0 & \ddots & \vdots \\ \vdots & \vdots & \ddots & 1 \\ 0 & 0 & \dots & 0 \end{bmatrix} \text{ and } C = \begin{bmatrix} 1 & 0 & \dots & 0 \end{bmatrix}.$$

The matrix Δ_θ, characterizing the high gain observer (3), is given by

$$\Delta_\theta = diag\left[\begin{array}{cccc} 1 & 1/\theta & \ldots & 1/\theta^{n-1} \end{array}\right]. \tag{5}$$

The matrix $\Lambda(\hat{x}\,(t))$, used in the state observer Eq. (3), is expressed in the following form:

$$\Delta(\hat{x}(t)) = \begin{bmatrix} I_{n-1} & 0 & \ldots & 0 \\ 0 & F_1\left(\hat{x}_1(t)\right) & \ldots & 0 \\ \vdots & 0 & \ddots & \vdots \\ 0 & 0 & \ldots & \prod_{i=1}^{p-1} F_i(\hat{x}(t)) \end{bmatrix}.$$

It is important to note that $S^{-1}C^{\mathrm{T}}$ can be expressed by

$$S^{-1}C = \left[\begin{array}{cccc} C_q^1 I_p & C_q^2 I_p & \ldots & C_q^q I_p \end{array}\right]^T \text{ with } C_n^p = \frac{n!}{p!(n-p)!}.$$

It is evident that to attain the minimum estimation error, the setting parameter θ has to be optimized. In the next section, an optimization algorithm for the optimal high gain observer synthesis is propounded.

3 High Gain Observer Optimization Approach

This section deals with the nonlinear high gain observer optimization, and more precisely, the optimization of a quadratic criterion in order to calculate the optimal observation gain.

Since 1980s, metaheuristic techniques appeared with a common intention to solve the most difficult optimization problems [32, 33]. These algorithms are iterative optimization methods designed to find decent solutions for difficult optimization problems for which no more adequate deterministic method is available and the direct search for the best solution could demand an excessive computation time. In the literature, numerous metaheuristic methods have been designed, others are in the procedure of being introduced. A state of the art for this topic, presenting a good number of variants and hybridizations between methods, is presented in [34].

In this paper, it is obvious that the choice of the setting parameter θ is very important for improving the efficiency of the high gain state observer and more exactly for the convergence of the observation error. The choice of this parameter is accomplished so far in a practical form.

In what follows, we propose a new approach to optimize the parameter θ by using a quadratic criterion achieving a compromise between the performances of the state observer and its observation gain.

3.1 Proposed High Gain Optimization Criterion

It should be noted that the research for the minimal observation error amounts to the research for an optimal parameter θ_{opt}. As a matter of fact, to search θ_{opt}, it is proposed to minimize the following quadratic criterion:

$$J = \int_0^\infty \left(e^T(t)Qe(t) + v^T(t)Rv(t)\right)dt \tag{6}$$

where $v(t) = \theta\Lambda^+(\hat{x}(t))\Delta_\theta^{-1}S^{-1}C^TC(x(t) - \hat{x}(t))$ reflects the correction term of the high gain observer, Q is a non-negative symmetric matrix and R is a positive definite symmetric matrix of appropriate dimensions.

It is worth noting that the quadratic criterion (6) realizes a compromise between the performances described by the term $\int_0^\infty e^T(t)Qe(t)dt$ and the energy of observation expressed by the term $\int_0^\infty v^T(t)Rv(t)dt$, i.e., to pursue a minimal observation error with an optimum observation gain encompassed by the calculation of (t), allowing the observed state vector to track the real one with a suitable and sufficient energy.

This optimization criterion can be presented as follows

$$J = \int_0^\infty e^T(t)F_Ke(t)dt \tag{7}$$

with $F_K = Q + C^TK^TRKC$ and $K = -\theta\Lambda^+(\hat{x}(t))\Delta_\theta^{-1}S^{-1}C^T$ the observation gain.

3.2 Numerical Optimization Design Method

In order to optimize the quadratic criterion J, given by Eq. (6), it is necessary to calculate first, for all $(i = 1, \ldots,)$, the corresponding value of the proposed criterion, and second to search its minimal value among all the obtained values. Therefore, we have to look through all the admissible values of θ the sign of $\frac{dJ}{d\theta} < 0$ until it changes.

For the calculation of the gradient of J, we consider the approximation given by

$$\frac{dJ}{d\theta} = \frac{J(\theta_{i+1}) - J(\theta_i)}{\theta_{i+1} - \theta_i}. \tag{8}$$

The convergence of the gradient is illustrated by the following condition:

$$\frac{dJ}{d\theta} < 0. \tag{9}$$

Furthermore, by browsing all the permissible values of θ_i in a defined interval and with a selected incrementing step, we consider that $\theta_{i+1} - \theta_i > 0$. Hence, selecting $\frac{dJ}{d\theta} < 0$ is conditioned by

$$J(\theta_{i+1}) - J(\theta_i) < 0. \tag{10}$$

As a matter of fact, the calculation of (θ_i) and (θ_{i+1}) and the test of (10) are performed by an innovative optimization algorithm highlighted hereafter.

3.3 Proposed Optimization Algorithm

To validate the above-mentioned steps regarding the synthesis of the nonlinear state observer with optimal gain, we propose a novel algorithm, which aims to search the global extremum of the defined cost function.

Therefore, the developed algorithm serves to determine the value of θ_{opt} for the synthesis of the optimal high gain observer. The principle of this optimization method, based on the "For" loop for global extremum search, is described by the following algorithm:

Data: The systems described by Eqs. (2) and (3);

Results: Calculation of θ_{opt} and J_{opt}.

1	Begin
2	Initialization of the studied system and its observer; Initialization of the initial and final value of the parameter to be optimized: θ_i and θ_f; The initial solution θ_0, J_0 considered temporarily as the optimal solution θ_{opt}, J_{opt};
3	For θ from θi to θ_f with steps of k do
4	Determination of the state vector of the system and that of the observer;
5	Calculation of the observation error $e(t)$ and the correction term $v(t)$;
6	Calculation of the term inside the integral J given by equation (6);
7	Calculation of the integral J;
8	If $J < J_{\text{opt}}$ then $\theta_{\text{opt}} = \theta$ $J_{\text{opt}} = J$ End End
9	Displays of θ_{opt} and J_{opt};
10	End

The validation of this algorithm is demonstrated by numerical simulation dealing with the state synchronization of an application example of nonlinear perturbed chaotic system.

4 Numerical Simulation

To demonstrate the effectiveness of the proposed optimal high gain observer for the synchronization of nonlinear perturbed chaotic systems, let us consider the unified chaotic systems illustrated by the following state equations [35, 36]:

$$\begin{cases} \dot{x}_1(t) = (25\alpha + 10)\left(x_2 - x_1\right) + d_1(t) \\ \dot{x}_2(t) = (28 - 35\alpha)x_1 - x_1x_3 + (29\alpha - 1)x_2 + d_2(t) \\ \dot{x}_3(t) = x_1x_2 - \left(\dfrac{\alpha + 8}{3}\right)x_3 + d_3(t) \end{cases} \tag{11}$$

It is worth pointing out that system (11) is considered as the Lorenz system if $0 \leq \alpha < 0.8$. Besides, it suits to the original Chen system for $\alpha = 0.8$. Nevertheless, for $0.8 < \alpha \leq 1$ this system is considered as the Lü system.

Additionally, the exogenous disturbances inherent on such a system are specified by $d_1(t) = 0.28\cos(3t)$, $d_2(t) = 0.19\cos(4t)$ and $d_3(t) = 0.34\cos(5t)$.

Figures 1, 2 and 3 describe the attractor evolution of the unified chaotic systems with several values of α to demonstrate their chaotic behaviors.

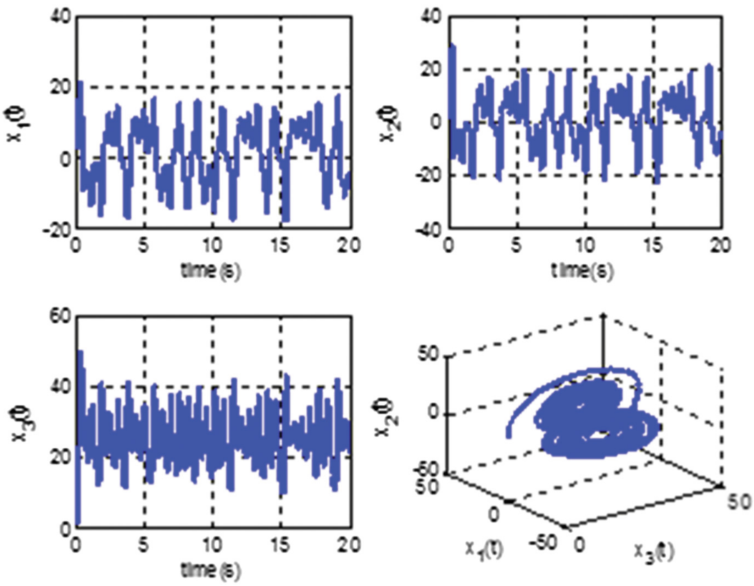

Fig. 1. Lorenz system state variables and their attractor for $\boldsymbol{\alpha} = \mathbf{0.1}$.

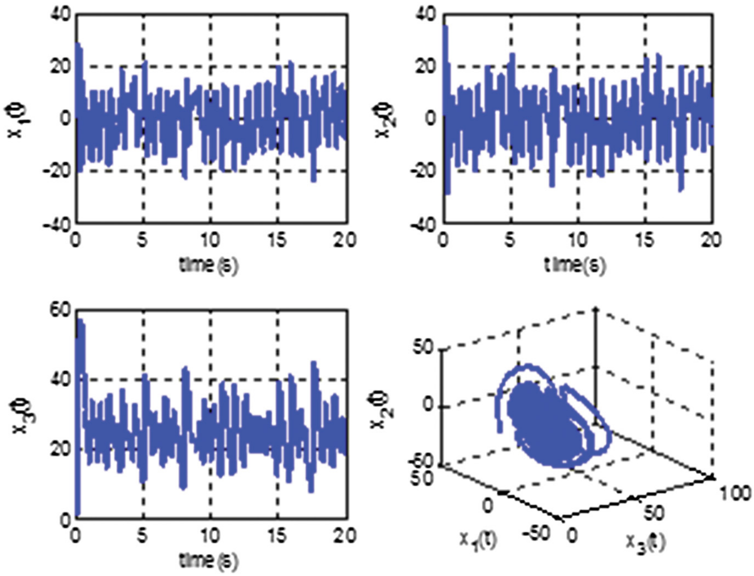

Fig. 2. Chen system state variables and their attractor for $\boldsymbol{\alpha} = \mathbf{0.8}$.

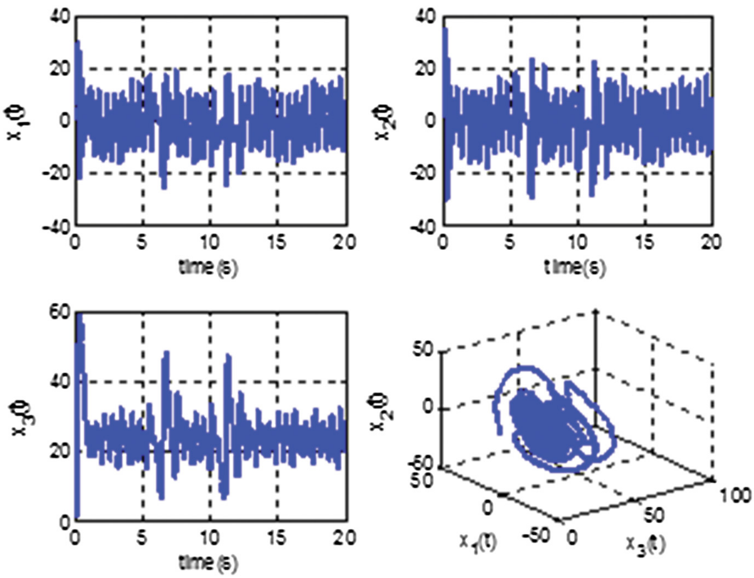

Fig. 3. Lü system state variables and their attractor for $\boldsymbol{\alpha} = \mathbf{1}$

It should be noted that the choice of the cost function must be accomplished carefully because it highly affects the state observer performance. Therefore, to compare the proposed optimization approach, we consider in the simulation study the quadratic criterion whose cost function is expressed by [37]

$$J = \int_0^T \left(\left(e_1(t)\right)^2 + \left(e_2(t)\right)^2 + \left(e_3(t)\right)^2 \right) dt \tag{12}$$

where $e_1(t) = \hat{x}_1(t) - x_1(t)$, $e_2(t) = \hat{x}_2(t) - x_2(t)$, $e_3(t) = \hat{x}_3(t) - x_3(t)$ are the observation errors between the high gain observer (3), with $n = 3$, and the unified chaotic systems (11). T is the simulation final time.

The most important part of this algorithm is the way that the cost function is defined. The cost function must be defined in a way that its minimization ensures the state observation of the system. Thus, it can be a positive semi definite function so it is adopted, in this case, the square of the error vector norm.

As a summary, the two proposed cost functions has the following properties:

- They can be calculated while the system is running;
- As the system tends to converge, the integration interval becomes smaller until it reaches some minimum length. This prevents chattering of response of system while its average remains constant near zero. The minimum interval length must be considered to allow the controller to influence the system behavior. As a result, the proposed algorithm will be able to analyze the effectiveness of the state observer.

Nevertheless, the minimization of the criterion J with respect to θ is analytically very difficult to achieve. To overcome this problem, we propose an iterative numerical approach to calculate the cost function J and to provide the parameter θ_{opt}.

To highlight the performances of the developed synchronization scheme relying on the optimal high gain observer, the initial conditions are fixed for the transmitter and the receiver as follows $x(0) = [1\ 1\ 0]$ and $\hat{x}(0) = [-0.25\ 0.25\ -5]$.

The simulation study of the designed optimization method for the design of the nonlinear optimal high gain observer, in the case where $\alpha = 0$, $\theta \in \{1, \ldots, 10\}$ and a step of $\varepsilon = 0.01$, enables calculating the global extremum of J for the two before-mentioned methods.

It is worth pointing out that the cost function (6) is illustrated in the numerical simulation by J_1, whereas the cost function characterized by (12) is illustrated by J_2 as shown in Table 1.

Owing to these results, the optimal values corresponds to $\theta_{\text{opt1}} = 3.5$ for the global minimum $J_{\text{opt1}} = 2.2478124e{+}3$ using the first cost function and $\theta_{\text{opt2}} = 3.51$ for $J_{\text{opt2}} = 3.362415218066241e{+}1$ using the second one.

Moreover, a comparison amongst the transmitter and the receiver state variables is highlighted in Figs. 4, 5 and 6, which specified the state variables $x_1(t)$, $x_2(t)$, $x_3(t)$ and their observed states related to the classic high gain observer with two arbitrarily cases of θ ($\theta = 1.1$ and $\theta = 5$), and the two distant optimal observers with $\theta_{\text{opt1}} = 3.5$ and $\theta_{\text{opt2}} = 3.51$.

Table 1. Values of the first and the second cost functions according to different $\boldsymbol{\theta}$-values related to the perturbed unified chaotic system.

θ	J_1	J_2
1	$4.4855297e^{+3}$	$7.577504021427615e^{+2}$
2	$7.6621877e^{+3}$	$4.469155184288474e^{+2}$
3	$2.4415966e^{+3}$	$4.848758400266978e^{+1}$
3.4	$2.4862039e^{+3}$	$3.779298238702135e^{+1}$
3.5	$\mathbf{2.2478124e^{+3}}$	$3.379379645232096e^{+1}$
3.51	$2.2512412e^{+3}$	$\mathbf{3.362415218066241e^{+1}}$
3.6	$4.5424828e^{+3}$	$5.2503468779104e^{+1}$
4	$156.3349796e^{+3}$	$3.707143853913085e^{+3}$
5	$28630.0455254e^{+3}$	$1.491342902435575e^{+4}$
7	$2160290.035445e^{+3}$	$2.065152629345135e^{+5}$
8	$28430.4026805e^{+3}$	$2.071352042070496e^{+6}$
9	$35394972.7125344e^{+3}$	$1.041385390053656e^{+6}$
10	$115257.2757344e^{+3}$	$9.066137482070914e^{+6}$

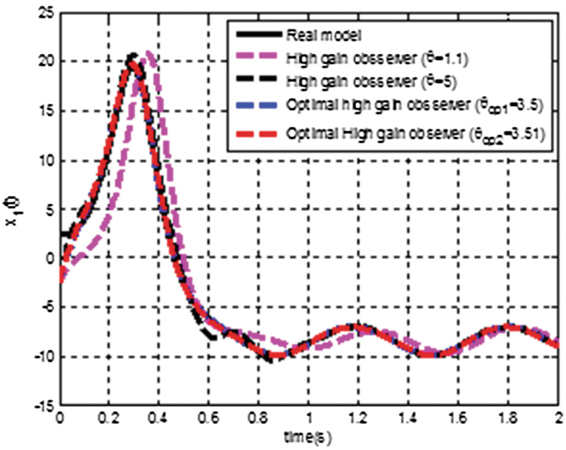

Fig. 4. Evolution of $\boldsymbol{x}_1(\boldsymbol{t})$ and their observed states for $\boldsymbol{\theta} = \mathbf{1.1}$, $\boldsymbol{\theta}$=, $\boldsymbol{\theta}_{\text{opt1}} = \mathbf{3.5}$ and $\boldsymbol{\theta}_{\text{opt1}} = \mathbf{3.51}$.

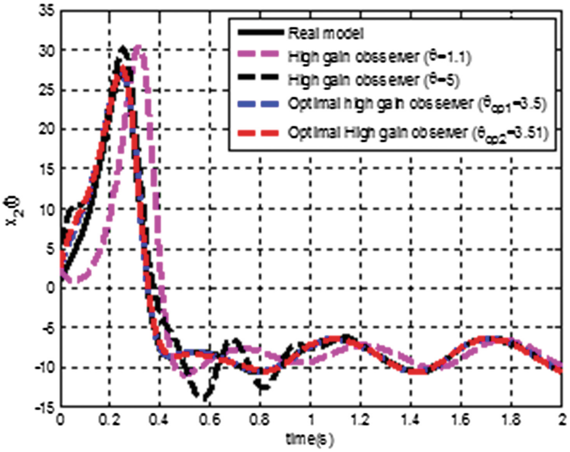

Fig. 5. Evolution of $\boldsymbol{x}_2(\boldsymbol{t})$ and their observed states for $\boldsymbol{\theta} = \mathbf{1.1}$, $\boldsymbol{\theta}$=, $\boldsymbol{\theta}_{\text{opt1}} = \mathbf{3.5}$ and $\boldsymbol{\theta}_{\text{opt1}} = \mathbf{3.51}$.

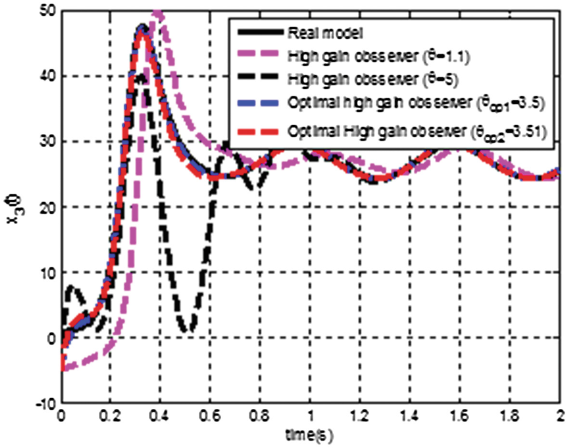

Fig. 6. Evolution of $\boldsymbol{x}_3(\boldsymbol{t})$ and their observed states for $\boldsymbol{\theta} = \mathbf{1.1}$, $\boldsymbol{\theta} = \mathbf{5}$, $\boldsymbol{\theta}_{\text{opt1}} = \mathbf{3.5}$ and $\boldsymbol{\theta}_{\text{opt1}} = \mathbf{3.51}$.

As a result, the performances of the optimal high gain observers are very compelling compared to those obtained by the classic observer for the three states variables.

Additionally, it is clearly seen that the first optimal high gain observer using the proposed cost function with θ_{opt1} converges more rapidly than the second one with θ_{opt2} to cover all the state variables of the transmitter.

5 Conclusion

In this paper, an innovative optimal high gain observer technique has been elaborated to improve the state synchronization performances of nonlinear disturbed chaotic systems. The necessary optimal value of the high gain observer setting parameter θ has been computed using an outstanding proposed optimization technique. The challenging feature of this approach lies in the realization of a compromise between the observation gain and the observation error of the studied observer by using a proposed quadratic optimization criterion. Moreover, a second cost function, dealing with square errors between the master and the slave systems, has been exhibited to improve the state synchronization quality.

The performances of the developed optimization strategies for the state synchronization of the nonlinear perturbed unified chaotic system application example have been demonstrated through numerical simulations. Owing to the simulation results, it has been proven that the designed approaches are highly trustworthy since they have enabled a convincing robust convergence of the optimal high gain observer towards the real states compared to the standard high gain observer despite the presence of significant external disturbances inherent on the nonlinear unified chaotic systems.

References

1. Pecora, L.M., Carroll, T.L.: Synchronization in chaotic systems. Phys. Rev. Lett. **64**(8), 21–24 (1990)
2. Carroll, T.L., Pecora, L.M.: Synchronizing chaotic circuits. IEEE Trans. Circuits Syst. **38**(4), 453–456 (1991)
3. Murali, K., Lakshmanan, M.: Secure communication using a compound signal from generalized synchronizable chaotic systems. Phys. Lett. A **241**(6), 303–310 (1998)
4. Aguilar-Lopez, R., Martinez-Guerra, R., Perez-Pinacho, C.A.: Nonlinear observer for synchronization of chaotic systems with application to secure data transmission. Eur. Phys. J. Spec. Top. **223**(8), 1541–1548 (2014)
5. Yavuz, E., Yazici, R., Kasapbasi, M.C., Yamac, E.: A chaos-based image encryption algorithm with simple logical functions. Comput. Electr. Eng. **54**, 471–483 (2016)
6. Martinez-Guerra, R., Perez-Pinacho, C.A., Gomez-Cortes, G.C., Cruz-Victoria, J.C., Mata-Machuca, J.L.: Experimental Synchronization by means of observers. J. Appl. Res. Technol. **12**(1), 52–62 (2014)
7. Loria, A., Panteley, E., Zavala, A.: Adaptive observers for robust synchronization of chaotic systems. IEEE Trans. Circuits Syst. Part 1 Fundam. Theory Appl. **56**(12), 2703–2716 (2009)
8. Wang, T., Jia, N.: Chaos control and hybrid projective synchronization of several new chaotic systems. Appl. Math. Comput. **218**(13), 7231–7240 (2012)
9. Ghamati, M., Balochian, S.: Design of adaptive sliding mode control for synchronization Genesio–Tesi chaotic system. Chaos, Solitons Fractals **75**, 111–117 (2015)
10. Ansteit, F., Millerioux, G., Bloch, G.: Polytopic observer design for LPV systems based on minimal convex polytope finding. J. Algorithms Comput. Technol. **3**(1), 23–43 (2009)
11. Han, X., Chang, X.: A chaotic digital secure communication based on a modified gravitational search algorithm filte. Inf. Sci. **208**, 14–27 (2012)
12. Morgül, O., Solak, E.: Observer based synchronization of chaotic systems. Phys. Rev. E **54**(5), 4803–4811 (1996)
13. Nijmeijer, H., Mareels, I.: An observer looks at synchronization. IEEE Trans. Circuit and Syst. **44**(10), 882–890 (1997)
14. Zhu, F.: Full-order and reduced-order observer-based synchronization for chaotic systems with unknown disturbances and parameters. Phys. Lett. A **372**(3), 223–232 (2008)

15. Shahnazi, R., Haghani, A., Jeinsch, T.: Adaptive fuzzy observer-based stabilization of a class of uncertain time-delayed chaotic systems with actuator nonlinearities. Chaos, Solitons Fractals **76**, 98–110 (2015)
16. Bowong, S., Kakmeni, F.M., Fotsin, H.: A new adaptive observer-based synchronization scheme for private communication. Phys. Lett. A **355**(3), 193–201 (2006)
17. Chen, F., Zhang, W.: LMI criteria for robust chaos synchronization of a class of chaotic systems. Nonlinear Anal. Theory Methods Appl. A **67**(12), 3384–3393 (2007)
18. Okamoto, T., Hirata, H.: SConstrained optimization using a multipoint type chaotic Lagrangian method with a coupling structure. Eng. Optim. **45**(3), 311–336 (2013)
19. Chaio-Shiung, C.: Optimal nonlinear observers for chaotic synchronization with message embedded. Nonlinear Dyn. **61**(4), 623–632 (2010)
20. Chaio-Shiung, C.: Chaotic secure communication with quadratic optimal performance via LMI-based observer design. Int. J. Bifurcat. Chaos **20**(10), 3311–3322 (2010)
21. Shirazi, M.J., Vatankhah, R., Boroushaki, M., Salarieh, H., Alasty, A.: Application of particle swarm optimization in chaos synchronization in noisy environment in presence of unknown parameter uncertainty. Commun. Nonlinear Sci. Numer. Simul. **17**(2), 742–753 (2012)
22. Kim, J., Jin, M.: Synchronization of chaotic systems using particle swarm optimization and time-delay estimation. Nonlinear Dyn. **86**(3), 2003–2015 (2016)
23. Outanoute, M., Lachhab, A., Ed-Dahhak, A., Guerbaoui, M., Selmani, A., Bouchikhi, B.: Synthesis of an optimal dynamic regulator based on linear quadratic Gaussian (LQG) for the control of the relative humidity under experimental greenhouse. Int. J. Electr. Comput. Eng. **6**(5), 2262–2273 (2016)
24. Tsai, J.S.H., Wu, C.Y., Lee, C.H., Guo, S.M., Su, T.J.: A new optimal linear quadratic observer-based tracker under input constraint for the unknown system with a direct feed-through term. Optim. Control Appl. Methods **37**(1), 34–71 (2016)
25. Marcelo, M., Bernard, O.: Robust interval observers for global Lipschitz uncertain chaotic systems. Syst. Control Lett. **59**(11), 687–694 (2010)
26. Ma, J., Zhang, A.H., Xia, Y.F., Zhang, L.P.: Optimize design of adaptive synchronization controllers and parameter observers in different hyperchaotic systems. Appl. Math. Comput. **215**(9), 3318–3326 (2010)
27. Tang, K.S., Man, K.F., Kwong, S., He, Q.: Genetic algorithms and their applications. IEEE Signal Process. Mag. **13**, 22–37 (1996)
28. Dorigo, M., Maniezzo, V., Colorni, A.: The ant system: optimization by a colony of cooperating agents. IEEE Syst. Man Cybern. Soc. **26**, 29–41 (1996)
29. Han, X., Chang, X.: Chaotic secure communication based on a gravitational search algorithm filter. Eng. Appl. Artif. Intell. **25**(4), 766–774 (2012)
30. Kennedy, J., Eberhart, R.: Particle swarm optimization. Proc. IEEE Int. Conf. Neural Netw. **4**, 1942–1948 (1995)
31. Gauthier, J., Hammouri, H., Othman, S.: A simple observer for nonlinear systems: application to bioreactors. Trans. Automat. Contr. **37**(6), 875–880 (1992)
32. Boussaïd, I., Lepagnot, J., Siarry, P.: A survey on optimization metaheuristics. Inf. Sci. **237**, 82–117 (2013)
33. Cerny, V.: Thermodynamical approach to the traveling salesman problem: an efficient simulation algorithm. J. Optim. Theory Appl. **45**, 41–51 (1985)
34. Bowong, S.: Stability analysis for the synchronization of chaotic systems with different order: application to secure communications. Phys. Lett. A **326**, 102–113 (2004)
35. Xu, F., Yu, P.: Chaos control and chaos synchronization for multi-scroll chaotic attractors generated using hyperbolic functions. J. Math. Anal. Appl. **362**, 252–274 (2010)

36. Qiang, J.: Hyperchaos generated from the Lorenz chaotic system and its control. Phys. Lett. A **366**(3), 217–222 (2007)
37. Shirazi, M.J., Vatankhah, R., Boroushaki, M., Salarieh, H., Alasty, A.: Application of particle swarm optimization in chaos synchronization in noisy environment in presence of unknown parameter uncertainty. Commun. Nonlinear Sci. Numer. Simul. **17**(2), 742–753 (2012)

An Adaptive Fuzzy Predictive Control Based on Support Vector Regression

I. Boulkaibet[1(✉)], S. Bououden[2], T. Marwala[1], B. Twala[1], and A. Ali[1]

[1] Institute for Intelligent Systems, University of Johannesburg, Johannesburg, South Africa
ilyes@aims.ac.za
[2] Faculty of Sciences and Technology, University Abbes Laghrour, Khenchela, Algeria
sofiane.bououden@univ-khenchela.dz

Abstract. In this paper, an adaptive fuzzy Generalized Predictive Control (GPC) is proposed for nonlinear systems via Takagi-Sugeno system based Support Vector Regression (TS-SVR). The adaptive T-S fuzzy model is created using a support vector regression while the online learning procedure is obtained in two steps: first, the antecedent parameters of the TS-SVR are initialized using a k-means clustering and then iteratively adjusted using a back-propagation algorithm. Next, a sequential minimal optimization (SMO) algorithm is used to obtain the consequent parameters. Furthermore, the new TS fuzzy model is integrated into the GPC in order to control nonlinear systems. The performance of the proposed adaptive TS-SVR GPC controller is investigated by controlling the continuous stirred tank reactor (CSTR) system. The proposed TS-SVR GPChas shown good performance and efficiently controlled the nonlinear plant.

Keywords: Generalized predictive control · Takagi-Sugeno fuzzy system
Support vector regression · k-means clustering
Sequential minimal optimization

1 Introduction

1.1 General Information

The Generalized Predictive Control (GPC), which has been proposed by Clark et al. [1], is considered as one of the most effective control strategies. The main advantage of this method is that a polynomial model is used for the system predictions. Thus, the number of parameters required by the controller is then limited which will eventually simplify the application of GPC [2]. The GPC has been widely applied to control industrial plants, and offered good results in dealing with unstable systems. Unfortunately, the algorithm of the GPC method is based on the quadratic optimization where this optimization can only be solved for linear models. Besides, the linear models used by the GPC, to perform system predictions, are assumed to be accurate, and this assumption cannot be true in real life applications [3]. Many researchers have tried to develop a nonlinear version of the GPC (NGPC) to deal with the nonlinearity (or the absence of the mathematical models) of the systems during the controlling process.

M. Chadli et al. (Eds.): ICEECA 2017, LNEE 522, pp. 182–197, 2019.
https://doi.org/10.1007/978-3-319-97816-1_14

The most common strategy used by many experts was to linearize the mathematical models of the plants. Despite that this technique is very simple, yet a poor performance of the controller is likely to be expected since the operating points of the systems may change over time.

Lately, the application of universal approximation methods such a: Fuzzy Logic [4–6] and Neural Networks (NNs) [7] have been widely used to model nonlinear systems. These methods can be used to obtain relatively simple mathematical models to describe the dynamic responses of the original nonlinear systems [8, 9]. Usually, the Takagi-Sugeno (TS) [10] fuzzy model has been considered as one of the effective universal approximators for nonlinear systems, and has the ability to accurately describe the relation between the inputs and the outputs of a complex system via experimental data and prior knowledge of the system [11]. The TS fuzzy model was integrated many times into GPC, and the fuzzy GPC method has been applied numerous times and reported decent results in term of stability and robustness [11, 12].

Recently, the application of kernel regression methods, such as the Support vector regression (SVR) [13–16], has been increased in system identification [17–20]. These methods can also be integrated within the fuzzy reasoning to model systems based on sampled data [21–24]. Juang et al. [22, 25] proposed a new offline training of a TS fuzzy model using a SVR. In this approach, the consequent parameters were obtained using a SVR while the antecedent parameters were attained by a simple clustering algorithm. Unfortunately, complex kernel functions were used to obtain the consequent parameters which complicates the training process. Also, the presence of the bias term in the SVR model makes it difficult to propose an online identification based on the SVR.

Motivated by Juang et al. [22, 25] work, Boulkaibet et al. [23, 24] have proposed an adaptive fuzzy predictive control for nonlinear systems based on kernel regression methods. In this paper, an adaptive fuzzy predictive control for nonlinear systems is introduced based on Support vector Regression (TS-SVR) where the online training procedure of the consequent parameters is achieved by a sequential minimal optimization (SMO) algorithm. Furthermore, the antecedent parameters are initialized and updated using k-means and back propagation algorithms, respectively. Finally, the TS-SVR is integrated into the GPC to create an adaptive TS-SVR GPC where this controller was used to control a continuous stirred tank reactor (CSTR) system.

2 The Takagi-Sugeno Fuzzy System Based Support Vector Regression (TS-SVR)

In this section, the structure of the TS-SVR is presented where the proposed TS system is based on the famous if-then Takagi-Sugeno fuzzy rules. The *i*-th rule of the proposed TS model [10] is described by:

$$\begin{aligned} R_i : \quad & \text{IF } x_1(k) \textit{ is } A_1^i \ldots \textit{ and } x_n(k) \textit{ is } A_n^i \\ & \text{THEN } y_i(k) = \theta_0^i + \theta_1^i x_1(k) + \ldots + \theta_n^i x_n(k) \\ & i = 1, \ldots, N_r \end{aligned} \tag{1}$$

where $R_i, i = 1, 2, \ldots, N_r$ are the i-th rule, N_r is number of rules, $x_1(k), \ldots, x_n(k)$ are input variables, k is the time increment, $y_i(k)$ is the system output of the i-th rule and $A^i_j, i = 1, 2, \ldots, N_r, j = 1, 2, \ldots, n$ are the linguistic terms which are characterized by the fuzzy membership functions $\mu_{A^i_j}(x_j)$, $i = 1, 2, \ldots, N_r$, $j = 1, 2, \ldots, n$. Figure 1 illustrates the main structure of the proposed TS-SVR which is divided in the five layers.

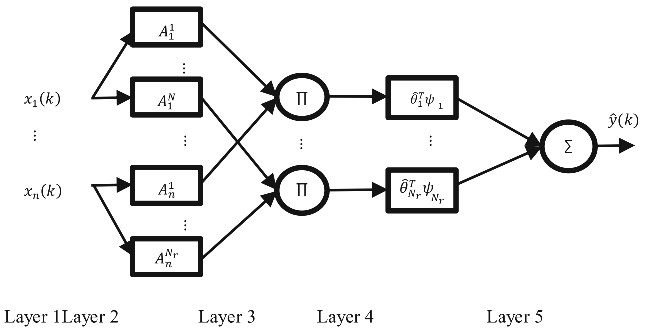

Fig. 1. The structure of the TS-LSSVR system

In this fuzzy system, the input vector of the fuzzy model represents the first layer. The input signal is transmitted to the second layer (also known as the fuzzification). Note that, each linguistic term A^i_j is defined by a membership function $\mu_{A^i_j}(x_j)$, and this function defines the value of the j-th input that satisfies the quantity A^i_j. Next, the product of all arrived input signals are computed in the third layer. The resulted signal of node i in the third layer characterizes the firing strength function $\mu_i(\boldsymbol{x})$. Then, the consequence values of each node i, $i = 1, 2, \ldots, N_r$ are computed in the fourth layer where the output of each node i, in layer 4, is computed as $\hat{\boldsymbol{\theta}}_i\psi_i$. Note that, ψ_i is the firing strength of node i multiplied by an augmented input vector $\dot{\boldsymbol{x}}(k) = (1, \boldsymbol{x}(k)) = (1, x_1(k), \ldots, x_n(k))^T$ (of the size $n+1$). $\hat{\boldsymbol{\theta}}_i = \left(\theta^i_0, \ldots, \theta^i_n\right)$ is the consequent parameters of node i. Finally, the defuzzification is performed in the fifth layer where the summation of all incoming signals from layer 4 represents the output $\hat{y}(k)$ of the TS fuzzy model. It is clear that the defuzzification procedure employed in the TS-SVR does not have any normalization procedure.

The Gaussian function is used to define the membership functions of the system:

$$\mu_{A^i_j}(x_j) = exp\left\{-\frac{\left(x_j - m_{ij}\right)^2}{2\sigma^2_{ij}}\right\}, i = 1, \ldots, N_r \; and \; j = 1, \ldots, n \tag{2}$$

where m_{ij} and σ_{ij} are the center and the standard deviation of the membership function, respectively. The firing strength of each node in the third layer are given as:

$$\mu_i(\boldsymbol{x}) = \prod_{j=1}^{n} \mu_{A_j^i}(x_j) = exp\left\{-\sum_{j=1}^{n} \frac{\left(x_j - m_{ij}\right)^2}{2\sigma_{ij}^2}\right\}, i = 1, \ldots, N_r \tag{3}$$

The functions ψ_i are given by: $\psi_i = \dot{\boldsymbol{x}}(k).\mu_i(\boldsymbol{x}), i = 1, 2, \ldots, N_r$. Finally the output of the fuzzy system, is given as:

$$\begin{aligned}\hat{y}(k) &= \sum_{i=1}^{N_r} \left(\hat{\boldsymbol{\theta}}_i^T \,\dot{\boldsymbol{x}}(k)\right).\mu_i(\boldsymbol{x}) \\ &= \sum_{i=1}^{N_r} \left(\hat{\theta}_0^i + \hat{\theta}_1^i x_1(k) + \cdots + \hat{\theta}_n^i x_n(k)\right).exp\left\{-\sum_{j=1}^{n} \left(\frac{\left(x_j - m_{ij}\right)^2}{2\sigma_{ij}^2}\right)\right\}\end{aligned} \tag{4}$$

In the next two sections, the procedure of identifying the consequent and the antecedent parameters of the TS-SVR are discussed in details.

3 Consequent Parameters of the Takagi-Sugeno Fuzzy System Based Support Vector Regression

In this section, the SVR is briefly discussed, and then this approach will be used to define the TS fuzzy system.

3.1 Support Vector Regression

Based on the concepts of kernel machine, the main idea of support vector regression (SVR) [16–18] is to implement a linear regression in high-dimensional feature space $\mathcal{Z}$ (Hilbert space), which is equivalent to a nonlinear regression in the original input space $\mathbb{R}^n$. Note that, the input space is mapped into a feature space $\mathcal{Z}$ with a nonlinear mapping function $\boldsymbol{\varphi}$. The SVR solution, using an ϵ-insensitive loss function, is given by the following optimization problem:

$$\max_{\boldsymbol{\alpha},\boldsymbol{\alpha}^*} \mathcal{W}(\boldsymbol{\alpha}, \boldsymbol{\alpha}^*) = \max_{\boldsymbol{\alpha},\boldsymbol{\alpha}^*} \left(-\frac{1}{2}\sum_{i=1}^{N_d}\sum_{j=1}^{N_d} \left(\alpha_i - \alpha_i^*\right)\left(\alpha_j - \alpha_j^*\right)\kappa\left(\boldsymbol{x}_i, \boldsymbol{x}_j\right) + \sum_{i=1}^{N_d} \left(\alpha_i(y_i - \varepsilon) - \alpha_i^*(y_i + \varepsilon)\right)\right) \tag{5}$$

Subject to the constraints (Karush-Kuhn-Tucker (KKT) conditions):

$$\begin{cases} 0 \leq \alpha_i, \alpha_i^* \leq C & i = 1, \ldots, N_d \\ \sum_{i=1}^{N_d} \left(\alpha_i - \alpha_i^*\right) = 0 & \end{cases} \tag{6}$$

where ε prescribes the insensitivity zone, C is a constant and α_i, α_i^* are the Lagrange multipliers. This optimization will be solved using a quadratic programming (QP), and the regression solution is given by:

$$\hat{y}(k) = \sum\nolimits_{i=1}^{N_d} \left(\alpha_i - \alpha_i^*\right) \kappa(\boldsymbol{x}, \boldsymbol{x}_i) + b \tag{7}$$

where $b \in \mathbb{R}$ is the bias and $\kappa(\boldsymbol{x}, \boldsymbol{x}_i), i = 1, \ldots, N_d$ represents a Kernel function that satisfies Mercer's theorem [26] (which is given in Theorem 1), and $\kappa(\boldsymbol{x}, \boldsymbol{x}_i) = \langle \boldsymbol{\varphi}(\boldsymbol{x}), \boldsymbol{\varphi}(\boldsymbol{x}_i) \rangle = \boldsymbol{\varphi}(\boldsymbol{x})^T \boldsymbol{\varphi}(\boldsymbol{x}_i)$.

Theorem 1 (Mercer's theorem): a function $\kappa(\boldsymbol{x}, \boldsymbol{z})$ of a two vectors $\boldsymbol{x}, \boldsymbol{z} \in \mathbb{R}^n$ is a positive semi-definite kernel if and only if it satisfies Mercer's theorem [26]:

$$\sum\nolimits_{i,j=1}^{N_d} \delta_i \delta_j \kappa\left(\boldsymbol{x}_i, \boldsymbol{x}_j\right) \geq 0 \tag{8}$$

$\forall \delta_i, \delta_j \in \mathbb{R}$, $\forall \boldsymbol{x}_i, \boldsymbol{x}_j \in \mathbb{R}^n$, $i.j = 1, \ldots, N_d$, and N_d represents the size of the training data. If the quantity presented in Eq. (8) is only equal to zero for $\delta_i, \delta_j = 0, i.j = 1, \ldots, N_d$, then $\kappa(\boldsymbol{x}, \boldsymbol{z})$ is called strictly positive kernel (also known as strictly positive kernel).

The optimization problem represented by Eqs. (5) and (6) can be further simplified by choosing a strictly positive kernel. The theorem presented by Poggio et al. [27] will eventually help in simplifying the SVR solution:

Theorem 2: if a kernel function $\kappa(\boldsymbol{x}, \boldsymbol{z})$ provides an implicit bias, then the bias term b in Eq. (7) can be omitted [27].

According to Theorem 2 [27–30], the bias term can be neglected ($b = 0$) if the kernel function used by the SVR provides an implicit bias, which is exactly the case of the strictly positive definite kernel functions [27].

As a result, the prediction model in Eq. (7) with an explicit bias, $\hat{y}(k) = \sum\nolimits_{i=1}^{N_d} \left(\alpha_i - \alpha_i^*\right) \kappa(\boldsymbol{x}, \boldsymbol{x}_i)$, performances well where the main advantage of discarding the bias term is that a simple algorithm will be used to identify Lagrange multipliers since no additional equality constraint are needed during the optimization (the equality constraint in Eq. (6) will be vanished).

3.2 The Online Identification of Lagrange Multipliers

Generally, the data collected from the target system is limited which will eventually reduce the accuracy of the prediction made using offline approaches. In this paper, an online, adaptive, training of the SVR is implemented for identifications and control. The online algorithms are used in real-time applications where the data arrive sequentially while an instant decision has to be made in a short period of time. In this paper, the sequential minimal optimization (SMO) [31, 32] is applied to iteratively identify the Lagrange multipliers. The SMO is considered to be a popular approach and widest used to perform online training for kernel methods. This method has the ability to update Lagrange multipliers α_i, α_i^* and satisfying the constraints in Eq. (6). In this paper, the SMO is modified where only the last M data pairs are stored (as a dictionary) and used to identify the systems. In this case, M represents the size of the dictionary. This will eventually reduce the computational costs of the SMO approach in performing a single iteration. Then, the online regression model of the SVR with an explicit bias is given by:

$$\hat{y}(k) = \sum_{i=1}^{M} \left(\alpha_i - \alpha_i^*\right)\kappa(\boldsymbol{x}, \boldsymbol{x}_i) \tag{9}$$

and the updates for the Lagrange multipliers $\Delta\alpha_i, \Delta\alpha_i^*, i = 1, \ldots, M$ for an explicit bias are given by:

$$\begin{cases} \Delta\alpha_i = \mu_i \frac{\partial \mathcal{W}}{\partial \alpha_i} = -\alpha_i^* - \frac{e_k(k+i-M-1)+\varepsilon}{\kappa(\boldsymbol{x}_i, \boldsymbol{x}_i)} \\ \Delta\alpha_i^* = \mu_i \frac{\partial \mathcal{W}}{\partial \alpha_i^*} = -\alpha_i + \frac{e_k(k+i-M-1)-\varepsilon}{\kappa(\boldsymbol{x}_i, \boldsymbol{x}_i)} \end{cases} \tag{10}$$

where $\mu_i = \frac{1}{\kappa(\boldsymbol{x}_i, \boldsymbol{x}_i)}$ and e_k is the error: $e_k(k) = y(k) - \hat{y}(k)$.

Finally, the updated multipliers have to satisfy the KKT condition presented in Eq. (6). Then, the updated values are:

$$\begin{cases} \alpha_i(k+1) = min(max(\alpha_i(k) + \Delta\alpha_i, 0), C) \\ \alpha_i^*(k+1) = min\left(max\left(\alpha_i^*(k) + \Delta\alpha_i^*, 0\right), C\right) \end{cases} \tag{11}$$

3.3 Defining Consequent Parameters Using Lagrange Multipliers

Based on Boulkaibet et al. [23, 24] work, a multi-kernel function is used to perform SVR, where better predictions will be expected since the training data usually represents different operating points (different clusters and each cluster describes a fuzzy rule) [44]. The multi-kernel function is defined as:

$$\begin{aligned} \kappa(\boldsymbol{x}, \boldsymbol{z}) &= \sum_{l=1}^{N_r} \kappa_l(\boldsymbol{x}, \boldsymbol{z}) = \sum_{l=1}^{N_r} \langle \boldsymbol{\varphi}_l(\boldsymbol{x}), \boldsymbol{\varphi}_l(\boldsymbol{z}) \rangle \\ &= \sum_{l=1}^{N_r} \boldsymbol{\varphi}_l(\boldsymbol{x})^T . \boldsymbol{\varphi}_l(\boldsymbol{z}) \end{aligned} \tag{12}$$

where this kernel function is a combination of N_r kernel functions, and each kernel function is associated with one cluster (one rule). Note that, the function $\kappa(\boldsymbol{x}, \boldsymbol{z})$ in Eq. (12) is a valid kernel function and this can be easily verified using Mercer's theorem (Theorem 1). Next, an appropriate strictly positive definite kernel functions $\kappa_l(\boldsymbol{x}, \boldsymbol{z}), l = 1, \ldots, N_r$ will be used in order to simplify the SVR where the mapping functions $\boldsymbol{\varphi}_l, l = 1, \ldots, N_r$ have to be carefully selected. In this paper, and based on Boulkaibet et al. work [24], a strictly positive definite kernel function can be obtained when the input vector of the system is augmented by adding a constant. As a result, the input vector is: $\dot{\boldsymbol{x}}(k) = (1, \boldsymbol{x}(k)) = (1, x_1(k), \ldots, x_n(k))^T, \dot{\boldsymbol{x}}(k) \in \mathbb{R}^{n+1}$, and the mapping functions for the augmented input vector $\dot{\boldsymbol{x}}(k)$ are chosen such as [23, 24]:

$$\begin{aligned} \boldsymbol{\varphi}_l(\dot{\boldsymbol{x}}) &= \dot{\boldsymbol{x}}.\mu_l(\dot{\boldsymbol{x}}) = \dot{\boldsymbol{x}}.\mu_l(\boldsymbol{x}) \\ &= \dot{\boldsymbol{x}}.exp\left\{ -\sum\nolimits_{j=1}^{n} \frac{\left(x_j - m_{lj}\right)^2}{2\sigma_{lj}^2} \right\}, l = 1, \ldots, N_r \end{aligned} \tag{13}$$

with: $\boldsymbol{m}_l = (m_{1l}, \ldots, m_{nl})^T$ and $\boldsymbol{\sigma}_l = (\sigma_{1l}, \ldots, \sigma_{nl})^T$ are the centroid and width vectors of the Gaussian functions, respectively. It is clear that the Gaussian term $\mu_l(\dot{\boldsymbol{x}})$ of Eq. (13) is similar to the Gaussian term with the original input vector $\boldsymbol{x}(k)$ $(\mu_l(\dot{\boldsymbol{x}}) = \mu_l(\dot{\boldsymbol{x}}))$, which is obvious since both vectors $\boldsymbol{x}$ and $\boldsymbol{m}_l$ were augmented by adding 1, and the augmented value cancels each other. Note that, the input vector is augmented to obtain a strictly positive definite kernel functions $\kappa_l(\dot{\boldsymbol{x}}, \dot{\boldsymbol{x}}_i), l = 1, \ldots, N_r$ which indicates that the multi-kernel function defined in Eq. (12) is also a strictly positive definite kernel. This can be verified using Theorem 1.

Proof:

$$\sum_{i,j=1}^{N_d} \delta_i \delta_j \kappa(\dot{\boldsymbol{x}}_i, \dot{\boldsymbol{x}}_j)$$

$$= \sum_{i,j=1}^{N_d} \delta_i \delta_j \sum_{l=1}^{N_r} \langle \boldsymbol{\varphi}_l(\dot{\boldsymbol{x}}_i), \boldsymbol{\varphi}_l(\dot{\boldsymbol{x}}_j) \rangle = \sum_{l=1}^{N_r} \sum_{i,j=1}^{N_d} \delta_i \delta_j \langle \boldsymbol{\varphi}_l(\dot{\boldsymbol{x}}_i), \boldsymbol{\varphi}_l(\dot{\boldsymbol{x}}_j) \rangle$$

$$= \sum_{l=1}^{N_r} \langle \sum_{i=1}^{N_d} \delta_i \boldsymbol{\varphi}_l(\dot{\boldsymbol{x}}_i), \sum_{j=1}^{N_d} \delta_j \boldsymbol{\varphi}_l(\dot{\boldsymbol{x}}_j) \rangle = \sum_{l=1}^{N_r} \left\| \sum_{i=1}^{N_d} \delta_i \boldsymbol{\varphi}_l(\dot{\boldsymbol{x}}_i) \right\|^2$$

$$= \sum_{l=1}^{N_r} \left\| \left(\sum_{i=1}^{N_d} \delta_i \mu_l(\dot{\boldsymbol{x}}_i), \sum_{i=1}^{N_d} \delta_i \mu_l(\dot{\boldsymbol{x}}_i)\, x_1^i(k), \ldots, \sum_{i=1}^{N_d} \delta_i \mu_l(\dot{\boldsymbol{x}}_i)\, x_n^i(k) \right)^T \right\|^2$$

$$= \sum_{l=1}^{N_r} \left(\left(\sum_{i=1}^{N_d} \delta_i \mu_l(\dot{\boldsymbol{x}}_i) \right)^2 + \sum_{j=1}^{n} \left(\sum_{i=1}^{N_d} \delta_i \mu_l(\dot{\boldsymbol{x}}_i)\, x_j^i(k) \right)^2 \right) \geq \sum_{l=1}^{N_r} \left(\left(\sum_{i=1}^{N_d} \delta_i \mu_l(\dot{\boldsymbol{x}}_i) \right)^2 \right)$$

$$= \sum_{l=1}^{N_r} \left(\left(\sum_{i=1}^{N_d} \delta_i \mu_l(\boldsymbol{x}_i) \right)^2 \right).$$

Clearly, the quantity: $\sum_{l=1}^{N_r}\left(\left(\sum_{i=1}^{N_d}\delta_i\mu_l(\dot{\boldsymbol{x}}_i)\right)^2\right) > 0,\ \forall \boldsymbol{x}_{i,j} \in \mathbb{R}^n, \exists\delta_i \neq 0(i = 1, \ldots, N_d)$. This means that, the quantity $\sum_{l=1}^{N_r}\left(\left(\sum_{i=1}^{N_d}\delta_i\mu_l(\dot{\boldsymbol{x}}_i)\right)^2\right)$ is equal to zero only for all $\delta_i = 0, i = 1, \ldots, N_d$. Note that, the membership functions: $\mu_l(\dot{\boldsymbol{x}}) = exp\left\{-\sum_{j=1}^{n}\frac{\left(x_j - m_{lj}\right)^2}{2\sigma_{lj}^2}\right\} > 0$. This indicates that the multi-kernel function with an augmented input vector space is a strictly positive definite kernel, and the SVR without a bias term can be used to define the consequent parameters.

To define the new TS fuzzy system based on the SVR model, the multi-kernel function in Eq. (12) is used where each kernel function is associated with a fuzzy rule. Moreover, the selected multi-kernel function has to be a strictly positive definite function which allows the use of Eq. (9).

By substituting Eq. (12) into Eq. (9), we obtain:

$$\begin{aligned}
\hat{y}(k) &= \sum_{i=1}^{M}\left(\alpha_i - \alpha_i^*\right)\kappa(\dot{\boldsymbol{x}}, \dot{\boldsymbol{x}}_{\boldsymbol{i}}) = \sum_{i=1}^{M}\left(\alpha_i - \alpha_i^*\right).\left(\sum_{l=1}^{N_r}\kappa_l(\dot{\boldsymbol{x}}, \dot{\boldsymbol{x}}_i)\right) \\
&= \sum_{i=1}^{M}\left(\alpha_i - \alpha_i^*\right).\left(\sum_{l=1}^{N_r}\boldsymbol{\varphi}_l(\dot{\boldsymbol{x}}_i)^T\boldsymbol{\varphi}_l(\dot{\boldsymbol{x}})\right) = \sum_{l=1}^{N_r}\left(\sum_{i=1}^{M}\left(\alpha_i - \alpha_i^*\right).\boldsymbol{\varphi}_l(\dot{\boldsymbol{x}}_i)^T\right)\boldsymbol{\varphi}_l(\dot{\boldsymbol{x}}) \\
&= \sum_{l=1}^{N_r}\left(\sum_{i=1}^{M}\left(\alpha_i - \alpha_i^*\right).\dot{\boldsymbol{x}}_i^T\mu_l(\dot{\boldsymbol{x}}_i)\right)\dot{\boldsymbol{x}}.\mu_l(\dot{\boldsymbol{x}}) \\
&= \sum_{l=1}^{N_r}\left(\sum_{i=1}^{M}\left(\alpha_i - \alpha_i^*\right).\dot{\boldsymbol{x}}_i^T\mu_l(\boldsymbol{x}_i)\right)\dot{\boldsymbol{x}}.\mu_l(\boldsymbol{x})
\end{aligned}$$

It is obvious that: $\hat{\boldsymbol{\theta}}_l = \left(\sum_{i=1}^{M}\left(\alpha_i - \alpha_i^*\right)\boldsymbol{\varphi}_l(\dot{\boldsymbol{x}}_i)\right) = \sum_{i=1}^{M}\left(\alpha_i - \alpha_i^*\right)\dot{\boldsymbol{x}}_i\mu_l(\boldsymbol{x}_i)$, the online version of the TS-SVR defined in Eq. (4) is attained where the consequent parameters are:

$$\begin{aligned}
\hat{\boldsymbol{\theta}}_l &= \sum\nolimits_{i=1}^{M}\left(\alpha_i - \alpha_i^*\right)\dot{\boldsymbol{x}}_i.\mu_l(\boldsymbol{x}_i) \\
&= \sum\nolimits_{i=1}^{M}\left(\alpha_i - \alpha_i^*\right)\dot{\boldsymbol{x}}_i.exp\left\{-\sum\nolimits_{j=1}^{n}\frac{\left(x_j - m_{lj}\right)^2}{2\sigma_{lj}^2}\right\}
\end{aligned} \tag{14}$$

and the TS-SVR fuzzy model is defined as:

$$\begin{aligned}
\hat{y}(k) &= \sum\nolimits_{l=1}^{N_r}\hat{\boldsymbol{\theta}}_l^T\phi_l(\dot{\boldsymbol{x}}) = \sum\nolimits_{l=1}^{N_r}\hat{\boldsymbol{\theta}}_l^T\dot{\boldsymbol{x}}.\mu_l(\boldsymbol{x}) \\
&= \sum_{l=1}^{N_r}\left(\hat{\boldsymbol{\theta}}_l^T.\dot{\boldsymbol{x}}\right).exp\left\{-\sum_{j=1}^{n}\frac{\left(x_j - m_{lj}\right)^2}{2\sigma_{lj}^2}\right\} \\
&= \sum\nolimits_{i=1}^{N_r}\left(\hat{\boldsymbol{\theta}}_0^i + \hat{\boldsymbol{\theta}}_1^i x_1(k) + \ldots + \hat{\boldsymbol{\theta}}_n^i x_n(k)\right).exp\left\{-\sum\nolimits_{j=1}^{n}\left(\frac{\left(x_j - m_{ij}\right)^2}{2\sigma_{ij}^2}\right)\right\}
\end{aligned} \tag{15}$$

Clearly, the consequent parameters of the proposed TS-SVRcan be computed by identifying Lagrange multipliers $\boldsymbol{\alpha} = (\alpha_1, \ldots, \alpha_M)^T$ from Eq. (11) and then the consequent parameters are computed from Eq. (14) work.

$$x(k+1) = A_i x(k) + + Bu(k) \tag{16}$$

4 Antecedent Parameters of the Takagi-Sugeno Fuzzy System Based Support Vector Regression

In this section, the antecedent parameters ($\boldsymbol{m}_l$ and $\boldsymbol{\sigma}_l$) of the TS-SVR system are first initialised by separating the training data into clusters. This can be done using a k-means clustering algorithm [33] where the i-th cluster defines the centroid and the width vectors of the firing strength $\mu_i(\boldsymbol{x})$. Then, the antecedent parameters are updated using a simple back-propagation learning algorithm. To perform an online updating of the antecedent parameters m_{ij} and σ_{ij}, an error function is computed at each sampling instant:

$$e(k) = \frac{1}{2}(y(k) - \hat{y}(k))^2 \tag{17}$$

where $y(k)$ and $\hat{y}(k)$ are the actual and the approximated (TS-SVR) outputs at the instant k, respectively. The updated values of m_{ij} and σ_{ij} at the instant $k+1$ are given by [39]:

$$m_{ij}(k+1) = m_{ij}(k) - \eta\frac{\partial e(k)}{\partial m_{ij}} = m_{ij}(k) + \eta(y(k) - \hat{y}(k))\frac{\partial \hat{y}(k)}{\partial m_{ij}} \tag{18}$$

$$\sigma_{ij}(k+1) = \sigma_{ij}(k) - \eta\frac{\partial e(k)}{\partial \sigma_{ij}} = \sigma_{ij}(k) + \eta(y(k) - \hat{y}(k))\frac{\partial \hat{y}(k)}{\partial \sigma_{ij}} \tag{19}$$

$\boldsymbol{\eta}$ is a positive learning rate $\boldsymbol{\eta} = \frac{\boldsymbol{\beta}}{\sum_{j=1}^{N}\sum_{i=1}^{n}\left(\left(\frac{\partial\hat{y}(k)}{\partial m_{ij}}\right)^2 + \left(\frac{\partial\hat{y}(k)}{\partial\sigma_{ij}}\right)^2\right)}$ with $\boldsymbol{\beta} = 0.09$.

5 The Adaptive TS-SVR GPC Controller

In this section, the TS-SVR fuzzy model is used to represent the nonlinear system and to develop the control law of NGPC where the nonlinear system is replaced by several local affine models in order to compute the control signal, and the nonlinear system is replaced by TS-SVR fuzzy rules similar to the fuzzy rules described in Eq. (1). Then, from Eq. (1) the adaptive TS-SVR predictor is given by:

$$\hat{y}(k) = \sum_{i=1}^{N_r}\left(a_i(z^{-1})y(k-1) + b_i(z^{-1})u(k-d-1) + C_i\right).exp\left\{-\sum_{j=1}^{n}\left(\frac{(x_j - m_{ij})^2}{2\sigma_{ij}^2}\right)\right\} \tag{20}$$

where the input vector is $x(k) = (x_1(k), \ldots, x_n(k)) = (y(k-1), \ldots, y(k-n_a), u(k-d-1), \ldots, u(k-n_b))$, C_i is a constant while $a_i(z^{-1})$ and $b_i(z^{-1})$ are linear polynomials defined by:

$$\begin{aligned} a_i(z^{-1}) &= a_i^1 z^{-1} + \ldots + a_i^{n_a} z^{-n_a} \\ b_i(z^{-1}) &= b_i^0 + b_i^1 z^{-1} + \ldots + b_i^{n_b} z^{-n_b} \end{aligned} \tag{21}$$

The consequent vectors $\hat{\boldsymbol{\theta}}_i = (a_i, b_i, C_i), i = 1, \ldots, N_r$ are obtained using Eq. (14). Obviously, all local affine models presented in Eq. (20) will be combined to obtain the flowing TS-SVR fuzzy model:

$$\bar{A}\left(z^{-1}\right)y(k) = \bar{B}\left(z^{-1}\right)u(k-d-1) + \bar{C} \tag{22}$$

where $\bar{A}(z^{-1}) = 1 - \bar{a}^1 z^{-1} - \ldots - \bar{a}^{n_a} z^{-n_a}$ and $\bar{B}(z^{-1}) = \bar{b}^0 + \bar{b}^1 z^{-1} + \ldots + \bar{b}^{n_b} z^{-n_b}$, and:

$$\begin{aligned} \bar{a}^j &= \textstyle\sum_{i=1}^{M} a_i^j.exp\left\{-\sum_{j=1}^{n}\left(\frac{\left(x_j - m_{ij}\right)^2}{2\sigma_{ij}^2}\right)\right\} \\ \bar{b}^j &= \textstyle\sum_{i=1}^{M} b_i^j.exp\left\{-\sum_{j=1}^{n}\left(\frac{\left(x_j - m_{ij}\right)^2}{2\sigma_{ij}^2}\right)\right\} \\ \bar{C} &= \textstyle\sum_{i=1}^{M} C_i.exp\left\{-\sum_{j=1}^{n}\left(\frac{\left(x_j - m_{ij}\right)^2}{2\sigma_{ij}^2}\right)\right\} \end{aligned} \tag{23}$$

and M is the size of the dictionary. The system in Eq. (21) can be rewritten to the controlled auto-regressive integrated moving average (CARIMA) form:

$$\bar{A}\left(z^{-1}\right)y(k) = \bar{B}\left(z^{-1}\right)u(k-d-1) + \frac{\xi(k)}{\Delta} \tag{24}$$

Note that, the constant $\bar{C}$ is integrated with the white noise $\xi(k)$, and the function $\xi(k)$ becomes the white noise with a mean equal to $\bar{C}$. The difference operator is given by $\Delta = 1 - \mathrm{z}^{-1}$. The control law of the GPC is obtained to minimize the cost function [1]:

$$\begin{aligned} J(k) = &\textstyle\sum_{j=d+1}^{N_p} (\hat{y}(k+j|k) - w(k+j))^2 \\ &+ \textstyle\sum_{j=d+1}^{N_u+d-1} \vartheta\left(\mathrm{z}^{-1}\right)\Delta u(k+j-d-1|k)^2 \end{aligned} \tag{25}$$

where $\hat{y}(k+j|k)$ is an optimum j step ahead prediction of the system on time k, N_p and N_u are the output and control signal horizons, respectively. $w(k+j)$ is the reference trajectory signal. The constant $\vartheta(\mathrm{z}^{-1}) = \vartheta$ is the weighting polynomial. According to Clarke [1], the incremental optimal control law is obtained as:

$$\Delta\boldsymbol{u}(k) = \left(\boldsymbol{G}^T\boldsymbol{G} + \vartheta\boldsymbol{I}\right)^{-1}\boldsymbol{G}^T\left(\boldsymbol{W} - \boldsymbol{F}\left(\mathrm{z}^{-1}\right)y(k) - \boldsymbol{L}\left(\mathrm{z}^{-1}\right)\right) \tag{26}$$

where $\boldsymbol{I}$ is an identity matrix and $\boldsymbol{W}$ is the reference vector. The matrices $\boldsymbol{G}$, $\boldsymbol{F}$ and $\boldsymbol{L}$ are obtained by recursively solving the Diophantine equations. Note that, we only apply the first element of the vector $\boldsymbol{u}(k)$ to the system. In this case, the increment of the control signal is:

$$\Delta u(k) = \boldsymbol{\Gamma}\left(\boldsymbol{W} - \boldsymbol{F}\left(\mathrm{z}^{-1}\right)y(k) - \boldsymbol{L}\left(\mathrm{z}^{-1}\right)\right) \tag{27}$$

where $\boldsymbol{\Gamma}$ is the first row of the matrix $\left(\boldsymbol{G}^T\boldsymbol{G} + \vartheta\boldsymbol{I}\right)^{-1}\boldsymbol{G}^T$, and the control signal applied to the system is given by:

$$\boldsymbol{u}(\boldsymbol{k}) = \boldsymbol{u}(\boldsymbol{k} - 1) + \boldsymbol{\Delta u}(\boldsymbol{k}) \tag{28}$$

6 Example: The Continuous-Stirred Tank Reactor

As an illustrative example, a nonlinear complex system: "the continuous-stirred tank reactor plant" (CSTR) [23, 24, 34] is used to validate the adaptive TS-SVR performance in system identification and control.

The nonlinear system is governed by the following differential equations:

$$\begin{aligned} \dot{C}_a(t) &= \frac{q}{v}\left(C_{a0} - C_a(t)\right) - k_0 C_a(t) e^{-\frac{E}{RT(t)}} \\ \dot{T}(t) &= \frac{q}{v}\left(T_0 - T(t)\right) + k_1 C_a(t) e^{-\frac{E}{RT(t)}} \\ &\quad + k_2 q_c(t)\left(1 - e^{-\frac{k_3}{q_c(t)}}\right)\left(T_{c0} - T(t)\right) \end{aligned} \tag{29}$$

In this system, the product A_a is converted into a new product B_b at the end of the process. $C_a(t)$ describes the concentration of product A_a. $T(t)$ represents the temperature of the mixture and the coolant flow rate $q_c(t)$ controls the reaction. The constant q represents the process flow rate. The rest of the thermodynamic and chemical constants are specified in Table 1. The parameters k_1, k_2 and k_3 are: $k_1 = \frac{\Delta H k_0}{\rho C_p}$, $k_2 = \frac{\rho_c C_{pc}}{\rho C_p v}$ and $k_3 = \frac{h_a}{\rho_c C_{pc}}$.

6.1 The Online Identification

To perform an online identification of the system, the sampling time is set to $t_s = 0.1$ min (6 s), and Eq. (29) is used to generate $N_S = 900$ samples. The first 400 samples are used for initialising the adaptive TS-SVR (number of fuzzy rules, and initial values of the antecedent parameters) while the adaptive TS-SVR is validated using the rest of the samples. The training samples are attained using the control signal presented in Fig. 2. The size of the input vector is 8 ($n_a = 5$ and $n_b = 3$); note that, the input vector size is augmented to become 9 according the TS-SVR approach. The number of clusters, which is typically equal to number of rules is ($N_r = 7$).

Table 1. Nominal parameters of the CSTR nonlinear system

Parameters	Explanation	Nominal value
q	Process flow-rate	100 l/min
k_0	Reaction rate constant	7.2×10^{10} min^{-1}
v	Volume of the Reactor	100 l
T_0	Feed temperature	350 K
E/R	Activation energy	1×10^4 K
T_{c0}	Inlet coolant temperature	350 K
ΔH	Reaction heat	2×10^5 cal/mol
ρ, ρ_c	Liquid densities	1×10^3 g/l
C_p, C_{pc}	Specific heats	1 cal/g/K
C_{a0}	Inlet feed concentration	1 mol/l
h_a	Coefficient of heat transfer	7×10^5 cal/min/K

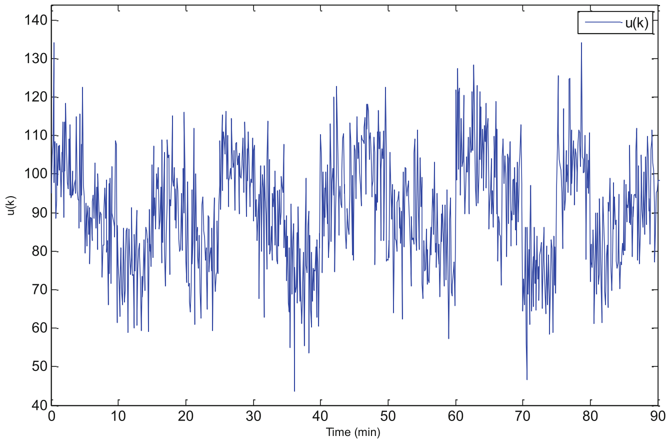

Fig. 2. Control signal used to generate samples

The dictionary size is set to $M = 50$. After performing the online identification, the results of the system output $C_a(t)$ are presented in Fig. 3.

The adaptive TS-SVR fuzzy model method performed well and provided a prediction that matches the original signal. The adaptive TS-SVR generates an error, the root mean squared error (RMSE), equal to $RMSE = 7.588 \times 10^{-3}$ which is considered small.

Next, the adaptive TS-SVR GPC controller is used to control the CSTR plant.

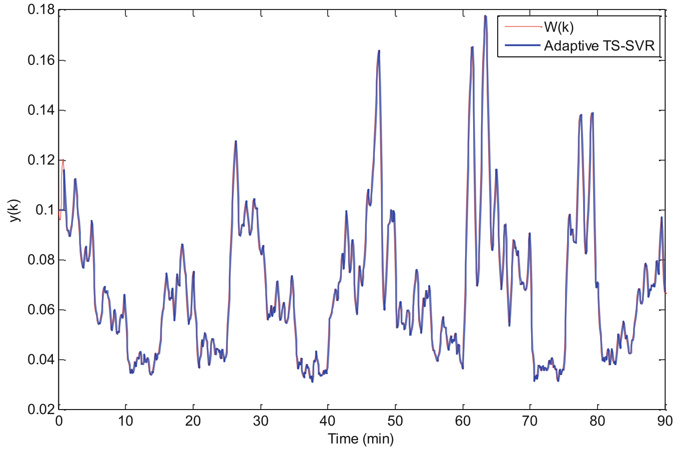

Fig. 3. Online identification using the proposed adaptive TR-SVR.

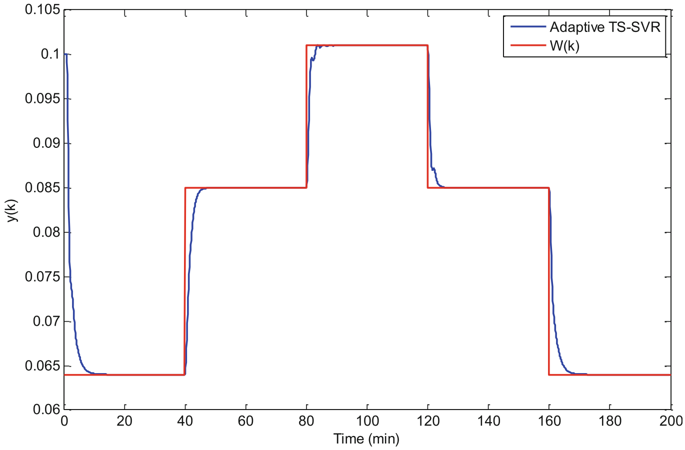

Fig. 4. Results of the proposed adaptive TS-SVR GPC

6.2 Adaptive TS-LSSVR GPC Controller

The adaptive TS-SVR GPC is investigated by controlling the CSTR plant. The same parameters used earlier in the identification process are kept for the control procedure while the parameters of the GPC algorithm are: $N_p = 10$, $N_u = 1$, $\vartheta = 0.0008$. The results of the system output and the control signal are illustrated in Figs. 4 and 5, respectively. Figure 4 shows that the adaptive TS-SVR GPC effectively control the CSTR system at the desired trajectory $W(k)$ and the response of this controller is relatively fast where the output signal moves from its initial value to the desired reference (as well as moving from one reference trajectory level to another) in a reasonable amount of time. The mean value of the execution time required in order to

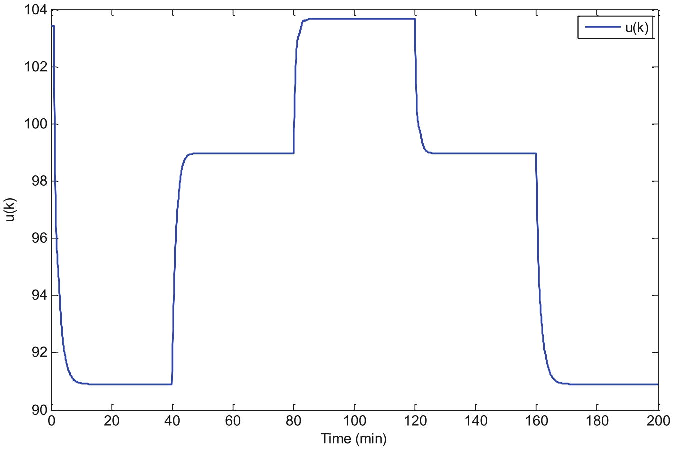

Fig. 5. Control signal obtained by the adaptive TS-SVR GPC.

implement one iteration for a window size of $M = 50$ is 0.00497 s, which is an acceptable duration (in this example: 0.00497 s $\ll$ $ts = 6$ s).

7 Conclusion

In this paper, an adaptive Takagi-Sugeno system based on support vector regression (TS-SVR) was proposed for system identification and control. In this approach, the antecedent parameters were initialized using a fuzzy k-means clustering while the updating is performed by a back-propagation algorithm. The consequent parameters, however, are defined as a support vector regression and the online updating is performed using the SMO algorithm. The proposed fuzzy model performed well and successfully used to identify a CSTR system. Then, the adaptive TS-SVR GPC efficiently controlled the CSTR system. In future work, more online kernel regression approaches will be used to introduce more effective adaptive TS fuzzy systems for system identification and control.

References

1. Clarke, D.W., Mothadi, C., Tuffs, P.S.C.: Generalized predictive control—part 1. The basic algorithm. Automatica **23**, 137–148 (1989)
2. Clarke, D.W., Mohtadi, C.: Properties of generalized predictive control. Automatica **25**(6), 859–875 (1989)
3. Camacho, F.E.: Constrained generalized predictive control. IEEE Trans. Autom. Control **38** (2), 327–332 (1993)
4. Zadeh, L.: Outline of a new approach to the analysis of complex systems and decision processes. IEEE Trans. Syst. Man Cybern. Part B **3**(1), 28–44 (1973)

5. Driankov, D., Hellendoorn, H., Reinfrank, M.: An Introduction to Fuzzy Control. Springer, Berlin (1993)
6. Wang, J., Gao, Y., Qiu, J., Ahn, C.K.: Sliding mode control for non-linear systems by Takagi–Sugeno fuzzy model and delta operator approaches. IET Control Theory Appl. **11**(8), 1205–1213 (2016)
7. Chen, S., Billings, S.: Neural networks for nonlinear dynamic system modelling and identification. Int. J. Control **56**, 319–346 (1992)
8. Soloway, D., Haley, P.J.: Neural generalized predictive control: a Newton–Raphson algorithm. In: Proceedings of the IEEE International Symposium on Intelligent Control, Dearborn, MI, USA, pp. 277–282 (1996)
9. Huang, Y.L., Lou, H.H., Gong, J.P., Edgar, T.F.: Fuzzy model predictive control. IEEE Trans. Fuzzy Syst. **8**, 665–678 (2000)
10. Takagi, T., Sugeno, M.: Fuzzy identification of systems and its application to modeling and control. IEEE Trans. Syst. Man Cybern. **15**, 116–132 (1985)
11. Mollov, S., Babuška, R., Abonyi, J., Verbruggen, H.B.: Effective optimization for fuzzy model predictive control. IEEE Trans. Fuzzy Syst. **12**(5), 661–675 (2004)
12. Sousa, J.M.D.C., Kaymak, U.: Model prediction control using fuzzy decision functions. IEEE Trans. Syst. Man Cybern. Part B Cybern. **31**(1), 54–65 (2001)
13. Vapnik, V.: The Nature of Statistical Learning Theory. Springer, London (1995)
14. Scholkopf, B., Burges, C.J.C., Smola, A.J.: Advances in Kernel Methods: Support Vector Learning. The MIT Press, Cambridge (1999)
15. Cortes, C., Vapnik, V.: Support-vector networks. Mach. Learn. **20**(3), 273–297 (1995)
16. Girosi, F.: An equivalence between sparse approximation and support vector machines. Neural Comput. **10**(6), 1455–1480 (1998)
17. Iplikci, S.: Support vector machines based generalized predictive control of chaotic systems. IEICE Trans. Fundam. Electron. Commun. Comput. Sci. **89**(10), 2787–2794 (2006)
18. Iplikci, S.: Online trained support vector machines-based generalized predictive control of non-linear systems. Int. J. Adapt. Control Signal Process. **20**(10), 599–621 (2006)
19. Guo, Z., Guan, X.: Nonlinear generalized predictive control based on online least squares support vector machines. Nonlinear Dyn. **79**(2), 1163–1168 (2015)
20. Li, L.J., Su, H.Y., Chu, J.: Generalized predictive control with online least squares support vector machines. Acta Autom. Sin. **33**(11), 1182–1188 (2007)
21. Chiang, J.H., Hao, P.Y.: Support vector learning mechanism for fuzzy rule-based modeling: a new approach. IEEE Trans. Fuzzy Syst. **12**(1), 1–11 (2004)
22. Juang, C.F., Hsieh, C.D.: TS-fuzzy system-based support vector regression. Fuzzy Sets Syst. **160**, 2486–2504 (2009)
23. Boulkaibet, I., Belarbi, K., Bououden, S., Marwala, T., Chadli, M.: A new T–S fuzzy model predictive control for nonlinear processes. Expert Syst. Appl. **88**, 132–151 (2017)
24. Boulkaibet, I., Belarbi, K., Bououden, S., Chadli, M., Marwala, T.: An adaptive fuzzy predictive control of nonlinear processes based on multi-kernel least squares support vector regression. Appl. Soft Comput. (2017) (under review)
25. Juang, C.F., Hsieh, C.D.: A fuzzy system constructed by rule generation and iterative linear SVR for antecedent and consequent parameter optimization. IEEE Trans. Fuzzy Syst. **20**(2), 372–384 (2012)
26. Mercer, J.: Functions of positive and negative type, and their connection with the theory of integral equations. Philos. Trans. R. Soc. Lond. A **209**, 415–446 (1909)
27. Poggio, T., Mukherjee, S., Rifkin, R., Raklin, A., Verri, A.: Uncertainty in Geometric Computations, pp. 131–141. Kluwer Academic Publishers, Boston (2002)
28. Vogt, M., Kecman, V.: Active-set methods for support vector machines. In: Support Vector Machines: Theory and Applications. Springer, Berlin, pp 133–158 (2005)

29. Huang, T.M., Kecman, V.: Bias term b in SVMs again. In: Proceedings of the 12th European Symposium on Artificial Neural Networks (ESANN 2004), Bruges, Belgium, pp. 441–448 (2004)
30. Kecman, V., Huang, T.M., Vogt, M. Iterative single data algorithm for training kernel machines from huge data sets: theory and performance. In: Support Vector Machines: Theory and Applications, pp. 605–605 (2005)
31. Platt, J.: Sequential minimal optimization: a fast algorithm for training support vector machines. Microsoft research technical report MSR-TR-98-14 (1998), p. 256
32. Kecman, V., Vogt, M., Huang, T.-M.: On the equality of Kernel AdaTron and sequential minimal optimization in classification and regression tasks and alike algorithms for Kernel machines. In: Proceedings of the 11 th European Symposium on Artificial Neural Networks, ESANN 2003, Bruges, Belgium, pp. 215–222 (2003). 256, 258, 269. http://www.support-vector.ws
33. MacQueen, J.B.: Some methods for classification and analysis of multivariate observations. In: Proceedings of 5-th Berkeley Symposium on Mathematical Statistics and Probability, vol. 1. University of California Press, Berkeley, pp. 281–297 (1967)
34. Oviedo, J.J.E., Vandewalle, J.P., Wertz, V.: Fuzzy Logic, Identification and Predictive Control. Springer, Berlin (2006)

Observer Based Model Predictive Control of Hybrid Systems

Zahaf Abdelmalek[1(✉)], Sofiane Bououden[2], Mohammed Chadli[3], Ivan Zelinka[4], and Ilyes Boulkaibet[5]

[1] Department of Electronics, University of the Brothers Mentouri Constantine, Constantine, Algeria
zaha_malek@yahoo.fr, zahaf.abdelmalek@umc.edu.dz
[2] Department of Industrial Engineering, University Abbes Laghrour, Khenchela, Algeria
sofiane.bououden@univ-khenchela.dz
[3] University of Picardie Jules Verne, MIS (EA 4029), 33 rue Saint-Leu, 80039 Amiens, France
mchadli@u-picardie.fr
[4] Faculty of Electrical Engineering and Computer Science, VŠB-TUO, Ostrava, Czech Republic
ivan.zelinka@vsb.cz
[5] RSA, Johannesburg University of Johannesburg, Johannesburg, South Africa
ilyes@aims.ac.za

Abstract. In this paper, we are investigating how to adopting a hybrid optimal control law for minimizing the optimization time for hybrid system, which is used for simultaneous estimation of both systems; in case of falling one of them, the propose design allowed to process the system properly and stable, based on the estimated error dynamics which gives a robustness for the system against the uncertainties, faults and disturbances. The stability is guaranteed based on the Lyapunov function which expressed on terms of LMIs. The simulations results are show the effectiveness of proposed approach.

Keywords: Hybrid system · Model Predictive Control (MPC) Observer · Linear Matrix Inequality (LMI)

1 Introduction

In this work we try to enrich the field of control Hybrid system, which take a big intention in tow last decades, for its tolerance and useful in the energy consumption. To be can able to predict the future behavior of the system the most technical used is MPC; it's based to use a model for the prediction of next performance; many schemes are presented to give more ideas how to improve the time of online optimization for medium and high speed systems, that's lead to put many theories about the conditions of processing as LMI's [1–5].

In the other hand, Hybrid model predictive control is knew as efficient technique for many researches in last year's, for studying the efficiency of power system as in [6, 7],

M. Chadli et al. (Eds.): ICEECA 2017, LNEE 522, pp. 198–207, 2019.
https://doi.org/10.1007/978-3-319-97816-1_15

the authors in [8] gives an idea for the optimization of hybrid linear system, also they make further investigation to how put a good control for studying system in [9] and [10]. In [11] researchers proposed a hybrid pseudo-spectral method to try solving the optimal control problem. In other hand, a solution for hybrid renewable energy systems is suggested [12]; in the same way an approach for managing the consumption of fuel for hybrid vehicles it's proposed by [13].

Furthermore, the stability of hybrid model predictive control problems is given a challenge for many researchers to find the best way to provide a robustness and stability for hybrid systems. using multi Lyapunov function and other tools for studying stability of hybrid and switched system is presented in [14], a robustness and stability of model predictive control for hybrid systems is investigated in [15]; in addition, stability and robustness approaches for hybrid dynamical systems are presented in [16].

But even so, in this topic there are many researches and still a future investigation, for the reason that this topic is not really developed as the other fields.

In this research, we consider to study the hybrid optimal control problems, based on the conception of estimator model predictive control for discrete hybrid dynamic model. The main idea is putting a procedure to recuperate the system performance in the case of falling down one of both system or in presence of uncertainties, faults and disturbances signals, that can ensure the stability and robustness of process by calculate the gains of hybrid optimal control law by solving the online optimization of the LMIs constrained problem at each sampling time. The stability and also the robustness are improved by using Lyapunov function. The results show the effectiveness of the studying control law by stabilizing the constrained systems.

This work is presented as follows: Sect. 2 introduces the notations and results of the basic elements. Section 3 presents the proposed approach to generate the hybrid optimal control law of the closed-loop hybrid system. In Sect. 4, simulation results are presented.

2 Problem Formulation and Preliminaries

We consider the following hybrid discrete-time system represented as:

$$\begin{cases} x(k+1) = A_i x(k) + + Bu(k) \\ y(k+1) = Cx(k) \end{cases} \tag{1}$$

To estimate the state in the feedback channel, an observer is designed,

$$\begin{cases} \hat{x}(k+1) = A_i \hat{x}(k) + Bu(k) + L(y(k) - \hat{y}(k)) \\ \hat{y}(k+1) = C\hat{x}(k) \end{cases} \tag{2}$$

Therefore, the control estimation to be generated on the controller side is

$$u(k) = K\hat{x}(k) = FG^{-1}\hat{x}(k) \tag{3}$$

Where A_i, B *and* C are state matrices, K is the controller gain matrix and L is the observer gain matrix which can be designed by standard methods such as the Lyapunov method.

Let us consider the following problem, which minimizes the given objective function in an infinite horizon [27]:

$$\begin{aligned} &\min_{u(k+i/k)=k\hat{x}(k+i/k)} \max_{i>0} J_{\infty}(k) \\ &\hat{y}_{h,min} \leq \hat{y}_h(k+i/k) \leq \hat{y}_{h,max}, \quad i \geq 0, \quad h = 1, 2, \ldots, q \\ &u_{h,min} \leq u_h(k+i/k) \leq u_{h,max}, \quad i \geq 0, \quad h = 1, 2, \ldots, p \end{aligned} \tag{4}$$

$$J_{\infty}(k) = \sum\nolimits_{i=0}^{\infty} \left[\hat{X}(k+i) + U(k+i)\right] \tag{5}$$

$$\text{With} \quad \begin{cases} \hat{X}(k+i) = \hat{x}^T(k+i/k)Q_0\hat{x}(k+i/k) \\ U(k+i) = u^T(k+i/k)R_0 u(k+i/k) \end{cases} \tag{6}$$

Assumption: For any matrices W, V and a symmetric matrix Z > 0, the following statements are equivalent and hold:

$$1/(W+V)^T Z(W+V) > 0 \tag{7}$$

$$2/ - W^T ZW - V^T ZV < 2\left(W^T ZV + V^T ZW\right) \tag{8}$$

Proof:

$$\begin{aligned} &(W+V)^T Z(W+V) > 0 \Rightarrow \\ &W^T ZW + V^T ZV + \left(W^T ZV + V^T ZW\right) > 0 \\ &- W^T ZW - V^T ZV < \left(W^T ZV + V^T ZW\right) \end{aligned}$$

To be sure that inequality is always verified and the first term is always borne we can write:

$$-W^T ZW - V^T ZV < 2\left(W^T ZV + V^T ZW\right)$$

A. Augmented System

The estimation error dynamics is defined as:

$$e(k) = x(k) - \hat{x}(k) \tag{9}$$

Using (1) and (2) we get the next closed loop discrete-time system:

$$\begin{cases} \hat{x}(k+1) = (A_i + BK)\hat{x}(k) + +LCe(k) \\ e(k+1) = (A_i - LC)e(k) \end{cases} \tag{10}$$

The previous augmented system can be written as:

$$\tilde{x}(k+1) = \tilde{A}(k)\tilde{x}(k) \tag{11}$$

Where:

$$\tilde{x}(k) = \left[\hat{x}^T(k)e^T(k)\hat{x}^T(k-1)e^T(k-1)\right]^T \tag{12}$$

$$\tilde{A}(k) = \begin{bmatrix} \tilde{A}_1(k) \\ \tilde{A}_2(k) \\ \tilde{A}_3(k) \\ \tilde{A}_4(k) \end{bmatrix} = \begin{bmatrix} (A_i + BK) & LC & 0_n & 0_n \\ 0_n & (A_i - LC) & 0_n & 0_n \\ I_n & 0_n & 0_n & 0_n \\ 0_n & I_n & 0_n & 0_n \end{bmatrix} \tag{13}$$

The new system can describe as follows:

$$\hat{x}(k+1) = \tilde{A}_1(k)\tilde{x}(k), \quad e(k+1) = \tilde{A}_2(k)\tilde{x}(k)$$
$$\hat{x}(k) = \tilde{A}_3(k)\tilde{x}(k), \quad e(k) = \tilde{A}_4(k)\tilde{x}(k).$$

3 Robust Hybrid Optimal Control

Theorem: Let us consider the closed loop estimate system (10). Let the input feedback controller be defined by (3), which is based on the extended state observer, which meets the performance (2) for calculate the hybrid optimal control problem; is globally asymptotically stable if there exists a positive define matrix $Q > 0$; L, F and G satisfying the following convex optimization problem:

$$\min_{Q,F,G,L} \gamma \tag{14}$$

$$\begin{bmatrix} -1 & x^T(k/k) \\ x(k/k) & Q \end{bmatrix} < 0 \tag{15}$$

$$\begin{bmatrix} G^T\tilde{A}_3^T + \tilde{A}_3 G - P^{-1} & * & * & * & * \\ \frac{1}{4}(A_i G + BF)\tilde{A}_3 & Q & * & * & * \\ \frac{1}{4}\tilde{L}\tilde{A}_4 & 0_n & Q & * & * \\ Q_0^{1/2}\tilde{A}_3 G & 0_n & 0_n & \gamma I & * \\ R_0^{1/2}F\tilde{A}_3 & 0_n & 0_n & 0_n & \gamma I \end{bmatrix} < 0 \tag{16}$$

$$\begin{bmatrix} u_{max}^2 & F \\ F^T & G^T + G - Q \end{bmatrix} < 0 \tag{17}$$

Proof: Recall the closed-loop system in (10) and consider the following Lyapunov function candidate:

$$V(x(k/k)) = \hat{x}^T(k/k)P\hat{x}(k/k) \tag{18}$$

To ensure the stability of (2), we have:

$$V(\hat{x}(k+i+1/k)) - V(\hat{x}(k+i/k)) \leq -[X(k+i) + U(k+i)] \tag{19}$$

$$-V(\hat{x}(k/k)) \leq -J_\infty(k) \tag{20}$$

We can write it:

$$max_{A_i,B,i>0} J_\infty(k) \leq V(\hat{x}(k/k)) \leq \gamma \tag{21}$$

While the problem of minimization become

$$min_{Q,F,G,L}\ \gamma \tag{22}$$

With:

$$\hat{x}^T(k/k)P\hat{x}(k/k) \leq \gamma \Leftrightarrow -\gamma + \hat{x}^T(k/k)P\hat{x}(k/k) \geq 0 \tag{23}$$

Using Schur's complement to (23) we obtain:

$$\begin{bmatrix} -1 & \hat{x}^T(k/k) \\ \hat{x}(k/k) & Q \end{bmatrix} < 0 \tag{24}$$

– To ensure the stability of system (2), we have (10) it will be:

$$V(\hat{x}(k+1/k)) - V(\hat{x}(k/k)) \leq -\left[\left(\hat{x}^T(k/k)Q_0\hat{x}(k/k)\right) + \left(u^T(k/k)R_0u(k/k)\right)\right]$$

That can be writing as:

$$\begin{aligned}\left[\hat{x}^T(k+1/k)P\hat{x}(k+1/k)\right] - \left[\hat{x}^T(k/k)P\hat{x}(k/k)\right] < \\ -\left[\left(\hat{x}^T(k/k)Q_0\hat{x}(k/k)\right) + \left(u^T(k/k)R_0u(k/k)\right)\right]\end{aligned}$$

We replace $u(k+i/k)$ by (3):

$$\left[\hat{x}^T(k+1/k)P\hat{x}(k+1/k)\right] - \left[\hat{x}^T(k/k)P\hat{x}(k/k)\right] < -\hat{x}^T(k/k)[Q_0 + K^TR_0K]\hat{x}(k/k)$$

With substitution of $\hat{x}(k+1/k)$ by (2) we obtain:

$$[((A_i + BK)\hat{x}(k/k) + LCe(k))^T P((A_i + BK)\hat{x}(k/k) + LCe(k)) - [\hat{x}^T(k/k)P\hat{x}(k/k)]] < \\ -\hat{x}^T(k/k)[Q_0 + K^T R_0 K]\hat{x}(k/k)$$

We can write:

$$((A_i + BK)\tilde{A}_3 + LC\tilde{A}_4)^T P((A_i + BK)\tilde{A}_3 + LC\tilde{A}_4) - \tilde{A}_3^T P\tilde{A}_3 < -\tilde{A}_3^T Q_0\tilde{A}_3 \\ -\tilde{A}_3^T K^T R_0 K\tilde{A}_3 \Leftrightarrow$$

We multiple in the left by G^T and by G in the right we get:

$$((A_iG + BF)\tilde{A}_3 + LCG\tilde{A}_4)^T P((A_iG + BF)\tilde{A}_3 + LCG\tilde{A}_4) - G^T\tilde{A}_3^T P\tilde{A}_3 G < \\ -G^T\tilde{A}_3^T Q_0\tilde{A}_3 G - \tilde{A}_3^T F^T R_0 F\tilde{A}_3 \Leftrightarrow$$

Then we obtain:

$$G^T\tilde{A}_3^T P\tilde{A}_3 G + ((A_iG + BF)\tilde{A}_3 + LCG\tilde{A}_4)^T P((A_iG + BF)\tilde{A}_3 + LCG\tilde{A}_4) + G^T\tilde{A}_3^T Q_0\tilde{A}_3 G \\ \mp \tilde{A}_3^T F^T R_0 F\tilde{A}_3 < 0 \tag{25}$$

The term $G^{T\tilde{A}_3^T}P\tilde{A}_3G$, can be writing as follows:

$$\left(G^T\tilde{A}_3^T - P^{-1}\right)P\left(\tilde{A}_3G - P^{-1}\right) \geq 0 \Rightarrow$$

$$G^T\tilde{A}_3^T P\tilde{A}_3 G - G^T\tilde{A}_3^T PP^{-1} - P^{-1}P\tilde{A}_3 G + P^{-1}PP^{-1} \geq 0 \Leftrightarrow$$

$$G^T\tilde{A}_3^T P\tilde{A}_3 G - G^T\tilde{A}_3^T - \tilde{A}_3 G + P^{-1} \geq 0 \Leftrightarrow G^T\tilde{A}_3^T + \tilde{A}_3 G - P^{-1} \leq G^T\tilde{A}_3^T P\tilde{A}_3 G \Leftrightarrow$$

$$G^T\tilde{A}_3^T + \tilde{A}_3 G - P^{-1} \leq G^T\tilde{A}_3^T P\tilde{A}_3 G \tag{26}$$

We hold (26) in (25):

$$G^T\tilde{A}_3^T + \tilde{A}_3 G \\ - P^{-1} + ((A_iG + BF) + LCe(k))^T P((A_iG + BF) + LCe(k)) + G^T Q_0 G + F^T R_0 F < 0$$

We replace $P = \gamma Q^{-1}$ to the precedent inequality, we find:

$$(G^T\tilde{A}_3^T + \tilde{A}_3 G - P^{-1}) + ((A_iG + BF)\tilde{A}_3 + LCG\tilde{A}_4)^T P((A_iG + BF)\tilde{A}_3 + LCG\tilde{A}_4) \\ - G^T\tilde{A}_3^T Q_0\tilde{A}_3 G - \tilde{A}_3^T F^T R_0 F\tilde{A}_3 > 0 \tag{25}$$

We put: $\tilde{L} = LCG$

Using the previous assumption in this inequality we get:

$$\begin{aligned}(G^T\tilde{A}_3^T + \tilde{A}_3 G - P^{-1}) + 1/2((A_i G + BF)\tilde{A}_3)^T P((A_i G + BF)\tilde{A}_3) + \\ 1/2\Big(\big(\tilde{L}\tilde{A}_4\big)^T P\big(\tilde{L}\tilde{A}_4\big)\Big) + G^T\tilde{A}_3^T Q_0 \tilde{A}_3 G + \tilde{A}_3^T F^T R_0 F\tilde{A}_3 < 0\end{aligned} \tag{27}$$

Using generalized Schur's complement to (27), we obtain:

$$\begin{bmatrix} G^T\tilde{A}_3^T + \tilde{A}_3 G - P^{-1} & * & * & * & * \\ \frac{1}{4}(A_i G + BF)\tilde{A}_3 & Q & * & * & * \\ \frac{1}{4}\tilde{L}\tilde{A}_4 & 0_n & Q & * & * \\ Q_0^{1/2}\tilde{A}_3 G & 0_n & 0_n & \gamma I & * \\ R_0^{1/2} F\tilde{A}_3 & 0_n & 0_n & 0_n & \gamma I \end{bmatrix} < 0 \tag{28}$$

Now, we put the input constraints in the form of LMIs.

– <u>Input Constraints</u>

$$u_{h,min} \le u_h(k+i/k) \le u_{h,max}, \quad i \ge 0, \quad h = 1, 2, \ldots, p$$

$$|u_h(k+i/k)| \le u_{h,max}, \quad i \ge 0, \quad h = 1, 2, \ldots, p$$

$$u_{max} = U$$

$$\|u(k+i/k)\|_{max} \triangleq \max_i u_i(k+i/k)$$

With (6), we can write:

$$\max_{i>0} \|u(k)\|_{max} \ge \max_{i>0} \left\|FG^{-1}P\hat{x}(k)\right\|_{max}$$

Use again the LMI constraints in [5]. We obtain:

$$\begin{bmatrix} -u_{max}^2 & FG^{-1}) \\ (FG^{-1})^T & P \end{bmatrix} > 0$$

By using Congruence property with full rank matrix $\begin{bmatrix} I & 0 \\ 0 & G^T \end{bmatrix}$ gives:

$$\begin{bmatrix} u_{max}^2 & F \\ F^T & G^T + G - Q \end{bmatrix} < 0 \tag{29}$$

End of proof.

4 Simulation Results

In this section, we validate the effectiveness of the proposed approach for guaranteeing the stability and robustness of systems.

Example

Using a servo control system; we consider the hybrid discrete time model as follows:

$$A_1 = \begin{bmatrix} 1.120 & 0.213 & -0.335 \\ 1 & 0 & 0 \\ 0 & 1 & 0 \end{bmatrix},$$

$$A_2 = \begin{bmatrix} -0.5 & -0.053 & 0.1 \\ 0.8 & 0.1 & 0 \\ 0 & 0 & 1 \end{bmatrix},$$

$$B = \begin{bmatrix} 1 \\ 0 \\ 0 \end{bmatrix}, C = \begin{bmatrix} 0.0541 & 0.1150 & 0.0001 \end{bmatrix}$$

The weighting matrices are:

$$\mathrm{Q}_0 = \begin{bmatrix} 1 & 0 & 0 \\ 0 & 1 & 0 \\ 0 & 0 & 1 \end{bmatrix}, \mathrm{R}_0 = 0.5,$$

The initials conditions are:

$$x = [55-5]^T, \quad \hat{x} = [000]^T$$

In Fig. 1, the estimated error dynamics show that the proposed approach lead the system to a good performance during the processing.

The result in Fig. 2 shows that the conception of hybrid optimal control law gives a good control with time. It is also clearly that the stability of process is guarantee.

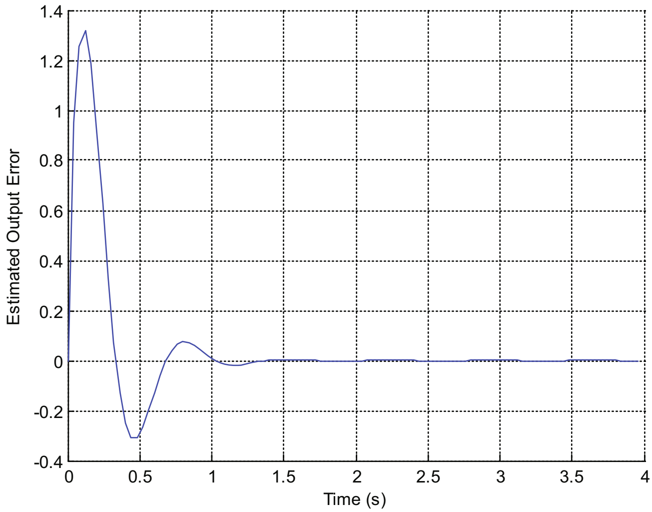

Fig. 1. Estimated output error

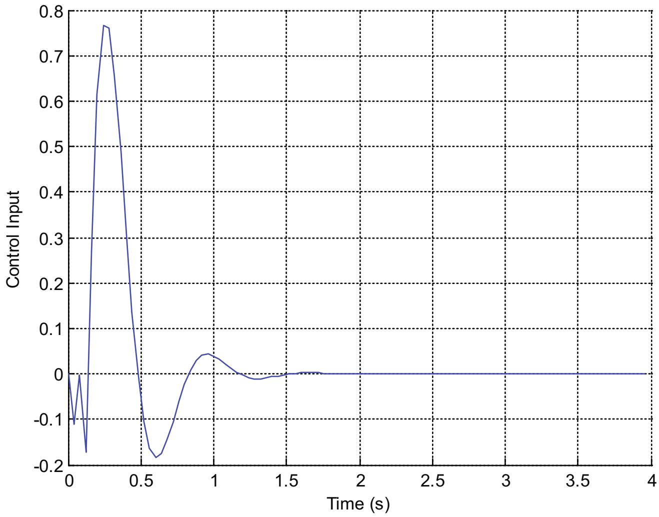

Fig. 2. Response of control input

5 Conclusion

In this work, a hybrid optimal control problem scheme was introduced. We were trying to use an observer controller to make progress the performance of system in case of uncertainties or defaults of system; to calculate the gains of the optimal controller is based on solving the set of LMIs, when the best solution is finding at each sampling time where consequence parameters of the system are optimized so as it. Furthermore, the stability of systems and the feasibility of solution were ensured for a class of nonlinear systems.

References

1. Camacho, E.F., Bordons, C.: Model Predictive Control. Springer, London (2004)
2. Zeilinger, M.N., Raimondo, D.M., Domahidi, A., Morari, M., Jones, C.N.: On real-time robust model predictive control. Automatica **50**, 683–694 (2014)
3. Ferreau, H.J., Bock, H.G., Diehl, M.: An online active set strategy to overcome the limitations of explicit MPC. Int. J. Robust Nonlinear Control **18**, 816–830 (2008)
4. Wang, Y., Boyd, S.: Fast model predictive control using online optimization. IEEE Trans. Control Syst. Technol. **18**(2), 267–278 (2010)
5. Kothare, M.V., Balakrishnan, V., Morari, M.: Robust constrained model predictive control using linear matrix inequalities. Automatica **32**(10), 1361–1379 (1996)
6. Mohanty, A., Viswavandya, M., Ray, P.K., Mohanty, S.: Reactive power control and optimisation of hybrid off shore tidal turbine with system uncertainties. J. Ocean Eng. Sci. **1** (4), 256–267 (2016)
7. Ferrari-Trecate, G., Gallestey, E., Letizia, P., Spedicato, M., Morari, M.: Modeling and control of co-generation power plants: a hybrid system approach. IEEE Trans. Control Syst. Technol. **12**(5), 694–705 (2004)
8. Borrelli, F., Baotic, M., Bemporad, A., Morari, M.: Dynamic programming for constrained optimal control of discrete-time linear hybrid systems. Automatica **41**, 1709–1721 (2005)
9. Borrelli, F., Bemporad, A., Fodor, M., Hrovat, D.: An MPC/hybrid system approach to traction control. IEEE Trans. Control Syst. Technol. **14**(3), 541–552 (2006)
10. Borrelli, F., Falcone, P., Pekar, J., Stewart, G.: Reference governor for constrained piecewise affine systems. J. Process Control **19**(8), 1229–1237 (2009)
11. Khosrow, M., Asyieh, E.: An efficient hybrid pseudo-spectral method for solving optimal control of Volterra integral systems. Math. Commun. **19**, 417–435 (2014)
12. Bernal-Agustın, J.L., Dufo-Lopez, R.: Simulation and optimization of stand-alone hybrid renewable energy systems. Renew. Sustain. Energy Rev. **13**, 2111–2118 (2009)
13. Zheng, C.H., Park, Y.I., Lim, W.S., Cha, S.W.: Fuel economy evaluation of fuel cell hybrid vehicles based on optimal control. Int. J. Automot. Technol. **13**(3), 517–522 (2012)
14. Branicky, M.: Multiple Lyapunov functions and other analysis tools for switched and hybrid systems. IEEE Trans. Autom. Control **43**, 475–482 (1998)
15. Lazar, M.: Model Predictive Control of Hybrid Systems: Stability and Robustness. University of Technology, Eindhoven (2006)
16. Goebel, R., Sanfelice, R.G., Teel, A.R.: Hybrid Dynamical Systems: Modeling, Stability, and Robustness. Princeton University Press, Princeton (2012). http://www.jstor.org/stable/j.ctt7s02z

Optimal Indirect Robust Adaptive Fuzzy Control Using PSO for MIMO Nonlinear Systems

Bounemeur Abdelhamid[1(✉)], Chemachema Mouhamed[1], and Essounbouli Najib[2]

[1] Laboratory of Automatic, Robotic and Control Systems, Department of Electronics, Faculty of Engineering, University Frères Mentouri Constantine 1, Constantine, Algeria
hamidsie4@gmail.com, m_chemachema@yahoo.fr

[2] Laboratory of Research in Science and Information Technical and Communication, Department of Mechanical Engineering, University of Troyes, Troyes Cedex, France
najib.essounbouli@univ-reims.fr

Abstract. This brief addresses The fuzzy adaptive control for class of MIMO nonlinear systems using Particle Swarm Optimization metaheuristic (PSO). To estimate the uncertain parts of the process, fuzzy logic systems are used. The uncertain nonlinearities of the system are captured by fuzzy systems that have been proven to be universal approximators. The Adaptations parameters are set to be approximated using PSO. The proposed control scheme completely overcomes the singularity problem that occurs in the indirect adaptive feedback linearizing control. Projection in the estimate parameters is not required and the stability analysis of the closed-loop system is performed using Lyapunov approach. Simulation results are provided to perform the effectiveness of the proposed control design.

Keywords: Adaptive fuzzy control · Feedback linearization
Nonlinear systems · Lyapunov stability · PSO

1 Introduction

Recent years have witnessed numbers of adaptive techniques [1], fuzzy system based adaptive control methodologies have received much attention for controlling uncertain and nonlinear dynamical systems. Based on the universal approximation theorem. During the last two decades, several adaptive fuzzy control schemes for a class of multi-input multi-output (MIMO) nonlinear uncertain systems are investigated [2–4]. Conceptually, there are two distinct approaches that have been formulated in the design of a fuzzy adaptive control system: direct and indirect schemes. The direct approach consists to approximate the ideal control law by a fuzzy system [5, 6]. However, in the indirect approach the nonlinear dynamics of the system are approximated by fuzzy systems to develop a control law based on these systems [3, 7]. In the indirect adaptive schemes, the possible controller singularity problems are usually met. In the

M. Chadli et al. (Eds.): ICEECA 2017, LNEE 522, pp. 208–224, 2019.
https://doi.org/10.1007/978-3-319-97816-1_16

aforementioned papers, the adjustable parameters of the fuzzy systems are updated by adaptive laws based on a Lyapunov approach, the parameter adaptive laws are designed in such a way to ensure the convergence of a Lyapunov function. However, for an effective adaptation, it is more judicious to directly base the parameter adaptation process on the identification error between the unknown function and its adaptive fuzzy approximation.

The initial adaptive controllers are constructed by some arbitrary values in the conventional nonlinear adaptive control schemes. Therefore, it is transparent that without sufficient and efficient fuzzy IF- THEN rules the convergence speed needs more time. Another challenging and yet rewarding problem in adaptive control scheme, DAF or IAF, is how properly determined the existing adaptation parameters in the adaptation law, which derived from the Lyapunov theory and designed by trial-and-error by the user.

Therefore, overcoming those restrictions and improving the tracking performance of DAF and IAF have gained a lot of attention these days. Many researchers have been focusing on using bio-inspired methods and evolutionary strategies to cope with those shortages, due to the lack of analytical approaches. Genetic algorithm (GA) has been widely applied to DAF and IAF. The GA is employed to optimize all the configuration parameters of the adaptive fuzzy such as the number of membership functions and rules [8, 9], the initial values of the consequent parameter vector [10], and the parameters in adaptive laws [11, 12]. Particle Swarm Optimization (PSO) has recently received much interest for achieving high efficiency and simpler implementation algorithm in comparison with GA. Commonly, PSO is utilized in adaptive fuzzy control such as optimizing both its structures and free parameters [13], simultaneously tune the shape of the fuzzy membership functions for all the consequences of rules in fuzzy rule-base [14]. Furthermore, PSO is used to update the premise part of the fuzzy system while the consequent part is updated by the other methods [15].

In this paper, an optimal indirect adaptive fuzzy controller is designed for a class of uncertain MIMO nonlinear continuous system by using the PSO algorithm. The PSO is utilized to construct an initial adaptive fuzzy controller with some adjustable parameters. In other words, the control knowledge of skilled human operators, fuzzy IF-THEN rules, is incorporated into the fuzzy controller through the setting of its initial parameters and simultaneously determining a suitable adaptation parameter by using the PSO; finally, an adaptive law is developed to tune the free parameters based on a Lyapunov theory. Inspired by the aforementioned papers, this paper presents indirect adaptive fuzzy control schemes for a class of continuous-time uncertain MIMO nonlinear dynamical systems. The proposed scheme is based on the results in [6] such that the fuzzy systems are used to approximate the system's unknown nonlinearities. To achieve the tracking of a desired output, new learning algorithms are proposed in the presented controller which permits superior control performance compared to the same class of controllers [16, 17]. In the proposed controller, a robustifying control term is added to the basic fuzzy controller to deal with approximation errors. The regularized inverse matrix is employed to solve problem of singularity and the stability of the closed-loop system is studied using Lyapunov method.

The outline of the paper is as follows. Section 2 presents the problem formulation. Section 3 presents a brief description of the used fuzzy system. In Sect. 4, a new control law and adaptive algorithms are proposed with PSO algorithm and stability analysis is given. Simulation examples are illustrated in Sect. 5. The conclusion is finally given in Sect. 6.

2 Problem Statement and Preliminaries

We consider a class of uncertain MIMO nonlinear systems given by

$$\begin{array}{c} y_1^{r1} = f_1(x) + \sum_{j=1}^{p} g_{1j}(x)u_j \\ \vdots \\ y_p^{rp} = f_p(x) + \sum_{j=1}^{p} g_{pj}(x)u_j \end{array} \tag{1}$$

where $x = \left[y_1, \dot{y}_1, \ldots, y_1^{(r_1-1)}, \ldots, y_p, \dot{y}_p, \ldots, y_p^{\left(r_p-1\right)}\right]^T$ is the overall state vector which is assumed available for measurement, $u = \left[u_1, \ldots, u_p\right]^T$ is the control input vector, $y = \left[y_1, \ldots, y_p\right]^T$ is the output vector, and $f_i(x)$ et $g_{ij}(x), i, j = 1, \ldots, p$ are unknown smooth nonlinear functions.

Let us denote

$$y^{(r)} = \left[y_1^{(r_1)} \ldots y_p^{(r_p)}\right]$$

$$F(x) = \left[f_1(x) \ldots f_p(x)\right]^T$$

$$G(x) = \begin{bmatrix} g_{11}(x) & \ldots & g_{1p}(x) \\ \vdots & \ddots & \vdots \\ g_{p1}(x) & \ldots & g_{pp}(x) \end{bmatrix}$$

Then, dynamic system (1) can be written in the following compact form

$$y^{(r)} = F(x) + G(x)u \tag{2}$$

The control objective is to design adaptive control $u_i(t)$ for system (1) such that the output $y_i(t)$ follows a specified desired trajectory $y_{di}(t)$ under boundedness of all signals.

Assumption 1: The matrix $G(x)$ is symmetric positive definite and bounded as $G(x) \geq \sigma_0 I_P$,where σ_0 is a positive constants.

Assumption 2: The desired trajectory $y_{di}(t), i = 1, \ldots, P$, is a known bounded function of time with bounded known derivatives $\dot{y}_{di}(t), \ldots, y_{di}^{(r_i)}$ i.e. $y_{di}(t) \epsilon C^{r_i}$.

Remark 1: Notice that Assumption 1 is a sufficient condition ensuring that the matrix $G(x)$ is always regular and, therefore, system (1) is feedback linearizable by a static state feedback. Although this assumption restricts the considered class of MIMO nonlinear systems, many physical systems, such as robotic system [18], fulfill such a property.

Define the tracking errors as

$$\begin{aligned} e_1(t) &= y_{d1}(t) - y_1(t) \\ &\vdots \\ e_p(t) &= y_{dp}(t) - y_p(t) \end{aligned} \tag{3}$$

while the feedback control is given by:

$$u = G(x)^{-1}[-F(x) + V] \tag{4}$$

where

$$V = \begin{bmatrix} v_1 \\ \vdots \\ v_p \end{bmatrix} = \begin{bmatrix} y_{d1}^{(r_1)} + k_{1r1}e_1^{(r_1-1)} + \ldots + k_{11}e_1 \\ \vdots \\ y_{dp}^{(r_p)} + k_{prp}e_p^{(r_p-1)} + \ldots + k_{p1}e_p \end{bmatrix} \tag{5}$$

we can write

$$\begin{cases} e_1^{(r_1)} + k_{1r1}e_1^{(r_1-1)} + \ldots + k_{11}e_1 = 0 \\ \vdots \\ e_p^{(r_p)} + k_{prp}e_p^{(r_p-1)} + \ldots + k_{p1}e_p = 0 \end{cases} \tag{6}$$

where the coefficients k_{ij} are chosen such that all the polynomials in Eq. 6 are of the type Hurwitz. So we can conclude that $\lim_{t\to\infty} e_i(t) = 0$ which is the main objective of the command. However in this case, the nonlinear functions $f_i(x)$ and $g_i(x) i = 1, \ldots, p$ are assumed unknown, then obtaining the feedback control law (4) is difficult. For this reason the dynamics of these functions is approximated by using fuzzy systems.

3 Description of Fuzzy Systems

In this work we will consider a fuzzy zero order (TS0).

Each rule has a numerical conclusion, the total output of the fuzzy system is obtained by calculating a weighted average, and in this manner the time consumed by the procedure of defuzzification is avoided. Then the output of fuzzy system is given by following relationship [19–21]:

$$y(x) = \frac{\sum_{k=1}^{N} \mu_k(x) f_k(x)}{\sum_{k=1}^{N} \mu_k(x)} \tag{7}$$

with $\mu_k(x) = \prod_{i=1}^{n} \mu_{\breve{F}_i^k}, \breve{F}_i^k \in \left\{F_i^1, \ldots, F_i^{m_i}\right\}$ which represents the degree of confidence or activation rule R_k and $f_k(x)$ is a polynomial of zero order.

$$f_k(x) = a^k \tag{8}$$

We can simplify the output of fuzzy system as follows:

$$y(x) = \frac{\sum_{k=1}^{N} \mu_k(x) a^k}{\sum_{k=1}^{N} \mu_k(x)} \tag{9}$$

By introducing the concept of fuzzy basis functions [22], the output of fuzzy system TS0 can be written as:

$$y(x) = w^T(x)\theta \tag{10}$$

with

- $\theta = [a^1 \ldots a^N]$: Vector of parameters of the conclusion of rules fuzzy part.
- $w(x) = [w_1(x) \ldots w_N(x)]^T$: Basic function of the vector each component is given by:

$$w_N(x) = \frac{\mu_k(x)}{\sum_{j=1}^{N} \mu_j(x)}, k = 1, \ldots, N \tag{11}$$

4 Controller Design

4.1 Indirect Adaptive Fuzzy Control

In this section we propose to indirectly approximate the unknown ideal (4) by identifying the unknown functions $f_i(x)$ and $g_{ij}(x)$ using fuzzy systems.

$$\widehat{f}_i(x, \theta) = w_{f_i}^T(x)\theta_{f_i}, i = 1, \ldots, p \tag{12}$$

$$\hat{g}_{ij}(x, \theta) = w_{g_{ij}}^T(x)\theta_{g_{ij}}, i,j = 1, \ldots, p \tag{13}$$

With $w_{f_i}^T$ and $w_{g_{ij}}^T$ are vectors of fuzzy basic functions supposed properly fixed in prior by the user, θ_{f_i} and $\theta_{g_{ij}}$ are vectors of the fitted parameters. The functions $f_{ij}(x)$ and $g_{ij}(x)$ can be expressed in terms of fuzzy approximations in the following manner:

$$\begin{cases} f_i(x) = \hat{f}_i\left(x, \theta_{fi}^*\right) + \varepsilon_{f_i}(x) \\ g_{ij}(x) = \hat{g}_{ij}\left(x, \theta_{g_{ij}}^*\right) + \varepsilon_{g_{ij}}(x) \end{cases} \tag{14}$$

With $\varepsilon_{f_i}(x)$ and $\varepsilon_{g_{ij}}(x)$ represent the fuzzy approximation errors, $\theta^*_{f_i}$ and $\theta^*_{g_{ij}}$ are respectively of the optimum parameters of θ_{f_i} and $\theta_{g_{ij}}$, the values of parameters θ_{f_i} and $\theta_{g_{ij}}$ respectively minimizing the approximation errors $\varepsilon_{f_i}(x)$ and $\varepsilon_{g_{ij}}(x)$. These optimal parameters satisfy:

$$\theta^*_{fi} = arg\ \min_{\theta_{f_i}}\left\{\sup_x\left|f_i(x) - \hat{f}_i\left(x, \theta_{f_i}\right)\right|\right\} \tag{15}$$

$$\theta^*_{gij} = arg\ \min_{\theta_{f_i}}\left\{\sup_x\left|g_{ij}(x) - \hat{g}_{ij}\left(x, \theta_{gij}\right)\right|\right\} \tag{16}$$

Note that the optimal parameters $\theta^*_{f_i}$ and $\theta^*_{g_{ij}}$ are unknown constants artificial introduced only to the theoretical study of the stability of the control algorithm. In fact, the knowledge of their values is not necessary for implementation of adaptive control law. From the above analysis, we can write:

$$f_i(x) - \hat{f}_i\left(x, \theta_{f_i}\right) = w^T_{f_i}(x)\tilde{\theta}_{f_i} + \varepsilon_{f_i}(x) \tag{17}$$

$$g_{ij}(x) - \hat{g}_{ij}\left(x, \theta_{gij}\right) = w^T_{g_{ij}}(x)\tilde{\theta}_{g_{ij}} + \varepsilon_{g_{ij}}(x) \tag{18}$$

where

$\tilde{\theta}_{f_i} = \theta^*_{f_i} - \theta_{f_i}$ and $\tilde{\theta}_{g_{ij}} = \theta^*_{g_{ij}} - \theta_{g_{ij}}$, are the parameter estimation errors.

Assumption 3: The fuzzy approximation errors $\varepsilon_{f_i}(x)$ and $\varepsilon_{g_{ij}}(x)$ are bounded for all $x\epsilon\Omega_x$ as $\left|\varepsilon_{f_i}(x)\right| \le \bar{\varepsilon}_{f_i}$ and $\left|\varepsilon_{g_{ij}}(x)\right| \le \bar{\varepsilon}_{g_{ij}}$, where $\bar{\varepsilon}_{f_i}$ and $\bar{\varepsilon}_{g_{ij}}$ are unknown positive constants.

This assumption is reasonable, since we assume that fuzzy systems used for approximating unknown functions have the universal approximator property.

Denote

$$\hat{F}\left(x, \theta_f\right) = \left[\hat{f}_1\left(x, \theta_{f1}\right)\ldots\hat{f}_p\left(x, \theta_{fp}\right)\right]^T$$

$$\hat{G}\left(x, \theta_g\right) = \begin{bmatrix} \hat{g}_{11}(x) & \ldots & \hat{g}_{1p}(x) \\ \vdots & \ddots & \vdots \\ \hat{g}_{p1}(x) & \ldots & \hat{g}_{pp}(x) \end{bmatrix}$$

$$\theta_f = \left[\theta_{f1}, \ldots, \theta_{fp}\right]^T; \theta^*_f = \left[\theta^*_{f1}, \ldots, \theta^*_{fp}\right]^T$$

$$\theta_g = \begin{bmatrix} \theta_{g11} & \cdots & \theta_{g1p} \\ \vdots & \ddots & \vdots \\ \theta_{gp1} & \cdots & \theta_{gpp} \end{bmatrix}$$
$$\theta_g^* = \begin{bmatrix} \theta_{g11}^* & \cdots & \theta_{g1p}^* \\ \vdots & \ddots & \vdots \\ \theta_{gp1}^* & \cdots & \theta_{gpp}^* \end{bmatrix}$$

$$W_f(x) = diag\lfloor w_{f1}(x), \ldots, w_{fp}(x) \rfloor$$
$$W_g(x) = diag\lfloor w_{g1}(x), \ldots, w_{gp}(x) \rfloor$$

$$\varepsilon_f(x) = \left[\varepsilon_{f1}(x) \ldots \varepsilon_{fp}(x)\right]^T$$

$$\varepsilon_g(x) = \begin{bmatrix} \varepsilon_{g11}(x) & \cdots & \varepsilon_{g1p}(x) \\ \vdots & \ddots & \vdots \\ \varepsilon_{gp1}(x) & \cdots & \varepsilon_{gpp}(x) \end{bmatrix}$$

$$\overline{\varepsilon_f} = \left[\bar{\varepsilon}_{f1} \ldots \bar{\varepsilon}_{fp}\right]^T$$

$$\bar{\varepsilon}_g = \begin{bmatrix} \bar{\varepsilon}_{g11} & \cdots & \bar{\varepsilon}_{g1p} \\ \vdots & \ddots & \vdots \\ \bar{\varepsilon}_{gp1} & \cdots & \bar{\varepsilon}_{gpp} \end{bmatrix}$$

$$F(x) - \hat{F}(x, \theta_f) = \hat{F}\left(x, \theta_f^*\right) - \hat{F}(x, \theta_f) + \varepsilon_f(x) \tag{19}$$

$$G(x) - \hat{G}(x, \theta_g) = \hat{G}\left(x, \theta_g^*\right) - \hat{G}(x, \theta_g) + \varepsilon_g(x) \tag{20}$$

Now we can write an expression for the adaptive law

$$u_c = \hat{G}^T(x, \theta_g)\left(\varepsilon_0 I_P + \hat{G}(x, \theta_g)\hat{G}^T(x, \theta_g)\right)^{-1}\left[-\hat{F}(x, \theta_f) + V\right] \tag{21}$$

where ε_0 is a small positive constant.

In the control law (21), we replaced $\hat{G}(x, \theta_g)^{-1}$ by the regularized inverse

$$\hat{G}^T(x, \theta_g)\left(\varepsilon_0 I_P + \hat{G}(x, \theta_g)\hat{G}^T(x, \theta_g)\right)^{-1} \tag{22}$$

The regularized inverse given by (22) is always defined even when $\hat{G}(x, \theta_g)$ is not invertible, hence the control law (21) is well defined. Note that even if the control law (22) is well defined, it cannot alone ensure the stability of the closed loop system. This is due, on the one hand, the error introduced by the approximation of actual functions $F(x)$ and $G(x)$ by fuzzy systems and from one side to the error introduced by the use of the regularized inverse matrix in place of the inverse matrix. For these reasons and in order to have a control law does not depend on any initialization phase we propose, a control law which is composed of two terms, a term adaptive control u_c introduced to overcome the problems of non-linearity of the system, and a second term u_r proposed, to circumvent the problem of approximation errors and, compensate for the error due to the use of the inverse regularized instead of the inverse matrix, then the resulting control law is represented as follows:

$$u = u_c + u_r \tag{23}$$

The adaptive control term u_c is given by

$$u_c = \hat{G}^T(x,\theta_g)\left(\varepsilon_0 I_P + \hat{G}(x,\theta_g)\hat{G}^T(x,\theta_g)\right)^{-1}\left[-\hat{F}(x,\theta_f) + V\right] \tag{24}$$

The robust control term u_r is given by

$$u_r = \frac{B^T PE|E^T PB|\left(\hat{\varepsilon}_f + \hat{\varepsilon}_g|u_c| + |u_O|\right)}{\sigma_0\|E^T PB\|^2 + \delta} \tag{25}$$

where $u_r = \begin{bmatrix} u_{r1} \\ \vdots \\ u_{rp} \end{bmatrix}$

$$u_0 = \varepsilon_0\left[\varepsilon_0 I_p + \hat{G}(x,\theta_g)\hat{G}^T(x,\theta_g)\right]^{-1}\left(-\hat{F}(x,\theta_f) + V\right) \tag{26}$$

$\hat{\varepsilon}_f$ and $\hat{\varepsilon}_g$ are respectively the estimated of $\bar{\varepsilon}_f$ and $\bar{\varepsilon}_g$, δ is a time-varying parameter defined below. To achieve the control objectives, we define the parameter adaption laws as follows:

$$\dot{\theta}_f = -\gamma_f B^T PEw_f(x) \tag{27}$$

$$\dot{\theta}_{gij} = -\gamma_g B^T PEu_j w_{gi}(x) \quad i,j = 1,\ldots,p \tag{28}$$

$$\dot{\hat{\varepsilon}}_f = n_f\left|B^T PE\right| \tag{29}$$

$$\dot{\hat{\varepsilon}}_g = n_g\left|u_c^T\right|\left|B^T PE\right| \tag{30}$$

$$\dot{\delta} = -\eta\frac{|E^T PB|\left(\hat{\varepsilon}_f + \hat{\varepsilon}_g|u_c| + |u_O|\right)}{\sigma_0\|E^T PB\|^2 + \delta} \tag{31}$$

$\gamma_f > 0, \gamma_g > 0, n_f > 0, n_g > 0, \eta > 0$ and $\delta(0) > 0$.

4.2 Optimal Indirect Adaptive Fuzzy Control

Indirect Adaptive Fuzzy (IAF) controllers use fuzzy systems to approximate the unknown nonlinear functions inside the study system. In the other words, they incorporate fuzzy IF-THEN rules directly into themselves. It should be emphasize that the human expert knowledge (fuzzy IF-THEN rules) is incorporated through the initial parameters. Therefore, the major advantage of the FLS is emerged while the initial parameters are chosen accurately. Another significant parameter is, which is known as adaptation parameter. There is no specific approach to choose a suitable adaptation parameter. Therefore, an Optimization Method (OM) should be employed to determine the initial parameters and the adaptation parameter simultaneously. Moreover, the control objective in optimal adaptive control scheme is not only the X state vector of the system in Eq. (1), follows a given desired trajectory state but also the tracking error converges to zero asymptotically. The Mean Square Error (MSE) is defined in (32) to use as an objective function for evaluating the performance index in the optimal designing of direct fuzzy system, assigning the initial parameters and the adaptation parameter. The MSE formulates as follows:

$$MSE = \frac{1}{K}\sum (Y_d - Y)^2 \tag{32}$$

where, Y is actual state of system, Y_d is desired state. K is the total number of data.

The proposed optimization method chosen in this paper is PSO (particles swarm optimization), due to its popularity in the optimization approaches.

The particle swarm optimization, PSO

Particle swarm optimization is an evolutionary computation technique developed by Kennedy and Eberhart in 1995 [23, 24].The particle swarm concept originated as a simulation of a simplified social system. **PSO** is initialized with a population of random solutions. Each potential solution is assigned a randomized velocity. Each particle keeps track of its coordinates in the problem space which are associated with the best solution, ***pbest***, (fitness) it has achieved so far. Another best value that is tracked by the global version of the particle swarm optimizer is the overall best value, and its location, obtained so far by any particle in the population. This location is called ***gbest.*** At each step, the PSO concept consists of changing the velocity of each particle toward its *pbest* and *gbest* locations. The velocity is weighted by a random term, with separate random numbers being generated for acceleration toward *pbest* and *gbest* locations.

The original process for implementing the global version of PSO is as follows:

a. Initialize a population of particles with random positions and velocities in the problem space.
b. For each particle, evaluate the desired optimization fitness function.
c. Compare particle's fitness evaluation with particle's *pbest*. If current value is better than *pbest*, then set *pbest* value equal to the current value and *pbest* location equal to the current location.
d. Compare fitness evaluation with the population's overall previous best. If current value is better than *gbest*, then reset *gbest* to the current particle's array index value.

e. Change the velocity and position of the particle according to the Eqs. (33) and (34), respectively:

$$v_{id} = wv_{id} + c_1 r_1 (p_{bid} - x_{id}) + c_2 r_2 (p_{gb} - x_{id}) \tag{33}$$

$$x_{id} = x_{id} + v_{id} \tag{34}$$

f. Loop to step 2 until a criterion is met. where x_{id} particle position; v_{id} particle velocity; p_{bid} local best position; p_{gb} global best position; c_1, c_2 constants; r_1, r_2 random numbers between 0 and 1
The proposed control scheme based on an optimization method is shown in Fig. 1.

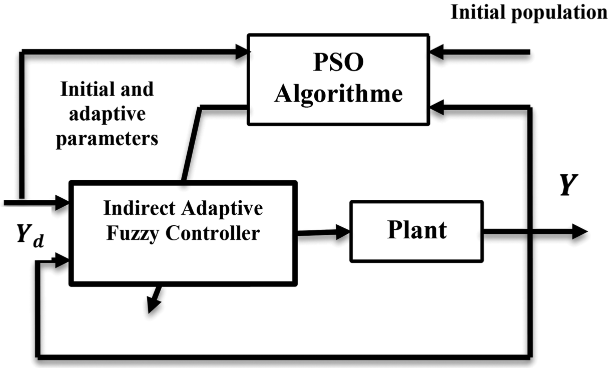

Fig. 1. The proposed controller scheme based on PSO

Remark 1: In this brief work we consider the on-line approximation of all adaptation parameters and also the first values of adaption laws, to make our proposed control law full automatics, so that no parameters are chosen manually, they are performed with our optimization method to make maximum performances even with changing the initial states.

Theorem: Consider the nonlinear system (1), and suppose that the assumptions (1–3) are satisfied. Then the control law defined by Eqs. (24)–(25) with adaptation law (27)–(31) applied to the system (1) ensures boundedness of all signals of the closed loop and the convergence to zero of tracking errors, $e_i^{(j)} \to 0$ when $t \to \infty$ for $i = 1, \ldots, P$ and, $j = 0, 1, \ldots, r_i - 1$.

Proof

$$E^{(n)} = Y_d^{(n)} - Y^{(n)} \tag{35}$$

$$E^{(n)} = Y_d^{(n)} - F(x) - G(x)u \tag{36}$$

We can write as follows:

$$E^{(n)} = Y_d^{(n)} - F(x) - G(x)u_c - G(x)u_r \tag{37}$$

substitute (24) and (26), Eq. (37) becomes

$$E^{(n)} = -K^T E - \left(F(x) - \hat{F}\left(x, \theta_f\right)\right) - \left(G(x) - G\left(x, \theta_g\right)\right)u_c - G(x)u_r + u_0 \tag{38}$$

substitute (19) and (20), Eq. (38) becomes

$$\begin{aligned} E^{(n)} = {} & -K^T E - \left(\hat{F}\left(x, \theta_f^*\right) - \hat{F}\left(x, \theta_f\right) + \varepsilon_f(x)\right) - \left(\hat{G}\left(x, \theta_g^*\right) - \hat{G}\left(x, \theta_g\right) + \varepsilon_g(x)\right)u_c \\ & - G(x)u_r + u_0 \end{aligned} \tag{39}$$

$$\begin{aligned} E^{(n)} = {} & -K^T E - \left(W_f^T \tilde{\theta}_f + \varepsilon_f(x)\right) - \left(\sum_{i=1}^{p} \sum_{j=1}^{p} W_{gi}^T \tilde{\theta}_{gij} u_{cj}\right) - \varepsilon_g(x)u_c \\ & - G(x)u_r + u_0 \end{aligned} \tag{40}$$

While the dynamics of the error can be written as follows:

$$\dot{E} = AE + B\left[-\left(W_f^T \tilde{\theta}_f + \varepsilon_f(x)\right) - \left(\sum_{i=1}^{p} \sum_{j=1}^{p} W_{gi}^T \tilde{\theta}_{gij} u_{cj}\right) - \varepsilon_g(x)u_c - G(x)u_r + u_0\right] \tag{41}$$

where

$$A = \begin{bmatrix} 0 & I_{n\times n} & \ldots & 0 \\ \vdots & \ddots & & \vdots \\ 0 & 0 & 0 & I_{n\times n} \\ -K_1 & -K_2 & \ldots & -K_n \end{bmatrix} B = \begin{bmatrix} 0 \\ \vdots \\ 0 \\ I_{n\times n} \end{bmatrix}$$

Until $(|sI - A|) = s^{(n)} + K_1 s^{(n-1)} + \ldots + K_n$ is stable (A stable), we know that there exists a symmetric positive definite matrix $P(n, n)$ that satisfies the Lyapunov equation:

$$A^T P + PA = -Q \tag{42}$$

where Q is a symmetric positive definite matrix of arbitrary dimensions $(n \times n)$.

To minimize the tracking error and the approximation error, we consider the following Lyapunov function:

$$V = \frac{1}{2}E^T PE + \frac{1}{2\gamma_f}\tilde{\theta}_f^T \tilde{\theta}_f + \frac{1}{2\gamma_g} tr(\tilde{\theta}_g^T \tilde{\theta}_g) + \frac{1}{2\eta_f}\tilde{\varepsilon}_f^T \tilde{\varepsilon}_f + \frac{1}{2\eta_g} tr\left(\tilde{\varepsilon}_g^T \tilde{\varepsilon}_g\right) + \frac{1}{2\eta}\delta^2 \tag{43}$$

with δ is a time-varying parameter, $\tilde{\varepsilon}_f = \bar{\varepsilon}_f - \hat{\varepsilon}_f$, $\tilde{\varepsilon}_g = \bar{\varepsilon}_g - \hat{\varepsilon}_g$

Using (38) and (39), the time derivative of V can be write in the following form

$$\dot{V} = -\frac{1}{2}E^T QE + E^T PB\Big[-\Big(W_f^T\tilde{\theta}_f + \varepsilon_f(x)\Big) - \Big(\sum_{i=1}^{p}\sum_{j=1}^{p} W_{gi}^T\tilde{\theta}_{gij}u_{cj}\Big) - \varepsilon_g(x)u_c - G(x)u_r + u_0\Big] - \frac{1}{\gamma_f}\tilde{\theta}_f^T\dot{\theta}_f - \sum_{i=1}^{p}\sum_{j=1}^{p}\frac{1}{\gamma_{gij}}\tilde{\theta}_{gij}^T\dot{\theta}_{gij} - \frac{1}{\eta_f}\tilde{\varepsilon}_f^T\dot{\hat{\varepsilon}}_f - \frac{1}{\eta_g}tr\Big(\tilde{\varepsilon}_g^T\dot{\hat{\varepsilon}}_g\Big) + \frac{1}{\eta}\delta\dot{\delta} \tag{44}$$

Equation (44) can be simplified

$$\dot{V} = -\frac{1}{2}E^T QE + \dot{V}_1 + \dot{V}_2 \tag{45}$$

Remark 2: Writing the derivative of the Lyapunov function described in Eq. (45) facilitates the task of demonstrating negativity of the derivative $\dot{V}$

$$\dot{V}_1 = -\frac{1}{\gamma_f}\tilde{\theta}_f^T\Big[\gamma_f B^T PEW_f + \dot{\theta}_f\Big] - \frac{1}{\gamma_g}\sum_{i=1}^{p}\sum_{j=1}^{p}\tilde{\theta}_{gij}^T\Big[\gamma_g B^T PEu_j w_{gi} + \dot{\theta}_{gij}\Big] \tag{46}$$

If adaptation laws (27) and (28), Eq. (46) becomes

$$\dot{V}_1 = 0 \tag{47}$$

$$\dot{V}_2 = -E^T PBG(x)u_r - E^T PB\varepsilon_f(x) - E^T PB\varepsilon_g(x)u_c + E^T PBu_0 - \frac{1}{\eta_f}\tilde{\varepsilon}_f^T\dot{\hat{\varepsilon}}_f - \frac{1}{\eta_g}tr\Big(\tilde{\varepsilon}_g^T\dot{\hat{\varepsilon}}_g\Big) + \frac{1}{\eta}\delta\dot{\delta} \tag{48}$$

Then $\dot{V}_2$ can be bounded as follows

$$\dot{V}_2 \le -E^T PB\sigma_0 u_r + \left|E^T PB\right|\overline{\varepsilon_f} - \left|E^T PB\right|\overline{\varepsilon_g}|u_c| + \left|E^T PB\right||u_0| - \frac{1}{\eta_f}\tilde{\varepsilon}_f^T\dot{\hat{\varepsilon}}_f - \frac{1}{\eta_g}tr\Big(\tilde{\varepsilon}_g^T\dot{\hat{\varepsilon}}_g\Big) + \frac{1}{\eta}\delta\dot{\delta} \tag{49}$$

If we use the adaption laws (29) and (30), Eq. (49) becomes

$$\dot{V}_2 \le -E^T PB\sigma_0 u_r + \left|E^T PB\right||u_0| + \frac{1}{\eta}\delta\dot{\delta} + \hat{\varepsilon}_f\left|E^T PB\right| + \hat{\varepsilon}_g\left|E^T PB\right||u_c| \tag{50}$$

Using (25) et (31), then (50) becomes

$$\dot{V}_2 = 0 \tag{51}$$

From results (47) and (51), (45) can be bounded as follows

$$\dot{V} \leq -\frac{1}{2} E^T Q E \leq 0 \tag{52}$$

$$\dot{V} \leq -\frac{1}{2} \lambda_{Qmin} E^2 \tag{53}$$

where λ_{Qmin} The minimum eigen value of the matrix Q,then by integrating both sides of Eq. (53) from $[0, t]$

$$\int_0^t \|E(\tau)\|^2 d\tau \leq \frac{2}{\lambda_{Qmin}} [V(0) - V(t)] \tag{54}$$

which gives us

$$\int_0^t \|E(\tau)\|^2 d\tau \leq \frac{2}{\lambda_{Qmin}} [\|V(0)\| + \|V(t)\|] \tag{55}$$

As shown by [25], this implies that $E(t) \in L_2$, according to the theory of Lyapunov, $E(t)$ is bounded. On the other hand, from (38) $\dot{E}(t) \in L_\infty$ (bounded) because all members of the right are bounded. According to Barbalat's lemma, we conclude that $\lim_{t\to\infty} \|E(t)\| = 0$.

5 Simulation Results

In this section, we test the proposed indirect adaptive fuzzy control scheme on the tracking control of two-link rigid robot manipulator with the following dynamics [26]:

$$\begin{pmatrix} \ddot{q}_1 \\ \ddot{q}_2 \end{pmatrix} = \begin{pmatrix} M_{11} & M_{12} \\ M_{21} & M_{22} \end{pmatrix}^{-1} \left\{ \begin{pmatrix} u_1 \\ u_2 \end{pmatrix} - \begin{pmatrix} -h\dot{q}_2 & -h\dot{q}_2(\dot{q}_1 + \dot{q}_2) \\ h\dot{q}_1 & 0 \end{pmatrix} \begin{pmatrix} \dot{q}_1 \\ \dot{q}_2 \end{pmatrix} \right\} \tag{56}$$

where

$$M_{11} = a_1 + 2a_3 \cos(q_2) + 2a_4 \sin(q_2)$$
$$M_{22} = a_2$$
$$M_{21} = M_{12} = a_2 + a_3 \cos(q_2) + a_4 \sin(q_2)$$

$$h = a_3 \sin(q_2) - a_4 \cos(q_2)$$

$$a_1 = I_1 + m_1 l_{c1}^2 + I_e + m_e l_{ce}^2 + m_e l_1^2$$

with

$$a_2 = I_e + m_e l_{ce}^2$$
$$a_3 = m_e l_1 l_{ce} \cos(\delta_e)$$
$$a_4 = m_e l_1 l_{ce} \sin(\delta_e)$$

In the simulation, the following parameter values are used $m_1 = 1,\ m_e = 2,\ l_1 = 1,\ l_{c1} = 0.5,\ l_{ce} = 0.6,\ I = 0.12,\ I_e = 0.5,\ \delta_e = 30^\circ$.

$$y = [q_1 q_2] u = [u_1 u_2]$$

$$x = [q_1 \dot{q}_1 q_2 \dot{q}_2]$$

$$F(x) = \begin{pmatrix} f_1(x) \\ f_2(x) \end{pmatrix} = -M^{-1} \begin{pmatrix} -h\dot{q}_2 & -h\dot{q}_2(\dot{q}_1 + \dot{q}_2) \\ h\dot{q}_1 & 0 \end{pmatrix} \begin{pmatrix} \dot{q}_1 \\ \dot{q}_2 \end{pmatrix}$$

$$G(x) = \begin{pmatrix} g_{11}(x) & g_{12}(x) \\ g_{21}(x) & g_{22}(x) \end{pmatrix} = M^{-1} = \begin{pmatrix} M_{11} & M_{12} \\ M_{21} & M_{22} \end{pmatrix}^{-1}$$

Then, the robot system given by (54) can be expressed as $\ddot{y} = F(x) + G(x)u$

The control objective is to force the system output q_1 and q_2 to track the desired trajectories $y_{d1} = \sin(t)$ and $y_{d2} = \sin(t)$, respectively.

To synthesize the indirect adaptive fuzzy controller, six fuzzy systems in the form of (11) are used. Each fuzzy system has $x_1(t)$, $x_2(t)$, $x_3(t)$, and $x_4(t)$ as input, and for each input variable $x_i(t)$, five Gaussian functions are defined as

$$\mu_{F_i^1}(x_i) = \exp\left\{ -\frac{1}{2} \left(\frac{x_i + c_i}{\sigma} \right)^2 \right\} i = 1, 2, 3, 4$$

where $c_i = [-1.25, -0.75, 0, 0.75, 1.25]$ and $\sigma = 0.7$

The robot initial conditions are $x(0) = [0.5; 0; 0.5; 0]$, and the initial values and all parameters of the adaption laws are setting automatically with our proposed OM method.

$$p = [8.12\,0\,2.75\,0; 0\,8.12\,0\,2.75;\ 2.75\,0\,2.62\,0; 0\,2.75\,0\,2.62],$$

$Q = diag(5.5, 5.5, 5, 5),\ k = [10; 01; 20; 02]$, The simulation results for the first link are shown in Fig. 2, those for the second link are shown in Fig. 3, and the control input signals are shown in Fig. 4. We can note that the actual trajectories converge to the desired trajectories and the control signals are almost smooth. These simulation results demonstrate the tracking capability of the proposed indirect adaptive controller and its effectiveness for control tracking of uncertain MIMO nonlinear systems.

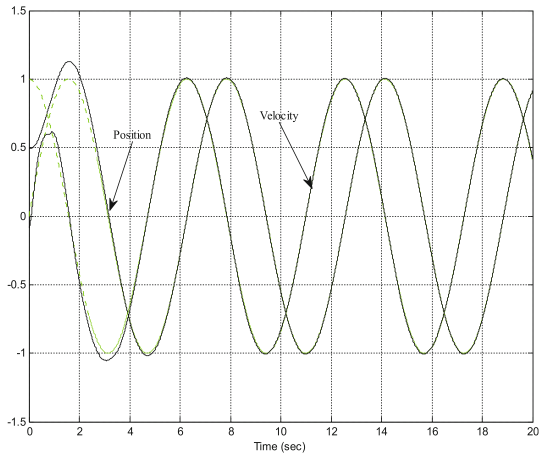

Fig. 2. Tracking curves of link 1: actual (black lines); desired (green lines).

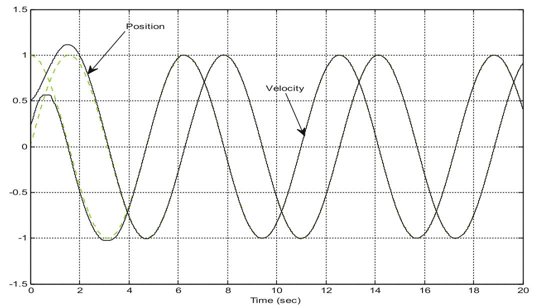

Fig. 3. Tracking curves of link 2: actual (black lines); desired (green lines).

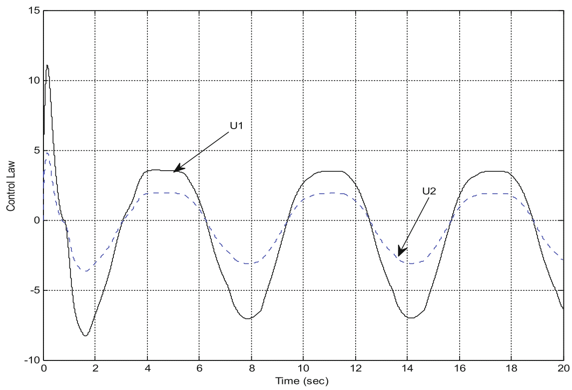

Fig. 4. Control input signals: u_1(black line); u_2(blue line).

6 Conclusion

In this paper, the main contribution of this paper is to propose the indirect adaptive fuzzy controller based on the PSO. The PSO is used to determine the initial knowledge and the adaptation parameters simultaneously. In the other words, the human experts knowledge, fuzzy IF-THEN rules, are incorporated through the initial parameters into the indirect fuzzy control scheme via the PSO. The scheme consists of an adaptive fuzzy controller with a robust control term used to compensate for approximation errors. The adaptive schema is a free from singularity, and new adaptive parameters update law are used, besides, the proposed adaptive schemes allow initialization to zero of all adjustable parameters of the fuzzy systems. This approach do not require the knowledge of the mathematical model of the plant, guarantee the uniform boundedness of all the signals in the closed-loop system, the smooth control signal and asymptotic convergence for error tracking are achieved in the proposed control scheme. Simulation results performed on a two-link robot manipulator illustrate the method. Future works will focus on extension of the approach to more general MIMO nonlinear systems and its improvement by introducing a state observer to provide an estimate of the state vector.

References

1. Lilly, J.H.: Fuzzy Control and Identification, 1st edn. Wiley, New York (2011)
2. Shi, W., Zhang, M., Guo, W., Guo, L.: Stable adaptive fuzzy control for MIMO nonlinear systems. Comput. Math. Appl. **62**, 2843–2853 (2011)
3. Qi, R.: T-S model based indirect adaptive fuzzy control for a class of MIMO uncertain nonlinear systems. In: IEEE Proceedings of the 6th World Congress on Intelligent Control and Automation, pp. 3943–3947, June 2006
4. Gao, Y.: Online adaptive fuzzy neural identification and control of a class of MIMO nonlinear systems. IEEE Trans. Fuzzy Syst. **11**, 3900–3904 (2003)
5. Tlemcani, A., Chekireb, H., Boucherit, M.S., Labiod, S.: Decentralized direct adaptive fuzzy control of nonlinear interconnected MIMO system class. Arch. Control Sci. **17**(4), 357–374 (2007)
6. Labiod, S., Guerra, T.M.: Direct adaptive fuzzy control for a class of MIMO nonlinear systems. Int. J. Syst. Sci. **38**(8), 665–675 (2007)
7. Wang, L.-X.: A Course in Fuzzy Systems and Control, 2nd edn. Prentice-Hall Inc., Englewood Cliffs (1997)
8. Giordano, V., Naso, D., Turchiano, B.: Combining genetic algorithms and Lyapunov-based adaptation for online design of fuzzy controllers. IEEE Trans. Syst. Man Cybern. Part B **36** (5), 1118–1227 (2006)
9. Navale, R.L., Nelson, R.M.: Use of genetic algorithms to develop an adaptive fuzzy logic controller for a cooling coil. Energy Build. **42**(5), 708–716 (2010)
10. Chen, P.C., Chen, C.W., Chiang, W.L.: GA-based modified adaptive fuzzy sliding mode controller for nonlinear systems. Expert Syst. Appl. **36**(3), 5872–5879 (2009)
11. Leu, Y.G., Hong, C.M., Zhon, H.J.: GA-based adaptive fuzzy-neural control for a class of MIMO systems. In: Advances in Neural Networks–ISNN 2007, vol. 4491, pp. 45–53 (2007)

12. Yu, M., Cong, S.: Design of nonlinear motor adaptive fuzzy sliding mode controller based on GA. In: Advanced Intelligent Computing Theories and Applications. With Aspects of Theoretical and Methodological Issues, vol. 5681, pp. 445–451 (2007)
13. Sharma, K.D., Chatterjee, A., Rakshit, A.A.: Hybrid approach for design of stable adaptive fuzzy controllers employing Lyapunov theory and particle swarm optimization. IEEE Trans. Fuzzy Syst. **17**(2), 329–342 (2009)
14. Chatterjee, A., Siarry, P.: A PSO-aided neuro-fuzzy classifier employing linguistic hedge concepts. Expert Syst. Appl. **33**(4), 1097–1109 (2007)
15. Li, C., Wu, T.: Adaptive fuzzy approach to function approximation with PSO and RLSE. Expert Syst. Appl. **38**(10), 13266–13273 (2011)
16. Labiod, S., Guerra, T.M.: Direct and indirect adaptive fuzzy control for a class of MIMO nonlinear systems. In: Advances in Robot Manipulators, vol. 31, pp. 280–298, April 2010
17. Babaie, A., Nikranjbar, A.: Adaptive fuzzy control of uncertain (P-R) robot manipulator using Lyapunov method compared to RLSE. MAjlesi J. Mechatron. Syst. **1**(2), 37–45 (2012)
18. Slotine, J.J., Li, W.: Applied Nonlinear Control. Prentice-Hall Inc., New Jersey (1991)
19. Kosko B.: Fuzzy systems as universal approximator. In: Proceedings of the IEEE Conference on Fuzzy Systems, San Diego, USA, pp. 1153–1162 (1992)
20. Jang, J.R.: ANFIS: adaptive-network-based fuzzy inference system. IEEE Trans. Syst. Man Cybern. **23**(3), 665–685 (1993)
21. Jang, J.S.R., Sun, C.T.: Neuro-fuzzy modeling and control. Proc. IEEE **83**(3), 378–406 (1995)
22. Wang, L.X.: Adaptive Fuzzy Systems and Control. Prentice-Hall, Englewood Cliffs (1994)
23. Eberhart, R.C., Shi, Y.: Particle swarm optimization: developments, applications and resources. In: Proceedings of the Congress on Evolutionary Computation 2001, Seoul, Korea (2001)
24. Clerc, M., Kennedy, J.: The particle swarm—explosion, stability, and convergence in a multidimensional complex space. IEEE Trans. Evol. Comput. **6**(1), 58–73 (2002)
25. Wang, L.X.: Stable adaptive fuzzy control of nonlinear systems. IEEE Trans. Fuzzy Syst. **1** (2), 146–155 (1993)
26. Tong, S., Tang, J., Wang, T.: Fuzzy adaptive control of multivariable nonlinear systems. Fuzzy Sets Syst. **111**, 153–167 (2000)

Renewable Energy (RE)

Comparison Between Three Hybrid System PV/Wind Turbine/Diesel Generator/Battery Using HOMER PRO Software

Chouaib Ammari[1](✉), Messaoud Hamouda[2], and Salim Makhloufi[3]

[1] University Ahmed Draya-Adrar, Adrar, Algeria
chocho.math@gmail.com
[2] LDDI Laboratory, University Ahmed Draya-Adrar, Adrar, Algeria
jhamouda@yahoo.fr
[3] LEESI Laboratory, University Ahmed Draya-Adrar, Adrar, Algeria
makhlofi_s@yahoo.fr

Abstract. In this paper, we will compare between three hybrid systems containing from solar photovoltaic, wind turbine, battery and diesel generator, this last will use for feeding the village when renewable source is insufficient. The hybrid central will distribute energy to rural village in southwest of Algeria called "Timiaouine", the consumption of this village will be detailed in the all the years because the precise sizing is the key to choose optimum configuration for hybrid central. The program used for simulation and optimization is Hybrid Optimization Model for Electric Renewable (HOMER PRO), this program will simulate the central and propose all the configuration possible but just the best configuration economic and ecologic will be choose with take consideration the security energetic of the village.

Keywords: Hybrid central · HOMER PRO · Renewable energy · Solar energy
Wind energy · Diesel generator

1 Introduction

The energy demand growths exponentially every day due to the increase in industry and population, for this reason the world bank and international energy agency estimate doubling in installing capacity of energy over the 4 following decades [1]. Renewable energy sources are powerless to meet energy demand because some sources richness with season like solar and wind energy, or depend on the location like hydroelectric, and produce clean electricity [2, 3]. However, the drawbacks of renewable energy sources can be limited by using solar energy in a hybrid system [4].

The electric energy system made up of one renewable source and another conventional source named Hybrid Renewable Energy Systems (HRES) [5], that system can work in off-grid (standalone) or grid connected mode.

The hybrid energy systems composed essentially from renewable energy generators (AC/DC sources), nonrenewable generators (AC/DC sources), power conditioning unit, storage, load (AC/DC) and sometimes may include grid [6].

M. Chadli et al. (Eds.): ICEECA 2017, LNEE 522, pp. 227–237, 2019.
https://doi.org/10.1007/978-3-319-97816-1_17

HRES can use one or both of the renewable sources (solar photovoltaic and wind turbine) in combination with storage system like fuel cell, batteries or ultra-capacitor. This back up energy devices (or named also secondary sources) are introduced into the system to supply the shortage power and to cover the pic consumption [5].

In some cases, the system can be 100% on renewables source by eliminating the diesel generators and replace via large storage capacity, but this has a strong impact on overall system cost [7]. There are many combinations for hybrid energy systems such as solar, wind, hydroelectric, or geothermal with conventional sources like diesel generator and storage device (battery or fuel cell) [8].

We can classify HRES by capacity installed, these systems vary from few kW to hundreds of kW, with a capacity less than 5 kW can be treated as the small systems, this kind of systems is generally used to serve the loads of a remotely located home or a telecommunication relay system. Then the systems with the capacity more than 5 kW and less than 100 kW can be treated as the medium systems, these are used to power remotely located community which contains several homes another required amenities. The medium systems in most cases work in stand-alone mode and sometimes may be connected to utility grid, if it is nearby. The other type of the system is able to cover the energy of a region, with the capacity of more than 100 kW can be called as the large system. These systems are generally connected to grid, to enable the power exchange between the grid and the system in case of surplus or deficiency [9] and stay the uses of small isolated HRES is predictable to grow extremely in the near future [10].

In order to find the optimal sizing and operational strategy for a hybrid renewable energy system, HOMER PRO software is one of the best program work in hybrid system. This soft-ware based on three principal tasks which are simulation, optimization and sensitivity analysis [11].

HRES will become popular for standalone power generation because is its very improvement and efficiency increment in renewable energy technologies and power electronic converters [12].

2 System Description

The hybrid central are composed from:

- Solar photovoltaic.
- Wind turbine.
- Diesel generator.
- Storage system.

The connection of hybrid system is illustrated in the below Fig. 1:

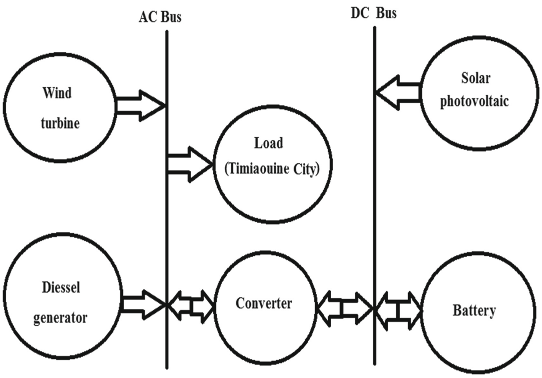

Fig. 1. Hybrid system connection

3 Hybrid Central Sizing

For size a hybrid central in HOMER PRO, we should follow these steps:

3.1 Load Consumption

The load profile is an important step to find whether the energy produced by the central is matching the load demand [9], Arabali et al. [13] propose a method for the hourly load variation by using Gaussian distribution with specific limits. The statistical methods are also generally used for the estimation of the residential energy consumption [14].

The HOMER PRO program filed loads according to their type (home, commercial, industrial or city) and proposed model for each type.

In our case, the load is consumption of Timiaouine city. We will describe in this part just the consumption for houses, because it presents 98% from global consumption of this rural village.

3.2 Housing Consumption

We classified the consumption in two seasons; a season when consumption is low (winter), and a season when consumption is high (summer).

In winter season, we noticed that most consumption of houses is in the refrigerator and light (45%), the other consumption divided between the rest devices, the consumption rest low and equal 16,17 kWh/day

In the high season consumption, the air-conditioner presents more than 60% from the global house load, the daily consumption is 46,9 kWh.

3.3 Total Village Consumption

Timiaouine town consumes 7,52 MWh every day in winter and 23 MWh/day in summer (Fig. 2), the household presents 93% from global consumption, the second most consumption is the schools by 5% (secondary and primary).

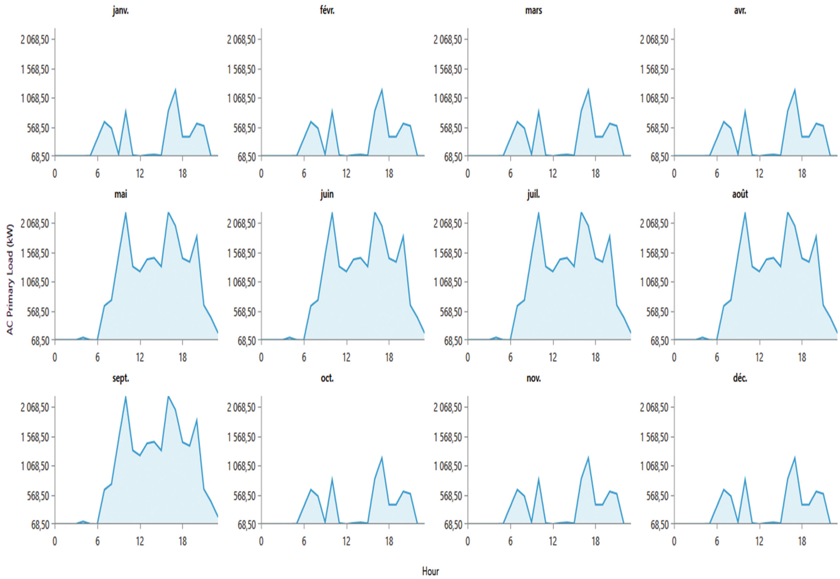

Fig. 2. Annual village consumption

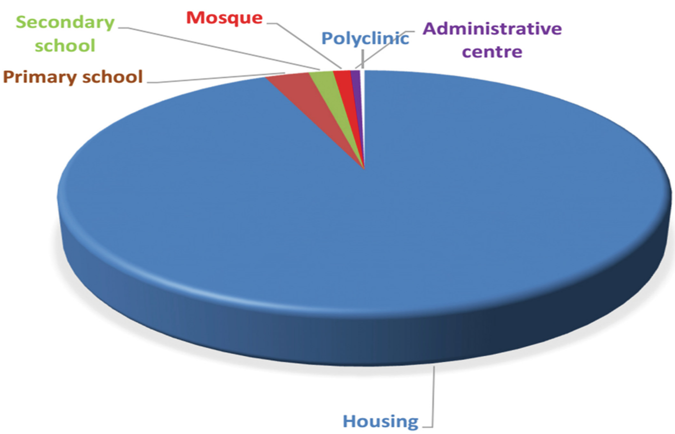

Fig. 3. Description of consumption [15]

Figure 3 present description of consumption in rural village, on note that houses present most village consumption due number of houses and low commercial and industrial activity in this place.

3.4 Weather Data

The climatic conditions play a major role, as the entire power generation is dependent on this. For every different location, the weather conditions will be different. Therefore, for a feasibility study or for optimal sizing of the hybrid systems, weather data is a very

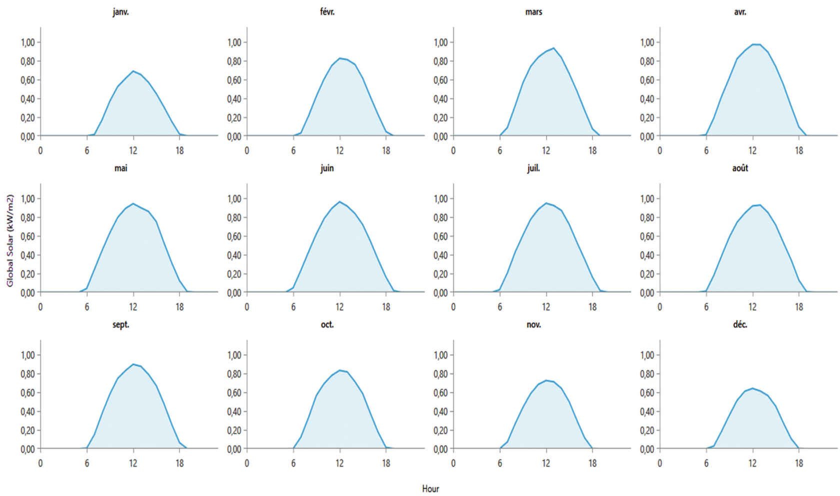

Fig. 4. Global solar daily profile

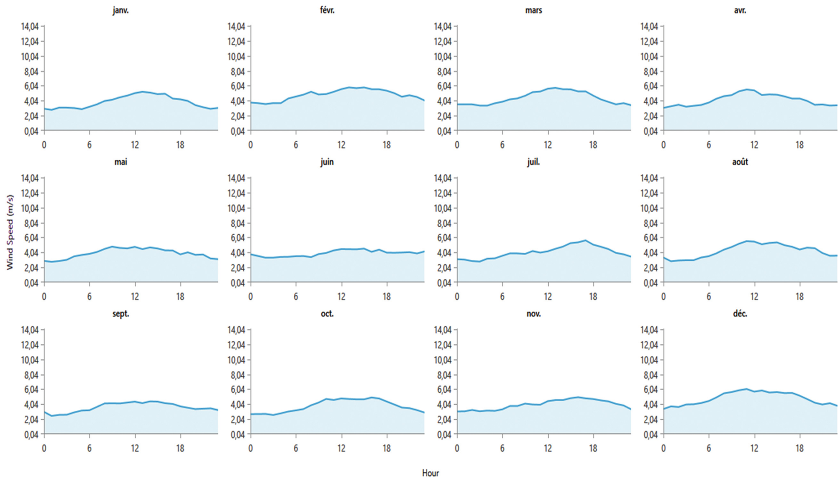

Fig. 5. Wind speed daily profile

important tool for analyzing the climatic conditions thoroughly before setting up a plant. Such data is mostly available at the local meteorological stations, for some potential sites, the space research agencies like national aeronautics and space administration (NASA) have made the data available through the web resources [9], the Figs. 4 and 5 characterize the weather data for Timiaouine city.

4 Generator Sizing

4.1 Solar Photovoltaic

The initial capital cost is 138600DZD/kWh (1€ = 126DZD), 138600DZD for the replacement and the cost of maintenance it takes 1260DZD, the lifetime of panel is 25 years.

Photovoltaic generator is size with 2800 kW in first configuration used PV/DG/Battery and 2300 kW in second configuration when this system combined from PV/Wind turbine/DG.

4.2 Wind Turbine

In third configuration, hybrid system composes from WT/DG/Battery use eight (8) wind turbines but the second configuration (PV/WT/DG/battery) use just four (4) wind turbine in hybrid central.

Wind turbine uses in all configuration proposed in this study is wind turbine mark GAMESA, type G52 with 850 kW power output, the cost of this type is 1,8 million euro and is the same for replacement, the maintenance costed at 2309958DZD.

4.3 Diesel Generator

Generator diesel is used like support in peak load or absence of the renewable generators production (solar or wind). The initial cost is 63000DZD/kWh, this price is the same price for replacement with 15000 h for the lifetime. The next table summarizes the capacity of DG for three configurations (Table 1):

Table 1. Comparison between capacities of DG in three-hybrid systems

Hybrid system component	Capacity of DG proposed from HOMER PRO (kW)
PV/DG/battery	1800
PV/DG/WT/battery	2300
WT/DG/battery	2200

5 Results and Comparison

To select best hybrid systems, full comparison technique, economic and ecologic between three-hybrid systems to choose the better between them, the simulation and optimization of these systems are doing it by HOMER PRO software.

HOMER PRO software simulates and optimized systems based on three steps:

1- Selection of components (load profile, meteorological data and generator installed on system).
2- Comparison a wide range of generators with different constraints and sensitivities in techno-economic analysis, this analysis uses life-cycle cost (LCC) of the system and equal to present value of all the costs of installing and operating that component over the project lifetime, minus the present value of all the revenues that it earns over the project lifetime.
3- The final step is optimization; simulated systems are arranged and filtered due to criteria that choose in step two [16, 17].

Figures 6, 7 and 8 present result of simulation for PV/DG/battery, PV/WT/DG and WT/DG/battery respectively.

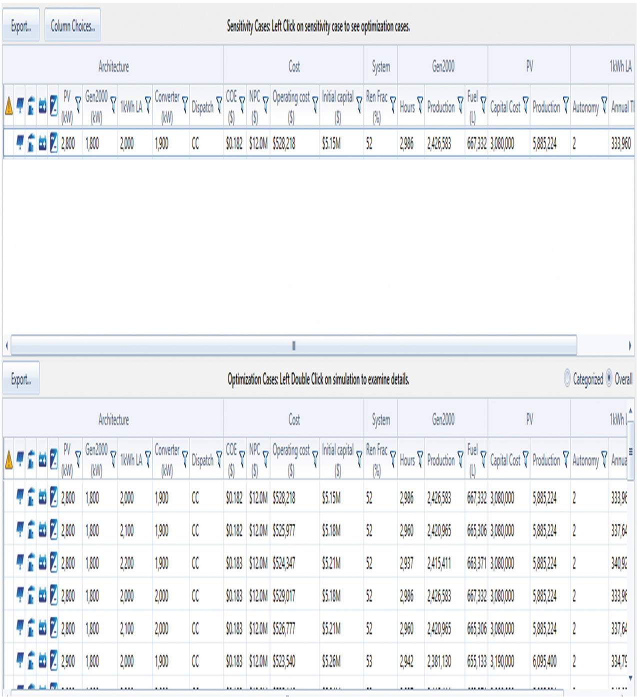

Export... Column Choices... Sensitivity Cases: Left Click on sensitivity case to see optimization cases.

Architecture					Cost				System	Gen2000			PV		1kWh LA	
PV (kW)	Gen2000 (kW)	1kWh LA	Converter (kW)	Dispatch	COE ($)	NPC ($)	Operating cost ($)	Initial capital ($)	Ren Frac (%)	Hours	Production	Fuel (L)	Capital Cost	Production	Autonomy	Annual Tl
2,800	1,800	2,000	1,900	CC	$0.182	$12.0M	$528,218	$5.15M	52	2,986	2,426,583	667,332	3,080,000	5,885,224	2	333,960

Export... Optimization Cases: Left Double Click on simulation to examine details. Categorized Overall

Architecture					Cost				System	Gen2000			PV		1kWh L	
PV (kW)	Gen2000 (kW)	1kWh LA	Converter (kW)	Dispatch	COE ($)	NPC ($)	Operating cost ($)	Initial capital ($)	Ren Frac (%)	Hours	Production	Fuel (L)	Capital Cost	Production	Autonomy	Annua
2,800	1,800	2,000	1,900	CC	$0.182	$12.0M	$528,218	$5.15M	52	2,986	2,426,583	667,332	3,080,000	5,885,224	2	333,96
2,800	1,800	2,100	1,900	CC	$0.182	$12.0M	$525,977	$5.18M	52	2,960	2,420,965	665,306	3,080,000	5,885,224	2	337,64
2,800	1,800	2,200	1,900	CC	$0.183	$12.0M	$524,347	$5.21M	52	2,937	2,415,411	663,371	3,080,000	5,885,224	2	340,92
2,800	1,800	2,000	2,000	CC	$0.183	$12.0M	$529,017	$5.18M	52	2,986	2,426,583	667,332	3,080,000	5,885,224	2	333,96
2,800	1,800	2,100	2,000	CC	$0.183	$12.0M	$526,777	$5.21M	52	2,960	2,420,965	665,306	3,080,000	5,885,224	2	337,64
2,900	1,800	2,000	1,900	CC	$0.183	$12.0M	$523,540	$5.26M	53	2,942	2,381,130	655,133	3,190,000	6,095,400	2	334,7

Fig. 6. Simulation of PV/DG/battery system

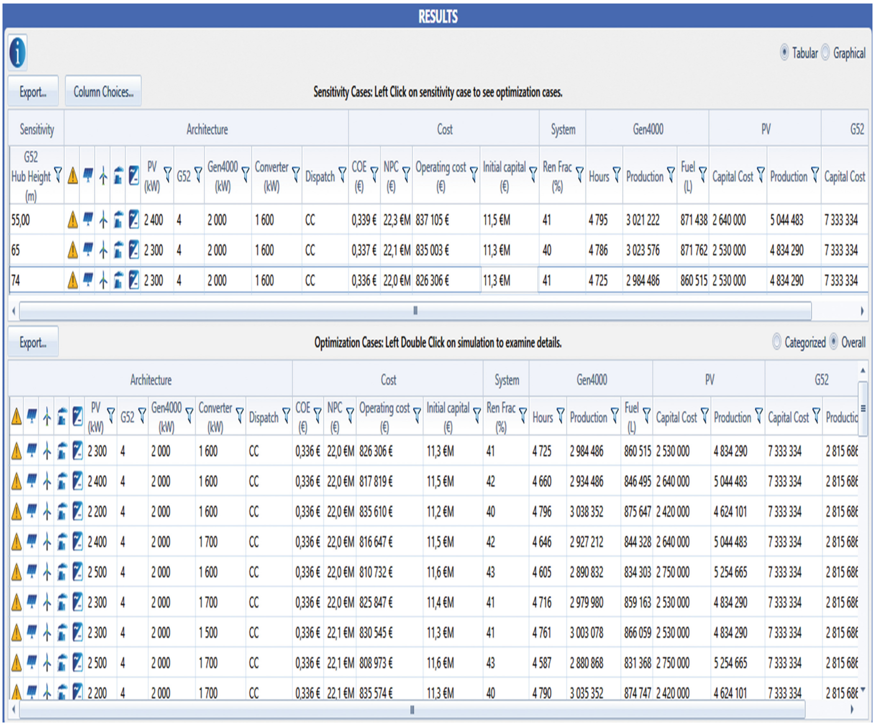

RESULTS

Sensitivity Cases: Left Click on sensitivity case to see optimization cases.

Sensitivity	Architecture					Cost				System	Gen4000			PV		G52
G52 Hub Height (m)	PV (kW)	G52	Gen4000 (kW)	Converter (kW)	Dispatch	COE (€)	NPC (€)	Operating cost (€)	Initial capital (€)	Ren Frac (%)	Hours	Production	Fuel (L)	Capital Cost	Production	Capital Cost
55,00	2 400	4	2 000	1 600	CC	0,339 €	22,3 €M	837 105 €	11,5 €M	41	4 795	3 021 222	871 438	2 640 000	5 044 483	7 333 334
65	2 300	4	2 000	1 600	CC	0,337 €	22,1 €M	835 003 €	11,3 €M	40	4 786	3 023 576	871 762	2 530 000	4 834 290	7 333 334
74	2 300	4	2 000	1 600	CC	0,336 €	22,0 €M	826 306 €	11,3 €M	41	4 725	2 984 486	860 515	2 530 000	4 834 290	7 333 334

Optimization Cases: Left Double Click on simulation to examine details.

Architecture					Cost				System	Gen4000			PV		G52	
PV (kW)	G52	Gen4000 (kW)	Converter (kW)	Dispatch	COE (€)	NPC (€)	Operating cost (€)	Initial capital (€)	Ren Frac (%)	Hours	Production	Fuel (L)	Capital Cost	Production	Capital Cost	Productic
2 300	4	2 000	1 600	CC	0,336 €	22,0 €M	826 306 €	11,3 €M	41	4 725	2 984 486	860 515	2 530 000	4 834 290	7 333 334	2 815 68
2 400	4	2 000	1 600	CC	0,336 €	22,0 €M	817 819 €	11,5 €M	42	4 660	2 934 486	846 495	2 640 000	5 044 483	7 333 334	2 815 68
2 200	4	2 000	1 600	CC	0,336 €	22,0 €M	835 610 €	11,2 €M	40	4 796	3 038 352	875 647	2 420 000	4 624 101	7 333 334	2 815 68
2 400	4	2 000	1 700	CC	0,336 €	22,0 €M	816 647 €	11,5 €M	42	4 646	2 927 212	844 328	2 640 000	5 044 483	7 333 334	2 815 68
2 500	4	2 000	1 600	CC	0,336 €	22,0 €M	810 732 €	11,6 €M	43	4 605	2 890 832	834 303	2 750 000	5 254 665	7 333 334	2 815 68
2 300	4	2 000	1 700	CC	0,336 €	22,0 €M	825 847 €	11,4 €M	41	4 716	2 979 980	859 163	2 530 000	4 834 290	7 333 334	2 815 68
2 300	4	2 000	1 500	CC	0,336 €	22,1 €M	830 545 €	11,3 €M	41	4 761	3 003 078	866 059	2 530 000	4 834 290	7 333 334	2 815 68
2 500	4	2 000	1 700	CC	0,336 €	22,1 €M	808 973 €	11,6 €M	43	4 587	2 880 868	831 368	2 750 000	5 254 665	7 333 334	2 815 68
2 200	4	2 000	1 700	CC	0,336 €	22,1 €M	835 574 €	11,3 €M	40	4 790	3 035 352	874 747	2 420 000	4 624 101	7 333 334	2 815 68

Fig. 7. Simulation of PV/WT/DG system

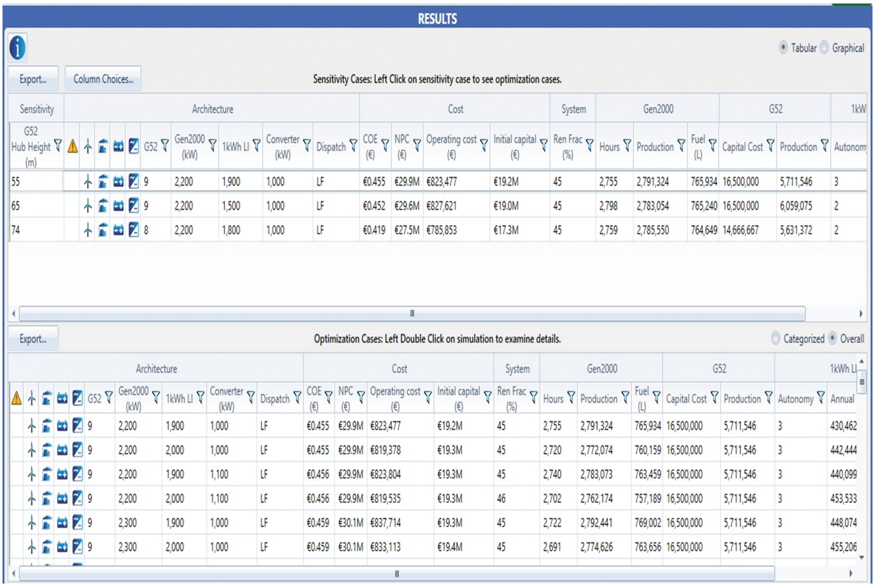

RESULTS

Sensitivity Cases: Left Click on sensitivity case to see optimization cases.

Sensitivity	Architecture					Cost				System	Gen2000			G52		1kW
G52 Hub Height (m)	G52	Gen2000 (kW)	1kWh LI	Converter (kW)	Dispatch	COE (€)	NPC (€)	Operating cost (€)	Initial capital (€)	Ren Frac (%)	Hours	Production	Fuel (L)	Capital Cost	Production	Autonom
55	9	2,200	1,900	1,000	LF	€0.455	€29.9M	€823,477	€19.2M	45	2,755	2,791,324	765,934	16,500,000	5,711,546	3
65	9	2,200	1,500	1,000	LF	€0.452	€29.6M	€827,621	€19.0M	45	2,798	2,783,054	765,240	16,500,000	6,059,075	2
74	8	2,200	1,800	1,000	LF	€0.419	€27.5M	€785,853	€17.3M	45	2,759	2,785,550	764,649	14,666,667	5,631,372	2

Optimization Cases: Left Double Click on simulation to examine details.

Architecture					Cost				System	Gen2000			G52			1kWh LI
G52	Gen2000 (kW)	1kWh LI	Converter (kW)	Dispatch	COE (€)	NPC (€)	Operating cost (€)	Initial capital (€)	Ren Frac (%)	Hours	Production	Fuel (L)	Capital Cost	Production	Autonomy	Annual
9	2,200	1,900	1,000	LF	€0.455	€29.9M	€823,477	€19.2M	45	2,755	2,791,324	765,934	16,500,000	5,711,546	3	430,462
9	2,200	2,000	1,000	LF	€0.455	€29.9M	€819,378	€19.3M	45	2,720	2,772,074	760,159	16,500,000	5,711,546	3	442,444
9	2,200	1,900	1,100	LF	€0.456	€29.9M	€823,804	€19.3M	45	2,740	2,783,073	763,459	16,500,000	5,711,546	3	440,099
9	2,200	2,000	1,100	LF	€0.456	€29.9M	€819,535	€19.3M	46	2,702	2,762,174	757,189	16,500,000	5,711,546	3	453,533
9	2,300	1,900	1,000	LF	€0.459	€30.1M	€837,714	€19.3M	45	2,722	2,792,441	769,002	16,500,000	5,711,546	3	448,074
9	2,300	2,000	1,000	LF	€0.459	€30.1M	€833,113	€19.4M	45	2,691	2,774,626	763,656	16,500,000	5,711,546	3	455,206

Fig. 8. Simulation of WT/DG/battery system

In sensitivity case present different technical parameter influence to size or cost of systems like height of wind turbine, below sensitivity case, they are optimization case, in this part on show different systems proposed with different cost and size.

5.1 Technique Comparison

The table below summarized the technical parameter for three different configurations:

The hybrid system uses PV/WT/DG is the best technically, because it produces energy more than the other configuration, use all the renewable resource available in the site and cover all the consumption over the year (Table 2).

Table 2. Technical comparison between three-hybrid systems

Hybrid system component	Annual production (GWh)	Energy renewable %	Unmet load kW/year	PV kW	WT quantity	DG kW	Battery kWh
PV/DG/battery	8.31	71%	0	2800	0	1800	2000
PV/DG/WT/battery	10.63	71%	0	2300	4	2000	0
WT/DG/battery	8.41	67%	69	0	8	2200	1800

5.2 Economic and Ecologic Comparison

In this section, the comparison between three systems will be hold on economic parameter (levelized cost, global investment cost) and ecologic parameter (fuel annually consumption, dioxide emission) (Table 3).

Table 3. Economic and ecologic comparison between three-hybrid systems

Hybrid system component	Investment cost (billion Dinnar)	Levelized cost (DZD/kWh)	Fuel cons (L/year)	CO2 Emissions (kg/year)
PV/DG/battery	1.49	22.932	667332	1757305
PV/DG/WT/battery	2.77	42.336	860515	2266018
WT/DG/battery	3.45	52.794	764649	2013572

After comparison between three configuration, the hybrid systems best economically is the system who use PV/DG/battery, this system have low investment cost than the other and produce energy with attractive cost more than the last two systems, in same time this systems produce dioxide carbon too much low than others, that main this hybrid systems is the most systems economic and produce green energy more than the other configuration.

In the end, the best system proposed from HOMER PRO is the systems who uses PV/DG/battery, because he produce green energy with attractive cost, cover all the consumption of this rural village and offer for this people to live life better than what he lives now.

6 Conclusion

In this study, a comparison between three different hybrid systems has simulated and optimized using HOMER PRO software for feeding rural village situated in southwest Algeria named “Timiaouine”.

The optimum configuration proposed is a hybrid central produce more than 8 GWh every year, most of this energy is produced from renewable source (71%), this result is better than other study by Sen and Bhattacharyya [16] when he use hybrid central base on solar photovoltaic, bio diesel, hydropower and batteries with levelized cost of energy (LCOE) equal 55.692DZD/kWh.

After comparison between different configurations, the better is the uses of PV/DG/ battery to produce clean energy with acceptable cost.

References

1. Türkay, B.E., Telli, A.Y.: Economic analysis of standalone and grid connected hybrid energy systems. Renew. Energy **36**(7), 1931–1943 (2011)
2. Hepbasli, A.: A key review on energetic analysis and assessment of renewable energy resources for a sustainable future. Renew. Sustain. Energy Rev. **12**(3), 593–661 (2008)
3. Nayar, C.V., Islam, S.M., Dehbonei, H., Tan, K., Sharma, H.: Power electronics for renewable energy sources. In: Rashid, M.H. (ed.) Power Electronics Handbook, 2nd edn. Academic Press – Imprint of Elsevier Inc, United Kingdom, pp. 673–716 (2007)
4. Ijumba, N.M., Wekesah, C.W.: Application potential of solar and mini-hydro energy sources in rural electrification. In: 1996 IEEE AFRICON 4th AFRICON (1996)
5. Bajpai, P., Dash, V.: Hybrid renewable energy systems for power generation in stand-alone applications: a review. Renew. Sustain. Energy Rev. **16**, 2926–2939 (2012)
6. Upadhyay, S., Sharma, M.P.: A review on configurations, control and sizing methodologies of hybrid energy systems. Renew. Sustain. Energy Rev. **38**, 47–63 (2014)
7. AndreMalheiro, P.M., Castro, R.M., Lima, A.E.: Integrated sizing and scheduling of wind/PV/diesel/battery isolated systems. Renew. Energy **83**, 646–657 (2015)
8. Díaz, P., Arias, C.A., Peña, R., Sandoval, D.: FAR from the grid: a rural electrification field study. Renew. Energy **35**(12), 2829–2834 (2010)
9. Mahesh, A.: Kanwarjit Singh Sandhu Hybrid wind/photovoltaic energy system developments: critical review and findings. Renew. Sustain. Energy Rev. **52**, 1135–1147 (2015)
10. Al Busaidi, A.S., Kazem, H.A., Al-Badi, A.H., Khan, M.F.: A review of optimum sizing of hybrid PV– Wind renewable energy systems in Oman. Renew. Sustain. Energy Rev. **53**, 185–193 (2016)
11. Razak, N.A.A., bin Othman, M.M., Musirin, I.: Optimal sizing and operational strategy of hybrid renewable energy system using HOMER. In: The 4th International Power Engineering and Optimization Conference/MALAYSIA, 23–24 June 2010
12. Marques, A.J., Boccaletti, C., Ribeiro, E.F.F.: Uninterruptible energy production in standalone power systems for tele-communications. Presented at the International Conference on Renewable Energies and Power Quality (ICREPQ 2009), Valencia, Spain (2009)
13. Arabali, A., Ghofrani, M., Etezadi-Amoli, M., Fadali, M.S., Baghzouz, Y.: Genetic algorithm-based optimization approach for energy management. IEEE Trans. Power Deliv. **28**(1), 162–170 (2013)

14. Nelson, F., Biswas, M.A.R.: Regression analysis for prediction of residential energy consumption. Renew. Sustain. Energy Rev. **47**, 332–343 (2015)
15. Chouaib, A., Messaoud, H., Salim, M.: Sizing, modelling and simulation for Hybrid Central PV/wind turbine/diesel generator for feeding rural village in South Algeria. EAI Endorsed Trans. Energy Web Inf. Technol. **4**(15). https://doi.org/10.4108/eai.13-12-2017.153470
16. Sen, R., Bhattacharyya, S.C.: Off-grid electricity generation with renewable energy technologies in India: an application of HOMER. Renew. Energy **62**, 388–398 (2014)
17. Barbier, T.: Optimisation de la stratégie et du dimensionnement des systèmes hybrides Eolien, Diesel, Batteries pour sites isoles, mémoire en Génie Industrie, Septembre 2013

Indoor and Outdoor Measurements of PV Module Performance of Different Manufacturing Technologies

Lazhar Lalaoui[1(✉)], Mohamed Bouafia[1], Said Bouzid[1], Matthias Kugler[2], Maximilian Zentgraf[2], Philip Schinköthe[2], and Sabine Nieland[2]

[1] Applied Optics Laboratory, Institute of Optics and Precision Mechanics, University Setif -1-, Campus (Ex-Travaux Publics), Avenue Saïd Boukhraïssa, 19000 Maabouda, Setif, Algeria
lalaoui-lazhar@univ-setif.dz, Bouafia_med@yahoo.fr, said_bouzid@yahoo.fr

[2] SolarTestLab Laboratory, CiS Forschungsinstitut für Mikrosensorik und Photovoltaik GmbH, Konrad-Zuse-Str. 14, 99099 Erfurt, Germany
{mkugler,mzentgraf,pschinkoethe,snieland}@cismst.de

Abstract. In the present paper, an experimental analysis of the PV modules efficiency of different photovoltaic comprising monocrystalline silicon, poly-crystal-line silicon and thin-film silicon technologies has been made. The PV modules were first subjected to thorough indoor evaluation (Sun simulator, Electroluminescence) to check the real characteristics and internal defects that make the effectiveness of these modules lower compared to characteristics declared by the manufacturer under the terms of DIN EN ISO/IEC 17025:2005. Results of the first analysis have been taken as a reference for the second part, which consist of ex-posing the PV modules to various natural factors in outdoor environment (solar radiation, temperature, wind, humidity…) versus time. Then, using the peak power measuring device PVPM, different electrical characteristics of the photovoltaic module during the exposure in operating site were determined. Significant differences in the energy efficiency of PV modules have been presented. The analysis of the photovoltaic efficiency has allowed a better comparison between PV technologies better for a specific environment (semi-humid region).

Keywords: Photovoltaic efficiency · Sun simulator test · Electroluminescence image test · Climate environment

1 Introduction

For a very long time, the man has searched to use the energy emitted by the sun [1, 2]. Most uses are direct as in agriculture, through the photosynthesis, or in the various applications of drying and heating, as much handmade but not as industrial [1]. This energy is available in abundance on all earth surface, and despite an important mitigation during the atmosphere passage, the remaining amount remains still important when it reaches the ground. Thus, we can count crest on 1000 W/m^2 in the temperate zones and to 1400 W/m^2 when the atmosphere is weakly polluted in dust or water [2, 3]. The various

M. Chadli et al. (Eds.): ICEECA 2017, LNEE 522, pp. 238–250, 2019.
https://doi.org/10.1007/978-3-319-97816-1_18

studies undertaken so far on the potential energizing solar make to appear a considerable potential for the using and the exploitation of this form of energy [1–4]. The photovoltaic (PV) technology is the most simple and elegant way to harness solar energy. PV converts insolation (solar radiation) directly into electricity by solar cells [4]. Today, energy production through PV technology is growing rapidly compared to other conventional power generation technologies. However, environment (temperature [5], wind [6], humidity [6], solar radiation [7]) has a significant impact on the performance (i.e. efficiency) of a PV module technology. The geographic location, tilt angle, operating condition, and equipment used are important parameters in the evaluation and discussion of the results of our work. Their effects make it possible to choose the best conditions for achieving the best photovoltaic efficiency [8]. Over the years, photovoltaic (PV) modules have gained a reputation for their reliability. Hence, some modules degrade or even fail when exposed outdoors for extended periods of time, especially when conditions are severe. Factors such as thermal cycling [9, 10], ultraviolet absorption [11], loss of adhesion and moisture ingress [12] may be the causes of the degradation of these PV modules [13–16]. The global objective of the present paper is the demonstration effect of the environment on the efficiency of PV modules, by analysis of various parameters that can contribute to the optimisation of the energy efficiency. Three different technologies of photovoltaic modules are used:

- Crystalline silicon (c-Si):
  - Monocrystalline silicon (m-Si); (three PV modules).
- Polycrystalline silicon (p-Si); (three PV modules).
  - Thin film silicon.
  - Amorphous silicon single junction; (1j, a-Si); (one PV module).

The indoor and outdoor measurements of photovoltaic modules performance allowed us to know the environmental impact on performance behaviour quantified for different PV modules in the same climate. we compared various photo-voltaic module technologies in taking into account the cost, the efficiency and the variability of the power delivered according to the illumination: the central objective being to determine the technology most adapted to a region like Thuringia, relatively not very sunny (cloudy, semi-humid region).

2 Equipment and Experimental Setup

2.1 Peak Power Measuring Device for PV-Modules

The devices of type (PVPM/1000C100) enables the measurement of the I-V curve of photovoltaic modules as well as of strings. By a new developed procedure [17], the device can measure and calculate the peak power Ppk, the Rs and Rp directly at the place of assembly of the PV system. Calculation results and the diagram can be displayed on the internal LCD-display. The PVPM automatically measures the I-V-characteristic of the generator at a capacitive load. From the measured data, the PVPM calculates: Pmax, Rs, Rp, FF, and plots the I-V characteristic of photovoltaic module [17, 18] (see Fig. 1). The measurements and data are automatically stored in an integrated permanent memory (can store 1000 measurements), and thus are available to be transferred to a computer [18, 19]. The device is equipped with a standard solar radiation sensor for a measurement range [0–1300 W/m^2] and a thermocouple [−40 °C/+ 120 °C], and PC software PVPMdisp 2.3.3.4 © 13 PV engineering GmbH [19]. The peak power is the power of a module under Standard Test Conditions (STC) IEC60904-3: STC Irradiance 1000 W/m^2, Spectrum AM = 1.5, Cell Temper. 25 °C. So far, the very sumptuous measurement of the peak power was possible only in particularly suited laboratories. By a new procedure [17], which was developed by Professor Wagner at the University of Applied Sciences Dortmund (patented), the measurement with the PVPM can easily be performed.

Fig. 1. Peak power measuring device PVE Photovoltaik engineering (PVPM/1000c100).

2.2 Photovoltaic (PV) Modules

All the following characteristics are given by the manufacturers of photovoltaic modules.

2.2.1 Bosch m-Si M60 Eu 44 117

Crystalline Solar Module compound of 60 cells monocrystalline silicon in the format of 156 mm × 156 mm are connected in series with a maximum power of 240 Wp. This module is protected by a tempered glass plate and an EVA resin, an impermeable back sheet, an anodized aluminum frame, connection box (IP65) with three bypass diodes. (IEC 61215 and IEC 61730 safety class II).

2.2.2 PVTEC POLSKA MU 235

Polycrystalline technology module is composed of 60 cells, format 156 mm × 156 mm connected in series with a maximum power of 235 Wp, protected by a glass plate with 4 mm ESG (laminated safety glass) and EVA resin, an impermeable back sheet, an anodized aluminum frame, connection box (IP65) with three by-pass diodes 12A (Table 1). Certified according to IEC 61730 and IEC 61215 norms.

Table 1. Specifications of the photovoltaic modules tested (datasheet).

	m-Si Bosch Solar m-Si M 60	p-Si PVTEC MU 235	a-Si GET-100-AT
Performance at standard test conditions STC: 1000w/m^2 AM 1.5, 25 °C			
P_{mpp} [W_p]	240 (–0/+ 4,99)	235 (–0/+ 3%)	101.39
V_{mpp} [V]	30.00	28.9	76.58
I_{mpp} [A]	8.10	8.16	1.32
V_{oc} [V]	37.40	37.2	95.84
I_{sc} [A]	8.60	8.68	1.50
η [%]	15.77	14.47	7.03
V_{max} [V] $_{system}$	1000	1000	1000
L × W × H [mm]	1660 × 990 × 50	1680 × 1030 × 30	1100 × 1335 × 7
Weight [Kg]	21	21	25
Connector	MC4	MC4	MC4

2.2.3 Green Energy Technology GET-100-AT

Thin film technology module is thin film single junction amorphous silicon module formed by a multilayer of thin-film of different materials, this multilayer is protected by a tempered glass plate and EVA resin, anodized aluminum alloy, silver, UL1703 certified, the connection box (IP67) with 03 bypass diodes 10 A (Table 1). Produced with accordance with IEC 61646/61730 norms.

2.3 Characterization Techniques

The aging phenomenon and degradation of characteristics over time [5, 6, 8], occur for non-equilibrium systems that evolve over time to reach their states of more stable equilibrium [9, 20]. Considering the latter phenomenon, it is necessary to know the initial characteristics of PV modules, for this reason, preliminary measurements have been made at the CIS SolarTestLab laboratory, Erfurt (Germany). We have applied two characterization techniques (Electrical and Optical), the first to study the I-V characteristics of photovoltaic modules and the efficiency (Flash-test or Sun Simulator), and the second to study the internal structure of solar cells (Electroluminescence image).

2.3.1 Sun Simulator/Flash-Test (Indoor)

The purpose of the Sun Simulator is to provide a controllable indoor test facility under laboratory conditions, used for the testing of Si wafer, solar cells, PV module. Most manufacturers call this technique the flash-test or Sun Simulator (BERGER Module tester type PSS 8-AU) (see Fig. 2). The Sun Simulator is a test to measure the output performance of a solar photovoltaic module, and also is a standard procedure at manufacturers to ensure the operability of each module. During a flash-test, the photovoltaic module is exposed to a short (3 ms) bright (100 mW per sq.cm), the flash light from a xenon filled arc lamp. The output spectrum of this lamp is as close to the spectrum of the sun as possible. The out-put signal is collected by PSL SCD device (Pulsed Solar

Load and Measuring Device) simulating the resistance controlled by a computer, and then the data is compared to a reference solar module. The Sun Simulator is periodically standardized by calibration using a standard module with traceability of its measurements to TGA GmbH under the terms of DIN EN ISO/IEC 17025:2005) [21]. In-deed, the measurement on Sun Simulator can be considered as reference data that is geared to the power output calibrated to standard solar irradiation. The Sun Simulator results are compared to the specifications of the photovoltaic module datasheet printed on the label on the module's backside [15, 16, 22]. The objective of the presented experimental investigation is to determine the performance degradation of the photovoltaic modules, which were exposed already to various factors during exposure on natural site (outside), and then to check the peak power and the efficiency of these photovoltaic modules.

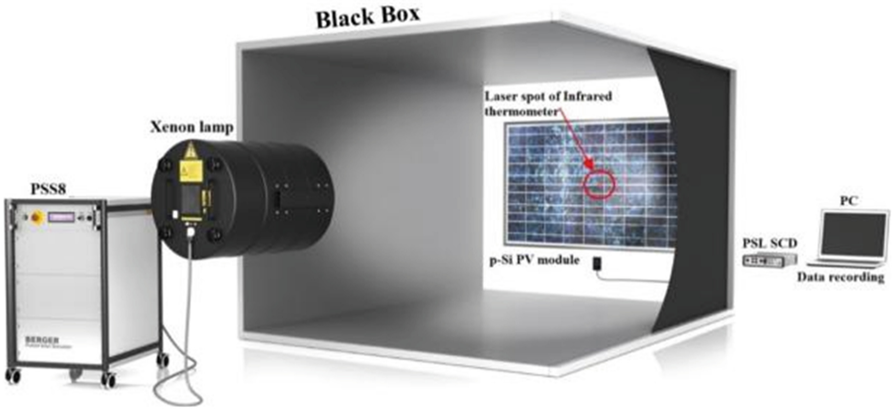

Fig. 2. BERGER Module tester type PSS 8-AU: Sun simulator (from BERGER Lichttechnik February 2018).

2.3.2 Electroluminescence Solar Module Tester (Indoor)

The inspection of PV modules through electroluminescence test becomes fundamental due to the improvement of material and production processes. The electroluminescence PV module tester (EL) is an imaging measurement process that allows us to peer directly into the cells of a solar module and locate potential defects that could have a negative impact on power as well as a module's lifespan [23]. In particular it is possible to identify micro cracks, degradation and shunted area on cells. A tension V (for I = 9A) extern is applied to the borders of the module (with measuring temperature 23 °C) which causes a recombination of electrons in cells, which also causes an emission of photons in the near infrared range, which is invisible to the human eye. In a general way: more the brilliance of photons emitted by a part of the cell is important, more this part will be active during the electricity production. this phenomenon has been discussed in detail [24]. In this test, the PV module investigations were performed with a CCD cam-era IR, which has a spectral response approximately 300 to 1100 nm. The camera is cooled to −50 °C below ambient temperature to improve accuracy and prevent noise in the image from thermally generated carriers in the detector. The experimental setup is illustrated in (see Fig. 3). The image captured shows the intensity distribution of the luminescence radiation. Although a homogeneous distribution would be expected for an ideal solar cell, electroluminescence images of actual solar cells always show inhomogeneities.

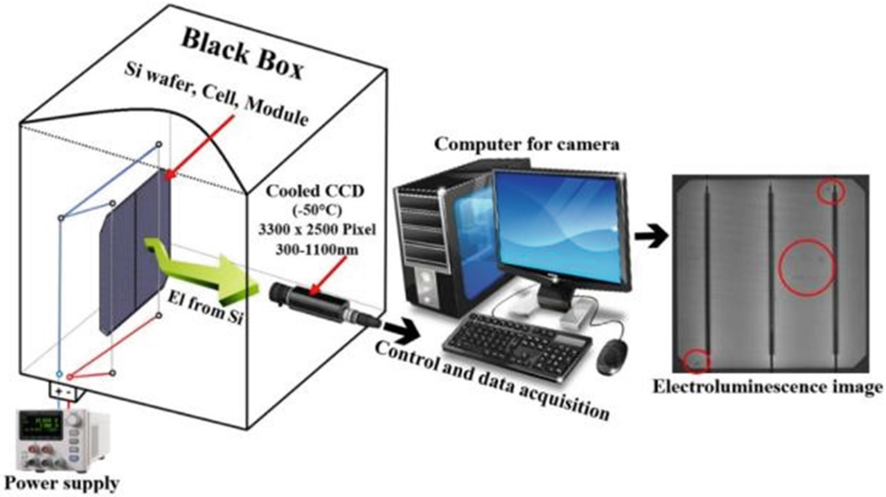

Fig. 3. Schematic of EL experimental setup PV module inspection.

3 Experimental Results

In order to determine the environmental impact on performance behaviour, a site with composite climate has been selected to perform the experimental study. The details of the selected site (experimental setup and experiment procedure) are explained below.

3.1 Indoor Measurements

3.1.1 Sun Simulator Results

The performance of a PV module will decrease over time. The degradation rate is typically higher in the first year upon initial exposure to light and then stabilises [8, 9, 20]. The results of detailed I-V Measurements (as described in Sect. 2.3.1.) on six crystalline silicon (Si) modules (03 m-Si and 03 p-Si) plus one amorphous module located at Solar-TestLab at CiS Research Institute for Microsensors and Photovoltaics, Erfurt (Germany) have been presented in Table 2.

Table 2. Sun simulator results under STC (IEC60904-3). (IEC60904-3: STC Irradiance 1000 W/m^2, Spectrum AM = 1.5, Cell Temper. 25 °C).

Ref	m-Si M60 EU 30117			p-Si LLC-PV MU 235			a-Si GET
	#062	#677	#787	#08	#10	#11	#78PI
P_{mpp} [W_p]	239.51	239.50	238.89	226.29	229.58	229.86	90.69
V_{mpp} [V]	29.51	29.59	29.70	28.65	28.75	28.76	67.96
I_{mpp} [A]	8.12	8.09	8.04	7.90	7.99	7.99	1.33
V_{oc} [V]	36.77	36.80	36.78	36.29	36.28	36.33	90.94
I_{sc} [A]	8.65	8.62	8.68	8.43	8.52	8.51	1.66
FF [%]	75.33	75.49	74.87	73.97	74.34	74.34	60.05
η [%]	14.57	14.57	14.54	13.61	13.80	13.82	6.74

3.1.2 Electroluminescence Solar Module Tester Results

The PV modules that suffer from efficiency losses have of course a bad impact on the system energy bill. As this test is the complement to the sun simulator investigation to justify the efficiency losses in each PV module and complete the quality assessment of these modules. In the case of amorphous module, an electric current of 9A presents a risk of destruction of cells outright, because this type of module only works with low electric current. Whereas, the EL-images of monocrystalline and polycrystalline PV modules are presented below in Fig. 4.

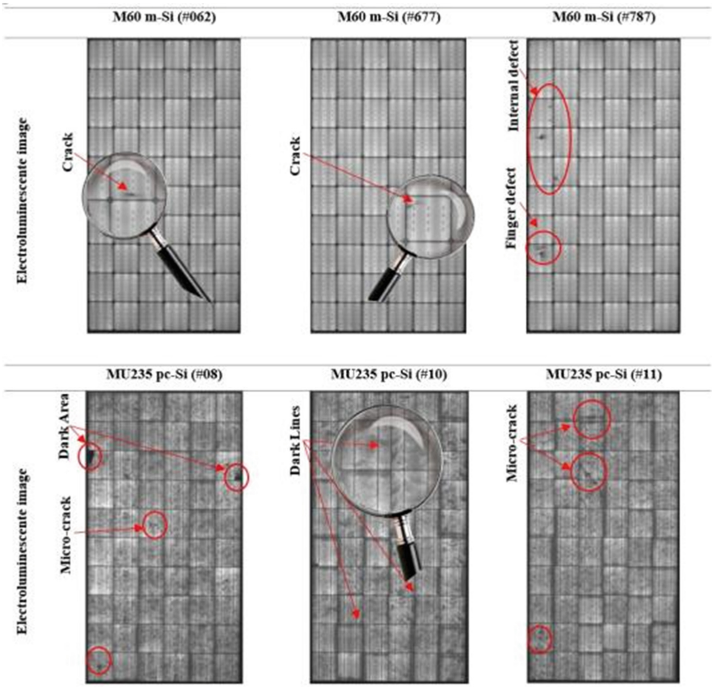

Fig. 4. The EL-images and quality inspections of PV modules.

Figure 4 shown is an image of a monocrystalline and polycrystalline solar cells operated under forward bias condition. The electroluminescence of the solar cells below the grid electrodes is clearly visible. The EL-images in Fig. 4 reveal wide optical differences between both PV modules m-Si and p-Si. The darker areas and vertical dark lines in the image indicate regions of minor quality (not operating properly) within the solar cells. Some close-up views and the red circles show the location of the micro-cracks and finger defects, who have a negative impact on electrical characteristics (especially efficiency) that were deter-mined from their electrical characteristics illuminated I-V measurements in the first part (Sun simulator).

3.1.3 Discussion

Bosch M60 EU 30117 PV modules (m-Si #062, #677 and #787): presented modules are never operating in real conditions and as seen in Table 2 their performance is reduced by 1.20% over the initial efficiency. The state of these modules presents a power loss of >0.30% (during degradation). There-fore, these modules were not visibly degraded in any way as seen in Fig. 4. In fact, to stabilize the power loss, the PV module must be operated in real conditions for an optimal period until more stable characteristics are obtained. Usually, manufacturers guarantee at least 80% of the starting power after 20 to 25 years. As any mechanical damage affects the performance, and results in decreased efficiency of PV module. After inspecting the EL images in Fig. 4, the modules (#062 and #677) present only one mechanical damage (crack), which explains how these modules have a power very close to the power declared by the manufacturer.

PVTEC POLSKA LLC-PV MU 235 (p-Si #08, #10 and #11): have been operated outdoors for one-year. Therefore, according to results in Table 2 (Sun Simulator), the performance of these modules is already slightly degraded, with a loss 3% of the nominal power. The intensity in this case is lower than the first type of modules, with the existence of dark lines on the interconnections of cells and black local areas (crack, micro-crack, finger defects,) show that these cells are not functional and no longer participate in photovoltaic con-version. which explains the degradation of the photovoltaic efficiency of this module, see Fig. 4.

Green Energy Tech GET-100-AT (a-Si #78PI): has been operated outdoors for two years. Hence, from the results shown in Table 2, a considerable decrease in efficiency of this module almost 10% less than the initial performance declared by the manufacturer GET has been measured.

3.2 Outdoor Measurements

The solar spectrum, insolation, temperature, wind-speed and wind-direction (see Fig. 5) are highly variable parameters depending on the geographical site. The outdoor measurements for different technologies of PV modules were carried out at Research Institute for Microsensors and Photovoltaics (CIS), Erfurt, (Ger-many). The geographical location of CIS is latitude 50° 58′ 41″ North and longitude 11° 01′ 45″ East with an elevation of 294 m from sea level. The maximum solar irradiance was recorded during an exposure test of 15 days was 1466.02 W/m^2, and an average wind speed of 2.07 m/s (see Fig. 5), an average temperature of 16.67 °C, with Tmax = 35.7 °C and Tmin = 7.1 °C. An angle of inclination of the PV modules of 31° to the south, has been chosen as an optimal angle of this region.

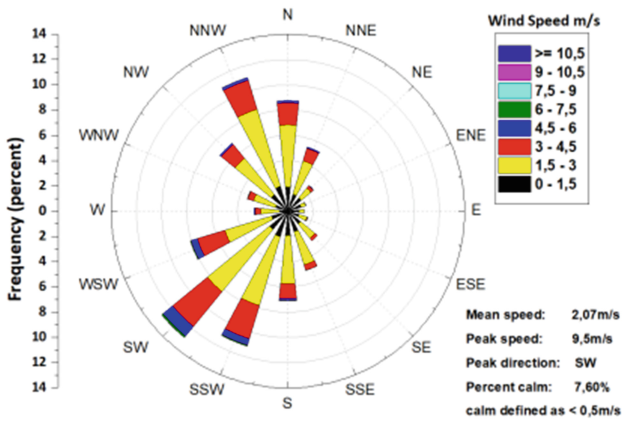

Fig. 5. Wind-rose diagram of meteorological site (CIS): wind-direction and wind-speed data.

3.2.1 Peak Power Measuring Device Results

The current-voltage and power-voltage characteristics for the considered modules are measured and recorded in various natural factors conditions (insolation, temperature, humidity). The insolation and temperature corrections for determining current-voltage characteristics are determined according to standard IEC 60904-1 [25]. The incident solar radiation is monitored by solar radiation sensor (SOZ-03) while the cell and module temperatures are monitored by placing a temperature sensor (thermocouple Pt1000) at the modules' back under con-sideration for each photovoltaic module technology (see Fig. 6).

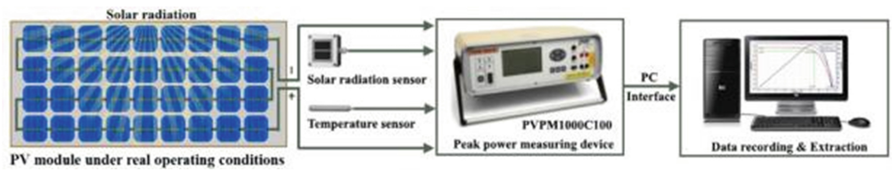

Fig. 6. Schematic of experimental setup (outdoor).

Before carrying out the measurements with peak power PVPM, it is necessary to maintain the modules in the operating site for some time to adapt and integrate with the site environment (semi-humid region).

The software **PVPMdisp** traces the current-voltage curves and calculates all the other parameters which are indicated above in Table 3 with the different measurement conditions. According to peak power measuring device PVPM results indicated in

Table 3 for three different technologies of PV module that were tested in operational site [26, 27], remarks were noted as follows:

Table 3. Electrical characteristic measured by peak power measuring device (out-door results)

	m-Si M60 EU 30117 #787		p-Si LLC-PV MU 235 #10		a-Si GET-100-AT #78PI	
	STC	Measured	STC	Measured	STC	Measured
P_{mpp} [W_p]	218.0	191.5	210.5	158	87.1	52.1
V_{mpp} [V]	27.90	25.7	26.7	26.2	73.6	64.39
I_{mpp} [A]	7.83	7.44	7.89	6.57	1.18	0.81
V_{oc} [V]	36.10	34.0	35.63	34.3	98.6	86.2
I_{sc} [A]	8.64	8.22	8.60	8.60	1.47	1.01
FF [%]	69.9	68.4	68.7	70.2	59.91	60
T_{mod} [°C]	25	42.2	25	31.3	25	23.6
E_{eff} [w/m^2]	1000	951	1000	949	1000	684

Bosch M60 EU 30117 PV modules (m-Si #062): A temperature module increase to 42.2 °C was recorded. In efficiency terms, it's the most damaging factor for this technology (m-Si). Nevertheless, this PV modules type has a fairly good efficiency even in low solar irradiation. Therefore, temperature increase affects efficiency and presents a power loss of almost 20% and 8.89% under STC compared to Sun simulator results in Sect. 3.1.1 (reference), see Fig. 7(a).

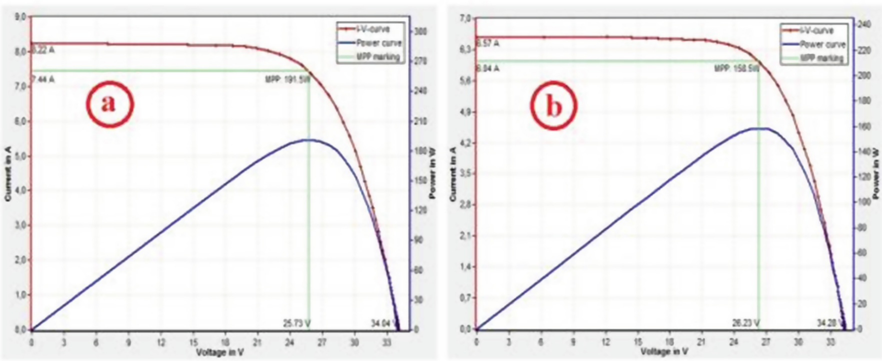

Fig. 7. Characteristic curve I-V example of **(a)** The monocrystalline, **(b)** The polycristalline Si PV module obtained by peak power measuring device PVPM1000C100.

PVTEC POLSKA LLC-PV MU 235 (p-Si #10): This type of module loses 8.31% of energy under operating real conditions compared to the initial energy of the simulation obtained by the flash test under STC. Indeed, this polycrystal-line module under low irradiation with a temperature of 31.1 °C loses about 31.17% of its initial efficiency.

Polycristalline module requires a good illumination to obtain a good efficiency but which is always lower than that of a monocrystalline PV see Fig. 7 (b).

Green Energy Tech GET-100-AT (a-Si #78PI): This PV module type has a high voltage delivered with a low power loss of 3.95% under STC. Its efficiency (< 7%) is always stable in high temperature and the short lifetime com-pared to m-Si or p-Si PV modules is only its disadvantage.

3.2.2 Discussion

Further to this experimental analysis, Germany, cloudy country (low luminous intensity) the first conclusion would be to think that the m-Si is better than the p-Si, at this stage, we will have a tendency to say that the two technologies are really holding hands. We notice that the monocrystalline PV technology provides a power superior than poly-crystalline. In particular, when the conditions are marked by a freshness and little sunshine (mornings for example), On the other hand, it is the opposite during high illu-mination and high temperature [22]. For thin-film modules this technology simply arises, at first, from a will to decrease the manufacturing costs of modules.

4 Conclusion

The global objective of this work is the demonstration effect of the environment on the efficiency of PV modules, and analysis of various parameters that can contribute to the optimisation of the energy efficiency. The optimal operation of the photovoltaic module is closely related to the climatic conditions on the one hand and the charge used on the other hand. With regard to the climatic conditions, the PV modules must be placed in a locality with strong insolation so as to extract the maximum power while taking into account the increase of the temperature which decreases the energy efficiency. Depending on the environment, each technology has advantages and disadvantages, so to optimise PV performance, it is necessary to make a meteorological analysis on the geographical location. Through techniques of electrical (Sun Simulator) and optical characterization (El image) of PV modules. we can determine actual electrical and mechanical defects located in solar cells, which may explain any decrease in photo-voltaic efficiency. The obtained results allowed us to analyse the functioning of the system PV for three photovoltaic technologies at the Erfurt city in Germany as experi-mental site characterised by a strong fluctuation in temperature and a high humidity [26, 27]. Practically, it is difficult to isolate the effect of each parameter as many parameters can influence this investigation (insolation, temperature, wind, angle, orientation,). As a perspective, in order to develop a standardisation of photovoltaic modules working in arid and semi-arid conditions by in-situ analysis of photovoltaic efficiency, it's necessary to install in other operating site (arid or semi-arid region), to make a comparison between the impact of two environment's regions.

Acknowledgement. The authors would like to thank Prof. Dr. Gerhard Gobsch to have initiated this project.

References

1. Perlin, J.: From Space to Earth, the Story of Solar Electricity. Earthscan (1999)
2. Villoz, A.L.-M.: énergie solaire photovoltaïque: le manuel du professionnel. Dunod (2003)
3. Labouret, A., Villoz, M.: Energie solaire photovoltaïque-4ème édition. Dunod (2009)
4. Tiwari, G.N., Dubey, S.: Fundamentals of photovoltaic modules and their applications. Royal Society of Chemistry (2009)
5. Skoplaki, E., Palyvos, J.A.: On the temperature dependence of photovoltaic module electrical performance: A review of efficiency/power correlations. Sol. Energy **83**(5), 614–624 (2009)
6. Cañete, C., Carretero, J., Sidrach-de-Cardona, M.: Energy performance of different photovoltaic module technologies under outdoor conditions. Energy **65**, 295–302 (2014)
7. Belkaid, A., Colak, I., Isik, O.: Photovoltaic maximum power point tracking under fast varying of solar radiation. Appl. Energy **179**, 523–530 (2016)
8. Schweiger, M., et al.: Understanding the energy yield of photovoltaic modules in different climates by linear performance loss analysis of the module performance ratio. IET Renew. Power Gener. **11**(5), 558–565 (2017)
9. King, D.L., et al.: Photovoltaic module performance and durability following long-term field exposure. AIP Conf. Proc. **462**(1), 565–571 (1999)
10. Wohlgemuth, J.H., et al.: Long term reliability of photovoltaic modules. In: IEEE 4th World Conference on Photovoltaic Energy Conversion, Conference Record of the 2006, vol. 2, pp. 2050–2053. IEEE (2006)
11. Mani, M., Pillai, R.: Impact of dust on solar photovoltaic (PV) performance: research status, challenges and recommendations. Renew. Sustain. Energy Rev. **14**(9), 3124–3131 (2010)
12. Jorgensen, G.J., et al.: Moisture transport, adhesion, and corrosion protection of PV module packaging materials. Sol. Energy Mater. Sol. Cells **90**(16), 2739–2775 (2006)
13. Quintana, M.A., et al.: Commonly observed degradation in field-aged photovoltaic modules. In: Conference Record of the Twenty-Ninth IEEE Photovoltaic Specialists Conference, pp. 1436–1439. IEEE (2002)
14. Jordan, D.C., Kurtz, S.R.: Photovoltaic degradation rates—an analytical review. Prog. Photovoltaics Res. Appl. **21**(1), 12–29 (2013)
15. Mahammed, I.H., et al.: Outdoor study of partial shading effects on different PV modules technologies. Energy Procedia **141**, 81–85 (2017)
16. Bana, S., Saini, R.P.: Experimental investigation on power output of different photovoltaic array configurations under uniform and partial shading scenarios. Energy **127**, 438–453 (2017)
17. Wagner, A.: Peak-power and internal series resistance measurement under natural ambient conditions. In: Proceedings EuroSun, vol. 5, (2000)
18. Bendel, C., Wagner, A.: Photovoltaic measurement relevant to the energy yield. In: Proceedings of 3rd World Conference on Photovoltaic Energy Conversion, vol. 3, pp. 2227–2230. IEEE (2003)
19. Schulte, K.M., Wagner, A.: Die Effektive Solarzellenkennlinie.-Anwendung in der Teillast-Berechnung. In: Proceedings, vol. 17 (2002)
20. Jorgensen, G.J., McMahon, T.J.: Accelerated and outdoor aging effects on photovoltaic module interfacial adhesion properties. Prog. Photovoltaics Res. Appl. **16**(6), 519–527 (2008)
21. ISO, BSEN: IEC 17025: 2005 General requirements for the competence of testing and calibration laboratories. ICS, vol. 3 (2005)
22. Alonso-Garcia, M.C., Ruiz, J.M., Chenlo, F.: Experimental study of mismatch and shading effects in the I-V characteristic of a photovoltaic module. Sol. Energy Mater. Sol. Cells **90**(3), 329–340 (2006)

23. Crozier, F.J.J.L., van Dyk, E.E., Vorster, F.J.: high resolution spatial electroluminescence imaging of photovoltaic modules. Vor. Nelson Mand. Metrop. Univ (2009)
24. Rau, U.: Reciprocity relation between photovoltaic quantum efficiency and electroluminescent emission of solar cells. Phys. Rev. B **76**(8), 085303 (2007)
25. International Electrotechnical Commission. "Photovoltaic Devices-Part 1: Measurement of photovoltaic current-voltage characteristics. IEC 60904-1 (2006)
26. Osterwald, C.R., et al.: Comparison of degradation rates of individual modules held at maximum power. In: Conference Record of the 2006 IEEE 4th World Conference on Photovoltaic Energy Conversion, vol. 2, pp. 2085–2088. IEEE (2006)
27. Tina, G.M., Abate, R.: Experimental verification of thermal behaviour of photovoltaic modules. In: The 14th IEEE Mediterranean Electrotechnical Conference. MELECON 2008, pp. 579–584. IEEE (2008)

Optimization of Energy Pile Conductance Using Finite Element and Fractional Factorial Design of Experiment

Khaled Ahmed[1(✉)], Mohammed Al-Khawaja[1], and Muhannad Suleiman[2]

[1] Mechanical and Industrial Engineering Department, Qatar University, Doha 2713, Qatar
Kh.ahmed@qu.edu.qa
[2] Civil and Environmental Engineering, Lehigh University, Bethlehem, PA 18015, USA

Abstract. In Ground Source Heat Pumps (GSHP), Energy Piles pose as heat exchangers that transfer the heat from the buildings to the shallow ground lower temperature in order to decrease the energy consumption whilst cooling the buildings. These piles are mainly designed for highest possible thermal conductance. In this paper, nine factors influencing the thermal conductance of the energy pile are defined and statistically evaluated. These nine factors are; number of tubes, pile diameter, tube diameter, tube thickness, tube location, pile conductivity, tube conductivity, soil conductivity, and water flow rate. The thermal conductance of the energy pile is calculated using finite element model. The significance of these factors is evaluated using fractional factorial uniform design of experiment. The results show significance increase in the pile thermal conductance with the increase of the tube diameter, number of tubes, water flow rate, and tube and pile thermal conductivities. Furthermore, the tubes location near the pile outer surface show significant increase in the pile thermal conductance. On the other hand, decreasing pile diameter slightly increases the pile thermal conductance. Nevertheless, the soil thermal conductivity has shown insignificant effects on the pile thermal conductance.

Keywords: Energy piles · Geothermal · GSHP · Composite cylinder model Thermal resistance · Finite element · Renewable energy · DOE

1 Introduction

Ground Source Heat Pumps (GSHP) are a geothermal free form of energy utilizes the constant temperature of the shallow ground all year round to reduce energy consumption in cooling buildings through its energy piles [1]. The significant advantage of using energy piles over boreholes systems is that they require no additional structural or hydraulic measures because they are installed within elements that are already needed for structure [2]. Energy piles utilize renewable geothermal energy for buildings heating and cooling purposes and need proper design and sizing in order to end up with high plant efficiency [3].

M. Chadli et al. (Eds.): ICEECA 2017, LNEE 522, pp. 251–266, 2019.
https://doi.org/10.1007/978-3-319-97816-1_19

Research on the controlling factors of the energy piles have shown that maximizing the pile surface, maximizing the concrete thermal conductivity, and maximizing the number of water tubes will increase the heat exchanging through the energy pile [4]. These reports neither include all elements affecting the thermal conductance of energy pile nor their interconnection effects. The analytical formulae proposed by [5] have shown nine factors affecting the energy pile steady state thermal conductance. These nine factors are; number of tubes, pile diameter, tube diameter, tube thickness, tube location, water flow rate, and the thermal conductivities of the pile, tube and soil. Investigating these factors together require unreachable number of experiments to evaluate the interrelation between these controlling factors. Statistical design of experiments methods like uniform fractional factorial design can solve this problem.

Based on either the finite-element method or the finite-volume method, various numerical approaches for full discretization of the Ground source heat exchangers like boreholes or energy piles have been formed. These models are employed to solve the heat-exchanging problem to optimize the heat exchanger geometry [6–9]. These models require extensive CPU time for being 3D models or for solving the transient effects. In order to decrease the time of calculations, the current analysis will be restricted to 2D steady state model.

The objective of the current work is to build a 2D steady state finite element thermal model to predict the energy pile thermal conductance at different combinations of the controlling factors. Then statistical regression method will be used to define a correlation between these controlling factors based on the significance of each of these factors on the energy pile steady state thermal conductance whilst changing other factors using uniform fractional factorial design of experiment method.

2 Energy Pile Factors and FE Model

The current work considers the energy pile cross sectional in plane factors assuming same behaviors and relations through the pile height. Figure 1 shows schematic configurations of the studied energy pile in the current work.

The energy pile is symmetrical with repeated pattern. Half of the repeated sector can represent the whole energy pile cross section as shown in Fig. 1. The angle "θ" depends on the number of U-tubes in the pile and equal ($90/n$) where 'n' is the number of U-tubes. Lines "O–A" and "O–B" are symmetry lines. The energy pile model considers the variation of five geometrical factors; number of U-tubes (n), pile diameter (d_p), tube inner diameter (d_i), tube thickness (t), and tubes spacing (S). In addition, it considers the variation of thermal conductivities of the pile (K_p), the HDPE tube (K_t) and the sand (K_s). The study will consider one operational factor, which is the heat transfer coefficient of the circulating water (H). The sand width will not affect the steady state conductance of the energy pile so that it will assumed with constant value in the current study (L_s = 1.0 m). The energy pile studied factors throughout the current study are listed in Table 1.

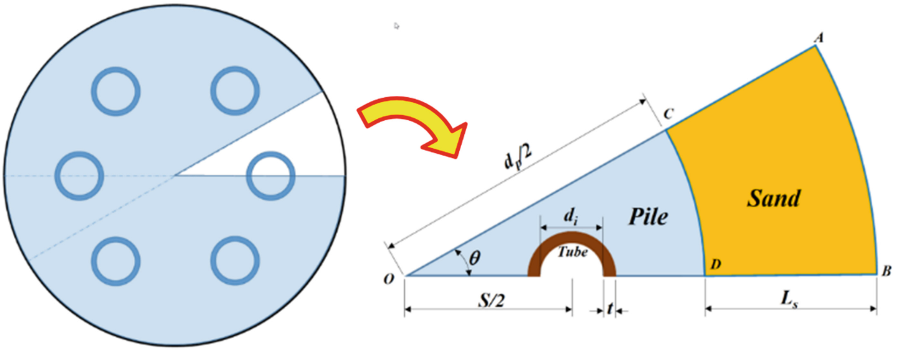

Fig. 1. Energy pile geometrical factors.

Table 1. Studied factors and their levels.

Level	n	d_p	d_i	T	S	K_p	K_s	K_t	H
−1	1	0.4	0.02	0.002	0.40 d_p	1.0	0.5	0.5	10
0	2	0.7	0.03	0.003	0.60 d_p	1.75	1	16	55
+1	3	1.0	0.04	0.004	0.80 d_p	2.50	1.5	32	100

Using Galerkin method and the divergence theorem [10], the discretized 2D finite element equation of a steady state condition, with no heat generation, takes the following form;

$$\left[\int_A [B]^T[K][B]\,dA + \int_S [N^s]^T[N^s]dS\right]\{\bar{T}\} = \int_S q^s[N^s]^T dS + \int_S hT_f[N^s]^T dS \quad (1)$$

where [B] is the temperature gradient interpolation matrix and {T} is the nodal temperature vector.

The boundary conditions of this equation take the following form with respect to Fig. 1;

Symmetric boundary conditions at lines "O–A" and "O–B" (Adiabatic BC).

$$\frac{\partial \mathrm{T}}{\partial \mathrm{S}} = 0 \quad (2)$$

where S is the normal vector at symmetric lines.

Convection heat exchange at the inner surface of the HDPE tube.

$$-\mathrm{K_s}\frac{\partial \mathrm{T}}{\partial \mathrm{S}} = \mathrm{H}(\mathrm{T_s} - \mathrm{T_f}) \quad (3)$$

where;

S is the normal vector at the inner surface of the HDPE tube.
T_s is calculated temperature at the inner surface of the HDPE tube.
T_f is the bulk temperature of the circulating water (45 °C).
H is the studied heat transfer coefficient.

Specified constant temperature at the outer surface of the sand line "A–B".

$$T_{A-B} = 25\,^{o}C \tag{4}$$

The set of linear equations represented by Eq. (1) and the boundary conditions represented by Eqs. (2–4) are assembled to form the global system matrix equations to be solved to calculate the temperatures at the inner surface of the HDPE tube "T_t" and the outer surface of the energy pile at line "C–D" "T_{C-D}". Also, the heat flow at the inner tube surface and the outer surface of the sand line "A–B" are calculated for convergence checking and for thermal conductance calculations. The energy pile steady state thermal conductance is calculated by the following equation;

$$C_{p,FE} = \frac{Q_{A-B}}{T_t - T_{C-D}} \tag{5}$$

2.1 FE Model Validation and Mesh Density Sensitivity

The finite element model of each design point is built and solved, autonomously, using ANSYS Parametric Design Language offered by ANSYS_MAPDL. This powerful scripting language allows parameterizing the finite element model and automating all related tasks of solution and post processing.

The current finite element model is verified against an analytical model of the steady state thermal resistance, which is the reciprocal of the thermal conductance, for these energy pile configurations. The model is proposed by [5] and approximated the thermal resistance of double U-tube energy pile as follows;

$$R_p = \frac{1}{4\pi K_p}\left[\ln\left(\frac{d_p^{2n}}{2nd_o S^{2n-1}}\left(\frac{d_p^{2n}}{d_p^{4n} - S^{4n}}\right)^{\left(\frac{K_p - K_s}{K_p + K_s}\right)}\right)\right] + \frac{1}{2n\pi}\left(\frac{1}{2K_t}\ln\left(\frac{d_o}{d_i}\right) + \frac{1}{d_i H}\right)_t \tag{6}$$

where;

R_p [m.K/W]: Energy pile thermal resistance.
n: Number of U-tubes.
$m = 2(n - 1)$.
d_p [m]: Pile diameter.
d_i [m]: Tube inner diameter.
t [m]: Tube thickness.

S [m]: Tubes spacing.
K_p [W/m.K]: Pile thermal conductivity.
K_s [W/m.K]: Soil thermal conductivity.
K_t [W/m.K]: Tube thermal conductivity.
H [W/m^2.K]: Convection heat transfer coefficient.

The FE results are usually sensitive to the mesh density. A proper mesh density that gives acceptable result within applicable CPU time is important to be achieved ahead of the investigation. A model with mid factors listed in Table 1 is used in the validation and the study of mesh density sensitivity. The mesh density in this model is parameterized to the number of elements through the HDPE tube thickness. The rest of elements sizes are assigned to be within the recommended aspect ratio (<1:5). The results of the validation and mesh density sensitivity study are shown Fig. 2. Domain discretization with 20 elements through HDPE thickness is the most compromised pattern between predicted results and calculation time. This pattern shows deviation percentage less than 0.02% with 10 s of CPU time.

3 Uniform Design of Experiment

Design of experiment methods are widely used in factors correlations and performance optimizations of multivariable systems [11]. Fractional factorial design of experiment is optimally suitable for systems with large number of factors. The Uniform design is an efficient fractional factorial design [12]. The uniform design is one of the robust space-filling designs that is significantly important in investigating large engineering systems [13].

3.1 Design Selection

The domain of each factor of the energy pile system factors is levelled to three levels (−1, 0, +1). The related values of these levels for each factor are listed in Table 1. The designs incorporated with 9 factors at three levels (3^9) can be investigated using number of simulation experimental runs as low as 9 runs and as high as 51 runs. The number of runs affect the uniformity discrepancy of the selected design. Figure 3 presents the effect of the number of runs on the discrepancy CD_2 of the design $U_n(3^9)$ [14]. The current work uses the uniform designs $U_{27}(3^9)$, $U_{36}(3^9)$ and $U_{51}(3^9)$ with 27, 36 and 51 runs respectively [14].

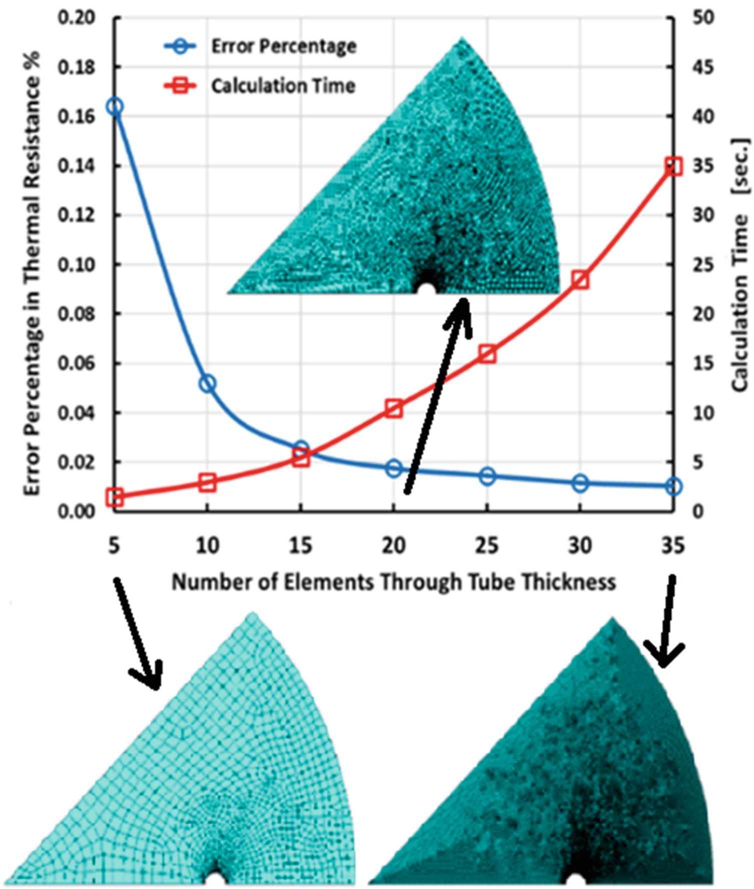

Fig. 2. Deviation in the predicted energy pile thermal resistance and the CPU calculation times at different mesh densities showing the pile mesh layouts of; 5, 20, and 35 elements through tube thickness.

3.2 Signal to Noise Ratio

Measured quantities are affected by significant and insignificant factors. Significant factors produce strong signal while insignificant factors produce noise. Magnification of the signal to noise ratio emphasizes the effect of each factor on the measured data. This leads to optimizing the controlling factors for better performance. The signal to noise ratio in the current work is calculated with the Taguchi larger the better relation as follows [15];

$$S/N = -10\ \log_{10}\left(\frac{1}{m}\sum\nolimits_{i=1}^{m}\frac{1}{C_{p,i}^{2}}\right) \tag{7}$$

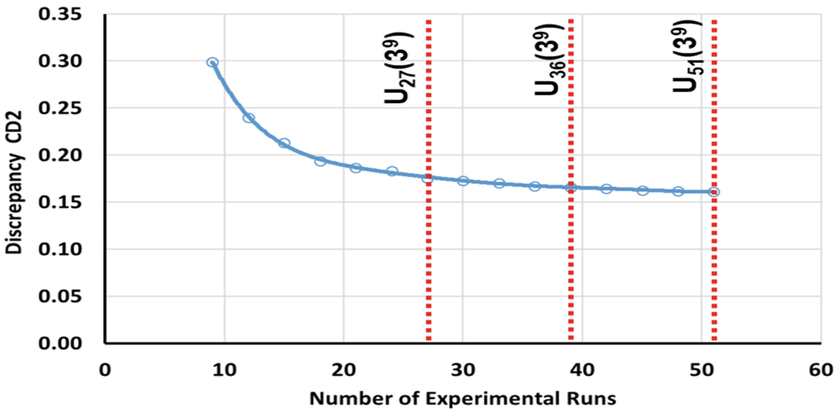

Fig. 3. Effect of number of runs on the uniform design $U_n(3^9)$ discrepancy CD_2 edited based on the data published by [14].

where;

m: is the number of observations for each factor.
$C^2_{p,i}$: is the FE predicted thermal conductance of the energy pile at experiment number i.

Another method to investigate the significance for each factor is the estimation of the cubic least square regression of the observed data at all experiments. The common cubic correlation is simply expressed as follows;

$$Y = a_0 + \sum_{k=1}^{9} a_k x_k + \sum_{i=1}^{9} \sum_{j=i}^{9} b_{ij} x_i x_j + \sum_{i=1}^{9} \sum_{j=i}^{9} \sum_{k=j}^{9} c_{ijk} x_i x_j x_k \quad (8)$$

where;

Y represents a function of the equivalent thermal conductance of the energy pile including water tubes.
a_o, a_k, b_{ij} and c_{ijk} are the correlation coefficients of the cubic model. These coefficients can be calculated using stepwise least square method.
x_i represents the controlling factors as shown in Table 2.

The first part is the intercept constant, the second part represents the linear weight of each factor separately, and the third part represents the cubic and the interaction between controlling factors in a pair wise manner.

Table 2. The related factors for each variable in the cubic correlation.

x_1	x_2	x_3	x_4	x_5	x_6	x_7	x_8	x_9
n	d_p	d_i	t	S	K_p	K_s	K_t	H

4 Results

4.1 Effect of Factors Means

The current work investigated the energy pile conductance using three designs $U_{27}(3^9)$, $U_{36}(3^9)$ and $U_{51}(3^9)$ with 27, 36 and 51 runs respectively [14]. Uniform design $U_{51}(3^9)$ is shown in Table 3, and the other designs are available at the Uniform Design Tables book [14]. The significance of each factor is measured by calculating the mean thermal conductance for each factor with all other factors. The three designs have shown consistent behaviour with the most significant factors as shown Fig. 4. On the other hand, the less significant factors have shown non-consistent behaviour with the three designs. The significance of the controlling factors on the mean thermal conductance is shown in Fig. 5. The most five significant factors with direct proportionality are the convection heat transfer coefficient "H", the number of tubes "n", the pile thermal conductivity "K_p", the distance between tubes "S", and the tube inner diameter "d_i", respectively in significance order. The other four factors are either less significant or with inverse proportionality.

4.2 Signal to Noise Ratio Measurements

The calculated thermal conductance of the energy pile at the different runs using the uniform designs of experiment are analyzed using Eq. (7). The significance of the factors have been better emphasized. The three designs have shown more consistence results with the Signal to Noise ratio measure than that obtained by the means measure as shown in Fig. 6.

The three designs have shown that the least significant factors; are tube thickness "t", soil thermal conductivity "K_s", and the tube thermal conductivity "K_t". The other factors have shown highest signal to noise ratio at the highest level "+1". These factors are the convection heat transfer coefficient "H", the number of tubes "n", the pile thermal conductivity "K_p", the tube inner diameter "d_i", and the distance between tubes "S" respectively in significance order, as shown in Fig. 6. On the other hand, the pile diameter has shown the highest signal to noise ratio at level "−1". This implies that the thermal conductance of the energy pile is slightly decrease with the increase of the energy pile diameter.

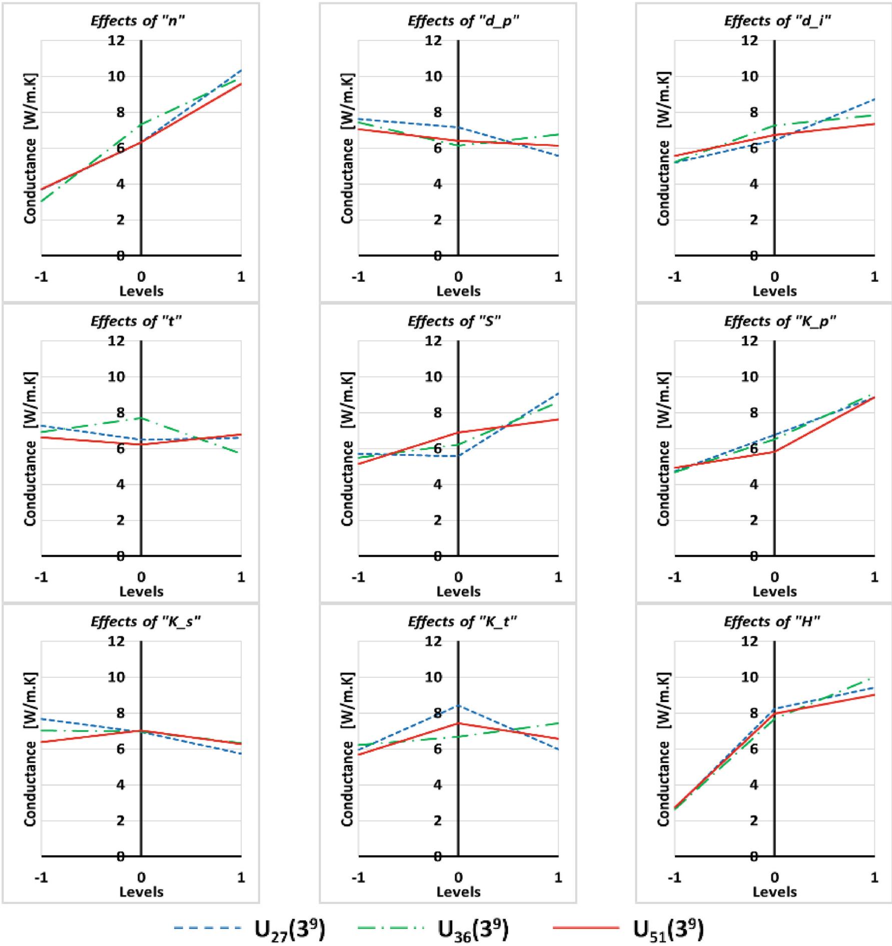

Fig. 4. Effects of each factor separately on the energy pile conductance.

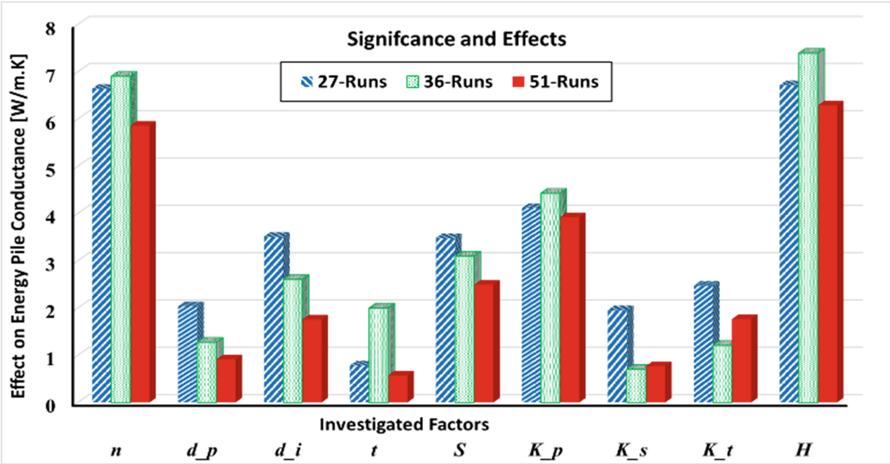

Fig. 5. Effects and significance of each factor separately on the energy pile conductance.

4.3 Cubic Least Square Model

Using the stepwise least square regression, the coefficients of the cubic Eq. (8) are calculated using the three uniform designs $U_{27}(3^9)$, $U_{36}(3^9)$ and $U_{51}(3^9)$. As shown in Fig. 7, the three designs show direct proportionality of the energy pile thermal conductance with the five most significant factors; (H, n, K_p, d_i, and S) and inverse proportionality with d_p. However, the other three factors are controversial because they have minor effects. Design $U_{27}(3^9)$ shows dependency of the pile conductance on the t and K_s, however, the other two designs show no dependency. On the other hand, design $U_{27}(3^9)$ shows no dependency on K_t, however, the other two designs show direct proportionality of the pile conductance and K_t as shown in Fig. 7.

4.4 Regression Model Verification

Three cubic regression models have been created from the three designs. To examine these models, the thermal conductance of a base case with all factors are at mid-level is calculated. Then each factor is changed to the extreme levels separately whilst other factors are at the mid-level. The energy pile conductance of these cases are compared to that predicted by the three cubic regression models. As shown in Fig. 7, the models achieved by designs $U_{36}(3^9)$ and $U_{51}(3^9)$ are in better correlation with the simulation experiment results. However, model achieved by design $U_{27}(3^9)$ is slightly deviated.

Table 3. Uniform design $U_{51}(3^9)$ [14].

Exp.	n	d_p	d_i	t	S	K_p	K_s	K_t	H	Pile cond. C_p
1	1	1	1	1	1	0	−1	−1	1	16.8501
2	0	1	−1	0	1	−1	0	1	1	6.3859
3	1	−1	1	1	−1	0	1	0	0	10.4425
4	0	−1	1	−1	0	1	−1	−1	−1	4.0793
5	−1	0	0	1	1	−1	1	0	1	4.1772
6	−1	1	0	1	0	−1	1	1	0	2.9434
7	1	0	0	−1	−1	1	1	−1	1	11.5765
8	0	0	0	0	0	0	0	0	0	8.3735
9	0	0	0	1	1	−1	−1	−1	0	6.3752
10	0	1	−1	−1	0	1	1	0	1	9.8099
11	0	1	0	1	−1	1	−1	0	−1	2.9456
12	0	1	1	0	−1	−1	1	−1	1	4.8182
13	1	1	0	1	1	1	0	1	0	16.6359
14	0	0	0	0	0	0	0	0	0	8.3735
15	−1	0	0	1	−1	0	0	−1	−1	1.406
16	−1	−1	1	0	1	1	1	0	1	10.1626
17	1	1	1	0	0	1	0	0	0	15.3738
18	0	0	1	1	1	1	1	0	−1	4.3231
19	0	−1	0	0	0	0	0	−1	1	10.0505
20	1	−1	0	0	−1	−1	−1	0	1	6.6228
21	1	0	1	−1	0	−1	0	0	1	9.4316
22	−1	0	−1	0	−1	1	1	1	0	3.8853
23	1	0	−1	−1	1	1	−1	0	0	12.8852
24	−1	0	−1	−1	0	−1	−1	−1	1	2.7331
25	−1	1	1	0	1	−1	−1	0	−1	1.6183
26	−1	0	1	1	0	1	−1	1	1	8.1579
27	−1	1	−1	0	1	1	0	−1	−1	1.0582
28	1	−1	0	−1	1	−1	0	−1	−1	4.3068
29	1	1	−1	1	0	−1	1	−1	−1	2.5104
30	−1	1	0	−1	1	0	1	−1	0	4.0124
31	0	1	1	0	0	0	1	1	−1	3.672
32	1	−1	0	0	0	1	1	1	−1	4.761
33	1	−1	−1	0	0	−1	−1	1	0	7.1593
34	−1	1	1	−1	−1	1	0	−1	0	5.1449
35	0	0	−1	−1	1	0	0	0	−1	2.1749
36	0	−1	−1	0	1	0	1	−1	0	7.1671
37	0	−1	1	1	−1	−1	0	1	−1	3.0084
38	1	1	−1	−1	−1	0	0	1	−1	2.7471
39	−1	−1	1	−1	−1	0	0	1	1	6.6467
40	0	1	0	−1	−1	−1	−1	1	0	4.2251
41	−1	−1	−1	−1	−1	−1	1	0	−1	0.9637
42	−1	1	−1	0	−1	0	−1	0	1	3.8843
43	1	−1	−1	1	0	1	0	0	1	15.8726
44	1	0	1	0	−1	0	−1	−1	−1	4.4323
45	0	−1	0	−1	1	1	−1	1	1	17.7434
46	−1	0	0	−1	0	0	−1	1	−1	1.5073

(*continued*)

Table 3. (*continued*)

Exp.	n	d_p	d_i	t	S	K_p	K_s	K_t	H	Pile cond. C_p
47	−1	−1	−1	1	1	0	−1	1	−1	1.0998
48	0	−1	−1	1	−1	1	−1	−1	0	6.1027
49	1	0	1	−1	1	−1	1	1	0	12.7236
50	1	0	−1	1	−1	0	1	1	1	8.5339
51	−1	−1	1	1	0	−1	0	−1	0	3.913

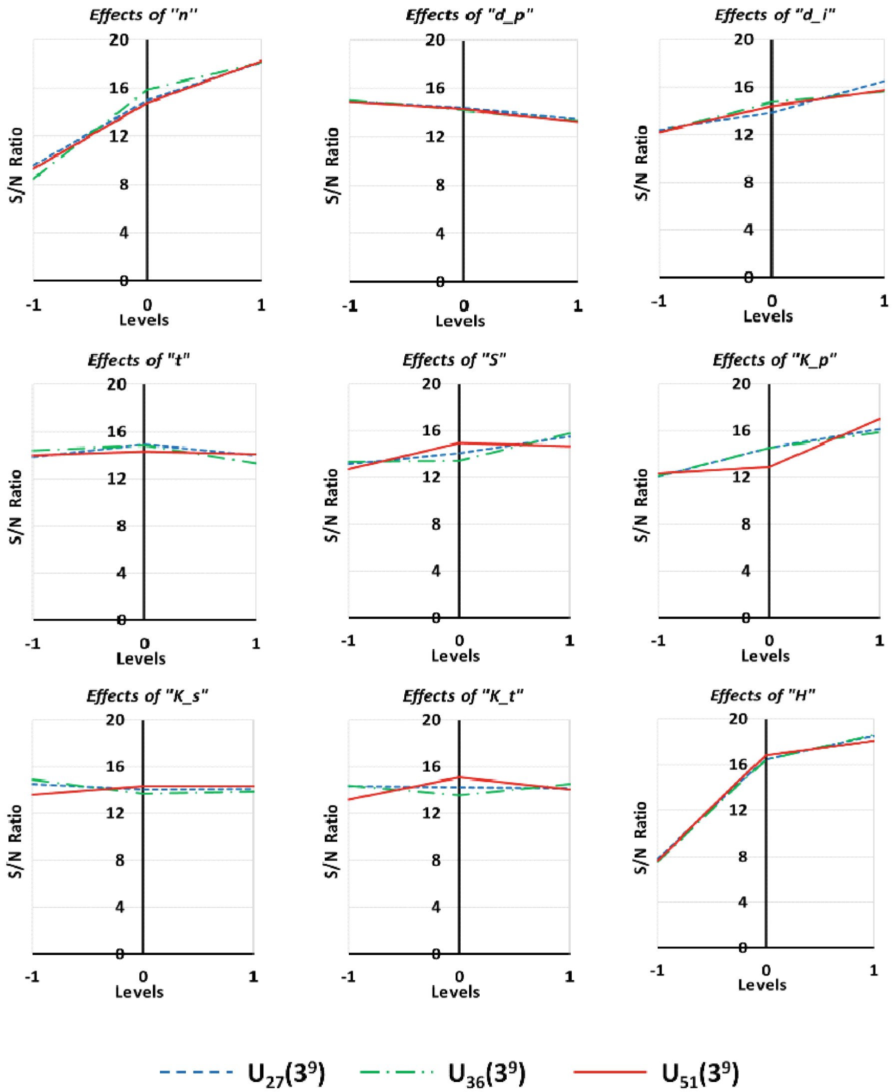

Fig. 6. Signal to noise ratios of the energy pile thermal conductance predicted at different uniform designs runs.

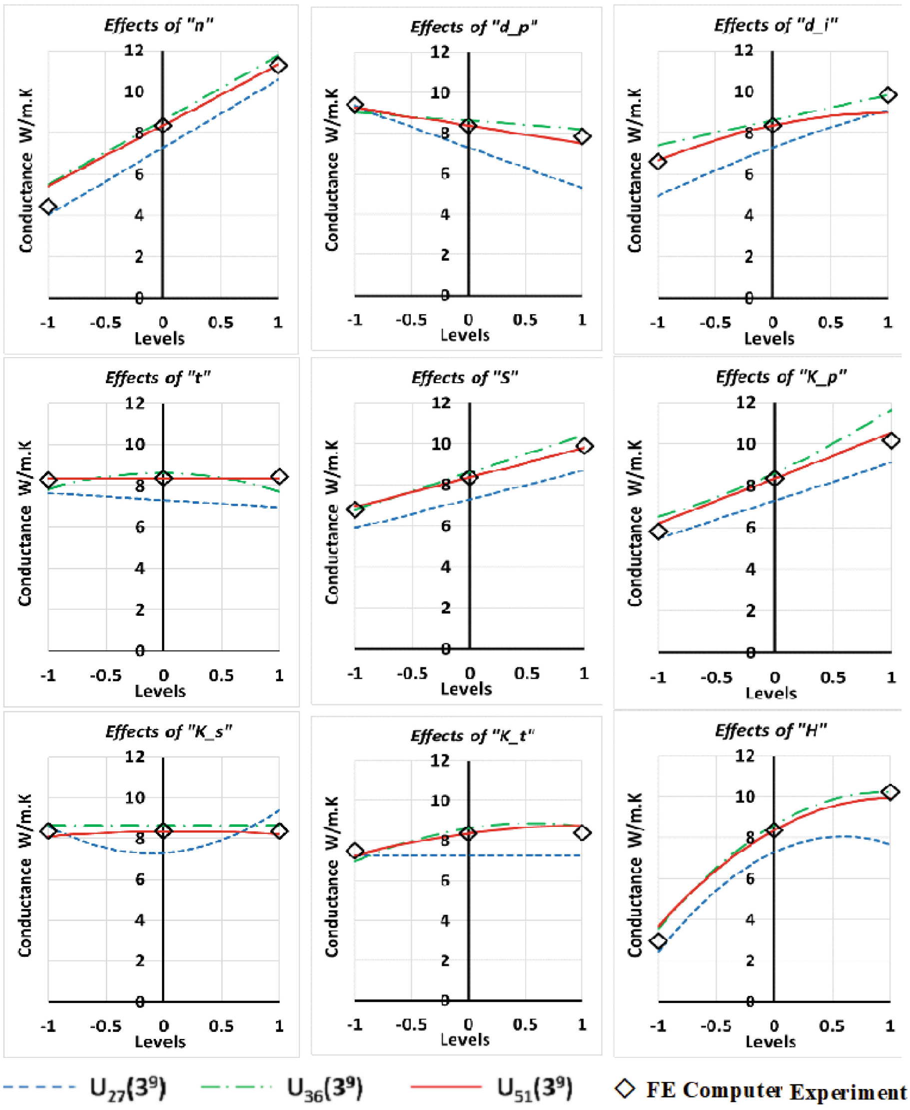

Fig. 7. Predicted energy pile conductance using the cubic regression models and FE experiments.

Table 4. Maximum conductance achieved by each design and the optimum factors for all cases.

	$U_{27}(3^9)$	$U_{36}(3^9)$	$U_{51}(3^9)$	Opt.
Number of tubes (n)	+1	+1	0	+1
Pile diameter (d_p)	−1	+1	−1	−1
Tube inner diameter (d_i)	+1	0	0	+1
Tube thickness (t)	−1	−1	−1	0
Distance between tubes (S)	+1	+1	+1	+1
Pile thermal conductivity (K_p)	+1	+1	+1	+1
Ground thermal conductivity (K_s)	−1	0	−1	0
Tube thermal conductivity (K_t)	0	0	+1	+1
Heat transfer coefficient (H)	0	+1	+1	+1
Energy pile thermal conductance (C_p)	24.4	21.33	17.75	34.52

Table 5. Maximum thermal conductance verification.

n	d_p	d_i	t	S	K_p	K_s	K_t	H	C_p
-1	-1	1	0	1	1	0	1	1	9.896524
0	-1	1	0	1	1	0	1	1	22.66916
1	-1	1	0	1	1	0	1	1	34.5194
1	-1	1	0	1	1	0	1	1	34.5194
1	0	1	0	1	1	0	1	1	28.37823
1	1	1	0	1	1	0	1	1	25.5727
1	-1	-1	0	1	1	0	1	1	20.5455
1	-1	0	0	1	1	0	1	1	27.63778
1	-1	1	0	1	1	0	1	1	34.5194
1	-1	1	-1	1	1	0	1	1	33.8404
1	-1	1	0	1	1	0	1	1	34.5194
1	-1	1	1	1	1	0	1	1	35.17938
1	-1	1	0	-1	1	0	1	1	15.69314
1	-1	1	0	0	1	0	1	1	23.04178
1	-1	1	0	1	1	0	1	1	34.5194
1	-1	1	0	1	-1	0	1	1	19.84264
1	-1	1	0	1	0	0	1	1	28.39127
1	-1	1	0	1	1	0	1	1	34.5194
1	-1	1	0	1	1	-1	1	1	34.25466
1	-1	1	0	1	1	0	1	1	34.5194
1	-1	1	0	1	1	1	1	1	34.72366
1	-1	1	0	1	1	0	-1	1	26.92667
1	-1	1	0	1	1	0	0	1	34.14625
1	-1	1	0	1	1	0	1	1	34.5194
1	-1	1	0	1	1	0	1	-1	6.734525
1	-1	1	0	1	1	0	1	0	25.07089
1	-1	1	0	1	1	0	1	1	34.5194

4.5 Optimized Thermal Conductance

Each of the uniform designs have shown different maximum conductance within the investigated combinations. The combinations related to the maximum conductance for each design is shown in Table 4. By using the three measures; mean of means, Signal to noise ratio, and cubic regression model, applied to the three designs U27(3^9), U36(3^9), and U51(3^9) we can optimize the energy pile factors for maximum thermal conductance to the values shown in Table 4. The energy pile with these configurations has achieved thermal conductance of 34.52 W/m.K. To examine this result, a set of 27 simulation experiments is carried out with the optimum combination achieved as base combination. Then each factor is examined separately whilst keeping the other factors at the optimum value. As shown in Table 5, the optimum combinations shows the maximum energy pile conductance in almost all cases. A slight increase (<2%) is observed with choosing thicker tube. This test also shows that using Stainless steel tube (K = 16 W/m.K) instead of HDPE tubes (K = 0.5 W/m.k) increases the pile conductance (27%). However, using galvanized steel (K = 32 W/m.K) increases the pile conductance (1.7%). It is worth noting that these results are limited to the investigated boundaries of each factor.

5 Conclusions

Energy piles are crucial member of GSHP system to reject or pump heat into ground to reduce the consumption of fossil fuel and CO_2 emission. The efficiency of the energy pile increases with the increase of its steady state thermal conductance. The current work present a statistical approach to define the optimum condition with the least number of experiments using uniform design. Uniform design U36(3^9) has shown acceptable level of error with significantly low number of experiments. The maximum energy pile steady state thermal conductance is achieved with the highest number of tubes, largest tube diameter, largest distance between tubes, highest pile thermal conductivity and highest heat transfer coefficient. Although, smaller pile diameter slightly increase the energy pile thermal conductance, the constructional limitation might stand against reducing these factors with slight insignificant decrease in the energy pile thermal conductance.

Acknowledgement. This publication was made possible by grant No. **NPRP 7-725-2-270** from the Qatar National Research Fund (a member of Qatar Foundation). The statements made herein are solely the responsibility of the authors.

References

1. Kharseh, M., Al-Khawaja, M., Suleiman, M.T.: Potential of ground source heat pump systems in cooling-dominated environments: residential buildings. Geothermics **30**(57), 104–110 (2015)
2. Brandl, H.: Energy foundations and other thermo-active ground structures. Geotechnique **56** (2), 81–122 (2006)

3. Fadejev, J., Simson, R., Kurnitski, J., Haghighat, F.: A review on energy piles design, sizing and modelling. Energy **24**(122), 390–407 (2017)
4. Cecinato, F., Loveridge, F.A.: Influences on the thermal efficiency of energy piles. Energy **15**(82), 1021–1033 (2015)
5. Hu, P., Zha, J., Lei, F., Zhu, N., Wu, T.: A composite cylindrical model and its application in analysis of thermal response and performance for energy pile. Energy Build. **31**(84), 324–332 (2014)
6. He, M., Rees, S.J., Shao, L.: Applications of a dynamic three-dimensional numerical model for borehole heat exchangers. In: Proceedings of Effstock, The 11th International Conference on Thermal Energy Storage, Stockholm International Fairs, Stockholm, Sweden (2009)
7. Lamarche, L., Kajl, S., Beauchamp, B.: A review of methods to evaluate borehole thermal resistances in geothermal heat-pump systems. Geothermics **39**(2), 187–200 (2010)
8. Śliwa, T., Gołaś, A., Wołoszyn, J., Gonet, A.: Numerical model of borehole heat exchanger in Ansys CFX software/Numeryczny Model Otworowego Wymiennika Ciepła W Pakiecie Ansys Cfx. Arch. Mining Sci. **57**(2), 375–390 (2012)
9. Wołoszyn, J., Gołaś, A.: Modelling of a borehole heat exchanger using a finite element with multiple degrees of freedom. Geothermics **31**(47), 13–26 (2013)
10. Nikishkov, G.: Finite element equations for heat transfer. In: Programming Finite Elements in Java™, pp. 13–19 (2010)
11. Weissman, S.A., Anderson, N.G.: Design of experiments (DoE) and process optimization: a review of recent publications. Org. Process Res. Dev. **19**(11), 1605–1633 (2014)
12. Fang, K.T., Lin, D.K., Winker, P., Zhang, Y.: Uniform design: theory and application. Technometrics **42**(3), 237–248 (2000)
13. Yang, J., Li, L., Yang, L., Li, J.: Uniform design for the parameters optimization of pin-fins channel heat sink. Appl. Thermal Eng. **25**(120), 289–297 (2017)
14. Fang, K.T., Wang, Y.: Number-theoretic methods in Statistics. CRC Press, Boca Raton (1993)
15. Roy, R.K.: Design of Experiments Using the Taguchi Approach: 16 Steps to Product and Process Improvement. Wiley, New York (2001)

Seasonal Variations of Solar Radiation on the Performance of Crystalline Silicon Heterojunction (c-Si-HJ) Solar Cells

Abla Guechi[1(✉)] and Mohamed Chegaar[2]

[1] Institute of Optics and Precision Mechanics, Ferhat Abbas University, 19000 Sétif, Algeria
ab_guechi@yahoo.fr

[2] Physics Department, Ferhat Abbas University, 19000 Setif, Algeria
chegaar@yahoo.fr

Abstract. This work investigates the feasibility of using a solar spectral radiation model SMARTS2 to estimate the global, beam and diffuse solar irradiance and assess the influence of variation seasonal on the conversion efficiency of the c-Si-HJ solar cell. The variation of the common performance indicators such as short circuit current, fill factor, open circuit voltage, and efficiency are shown and discussed for each month and under different solar compounds. The results show that the variations in the solar spectrum affect this device to a different extent. For global and beam irradiance, the maximum efficiency is obtained in the summer months, however, the lower efficiency is obtained during winter. On the other hand, in the diffuse solar irradiance, the maximum efficiency is found in the winter months whereas the lower efficiency is obtained in summer months.

Keywords: c-Si-HJ solar cells · Season variation · Spectral effects · Performance SMARTS model

1 Introduction

Manufacturers report photovoltaic module power output at standard testing conditions (STC), which correspond to 1000 W/m^2, 25 °C, air mass 1.5 and normal incidence. In real operating conditions, the module output is strongly affected by various environmental conditions such as irradiation intensity, temperature, and spectral effects. Furthermore, the impact of each climatic factor on the energy production varies according to the module technology in use.

The spectrum of incident irradiance has become an important factor in the performance of photovoltaic devices since many emergent thin film technologies are highly spectrally selective. This can give rise to significant variations in performance as the spectrum changes. Such variation occurs on a daily and a seasonal basis, in a manner and magnitude determined by location and local atmospheric parameters.

The variations of the conversion efficiency of the different solar cell are the result of a superposition of several effects [1–3]. The increasing operating temperatures may

M. Chadli et al. (Eds.): ICEECA 2017, LNEE 522, pp. 267–276, 2019.
https://doi.org/10.1007/978-3-319-97816-1_20

provoke an annual effect of the light-generated defects. This makes the performance of photovoltaic solar module higher in summer than in winter [4–7]. In summer the sun appears to be high in the sky, the sunlight travels less through the earth's atmosphere and suffers fewer scattering losses. The losses are most significant in the short wavelength range. The resulting better spectral matching in summer leads to increased short-circuit current in the device and therefore to increased performance [8]. The efficiency of a solar module increases with the irradiance when the series resistance is small enough [9].

The spectral effect on the performance of the different photovoltaic devices is not yet quantified on a large scale because of the difficulty to obtain spectral solar measurements. Therefore, it is rather important to elaborate methods to quantify this effect on the different types of solar cells performance.

Crystalline silicon (c-Si) solar cells have a lifetime reliability and high performance [12]. Amorphous silicon/crystalline silicon (a-Si: H/c-Si) heterojunction solar cells are also interesting because their structures have developed and achieved a high conversion efficiency. Moreover, the low-temperature coefficients of crystalline silicon heterojunction (c-Si-HJ) solar cells, when suitably applied in a high-temperature environment, have resulted in higher energy yields when compared to conventional c-Si homojunction solar cells.

Setif is located in Algeria, at approximately 1.080 km above the sea level, its dry Mediterranean climate is characterized by a dry and hot summer during June August, whilst its winters are cool and somewhat moist during December March. Furthermore, the summer is fairly hot where extreme heat waves are common around the month of July where temperatures can sometimes even reach 40 °C. However, the humidity is lower, besides, it's hotter during the day and cooler at night. Winter is rather cold, especially when cold air masses prevail, which can at times bring even snow and frost. Due to Setif location on the High Plateaus, it one of the coldest regions during winter in Algeria.

This paper aims to investigate the performance of c-Si-HJ solar cell due to the influence of spectral irradiance throughout the year in Setif (Algeria) climate using the spectral model SMARTS 2 for clear skies considering the measured spectral response of this solar cell.

2 Calculation Procedure

2.1 Spectral Solar Irradiance Calculation

A large range of atmospheric radiation models has been elaborated by different authors for calculating the spectral solar irradiation [10]. Several of these models have been developed by various climate research centers and are highly complex numerical models utilizing the satellite observations as inputs. A physical spectral model is proposed by Gueymard [11] and called SMARTS2 (Simple Model of Atmospheric Radiative Transfer of Sunshine) is introduced here to examine the seasonal variation on the thin film solar cells output. It can be used in a variety of applications to predict full terrestrial spectra under any cloudless atmospheric condition. It gained acceptance in both the atmospheric and engineering fields due to its low number of inputs, ease of use, to its versatility, execution speed, and various refinements. It can calculate punctual estimations of spectral irradiances using as input parameters the local geographic coordinates, atmospheric water vapor content, atmospheric pressure and aerosol optical thickness.

SMARTS2 is used to generate the global component of the solar spectra for the site of Setif (36.18 °N, 5.41 °E and 1081 m) which is characterized by a clear sky most of the time. The calculations are for a horizontal surface at noon time for the typical meteorological day of each month (approximately the 15th day of each month) of the year. The inputs we introduced in the model are water vapor content, atmospheric turbidity, noon-time, albedo, altitude, longitude, latitude, and aerosol model and reference atmosphere.

2.2 Spectral Solar Irradiance Calculation

The fill factor and the conversion efficiency λ of the solar cell are associated through:

$$\eta = FF\frac{V_{oc} I_{sc}}{P_i S} \tag{1}$$

where *Pi* is the incident irradiation in W/m^2 and is given by:

$$P_i = \int_0^{\infty} E(\lambda)\, d\lambda \tag{2}$$

with *E* (λ) is the spectral irradiance, *S* is the area of the device, *Isc* is the short circuit current and *Voc* is the open circuit voltage.

The fill factor FF is defined as [12]:

$$FF = \frac{v_{oc} - \ln\left(v_{oc} + 0.72\right)}{v_{oc} + 1} \tag{3}$$

where:

$$v_{oc} = \frac{V_{oc}}{n\left(\frac{kT}{q}\right)} \tag{4}$$

The open circuit voltage is given by:

$$V_{oc} = n\frac{kT}{q}\ln\left(\frac{I_{ph}}{I_s} + 1\right) \tag{5}$$

The photocurrent has been taken directly as the short circuit current according to the approximation $I_{ph} = |I_{sc}|$.

The ideality factor, n, the saturation current, Is, and the parasite resistances (series and shunt) are computed from the I–V characteristics using an approach which involves the use of an auxiliary function and a computer-fitting routine. The short circuit density Jsc of the device, which is the value of the photocurrent density [12], is directly linked to the spectral irradiance E (λ) and can be calculated as:

$$J_{sc} = \int E(\lambda)\, SR\,(\lambda)\, d\lambda \tag{6}$$

where $E(\lambda)$ is the energy of the incident light and $SR(\lambda)$ is the measured spectral response at the given wavelength, λ.

Figure 1 shows the measured spectral response of the different thin film solar cells considered in this study. It is clear that this technology has a specific spectral response and, associated with this, an effective spectral range.

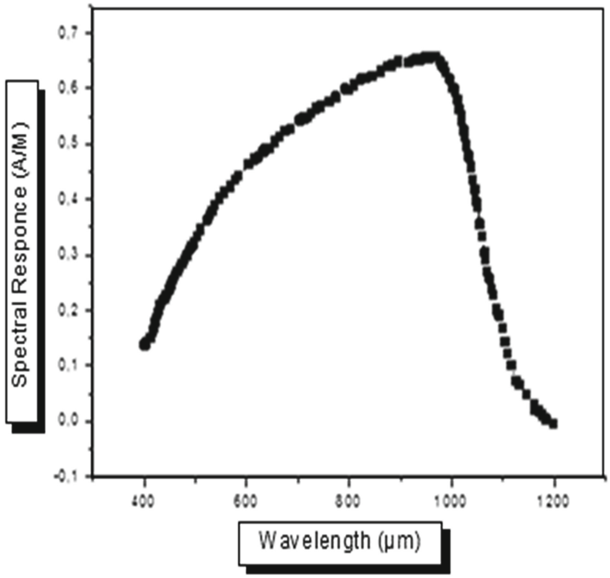

Fig. 1. The measured spectral response of c-Si-HJ solar cell [13]

3 Results and Discussion

Figures 2, 3 and 4 show clear-sky spectra for different months of the seasons at noontime in Setif (Algeria). All compounds of solar irradiance (direct, global and diffuse) show monthly spectral variations which correlate strongly with the observed efficiency of this solar cell. It is apparent from these figure that the global and beam solar irradiance becomes higher in the summer months due to the higher elevation of the sun and subsequent lower air mass and by elevated diffuse component over the direct, resulting in a greater proportion of the irradiance being absorbed by the solar devices whereas the lower solar irradiance in Setif in winter is likely due to higher air mass. An increase observed from November to December, can be linked to the advent and upsurge of dust in December while the slight reduction of the value in January, is due to a decline in atmospheric turbidity during the month compared to December. Linked to the fact that while February, was a relatively clear-sky month and March, an appreciably clear sky month with little cloudiness, subsequent months witnessed considerable cloudiness which sometimes resulted into rainfall.

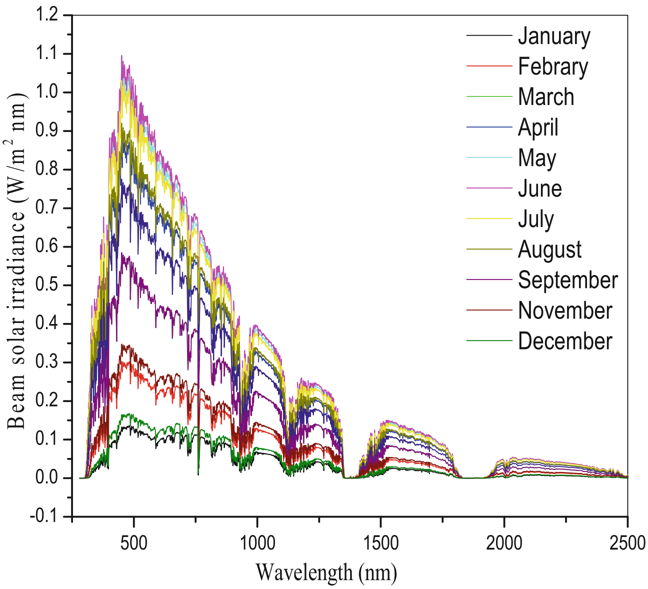

Fig. 2. Beam spectral irradiance as a function of wavelength for different months of the seasons at noontime

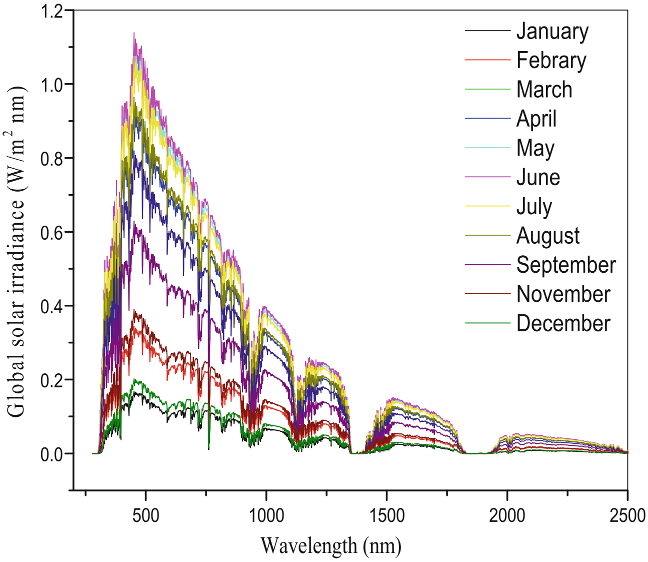

Fig. 3. Global spectral irradiance as a function of wavelength for different months of the seasons at noontime

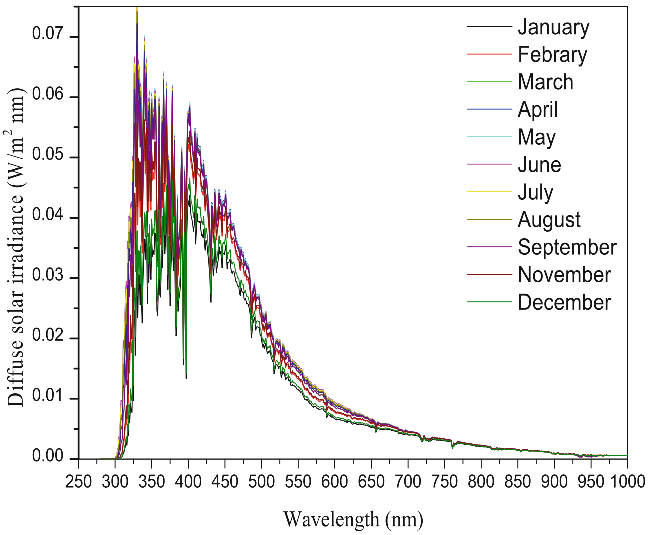

Fig. 4. Diffuse spectral irradiance as a function of wavelength for different months of the seasons at noontime

In the majority of the solar cell, the efficiency of the transformation of light into electricity depends directly on the irradiation. It is clear that the devices will operate with a higher efficiency in summer rather than in winter.

The spectral distribution of global solar irradiance for each month has been calculated. Then we have translated the performance changes into output power changes for this cell.

The monthly variations of the efficiency for the c-Si-HJ solar cell under diffuse, global and beam irradiance are presented in Figs. 5(a), 5(b) and 5(c). These depict average efficiency data plotted versus month, for a horizontal surface at noon time for the typical meteorological day of each month (approximately the 15th day of each month), for the c-Si-HJ solar cell. It can be seen that changes in the incident solar spectral irradiance are responsible for the majority of the seasonal variation in the different materials and to different extents. The maximum efficiency of the c-Si-HJ device is seen in the summer months, whereas in the winter months, a significant reduction in the efficiency is seen for this device for global and beam solar irradiance respectively. This could be expected, as the average AM is significantly higher than 1.5. However, the maximum efficiency of the c-Si-HJ device is seen in the winter months, while in the summer months a significant reduction in the efficiency is seen for this device for diffuse solar irradiance.

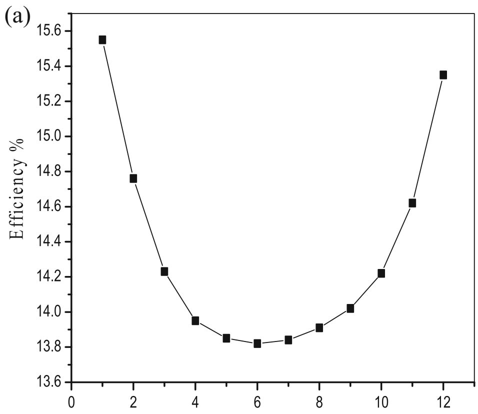

Fig. 5a. Monthly variations of the efficiency of the c-Si-HJ solar cell under diffuse spectral irradiance

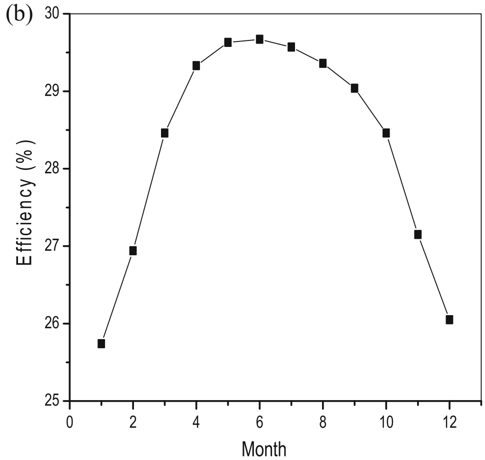

Fig. 5b. Monthly variations of the efficiency of the c-Si-HJ solar cell under global spectral irradiance

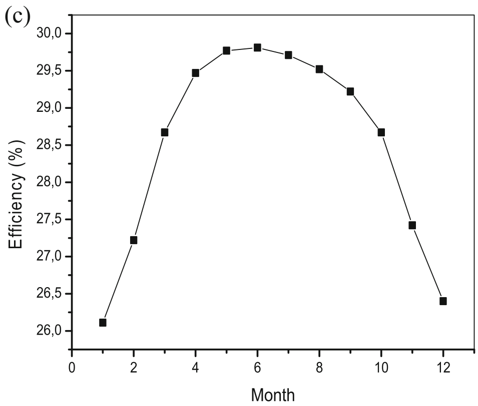

Fig. 5c. Monthly variations of the efficiency of the c-Si-HJ solar cell under global spectral irradiance

The variations of the performance of c-Si-HJ solar cell under global, direct and diffuse solar irradiance are shown in Tables 1, 2 and 3. As illustrated, c-Si-HJ shows an unusual performance variation in the course of the year in that they typically obtain maximum cells parameters in the summertime, when the air mass is lowest. There is a small variation in FF with changing spectrum solar of irradiance. A similarly weak trend was observed for Voc. During the summer months increases the solar flux leads to an increase in Voc, whereas in November, December, and January Voc decreases as the sunlight of the device is gradually decreased. This reinforces earlier research that spectral effects on efficiency are primarily due to changes in Isc as expected from changes in the spectral radiation. The absolute influence of varying solar spectrum is mainly dependent on the band gap of the material. A significant difference in the performance of the c-Si-HJ solar cell is observed under different solar compounds.

Table 1. Spectral effect on the c-Si-HJ solar cell parameters for global irradiance

Month	Jsc (mA/cm^2)	Voc (V)	FF
January	4.972	0.600	0.7503
February	10.223	0.631	0.7588
March	18.807	0.658	0.7650
April	28.089	0.676	0.7697
May	33.386	0.683	0.7715
June	34.358	0.685	0.7718
July	32.396	0.682	0.7712
August	29.013	0.677	0.770
September	24.605	0.604	0.7683
October	18.808	0.658	0.7655
November	11.591	0.637	0.7602
December	5.981	0.684	0.7525

Table 2. Spectral effect on the c-Si-HJ solar cell parameters for beam irradiance

Month	Jsc (mA/cm^2)	Voc (V)	FF
January	4.6179	0.597	0.7494
February	9.81804	0.6301	0.7583
March	18.37647	0.6576	0.7653
April	27.64883	0.6755	0.7695
May	32.94482	0.6832	0.7713
June	33.91953	0.6845	0.7716
July	31.96092	0.6819	0.7710
August	28.57861	0.6769	0.7699
September	24.17123	0.6696	0.7682
October	18.37918	0.6576	0.7653
November	11.18006	0.6358	0.7598
December	5.61135	0.6056	0.7518

Table 3. Spectral effect on the c-Si-HJ solar cell parameters for diffuse irradiance

Month	Jsc (mA/cm^2)	Voc (V)	FF
January	0.3541	0.4844	0.7123
February	0.4049	0.4903	0.7146
March	0.4314	0.4931	0.7156
April	0.4410	0.494	0.716
May	0.4412	0.494	0.716
June	0.4382	0.497	0.7159
July	0.4357	0.4935	0.7158
August	0.4347	0.4934	0.7157
September	0.4430	0.4933	0.7157
October	0.4293	0.4928	0.7155
November	0.4112	0.491	0.7148
December	0.3696	0.4863	0.713

4 Conclusion

The main purpose of this paper is to know how c-Si-HJ solar cell performs under possible spectral solar irradiance variations throughout the year. As there are not many measurement systems in the word for spectral irradiance, modeling global, diffuse and direct solar spectral is very significant for c-Si-HJ devices. This can be done by clear sky models such as SMART especially for developing countries where it is difficult to afford equipment and techniques involved.

The results show that c-Si-HJ solar cell illustrates an unusual performance variation in the course of the year in that they typically obtain maximum cells parameters in the summertime when the air mass is lowest for global and direct solar irradiance. There is a small variation in FF with changing spectrum solar irradiance. A similarly weak trend was observed for Voc.

The work has clearly demonstrated that the chosen approach is suitable for the modeling spectral effects on solar devices. Further work is required to point out combined measured seasonal variations especially temperature effects on this device at various geographical locations.

References

1. Ohtake, H., Gari da Silva Fonseca Jr., J., Takashima, T., Oozeki, T., Shimose, K., Yamada, Y.: Regional and seasonal characteristics of global horizontal irradiance forecasts obtained from the Japan Meteorological Agency mesoscale model. Sol. Energy **116**, 83–99 (2015)
2. Inman, R.H., Edson, J.G., Coimbra, C.F.M.: Impact of local broadband turbidity estimation on forecasting of clear sky direct normal irradiance. Sol. Energy **117**, 125–138 (2015)
3. El-Nouby Adam, M., El-Nobi, E.F.: Correlation between air temperature and atmospheric turbidity at a subtropical location. World Environ. **7**(1), 1–9 (2017)
4. Park, H.T., Hattori, S., Tanaka, T., Cha, G.S.: Seasonal variations in radiation and energy balance in a deciduous broad-leaved forest. J. For. Res. **4**, 261–269 (1999)
5. Ogueke, N.V., Abam, F., Nwaigwe, K.N., Okoronkwo, C.A., Ugwuoke, P.E., Anyanwu, E.E.: The effect of seasonal variation and angle of inclination on the performances of photovoltaic panels in South Eastern Nigeria. Res. J. Appl. Sci. Eng. Technol. **5**(3), 794–800 (2013)
6. Magare, D.B., Sastry, O.S., Gupta, R., Betts, T.R., Gottschalg, R., Kumar, A., Bora, B., Singh, Y.K.: Effect of seasonal spectral variations on performance of three different photovoltaic technologies in India. Int. J. Energy Environ. Eng. **7**, 93–103 (2016)
7. Vasisht, M.S., Srinivasan, J., Ramasesha, S.K.: Performance of solar photovoltaic installations: effect of seasonal variations. Sol. Energy **131**, 39–46 (2016)
8. Ye, J., Reindl, T., Luther, J.: Seasonal variation of PV module performance in tropical regions. In: 38th Photovoltaic Specialists Conference (PVSC), IEEE, Austin, TX, USA (2012)
9. Limmanee, A., Udomdachanut, N., Songtrai, S., Kaewniyompanit, S., Sato, Y., Nakaishi, M., Kittisontirak, S., Sriprapha, K., Sakamoto, Y.: Seasonal variations in performance loss of photovoltaic modules: a case study in Thailand Science Park. J. Renew. Sustain. Energy **7**, 053120 (2015)
10. Gueymard, A.: SMARTS user's manual. Solar Consulting Services, Bailey (2003)
11. Gueymard, A.: Variability in direct irradiance around the Sahara: are the modeled datasets of bankable quality. In: SOLARPACES Conference, Perpignan, France (2010)
12. Green, M.A.: Solar Cells, Operating Principals, Technology, and System Applications. Prentice-Hall Inc., Englewood Cliffs (1982)
13. Krajangsang, T., et al.: An intrinsic amorphous silicon oxide and amorphous silicon stack passivation layer for crystalline silicon heterojunction solar cells. Thin Solid Films **628**, 107–111 (2017)

Advanced Controls for Wind Power Plant Ancillary Services

Imen Karray(✉), Khadija Ben Kilani, and Mohamed Elleuch

ENIT-LSE, University of Tunis El Manar, B.P 37 Le Belvédère, 1002 Tunis, Tunisia
imenkarray22@gmail.com, {khadija.kilani, mohamed.elleuch}@enit.utm.tn

Abstract. This paper develops advanced controls to improve wind turbines ancillary services. Different controls are proposed to enhance the reactive power capabilities of a permanent magnet synchronous generator (PMSG). Recently, due to their substantial energy integration into power systems, wind power plants have to comply with Grid Code Requirements (GCR) set by power system operators. Voltage Ride Through (VRT) is one of the most important GCR of the Tunisian Power System Operator "STEG" (SociétéTunisienned'Electricité et de Gaz). The developed controls enable wind turbines reactive power production or absorption based on two hierarchical control signals emanating from the dispatching, or from voltage regulation controller at the Point of connection (Poc). The ramp up and down rates in reactive power absorption or supply must comply with the GCR. A recent control concept named synchronverter is used to control the reactive for compliance with the Tunisian GCR. With both Voltage Oriented (VOC) and synchronverter controls, the desired wind plant reactive capabilities are achieved with or without sufficient wind velocity. Thus, wind turbines are able to operate as static synchronous condensers (STATCOMs) under the so called "WindFree-Reactive Power" Control.

Keywords: Wind power · Ancillary services · Grid code requirements
Synchronverter control · Voltage oriented control · STATCOM

1 Introduction

Recently, the role of wind energy is becoming vital in the world's energy markets as the growth rate gets faster. By the end of 2016, the worldwide wind installed capacity has reached 486,661 MW, with a growth rate of 11.8%. (54,846 MW installed in the year 2016). By the end of 2016, 5% of the world's electricity demand is generated by wind turbines [1]. Parallelizing this growth, new operational challenges have intrigued power system grid operators concerning voltage regulation of the grid. Indeed, under substantial wind energy integration, large amounts of reactive power need to be recovered in response to large voltage excursions such as in short-circuit post fault conditions. Wind power plants are required to stay connected and withstand specific voltage profiles, known as Low Voltage Ride Through (LVRT) or High Voltage Ride

M. Chadli et al. (Eds.): ICEECA 2017, LNEE 522, pp. 277–292, 2019.
https://doi.org/10.1007/978-3-319-97816-1_21

Through (HVRT) [2, 7]. Further requirements on grid reactive power supports have been set by power system operators in many countries, including Tunisia [3].Wind turbines are required to absorb or supply reactive power with maximum ramp up and ramp down rates dictated by the Grid Code. A hierarchical control scheme comprises two levels: A control signal issued from the dispatching constitutes the primary control, assuring global voltage control. The secondary control level is local, where the reactive power setpoint is based on the voltage at the wind power plant Poc (Fig. 1). Under such scheme, priority is for reactive power settings coming from the Dispatching, as indicated in Fig. 1. In low wind power conditions, reactive power capabilities may be achieved by operating the wind plant as a STATCOM, realized with both voltage oriented and synchronverter controls. The latter control method is based on the concept of synchronverter, where the grid side inverter emulates the mathematical model of a conventional synchronous generator [9–11]. Both control methods assure participation of wind turbines in reactive power regulation, as well as STATCOM operation in zero wind power conditions. Such “WindFree-Reactive Power” operation of wind turbines has been used in wind power plant controls, provided by General Electric [12].

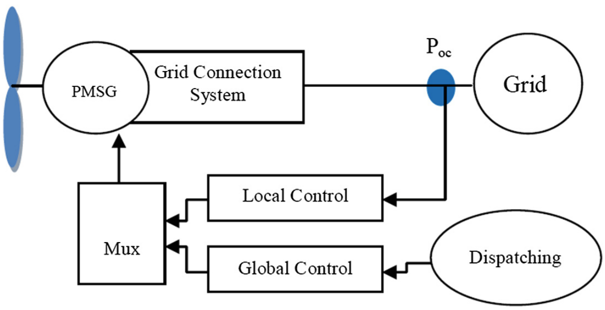

Fig. 1. Control hierarchy of wind power plant

Wind power plant controls presented in this paper coordinate the behaviors of the wind turbines to meet the grid code requirements and to get close to the ancillary services of synchronous machine. Different control loops are developed in order to guarantee reactive power support of the grid, while respecting the Grid Code requirements.

2 Wind Power System Description

The studied system shown in Fig. 2 is based on a permanent magnet synchronous generator (PMSG). The wind generator is connected to the grid via two power converters linked by a DC bus. The machine side converter is a diode bridge followed by a DC/DC chopper, while the grid side converter is based on an IGBT Pulse Width.

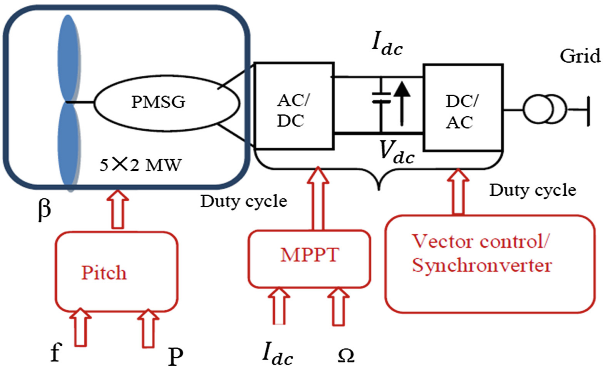

Fig. 2. Structure of a wind power system based on a Permanent Magnet Synchronous Generator (PMSG). P: active power, f: frequency, Ω: rotational speed, β: pitch angle, V_{dc}: DC bus voltage,I_{dc}: DC bus current

Modulation (PWM) control. The grid side converter controls the DC bus voltage and the reactive power exchanged with the grid, by two control methods: voltage oriented control, and synchronverter based control. The machine-side converter controls the machine torque and its rotational speed. The nominal power is generated for a nominal wind speed. The active power produced by the turbine is given by [2]:

$$P_m = \frac{1}{2} C_p(\lambda, \beta)\rho S V^3 \tag{1}$$

Where:
C_p: power coefficient; V: wind speed; $\lambda = R\Omega/V$: tip speed ratio (with R: length of blade; Ω: turbine speed); β: pitch angle; ρ: air density [kg/m^3]; S: area swept by wind turbine blades.

3 Grid Code Requirements

3.1 Low Voltage Ride Through Profile

In case of a grid voltage deviation resulting from large load changes or grid faults, wind generators are required to fulfill the LVRT. Power grid operators developed grid codes by specifying the desired LVRT behavior to maintain the grid voltage stability and avoid its collapse. It is worth noting that grid code requirements were originally developed for synchronous generators in conventional power plants. For the recent GCRs, they involve wind turbine generators which characteristics differ from the conventional ones. In the Tunisian Grid Code [3], renewable energy power plants of generation capacity greater than 1 MW must remain in operation when a voltage dip appears at the wind plant connection point Poc as shown in Fig. 3. For asymmetric faults, the curve is applied to the lowest voltage of the three phases. After a disturbance, renewable energy power plants have to contribute to the grid restoration of its normal operating conditions in voltage and frequency. Active power ought to be restored within a maximum time not exceeding the second, after voltage restoration.

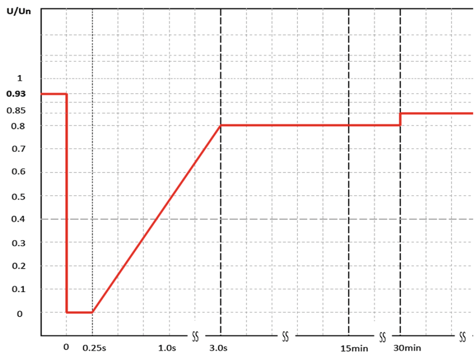

Fig. 3. Under-voltage during which the Renewable Power Plants must remain in service [3]

3.2 Reactive Power Management

Reactive power supply or absorption for wind and photovoltaic systems are constrained by operating limits which depend on their active power generation. For the Tunisian GCR, these limits in HV or MV grids are expressed by the power factor under nominal voltage Un, as depicted in Fig. 4. In addition, the power plant's installation equipment such as cables, shall not limit the reactive power availability at the connection point. In the Tunisian Grid Code, failure to comply with reactive power requirements may result in a restriction of active power generation output. On the other hand, reactive power shall be supplied in response to the grid disturbances. Its control setting may target a desired operating power factor cosφ, a reactive power reference value Q, or a desired Poc voltage set point. For instance, wind or photovoltaic plants connected to the Tunisian (STEG) HV grid should be capable of providing or absorbing reactive power over the entire allowed steady-state voltage range (93% Un < U < 107% Un), which corresponds to a minimum of 0.95 power factor "lag to lead" at the Poc. For voltage levels greater than 107% or less than 93%, the reactive power limits could be reduced according to the diagram depicted in Fig. 5.

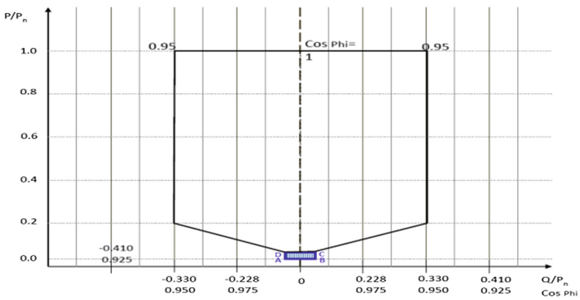

Fig. 4. Reactive power operating limits function of the active power (U = Un) for an HV or MV connection point for renewable energy plants [3]

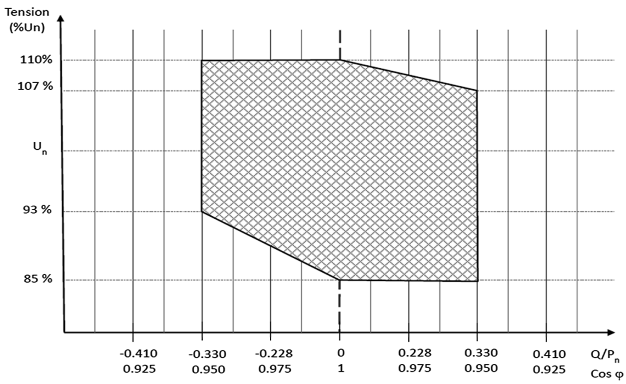

Fig. 5. The limits of reactive power function of voltage at the Poc according to [3].

4 Reactive Power Management with Vector Control

4.1 Grid Side Converter Control

The grid side converter ensures a dual function of interfacing the wind turbine to the grid while independently controlling active and reactive powers for a reference power factor, for all wind speeds. The vector control using PI control loops is required (Fig. 6).

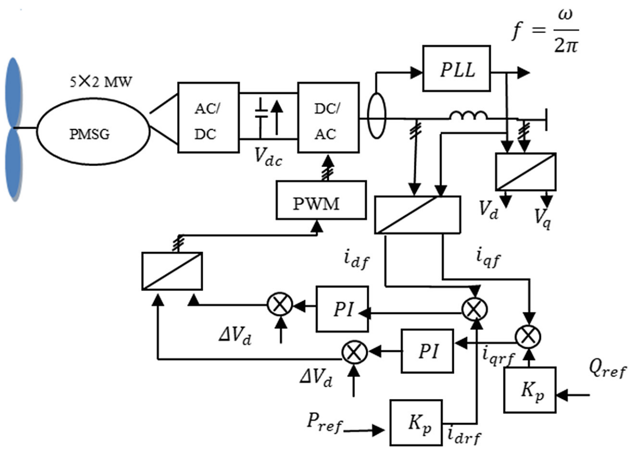

Fig. 6. Grid side converter control strategy (VOC)

Direct and quadrature currents are regulated by PI controllers in the inner control loop. The DC voltage is stabilized at the reference value by the DC-voltage PI controller [4]. The relationship between grid inverter voltages and line currents is:

$$\begin{bmatrix} e_a \\ e_b \\ e_c \end{bmatrix} = R_f \begin{bmatrix} i_a \\ i_b \\ i_c \end{bmatrix} + L_f \frac{d}{dt} \begin{bmatrix} i_a \\ i_b \\ i_c \end{bmatrix} + \begin{bmatrix} v_a \\ v_b \\ v_c \end{bmatrix} \tag{2}$$

With e_a, e_b, e_c *are the* voltages at the inverter system output, i_a, i_b, i_c are the line currents, v_a, v_b, v_c are the grid voltage components, R_f *is the* filter resistance, and L_f : filter inductance. The model for the grid-side converter is expressed by [5]:

$$v_q = e_q - R_f i_{qf} - L_f \frac{di_{qf}}{dt} - \omega L_f i_{df} \tag{3}$$

$$v_d = e_d - R_f i_{df} - L_f \frac{di_{df}}{dt} - \omega L_f i_{qf} \tag{4}$$

where v_d, v_q: voltage components in d–q reference frame, e_d, e_q : inverter voltage components in d–q reference frame, i_{df}, i_{qf} : grid current in the d–q reference frame. $\omega = 2f$*is* the grid angular frequency detected by the Phase Locked Loop (PLL) and used for the abc/dq transformation and synchronization. The rotating reference frame shown in Fig. 7 is used in the vector control. The instantaneous active and reactive powers are expressed by:

$$Q = \frac{3}{2}\left(v_d i_{qf} - v_q i_{df}\right) \tag{5}$$

$$P = \frac{3}{2}\left(v_d i_{df} - v_q i_{qf}\right) \tag{6}$$

As the Vector Control scheme used is based on a synchronously rotating reference frame as shown in Fig. 7, then:

$$V_d = V \tag{7}$$

$$V_q = 0 \tag{8}$$

Therefore, (3) and (4) can be expressed by:

$$L_f \frac{di_{df}}{dt} = e_d - R_f i_{df} + \omega L_f i_{qf} - V \tag{9}$$

$$L_f \frac{di_{qf}}{dt} = e_q - R_f i_{qf} - \omega L_f i_{df} \tag{10}$$

Using (5) and (6), active and reactive powers are expressed by:

$$P = \frac{3}{2} V i_{df} \tag{10}$$

$$Q = \frac{3}{2} V i_{qf} \tag{11}$$

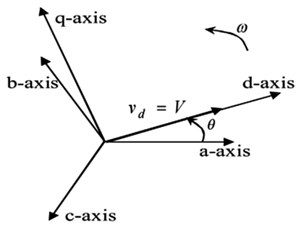

Fig. 7. abc axis and rotating d,q reference frame

4.2 Voltage Regulation and Q-ramp Control Loop

Generating electricity with variable power factors helps reducing the cost of adding capacitors for reactive power support. Such advantageous operation is sought from both distributors and producers [6]. A reactive power control loop is implemented using PI controllers (Fig. 8). The reactive power control must comply with the Tunisian GCR. Injecting or absorbing reactive power to support the grid voltage must be controlled with ramp up and ramp down. The limits of these ramp up and downs are also mentioned in other operators GCRs [7, 8].

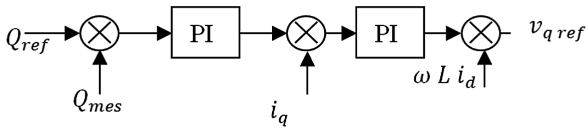

Fig. 8. abc axis and Reactive power control loop

4.3 Control Implementation for STATCOM Operation

For low wind speeds $(P_{active} = 0)$, the wind power plant could be operated as STATCOM to regulate reactive power interchange with the grid. The control structure of a STATCOM consists of a double control loop, as indicated in Fig. 11. The active current reference i_{d_ref} and reactive current reference i_{q_ref} are calculated by the external control loop to control the active and reactive power exchange (Fig. 9). Controlling the active power allows controlling the DC bus voltage. The reference reactive current is calculated to keep the DC bus voltage constant. For reactive power, two control strategies are used: power factor control and voltage control. The power factor is controlled at the point of connection to the grid to a reference value suggested by the GCR, or imposed by the dispatching. The power factor is maintained at a reference value by an integral proportional corrector. The voltage at the point of connection to the grid is maintained at a reference value by injecting or absorbing reactive power [12]. The voltages are calculated by the internal control loop for the pulse width modulation PWM which determines the opening and closing signals of IGBTs. The structure of the internal current control loop is shown in Fig. 10 [4].

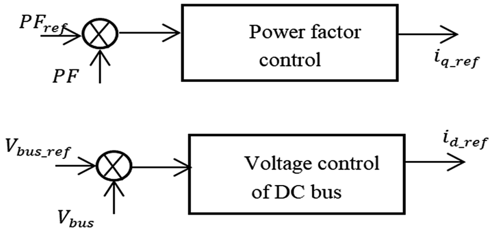

Fig. 9. External control structure

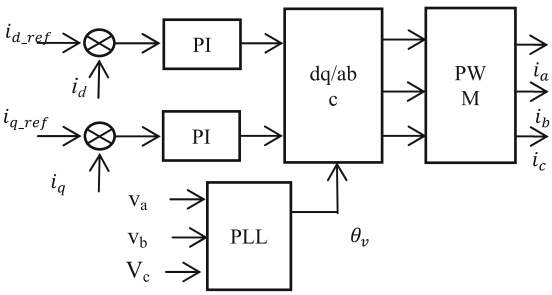

Fig. 10. Internal control structure

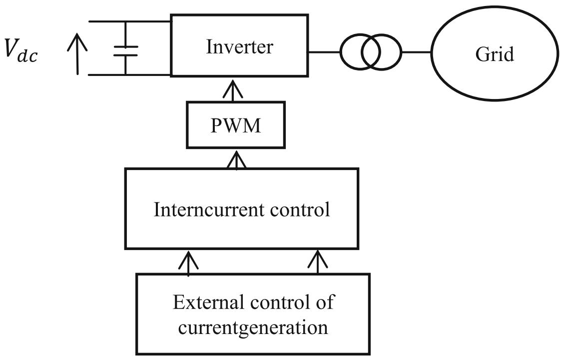

Fig. 11. Control diagram under STATCOM operation

5 Reactive Power Management with Synchronverter Control

5.1 The Concept of Synchronverter

A synchronverter is an inverter that mimics the synchronous generator. The control of the inverter is based on emulating the mathematical model of a synchronous generator [9, 10]. The structure of the three phase rotor of a synchronous machine is shown in Fig. 12. The stator and rotor windings in the *abc* frame lead to a self-inductance L and a mutual inductance ($-M$). The field winding can be viewed as a concentrated coil having a cyclic inductance L_s [9]. The phase voltages vector is:

$$V_{a,b,c} = -R_s i_{a,b,c} - L_s \frac{di_{a,b,c}}{dt} + e_{a,b,c} \tag{13}$$

Where $i_{a,b,c} = [i_a, i_b, i_c]^T$ is the stator phase current vector, L_s is the stator cyclic inductance and R_s is the stator windings resistance [11].

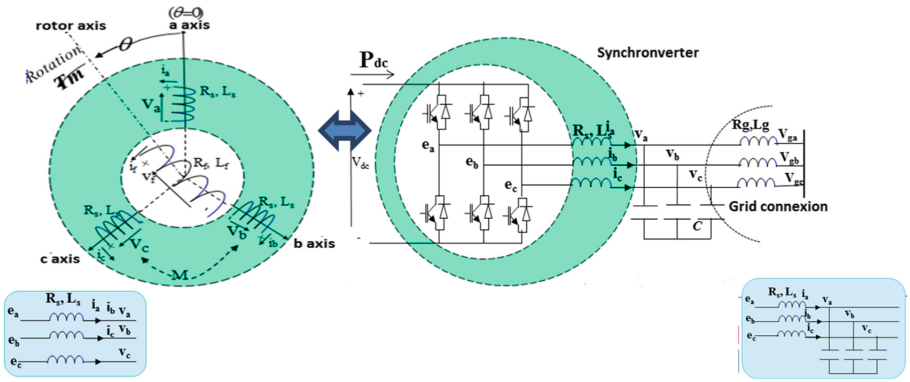

Fig. 12. Scheme of the Synchronverter Concept: emulation of synchronous machine (on the left) by three phase PWM inverter (on the right)

The mutual inductance between the stator coils and the rotor coils changes with the rotor angle as follows ($M_f > 0$):

$$M_{af} = M_f \cos\theta$$
$$M_{bf} = M_f \cos\left(\theta - \frac{2\pi}{3}\right) \tag{14}$$
$$M_{cf} = M_f \cos\left(\theta - \frac{4\pi}{3}\right)$$

$e_{a,b,c} = [e_a, e_b, e_c]^T$ is the back emf vector which can be expressed by:

$$e_{a,b,c} = M_f i_f \dot{\theta} \widetilde{\sin\theta} - M_f \frac{di_f}{dt} \widetilde{\cos\theta} \tag{15}$$

Where:

$$\widetilde{\sin\theta} = \begin{bmatrix} \sin\theta \\ \sin\left(\theta - \frac{2\pi}{3}\right) \\ \sin\left(\theta - \frac{4\pi}{3}\right) \end{bmatrix} \text{ and } \widetilde{\cos\theta} = \begin{bmatrix} \cos\theta \\ \cos\left(\theta - \frac{2\pi}{3}\right) \\ \cos\left(\theta - \frac{4\pi}{3}\right) \end{bmatrix}$$

θ is the rotor angle and i_f is the rotor excitation current. The mechanical equation of the synchronous machine is expressed by:

$$J_r \ddot{\theta} = T_{mr} - T_{er} - D_{pr} \dot{\theta} \tag{16}$$

Where J_r is the moment of inertia of both generator and turbine, T_{mr} is the mechanical torque, T_{er} is the electromagnetic torque, and D_{pr} is a damping factor. T_{er} can be expressed by:

$$T_{er} = M_f i_f \left\langle i_{a,b,c}, \widetilde{\sin\theta} \right\rangle \tag{17}$$

where $\langle . \,, . \rangle$ is the conventional inner product in R^3.

The real and reactive powers generated by the synchronous machine are given respectively by (18) and (19):

$$P = \dot{\theta} M_f i_f \left\langle i_{a,b,c}, \widetilde{\sin\theta} \right\rangle \tag{18}$$

$$Q = -\dot{\theta} M_f i_f \left\langle i_{a,b,c}, \widetilde{\cos\theta} \right\rangle \tag{19}$$

The development of the concept of the synchronverter is based on (13) to (19) equations. This concept consists of controlling the inverter similarly to conventional synchronous generators [10, 12].

5.2 Synchronverter Operating as STATCOM

The basic principles of rotational synchronous generator and STATCOMs operating as reactive power compensators are similar. Nonetheless, most control methods proposed to control STATCOM do not take into consideration the mathematical model of synchronous machines [11]. In [11], there is a trend to use the characteristics of a synchronous machine when the grid side inverter is operating as a STATCOM. In this case, the grid considers the converter as a synchronous machine operating in compensating mode. The synchronverter control enables reactive power regulation capabilities for zero active power generation. Thus, the grid side inverter operates as a STATCOM under "WindFree Reactive Power Control" [12]. The controller shown in Fig. 13 is proposed. It is composed of two regulators: The first regulates the DC voltage V_{dc} to keep itconstant. The second regulates the reactive power absorbed or generated by the inverter to a reference value Q_{ref} [11].

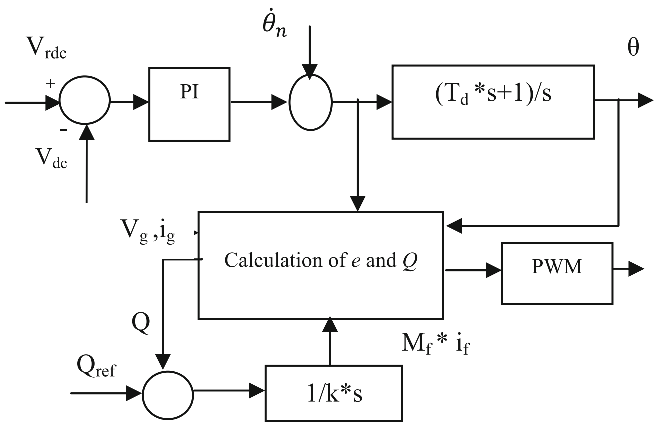

Fig. 13. STATCOM control loop with synchronverter concept

6 Simulation Results

6.1 Reactive Power Control

A variable wind speed is applied as shown in Fig. 14a. We depict from Fig. 14b, that the nominal active power (1 pu) is generated at nominal wind speed valued at 15 m/s. For wind speeds above nominal, the active power is curtailed at 1 pu.

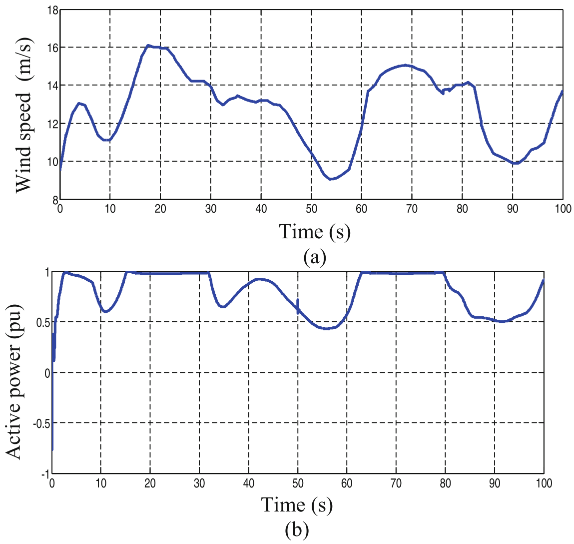

Fig. 14. (a) Wind profile. (b) Generated active power

6.1.1 Local Control

For this test, the grid voltage at the Poc is affected by a very fast transient increase (+0.2 pu) at t = 50 s (Fig. 15a) due to an important loss of load. As a response, the reactive power output of the wind plant switches from Q = 0 to Q = −0.45 pu (Fig. 15b). Thus, the wind turbines absorbed reactive power to bring the Poc voltage within the acceptable range. On the other hand, Fig. 16b shows reactive power injection at the point of connection in case of a Poc voltage drop of 4% (ΔV_POC = −4%) (Fig. 16a) and where the wind power plant provides the grid with reactive power.

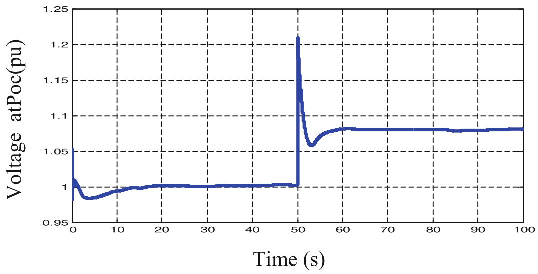

(a)

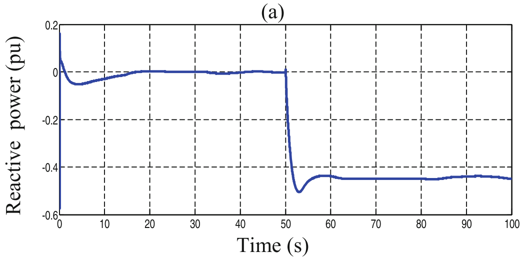

(b)

Fig. 15. (a) Grid voltage transient, (b) resulting reactive power response

6.1.2 Global Control

In order to verify the hierarchy between local and global controls, it is essential to check that the global control loop prioritizes the local one. That is, once a reactive power reference value Qref is received from the Dispatcher, local voltage controls are terminated. The wind power plant will operate under the Q Dispatching requirement. Figure 17 shows the reactive power delivered by the power plant following an order received from the Dispatching which requires an operation with Q = 0 (cos φ = 1), regardless of the voltage value at the Poc, which is successfully achieved.

6.2 Emergency Disconnection and P–Q Ramp Control

The wind turbine is controlled for emergency disconnection (for example, in storm situations). This is an important security function that must be guaranteed. To test this function, a dispatching command is applied at t = 40 s. The Tunisian grid code requires a ramp down of 10% for both active and reactive powers. Figures 18 and 19 depict that the ramp downs are respected according to the GCR for both active and reactive powers.

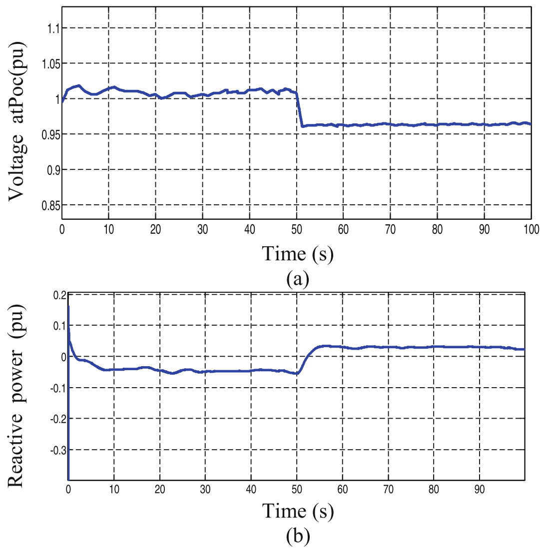

Fig. 16. (a) Drop of the Poc grid voltage, (b) resulting reactive power response

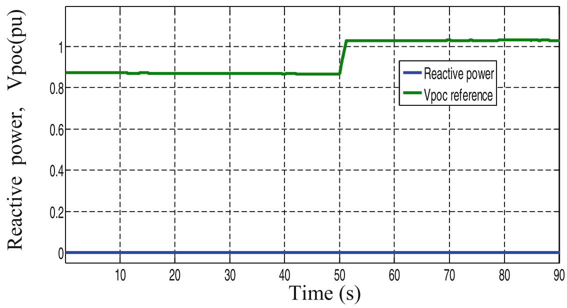

Fig. 17. Response of power plant reactive power during a variation in Vpoc reference under the Dispatching order: Q = 0.

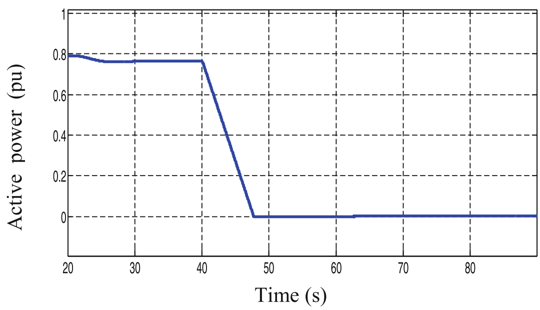

Fig. 18. Active power ramp down controlled

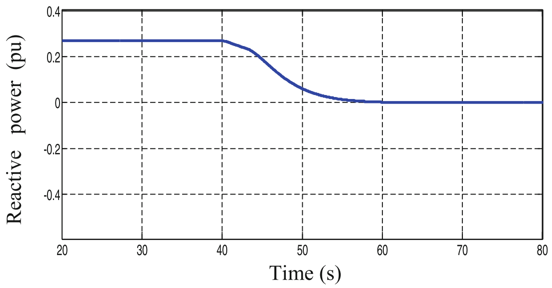

Fig. 19. Reactive power ramp down controlled

6.3 STATCOM Operation with VOC and Synchronverter Controls

In this section, the control loops described ahead have been tested under zero wind speed (Active power is set to zero).First, a voltage increase is applied to the Poc at t = 50 s. The reactive power responses from STATCOM operation with voltage oriented control and synchronverter control are shown in Fig. 20. With both controls, the reactive power decreases from 0 pu to −0.38 pu at t = 50 s; but, the synchronverter control response was faster and without overshoot. Then, we apply a decrease in the grid voltage at t = 50 s. The resulting reactive power responses under vector control and synchronverter control are shown in Fig. 21. They both increase at t = 50 s from 0 to 0.35 pu, with the same performances as the previous case.

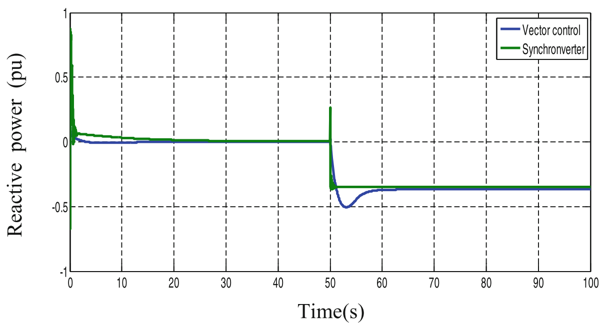

Fig. 20. Response of reactive power in STATCOM operation for a voltage increase

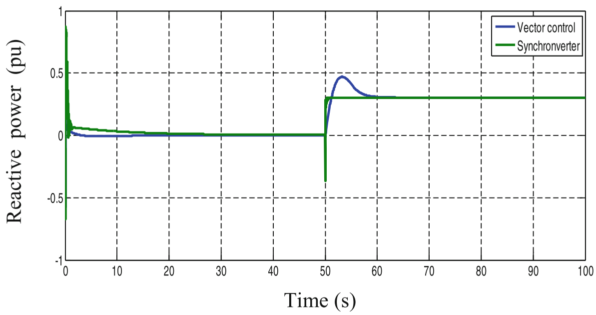

Fig. 21. Response of reactive power in STATCOM operation for a voltage decrease

7 Conclusions

In the present paper, advanced controls have been elaborated and implemented to improve the wind plant participation in the grid ancillary services. The wind power plants are required to support the grid with reactive power in case of voltage deviations or grid faults. Reactive power management of power plant has to comply with the grid code requirement specific to each country. The purpose of these requirements is to ensure the reliability and the stability of the electrical power grid.

In this work, reactive power control loops using PI controllers are developed for a system based on a Permanent Magnet Synchronous Generator. The ramp up and the ramp down for both active and reactive power have been taking into account as required by the Tunisian Grid Code. The hierarchical control, tested in this paper, gives the priority to the dispatching orders.

The recent concept of the synchronverter has successfully been used to control the grid side converter with a mathematical model similar to the synchronous generator one. The "free wind" reactive power capability of the modern wind power plant has been successfully tested in this paper, where the wind plant operated as a STATCOM. The regulation of reactive power as well as the voltage of wind plant connection have been successfully tested with two types of controls: VOC and Sychronverter. Better performance was shown by the last control. The simulation results have confirmed the respect of the hierarchy of controls by the priority given to the dispatching orders. In addition, voltage and reactive power regulations have complied well with the grid code requirements established by the power system operator.

References

1. World Wind Energy Association.: World Wind Market has reached 486 GW from where 54 GW has been installed last year, June 2017. www.wwindea.org
2. Zhou, X., Tang, Y., Shi, J.: Enhancing LVRT capability of DFIG-based wind turbine systems with SMES series in the rotor. Int. J. Rotating Mach. (2016)

3. SociétéTunisienned’Electricité et de Gaz STEG.: Cahier des Exigences Techniques de Raccordement et d’Evacuation de L’EnergieProduite à Partir des Installations d’EnergiesRenouvelablessureeReseau Haute et Moyenne Tension (2015). www.steg.com.tn
4. Errami, Y., Ouassaid, M., Mohamed.: Modelling and optimal power control for permanent magnet synchronous generator wind turbine system connected to utility grid with fault conditions. Inst. Eng. Technol. J. (2015)
5. Gajewski, P., Pieńkowski, K.: Analysis of a wind energy converter system with PMSG. IEEE Power Energy (2016)
6. Monteiro Pereira, R.M., Machado Ferreira, C.M., Maciel Barbosa, F.P.: Reactive power management of a wind farm to prevent voltage collapse of an electric power system. In: 50th International Universities Power Engineering Conference, Stafforshire University, UK (2015)
7. Yang, Y., Chen, W., Blaabjerg, F.: Advanced control of photovoltaic and wind turbines power systems. In: Power Electronics and Drives. Studies in Computational Intelligence, vol. 531. Springer International Publishing Switzerland (2014). https://doi.org/10.1007/978-3-319-03401-0_2
8. Monteiro Pereira, R.M., Machado Ferreira, C.M., Ghulam Sarwar Kaloi, F., Wang, J., Balochen, M.H.: Active and reactive power control of the doubly fed induction generator based on wind energy conversion. Energy Reports, pp. 194–200. Elsevier (2016)
9. Aouini, R., Marinescu, B., Ben Kilani, K., Elleuch, M.: Synchronverter-based emulation and control of HVDC transmission. IEEE Trans. Power Syst. **31**(1), 278–286 (2016)
10. Zhong, Q.-C., Konstantopoulos, G.C., Ren, B., Miroslav.: Improved synchronverters with bounded frequency and voltage for smart grid integration. IEEE Trans. Smart Grid Issue, vol. pp, issue 99, May 2016 (2016)
11. Nguyen, P.-L., Zhong, Q.-C., Blaabjerg, F., Guerrero, J.M.: Synchronverter-based operation of STATCOM to mimic synchronous condensers. In: 7th IEEE Conference on Industrial Electronics and Applications, USA (2012)
12. Miller, N.W.: Voltage and reactive power control-general electric. In: BPA Voltage Control Technical Conference, 23 August 2011

Damping of Forced Oscillations Caused by Wind Power

Ikram Nacef(✉), Khadija Ben Kilani, and Mohamed Elleuch

ENIT-LSE-RL11ES15, University of Tunis El Manar, Tunis le Belvédère, Tunis, Tunisia
ikramnacef28@gmail.com,
{khadija.kilani,mohamed.elleuch}@enit.utm.tn

Abstract. This paper investigates the issue of forced oscillations caused by wind power fluctuations and their damping by standards power system controls. The purpose is twofold: First, we study the difference between variable-speed and fixed speed wind turbine generators in inducing forced oscillations and causing resonance. Second, we demonstrate how standards power system controls can damp these forced oscillations and avoid the resonance in power systems. Modal analysis, frequency domain analysis and general forced oscillation mechanism (GFO) are performed to study this issue. The study is applied on four-machines two areas power system. The results demonstrate that power system controls damp forced oscillations and shift the frequencies of these oscillations far away from the dominant frequency band of wind power generation.

Keywords: Forced oscillations · Power system controls · Modal analysis
Variable speed · Wind power generation fixed speed

1 Introduction

1.1 General Information

The resonance is a well known phenomenon in physics. It is the tendency of a system to oscillate with greater amplitude at some frequencies than the others. Indeed, an external periodic disturbing force with a frequency at one of the natural system frequencies of poorly damped modes will lead to resonance [1]. Many studies investigated the forced oscillation mechanism in power systems. They point out that forced oscillations can emerge when power system is perturbed by periodic disturbances at frequencies close or equal to natural frequencies of system modes [2]. Such oscillations have been observed from the western North American Power System (wNAPS), US Western Electricity Coordinating Council (WECC) system, and the Nordic power system [3].

Various power system disturbances have been found to be the origins of forced oscillations, such as cyclic loads [4], turbo-pressure pulsations [5, 6], and mechanical oscillations of generator turbines [7]. Besides, the variability and the randomness of wind power generation may be considered as a potential forced oscillation source. In [8], the effects of wind shear and tower shadow are investigated. It was demonstrated that forced oscillations are caused by wind shear and tower shadow. In [9], the general forced oscillation mechanism GFO has been

M. Chadli et al. (Eds.): ICEECA 2017, LNEE 522, pp. 293–303, 2019.
https://doi.org/10.1007/978-3-319-97816-1_22

applied to study the inter-area oscillations observed on the power grid of China. It has been proved that the observed oscillation may be a forced oscillation caused by wind power fluctuations. Therefore, forced oscillation becomes not only an important issue of power system but also one concern of integrating wind energy into modern power grid.

Since wind turbine generators dynamic characteristics differ, it is essential to demonstrate if there is a difference between the variable speed and fixed speed wind turbines in exciting forced oscillations. On the other hand, if the frequencies of the wind power fluctuations coincide with the natural frequency of poorly damped oscillation mode, then the forced oscillation might result in a large amplitude oscillation, that is, the resonance.

Resonance in power systems is a dangerous situation; it may cause catastrophic blackouts, especially in the poorly damped operating condition [8]. Thus, it is necessary to avoid resonance. In this context, there are three methods could be used, namely, to reduce the input source oscillation, to move the input frequency far away from the natural frequency, and to improve the damping of the natural oscillation mode [8].

The purpose of this paper is twofold: First, we study the difference between variable-speed and fixed speed wind turbine generators in inducing forced oscillations and causing resonance. Second, we demonstrate how standards power system controls including Automatic Voltage regulators (AVR), Turbine Governors (TG) and Power System Stabilizers (PSS) can damp forced oscillations caused by wind fluctuations and move the frequencies of these oscillations far away from the dominant frequency band of wind power generation. Modal analysis, frequency domain analysis and general forced oscillation mechanism (GFO) are performed to study this issue. The study is applied on four-machines two areas power system.

2 Related Forced Oscillations in Power Systems

The general forced oscillation (GFO) can be excited when the frequency band of the random excitation covers the natural frequencies of poorly damped system modes. This mechanism is applied to study the oscillations in real power systems [10].

The linear system is modeled in the frequency domain as [10]:

$$S_y(f) = |H(f)|^2 S_u(f) \tag{1}$$

where $H(f)$ is the frequency-domain transfer function of the linear system and $S_u(f)$ and $S_y(f)$ are the power spectral density (PSD) of the input stationary random process and the PSD of the output stationary random process respectively.

Since, we can't easily obtain the exact value of $|H(f)|^2$, Eq. (1) will be used to make a qualitative analysis. From Eq. (1), it's clear that the system response depends on the input random excitation $S_u(f)$ and the squared amplitude-frequency property of the transfer function $|H(f)|^2$. For example, if the power system has three oscillation modes with natural frequencies f_1, f_2 and f_3 and if the power spectral density of the input random excitation covers one mode frequency f_1, the power spectral density of the output random excitation is very large at f_1, and small at f_2 and f_3 as shown in Fig. 1(a). Similarly, if the frequency band of the input random excitation changes (covers the modes with frequencies f_2 and f_3, as shown in Fig. 1(b), the PSD of the output variable is small at f_1 and becomes large at f_2 and f_3. Therefore, the mechanism of general forced oscillation (GFO) indicates that if the frequency bands observed in the PSD of the input random excitations cover the natural frequencies of some poorly damped modes of power systems, a forced oscillation with frequency bands around the covered mode frequencies is excited [10].

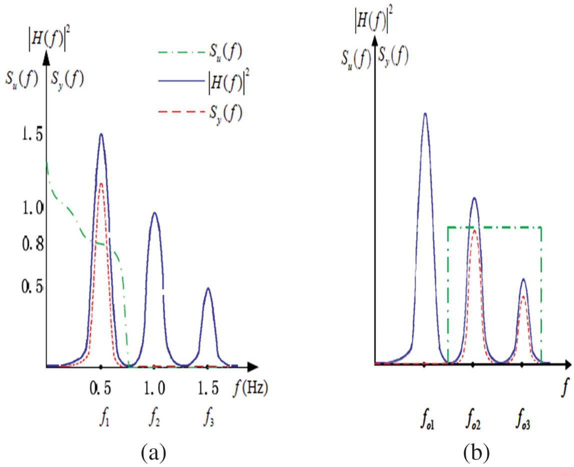

Fig. 1. Principe of GFO

The study is applied on a four-machines two areas power system [11]. It consists of two areas connected together by two 230 kV lines of 220 km length. It was designed in [11] to study low frequency electromechanical oscillations in large interconnected power systems. Each area comprises two identical generators rated 20 kV/900 MVA. The synchronous generators are presented by a six-order model with magnetic saturation neglected. There is 2800 MW installed generation capacity in this system (1400 MW in each area), and

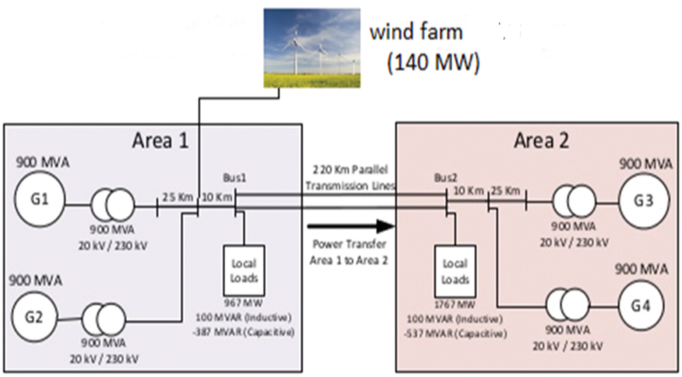

Fig. 2. Four-machines two areas power system with wind farm

400 MW of the total active power is transmitted from area 1 to area 2. We connect a wind farm at the sending end of area 1 at bus 6. The penetration level is 10% of the total installed active power of area 1 (140 MW). The test system is shown in Fig. 2. Simulation results were carried out using a Power System Analysis Toolbox (PSAT), which is a MATLAB-based toolbox for power system studies. Table 1 presents the study cases.

Table 1. Study Cases

Cases		Linear modal analysis	PSD of wind power generation
No WTGs	No(AVR/TG/PSS)	X	–
	(AVR/TG/PSS)	X	–
DFIG	No(AVR/TG/PSS)	X	X
	(AVR/TG/PSS)	X	X
DDSG	No(AVR/TG/PSS)	X	X
	(AVR/TG/PSS)	X	X
SCIG	No(AVR/TG/PSS)	X	X
	(AVR/TG/PSS)	X	X

First, linear modal analysis is performed for different cases to assess the resulting oscillation modes and to determine if wind turbine generators excite forced oscillations. Second, the wind power generation of each wind turbine (the Doubly Fed Induction Generator (DFIG), the Direct Drive Synchronous Generator (DDSG) and the Squirrel Cage Induction Generator (SCIG)) is frequency analysed by the power spectral density (PSD) in search of correlation between the band frequency of wind power output and the frequencies of oscillation modes indicated by linear modal analysis. Finally, we demonstrate how standards power system controls, namely, Automatic Voltage Regulator (AVR), Turbine Governor (TG) and Power System Stabilizer (PSS) can move the frequency of forced oscillations far away from the dominant frequency band of wind power generation and then avoid resonance of power system.

3 Simulation Results

3.1 Forced Oscillations in Power Test System Without (AVR/TG/PSS)

3.1.1 Modal Analysis

The resulting oscillation modes of the different cases without power system controls (AVR/TG/PSS) are summarized in Table 2.

From Table 2, it can be noticed that without wind farm, there are three oscillation modes. The integration of wind farm induces another oscillation mode. Its frequency depends on the type of the wind turbine generator, which is approximately (0.136 Hz, 0.09 Hz and 0.67 Hz), in case of (DFIG, DDSG and SCIG) respectively. Thus, wind power generation may be the source of this new mode.

Table 2. Resulting oscillation modes

Cases	Modes	Frequency f (Hz)	Damping ratio $\zeta(\%)$
No WTGs	Mode 1	0.98601	8.37
	Mode 2	0.95794	8.48
	Mode 3	0.49816	4.06
DFIG	Mode 1	0.98586	8.35
	Mode 2	0.94782	9.5
	Mode 3	0.51425	2.73
	New mode	**0.13638**	**9**
DDSG	Mode 1	0.99186	8.45
	Mode 2	0.95055	9.45
	Mode 3	0.51333	3
	New mode	**0.09013**	**2.24**
SCIG	Mode 1	0.99081	8.35
	Mode 2	0.94844	9.45
	Mode 3	0.51175	5.83
	New mode	**0.67923**	**22.7**

The participation factor of each generator to the new mode is illustrated by Figs. 3, 4 and 5 in the case of (DFIG, DDSG and SCIG) respectively. It's clear that in the case of variable speed WTGs (DFIG and DDSG) all generators contribute to the new mode. Whereas, in the case of fixed speed WTGs, only the SCIG contribute to the new mode and the participation factor of the synchronous generators is negligible.

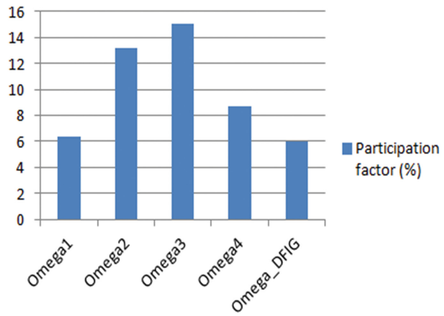

Fig. 3. Participation factors in case of DFIG

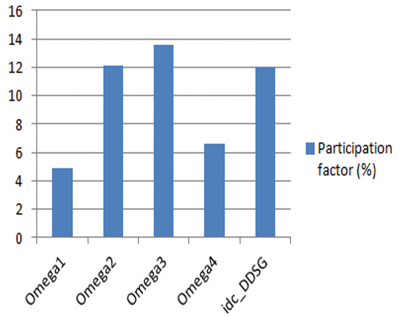

Fig. 4. Participation factors in case of DDSG

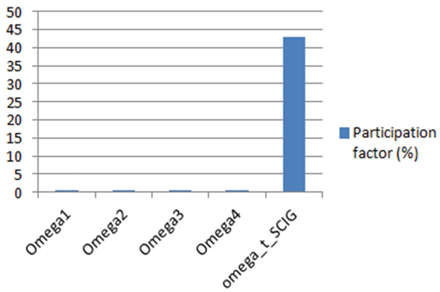

Fig. 5. Participation factor in case of SCIG

The low contribution of the synchronous generators in the mode introduced by the fixed speed turbines (SCIG) may justify the high value of the damping of this mode which will remain without great impact as long as the penetration rate of the wind power remains reduced. On the other hand, the high participation of synchronous machines in the modes introduced respectively by variable speed turbines (DFIG and DDSG) may explain the low damping of those modes, which could be maintained or amplified in the power system.

3.1.2 Power Spectral Density

Power spectral density (PSD) is performed to demonstrate the correlation between the new oscillation mode indicated by modal analysis and the dominant frequency band of power generated by variable speed and fixed speed turbine generators. If there is a correlation, thus, wind power generation can be considered as a forced oscillation source.

Power generated by variable speed and fixed speed wind turbine generators (DFIG, DDSG, and SCIG) and their respective PSD are depicted in Figs. 6, 7, 8, 9, 10 and 11.

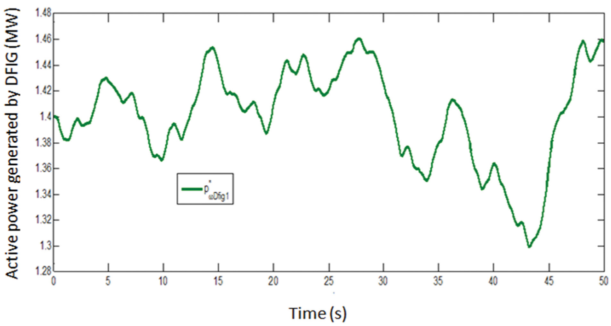

Fig. 6. Power generated by DFIG

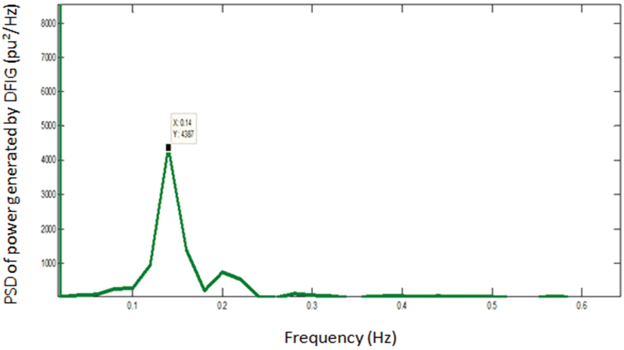

Fig. 7. PSD of power generated by DFIG

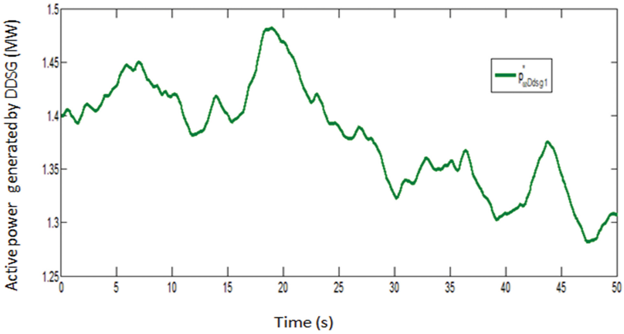

Fig. 8. Power generated by DDSG

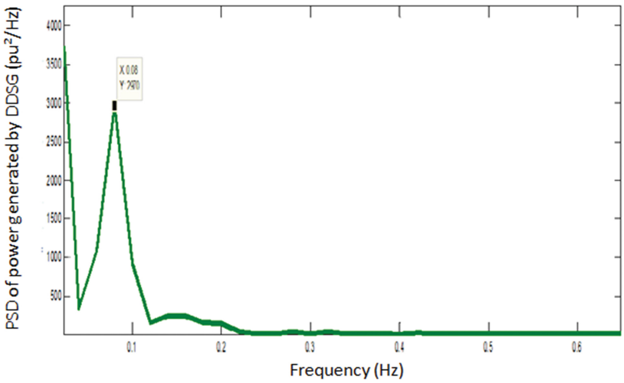

Fig. 9. PSD of power generated by DDSG

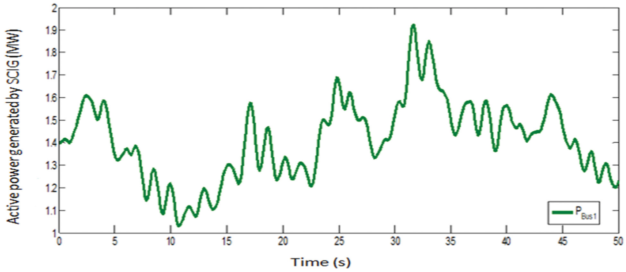

Fig. 10. Power generated by SCIG

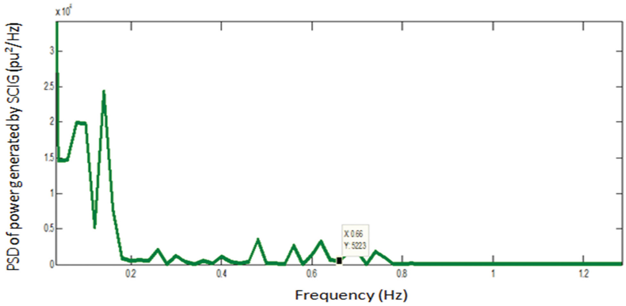

Fig. 11. PSD of power generated by SCIG

From Figs. 7, 9 and 11, it can be seen that wind power generation is distributed on a narrow frequency band which depends on the type of the wind turbine generator. In case of variable speed wind turbine generators (DFIG and DDSG), the frequency band of the power output covers the frequency of the new mode indicated by modal analysis (Table 2):

- The peak of the dominant frequency band of DFIG's power output is 0.14 Hz (Fig. 7) and it coincides approximately with the frequency of the new oscillation mode (0.136 Hz).
- The peak of the dominant frequency band of DDSG's power output is 0.08 Hz (Fig. 9) and it coincides approximately with the frequency of the new oscillation mode (0.09 Hz).

Therefore, Based on the general forced oscillation mechanism (GFO), we can speculate that the new oscillation mode indicate by modal analysis is a forced oscillation caused by wind power generation. And the phenomenon of resonance may occur.

In case of fixed speed wind turbine generator (SCIG), the frequency band of the power output is large and it comprises the frequency of the excited oscillation mode which is approximately (0.67 Hz). Whereas this mode is well damped (22.7%) and its frequency is far away from the peak of the frequency band of wind power generation. Thus, the new oscillation mode in this case is not dangerous and the power system will not undergo a resonance.

3.2 Control of forced Oscillations

Table 3 presents the frequency and the damping ratio of the forced oscillation mode for the different cases where the synchronous generators of the power system are equipped by the standards controls (AVR/TG/PSS). The parameters of (AVR/TG/PSS) are tuned as in [11].

Table 3. Frequency and damping of the forced oscillation mode

Cases	Frequency *f* (Hz)	Damping ratio (%)
DFIG	0.17027	62.29
DDSG	0.12247	82
SCIG	0.66987	23.48

Figures 12, 13 and 14 illustrate the PSD of the power generated by the different wind turbine generators (in cases with (AVR/TG/PSS)).

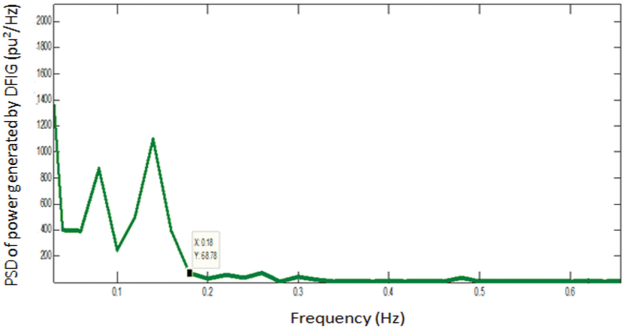

Fig. 12. PSD of power generated by DFIG (case with (AVR/TG/PSS))

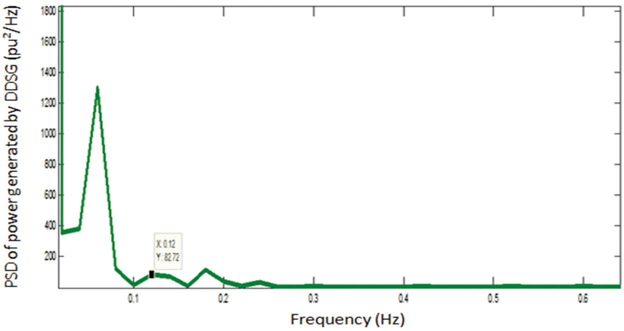

Fig. 13. PSD of power generated by DDSG (case with (AVR/TG/PSS))

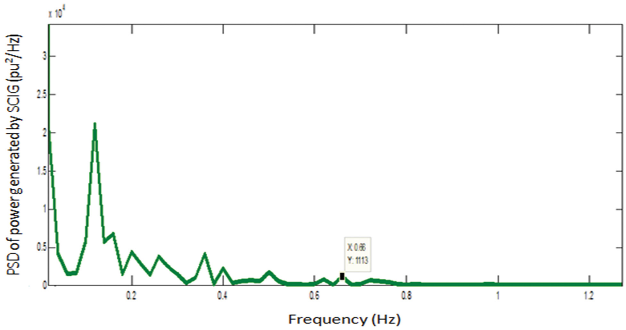

Fig. 14. PSD of power generated by SCIG (case with (AVR/TG/PSS))

It can be seen from Table 3 that:

- The oscillation mode induced by the wind power generated by SCIG is not influenced by the power system controls.
- In the case of DFIG and DDSG, the damping of the forced oscillation mode mentioned in section A increases significantly. Indeed, without power system controls, this oscillation mode was poorly damped (9% and 2.24%) in cases of (DFIG and DDSG) respectively. Whereas, when the synchronous generators are equipped by (AVR/TG/PSS), the damping of the forced oscillation reaches (62.29% and 82%) in cases of (DFIG and DDSG) respectively. On the other hand, it can be noticed from Figs. 9 and 10 that the frequency of the forced oscillation mode is far away from the peak of dominant frequency band of the wind power generation.

Thus, we can speculate that standards power system controls (AVR/TG/PSS) are able to damp forced oscillations and move their frequencies far away from the peak of the frequency band of wind power generation. As a result, resonance can be avoided.

4 Conclusion

This paper has investigated the issue of forced oscillations caused by wind power generation and their control. On the first hand, we studied the difference between variable speed and fixed speed wind turbine generators in inducing forced oscillations and causing resonance of power system. On the second hand, it was demonstrated how standards power system controls, namely, AVR, TG and PSS, can damp forced oscillations and avoid resonance of power system. The wind power generation was frequency analyzed and the general forced oscillation mechanism (GFO) was used to demonstrate the correlation between the frequencies of oscillation modes indicated by modal analysis and the wind power spectrum.

There is a correlation between the frequency of the wind power fluctuations and the natural frequency of system mode. Thus, wind power generation can be considered as a forced oscillation source. Whereas, there is a difference between variable speed and fixed speed wind turbine generators in inducting forced oscillations and causing resonance of power system. Indeed, variable-speed WTGs may cause resonance as the peak of the dominant frequency band of power output coincides with the natural frequency of poorly damped mode. Contrary to fixed-speed WTGs.

From a control point of view, it was demonstrated that standards power system controls, namely, AVR, TG and PSS can damp forced oscillations and move their frequencies from the dominant frequency band of wind power. Therefore, these controls can be an efficient way to avoid resonance of interconnected power system integrated substantial wind power generation.

References

1. Sarmadi, S.A.N., Venkatasubramanian, V.: Inter-area resonance in power systems from forced oscillations. IEEE Trans. Power Syst. **31**, 378–386 (2015)
2. Magdy, M.A., Coowar, F.: Frequency domain analysis of power system forced oscillations. IEE Proc. C Gen. Transm. Distrib. **137**(4), 261–268 (1990)
3. Vanfretti, L., Dosiek, L., Pierre, J.W., Trudnowski, D., Chow, J.H., García-Valle, R., Aliyu, U.: Application of ambient analysis techniques for the estimation of electromechanical oscillations from measured PMU data in four different power systems. Eur. Trans. Electr. Power **21**(4), 1640–1656 (2011)
4. Yu, Y., Min, Y., Chen, L., Ju, P.: The disturbance source identification of forced power oscillation caused by continuous cyclical load. In: Proceedings of the International Conference on Electric Utility Deregulation and Restructuring and Power Technologies (DRPT), Weihai, China, 6–9, pp. 308–313 (2011)
5. Hayashi, I., Kaneko, S.: Pressure pulsations in piping system excited by a centrifugal turbomachinery taking the damping characteristics into consideration. J. Fluid. Struct. **45**, 216–234 (2014)
6. Han, Z.X., Zhu, Z.L., Tian, X.S., Li, F.: Analysis and simulation research on power system low frequency oscillation. In: Proceedings of the International Conference on Computer Modeling and Simulation (ICCMS), Sanya, China, 22–24; pp. 223–228 (2011)
7. Wang, X., Li, X., Li, F.: Analysis on oscillation in electro-hydraulic regulating system of steam turbine and fault diagnosis based on PSOBP. Expert Syst. Appl. **37**(5), 3887–3892 (2010)
8. Su, C., Hu, W., Chen, Z., Hu, Y.: Mitigation of power system oscillation caused by wind power fluctuation. IET Renew. Power Gener. **7**(6), 639–651 (2013)
9. Ju, P., Liu, Y., Wu, F., Dai, F., Yu, Y.: General forced oscillations in a real power grid integrated with large scale wind power. Energies **9**, 525 (2016)
10. Liu, Y., Ju, P., Chen, J., Zhang, Y., Yu, Y.: Contrastive analysis of general and special forced oscillations of power systems. CSEE J. Power Energy Syst. **1**, 61–68 (2015)
11. Kundur, P.: Power System Stability and Control. McGraw-Hill, New York (1994)

High Performance Analysis of Hetero-Junction $In_{1-X}Ga_XN/GaAs$ Solar Cell Using SCAPS

Abdelkader Nassour[1(✉)], Malika Kandouci[1], and Abderrahmane Belghachi[2]

[1] Laboratory of Electronic Photonic and Optoelectronic (LEPO), University of Sidi Bel-Abbes, 22000 Sidi Bel-Abbes, Algeria
nassour.2011@gmail.com, maikand04@gmail.com
[2] Laboratory of Physics of Semiconductors Devices (LPDS), University of Béchar, 08000 Béchar, Algeria
abelghachi@yahoo.fr

Abstract. The group-III nitride based semiconductors have proved their potential application in optoelectronic devices. The effects of layers thickness and doping on the photovoltaic cell parameters in p-$In_{1-x}Ga_xN$/i-GaAs/n-$In_{1-x}Ga_xN$ hétérojunction solar cell have been investigated using solar cell capacitance simulator (SCAPS). The impacts of gallium (Ga) content, doping and thickness variation on the cell's output parameters were extensively simulated. In this work, the p and n-$In_{1-x}Ga_xN$ band gap (E_g) are first defined and formulated as mathematical functions of gallium (Ga) content ("x"). Our numerical analysis highlights that the E_g value of 1.27 eV corresponding to x = 0.3 is optimal. Our results showed that the best structure must have a p-doped $In_{0.7}Ga_{0.3}N$ layer, an active intrinsic GaAs layer, and n-doped $In_{0.7}Ga_{0.3}N$ layer that have thicknesses of 0.15, 1.2 and 0.15 µm, respectively and doped with $N_A = 10^{16}$ cm^{-3} and $N_D = 10^{17}$ cm^{-3}. Cells with these optimization results are found to give conversion efficiency of 25.88%.

Keywords: Solar cells · InGaN · SCAPS · GaAs · Efficiency Thin film

1 Introduction

Solar Cells are currently the subject of multiple investigations in order to reach the highest ratio efficiency/cost. With a direct band gap, the absorber-layer of thin-film solar cells has a high optical absorption coefficient which allows using absorbers of only a few microns thick [1].

Group III-nitride compound semiconductor materials have recently become one of the most interesting research topics due to their use in optoelectronic devices operating in the infrared, red, green, blue, violet and ultraviolet spectral wavelength regions [2].

InGaN ternary alloy is one of the most important materials in III-nitride family with direct band gap, and has a strong absorption coefficient [3]. The $In_{1-x}Ga_xN$ alloy has been studied extensively in recent years. High-quality wurtzite-structured In-rich

M. Chadli et al. (Eds.): ICEECA 2017, LNEE 522, pp. 304–313, 2019.
https://doi.org/10.1007/978-3-319-97816-1_23

$In_{1-x}Ga_xN$ films ($0 \leq x \geq 0.5$) have been grown on sapphire substrates by molecular-beam epitaxy [4].

The $In_{1-x}Ga_xN$ material systems can partly cover most parts of the solar spectrum from ultraviolet to infrared spectra due to their ability to vary their band gap with ranges 0.77 eV to 3.44 eV and have a substantial potential to develop ultrahigh efficiency solar cells [5, 6]. The extrinsic absorptions take place which causes the band gap value is lower than it is expected. And the acceptors and donors are mainly due to the doping or some defect structure. That's basically how the bowing behavior is coming from for the ternary semiconductor material. The measured bowing parameters vary from 1 to 5 eV according to work reported in literature [2].

The GaAs thin-film solar cell is a top contender in the thin-film multijunction (MJ) solar cells market in that it has a high power conversion efficiency (PCE) compared to that of other thin-film solar cells [7], but all are limited to some degree by the present lack of efficient photovoltaic materials with band gaps greater than ~ 1.9 eV. To achieve a high efficiency, it is likely that future MJ cell architectures will need to include materials with larger band gaps to improve the utilization of photons in the high energy portion of the solar spectrum, InGaN appears to be an ideal material for meeting this challenge [8].

In the present contribution, a numerical study has been realized in order to investigate the effect of a variation of material parameters to the final solar cell characteristics in order to improve their performances. In this article, examples of such simulation are shown for *p*-*i*-(GaAs)-*n* InGaN hétérojunction solar cell structure which it is composed of five layers, namely a transparent conductive oxide (TCO) contact, a *n*-doped InGaN layer, an active intrinsic GaAs layer, an *p*-doped InGaN layer, and a metal contact, as shown in Fig. 1. The calculations have been performed using a numerical model with the solar cell capacitance simulator (SCAPS) program.

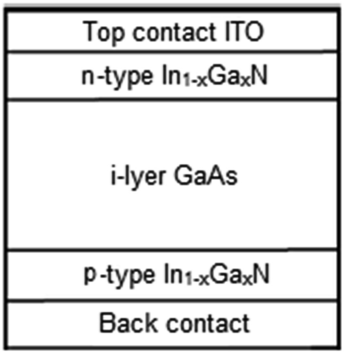

Fig. 1. Schematic view of proposed *p*-InGaN/*i*-GaAs/*n*-InGaN hetrojunction solar cell.

2 Numerical Simulations

In this paper, numerical modeling of *p*-$In_{1-x}Ga_xN$/*i*-GaAs/*n*-$In_{1-x}Ga_xN$ thin film solar cell has been performed using SCAPS computer software program [9] so as to investigate the effect of gallium grading on the cell performance, doping of InGaN layers and the effects of thickness of itch layers. It is possible to simulate structures formed from a defined number of layers with different doping profiles and with a given energetic distributions of donor and acceptor levels in bulk and at interfaces for arbitrarily light spectrum [10].

Recombination in deep bulk levels and their occupation is described by the Shockley–Read–Hall (SRH) formalism. Recombination at the interface states is described by an extension of the SRH formalism allowing the exchange of electrons between the interface state and the two adjacent conduction bands, and of holes between the state and the two adjacent valence bands [11, 12].

The total density of deep states in doped layers has been chosen higher than in the intrinsic one [13]. This gap state distribution does not completely account for correlation effects but it has been shown [14] that it is always a good approximation in computing the amount of trapped charges. The material properties that are used for the constituent layers are extracted from the reported literature [6, 15, 16].

The parameter values used in simulation are displayed in Table 1. For achieving the best performance of a cell under an AM 1.5 light spectrum and 1000 (w/m_2) light intensity, band gap and doping of *p*, *n* region then should be optimized, the thickness of two layers is kept unchanged and those of the third layer are optimized. All SCAPS simulations have been modeled at a room temperature T = 300 K. The measurement of the photovoltaic parameters has been made by considering null series resistance and infinitely large shunt resistance.

Table 1. Physical parameters used in the simulation of InGaN and GaAs layers.

Parameters	IGaN	GaAs
d(nm)	Variable	Variable
E_g(eV)	Variable	1.42
χ (eV)	4.5	4.07
$\varepsilon/\varepsilon_0$	13.6	12.9
N_c(cm^{-3})	2.2×10^{18}	2×10^{18}
N_v(cm^{-3})	1.8×10^{19}	1×10^{19}
μ_e(cm^2/V.s)	100	1000
μ_h(cm^2/V.s)	25	170
N_D (cm^{-3})	Variable	10^{16}
N_A (cm^{-3})	Variable	10^{16}
m_e	0.118	0.067
m_{hh}	0.064	0.027
υ_e *(cm/s)*	5×10^{-13}	10^{-16}
υ_h *(cm/s)*	10^{-15}	10^{-16}
N_t *(cm^{-3})*	10^{15}	10^{14}
$\alpha(\lambda)$	10^5	From file

3 Results and Discussions

3.1 The Effect of Gallium Grading on InGaN Cell Performance

Bandgap of $In_{1-x}Ga_xN$ depends on the Ga fraction, and can be expressed as [17]:

$$E_g(x) = xE_{gGaN}(1-x)E_{gInN} - mx(1-x) \tag{1}$$

Where E_{gGaN} is bandgap of GaN, E_{gInN} is bandgap of InN, and m is a bowing parameter in ternary $In_{1-x}Ga_xN$ alloys, there are equal to 3.44 eV to 0.77 eV and 1.4, respectively [4, 6].

Figure 2 and Table 2 show the effect of the mole fraction of Ga on the cell performance for: E_{gGaAs} = 1.42 eV. Increasing the bandgap of this layer reduces the absorption within this layer and therefore the short-circuit current decreases. However, the open circuit voltage increases, as it varied linearly with the bandgap. The compromise between these two phenomena, Simulation results show the best value of bandgap is 1.27 eV and when we choose x = 0.3, $In_{1-x}Ga_xN$ equal to 1.27 eV. This simulation results have a good agreement with the theoretical estimation to achieve the best performance of the typical photovoltaic devices with the optimal Ga/(Ga + In) ration 'x' in the range from 0 to 0.5 eV [4].

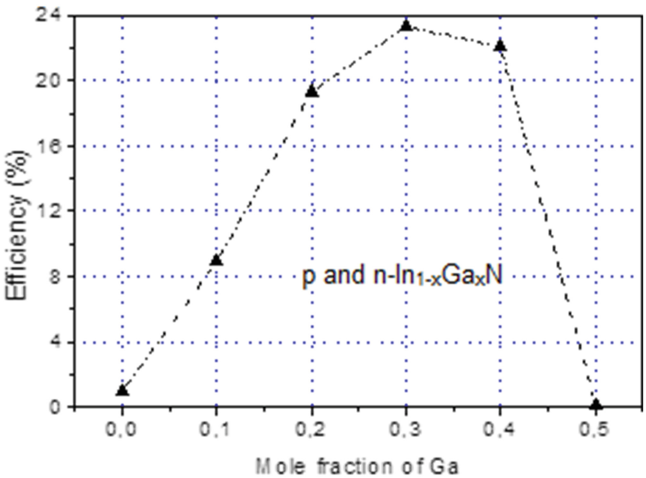

Fig. 2. Variation of cell efficiency due to increase Ga content in p and n-$In_{1-x}Ga_xN$ composition.

Table 2. Cell photovoltaic parameters for various p and n-layers gallium content $In_{1-X}Ga_XN$.

Ga/(Ga + In) ration	η %	FF %	J_{SC} (mA/cm^2)	V_{oc} (V)
0	0.98	49.77	4.736×10^{-3}	0.417
0.1	8.93	55.89	33.130	0.482
0.2	19.31	82.95	36.171	0.643
0.3	23.29	85.47	32.737	0.832
0.4	22.1	82.57	27.234	1.045
0.5	0.1	77.63	8.736×10^{-3}	1.087

3.2 The Effect of i-GaAs Layer Thickness on Conversion Efficiency

Variation of efficiency (η), as a function of *i*-GaAs thickness, under 1.5 AM one sun condition, has shown in Fig. 3. In Fig. 3, we assumed that *i*-region defect density N_t is about 10^{14} cm^{-3}. Table 3 shows that by increasing *i*-region thickness from 0.1 µm to 2.5 µm, J_{sc} increase but V_{oc} is unchanged. It is clear that by increasing the thickness from 0.1 µm to about 1.2 µm, J_{sc} significantly arise and after above thickness has no significant increase.

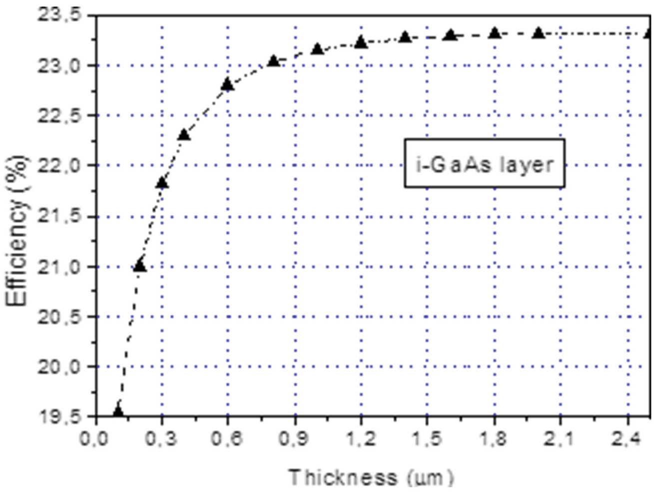

Fig. 3. Variation of efficiency versus thickness of GaAs intrinseque layer.

Furthermore, in Fig. 3, it is clear that in the 1.2 µm *i*-region thickness, efficiency is about 23.22% and after this thickness, due to electric field limits, η does not significantly increase. From the simulation results, it was found that the optimized value of *i*-GaAs thickness is 1.2 µm, which leads to a thinner and cheaper solar cell. Hence, *i*-region thickness has to be limited to 1.2 µm to maintain drift transport of charges across it. Decreasing *i*-region thickness increases the electric field in it, so our result with i-GaAs is more important than those found with *i*-InGaN [6].

Table 3. Cell photovoltaic parameters for various i-layer thicknesses GaAs.

Thickness of i-GaAs layer (μm)	η %	FF %	J_{SC} (mA/cm^2)	V_{oc} (V)
0.1	19.54	83.01	27.174	0.832
0.4	22.3	85.19	31.476	0.832
0.8	23.03	85.43	32.390	0.832
1	23.15	85.47	32.544	0.832
1.2	23.22	85.49	32.833	0.832
1.6	23.29	85.49	32.724	0.832
2	23.31	85.47	32.765	0.832
2.5	23.31	85.39	32.789	0.832

3.3 The Effect of p and n $In_{0.7}Ga_{0.3}N$ Layers Thickness on Conversion Efficiency

In Fig. 4 the efficiency is plotted against the thickness of p and n-InGaN layers. For the thickness of p and n region we have proceeded from 20 nm up to 170 nm. Our results regarding the cell photovoltaic parameters for various thicknesses of p and n region are listed in Table 4. From an inspection of Table 4 we notice that as the thickness of the p and n layer increases on going from 20 nm up to 170 nm, the form factor increases slightly. The same trend can be observed for the efficiency which increases from 23.06% to 23.47%.

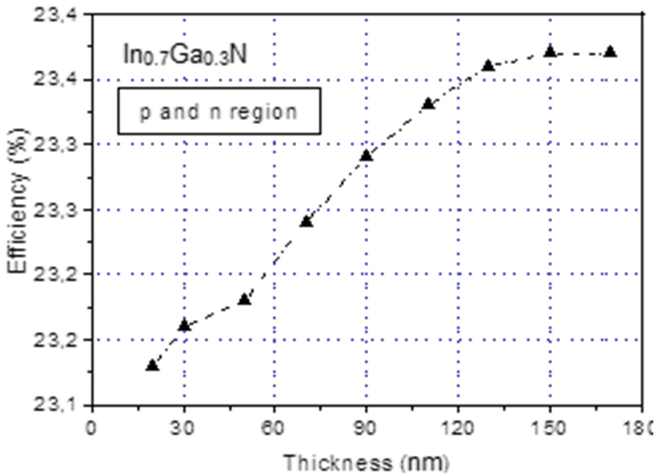

Fig. 4. Variation of efficiency versus thickness of p and n-$In_{0.7}Ga_{0.3}N$ layers.

The influence of the thickness of p and n region on the current density of the short circuit (J_{sc}) results in the monotonic increase of J_{sc}. As regards the open circuit voltage V_{oc}, it seems that V_{oc} is not sensitive to the variation of p and n layer thickness of InGaN. As reported in Table 4 and Fig. 4, the highest value of the electric efficiency

Table 4. Cell photovoltaic parameters for various p and n-layer thicknesses $In_{0.7}Ga_{0.3}N$.

Thickness of p and n $In_{0.7}Ga_{0.3}N$ layers (nm)	η %	FF %	J_{SC} (mA/cm^2)	V_{oc} (V)
20	23.13	85.42	32.297	0.832
30	23.16	85.42	32.34	0.832
50	23.18	85.41	32.379	0.832
70	23.24	85.4	32.466	0.832
90	23.29	85.39	32.537	0.832
110	23.33	85.38	32.594	0.832
130	23.35	85.37	32.641	0.832
150	23.47	85.77	32.653	0.832
170	23.37	85.8	32.398	0.832

could be achieved for a p and n layer thickness of 150 nm. As the material is used as *i*-region of the *p-i-n* structure and it is intended to maximize the thickness of this field bearing region, the thickness of the *p* and *n* junctions need to be minimal. This is consistent with the previous results reported in Ref. [6].

3.4 Influence of Doping of p and n-$In_{0.7}Ga_{0.3}N$ Layer on Conversion Efficiency

The variation of the efficiency as a function of doping (N_D) of *n*-$In_{0.7}Ga_{0.3}N$ layer with a thickness of 150 nm is displayed in Fig. 5. Note that as the value of N_D is increased, the efficiency increases as well and becomes almost constant when reaching a value of 25.8% for N_D = $10^{17}cm^{-3}$. In fact the increase of the dopant number may improve the

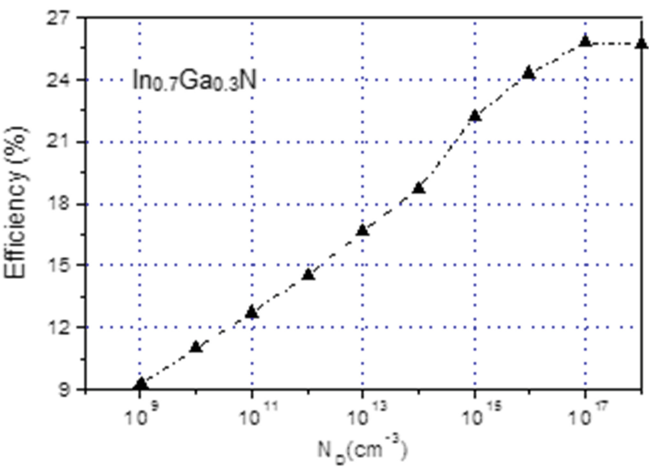

Fig. 5. Variation of efficiency versus doping of n-$In_{0.7}Ga_{0.3}N$ layer.

collection of photo-generated carriers and consequently favors the increase of electrical efficiency.

It is also interesting to see how the conversion efficiency is affected by the change of doping (N_A) of the p-$In_{0.7}Ga_{0.3}N$ layer. In this regard, we have displayed the variation of the efficiency as a function of the doping N_A in Fig. 6. Note that as N_A increases from 10^9 to 10^{16} cm^{-3}, the electric efficiency increases rapidly from 12.42% to 23.75%. This indicates that the doping of the p region has a strong effect on the efficiency of the solar cell. This is due to the fact that the increase of the number of dopant may improve the collection of photo-generated carriers leading thus to the increase of electric efficiency.

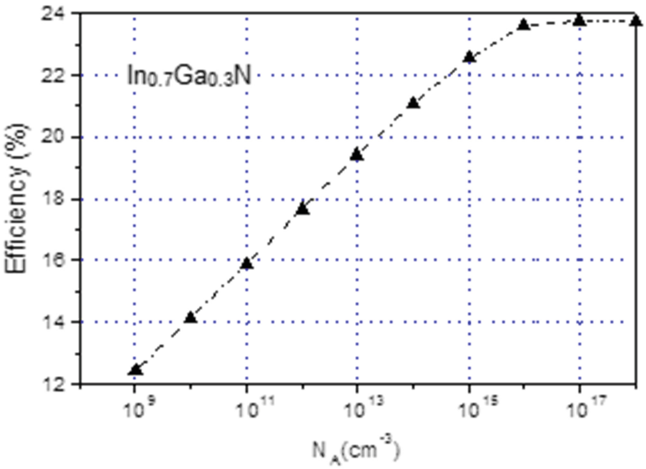

Fig. 6. Variation of efficiency versus doping of p-$In_{0.7}Ga_{0.3}N$ layer.

By combining the obtained optimal parameters of each layer, we have conceived the optimal structure of the p-$In_{0.7}Ga_{0.3}N$/i-GaAs/n-$In_{0.7}Ga_{0.3}N$ solar cell of interest. Our results are listed in Table 5. Regarding the efficiency, this is in good accord with the previous CIGS solar cell results reported in Refs. [10]. Furthermore, our result is clearly improved with respect to those previously conventional CIGS based solar cell and InGaN p-i-n homojuction solar cell reported in Refs. [1, 6, 18].

Table 5. Photovoltaic parameters comparison.

Photovoltaic values	η %	FF %	J_{SC} (mA/cm^2)	V_{oc} (V)
This work	25.88	87.15	32.944	0.906
Reference [1]	21.8019	83.75	35.0077	0.743
Reference [6]	20.43	85.2	28.5	0.84
Reference [18]	21.32	82	33.5	0.78

4 Conclusion

In this study, we have optimized a p-$In_{1-x}Ga_xN$/i-GaAs/n-$In_{1-x}Ga_xN$ solar cell. The cell performance is analyzed and simulated by the functions of Ga content in p and n region layer. The p and n-InGaN layer band gap was defined as the mathematical functions of Ga/(Ga + In) ratio. The numerical simulation results that were obtained with SCAPS show that the cell with $In_{0.7}Ga_{0.3}N$ as the p and n layers gives the higher efficiency in comparison with cells with other amount of Ga content in the p and n region. Variation of cell characteristics parameters in terms of thickness and doping in p-layer, i-GaAs layer, and n-layer has been calculated and it was found that the best structure must have a p and n layer ($In_{0.7}Ga_{0.3}N$) of thickness of 0.15 µm with $N_A = 10^{16}$ cm^{-3} and $N_D = 10^{17}$ cm^{-3} respectively and it was found that optimized value of the intrinsic GaAs layer thickness is 1.2 µm. Simulation results show that cell efficiency strongly depends on i-layer (GaAs) quality to maintain drift transport of charges across it and the high doping in p/n region ($In_{0.7}Ga_{0.3}N$) may improve the collection of photo-generated carriers. The p-i-(GaAs)-n $In_{1-x}Ga_xN$ solar cells with these parameters give an electric efficiency of 25.88% with a form factor of 87.15%, current density of 32.944 mA/cm^2 and voltage of open circuit of 0.906 V. The obtained efficiency in the present study is better than several those reported in the literature.

Acknowledgments. The authors acknowledge the use of SCAPS-1D program developed by Marc Burgelman and colleagues at the University of Gent in all the simulations reported in this study.

References

1. Benmir, A., Aida, M.S.: Analytical modeling and simulation of CIGS solar cells. Energy Procedia **36**, 618–627 (2013)
2. Wang Ms, J.: Optical properties of $In_{1-x}Ga_xN$ epilayers grown by HPCVD, Thesis, Georgia State University (2010)
3. Bennacer, H., Berrah, S., Boukortt, A., Ziane, M.I.: First principal calculations of optical properties of InGaN2 using in solar cells applications. In: Haddar, M., et al. (eds.) Multiphysics Modelling and Simulation for Systems Design and Monitoring. Applied Condition Monitoring, vol. 2. Springer, Cham (2015)
4. Wu, J., et al.: Small bandgap bowing in $In_{1-x}Ga_xN$ alloys, PACS numbers: 78.66.Fd, 72.80. Ey (2002)
5. Wu, J., Walukiewicz, W., Yu, K.M., Ager III, J.W., Haller, E.E., Lu, H., Schaff, W.J., Saito, Y., Nanishi, Y.: Appl. Phys. Lett. **80**, 3967 (2002)
6. Movla, H., Salami, D., Sadreddini, S.V.: Simulation analysis of the effects of defect density on the performance of *p-i-n* InGaN solar cell. Appl. Phys. A **109**, 497–502 (2012)
7. Moon, S., et al.: Highly efficient single-junction GaAs thin-film solar cell on flexible substrate. Sci. Rep. **6**, 30107 (2016). https://doi.org/10.1038/srep30107
8. Farrell, R.M., Friedman, D.J., Young, N.G.: InGaN-based solar cells and high-performance broadband optical coatings for ultrahigh efficiency hybrid multijunction device designs. In: Conference on Lasers and Electro-Optics (CLEO). IEEE Explore (2013)
9. Burgelman, M.: SCAPS User Manual. Elis-University of Gent, p. 10 (2007)

10. Heriche, H., Rouabah, Z., Bouarissa, N.: High-efficiency CIGS solar cells with optimization of layers thickness and doping. Optik Int. J. Light Electron Opt. **127**, 11751–11757 (2016)
11. Burgelman, M., Nollet, P., Degrave, S.: Modelling polycrystalline semiconductor solar cells. Thin Solid Films **361–362**, 527–532 (2000)
12. Burgelman, M., Verschraegen, J., Degrave, S., Nollet, P.: Prog. Photovolt. **12**, 143–153 (2004)
13. Street, R.A.: J. Non-Cryst. Solids **77**, 1–16 (1985)
14. Halpern, V.: Philos. Mag. **B 54**, 473–482 (1986)
15. Feng, S.-W., Lai, C.-M., Chen, C.-H., Sun, W.-C., Tu, L.-W.: J. Appl. Phys. **108**, 093118 (2010)
16. Levinshtein, M.E., Rumyanstev, S.L., Shur, M.S.: Properties of Advanced Semiconductor Materials: GaN, AlN, InN, BN, SiC, SiGe. Wiley, New York (2001)
17. Vurgaftman, I., Meyer, J.R.: J. Appl. Phys. **94**, 3675–3696 (2003)
18. Chelvanathan, P., Hossain, M.I., Amin, N.: Performance analysis of copper-indium-gallium-diselenide (CIGS) solar cells with various buffer layers by SCAPS. Curr. Appl. Phys. **10**, S387–S391 (2010)

Predictive Control Strategy for Double-Stage Grid Connected PV Systems

Abdelbaset Laib(✉), Fateh Krim, Billel Talbi, Abbes Kihal, and Abdeslem Sahli

LEPCI Laboratory, Electronics Department, Ferhat Abbas Setif-1-University, Route Bejaia, Setif, Algeria
laibabdelbasset42@gmail.com, krim_f@ieee.org, bilel_ei@live.fr, kihalabbas.87@gmail.com, sahli_abdeslem@yahoo.fr

Abstract. This paper presents a control of three phase two-stage grid-connected photovoltaic (PV) system based on predictive control strategy. The main goals are: extract the maximum power point (MPP) delivered by PV arrays under irradiation variations and to inject it into the network with a high grid current quality. MPPT current oriented loop based on predictive control strategy is proposed and applied into the first stage (DC–DC Boost converter) in order to achieve high performance tracking. Furthermore, a Voltage oriented control based on predictive control strategy and space vector modulation SVM (VOC-PC-SVM) is applied into the second stage (Tow-level inverter) in order to control the grid currents. The proposed system is simulated using Matlab/Simulink and Simpower system packages. The obtained results prove that the proposed control strategy provides high performance control in term of MPP tracking and grid current quality under irradiation variations in accordance with international standards (IEEE-519).

Keywords: PV system · Double-stage · Predictive control strategy
Maximum power point tracking (MPPT) · Grid current control

1 Introduction

Grid connected photovoltaic (PV) systems have been used to inject the energy delivered by PV arrays into the network [1–3]. The current challenge is to extract the maximum power from the PV arrays and deliver it to the network with high grid current quality under climatic changes. For this reason, several researchers are working on these challenges in two grid PV system topologies which are single and dual-stage [1–4]. The latter is widely used due to the fact that, the maximum power point tracking (MPPT) and the control of the power injected into the grid are decoupled with different converters. This advantage eases the MPP tracking as well as boosting the DC-link voltage value above the grid peak voltage value whatever is the quantity of the produced power from PV arrays [1].

PV arrays still do not deliver a maximum efficiency, since their performance depends on climatic conditions. The random variation of these factors reduces the PV arrays output power. For this reason, many MPPT techniques have been proposed in the literature in order to enforce PV array systems to continuously pursuing and expeditiously extracting the maximum power from the PV arrays. Conventional MPPT algorithms such as perturb

M. Chadli et al. (Eds.): ICEECA 2017, LNEE 522, pp. 314–327, 2019.
https://doi.org/10.1007/978-3-319-97816-1_24

and observe (P&O) [5] or Incremental conductance (IncCon) [6] have been intensively investigated in the last decade. Nevertheless, these techniques possess two major weakness: low speed in reaching the maximum power and broad oscillations around it. Recently, several intelligence techniques such as fuzzy logic [7–10] and neural networks [11] genetic algorithm [12], particle swarm optimization [2], have been introduced in order to enhance the performance, however, it still difficult to implement them in practice. In addition, due to the implementation simplicity of the conventional MPPT algorithms, other control schemes based on these algorithms have been proposed to improve the efficiency of PV array by including an intern voltage loop in the case of MPPT voltage-oriented loop [13, 14] or an intern current loop in the case of MPPT current oriented loop [15–20]. These latter afford an accurate MPP tracking as well as a satisfactory fluctuation reduction around the MPP, this is achieved by virtue of the linear relation between the PV array current and solar irradiation [16]. Several current controllers are employed in MPPT current oriented loop methods such as *PI* controller [17], predictive controller [15], Finite set model predictive controller (FS-MPC) [18–20] and sliding mode controller (SMC) [16]. Predictive current controller offers significant advantages like implementation simplicity and high performances regarding time response and PV current ripple compared to *PI* controller. Besides, it has fixed frequency compared to SMC and FS-MPC controllers.

In order to obtain high performance tracking, this paper proposes a MPPT current oriented loop based on fixed switching predictive current control as first part of this work.

The second stage is used to inject the extracted PV power into the network with assuring high gird current quality. For this purpose, many control techniques are proposed. One of them, control methods without modulation stage such as: grid current control based on hysteresis controllers [21] or finite set model predictive control strategies [22–24], direct power control DPC based on switching table [25]. Those control methods provide a high performance; however, they possess a variable switching frequency which is considered as a major drawback. Control method with modulation stage such as: Voltage-oriented control (VOC) [26], Voltage-based direct power control (V-DPC) [27], Virtual flux oriented control (VFOC) [28]. These techniques employ *PI* regulators in their inside current control loop in addition to modulation stage (PWM or SVM). It offers a fixed switching frequency however the slow regulation of *PI* regulators and the control delay degrade the obtained performance (grid current quality). These drawbacks are under consideration in the second part of this work.

A predictive control strategy is introduced to voltage-oriented control (VOC) for eliminate the delay control and *PI* regulators drawbacks under PV power injection to the grid with assuring a high grid current quality.

The proposed global system is simulated using Matlab/Simulink and Simpower system packages, where different tests are carried out under irradiation condition changes in order to check the system performance (grid current quality). More details are addressed in subsequent sections.

2 Overall System Configuration

The global system consists of the main components: PV array, DC/DC converter (boost), two level inverter, and $R_g L_g$ filter tied to grid as shown in Fig. 1.

The PV array generates the power depending on solar radiations. The boost converter is used to track the MPP and deliver it to the DC-link continuously. The two-level inverter injects the power coming from the boost into the grid following high grid current quality.

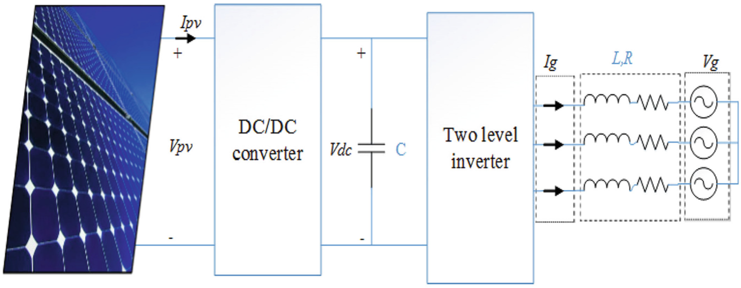

Fig. 1. Overall system configuration

3 Overall System Control

As shown in Fig. 2, a three steps technique are employed to control the overall system which are:

- A MPPT current oriented loop based on fixed switching predictive current control strategy is applied to track the MPP rapidly and accurately.
- A conventional *PI* controller is used to regulate the DC-link voltage.
- While, the grid currents are controlled by predictive control strategy through SVM (VOC-PC-SVM).

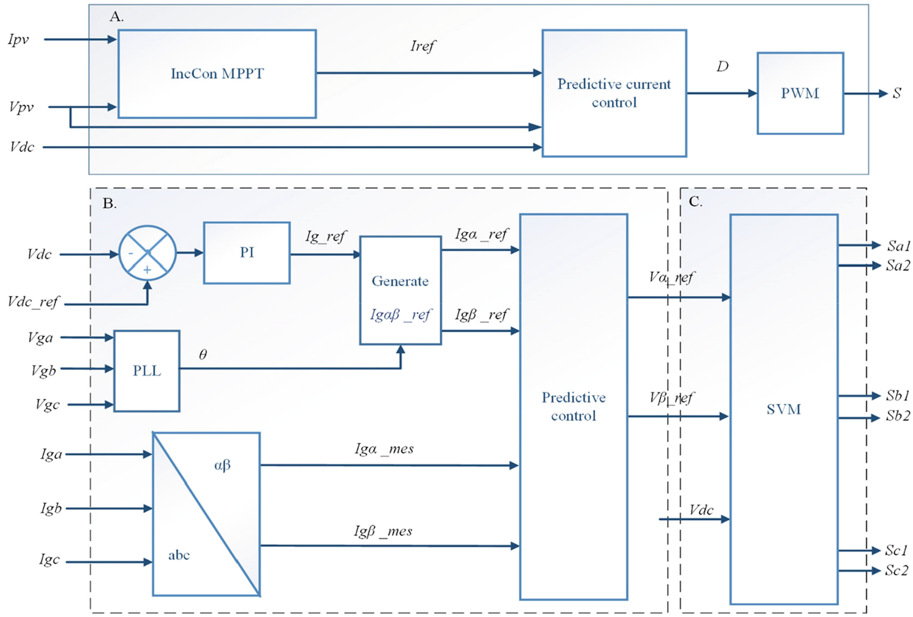

Fig. 2. Overall system control

3.1 MPPT Control

The current *Impp* must be tracked rapidly with less fluctuation where maximum power *Pmpp* is reached under solar radiation changes conditions. In this paper, MPPT method based on the combination of the conventional current IncCon algorithm, and fixed switching predictive current control loop is proposed.

IncCond Current MPPT

The Current Incremental algorithms as the conventional method are based on the slop of the PV power curve [6, 18]. It identifies of the instantaneous position value to the maximum power point; zero at the MPP, positive on the left-hand side of the MPP and negative on the right-hand side of the MPP.

The basic equations of this method are as follows [18]:

$$\frac{dP_{pv}}{dI_{pv}} > 0 \text{ at right of MPP} \tag{1}$$

$$\frac{dP_{pv}}{dI_{pv}} < 0 \text{ at left of MPP} \tag{2}$$

$$\frac{dP_{pv}}{dV_{pv}} = 0 \text{ at the MPP} \tag{3}$$

Since

$$\frac{dp_{pv}}{dI_{pv}} = \frac{d(V_{pv} * I_{pv})}{dI_{pv}} = \frac{dV_{pv}}{dI_{pv}} I_{pv} + V_{pv} \tag{4}$$

Equation (1) can be rewriting as:

$$\frac{dV_{pv}}{dI_{pv}} I_{pv} + V_{pv} > 0 \text{ at right of the MPP} \tag{5}$$

$$\frac{dV_{pv}}{dI_{pv}} I_{pv} + V_{pv} < 0 \text{ at left of the MPP} \tag{6}$$

$$\frac{dV_{pv}}{dI_{pv}} I_{pv} + V_{pv} = 0 \text{ at the MPP} \tag{7}$$

As illustrated in the flowchart in Fig. 3, the objective is to operate the PV current reference even *Iref* equals to *Impp* by comparison between the instantaneous conductance (I/V) and the incremental conductance (ΔI/ΔV) [6].

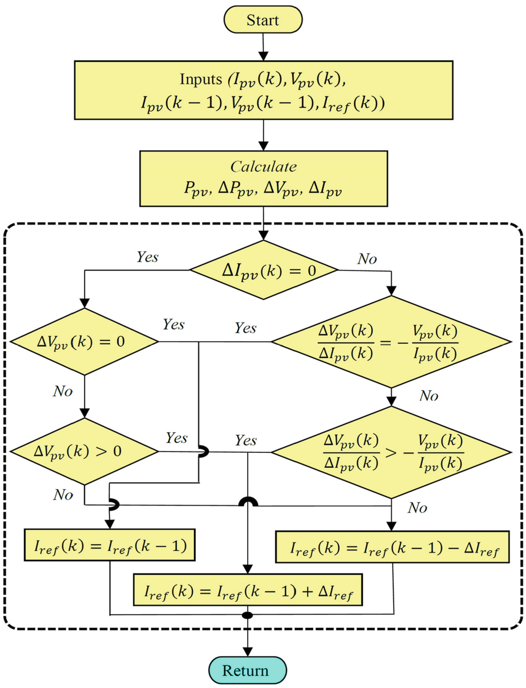

Fig. 3. IncCon current flowchart

Predictive Current Control

A fixed switching predictive current control is designed in this section in order to enforce the *Ipv* to track the *Iref* which delivered by the IncCon current MPPT algorithm. The determination of the future duty cycle is based on knowledge exact of DC-DC boost converter model [15]. Figure 4 illustrates the equivalent circuit of the boost converter considering the on and off switching state.

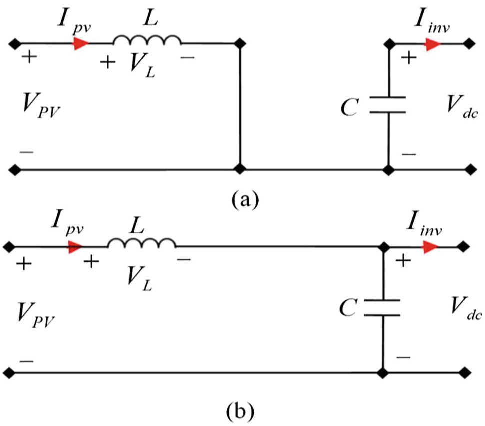

Fig. 4. DC–DC equivalent circuit

When the switch is OFF, the boost converter equations can be described as follows:

$$\begin{cases} L\dfrac{dI_{pv}(t)}{dt} = V_{pv}(t) \\ C\dfrac{dV_{dc}(t)}{dt} = -I_{inv}(t) \end{cases} \tag{8}$$

When the switch is ON, the boost converter equations yield:

$$\begin{cases} L\dfrac{dI_{pv}(t)}{dt} = V_{pv}(t) - V_{dc}(t) \\ C\dfrac{dV_{dc}(t)}{dt} = I_{pv}(t) - I_{inv}(t) \end{cases} \tag{9}$$

Equations (7) and (8) can be rewritten in term of duty cycle form as:

$$\begin{cases} L\dfrac{dI_{pv}(t)}{dt} = V_{pv}(t) - V_{dc}(t) + V_{dc}(t)d(t) \\ C\dfrac{dV_{dc}(t)}{dt} = I_{pv}(t) - I_{inv}(t) - I_{pv}(t)d(t) \end{cases} \tag{10}$$

The discrete time system of Eq. (9) considering the sampling frequency is *Ts* is given as:

$$\begin{cases} I_{pv}(k+1) = I_{pv}(k) + \frac{Ts}{L}[V_{pv}(k) + (d(k)-1)V_{dc}(k)] \\ V_{dc}(k+1) = V_{dc}(k) + \frac{Ts}{C}[(1-d(k))I_{pv}(k) - I_{inv}(k)] \end{cases} \tag{11}$$

In order to obtain the future duty cycle, Eq. (10) can be rewritten as:

$$I_{pv}(k+2) = I_{pv}(k+1) + \frac{Ts}{L}[V_{pv}(k+1) + (d(k+1)-1)V_{dc}(k+1)] \tag{12}$$

The current *Ipv* should track the current *Iref* delivered by MPPT unit in three control cycles [15]:

$$I_{pv}(k+2) = I_{ref}(k) \tag{13}$$

The future voltage *Vpv* (*k* + *1*) and *Vdc* (*k* + *1*) are supposed does not change considerably during one switching period and, thus, can be estimated as:

$$\begin{cases} v_{pv}(k+1) = v_{pv}(k) \\ v_{dc}(k+1) = v_{dc}(k) \end{cases} \tag{14}$$

From (11), (12) and (13), the future duty cycle can be derived as:

$$d(k+1) = \frac{\frac{L}{T_p}[i_{ref}(k) - i_{pv}(k+1)] - v_{pv}(k)}{v_{dc}(k)} + 1 \tag{15}$$

3.2 Grid Current Control

In this section, fixed switching grid current control is performed trough predictive control strategy and space vector modulation. The proposed model predictive control is based on the calculation of the voltage vector reference which is applied during the next simple time through SVM in order to closes the error between the predicted currents $I_{g\alpha\beta}(k+1)$ and their reference $I_{g\alpha\beta\_ref}$.

To apply the predictive control strategy, the inverter grid-connected model is necessary. The equation under illustrates the required mathematical model in natural frame (*abc*) [22]:

$$\frac{dI_g(t)}{dt} = \frac{1}{L}[V - V_g - RI_g] \tag{16}$$

where *V*, *Vg*, *Ig*, *LR* are the inverter voltage, grid voltage, grid current and filter inductance respectively.

From (16), the grid-connected inverter model in α-β frame can be expressed as follow:

$$\begin{cases} \dfrac{dI_{g\alpha}(t)}{dt} = \dfrac{1}{L}[-RI_{g\alpha}(t) - e_{g\alpha}(t) + V_{\alpha}] \\ \dfrac{dI_{g\beta}(t)}{dt} = \dfrac{1}{L}[-RI_{g\beta}(t) - e_{g\beta}(t) + V_{\beta}] \end{cases} \tag{17}$$

Euler forward method is used to approximate the derivatives in (9) in order to obtain discrete time model which is given bellow [22]:

$$\begin{cases} \dfrac{dI_{g\alpha}(t)}{dt} = \dfrac{I_{g\alpha}(k+1) - I_{g\alpha}(k)}{T_s} \\ \dfrac{dI_{g\beta}(t)}{dt} = \dfrac{I_{g\beta}(k+1) - I_{g\beta}(k)}{T_s} \end{cases} \tag{18}$$

where Ts is the sampling time.

The discrete time model of Eq. (17) yields:

$$\begin{cases} I_{g\alpha}(k+1) = \dfrac{T_s}{L}[-RI_{g\alpha}(k) - e_{g\alpha}(k) + V_{\alpha}(k)] - I_{g\alpha}(k) \\ I_{g\beta}(k+1) = \dfrac{T_s}{L}[-RI_{g\beta}(k) - e_{g\beta}(k) + V_{\beta}(k)] - I_{g\beta}(k) \end{cases} \tag{19}$$

To calculate the voltage vector reference, the currents $I_{g\alpha}$-$I_{g\beta}$ should track their references $I_{g\alpha\_ref}$-$I_{g\beta\_ref}$ during the next sampling time which means:

$$\begin{cases} I_{g\alpha}(k+1) = I_{g\alpha\_ref} \\ I_{g\beta}(k+1) = I_{g\beta\_ref} \end{cases} \tag{20}$$

Where:

$$\begin{cases} I_{g\alpha}(k) = I_{g\alpha\_mes} \\ I_{g\beta}(k) = I_{g\beta\_mes} \end{cases} \tag{21}$$

$$\begin{cases} e_{g\alpha}(k) = e_{g\alpha\_mes} \\ e_{g\beta}(k) = e_{g\beta\_mes} \end{cases} \tag{22}$$

By replacing the Eqs. (20), (21), (22) in (19), the voltage vector reference can be given as:

$$\begin{cases} V_{\alpha} = \dfrac{L}{Ts}(I_{g\alpha\_ref} - I_{g\alpha\_mes}) + RI_{g\alpha\_mes} + e_{g\alpha\_mes} \\ V_{\beta} = \dfrac{L}{Ts}(I_{g\beta\_ref} - I_{g\beta\_mes}) + RI_{g\beta\_mes} + e_{g\beta\_mes} \end{cases} \tag{23}$$

The reference voltage vector $V\alpha$, $V\beta$ is applied during the next sampling time through space vector modulation (SVM).

4 Simulation Results

In this section, a simulation with the parameters shown in Table 1 are carried out on the global system using MATLAB/Simulink and Simpower system packages in order to evaluate the performance of the proposed control scheme under irradiation change. This study is divided into two parts.

Table 1. System global parameters

Electrical parameters of the PV Siemens SM110	Value
Maximum power (Pmpp)	110 Watts
Open circuit voltage (Voc)	43.5 V
Short circuit current (Isc)	3.45 A
Voltage at Pmax	35
Current at Pmax	3.15
Number of cells connected in parallel (Np)	1
Number of cells connected in series (Ns)	72
Number of modules connected in series (Nss)	2
Number of modules connected in parallel (Npp)	2
Electrical parameters of the boost converter	**Value**
Resistor R	50 Ω
Inductor L	40 mH
Capacitor C	1100 μF
Electrical parameters of the Filter LR	**Value**
L	10 mH
R	0.1 Ω

In the first case, the purpose is to compare the performance of the IncCon/PPC with conventional MPPT in terms of MPP tracking speed and oscillations around it.

The second part, predictive control strategy based on space vector modulation is applied to control the second stage of the global system in order to inject the extract PV power with high grid current quality under irradiation changes.

4.1 Performance of IncCon/PCC MPPT

Under the irradiation changes represented by Fig. 5a, the IncCon algorithm based on PCC and classical IncCon are tested by numerical simulation. Initially, the irradiance level is set to 500 W/m^2. After that, at 0.1 s, a sudden increase irradiation change from 500 to 700 W/m^2 is occurred. The IncCon/PCC method reaches the MPP during 0.018 s, while the conventional method takes 0.036 s. Then the irradiance level is decreased slowly from 800 to 400 W/m^2 during 0.2 s, the IncCon/PCC method exhibited better accuracy tracking than the conventional IncCon. Finally, a sudden irradiation from 400 to 1000 W/m^2 is occurred at 0.5 s, the IncCon/PCC shows also a faster tracking than the conventional MPPT, where the proposed MPPT took just 0.056 s to reach the MPP while the conventional needs 0.1 s as shown in Fig. 5d.

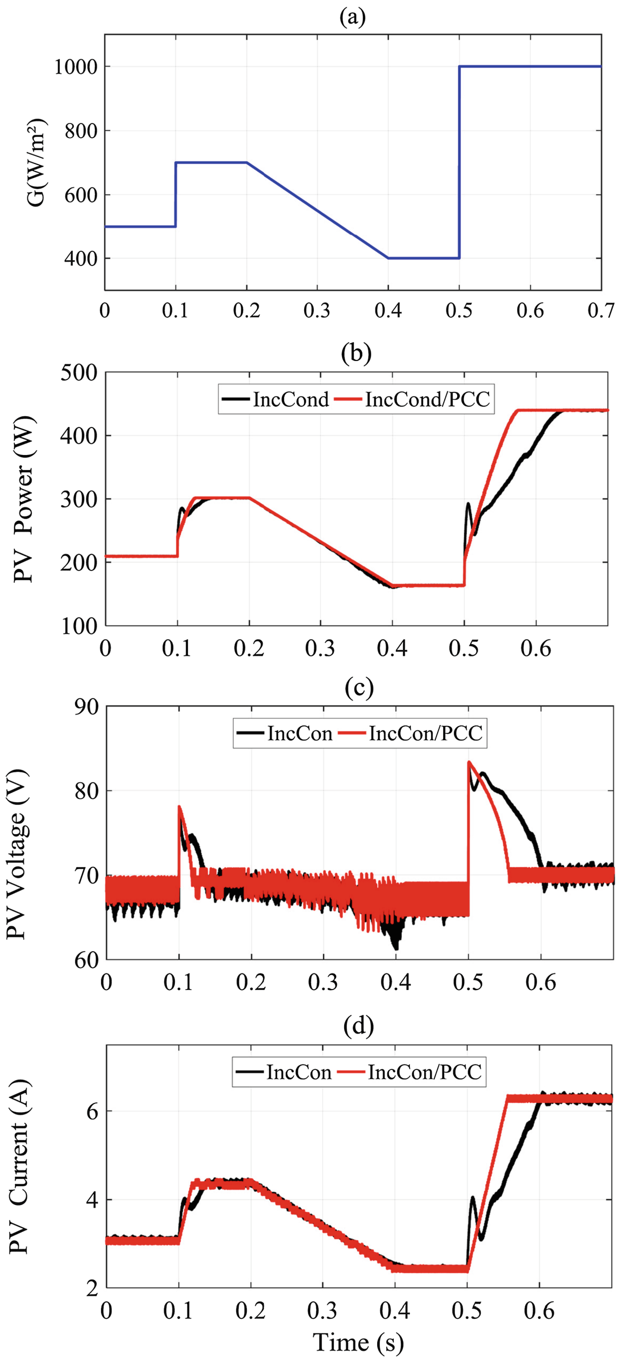

Fig. 5. Performance of IncCon/PCC, IncCon under irradiation changes

In another side, the IncCon/PCC method shows a high performance in term of power oscillation compared to the conventional one. Where the oscillation widths around MPPs, by using the proposed method, under different steady irradiations levels (500, 700, 400 and 1000 W/m^2) are [209.7 208.5], [302, 300.5], [163.8, 162.2], [440, 439.4], respectively. In counterpart, the widths of power oscillation by using the IncCon method are [209.7, 206], [302, 299], [163.8, 161], [440, 437.2] respectively.

4.2 Performance of Global System Under Irradiation Change

This section deals with test of the global system performance under different irradiation changes and presents the efficiency of the applied method in terms of grid current THD.

Firstly, as illustrated in Fig. 6a, for a fixed irradiation condition at 500 W/m^2 during the interval [0, 0.1 s [, the PV array output is oscillating around the MPP and the V_{dc} is completely regulated to its reference. Furthermore, the grid currents are in balance and sinusoidal form.

Afterward, the sudden irradiation changes from 500 to 700 W/m^2 at instant 0.1 s led to an increase in the PV power output and a small sharped deviation in V_{dc} over its

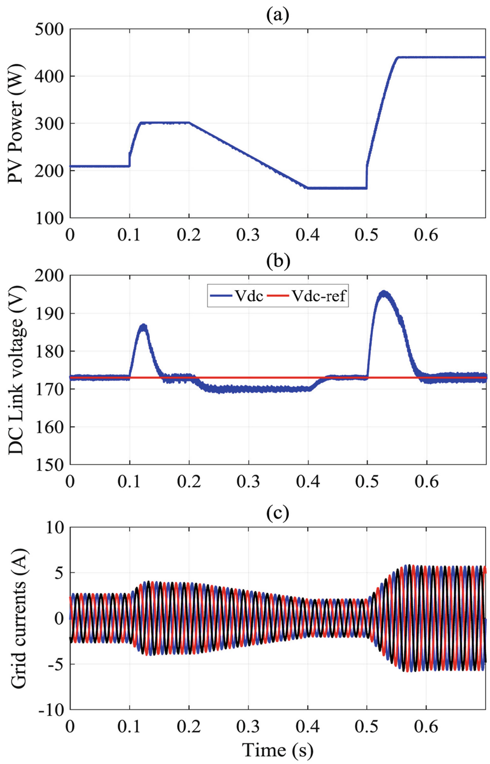

Fig. 6. Performance of global system under irradiation change

reference as showing in Fig. 6a, b. Despite that, the grid currents are increased with keeping their sinusoidal form due to the competence of the proposed method.

Finally, a large sudden change in the irradiation is occurred at instant 0.5 s. The PV power output is rapidly increased the reason behind a large deviation of V_{dc} over its reference as Then, under the slow irradiation change from 700 to 400 W/m^2, the PV power is slowly decreasing from 0.2 to 0.4 s. Also, the V_{dc} is a bit diverged from its reference as illustrated in Fig. 6b in the meanwhile the grid currents are decreasing with a sinusoidal form. As showing in Fig. 6b. even though, the grid currents are increased with keeping their sinusoidal form. This control ability is back to the ability of the proposed method.

As presented in Table 2, the proposed method (VOC based on predictive strategy trough SVM) provided high grid current quality under all irradiation change cases regardless to the international standards (IEEE-519).

Table 2. Obtained THD under all irradiation levels

G (W/m^2)	500 W/m^2	700 W/m^2	Increase 700–400 W/m^2	400 W/m^2	1000 W/m^2
THD%	2.35	1.55	2.62	3.08	1.08

5 Conclusions

In this paper, a control of three phase two-stage grid-connected PV system based on predictive control strategy is presented and discussed. The simulation results show a significant enhancement by applying the IncCon/PCC MPPT method in comparison with the conventional method in terms of response time and stability around the maximum power point under irradiation changes. Moreover, the proposed control of two stage (VOC-PC-SVM) inject the PV power with high grid current quality compare to the international standards (IEEE-519) in all irradiance changes levels.

References

1. El-Sayed, A.M., Orabi, M., AbdelRahim, O.M.: Two-stage micro-grid inverter with high-voltage gain for photovoltaic applications. IET Power Electron. **6**(9), 1812–1821 (2013)
2. de Oliveira, F.M., Oliveira da Silva, S.A., et al.: Grid-tied photovoltaic system based on PSO MPPT technique with active power line conditioning. IET Power Electron. **9**(6), 1180–1191 (2016)
3. Menadi, A., Abdeddaim, S., et al.: Implementation of fuzzy-sliding mode-based control of a grid connected photovoltaic system. ISA Trans. **58**, 586–594 (2015)
4. Chen, L., Amirahmadi, A., et al.: Design and implementation of three-phase two-stage grid-connected module integrated converter. IEEE Trans. Power Electron. **29**(8), 3881–3892 (2014)
5. Wai, R.-J., Wang, W.-H., Lin, C.-Y.: High-performance stand-alone photovoltaic generation system. IEEE Trans. Ind. Electron. **55**(1), 240–250 (2008)
6. Safari, A., Mekhilef, S.: Simulation and hardware implementation of incremental conductance MPPT with direct control method using Cuk converter. IEEE Trans. Ind. Electron. **58**(4), 1154–1161 (2011)

7. Bendib, B., Belmili, H., Krim, F.: A survey of the most used MPPT methods: Conventional and advanced algorithms applied for photovoltaic systems. Renew. Sustain. Energy Rev. **45**, 637–648 (2015)
8. Zainuri, M.A.A.M., Radzi, M.A.M., Soh, A.C., AbdRahim, N.: Development of adaptive perturb and observe-fuzzy control maximum power point tracking for photovoltaic boost dc–dc converter. IET Renew. Power Gener. **8**(2), 183–194 (2013)
9. Radjai, T., Rahmani, L., Mekhilef, S., Gaubert, J.P.: Implementation of a modified incremental conductance MPPT algorithm with direct control based on a fuzzy duty cycle change estimator using dSPACE. Sol. Energy **110**, 325–337 (2014)
10. Algazar, M.M., Al-Monier, H., Abd El-Halim, H., Ezzat El Kotb Salem, M.: Maximum power point tracking using fuzzy logic control. Electr. Power Energy Syst. **39**, 21–28 (2012)
11. Houria, B., Talha, A., Bouhali, O.: A three-phase NPC grid-connected inverter for photovoltaic applications using neural network MPPT. Renew. Sustain. Energy Rev. **49**, 1171–1179 (2015)
12. Harrag, A., Messalti, S.: Variable step size modified P&O MPPT algorithm using GA-based hybrid offline/online PID controller. Renew. Sustain. Energy Rev. **49**, 1247–1260 (2015)
13. Raseswari, P., Subudhi, B.: Double integral sliding mode MPPT control of a photovoltaic system. IEEE Trans. Control Syst. Technol. **24**(1), 285–292 (2016)
14. Kihel, A., Krim, F., Laib, A.: MPPT voltage oriented loop based on integral sliding mode control applied to the boost converter. In: IEEE 6th International Conference on Systems and Control (ICSC), Batna, Algeria, pp. 205–209, 7–9 May 2017
15. Panagiotis, K.E., Kladas, A.G., Manias, S.N.: Fast photovoltaic-system voltage-or current-oriented MPPT employing a predictive digital current-controlled converter. IEEE Trans. Ind. Electron. **60**(12), 5673–5685 (2013)
16. Enrico, B., et al.: A fast current-based MPPT technique employing sliding mode control. IEEE Trans. Ind. Electron. **60**(3), 1168–1178 (2013)
17. Kollimalla, S.K., Mishra, M.K.: A novel adaptive P&O MPPT algorithm considering sudden changes in the irradiance. IEEE Trans. Energy Convers. **29**(3), 602–610 (2014)
18. Kakosimos, P.E., Kladas, A.G.: Implementation of photovoltaic array MPPT through fixed step predictive control technique. Renew. Energy **36**, 2508–2514 (2011)
19. Talbi, B., Krim, F., Rekioua, T., Laib, A., Feroura, H.: Design and hardware validation of modified P&O algorithm by fuzzy logic approach based on model predictive control for MPPT of PV systems. J. Renew. Sustain. Energy **9**(4), 043503 (2017)
20. Talbi, B., Krim, F., Rekioua, T., Mekhilef, S., Laib, A., Belaout, A.: A high-performance control scheme for photovoltaic pumping system under sudden irradiance and load changes. Sol. Energy **159**, 353–368 (2018)
21. Jain, C., Singh, B.: A three-phase grid tied SPV system with adaptive DC-link voltage for CPI voltage variations. IEEE Trans. Sustain. Energy **7**(1), 337–344 (2016)
22. Rodriguez, J., et al.: Predictive current control of a voltage source inverter. IEEE Trans. Ind. Electron. **54**(1), 495–503 (2007)
23. Feroura, H., Krim, F., Talbi, B., Laib, A.: Finite-set model predictive voltage control for islanded three phase current source inverter. In: IEEE 5th International Conference on Electrical Engineering (ICEE-B), Boumerdes, Algeria, pp. 1–5, 29–31 October 2017
24. Feroura, H., Krim, F., Talbi, B., Laib, A., Belaout, A.: Finite-set model predictive direct power control of grid connected current source inverter. Elektronika ir Elektrotechnika **23**(5), 36–40 (2017)
25. Hu, J., Zhu, Z.Q.: Investigation on switching patterns of direct power control strategies for grid-connected DC–AC converters based on power variation rates. IEEE Trans. Power Electron. **26**, 3582–3598 (2011)

26. Remus, T., Marco, L., Pedro, R.: Grid converters for photovoltaic and wind power systems. Wiley, Hoboken (2011)
27. Malinowski, M., Jasiniski, M., Kazmierkowski, M.P.: Simple direct power control of three-phase PWM rectifier using space-vector modulation (DPC-SVM). IEEE Trans. Ind. Electron. **51**, 447–454 (2004)
28. Malinowski, M., Kazmierkowski, M.P., Hansen, S., Blaabjerg, F., Marques, G.D.M.: Virtual flux based direct power control of three-phase PWM rectifiers. IEEE Trans. Ind. Appl. **37**, 1019–1027 (2001)

Total Harmonic Distortion Performance in PV Systems Using Fuzzy Logic Controller

Ahmed Ali(✉), Bhekisipho Twala, Tshilidzi Marwala, and Ilyes Boulkaibet

Faculty of Engineering and Built Environment, University of Johannesburg, Johannesburg, South Africa
axmedee@live.com, {btwala,T.Marwala,ilyesb}@uj.ac.za

Abstract. Solar photovoltaic (PV) and wind farm systems of renewable energy installations have been considered as the promising generating source that would cover the continuous energy demand. With the high incoming penetration of distribution generators (DG), both the end users of the electric power as well as the electric utilities have become more concerned on the issue of the electric network quality. A particular issue falling under the umbrella concept is capacitive coupling with the grounding systems that have become essential as a result of the high-frequency current that is imposed by the converters of power. Total harmonic distortion (THD) is limited by the quality standards of power (IEEE-519) within the range that is acceptable caused by power electronic equipment rapid usage. Thus, the primary aim of the work is to broaden the investigation of the power systems quality problems.

Keywords: Fuzzy logic controller (FLC) · Variable frequency drivers (VFDs) Active power filters (APF) · Flying capacitor multilevel inverter (FCMLI)

1 Introduction

The power quality distortion is one of the most serious problem affecting the electric power systems because of the increase in the non-linear drawing non-sinusoidal currents. The use of active filters is harmonic migration and compensation of reactive power, voltage regulation, and load balancing as well as compensation of voltage flicker. The non-linear loads four wire three phase system a harmonic current which is of high levels in the natural wire and three line conductors enrolled. The supply quality declination is as a result of the unbalanced load. In reduction of harmonic effect, various techniques of harmonic migration are proposed.

The shunt active power filter is viewed as the most popular APFs, the technique include passive filters, phase multiplication, harmonic injection as well as active power filters (APFs). Mainly, it is a current sources, and is connected in a parallel manner to the non-linear loads. Shunt AFC conventionally is controlled in a manner which allows injection of reactive and harmonic compensation current on the basis of reference

The original version of this chapter was revised: Incorrect fourth author name has been corrected. The correction to this chapter is available at https://doi.org/10.1007/978-3-319-97816-1_45

M. Chadli et al. (Eds.): ICEECA 2017, LNEE 522, pp. 328–337, 2019.
https://doi.org/10.1007/978-3-319-97816-1_25

currents which are calculated. The purpose of injection current is to cancel the reactive and harmonic currents which non-linear loads draw. As of the recent times, the fuzzy logic controller is generating much interest in numerous application and is being introduced in the field of power electronics [3].

According to a number or strategies of controls developed, still, two theory methods of controls have always been dominant. They include the instantaneous reactive and active current ($id - iq$) methods as well as the instantaneous reactive and active power ($p - q$). In the proposed work, we have concentrated on the two control strategies (($p - q$) and ($id - iq$) combined with the fuzzy controller aimed at validating the present observations. Simulations that are extensive have been conducted with fuzzy controller for the ($id - iq$) and ($p - q$) methods for various conditions of voltage such as non-sinusoidal, sinusoidal as well as the conditions which are unbalanced to adequate results. Upon observation of the ($id - iq$) strategy of control performance with the fuzzy controller, it can be observed that it is quite adequate over $p{-}q$ strategy of control with fuzzy controller [4].

According to the works, the work will undertake a number of steps in validating the objectives. Analysis and design of five-level capacitor multilevel inverter circuit in applying an equal but opposite to the harmonics that are distorted in to the source current line to help cancel the harmonic design of non-linear load, a fuzzy logic response of the shunt active system of power. Visualization on the simulation of instantaneous reactive and active theory based shunt active filter with Simulink/MATLAB, as a better solution in reducing harmonics. Fuzzy controller will carry out the simulations for both p-q method for various voltage conditions. The primary reason for the concern of the capacitive coupling are:

(a) Harmonics increase, thus, the converters of power loses in both the consumer and utility equipment.
(b) Currents of ground capacities have the potential to cause malfunctioning of control devices and sensitive load.
(c) The capacitive current circulation trough the power equipment may provoke their lifetime production and this limits the capability of power.
(d) As a result of capacitive ground current, the ground potential rise, representing unsafe working conditions along the electric network or installations.
(e) Interference of electromagnetic in the systems of communications and metering infrastructure.

As such, the importance of renewable energy modelling installation has been noticed considering capacitive coupling with the grounding system, thereby simulating accurately AC and DC component of the current waveforms which electric network is used to measure.

2 Background

2.1 Shunt Active Power Filter

In the system of electric distribution development, sudden increment of non-linear load has been experienced, like domestic appliances, rectifier equipment, power supply as well as adjustable speed drivers (ASD). With the increase in these loads, the generated harmonics current that the loads generates is very significant. Different problems associated with power system can result as a result of these harmonics, some of the problems include inaccurate metering of power flow, light flicker, excessive neutral currents, system protection malfunctioning, as well as equipment overheating and distorted voltage waveform. In addition, they are responsible for the reduction of efficiency by drawing the components of reactive current from the networks of distribution [5].

From Fig. 1 the concept of cancellation of harmonic current is demonstrated so that the current supply is sinusoidal from the source, the used inverter of the voltage source in active filters makes possible the harmonic control. APFs has been developed where the voltage-source inverter (VSI) based shunt active power filter is employed recently and has been recognized as the control scheme available solution, where the needed compensation current are determined through only sensing line currents, which is easy and simple in implementing [6].

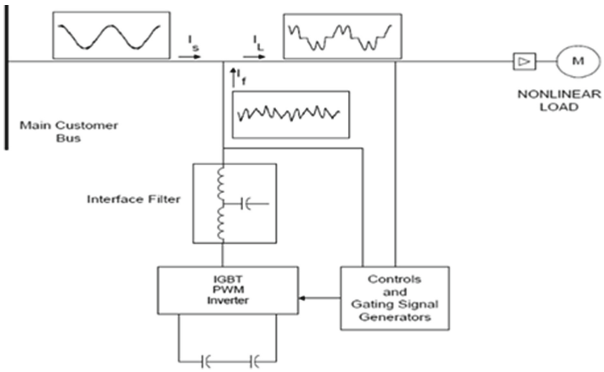

Fig. 1. Illustration of the shunt connected active components with the waveform to show the harmonics cancellation.

2.2 Flying Capacitor Multilevel Inverters (FCMLI)

From Fig. 1 the apology for five level capacitor multilevel converter circuit is demonstrated. The topology of Flying Capacitor Converter (FCC) is being introduced and pros and cons compared with other forms of multilevel topologies. FCC utilizes various float capacitors in each phase which is connected to a number of points at the converter to ensure the achievement of different levels of voltage in the output signals.

The recently developed converter topology is the flying capacitor multilevel converter that assures flexible monitoring, control as well as modular design. The multilevel FCC needs a DC voltage distribution which is balanced. To realize this, the use of special control is recommended leading to natural balancing or one can measure the voltages and go ahead to select the most appropriate switching state. There are three factors that influence the balancing, they include the switching frequency, the harmonic contact of the reference waveform and the load impendence. The output voltage must make sure that the load control in addition to the balancing of voltage of the FCC multilevel e.g. the AC machine three face [7].

2.3 Instantaneous Real and Reactive Power Method $(p - q)$

The non-linear load instantaneous reactive and active powers p and q is where the active filter currents can be obtained. The phase voltages transformation Va, Vb *and* Vc as well as the load current (La, Lb *and* Lc) into á – â the orthogonal coordinates have been provided from Eqs. 1 and 2 below.

The active power filters compensation objectives are the present harmonic in the input current. Presented in the present architecture is the three phase four wire, which has been realized with the control strategy of constant power. The circulation of power is further given from Eq. (3) [8].

$$\begin{pmatrix} V_0 \\ V_\alpha \\ V_\beta \end{pmatrix} = \frac{\sqrt{2}}{\sqrt{3}} \begin{pmatrix} 1/\sqrt{1/2} & 1/\sqrt{1/2} & 1/\sqrt{1/2} \\ 1 & -1/2 & -1/2 \\ 0 & \sqrt{3}/2 & -\sqrt{3}/2 \end{pmatrix} \begin{pmatrix} V_a \\ V_b \\ V_c \end{pmatrix} \tag{1}$$

$$\begin{pmatrix} I_0 \\ I_\alpha \\ I_\beta \end{pmatrix} = \frac{\sqrt{2}}{\sqrt{3}} \begin{pmatrix} 1/\sqrt{1/2} & 1/\sqrt{1/2} & 1/\sqrt{1/2} \\ 1 & -1/2 & -1/2 \\ 0 & \sqrt{3}/2 & -\sqrt{3}/2 \end{pmatrix} \begin{pmatrix} I_a \\ I_b \\ I_c \end{pmatrix} \tag{2}$$

$$\begin{pmatrix} P_0 \\ P_\alpha \\ P_\beta \end{pmatrix} = \begin{pmatrix} V_0 & 0 & 0 \\ 0 & V\propto & V\beta \\ 0 & V\beta & -V\alpha \end{pmatrix} \begin{pmatrix} I_0 \\ I_\alpha \\ I_\beta \end{pmatrix} \tag{3}$$

$$\begin{pmatrix} P \\ q \end{pmatrix} = \begin{pmatrix} V\alpha & V\beta \\ V\beta & -V\alpha \end{pmatrix} \begin{pmatrix} I_\alpha \\ I_\beta \end{pmatrix} \tag{4}$$

2.4 Fuzzy Logic Current Controller

Fuzzy set of theory is utilized by the fuzzy logic, where a variable is a member of a single or more than one set, with a particular membership degree. Fuzzy logic is beneficial because it allows emulation of the process of human reasoning in computers, make decision based on complete and vague data, qualification of information that is imprecise, and yet employ process of "Defuzzification, arriving at a defined conclusion. In the below block diagram, fuzzy logic controller (FLC) is demonstrated from Fig. 2 [9].

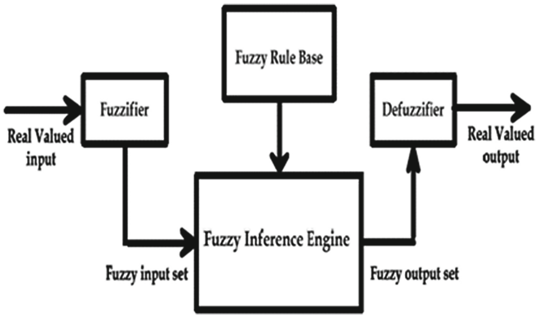

Fig. 2. FLC Block diagram

There are three blocks that makes up FLC, these are the Defuzzification, Inference as well as Fuzzification. The process above can be explained as below.

(1) *Fuzzification*
The requirement of the fuzzy logic controller is that each output/input variables defining the control surface to be expressed in the notations of fuzzy sets by use of linguistic levels. The values of linguistic of each variables of output and input divide its discourse universe into intervals that are adjacent in formation of functions of membership. The extent of belonging to a specific level is denoted by the member values. Thus, Fuzzification is viewed as the process that allows input/output variables to be converted into linguistic levels.

(2) *Inference*
Set rules governs the control surface behavior relating to the system output as well as input variables. A typical rule can be expressed as if A is x, then B is y, when the set of variables of input reach every rule that has any truth degree in its promise is fired, contributing to the control surface formation by modifying it approximately. After firing all the rules, the control surface that results is expressed as fuzzy set for the representation of the output constraints. The whole process is what is known to as the inference.

(3) *Defuzzification*
The process that converts into crisp quantity the fuzzy quantity is known as the Defuzzification. Several techniques are available for this process. However, the commonly prevalent one is the centroid strategy, which uses the formula that follows.

$\int (\mu(x)x)dx / \int \mu(x)dx$, ; In this case, the output x membership degree ì.

3 Literature Review

It has been noticed from the literature review that that the filter that is shunt active utilizes a technique that is simple for calculating the reference current compensation which is based on the fast Fourier transform. The shunt active power filter presented has the ability of operating in load conditions that are variable, unbalanced or balanced. In varying conditions that are fast, the classic filters may not have the capacity of having satisfactory performance.

In [11] the fuzzy logic controller is extended and applied to a three level APF shunt, the algorithm of logic control has been proposed for inverter dc voltage and harmonic current control to help in the improvement of performance of the three level active power filters as well as showing how three level inverter can be employed as a shunt active power filter.

The $p - q$ theory also known as the original instantaneous reactive power is systematically utilized in controlling the APFs. After connecting the APD in a parallel manner to an unbalanced and non-linear load, the application of p-q theory allows strategy of compensation which is commonly named as the constant power acquired in [12] demonstrating that any strategy of compensation may be developed into the frame of the theory of $p - q$. Besides, without the use of mapping matrices on p-q theory reformulation.

The shunt APF is shown in [13] for improvement of the quality of power with regards to the compensation of reactive power and harmonics in the network of distribution by the FLC or integral [PI].

Additionally, the electric network in [14] has a behavior of "a healthy carrier" of disturbances, and the generated disturbances by a single customer is distributed to the other clients, which causes equipment possible damage to the quality measurement.

Development of a shunt APF which is of low cost is described in [15] consisting of a digital control. This facilitates for correction of dynamic power factor and both compensation of the zero sequence and harmonics current. The controller of active filter is based on the p-q theory also known as the instantaneous power theory.

In [16] constructs and presents a fuzzy PID controller structure. The fuzzy logic controller application as a stabilizer of the system power is investigated by the use of simulation studies means on a single machine infinite bus system.

Also proposed a technique which is used in the characterization of the present total distortion of harmonic for inverters with a single phase. In calculation of average value of the harmonic distortion, the expression is made for each type of day (cloudy sky day) which is proposed by [17].

Total harmonic distortion (THD) is limited by the quality standards of power (IEEE-519) within the range that is acceptable caused by power electronic equipment rapid usage. Thus, the primary aim of the work is to broaden the investigation of the power systems quality problems. Where in the recent years there has been increase in the non-linear loads, the cost has also been affected. According to the works proposal, the work will undertake a number of steps in validating the objectives.

1. To conduct an analysis and design of five-level capacitor multilevel inverter circuit in applying an equal but opposite to the harmonics that are distorted in to the source current line to help cancel the harmonic design of non-linear load.
2. To design a fuzzy logic response of the shunt active system of power.
3. Visualization on the simulation of instantaneous reactive and active theory based shunt active filter with Simulink/MATLAB, as a better solution in reducing harmonics.
4. Fuzzy controller will carry out the simulations for both p-q method for various voltage conditions.

5. Conduct an analysis of the results obtained and making comparisons with other results that have been published.

4 System Model

A suitable capacitive coupling model is one that allows reproducing the injections of harmonic currents not only into the grid but also into the PV installations of the DC circuit that leads to current distortion, internal resonant and work conditions which are unsafe where the current discharged by capacitive goes far beyond the safety values of work threshold denoted as (IEEE Std. 80-2000, 2000). The capacitive coupling is considered as electric circuit part consisting of cable capacitive couplings, PV cells, the grid impedance and elements of AC filter and its effect has been appreciated in most of the large scale PV plants.

Under normal circumstances, the connection of PV modules happens on a panel in order to form a PV array as demonstrated from Fig. 1. The PV module circuit model is composed of current source that is ideal, a diode that is connected in parallel manner with the source of current and series resistor. For each PV modules, the input current is determined as demonstrated by the equation below:

$$I = I_{SC} - I_d = I_{SC} - I_0 \cdot \left\lfloor \exp\left(\frac{V + I.R_S}{n \cdot V_T}\right)\right\rfloor \tag{5}$$

In this case I_0 is the diode saturation current, while the module terminal voltage is represented by V, and the diode ideal constant is n, V_T is module thermal potential and $m\left(\frac{kT}{q}\right)$ gives the module thermal potential where k is the Boltzmann's constant denoted as $1.38E-23\ J/k$, in K, T cell temperature is measured, the Coulomb constant $(1.6E-19C)$ is represented by q and the cells number in module series is m. The module short circuit current under a specific solar irradiance is denoted by I_{SC}. Diode current is represented by I_d, which is provided by the current expression of classical diode. The R_s series resistance stands for the current flow intrinsic resistance.

The PV modules capacity coupling with the ground is parallel modelled as a Parallel resistant R_{pv} and capacitor C_{pv} arrangements simulating the dependency frequency on the grounding system that is normally represented in the grounding resistance R_g in the model.

Considering that current source for the AC and DC circuits of PV installation are represented by the converters, circuit which is equivalent is deduced in order to conduct analysis of the capacitive coupling effect over the voltage and current waveform.

The circuit that is equivalent of both the AC circuit for connection to the grid and the DC circuit of the PV installation as seen between the ground and inverter. In the AC circuit, the capacitors, inductance and resistance of the AC underground cables are represented by C_{ac_cable}, L_{ac_cable} and R_{ac_cable}, at saturation, the ground resistance is represented by R_{g_es} and the LC filter parameters connected at the inverter Ac terminals are the L_{filter} and C_{filter}.

The R_{pv} and C_{pv} inclusion on the equivalent of PV circuit allows the representation of the leakage path for components of high frequency between the Ground and the PV modules. This equivalent circuit of DC is represented by the continuous-time equation below, at the operating conditions that are normal.

$$\frac{di_1(t)}{dt} = \frac{1}{L_c}.v_{in}(t) - \frac{R_c}{L_c}.i_1(t) - \frac{1}{L_c}.v_2(t) \tag{6}$$

$$\frac{di_2(t)}{dt} = \frac{1}{C_c.(R_s + R_g)}.i_1(t) - \left[\frac{1}{C_c.(R_s + R_g)} + \frac{\psi}{C_{pv}.R_{pv}}\right].i_2(t) + \frac{1}{C_{pv}.R_{pv}.(R_s + R_g)}v_2(t) \tag{7}$$

$$\frac{dv_2(t)}{dt} = \frac{1}{C_c}.i_1(t) - \frac{1}{C_c}.i_2(t) \tag{8}$$

$$\begin{aligned} \frac{dv_{pv}(t)}{dt} &= \frac{R_g}{C_c.(R_s + R_g)}.i_1(t) + \left(\frac{R_{pv} + R_g}{C_{pv}.R_{pv}} + \frac{R_g}{C_c.(R_s + R_g)} + \frac{R_g.\psi}{C_{pv}.R_{pv}}\right).i_2(t) \\ &+ \frac{R_g}{C_{pv}.R_{pv}.(R_s + R_g)}.v_2(t) - \frac{1}{C_{pv}.R_{pv}}.v_{pv}(t) \end{aligned} \tag{9}$$

5 Results and Discussion

In this section, THD is compared with and without capacitive coupling, the results show that using capacitive coupling reduce the percentage of THD. Figs. 3 and 4 show THD with and without capacitive coupling. As shown, maximum THD without capacitive coupling about 3.9, while in case of capacitive coupling, it's about 3.4.

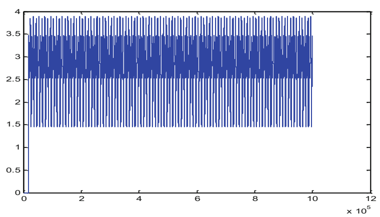

Fig. 3. THD without capacitive coupling for power in PV

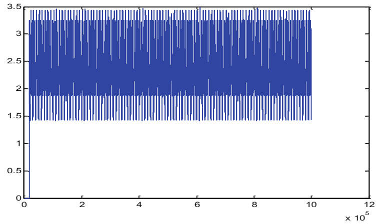

Fig. 4. THD with capacitive coupling for power in PV

On the other hand, THD for current source of PV are shown in Figs. 5 and 6. As shown, maximum THD without capacitive coupling about 0.34, while in case of capacitive coupling, it's about 0.26.

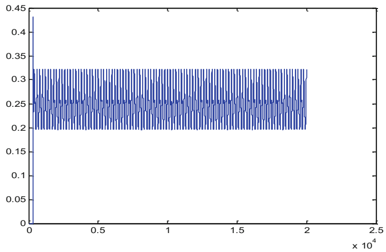

Fig. 5. THD without capacitive coupling for current in PV

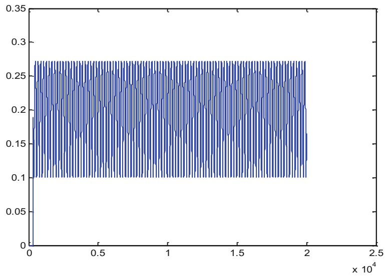

Fig. 6. THD with capacitive coupling for current in PV

6 Conclusions and Remarks

This paper presents THD in PV system in case of using capacitive coupling in order to reduce THD. Fuzzy logic controller is used in order to cancel the harmonic design of non-linear load. Results show that reduction in THD for power in PV systems around 13%, while the reduction in THD for current in PV systems around 23%.

References

1. Maercy, L.E., Karthick, R., Arumugam, S.: Fuzzy controlled shunt active filter for power quality improvement. Int. J. Soft Comput. **5**(2), 35–41 (2010). ISSN: 1816-9503
2. Suresh Kumar, B., Ramesh Reddy, K., Lalitha, V.: PI, fuzzy logic controlled shunt active power filter for three-phase four-wire systems with balanced, unbalanced and variable loads. J. Theor. Appl. Inf. Technol. (2005)
3. Mazari, B., Mekri, F., Fasla, S.: Fuzzy logic control of the energy storage capacitor of a three phase active power filter in unbalanced network, University of Sciences and Technology of Oran-Mohamed Boudiaf (2008)
4. Benachaiba, C., Mazari, B.: Contribution to the improvement of control strategies of the shunt active filter by a fuzzy PI controller, U.S.T. Oran BP 1505 Oran El M'aouar Algérie (2005)
5. Ali, A., Boulkaibet, I., Twala, B., Marwala, T.: Hybrid optimization algorithm to the problem of distributed generation power losses. In: IEEE International Conference on Systems, Man and Cybernetics (2016). https://doi.org/10.1109/SMC
6. Huang, J., Corzine, K.: Control strategies for series and shunt active filters. In: IEEE Bologna Power Tech Conference, June 2003
7. Venkatesh Kumar, C., Gomathi, V.: Extended Operationof Flying Capacitor Multilevel Inverters, 232 Emerson Hall, 1870 Miner Circle (2003)
8. Karuppanan, P., Mahapatra, K.: Cascaded Multilevel Inverter based Active filter for Power Line Conditioners using Instantaneous Reactive-Power Theory. IEEE (2003)
9. Farayola, A.M, Hasan, A.N, Ali, A.: Comparison of modified incremental conductance and fuzzy logic MPPT algorithm using modified CUK converter. In: Proceedings of 8th IEEE International Renewable Energy Congress (IREC) 2017, Amman Jordan (2017)
10. Singh, B., Singhal, V.: Fuzzy Pre-Compensated PI Control of Active Filters, Manuscript Received 10 December 2007, Revised 23 January 2008
11. Saad, S., Zellouma, L.: Fuzzy logic controller for three-level shunt active filter compensating harmonic sand reactive power, Received 1 July 2007, Received in revised form 19 January 2009, Accepted 6 April 2009. Accessed 21 May 2009
12. Salmern, P., Herrera, R.S.: Instantaneous reactive power theory—A general approach to poly-phase systems, Received 17 June 2008, Received in revised form 26 January 2009, Accepted 23 March 2009. Accessed 28 Apr 2009
13. Karuppanan, P., Mahapatra, K.: PI and fuzzy logic controllers for shunt active power filter, Received 8 March 2011, Received in revised form 11 September 2011, Accepted 12 September 2011
14. Ali, A.A., Hasan, A.N, Marwala, T.: Perturb and observe based on fuzzy logic controller maximum power point tracking (MPPT). In: IEEE International Conference on Renewable Energy Research 2014, Milwaukee, USA (2014)
15. Chang, G.W., Chen, S.K., Chu, M.: An efficient a–b–c reference frame-based compensation strategy for three-phase active power filter control, Received 4 January 2001, Received in revised form 17 September 2001, Accepted 3 October 2001
16. Bouafiaa, A., Krima, F., Gaubert, J.: Design and implementation of high performance direct power control of three-phase PWM rectifier, via fuzzy and PI controller for output voltage regulation, Received 5 February 2008, Accepted 6 September 2008. Accessed 23 Oct 2008
17. Farayola, A.M., Hasan, A.N., Ali, A.: Curve fitting polynomial technique compared to ANFIS technique for maximum power point tracking. In: Proceedings of 8th IEEE International Renewable Energy Congress (IREC), Amman, Jordan (2017)

A Robust Model Predictive Control of a DC/DC Converter for a Solar Pumping System

Omar Hazil[1,2,5](✉), Sofiane Bououden[2,5], Ilyes Boulkaibet[3,5], and Fouzia Maamri[4,5]

[1] Centre de Développement des Energies Renouvelables CDER, Algiers, Algeria
o.hazil@cder.dz

[2] Laboratory of Automatic and Robotic, University Constantine1, Constantine, Algeria
sofiane.bououden@univ-khenchela.dz

[3] Faculty of Sciences and Technology, University Abbes Laghrour Khenchela, Khenchela, Algeria
ilyes@aims.ac.za

[4] RSA, University of Johannesburg, Johannesburg, South Africa

[5] Faculty of Science and Applied Sciences, University Larbi Ben M'Hidi, Oum el Bouaghi, Algeria

Abstract. A robust model predictive control approach using linear matrix inequality (LMI) is proposed for uncertain nonlinear systems. A simulation study on a PV Pumping System which comprises a PV generator, a buck DC-DC converter and a DC motor-pump is presented to evaluate the performance of the proposed controller. The LMI-based RMPC algorithm is currently under experimental stage and in near future we will publish the first results if they are satisfactory.

Keywords: Buck DC-DC converter · PV generator · DC motor pump
Linear matrix inequality (LMI) · Robust predictive controller

1 Introduction

Water pumping systems powered by solar-cell generators is one of the most interesting applications for distributed energy generation. PV water pumping systems have the advantages of: reliability, low maintenance, ease of installation and the matching between the powers generated and the water usage needs [1, 2].

For a better optimization of the energy, PV water pumping systems have to operate at their maximum power point (MPP). This maximum power point varies largely in time according to temperatures and irradiation levels; it is difficult to maintain optimum matching at all set of climatic conditions. In order to avoid the energy losses, a DC-DC converter known as a maximum power point tracker (MPPT) is used to match continuously the output characteristics of a photovoltaic generator to the input characteristics of a motor pump [3, 4].

M. Chadli et al. (Eds.): ICEECA 2017, LNEE 522, pp. 338–347, 2019.
https://doi.org/10.1007/978-3-319-97816-1_26

In this paper, we present a PV water pumping systems which includes photovoltaic array generator, DC/DC converter and DC motor coupled to a centrifugal pump. A robust predictive controller [5] based on linear matrix inequalities (LMI) [6] is applied to keep the PV generator voltage at a reference value taking into account uncertainty in the PVG operation point.

The following sections will show the PV pumping system modeling with the state-space averaging method and will present the regulator design in details. Finally we will give some simulation results to test the robustness of the proposed control strategy.

2 Model Pumping System

A basic diagram of the analyzed photovoltaic system is depicted in Fig. 1. It is possible to identify three main blocks that need to be modeled. They are photovoltaic arrays, DC-DC converter and a DC motor coupled to a centrifugal pump.

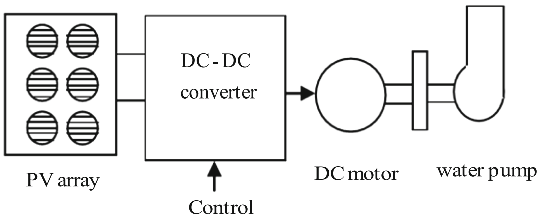

Fig. 1. Configuration of the PV pumping system

2.1 Photovoltaic Array Model

In order to appropriately represent the PVG, consider the equivalent circuit, shown in Fig. 2, where the photovoltaic cell is represented by an electric current generator which is equivalent to a current source parallel to a diode, i_{PH} represent the current (photo-current) generated by solar radiation (G), R_{SH} and R_S are intrinsic shunt and series resistances of the module, respectively. Note, R_{SH} is irradiation dependent and R_S is constant.

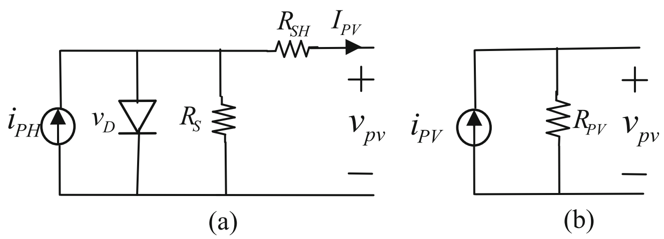

Fig. 2. Equivalent electrical scheme of the PVG: (a) Detailed, (b) Norton.

Photovoltaic generators are neither constant voltage sources nor current sources but in a real situation the array will be forced to operate at the boundaries of the constant current and constant voltage modes if a maximum power tracker is employed [7]. Consequently, the PV array may be represented by the simple Norton's equivalent circuit of Fig. 3 with

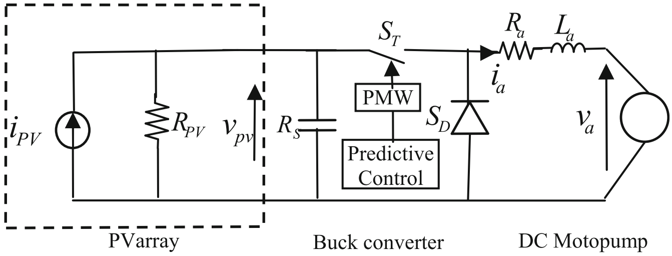

Fig. 3. Equivalent electrical scheme of the PV pumping system.

$$R_{PV} = R_S + R_{SH}//R_D \tag{1}$$

$$i_{PV} = i_{PH}\frac{R_{SH}//R_D}{R_{PV}} \tag{2}$$

It can be observed that the Norton equivalent circuit parameters are both environmental variables and operating point dependent.

2.2 Buck Converter Average Model

Resultant average model of PV pumping system is shown in Fig. 2, where v_{pv} is the photovoltaic array voltage. This voltage must be controlled in order to keep the array operation at the maximum power point; the output voltage va (DC motor voltage) is related to the photovoltaic array voltage by (3):

$$v_a = dv_{pv} \tag{3}$$

Where d is the duty cycle of the switch S_T

$$0 \le d \le 1 \tag{4}$$

The equations that describe the system can be described as the following:

$$\begin{aligned} L_a\dot{i}_a(t) &= -R_a i_a(t) - k_b\omega(t) + v_{pv}(t)d(t) \\ J\dot{\omega}(t) &= k_b i_a(t) - (k_T + F)\omega(t) \\ C\dot{v}_{pv}(t) &= I_{PV} - d(t)i_a(t) + v_{pv}(t)/R_{PV} \end{aligned} \tag{5}$$

Where ω and J are respectively the rotation speed and the moment of inertia of the group, k_b is the constant of the electric couple, k_T is the strength's constant against electrometrical. R_a and L_a represent respectively the armature resistance and inductance. F is the viscous friction coefficients of the DC machine.

The expression (5) can be compacted in the following manner,

$$\dot{x} = f(x(t), u(t)) \tag{6}$$

The total instantaneous quantities can be presented as the sum of the DC and AC components,

$$\begin{array}{ll} i_a(t) = \tilde{i}_a(t) + I_a & v_{pv}(t) = \tilde{v}_{pv}(t) + V_{pv} \\ \omega(t) = \tilde{\omega}(t) + \Omega & d(t) = \tilde{d}(t) + D \end{array} \tag{7}$$

Substituting this into (5) a small-signal model can be derived as follows:

$$\begin{aligned} &L_a\dot{\tilde{i}}_a(t) = -R_a\tilde{i}_a(t) - k_b\tilde{\omega}(t) + D\tilde{v}_{pv}(t) + V_{pv}\tilde{d}(t) \\ &J\dot{\tilde{\omega}}(t) = k_b\tilde{i}_a(t) - (k_T + F)\tilde{\omega}(t) \\ &C\dot{\tilde{v}}_{pv}(t) = -D\tilde{i}_a(t) - I_a\tilde{d}(t) + \tilde{v}_{pv}(t)/R_{PV} \end{aligned} \tag{8}$$

linearized around an operating point given by

$$\begin{aligned} &R_aI_a + k_b\Omega = V_{pv}D \\ &k_bI_a = (k_T + F)\Omega \\ &DI_a = I_{PV} - V_{PV}/R_{PV} \end{aligned} \tag{9}$$

We also introduce an added state variable to account for the integral of output regulation error. Let us define the new state variable as:

$$\dot{x}_e = v_{reff} - v_{pv} \tag{10}$$

The augmented averaged model of the PV system can be written as

$$\dot{x} = A\tilde{x} + B\tilde{u} + \tilde{f}(x(t), u(t)) \tag{11}$$

Where $\tilde{f}$ is a Lipschitz non-linearity, given by:

$$\tilde{f}(x(t), u(t)) = f(x(t), u(t)) - A\tilde{x} - B\tilde{u} \tag{12}$$

The nonlinear term is assumed to satisfy the Lipschitz condition as:

$$\left|\tilde{f}(X_1, t) - \tilde{f}(X_2, t)\right| \leq M|X_1 - X_2| \tag{13}$$

$$x = \begin{bmatrix} i_a \\ v_{pv} \\ \omega \\ x_e \end{bmatrix}, \qquad A = \begin{bmatrix} -\frac{R_a}{L_a} & \frac{D}{L_a} & -\frac{k_b}{L_a} & 0 \\ -\frac{D}{C} & \frac{1}{R_{PV}C} & 0 & 0 \\ \frac{k_b}{J} & 0 & -\frac{k_T+F}{J} & 0 \\ 0 & -1 & 0 & 0 \end{bmatrix}, \qquad B = \begin{bmatrix} \frac{V_{pv}}{L_a} \\ -\frac{I_a}{C} \\ 0 \\ 0 \end{bmatrix}$$

2.3 Uncertainty Model

We consider that the load R_{TH} at the operating point is uncertain or time-varying parameter. Then, matrices A and B depend on such uncertain which have been grouped in a vector p, and we can express (6) as a function of these parameter

$$\dot{x} = A(p)\tilde{x} + B\tilde{u} + \tilde{f}(x(t), u(t)) \tag{14}$$

In a general case, the vector p consists of N uncertain parameters $p = (p_1, \ldots, p_N)$, where each uncertain parameter p_i is bounded between a minimum and a maximum value $\bar{p}_i$ and $\underline{P}_i$

$$p_i \in \left[\underline{p_i}, \overline{p_i}\right] \tag{15}$$

The admissible values of vector p are constrained in an hyperrectangle in the parameter space R^N with $L = 2^N$ Vertices $\{\upsilon_1, \ldots, \upsilon_L\}$. The images of the matrix $[A(p), B(p)]$ for each vertex υ_1 corresponds to a set $\{\varsigma_1, \ldots, \varsigma_L\}$. The components of the set $\{\varsigma_1, \ldots, \varsigma_L\}$ are the extrema of a convex polytope, noted $Co\{\varsigma_1, \ldots, \varsigma_L\}$, which contains the images for all admissible values of p if the matrix $[A(p), B(p)]$ depends linearly on p, that is

$$[A(p), B(p)] \in Co\{\varsigma_1, \ldots, \varsigma_L\} = \left\{ \sum_{i=1}^{L} \lambda_i \varsigma_i, \quad \lambda_i \geq 0, \quad \sum_{i=1}^{L} \lambda_i \right\} \tag{16}$$

In this context, we consider that $N = 2$ and the parameter vector $p \in [1/R_{PV}]$ where:

$$1/R_{PV} \in [1/R_{PV\max}, 1/R_{PV\min}] \tag{17}$$

Since the PV system matrice A depend linearly on the uncertain parameter $1/R_{PV}$, we can define a polytope of $L = 2$ Vertices that contains all the possible values of the uncertain matrices. The vertices of the polytopic model are:

$$A_1 = \begin{bmatrix} -\frac{R_a}{L_a} & \frac{D}{L_a} & -\frac{k_b}{L_a} & 0 \\ -\frac{D}{C} & \frac{1}{R_{PV\max}C} & 0 & 0 \\ \frac{k_b}{J} & 0 & -\frac{k_T+F}{J} & 0 \\ 0 & -1 & 0 & 0 \end{bmatrix}, A_2 = \begin{bmatrix} -\frac{R_a}{L_a} & \frac{D}{L_a} & -\frac{k_b}{L_a} & 0 \\ -\frac{D}{C} & \frac{1}{R_{PV\min}C} & 0 & 0 \\ \frac{k_b}{J} & 0 & -\frac{k_T+F}{J} & 0 \\ 0 & -1 & 0 & 0 \end{bmatrix},$$

$$B_1 = B_2 = B$$

At maximum power transfer, the PV generator can be replaced by a voltage or a current source possessing high dynamic resistance in the former case and low dynamic resistance in the latter. In order to define range of changes for dynamic resistance, refer to PVG equivalent circuit of Fig. 3. At open circuit condition, R_D is low, dominating the parallel connection with R_{SH} [8, 9]. Thus we have:

$$R_{PV}|_{oc} \rightarrow R_S + R_D \tag{18}$$

bounded by

$$R_{PV}|_{oc} > R_{PV\min} = R_S \tag{19}$$

At short circuit and the reference condition, R_D is high, and R_{SH} dominates the parallel connection. Thus we have:

$$R_{PV}|_{sc} \rightarrow R_S + R_{SH} \tag{20}$$

Note that R_S is constant and R_{SH} is irradiation dependent [10]

$$\frac{R_{SH}}{R_{SH,ref}} = \frac{G}{G_{ref}} \tag{21}$$

$R_{SH,ref}$ is shunt resistance at STC (stands for Standard Test Conditions of 1 sun irradiation and *25 °C* PVG temperature). Finally as an approximation,

$$R_{PV}|_{sc} < R_{PV\max} = R_{SH.STC} \tag{22}$$

3 Robust Model-Based Predictive Control Using LMIs

Consider the infinite horizon quadratic performance index as follows:

$$J(k) = \sum_{i=0}^{\infty} x(k+i|k)^T Q x(k+i|k) + u(k+i|k)^T R u(k+i|k) \tag{23}$$

where $R(i)$, $Q(i)$ are two positive definite states and control weights respectively. Let us introduce a quadratic function $V(x) = x^T P x$, $P > 0$ of the state $x(k|k)$ of the system (14), with $V(0) = 0$. At sampling time k, suppose the following inequality is satisfied

$$V(k+i+1|k) - V(k+i|k) \geq -\left(x(k+i|k)^T Qx(k+i|k) + u(k+i|k)^T Ru(k+i|k)\right) \tag{24}$$

Summing (24) from $i = 0$ to $i = \infty$, we have

$$x(\infty|k)^T Px(\infty|k) - x(k|k)^T Px(k|k) \geq -J \tag{25}$$

If the resulting closed-loop system for (14) is stable, $x(\infty|k)$ must be zero and result in

$$J \leq x(k|k)^T Px(k|k) \leq -\gamma \tag{26}$$

where γ is a positive scalar and is regarded as an upper bound of the objective in (23)

$$\sum_{i=0}^{\infty} x(k+i|k)^T Qx(k+i|k) + u(k+i|k)^T Ru(k+i|k) \leq \gamma \tag{27}$$

Then, by substituting the state space Eq. (14) in the robust stability constraint (24), one has

$$\begin{aligned}
&\left[Ax(k+i|k) + Bu(k+i|k) + \tilde{f}(x(k+i|k), u(k+i|k)\right]^T P \\
&\left[Ax_i(k+i|k) + Bu(k+i|k) + \tilde{f}(x(k+i|k), u(k+i|k)\right] \\
&- x(k+i|k)^T Px(k+i|k) + x(k+i|k)^T Qx(k+i|k) \\
&+ u(k+i|k)^T Ru(k+i|k) \leq 0
\end{aligned} \tag{28}$$

Suppose the terms involving of $\tilde{f}$ in this inequality satisfy the following condition:

$$\begin{aligned}
&2[Ax(k+i|k) + Bu(k+i|k)]^T P\left[\tilde{f}(x(k+i|k), u(k+i|k)\right] \\
&+ \left[\tilde{f}(x(k+i|k), u(k+i|k)\right]^T P\left[\tilde{f}(x(k+i|k), u(k+i|k)\right] \\
&\leq \mu x(k+i|k)^T W^T Wx(k+i|k)
\end{aligned} \tag{29}$$

where $\mu = \lambda max(P)$ and W is the corresponding matrix of the quadratic bound which will be determined later in the next section. By replacing the condition (29) in the inequality (28), the following condition holds for all $i > 0$.

$$\begin{aligned}
&[Ax(k+i|k) + Bu(k+i|k)]^T P[Ax(k+i|k) + Bu(k+i|k)] \\
&- x(k+i|k)^T Px(k+i|k) + x(k+i|k)^T Qx(k+i|k) \\
&+ u(k+i|k)^T Ru(k+i|k) + \mu x(k+i|k)^T W^T Wx(k+i|k) \leq 0
\end{aligned} \tag{30}$$

the inequality can be expressed as:

$$P - (A_i + BK)^T P(A_i + BK) - Q - K^T RK - \mu W^T W \geq 0 \tag{31}$$

Define $P = \gamma G^{-1}$; $K = \gamma P^{-1}$ and $\alpha = \mu^{-1}\gamma$ and using Schur complement lemma twice, we have

$$\begin{bmatrix} G & (A_iG+BY)^T & (WG)^T & (Q^{1/2}G)^T & (R^{1/2}Y)^T \\ A_iG+BY & G & 0 & 0 & 0 \\ WG & 0 & \alpha I & 0 & 0 \\ Q^{1/2}G & 0 & 0 & \gamma I & 0 \\ R^{1/2}Y & 0 & 0 & 0 & \gamma I \end{bmatrix} \geq 0 \tag{32}$$

For robust constrained infinite horizon MPC, we incorporate both input constraint into the optimization problem. Then, the receding horizon state feedback gain K, which at the sampling time k minimizes the upper bound $V(x(k|k))$ on $J(k)$ and satisfies the specified input constraint, is given by $K = \gamma P^{-1}$, where $G > 0$ and Y are the solutions to the following LMIs:

$$\begin{gathered} \min_{G,Y,\gamma,\alpha} \gamma \quad \text{subjecte} \quad \text{to} \\ \begin{bmatrix} I & x(k|k)^T \\ x(k|k) & G \end{bmatrix} \geq 0 \\ \begin{bmatrix} G & (A_iG+BY)^T & (WG)^T & (Q^{1/2}G)^T & (R^{1/2}Y)^T \\ A_iG+BY & G & 0 & 0 & 0 \\ WG & 0 & \alpha I & 0 & 0 \\ Q^{1/2}G & 0 & 0 & \gamma I & 0 \\ R^{1/2}Y & 0 & 0 & 0 & \gamma I \end{bmatrix} \geq 0 \\ \begin{bmatrix} u_{\max}^2 I & Y \\ Y^T & G \end{bmatrix} \geq 0 \\ G - \alpha I > 0 \end{gathered} \tag{33}$$

4 Results, Analysis and Discussions

The performances of the proposed control design are illustrated through simulations. The numerical parameter values used are given by:

- PV generator: $R_{SH} = 13.5620\ \Omega$, $R_S = 0.2670\ \Omega$, $I_{pv} = 19.2000$ A,
- Capacitor: $C = 4000.10^{-6}$ F.
- The permanent magnet DC motor-pump is characterized by a nominal operating point: $Un = 24$ V and $In = 12$ A, $Wn = 3000$ round/mn (rpm) and a power $Pn = 0.3$ hp.

- The identified parameters of DC motor are in USI: $R_a = 1.072$, $L_a = 0.05$, $J = 476.10^{-6}$, $F = 88.10^{-5}$, $kT = 14.10^{-4}$, $kb = 45.10^{-3}$.

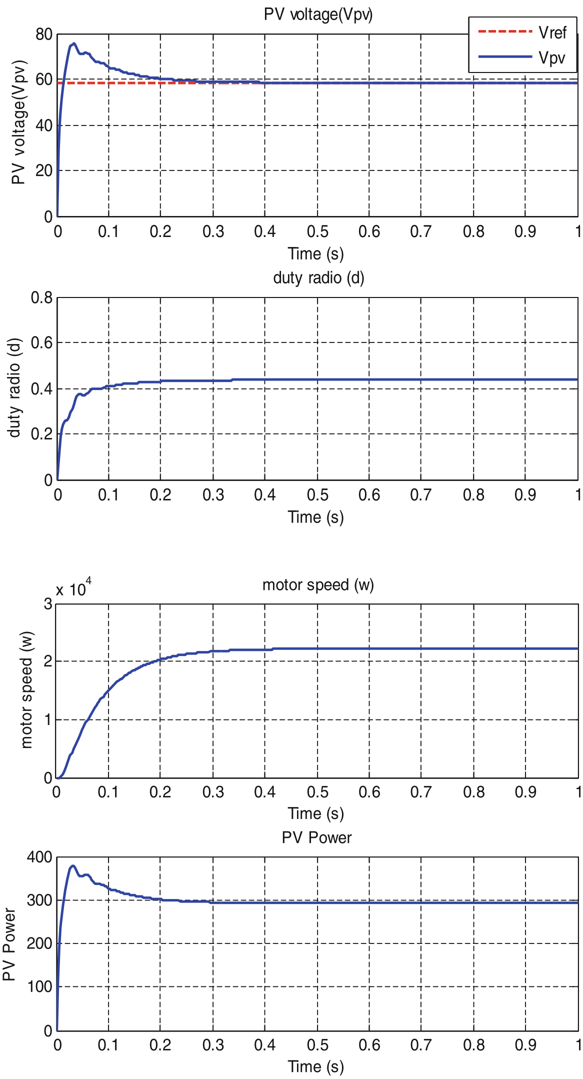

Fig. 4. The transient simulation of the PV system

Figure 4 depicts the transient simulation of the PV pumping system under the dynamic resistance perturbations. The waveforms depicted in the Fig. 4 are the duty-cycle d, PV voltage v_{pv}, PV power and motor speed ω. It can be noted that the voltage output response settle to their desired value with a saturated control input signal at

43%. Simulation results demonstrate that our controller guarantees better stabilization performance and better time response (*0.3* s). Moreover, the proposed controller is robust with respect to dynamic resistance change.

5 Conclusions

In this paper, a robust model predictive control approach based on linear matrix inequality has been proposed for the nonlinear systems subject to parametric uncertainties. The LMI-based RMPC controller has been applied to regulate the PV generator voltage of a photovoltaic pumping system.

At first the non linear state space averaging model of PV pumping system is generated and linearized around equilibrium point, this model take into account parametric uncertainty by means of a polytopic representation. Then, the state feedback control law is obtained by minimizing the upper bound of the infinite horizon cost function at each time instant. The stability condition of the closed-loop system is guaranteed over the whole uncertainty domain in the sense of Lyapunov.

References

1. Appelbaum, J., Bany, J.: Analysis of a direct coupled DC motor and a photovoltaic converter. In: 1st Commission of European Community Conference on Photovoltaic Solar Energy, Luxembourg, Reidel, Dordrecht, The Netherlands, 27–30 September 1979
2. Singer, S., Appelbaum, J.: Starting characteristics of direct current motors powered by solar cells. IEEE Trans. Energy Convers. **8**(1), 47–53 (1993)
3. Hua, C., Shen, C.: Study of maximum power tracking techniques and control of DC/DC converters for photovoltaic power system. In: Proceedings of 29th Annual IEEE PESC, pp. 86–93. IEEE Computer Society Press, New York (1998)
4. Masoum, M.A.S., Dehbonei, H., Fuchs, E.F.: Theoretical and experimental analyses of photovoltaic systems with voltage- and current-based maximum power-point tracking. IEEE Trans. Energy Conver. **17** (4) (2002)
5. Kothare, M., Balakrishnan, V., Morari, M.: Robust constrained model predictive control using linear matrix inequalities. Automatica **32**, 1361–1379 (1996)
6. Boyd, S., Ghaoui, L.E., Feron, E., Balakrishnan, V.: Linear Matrix Inequalities in Control Theory. SIAM, Philadelphia (1994)
7. Nakanishi, F., Ikegami, T., Ebihara, K., Kuriyama, S., Shiota, Y.: Modeling and operation of a 10 kw photovoltaic power generator using equivalent electric circuit method. In: Proceedings of IEEE Photovoltaic Specialists Conference (2000)
8. Sitbon, M., Schacham, S., Kuperman, A.: Disturbance observer based voltage regulation of current-mode-boost-converter-interfaced photovoltaic generator. In: IEEE Transactions on Industrial Electronics, pp. 0278–0046 (2015)
9. Elgendy, M.A., Zahawi, B., Atkinson, D.J.: Assessment of perturb and observe MPPT algorithm implementation techniques for PV pumping applications. IEEE Trans. Sustain. Energy **3**(1), 21–33 (2012)
10. Tian, H., Mancilla-David, F., Ellis, K., Muljadi, E., Jenkins, P.: A cell-to-module-to-array detailed model for photovoltaic panels. Sol. Energy **86**(9), 2695–2706 (2012)

Modeling of a Solar Cooling Machine by Absorption Using RBF Neural Networks

Kheireddine Lamamra[1,2(✉)], Djilali Khane[3,4], and Chokri Ben Salah[5]

[1] Department of Electrical Engineering, University of Oum El Bouaghi, Oum El Bouaghi, Algeria
l_kheir@yahoo.fr, Lamamra.kheireddine@ieee.org
[2] Laboratory of Mastering of Renewable Energies, University of Bejaia, Bejaia, Algeria
[3] Science and Technology Department, University Centre Morsli Abdallah of Tipaza, Tipaza, Algeria
[4] Green Energy Solar Company, Business Center, Office No. 13/4, Zéralda, Algiers, Algeria
djilkhane@gmail.com
[5] Control and Energy Management Laboratory (CEMLab), Department of Electrical Engineering, National School of Engineers of Sfax, Sfax, Tunisia
chokribs@yahoo.fr

Abstract. In this work, the modeling of a solar absorption cooling machine is presented using Artificial Neural Networks of the Radial Basic Function (RBF) type optimized by multi-objective genetic algorithms. The neural model obtained is compared with the results obtained with the Lansing model in order to validate its efficiency for the characterization of the coefficient of performance (COP) of absorption machines that produce cold with solar energy and the energy efficiency of this type of machine in order to reduce consumption. The optimization of the structure of the neural model and its learning are ensured by the NSGA-II genetic algorithms by optimizing two functions which are the learning error and the number of neurons in the hidden layer of the neural model. The obtained model offers the possibility of changing several parameters at the same time and facilitates the calculations and opens up fields of future research more push for this type of machine.

Keywords: Absorption machine · Lansing model · Modeling
RBF neural networks · Solar cold production

1 Introduction

Solar energy is the energy produced from the conversion of solar radiation. It is considered an inexhaustible source. The sun sends to the surface of the Earth a radiance that represents annually about fifteen thousand times the energy consumption of humanity

K. Lamamra, University of Oum El Bouaghi, Algeria

M. Chadli et al. (Eds.): ICEECA 2017, LNEE 522, pp. 348–362, 2019.
https://doi.org/10.1007/978-3-319-97816-1_27

[1]. This energy represents an instantaneous power received from about 1 Kilowatt peak per square meter (KWp/m^2) distributed over the entire spectrum, from ultraviolet to infrared. Studies have shown that the deserts receive in a few hours, more energy than that equivalent in annual consumption of all mankind [2].

Air conditioning helps maintain comfort and ambient air characteristics in temperature, humidity and air quality for human feel and due to power consumption; it is best to use cooling systems with solar energy. This procedure covers several positive aspects, mainly to limit the use of a conventional air conditioning known for its negative impacts on the environment [3–5]. A traditional air conditioner produces cold by compressing a so - called "refrigerant" or "refrigerant" fluid that has the ability to absorb large quantities of heat when it passes from its liquid phase to its gaseous phase at the evaporator. Therefore, it consumes electricity to operate the compressor and the refrigerant. Although it is in a closed circuit, fluid leaks are not uncommon [3, 4, 6]. In the case of solar air conditioning, the calorific energy delivered by the solar system is used by refrigeration or air-conditioning machines to produce refrigerating energy to ensure the refreshing of the premises [7, 8]. According to the French Environment and Energy Management Agency (ADEME: l'Agence De l'Environnement et de la Maîtrise de l'Energie), it is necessary to speak more precisely of "systems of air conditioning of the buildings assisted by the solar". In other words, the power supply to the installation is based on a mix: solar energy/conventional energy [ADEME], [4, 9].

In this work, simulations of a solar absorption cooling machine with an artificial neural network model of the RBF type are presented with the aim of replacing the mathematical models by a model which facilitates the numerical programming and which gives a flexibility in the choice of several variables simultaneously for the outputs which give rise interpretations of this machine. The neural model designed is optimized by multi-objective genetic algorithms, which are used to ensure the best possible learning of the neural model and to obtain an optimal structure by optimizing the neuron number in the hidden layer of the neural model.

2 Sorption Machines (Closed Systems)

Usually, refreshing systems using solar energy are divided into two categories: closed systems and open systems. Open systems cool the air directly, whereas closed systems produce chilled water which will then be used for cooling or dehumidifying the air. In sorption machines, mechanical compression is replaced by thermal compression in contrast to conventional electric air conditioning which produces cold by compressing a fluid. These systems also use a refrigerant and its phase changes (liquid/vapor) but they cause them through a supply of heat. The refrigerant is in this case water added with a second component. If the latter is a liquid, then it is called an absorbent and an absorption machine, if it is a porous solid, then we speak of adsorbent and adsorption machine [ADEME].

In absorption refrigeration machines used in air conditioning, the absorbing substance is generally lithium bromide (LiBr), the refrigerant fluid, water. The ammonia/

water couple can also be used. The temperature of the water used for the decomposition of water and absorbent must be between 80 and 120 °C (Fig. 1).

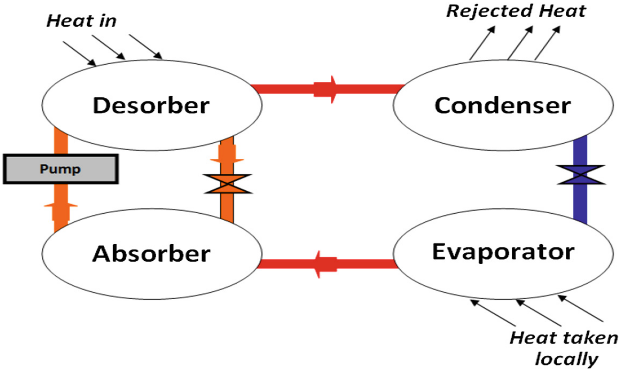

Fig. 1. Absorption Machine Operation [10].

A refrigerating machine is energy efficient if it requires little energy to provide a given refrigeration capacity. Its efficiency is evaluated by the calculation of the coefficient of performance (COP): ratio between the refrigerating power produced and the power supplied to the compressor. In the case of a traditional refrigerating machine, the power supplied is electric. The COP of such a machine can reach the value of 3 or more. In the case of an absorption refrigerating machine, the thermal COP rotates around 0.7; that of an adsorption machine ranges between 0.5 and 0.6. These sorption machines are already widespread in the industrial sector because some processes release a large amount of heat, from which it is possible to derive an otherwise useful refrigerating power. In the building sector, the idea is to couple these machines with a co-generator or solar panels. The heat required to separate the two products would therefore come from a co-generator or thermal solar panels. The challenge now is to reduce the size and power of machines so that they can be integrated into the building sector. Generally, current closed systems represent the majority of existing solar cooling systems, with a preponderant share for absorption systems [4, 8, 11].

The possibility of cold production from solar energy was initiated by technological developments in the solar sector. The calculation of any refrigeration cycle must lead to the determination of the different flow rates of the mixture as well as the operating conditions such as temperature, pressure and composition in each part of the system. In this work, the machine studied is an absorption using the LiBr-H2O couple and the thermodynamic study of the absorption cycle with a heat exchanger (Absorber-generator).

3 Absorption Refrigerating Machines Using the Torque (Libr-Water)

The cooling capacities of these machines are very high, their ranges range from 1 KW to 3.5 KW approximately, they are very used in Air conditioning [6, 12]. Figure 2 shows a diagram of an H2O/LiBr absorption plant. In this installation, the water represents the refrigerant while the absorber is LiBr. LiBr is a solid salt, but when mixed with sufficient water, a homogeneous liquid solution is obtained.

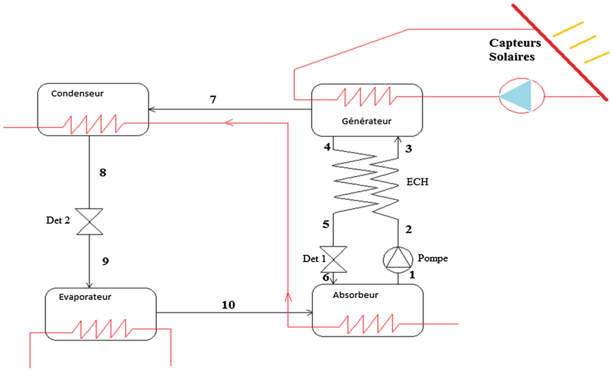

Fig. 2. Schematic diagram of a solar absorption machine (H2O/LiBr) [10]

The main advantage of this system is that the LiBr is not volatile. Thus, in the generator, only water vapor will be formed, but the main disadvantage is the supply of the solidification temperature of 0 °C. These installations are used in air conditioning (>0 °C) [6, 13].

3.1 Operation

The solution H2O/LiBr heated in the generator, the water separates as vapor, the solution remains diluted in LiBr (unlike the NH3 solution which it depletes in the boiler). The free water vapor is condensed in the condenser and then passes to the evaporator where it vaporizes. The water vapor produced is absorbed by the concentrated solution from the boiler which is depleted in the absorber. The pump returns this solution to the boiler for a new cycle. The low pressures combined with the boiler and the condenser on the one hand (1.6 bar absolute on average) and the evaporator and the absorber on the other hand allowing to concentrate in two blocks which are represented in the form of cylinders: Boiler and Condenser; Evaporator and Absorber. The very low overall pressure (evaporator/absorber) forces to maintain a high vacuum in this part of the installation so that the vaporization temperature of the water is close to 0 °C, this vacuum is maintained by a pump [6, 12, 13].

3.2 Representation of Absorption Cycle in Diagrams

It can be seen that for absorption machines, the number of independent variables makes it impossible to use the thermodynamic diagrams valid for mechanical compression systems, so two diagrams will be used [14–16]: Oldham Diagram and Merkel diagram. This is the most widely used diagram for a study of an absorption cycle. In this diagram, the lines of concentration are straight lines. It is useful for approximating a cycle and to check if the temperatures are compatible, but it does not provide thermodynamic information. For this purpose the Merkel diagram is used. The latter allows a complete study of the absorption machine because, in addition to the information given in the diagram, it gives information on the enthalpy of the liquid solution and the vapor of the refrigerant, it is a diagram (X, H) parameterized in pressure and temperature for the solution, pressure for steam [14–16].

4 Thermodynamic Calculation of an Absorption Machine (H2O/LiBr)

To determine the pressures and concentrations of the solution in the cycle, either: The diagrams mentioned above and mathematical models describing the different concentrations as a function of working temperatures. In our work we chose to work with the Lansing model [17].

4.1 Mass Balance

At the absorber, two mass balances can be carried out by [12]:

$$mr + mc - md = 0 \text{ (Overall assessment of the solution)}$$

$$mcXc - mdXd = 0 \text{ (Balance LiBr)}$$

From this we deduce an expression of *mc* and *md* in terms of *mr* and different titles of refrigerant.

$$m_d = m_r \frac{X_c}{X_c - X_d}; m_c = m_r \frac{X_d}{X_c - X_d}$$

4.2 Enthalpic Balance

The enthalpy balance is carried out on each component exchanging heat or working with the external environment [2]:

$$Qa + QC = Qe + Qg$$

Condenser: $Qc = mr(h7 - h8)$
Evaporator: $Qe = mr(h10 - h9)$
Generator: $Qg = mfh7 + mch4 - mdh3$
Absorber: $Qa = mdh1 - mrh10 - mch6$
Pump: $W_p = md(h2 - h1)$

4.3 Specific Solution Flow Rate (Circulation Rate)

The specific solution Flow Rate (FR), which is the ratio of the mass flows of the diluted solution (md) pumped by the pump and of vapor (mr) desorbed to the generator, is written [12]:

$$FR = \frac{md}{m_r} = \frac{X_c}{X_c - X_d} \text{où:}$$

Xc: the title of the concentrated solution leaving the generator to reach the absorber.
Xd: the title of the binary mixture rich in refrigerant leaving the absorber to join the generator.

4.4 The Degassing Range

The difference (Xc–Xd) is called the degassing range, it is noted (ΔX) [12]: $\Delta X = Xc–Xd$

A. Determination of Performance Coefficient COP

Using the above equations, we can express the COP by:

$$COP = \frac{Q_e}{Q_g + W_p} = \frac{m_r(h_{10} - h_9)}{m_r h_7 + m_c h_4 + m_d(h_2 - h_1 - h_3)}$$

5 Thermodynamic Analysis and Performance Calculation

In this work, a RBF neural model is elaborated. This model is optimized by NSGA-II multi-objective genetic algorithms and allows to determine the thermodynamic properties of each state in the cycle of an absorption refrigerating machine. L. Lansing has developed a mathematical model describing the different behaviors and the different thermodynamic properties of the absorption cycles for the couple (LiBr-Water) [17]. The established model works in the concentration range of solutions between 0.50 and 0.56 with an error of 0.2%.

The analysis of the simulation and the modeling procedure of a lithium bromide/water absorption system, are according to the following initial conditions: the temperature of the generator 90 °C, the temperature of the evaporator 7 °C, absorber and condenser temperature 40 °C, efficiency of exchanger 0.8, refrigeration capacity is 3024 kcal/h (3.5 kW).

The determination of the thermodynamic properties of each state in the cycle, the amount of heat transferred in each component and the flow rates of the different lines depends on the set of the following contribution parameters [6, 12, 14]:

- Temperature of generator Tg, [°C].
- Evaporator temperature Te, [°C].
- Condenser temperature Tc, [°C].
- Temperature of the absorber Ta, [°C].
- Liquid-liquid heat exchanger efficiency Eff.
- The refrigeration charge QE.

All parameters can be determined by actual measurements or assumed by a first reasonable estimate. The work of the pump, the pressure losses in the various components are neglected.

Thus, the first law of thermodynamics is [12]:

$$Q_C + Q_A = Q_G + Q_E$$

The coefficient of performance (COP)
It is defined by:

$$COP = \frac{refrigeration\,capacity}{motor\,power} = \frac{Q_E}{Q_G}$$

The ideal coefficient of performance
The maximum COP of an absorption machine is given by [17]:

$$(COP)_{max} = \frac{T_e\left(T_g - T_a\right)}{T_g\left(T_c - T_e\right)}$$

where Te, Ta, Tc and Tg are respectively: the absolute temperatures of the evaporator, the absorber, the condenser and the generator.

Hence the report of the COP (Cop ratio) [17]

$$Cop\ ratio = \frac{(COP)}{(COP)_{max}}$$

It is called the relative COP.

6 Modeling of the Solar Cold Production Machine by Absorption by RBF NN

In this work, the modeling of the machine of production of the solar cooling by absorption is carried out using the artificial neurons networks type of RBF optimized by the multi-objective genetic algorithms with the objective is simplifying the study in simulation of this machine by replacing several mathematical equations with a simple neural model and facilitated simulation testing and analysis which saves valuable time and avoiding complicated mathematical equations, allowing the use of this neural model by any user without the need to use these mathematical equations. The neural model also allows possible to make the variation of several parameters simultaneously which is very difficult using the mathematical equations [18].

6.1 Neural Networks

NN are data processing techniques able to modeling non-linear systems and approximating any function with some approximation error [19, 20]. In this work, the structure of the neural model of the solar absorption cooling machine is optimized by NSGA-II multi-objective genetic algorithms. This also ensures the learning of this model.

6.2 The NSGA-II Multi-objective Genetic Algorithm

The construction and the learning of the RBF neural model is performed by the Multi Objective Genetic Algorithm type of NSGA-II (Non-dominated Sorting Genetic Algorithm) developed and improved by chromo-somes. It's an elitist algorithm and in order to manage elitism, it evolves so that at each new generation, the best individuals encountered are retained. The functioning of this algorithm is as follows: At first, an initial population is randomly created, then a sorting operation is performed using the non-domination concept. for each solution it is assigned a rank equal to the level of non-dominance, the rank 1 for best, 2 for the next level, etc. Then, a tournament of parents selection is performed during the reproduction process.

Once two individuals of the population are randomly chosen, the tournament is performed on a comparison of the domination with constraints of the two individuals.

For a given generation *t*, after creating a children population Q_t from the previous population P_t (generated from the parents via the genetic operators, crossover and mutation), it is created a population R_t that includes the parents population P_t and the children population Q_t a manner that $R_t = P_t U Q_t$, that ensures the elite nature of the NSGA-II algorithm. Then the population R_t contains twice the size of a population (2 N individuals: N for parents and N for children).

As a result, the concept of non-dominance of Pareto is applied to sort Rt, then individuals of R_t will be grouped in successive fronts (F1, F2, … etc.) as F1 represents individuals of rank 1, F2 individuals of rank 2, etc.

After, the size of R_t should be reduced to N individuals in order to form the next population P_{t+1}, so N individuals from Rt must be excluded from the next population. If the size of the front F1 is less than N, then all its individuals are preserved and It is the same procedure for the other fronts while the number of the preserved individuals does not exceed the size N.

For example, fronts F1 and F2 can be fully preserved, by against the conservation of the front F3 will result in exceeding the size N of the population P_{t+1}, then, it's necessary to make a selection to determine individuals to keep. To do that, NSGA-II performs a mechanism for preserving the diversity in the population based on the evaluation of the individuals density around each solution across a calculating procedure of the "distance proximity". Thereby, a low value of the proximity distance for an individual is an individual "well surrounded".

It then proceeds to a descending sorting according to this proximity distance to preserve the necessary number of individuals of F3 front and remove some individuals from the densest areas. With this way, the population P_{t+1} is made up to N individuals and diversity is ensured. The individuals with extreme values of the criteria are maintained by this mechanism, which keeps the external bounds of the Pareto front.

At the end of this phase, the population P_{t+1} is created. Then a new population Q_{t+1} is generated from P_{t+1} by the reproduction operators.

The procedure described above is repeated by ensuring elitism and diversity until the satisfaction of the stopping criteria defined beforehand.

6.3 Learning of Neural Model by the NSGAII

The NSGA II is used to optimize the structure and parameters of the RBF NN by optimizing two objective functions that are: The number of neurons in the hidden layer (f_1) and the quadratic error which is the difference between the desired input of the output of the neural model (f_2).

The NSGA-II should find the best number of neurons in the hidden layer (Nn), find the parameters of the radial function of neurons of the same layer and also provide the best connection weights between neurons in the hidden layer and the output layer. Here we used a Gaussian form of the radial functions, and NSGA-II must find the best centers (C_i) and the best widths sigma (Sig_i) for these functions.

For that, the genetic chromosome contains: the number of neurons in the hidden layer, Gaussian functions centres and widths of the hidden layer neurons, and the weights of connections between the hidden layer and the output layer. It's structure has the following form:

$$[N_n C_1 C_2 \ldots C_{Nn} sig_1 sig_2 \ldots sig_{Nn} Z_1 Z_2 \ldots Z_{Nn}]$$

where:

- N_n: the number of neuron in the hidden layer.
- $C_2\ C_1 \ldots C_{Nn}$: the Gaussian functions centres of the hidden layer neurons.
- $sig_1\ sig_2 \ldots sig_{Nn}$: are the sigma widths of the Gaussian functions of the hidden layer neurons.
- $Z_1\ Z_2 \ldots Z_{Nn}$: the connection weights between the hidden layer neurons and the output layer neuron.

The length of the chromosome (L_{ch}) depends on the number of neurons in the hidden layer (N_n) and the number of neurons of the output layer (N_{ns}) because the inputs are fixed to six inputs. The general expression of the length of the chromosome (L_{ch}) is given by:

$$Lch = \left(2 + N_{ns}\right) * max\left(N_n\right) + 1$$

The population size T_m (population matrix) is given by:

$$Tm = N * ((2 + N_{ns}) * max\left(N_n\right) + 1))$$

N: number of individuals in the population.

The inputs of the neural model are: generator temperature Tg, evaporator temperature Te, condenser temperature Tc, absorbing temperature Ta and liquid-liquid heat exchanger *eff* efficiencies as well as the error of modeling *em.*

After the evolution of several generations of NSGA-II, an individual is chosen from the non-dominated individuals obtained from the Pareto front of the last generation. This individual represents the chosen neural model of the solar cooling machine by absorption is composed of 12 neurons in the hidden layer. The obtained results from this model are presented in the following section.

7 Results and Interpretations

The obtained results are presented below and it show that the NSG-II optimized RBF neural model obtained is identical to the model obtained via the mathematical equations of the Lansing model, with more flexibility concerning the variation of the input parameters. It should be noted that in order to have more precision and the neural model to learn better, a temperature step equal to 0.25°C was used for all the tests carried out.

Figures 3, 4, 5, 6, 7, 8, 9 and 10 respectively show: the variation of the coefficient of performance of the neural model COP_{nn} and that of the Lansing model COP_L as a function of the variation in temperatures: of the generator Tg, the absorber Ta, the condenser Tc, the Te evaporator. Each of these figures is followed by a figure of the corresponding instantaneous modeling error.

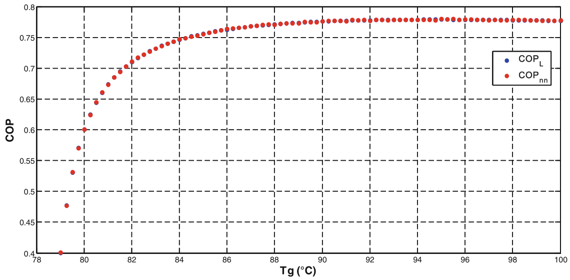

Fig. 3. Variation of Cop as a function of the generator temperature of the neuronal model and the Lansing model

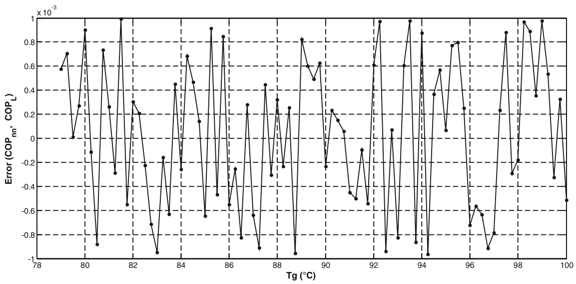

Fig. 4. Modeling error (Cop of neural model and Cop of Lansing model as a function of generator temperature).

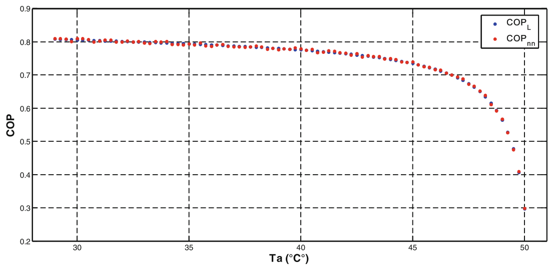

Fig. 5. Variation of the Cop of the neuronal model and that of the Lansing model as a function of the Absorber Temperature

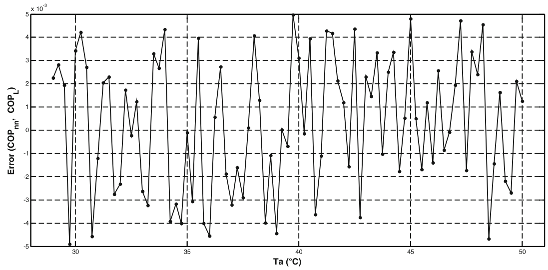

Fig. 6. Modeling error (Cop of neural model and Cop of Lansing model as a function of Absorber Temperature).

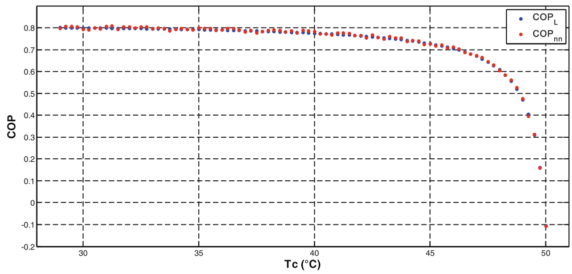

Fig. 7. Variation of the Cop of the neural model and that of the Lansing model as a function of the condenser temperature.

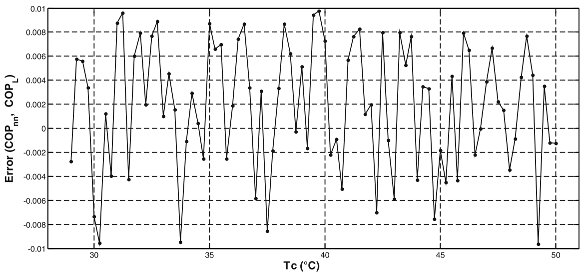

Fig. 8. Modeling error (Cop of neural model and Cop of Lansing model as a function of condenser temperature)

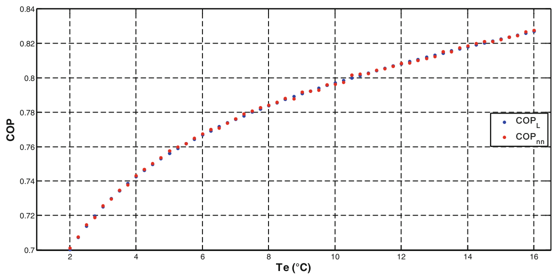

Fig. 9. Variation of the Cop of the neural model and that of the Lansing model as a function of the Evaporator Temperature.

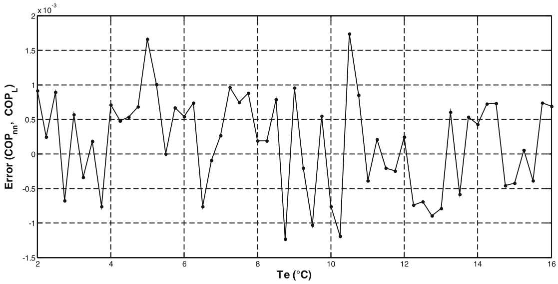

Fig. 10. Variation of the Cop of the neuronal model and that of the Lansing model as a function of the Evaporator Temperature.

Figures 11 and 12 show respectively, the variation of the COP of the neural model (COPnn) depending on the exchanger efficiency and its variation according to the generator temperature for different values of the exchanger efficiency.

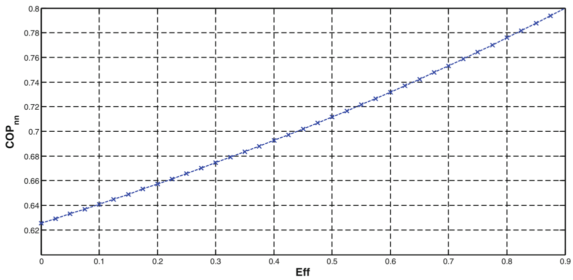

Fig. 11. Variation of the COP of the neural model as a function of the exchanger efficiency

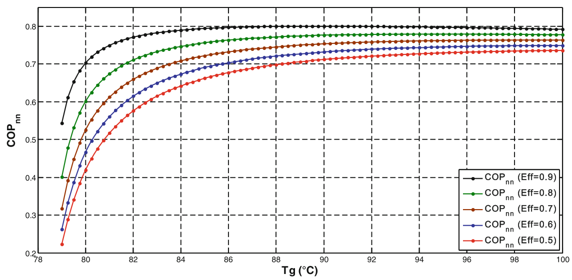

Fig. 12. Variation of the COP of the neural model as a function of the generator temperature Tg for different values of the exchanger efficiency.

Discussion of results

According to the obtained results, the following remarks can be made:

- In Fig. 3, the COPnn increases with the increase of Tg until reaching a maximum value 0.78, for Tg = 92 °C, with an instantaneous error of $e_{cop} = 0.97 \times 10^{-3}$ compared with the Lansing model, then the COPnn value remains almost constant and does not fall below 0.777 for *Tgmax* = 100°C. After this value, the investment is not important as long as the same COP is kept.
- The COPnn decreases with the increase of Ta and of Tc (Figs. 5 and 7). In the absorber there will be a need for cooling to ensure the proper functioning of the chemical reaction Lithium-water bromide. The water vapor leaving the generator passes to the condenser where it condenses at ambient temperature, the phenomenon of condensation is necessary in order to have the water completely liquid at the outlet of the condenser. If the ambient temperature (of the capacitor) increases, it will not have 100% liquid at the output of the condenser therefore the COPnn decreases.
- When Te increases (Fig. 9), the quantity of heat extracted by the evaporator Qe also increases and consequently increases the COPnn.
- According to all these results, it should be noted that the instantaneous modeling errors of all the tests are very low (Figs. 4, 6, 8 and 10). The largest quadratic modeling error is that of the neuronal model for Tc where $e_{qmoy}\,(T_c) = 2.8 \times 10^{-5}$.
- It is obvious from these results that the neural model conforms to the mathematical model, which is why we have adopted the neural model for the study of the variation

of the COPnn as a function of the exchanger efficiency and variation of the COPnn as a function of the generator temperature Tg for different values of the exchanger efficiency from 0.5 to 0.9 (Figs. 11 and 12).

- The COPnn increases with the increase of Eff, this behavior of the neural model is correct because if the heat exchanger accepts a good efficiency, it implies an increase of the temperature of the solution at the input of the generator, which helps to produce less energy to it according to the following equation $COP = \frac{Qe}{Qg}$; the COP_{nn} increases.
- For different values of the exchanger efficiency, the COPnn increases with the increase of Tg until reaching the maximum value for each curve of Eff.
- All the curves of COPnn (Fig. 10) tend towards the same constant value with a minor difference, so from this value the investment does not seem important.

8 Conclusion

In this work, artificial neural networks of type Radial Basis Function (RBF) were used to model the refrigeration absorption machine. The neural model is optimized by Non-dominated Sorting Genetic Algorithm (NSGA II). The obtained model makes possible to facilitate the calculation of the operating conditions of these types of absorption systems, knowing that the determination of the performance of a system by the conventional methods takes a long time.

The thermodynamic analysis of the solar absorption refrigeration machine modeled here by a neuronal model has shown that more the boiler temperature is high, more the COPnn of the refrigeration system is higher, since the heat flow captured by the solar heating sensor, directly affects the temperature of the boiler, thus influencing the coefficient of performance of the absorption refrigerating machine.

According to the simulation study of the solar absorption refrigeration system, a COPnn of the refrigerating machine can be reached by choosing a better solar collecting surface and ensuring the correct cooling of the condensers and the absorber.

From the obtained results, it is clear that the neuronal model optimized by the genetic algorithms is practically identical to the model obtained via the mathematical equations of the Lansing model. However, this neural model of RBF type, allowed us to avoid the use of mathematical equations, which will become very complicated by varying several parameters simultaneously. Through this neural model it was possible to study the variation of the COP as a function of the different temperatures and also as a function of the temperature of the generator for different values of the exchanger efficiency. In future work, we will exploit this neural model to study the behavior of the machine by varying several parameters simultaneously, which is difficult by the Lansing model but the neural model will save a lot of time. It is also interesting to determine the surface area of the solar thermal collectors needed for the operation of such machines, taking into account the ratio performance/investment price in order to optimize its efficiency.

References

1. Kamat, P.V., Tvrdy, K., Baker, D.R., Radich, J.G.: Beyond photovoltaics: semiconductor nanoarchitectures for liquid-junction solar cells. Chem. Rev. **110**(11), 6664–6688 (2010)
2. Da Rosa, A.V.: Fundamentals of Renewable Energy Processes. Academic Press, Cambridge (2012)
3. Ketfi, O., Merzouk, M., Merzouk, N.K., Metenani, S.E.: Performance of a single effect solar absorption cooling system (Libr-H2O). Energy Procedia **74**(Suppl. C), 130–138 (2015)
4. Kalogirou, S.A.: Solar Energy Engineering: Processes and Systems. Academic Press, Cambridge (2013)
5. Kalogirou, S.A.: Solar thermal collectors and applications. Prog. Energy Combust. Sci. **30**(3), 231–295 (2004)
6. Taieb, A., Mejbri, K., Bellagi, A.: Theoretical analysis of a diffusion-absorption refrigerator. Int. J. Hydrog. Energy **41**(32), 14293–14301 (2016)
7. Ma, H., Balthasar, F., Tait, N., Riera-Palou, X., Harrison, A.: A new comparison between the life cycle greenhouse gas emissions of battery electric vehicles and internal combustion vehicles. Energy Policy **44**, 160–173 (2012)
8. Allouhi, A., Kousksou, T., Jamil, A., Bruel, P., Mourad, Y., Zeraouli, Y.: Solar driven cooling systems: an updated review. Renew. Sustain. Energy Rev. **44**, 159–181 (2015)
9. Nikolakakis, T., Fthenakis, V.: The optimum mix of electricity from wind-and solar-sources in conventional power systems: evaluating the case for New York State. Energy Policy **39**(11), 6972–6980 (2011)
10. Closed systems: sorption machines - Solar air conditioning (in French). http://www.actu-environnement.com/ae/dossiers/climatisation_solaire/systemes_fermes.php4. Accessed 08 Oct 2016
11. Assilzadeh, F., Kalogirou, S.A., Ali, Y., Sopian, K.: Simulation and optimization of a LiBr solar absorption cooling system with evacuated tube collectors. Renew. Energy **30**(8), 1143–1159 (2005)
12. Reddy, T.A., Kreider, J.F., Curtiss, P.S., Rabl, A.: Heating and Cooling of Buildings: Design for Efficiency. CRC Press, Cambridge (2009)
13. Mendell, M.J., Lei-Gomez, Q., Mirer, A.G., Seppänen, O., Brunner, G.: Risk factors in heating, ventilating, and air-conditioning systems for occupant symptoms in US office buildings: the US EPA BASE study. Indoor Air **18**(4), 301–316 (2008)
14. Soli, N., Hafsia, N.B., Chaouachi, B.: Thermodynamic feasibility study of absorption diffusion machine working with hydrocarbons. Int. J. Hydrog. Energy **42**(1), 8881–8887 (2017)
15. Sun, D.-W.: Thermodynamic design data and optimum design maps for absorption refrigeration systems. Appl. Therm. Eng. **17**(3), 211–221 (1997)
16. Martz, W.L., Burton, C.M., Jacobi, A.M.: Local composition modelling of the thermodynamic properties of refrigerant and oil mixtures. Int. J. Refrig. **19**(1), 25–33 (1996)
17. Lansing, F.L.: Computer modeling of a single stage lithium bromide/water absorption refrigeration unit. Jet Propulsion Laboratory. California Institute of Technology, Pasadena, CA Deep Space Network Program Rep., no. 42–32, pp. 247–257 (1976)
18. Tehlah, N., Kaewpradit, P., Mujtaba, I.M.: Artificial neural network based modelling and optimization of refined palm oil process. Neurocomputing **216**, 489–501 (2016)
19. Azar, A.T., Vaidyanathan, S.: Computational Intelligence Applications in Modeling and Control. Springer, Berlin (2015)
20. Lamamra, K., Belarbi, K., Boukhtini, S.: Box and Jenkins nonlinear system modelling using RBF neural networks designed by NSGAII. In: Computational Intelligence Applications in Modeling and Control, pp. 229–254. Springer (2015)

Faults Diagnosis-Faults Tolerant Control (FTC)

Soft Fault Identification in Electrical Network Using Time Domain Reflectometry and Neural Network

A. Laib[1(✉)], M. Melit[1], B. Nekhoul[1], K. El Khamlichi Drissi[2], and K. Kerroum[2]

[1] LAMEL Laboratory, University of Jijel, BP 98 Ouled Aissa, 18000 Jijel, Algeria
abderrzaklaib@yahoo.fr, melit@univ-jijel.dz
[2] Pascal Institute, Blaise Pascal University, Clermont-Ferrand, France

Abstract. Time Domain Reflectometry (TDR) is commonly used to detect and localize hard faults in electric network. Unfortunately, in the case of soft fault especially in the case of complex network (network with several branches) it remains very difficult to detect the affected branch. In order to resolve this problem, we propose a new approach based on the Time Domain Reflectometry combined with Neural Network method (NN); the response of the electric network is obtained by applying the Finite Difference Time Domain method (FDTD) on the transmission line equations and the inverse problem is solved using Neural Network, very acceptable results are obtained basing on our new strategy which is capable to: define the fault by given the correct value of both of resistance and position, define the state of electrical network online, detect and localize more than one soft fault.

Keywords: Soft fault · Inverse problem · Neural network
Time domain reflectometry

1 Introduction

The most widely used technique for wire fault location and identification is Time Domain Reflectometry (TDR) where a specific signal is injected into the wiring network at the injection point and the reflected signal is analyzed. This last signal contains information about wire impedance, wire length, loads and sources …etc. In practice, different kinds of reflectometry methods are developed such as Time-Frequency Domain Reflectometry (TFDR), Spectrum Time Domain Reflectometry (STDR) [1, 2] and Multicarrier TDR (MCTDR) [3]), However, these techniques can locate hard faults (open and short circuits) that generate big reflection but they are not always capable to locate the small anomalies such as frays or chafes, diverse works have demonstrated success in locating faults such as [4] where TDR is combined with wavelet and Neural Network in order to detect and locate hard faults and in [5, 6], use the baseline method, in this last the output signal of the faulty wiring is compared with the output of the healthy wiring in order to detect and locate soft faults. This baseline approach is a

M. Chadli et al. (Eds.): ICEECA 2017, LNEE 522, pp. 365–376, 2019.
https://doi.org/10.1007/978-3-319-97816-1_28

natural efficient find of soft fault, but it is not able to define the nature of faults by given the exact resistance values. Another way although known reflectometry is an efficient method to diagnose simple topologies, it remains limited in the case of complex multi branch networks., also it remains limited in the case of electrical network affected by two simultaneous soft faults where they are not able to detect and locate theme in alternative approach Genetic Algorithm (GA) [7], Particle Swarm Optimization (PSO) [8], is to use a direct model in iterative procedure, where each one from previously methods is applied to the inverse process after generated TDR response and compared with measured one, however the inconvenient of these methods is computationally expensive where they need very long time for diagnosis. For solving these two problem (soft fault detection and localization, diagnosis online) a new approach is proposed for solving these two problems at the same time, it based on the combination of the Time Domain Reflectometry (TDR) and Neural Network (NN), where the response of the transmission line is obtained using the Finite Difference Time Domain method (FDTD) applied to transmission line equations, and NN method is applied to solve the inverse problem for identifying the faults.

2 Wave Propagation Model

RLCG circuit model is used for modeling Multiconductor Transmission Line (MTL) where the differential equations are defined by:

$$\frac{\partial}{\partial_z}[v(z,t)] = -[R]\cdot[i(z,t)] - [L]\cdot\frac{\partial}{\partial_t}[i(z,t)] \tag{1}$$

$$\frac{\partial}{\partial_z}[i(z,t)] = -[G]\cdot[v(z,t)] - [C]\cdot\frac{\partial}{\partial_t}[v(z,t)] \tag{2}$$

[R], [L], [C] and [G]: are the per-unit-length parameters, respectively, the series resistance, the series inductance, the shunt capacitance and the shunt conductance [9]. z and t: are space and time variables respectively.

This model is actualized by writing Kirchhoff's laws and taking the limit as $\Delta z \to 0$. Finite Difference Time Domain (FDTD) method is used to determinate the time-domain solution of the MTL, this method samples the space variable (line axis) in Δz increments also the time variable t is discretized in Δt increments, the finite differences is used to approximate the derivatives in MTL equations. The length of the spatial cell size Δz and the sampling interval Δt are chosen by insurance of the stability condition $\Delta t = \Delta z/v$.

v: is the wave propagation speed or velocity of propagation trough the transmission lines.

The currents and voltages are calculated by solving the matrix Eq. (3) [10].

$$f([x]) = [A][X] - [B] = [0] \tag{3}$$

The vector [X] includes the unknown currents and voltages at all nodes in the network and each line multiconductors. The [A] matrix is composed in two sub-matrices [A1] and [A2] where: [A1]: sub-matrix derived from terminal conditions for all tubes (coupled transmission line); [A2]: sub-matrix derived from the Kirchhoff's laws (KCL and KVL) for the junctions (extremities and interconnections networks). [B] Is the excitation vector. Once matrix [A] and vector [B] are determined the solution of matrix Eq. (3) at every time step Δt yields the currents and voltages in every node of the network.

3 Proposed Approach

3.1 Neural Network

In general, Genetic Algorithm (GA) and Particle Swarm Optimization (PSO) use a direct model in iterative procedure, where the parameters of theoretical model are fitted by adjusting the difference between the simulated response and the measured one using the iterative procedure. However the numerical solution is computationally expensive, furthermore, the diagnosis process will be more complicated. For solving this problem, the neural networks [11, 12] are good candidates, where it can be adjusted offline with a database includes information about the wiring network topology in order to use it online if required, also they can approximate a wide range provided which are previously trained. The topologies of used neural network is Multi-Layer Perceptron MLP, the retained structure containing input layer, one or more hidden layer and output layer. Each layer is composed of nodes and in the totally connected network considered, here each node connects to every node in subsequent layers (Fig. 1). The hidden unit nodes have the hyperbolic tangent activation functions and the outputs have linear activation. The Levenberg–Marquardt algorithm is used to adjust the variables of the NN.

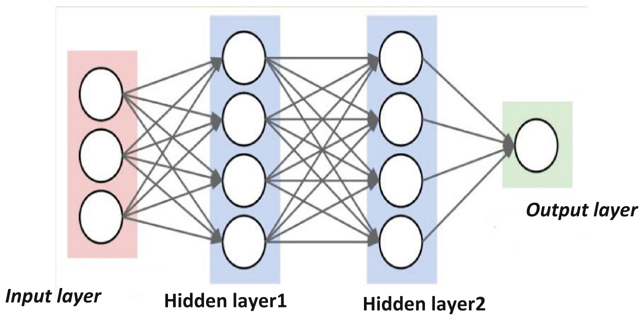

Fig. 1. Multi-layer perceptron neural network

3.2 Hybrid TDR-NN

At first, the signal of voltage difference between the response of healthy and the response of faulty network is used from the input of electrical network. Two groups of candidate features are extracted based on TDR difference signals. The max voltage amplitude in the signal of difference is selected with it corresponding time appearance, here the first group of candidate is the time appearance (t) of the magnitude max which is used to localize the fault and the second group of candidate is the max voltage magnitude which is used to define the nature of faults by given the exact resistance value. The inverse problem is used by applying the NN to detect and localize faults in electrical network. Multi-Layer Perceptron (MLP) NNs are used. The structure of MLP composed of two layers NNs with hyperbolic tangent activation functions in the hidden layer and of a single neuron having a linear activation function in the output layer. The datasets desired to train the NN were formed based on TDR method described above. The datasets are constituted of examples linking the time appearance (t) to the position of the fault, and the max voltage amplitude to it corresponding fault resistance Fig. 2, the training domain is as follow: the examples of the training dataset deduced to the NN, the output of the NN is compared to the one contained in the dataset. The error at the output obtained is reduced by Levenberg–Marquardt algorithm where is used to adjust the variables of the NN. The generalization capability of the NN is examined by calculating the Mean Square Error (MSE) obtained on the test set which contains input/output data not contained in the previous set.

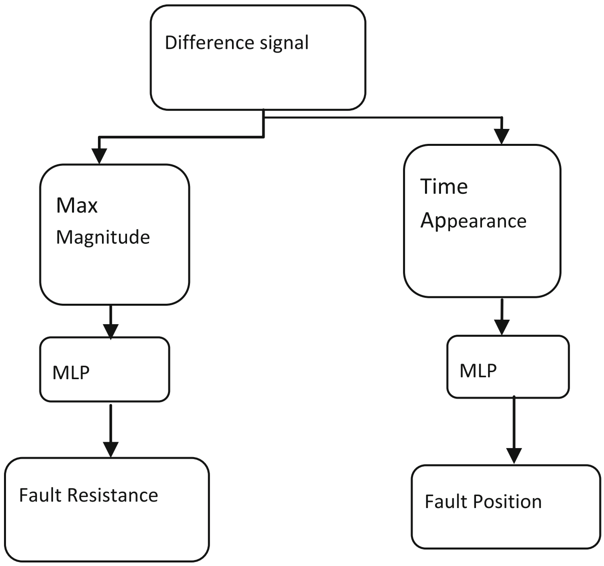

Fig. 2. Diagram of the proposed algorithm

4 Results and Discussion

4.1 Validation

In order to validate our MTL model, the configuration illustrated in Fig. 3b has been considered, this network consists of electric cable with cross section shown in Fig. 3a, this cable is largely used in embarked equipments (train, car, ship, aircraft …etc.), where r = 0.5e–3 m, and D = 2.06e–3 m. The distributed parameters L, and C, R, G can be calculated based on formulation proposed in [13]. The comparison between our numerical results and real measurements published by [7] is carried for a complex network; this last includes six open branches of L1 = 1 m, and L2 = 0.60 m, L3 = 2.25 m, and L4 = 4.25 m, L5 = 1.75 m, and L6 = 1 m.

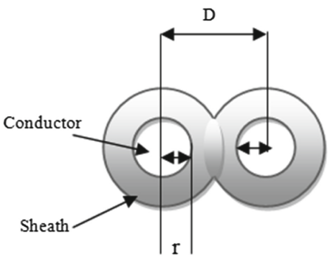

Fig. 3a. Cross-section of the used cable.

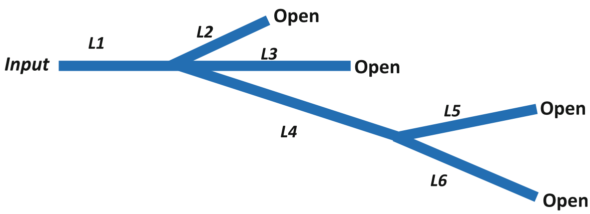

Fig. 3b. Configuration of network under study.

The source signal is a raised cosine pulse [14].

$$e(t) = \begin{cases} 0.5(1 - \cos(2\pi Ft)) & 0 < t < \frac{1}{F} \\ 0 & \text{otherwise} \end{cases} \tag{4}$$

Where F is the pulse frequency.

It is shown that our simulation results based on resolving the transmission line equations by FDTD (Fig. 3c) are practically the same to the published one in [7] (Fig. 3d). This fact confirms the validation of our proposed approach and permit to use our model to make a detailed investigation.

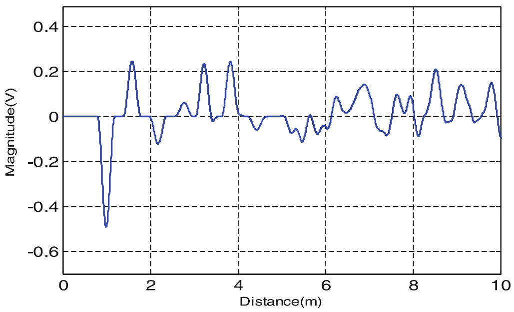

Fig. 3c. Network reflectometry response, our calculated result.

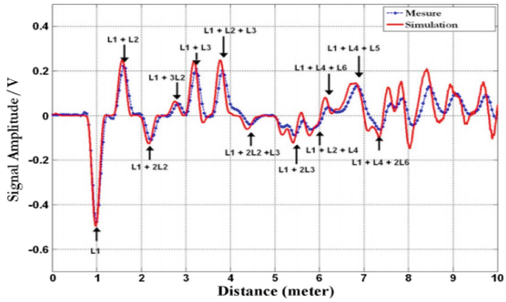

Fig. 3d. Network reflectometry response, published results by [7].

4.2 Parametric Study

In this part, we consider the network configuration represented in Fig. 3b. In the first case, a soft fault (local change on the characteristic impedance) in branch L2 at LF1 = 1.4 m from the input is considered (Fig. 4a). We notice that, the soft fault is represented by a localized change of characteristic impedance ΔL (ΔL = 2 cm) in the two cases. We consider different values of the fault impedance (Zc + ΔZc), each one is corresponding to ΔZc, different as illustrated in Fig. 4b.

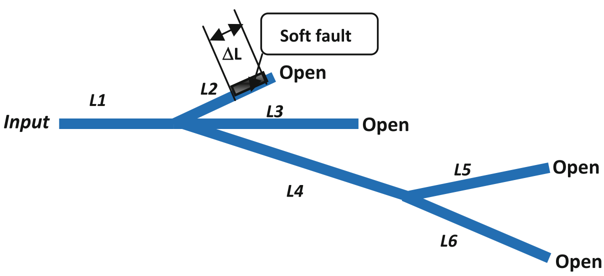

Fig. 4a. Configuration under study with soft fault at L2.

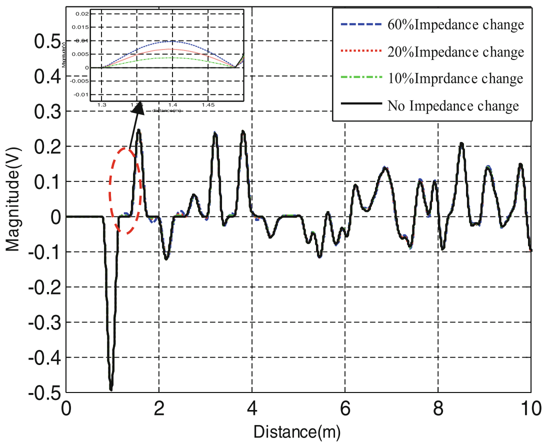

Fig. 4b. Network reflectometry response (input).

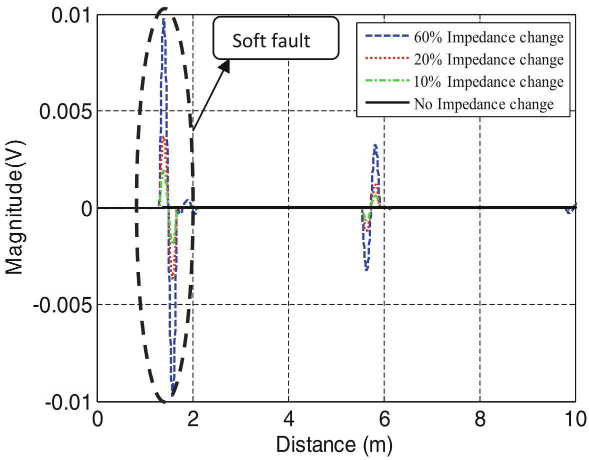

Fig. 4c. Difference signal between healthy and faulty network (input)

The second one involves networks affected by soft fault in branch L5 at LF2 = 6.25 m from the input (Fig. 5a).

Figures 4b and 5b shows the reflectometry response in case of one soft fault situated at two different positions (F_{L2} = 1.4 m at L2 (Fig. 4a) and F_{L5} = 6.25 m at L5 (Fig. 5a)), it is clear that in the two cases, the reflectometry signals of the soft fault (Figs. 4c and 5c) generates some small variation in the reflectometry response, based on these two figures it's not possible to deduce anything about the fault position or anything else. However, if we make a difference between the response of healthy and faulty networks as in Figs. 4c and 5c, we remark some reflections of the signal in the vicinity of the fault position which are proportional to the fault resistance.

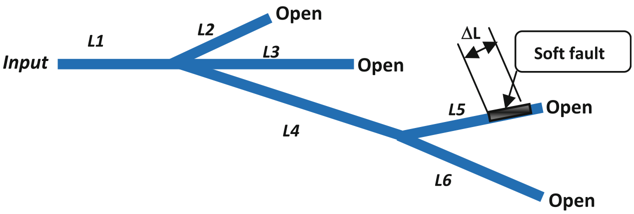

Fig. 5a. Configuration under study with soft fault at L5.

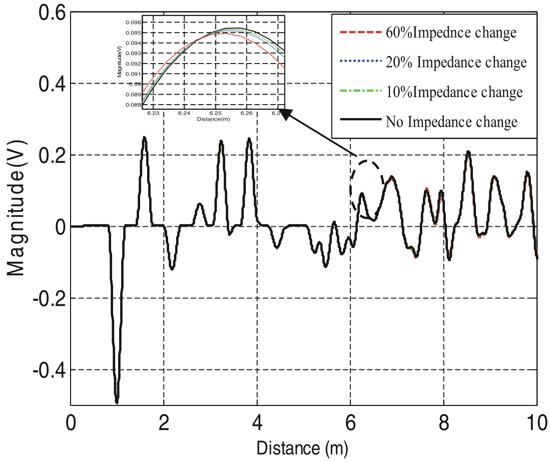

Fig. 5b. Network reflectometry response (input)

b. Network reflectometry response (input)

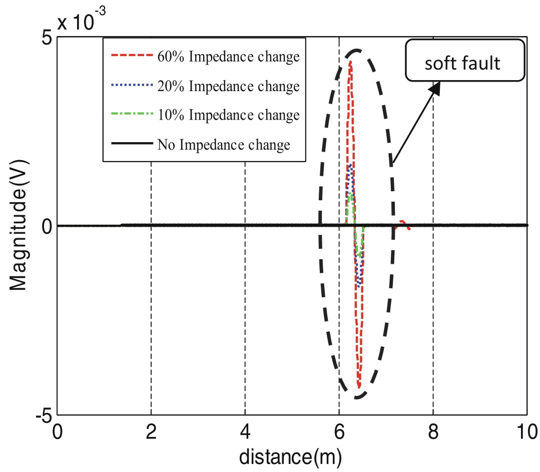

Fig. 5c. Difference signal between healthy and faulty network.

4.3 Case of Network Affected by Two Simultaneous Soft Faults

The case of electrical network affected by two soft faults has been considered; the two faults affect the branches called L2 and L5 respectively with 10% of impedance change at L2 and 60% impedance change at L5. Figure 6 shows the difference signal between healthy and faulty network in case of two simultaneous soft faults. It is shown that the location of the soft faults is clear but it is impossible to define the two soft faults by their resistances.

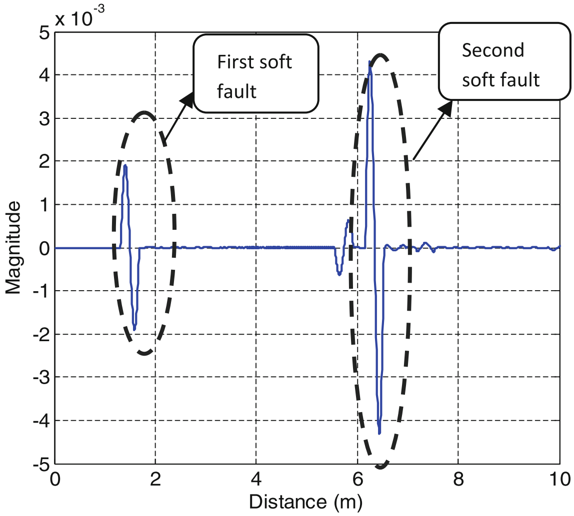

Fig. 6. Difference signal between healthy and faulty network in case of two simultaneous soft faults.

4.4 Inverse Problem

In order to give complete information about the soft faults by defining their resistances, a new proposed strategy has been considered basing of the inverse problem (Fig. 7); where the inverse problem is applied by using four (04) NNs for the two cases. We use the first NNp for the fault localizing in electrical network, the last three NNr are used for the estimation of the faults resistance; where the first NNr1 is used to characterize the faults situated before junctionJ1, the second NNr2 is used to characterize the faults situated between junction J1 and junction J2 and the third NNr3 is used to characterize the faults situated after junction J2 (Fig. 7). This distributed of NNr (NNr1, NNr2, NNr3) has been chosen because of the junction which divided the signal voltage between them; this separation is proposed in order to increase the efficiency of our analysis. The NNp contains two hidden layers (33,25) neurons with hyperbolic tangent activation functions and the output layer constituted of a single neuron having a linear activation function, and NNr contains one hidden layer of (25) neurons with hyperbolic tangent activation functions and the output layer constituted of a single neuron having a linear activation function. The datasets are constituted of examples linking the time appearance (t) to the position of the fault, and the max voltage amplitude to it corresponding fault resistance. The number of examples input/output database is 1580 examples for each NNr and about 1397 examples for NNp each dataset is randomly divided into two different sets: training set (80% of all samples) and testing set (20% of all samples).

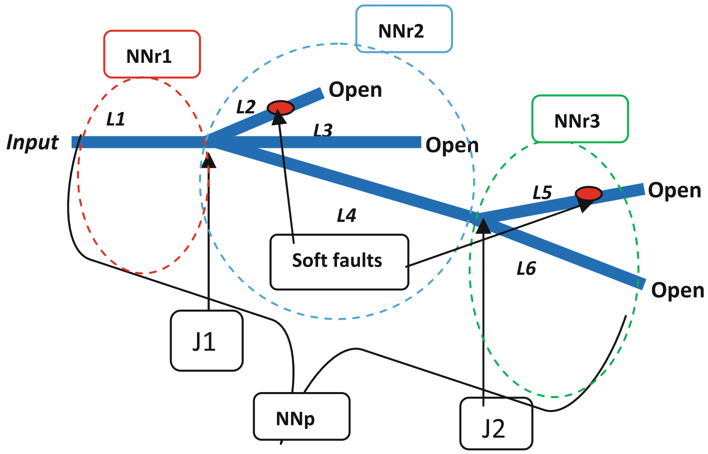

Fig. 7. Illustration of the distributed NN

Table 1. Our calculated results obtained using TDR-NN and published one based on Genetic Algorithm (GA).

	ΔZ = 10% ΔZ+Zc =86.49 Ω	ΔZ = 20 % ΔZ + Zc = 94.34Ω	ΔZ = 60 % ΔZ + Zc = 125.8Ω
soft fault at 1.4 m	86.49	94.34946 Ω	125.7996 Ω
	1.40027m	1.40027m	1.40027m
soft fault at 6.25 m	86.49Ω	94.34Ω	125.8Ω
	6.25034m	6.25034m	6.25034m

(A). CASE OF ELECTRICAL NETWORK AFFECTED BY SOFT FAULT IN BRANCH L2 AND L5

	ΔZ = 10 % ΔZ+Zc = 86.49 Ω	ΔZ = 20 % ΔZ+Zc = 94.34 Ω	ΔZ = 60 % ΔZ + Zc = 125.8 Ω
GA [7]	85.52 Ω	96.13 Ω	124.25 Ω
	5.96 m	6.03 m	5.91 m
NN	86.49Ω	94.34Ω	125.8Ω
	6.25034m	6.25034m	6.25034m

These results presented in Table 1a and b confirms the efficiency of our proposed approach in the identification of soft fault. It is shown that GA occurs some errors both on the localization and the identification (fault impedance) which prove that GA technique is not sufficient to detect and characterize the fault, For this raison, we have used the NN method to solve this problem; we see that the soft fault impedance has been accurately determined, either the soft fault is localized with exact precision (Table 1), we note that the error of soft fault identification $\Delta R = 6.37 * 10^{-5}\ \Omega$.

Table 2 Confirm the efficiency of our proposed approach in computational time diagnosis. The inversion carried out with NN is very fast (less than 1 s with $1.763 * 10^{-4}$ m for fault localization and $\Delta R = 6.37 * 10^{-5}\ \Omega$ for fault identification) and can be achieved "online." On the contrary, an iterative method (Genetic Algorithm; GA), requires 94.60 mn with an error $5.75 * 10^{-4}$ m and 26.36 mn with error $4.75 * 10^{-4}$ m in the case of Particle Swarm Optimization (PSO) to find the state of configuration includes five branches wiring network with hard fault which is generally easy to detect.

Table 2. Comparison of computational time diagnosis obtained with published results and the new approach based on neural network

	Error (m)	Computational time
Genetic Algorithm (GA) Published results by [7]	$5.75 * 10^{-4}$	94.60 mn
Particle Swarm Optimization (PSO) published results by [7]	$4.75 * 10^{-4}$	26.36 mn
Proposed approach based on Neural Network (NN)	$1.763 * 10^{-4}$	Less 1 s

5 Conclusion

In this paper, a new method is proposed for soft fault identification in complex electrical network. It is based on the TDR and NN. The electric wiring network is modeled using transmission line approach and the transmission line equations are resolved using the well-known FDTD method, the obtained results are validated by comparison with published ones [7], very acceptable results are obtained. It is showed in [7] that reflectometry and GA techniques occurs some errors in the faults characterization. To resolve this problem, the NN is proposed in order to reduce the error and ameliorate the identification of the faults and define the state of network online, our proposed approach has been compared with published results in [8]. Our simulation results prove the efficiency of the proposed strategy to detect and locate and define the soft fault in the case of complex electrical network.

References

1. Sharma, C.R., Furse, C., Harrison, R.R.: Low power STDR CMOS-sensor for locating faults in aging aircraft wiring. IEEE Sens. J. **7**(1), 43–50 (2007)
2. Furse, C., Safavi, M., Smith, P., Lo, C.: Feasibility of spread spectrum sensors for location of arcs on live wires. IEEE Sens. J **5**(6), 1445–1449 (2005)
3. Lelong, A., Carrion, M.: On line wire diagnosis using multicarrier time domain reflectometry for fault location. In: IEEE Sensors, pp. 751–754, October 2009
4. Laib, A., Melit, M., Nekhoul, B., Kerroum, K., Drissi, K.E.: A new hybrid approach using time-domain reflectometry combined with wavelet and neural network for fault identification in wiring network. In: 2016 8th International Conference on Modelling, Identification and Control (ICMIC), Algiers, Algeria, pp. 290–295 (2016)
5. Griffiths, L.A., Parakh, R., Furse, C., Baker, B.: The invisible fray: a critical analysis of the use of reflectometry for fray location. IEEE Sens. J **6**(3), 697–706 (2006)
6. Furse, C., Smith, P., Diamond, M.: Feasibility of reflectometry for nondestructive evaluation of prestressed concrete anchors. IEEE Sens. J. **9**(11), 1322–1329 (2009)
7. Smail, M.K., Pichon, L., Olivas, M., Auzanneau, F., Lambert, M.: Detection of defects in wiring networks using time domain reflectometry. IEEE Trans. Magn. **46**(8), 2998–3001 (2010)
8. Smail, M.K., Bouchekara, H.R.E.H., Pichon, L., Boudjefdjouf, H., Mehasni, R.: Diagnosis of wiring networks using Particle Swarm Optimization and Genetic Algorithms. Comput. Electr. Eng. **40**(7), 2236–2245 (2014)
9. Paul, C.R.: Analysis of Multiconductor Transmission Lines. Wiley, New York (1994)
10. Kaouche, S.: Analyse de Défauts dans un Réseau de Lignes ou de Câbles. Ph.D. thesis, Jijel University, June 2007
11. Coccorse, E., Martone, R., Morabito, F.C.: A neural network approach for the solution of electric and magnetic inverse problems. IEEE Trans. Magn. **30**(5), 2829–2839 (1994)
12. Smail, M.K., Hacib, T., Pichon, L., Loete, F.: Detection and location of defects in wiring networks using time-domain reflectometry and neural networks. IEEE Trans. Magn. **47**(5), 1502–1507 (2011)
13. Ulaby, F.T.: Fundamentals of Applied Electromagnetics. Prentice Hall (1999)
14. Parakha, R.: The invisible frays/a formal assessment of the ability of reflectometry to locate frays on aircraft wiring, M.S. thesis. Department of Electrical Engineering, Utah State University, Lagan, Utah (2004)

Tool Wear Condition Monitoring Based on Blind Source Separation and Wavelet Transform

Bazi Rabah[1](✉), Tarak Benkedjouh[2], and Rechak Said[1]

[1] Mechanical Engineering Laboratory, National Polytechnic School, El-Harrach Algiers, Algeria
Bazi.rabah2000@gmail.com, Said.rechak@gmail.com
[2] Laboratory of Structural Mechanics, Military Polytechnic School, Bordj El Bahri Algiers, Algeria
bktarek@gmail.com

Abstract. In this paper, a new intelligent method for the tool wear condition monitoring based on sparse components analysis (SCA) for blind sources separation and Continuous Wavelet Transform (CWT) have been applied. The CWT used to decompose the raw signals into coefficients; the independent sources obtained from wavelet coefficients estimated by SCA. The nodes energy computing from independent sources used for estimating the health assessment and remaining useful life of cutting tools. The PCA applied for the dimensionality reduction of the nodes energy data where the goodness of fit is measured; the idea is based on the computation of a nonlinear regression function in a high-dimensional feature space where the input data mapped via a nonlinear function. The results of its application in CNC machining show that this indicator can reflect effectively the performance degradation of cutting tools for milling process. The proposed method is applied on real world RUL estimation and health assessment for a given.

Keywords: Tool wear · Condition monitoring · Blind source separation RUL

1 Introduction

Machining process by material removal is the most important manufacturing in the mechanical industry. However, the influence of wear on the cutting tools on the quality of the surface state and the operating life of the cutting tool remains the main problem in machining.

The tool wear studies can be divided into two broad categories: First, model-based studies that use either pre-developed analytical models for certain types of tool wear, the Takeyema model of flank wear and the use crater wear model [1], or numerical derived models based on finite element analysis. The second one is data-based modelling, which relies on the empirical interpretation of input data and therefore requires a learning set. The advantage of these techniques is observed especially where a process model is not available. This feature is particularly useful for studying wear of tools that

M. Chadli et al. (Eds.): ICEECA 2017, LNEE 522, pp. 377–389, 2019.
https://doi.org/10.1007/978-3-319-97816-1_29

are based on hard materials due to the absence of models dealing with that phenomenon.

It is known from experimental results that the wavelet FNN model by detecting the cutting force, the NN regression model by spindle motor electric current and the FNN classification model by acoustic emission signal are all good at the fuzzy classification and can quickly and efficiently recognize the wear condition of the tool. It shows that the NN model has a strong function in the nonlinear mapping approach [2]. Following the application of signal extraction data analysis techniques, the increasing trend in the amplitude of the frequency spectra was more evident compared to the analysis of the raw signal. Therefore, the use of a blind signal extraction technique may be essential in a more complex environment, where there are potentially many causes for changing audio transmissions, making it difficult to distinguish the contribution associated with the stamping of the matrix wear [3]. The frequency bands from 2 to 6 kHz has been identified as containing the most important information related to wear in this sheet metal stamping applications. This knowledge will allow future studies to focus on these signals to identify the state of wear of the stamping process [4].

The time domain functions are selected for three frequency bands after the application of the FFT on the data acquired from the experimental configuration. The BPNN architecture has been optimized and the optimum BPNN parameters have been selected. A comparison between two nodes and single-node input BPNN architectures was made; an expert system for the diagnosis of rolling faults has been developed with a fault diagnosis accuracy of 98% and can be implemented in a CBM as a reliable method of diagnosing rolling faults [5].

The objective of this study is to investigate the applicability of sensory data fusion using low-cost detection technology, in particular the force signal and vibrations of the spindle to monitor the state of tools in milling. The organization of this work is the following: the theoretical history of continuous wavelet transformation, the analysis of the main components of the blind source separation are briefly presented in Sects. 2 and 3. The experimental configuration and the selected cutting conditions are explained in Sect. 4. In Sect. 5, data processing with CWT and SCA, regression of characteristics and outcomes are discussed, and a conclusion is provided in Sect. 6.

2 Continuous Wavelet Transforms (CWT)

A wavelet is a function with zero means and that is located in both frequency and time. We can characterize a wavelet by how localized it is in time (Δt) and frequency ($\Delta\omega$ or the bandwidth). The classical version of the Heisenberg uncertainty principle tells us that there is always a trade-off between localization in time and frequency. Without properly defining Δt and $\Delta\omega$, we will note that there is a limit to how small the uncertainty product $\Delta t \cdot \Delta\omega$ can be. One particular wavelet, the Morlet, is defined as

$$\psi_0(\eta) = \pi^{-1/4} e^{i\omega_0\eta} e^{-\frac{1}{2}\eta^2} \tag{1}$$

Where ω_0 is dimensionless frequency and η is dimensionless time. When using wavelets for feature extraction purposes the Morlet wavelet (with $\omega_0 = 6$) is a good choice, since it provides a good balance between time and frequency localization. We therefore restrict our further treatment to this wavelet, although the methods we present are generally applicable.

The idea behind the CWT is to apply the wavelet as a band pass filter to the time series. The wavelet is stretched in time by varying its scale (s), so that $\eta = s \cdot t$, and normalizing it to have unit energy. For the Morlet wavelet (with $\omega_0 = 6$) the Fourier period ($\lambda_{\omega t}$) is almost equal to the scale ($\lambda_{\omega t} = 1.03$ s) [6, 7].

The CWT of a time series ($x_n, n = 1, \ldots, N$) with uniform time steps δt is defined as the convolution of x_n with the scaled and normalized wavelet. We write

$$W_n^X(s) = \sqrt{\frac{\delta t}{s}} \sum_{n'=1}^{N} x_{n'} \psi_0 \left[\left(n' - n \right) \frac{\delta t}{s} \right] \tag{2}$$

In practice, it is faster to implement the convolution in Fourier's space. We define the wavelet power as $\left|W_n^X(s)\right|^2$, the complex argument $W_n^X(s)$ can be interpreted as the local phase.

CWT has edged artefacts because the wavelet is not completely localized in time. It is therefore useful to introduce a Cone of Influence (COI) in which edge effects cannot be ignored. Here we take the COI as the area in which the wavelet power caused by a discontinuity at the edge has dropped e^{-2} the value at the edge.

The statistical significance of wavelet power can be assessed relative to the null hypotheses that the signal is generated by a stationary process with a given background power spectrum (P_k). Many geophysical time series have distinctive red noise characteristics that can be modelled very well by a first order auto-regressive (AR1) process. The Fourier power spectrum of an AR1 process with lag-1 autocorrelations α.

$$P_k = \frac{1 - \alpha^2}{\left|1 - \alpha e^{-2i\pi k}\right|^2} \tag{3}$$

Where k is the Fourier frequency index.

The wavelet transforms can be thought of as a consecutive series of band-pass filters applied to the time series where the wavelet scale is linearly related to the characteristic period of the filter ($\lambda_{\omega t}$). Hence, for a stationary process with the power spectrum (P_k) the variance at a given wavelet scale, by the invocation of the Fourier convolution theorem, is simply the variance in the corresponding band of P_k. If P_k it is sufficiently smooth then we can approximate the variance at a given scale simply by P_k using the conversion $k^{-1} = \lambda_{\omega t}$. Monte Carlo methods it used to show that this approximation is very good for the AR1 spectrum, then show that the probability that the wavelet power, in a process with a given power spectrum (P_k), being greater than p is

$$D\left(\frac{\left|W_n^X(s)\right|^2}{\sigma_X^2} < p \right) = \frac{1}{2} P_k \chi_\nu^2(p) \tag{4}$$

Where ν is equal to 1 for real and 2 for complex wavelets.

There are clearly common features in the wavelet power of the two-time series such as the significant peak in the 5-year bands around 1940. Both series also have high power in the 2–7-year band in the period from 1860–1900, though for AO the power is not above the 5% significance level. However, the similarity between the portrayed patterns in this period is quite low and it is therefore hard to tell if it is merely a coincidence. The cross wavelet transforms help in this regard [7].

3 Blind Source Separation

3.1 Observing Mixtures of Unknown Signals

Consider a situation where there are a number of signals emitted by some physical objects or sources. These physical sources could be, for example, different brain areas emitting electric signals; people speaking in the same room, thus emitting speech signals; or mobile phones emitting their radio waves. Assume further that there are several sensors or receivers. These sensors are in different positions, so that each records a mixture of the original source signals with slightly different weights [8].

For the sake of simplicity of exposition, let us say there are three underlying source signals, and also three observed signals. Denote by $x_1(t)$, $x_2(t)$ and $x_3(t)$ the observed signals, which are the amplitudes of the recorded signals at the time point t, and by $s_1(t)$, $s_2(t)$ and $s_3(t)$ the original signals. They $x_i(t)$ are then weighed sums of the $s_i(t)$, where the coefficients depend on the distances between the sources and the sensors:

$$\begin{aligned} x_1(t) &= a_{11}s_1(t) + a_{12}s_2(t) + a_{13}s_3(t) \\ x_2(t) &= a_{21}s_1(t) + a_{22}s_2(t) + a_{23}s_3(t) \\ x_3(t) &= a_{31}s_1(t) + a_{32}s_2(t) + a_{33}s_3(t) \end{aligned} \tag{1.1}$$

There a_{ij} are constant coefficients that give the mixing weights. They are assumed unknown, since we cannot know the values of a_{ij} without knowing all the properties of the physical mixing system, which can be extremely difficult in general. The source signals s_i are unknown as well, since the very problem is that we cannot record them directly [9]. These are three linear mixtures x_i of some original source signals. They look as if they were completely noise, but actually, there are some quite structured underlying source signals hidden in these observed signals.

What we would like to do is to find the original signals from the mixtures $x_1(t)$, $x_2(t)$ and $x_3(t)$. This is the blind source separation (BSS) problem. *Blind* means that we know very little if anything about the original sources. We can safely assume that the mixing coefficients a_{ij} are different enough to make the matrix that they form invertible. Thus there exists a matrix W with coefficients w_{ij}, such that we can separate the s_i as

$$\begin{aligned} s_1(t) &= w_{11}x_1(t) + w_{12}x_2(t) + w_{13}x_3(t) \\ s_2(t) &= w_{21}x_1(t) + w_{22}x_2(t) + w_{23}x_3(t) \\ s_3(t) &= w_{31}x_1(t) + w_{32}x_2(t) + w_{33}x_3(t) \end{aligned} \tag{1.2}$$

Such a matrix W could be found as the inverse of the matrix that consists of the mixing coefficients a_{ij} in Eq. 1.2, if we knew those coefficients a_{ij}.

Now we see that in fact this problem is mathematically similar to the one where we wanted to find a good representation for the random data on $x_i(t)$, as in (1.1). Indeed, we could consider each signal $x_i(t), t = 1, \ldots, T$ as a sample of a random variable x_i, so that the value of the random variable is given by the amplitudes of that signal at the time points recorded [10].

3.2 Sparse Component Analysis Based (SCA) Undetermined BSS (UBSS)

Taking a p-degree-of-freedom-free linear vibration system for instance, the governing differential equations can be written as follows [10]:

$$M\ddot{q} + C\dot{q} + Kq = 0 \tag{2.1}$$

Where M, C and $K \in \mathbb{R}^{p \times p}$ are the mass, damping and stiffness matrix, respectively $\ddot{q}$, $\dot{q}$ and $q \in \mathbb{R}^p$ are the acceleration, velocity and displacement vectors, respectively. The transient oscillation for a proportionally lightly damped system can be expressed as follows:

$$q(t) = \sum_{i=1}^{p} \phi_i a_i \exp(-\xi\omega_i t)\cos(\omega_i t + \varphi_i) \tag{2.2}$$

In which ϕ_i is a constant vector corresponding to the mode shape a_i is a constant related to the initial conditions, ζ_i, ω_i, φ_i denote the damping ratio, natural frequency and initial phase angle, respectively. In practice, limited sensors (less than p) are available and the lower-order modes are focused on. By the mode truncation method, Eq. (2.2) can be rewritten in the matrix form

$$\begin{cases} \hat{q}(t) = \sum_{i=1}^{N} \phi_i a_i \exp(-\xi_i\omega_i t)\cos(\omega_i t + \varphi_i) \\ \hat{q}(t) = \Phi\Psi(t) = \Phi \operatorname{diag}(a_i)[\exp(-\xi_i\omega_i t)\cos(\omega_i t + \varphi_i)]) \end{cases} \tag{2.3}$$

In which $\hat{q}(t) \in \mathbb{R}^{M\times 1}$ is the truncated response vector $\Phi \in \mathbb{R}^{M\times N}$ is the mode shape matrix consisting of the mode shape vector ϕ_i, and $\Psi(t) \in \mathbb{R}^{N\times 1}$ is a vector consisting of single-mode signals. It should be noted that $M < N \le p$ in Eq. (2.3). Since the acceleration signals are common, Eq. (2.3) can be adapted as follows:

$$\begin{cases} \hat{q}^n(t) = \sum_{i=1}^{N} \phi_i b_i \exp(-\xi_i\omega_i t)\cos(\omega_i t + \theta_i) \\ \hat{q}^n(t) = \Phi\Psi^n(t) = \Phi \operatorname{diag}(b_i)\left[\exp(-\xi_i\omega_i t)\cos(\omega_i t + \theta_i)\right] \end{cases} \tag{2.4}$$

Where $b_i = a_i\omega_i^2$ and $\theta_i = \varphi_i + \beta_i$
with $\tan(\beta_i) = 2\xi_i/(\xi_i^2 - 1), 0 < \xi_i < 1$.

Considering Eq. (2.4), the modal analysis is to recover the mode shape matrix and the single mode signals for extracting natural frequencies and damping ratios. Similarly, BSS is developed to recover the sources and estimate the mixing matrix, using only the information of the observed signals. Introducing a linear TF transform, Eq. (2.4) could be rewritten as follows [10]:

$$\mathring{q}(t,f) = \Phi\Psi(t,f) \quad (t,f) \in \Omega \tag{2.5}$$

in which $\Omega = U_{i=1}^{N}\ \hat{\Omega}_i$ is the set of the TF sub-domains with the TF subdomain being defined [22] as follows:

$$\begin{cases} |q_i(t,f)| \gg 0(t,f) \in \hat{\Omega}_i \\ q_i(t,f) \approx 0(t,f) \notin \hat{\Omega}_i \end{cases} \tag{2.6}$$

When SCA-based UBSS in the TFD is introduced to estimate modal parameters, the TF subdomain $\hat{\Omega}_i, i = 1,\ldots,N$ is the domain one single-mode signal lies in, namely $\hat{\Omega}_i, i = 1,\ldots,N$ is a set of narrow frequency bands. Without loss of generality, a simple example is presented to state how the mixing matrix A (the mode shape Φ) is estimated:

$$\begin{cases} x_1(t) = a_{11}s_1(t) + a_{12}s_2(t) + a_{13}s_3(t) \\ x_2(t) = a_{21}s_1(t) + a_{22}s_2(t) + a_{23}s_3(t) \end{cases}. \tag{2.7}$$

Where a_{ij}, we have is where a_{ij}, we have is the coefficient of the mixing matrix. By a linear time–frequency transforms, such as short time Fourier transform (STFT) and wavelet transform (WT), Eq. (2.7) is transformed to be sparsely represented in the TFD. Because of sparseness in the TFD, the sub-domains exist, in which only one of the three sources is active, just as defined in Eq. (2.6). Assuming that s_1 is active in the subdomain $\hat{\Omega}_1$, we have.

$$\begin{cases} x_1(t_1,f_1) = a_{11}s_1(t_1,f_1) \\ x_2(t_1,f_1) = a_{21}s_1(t_1,f_1) \end{cases} \tag{2.8}$$

Furthermore $c_1 = a_{11}/a_{21} = x_1(t_1,f_1)/x_2(t_1,f_1)$. Similarly, $c_2 = a_{12}/a_{22}$ and $c_3 = a_{13}/a_{23}$ can be calculated. Then the mixing matrix A is estimated as follows:

$$A = \begin{bmatrix} 1 & 1 & 1 \\ c_1 & c_2 & c_3 \end{bmatrix}$$

As stated above, the important aspect of SCA is to find a suitable linear transform, by which the signals can be sparsely represented in the transformed domain. When SCA is applied in UBSS, the other two important aspects are the SSO (single source occupancy) point detection methods and the clustering algorithms. In TIFROM, the TF sub-domains are found as an optimization problem by analyzing the TF ratio

$(q_i(t,f) \big/ q_j(t,f), i \neq j)$ and SSO points of each $q_i(t,f), 1 = 1, \ldots,$ Mare extracted from the TF sub-domains to estimates the coefficients of the corresponding mode shape vector ϕ_j [10].

4 2010 Phm Society Conference Data Challenge

The machining experiments were carried out on a Roder CNC machining centre. The work piece is made of Inconel 718 which is a hard material to be cut and whose thermal and mechanical properties are of interest in the aeronautical field (it is used for components of aircraft reactors, for example). The piece used in the experiments is of square trapezoidal shape with a width of 112.5 mm and a high of 78 mm.

The cutting tools are six in number. They are made of tungsten carbide, round nose and have three cutting edges. They operate at a speed of 10360 rpm, and with an advance of 1.555 m/min. The passes made are 0.125 mm wide and 0.25 mm deep [12].

The data acquisition files are in.csv format, with seven. columns, corresponding to:

Column 1: Force (N) in X dimension
Column 2: Force (N) in Y dimension
Column 3: Force (N) in Z dimension
Column 4: Vibration (g) in X dimension
Column 5: Vibration (g) in Y dimension
Column 6: Vibration (g) in Z dimension
Column 7: AE-RMS (V) [12].

5 Results and Discussion

5.1 Organizational Chart

In SR-UBSS, the sub-domains are found based on the TF amplitude of mixtures and the mixing matrix is estimated by K-mean algorithm to cluster all the SSO points. The general steps of the proposed method in this study are illustrated in Fig. 1. It should be noted that it's not necessary to continue the SCA-based UBSS for recovering the sources since the natural frequencies can be directly extracted by analyzing the SSO points. Moreover, recovering sources is difficult because it's no longer simply inverse problem as that of the determined BSS while sources recovering is iteratively processed to estimate the natural frequencies and the corresponding damping ratios after the mixing matrix are worked out. If the damping ratios are focused on, singular value decomposition can be introduced to process the recovered sources [8].

5.2 Results of the Wavelet Transform (CWT)

The proposed method for evaluating the cutting tool state C2 is based on the prediction of RUL. The cutting tool is controlled by a set of sensors to detect the change in wear.

The sensors used are accelerometers for measuring vibrations caused by initial wear and acoustic emission sensors. The signals supplied by the sensors are then processed to extract the relevant characteristics. Several techniques for extracting the parameters exist in the literature. In this study, the wavelet transforms is used, it is a signal analysis tool; Compared to normal wavelet analysis, it has special abilities to achieve higher discrimination by analyzing the higher frequency ranges of a signal. The frequency domains separated by the wavelet can be easily selected and classified according to the characteristics of the signal analyzed. CWT considered a tree; the vertex is the original signal. The next level of the tree is the result of a step of the wavelet transform.

The following levels are constructed recursively by applying the wavelet transform, the low and high pass filter results from the previous wavelet. Then, when the transform process is completed, the energy in the different frequency bands can be calculated and taken as characteristics.

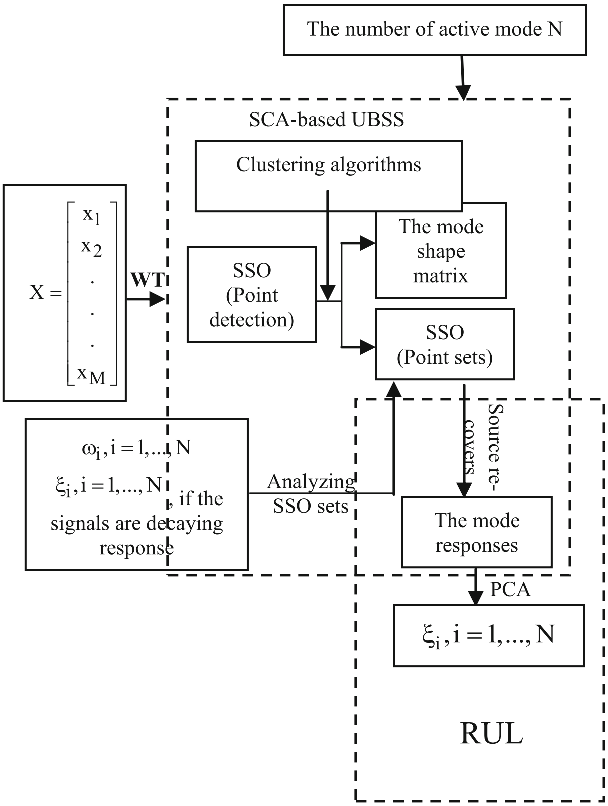

Fig. 1. The general organization chart of the proposed model using SCA-based UBSS

Figures 2, 3, 4 and 5 represent the RMS of the signal (force, vibration and AE), three different regions can be observed. In the first one the energy dissipation is observed to increase very rapidly, which means the sudden entry of the tool into the material (wear running-in). The second region represents the stability of the cutting tool which implies a rate of dissipation almost constant (stabilized wear) at the end of operations. The energy loss increases very rapidly, which means that the tool becomes unstable due to wear defects resulting from the progressive contact between tool and material (accelerated wear).

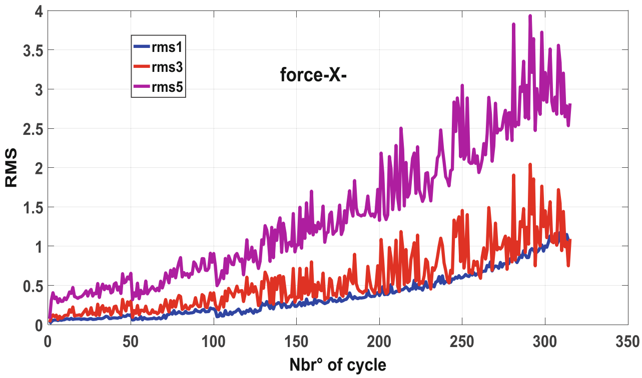

Fig. 2. Energy coefficients extracted from 07 levels of force X signals (tool C2).

5.3 Blind Signal Extraction from Wavelets Transform Coefficients

The application of (SR-UBSS) source separation allows the information to condense in a well-determined energy coefficient in order to keep the Monotonicity, Prognosability and trendability; Fig. 6 in this database indicates the strength is the best performing to determine the health indicator and the RUL; In order to validate the robustness of this model.

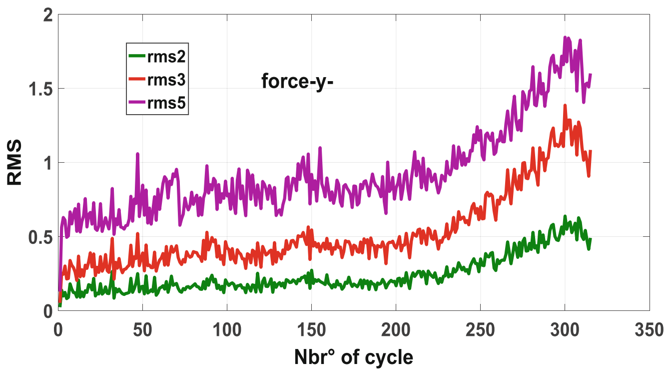

Fig. 3. Energy coefficients extracted from 07 levels of force Y signals (tool C2).

5.4 Cutting Tool Health Assessment

The application of Principal Components Analysis (PCA) allows the extraction of the health indicator; the latter is the best approach to increase the effectiveness of tool wear monitoring. In this work, the health indicators of the tools rely mainly on the signals of force, vibration and acoustics. The use of temporal domain features is allowed as health indicators for tools (Fig. 7).

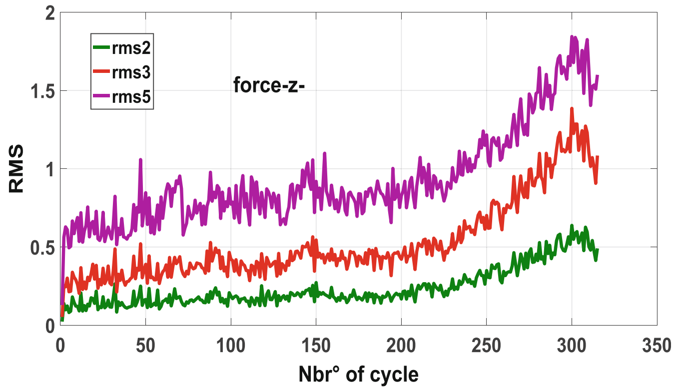

Fig. 4. Energy coefficients extracted from 07 levels of force Z signals (tool C2).

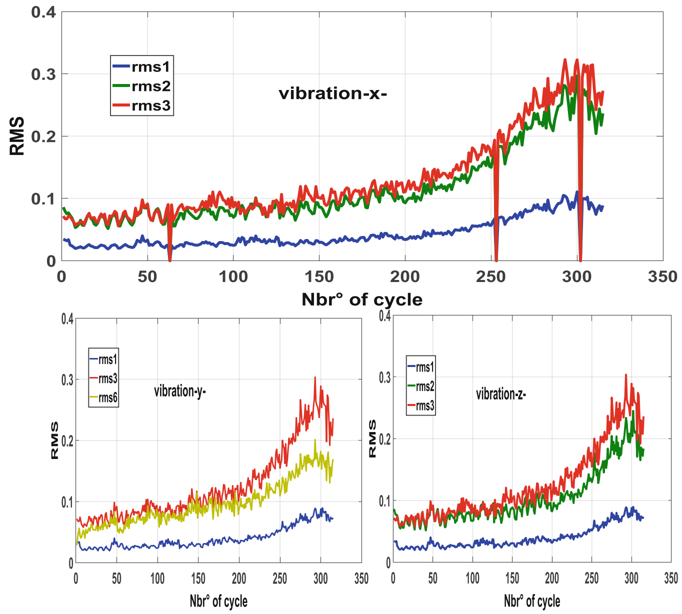

Fig. 5. Energy coefficients extracted from 07 levels of vibration X, Y, Z signals (tool C2).

5.5 Determination of the Remaining Useful Life (RUL)

In this study RUL prediction based on wear assessment threshold is known in advance. The threshold limit of 120% is considered. As shown in Fig. 8, the RUL estimated for the test experiments is also compared to the actual RUL, similar to the estimation process. To quantify the performance of the proposed approach, the precision metric for failure prognostic techniques is used for the RUL prediction proposed by [11]. This measurement is defined as 1 for the best performance and 0 for the worst. (Table 1) show the performance results of the RUL prediction using Cutters 1 and 2 as tests, respectively. The average performance accuracy value is 0.75 which is close to 1.

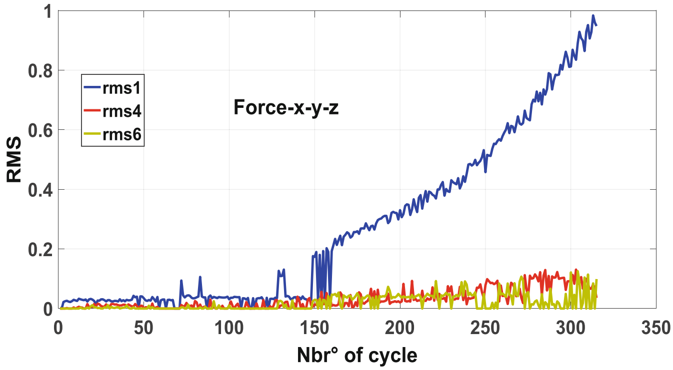

Fig. 6. Energy coefficients separated from force X-Y-Z signals (tool C2).

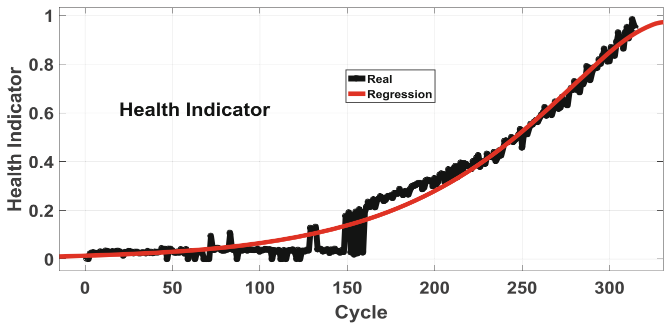

Fig. 7. The health indicator determined with the force signal.

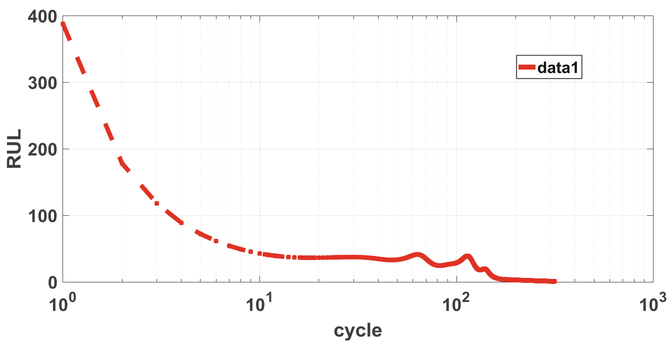

Fig. 8. RUL determined with the force signal.

Table 1. Prognostic metrics (C2).

Accuracy	Precision	MAPER	HP	R^2	RMSE
0.7562	5.65	6.41	4	0.9636	0.0225

6 Conclusion

The tool wear condition monitoring has been proposed in this work using the sensors signals measurements in milling process. The nodes energy is sensitive to process variations.

The nonlinear regression used in the work combines the advantages of CWT and SCA. As a result, significant improvements are obtained in the present work. The accuracy, MAPER and HP is suitable for industrial applications. The use of PCA makes it possible automatically to group the health states into force signals and the determination of the amount of health states from the given training data. The explicit relationship between the raw signals force and the wear state process is achieved by mapping the detected degradation into several degrees of wear increase value, which allows inline estimation and prediction RUL of wear values.

Finally, the proposed method can also be used for monitoring other machining operations such as turning and grinding as long as there are readily available data signals that are sensitive to tool wear.

References

1. Niaki, F.A., Ulutan, D., Mears, L.: Wavelets based sensor fusion for tool condition monitoring of hard to machine materials. In: 2015 IEEE International Conference on Multisensor Fusion and Integration for Intelligent Systems (MFI). IEEE (2015)
2. Jianping, Ye, B.: Fuzzy fusion of multi-sensor data for tool wear identifying. In: 2008 Fifth International Conference on Fuzzy Systems and Knowledge Discovery, FSKD 2008, vol. 3. IEEE (2008)

3. Teti, R., Jemielniak, K., O'Donnell, G., Dornfeld, D.: Advanced monitoring of machining operations. CIRP Ann.-Manufact. Technol. **59**(2), 717–739 (2010)
4. Ubhayaratne, I., Pereira, M.P., Xiang, Y., Rolfe, B.F.: Audio signal analysis for tool wear monitoring in sheet metal stamping. In: Mechanical Systems and Signal Processing, vol. 85, pp. 809–826 (2017). 10 September 2016
5. Gaud, D.K., Agrawal, P., Jayaswal, P.: Fault diagnosis of rolling elements bearing based on vibration and current signatures: an optimal network parameter selection. In: International Conference on Electrical, Electronics, and Optimisation Techniques (ICEEOT). IEEE (2016)
6. Grinsted, A., Moore, J.C., Jevrejeva, S.: Application of the cross wavelet transform and wavelet coherence to geophysical time series. Nonlinear Process. Geophys. **11**(5/6), 561–566 (2004)
7. Gao, R.X., Yan, R.: Wavelets: Theory and Applications for Manufacturing. Springer, New York (2010)
8. Comon, P.: Independent component analysis (1992)
9. Le, T.-P., Paultre, P.: Modal identification based on the time–frequency domain decomposition of unknown-input dynamic tests. Int. J. Mech. Sci. **71**, 41–50 (2013)
10. Hyvärinen, A., Karhunen, J., Oja, E.: Independent Component Analysis, vol. 46. Wiley, New York (2004)
11. Yu, K., Yang, K., Bai, Y.: Estimation of modal parameters using the sparse component analysis based undetermined blind source separation. Mech. Syst. Sig. Process. **45**(2), 302–316 (2014)
12. http://www.phmsociety.org/competition/phm/2010

Monitoring and Fault Diagnosis of Induction Motors Mechanical Faults Using a Modified Auto-regressive Approach

Ameur Fethi Aimer(✉), Ahmed Hamida Boudinar, Mohamed El Amine Khodja, Noureddine Benouzza, and Azeddine Bendiabdellah

Department of Electrical Engineering, Diagnosis Group, LDEE Laboratory, University of Sciences and Technology of Oran, Oran, Algeria
fethi.aimer@yahoo.fr, boud_ah@yahoo.fr

Abstract. Electric motors failure remains a very serious issue in the industrial world. This problem may not only result in the paralysis of the production but may also influence the operator safety. To resolve this problem, several methods have been developed for the monitoring and the diagnosis of faults from their appearances to avoid the industrial process interruption. With this objective in mind, this paper proposes a new diagnosis technique used in the identification of these faults based on stator current Auto-Regressive modeling. The proposed approach presents several advantages compared to the classical stator current spectral analysis using the conventional Periodogram technique. In fact, the proposed approach offers a very good frequency resolution for a very short acquisition time, which is impossible to achieve with the classical technique of the Periodogram. Simulation and experimental tests will be carried out later in this paper to verify the proposed method in bearing faults diagnosis.

Keywords: Auto-regressive model · Bearing fault · Diagnosis · Induction motor Outer race fault

1 Introduction

Advances in power electronics and control circuits lead to a growing use of induction motors in electric drive systems. The use of induction motors is due to their simple structure, their robustness and their manufacturing cost. Faced with this important position of induction motor in industry, researches are moving towards an effective fault diagnosis of induction motor to prevent the interruption of the entire drive system [1].

In this context, several statistical studies [1, 2] show that 52% of the induction motor faults concern the rolling-element bearings, hence the need to study this fault. Furthermore, these studies demonstrate that both inner and outer races faults occupies 39% of all bearing faults. In this aim, several research works investigated vibration analysis for bearing faults diagnosis [3–5]. Unfortunately, its main disadvantage is the vibration sensors location that must be placed in a specific position of the machine. Another technique is also used increasingly in recent years, based on the motor current signature analysis (MCSA). Indeed, several studies [6, 7] showed that the stator current bring

M. Chadli et al. (Eds.): ICEECA 2017, LNEE 522, pp. 390–410, 2019.
https://doi.org/10.1007/978-3-319-97816-1_30

information on almost all electrical and mechanical faults that may occur in the induction motor.

To analyze the stator current for extracting useful information on the existence or not of these faults, several signal processing methods have been developed. We can cite the methods that analyze behavior of the three phase currents in the time domain using Park's vector approach also known as Lissajou approach [8, 9]. Unfortunately, this approach is not efficient when fault signature (e.g. rotor faults) is very close to the fundamental. In addition, the interpretation of this approach remains complex.

For these reasons, several studies use the frequency approach, based on methods for the estimation of the Power Spectral Density (PSD) of the signal to be processed. These methods can be classified as following:

1.1 Nonparametric Methods

In this category, the most common method used in industry is that based on the estimation of the PSD by Periodogram. Several research works [10–12] justify the wide use of the PSD in the fault diagnosis field and its superiority with a fast and simple algorithm and an easy implementation.

In other hand, the PSD presents two major disadvantages, which are essentially due to:

- Its poor frequency resolution;
- A Smoothing effect and side effect introduced by the weighting window used in the estimation of the PSD by periodogram [12].

Both phenomena result in the appearance of side lobes in the stator current spectrum, reducing the level of analysis; which justifies the optimal choice of the weighting window to be used. In this context, different weighting windows can be used in improving the frequency resolution and to decrease both smoothing effect and side effect in some fault cases while the Hanning window seems to have better results [1].

Unfortunately, this choice is not always efficient in some operating modes (e.g. rotor faults at a small motor slip) because the fault signature will be embedded in the fundamental frequency. To resolve this problem, several works use both current and voltage signals to calculate the instantaneous power spectrum [13–15]. Nevertheless, in addition to being expensive because it requires the use of current and voltage sensors, this solution is still not reliable for other types of faults as is the case of bearing faults.

For this reason, several studies deal with the use of the Hilbert method in order to avoid the domination of the fundamental frequency in the current spectrum and resolve the problem of the weighting window choice [16, 17]. Moreover, although the Hilbert method is effective for rotor faults, it remains ineffective for other types of failures.

Other recent methods suggested analyzing the current spectrum in higher frequency bands, especially around the rotor slot harmonics to avoid the effect of the fundamental frequency [18]. Unfortunately, even these methods are characterized by poor frequency resolution. Indeed, these methods fail to distinguish between two harmonics very close of each other. Moreover, it is advisable to work on the low frequency bands as the fault signature is more important at low frequencies and attenuates as we increase in frequency.

1.2 Parametric Methods

These methods have been developed to estimate the PSD of signals and determine their characteristics with a better resolution. These methods are based on the establishment of a parametric model of the signal to be processed. The modeling assumes that this signal is the result of the excitation of a linear filter with white noise. The problem comes down to identify the filter parameters by minimizing the error between the measured signal and the filter output. This filter can be Auto Regressive (AR), Moving Average (MA) or a combination of both filters (ARMA).

However, this model requires human intervention on the model because:

- We must define the most suitable model for the signal;
- We must determine its order, i.e. the number of coefficients for a best modeling of the signal.

The choice of the model is generally based on the appearance of the spectrum, but the order of the model cannot be precisely determined without a more detailed analysis. The choice of the order is discussed in [19] which is generally done by minimizing some error criterion (e.g. Akaike, MDL, Final Prediction Error …) between the output signal of the model and the measured signal.

Finally, other methods known as High Resolution Methods based on the principle of the decomposition of the covariance matrix of the signal to be processed into two subspaces: signal subspace and noise subspace. These methods such as MUSIC [20, 21] and ESPRIT [22] are more robust to noise but require much more computation time due to the complexity of their algorithms. On other hand, the PRONY method [23], which is not based on the decomposition of spaces, is faster compared to MUSIC and ESPRIT, but more sensitive to noise.

In this paper, we propose to use the parametric AR method [24] in bearing faults diagnosis. However, the main drawback of the AR method is the computation time which can be considerable compared to conventional methods. In addition, the reliability of this method depends on the estimation of the model order. Indeed, several criteria give an estimation of the model order but it remains inexact and difficult to be optimal [19]. To solve these problems, we propose in this paper a new approach to improve the AR modeling on two points.

First of all, we perform the processing only on the frequency band in which, the fault signature is supposed to appear. This will reduce the number of analyzed samples, which reduces the computation time. In addition, this solution will allow us to determine the number of desired harmonic instead of estimating this number.

Secondly, we propose a clear presentation through stems representing the frequency of the signal obtained using the Root-AR approach presented later in this paper.

Finally, simulation tests and experimental results of the proposed Root-AR approach, will verify the merits of the proposed approach in the diagnosis of bearing faults.

2 Frequency Signatures of Bearing Faults

The rolling-element bearings act as an electromechanical interface between the stator and the rotor. In addition, they represent the holding element from the shaft of the machine to ensure proper rotation of the rotor [20].

The bearings are constituted by two races, the inner race and the outer race, balls and the cage which ensures equidistance between the balls as is shown in Fig. 1 [25].

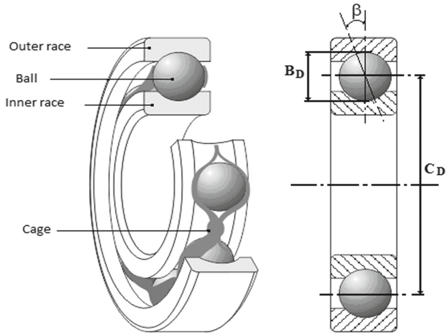

Fig. 1. Geometry of a rolling-element bearing.

Failures may affect the bearing on both races, on the ball or on the cage. Several studies have shown that the failure of each bearing element is manifested by a vibration frequency characterizing the fault type [20].

– Signature frequency of the outer race fault

$$f_o = \frac{N_b}{2} f_r \left(1 - \frac{B_D}{C_D} \cos\beta\right) \tag{1}$$

– Signature frequency of the inner race fault

$$f_i = \frac{N_b}{2} f_r \left(1 + \frac{B_D}{C_D} \cos\beta\right) \tag{2}$$

– Signature frequency of the ball fault

$$f_{ball} = \frac{C_D}{B_D} f_r \left(1 - \frac{B_D^2}{C_D^2} \cos^2\beta\right) \tag{3}$$

– Signature frequency of the cage fault

$$f_{cage} = \frac{1}{2} f_r \left(1 - \frac{B_D}{C_D} \cos\beta\right) \tag{4}$$

where N_b is the number of bearing balls, B_D and C_D respectively, are the ball and the cage diameter, β is the contact angle and f_r the mechanical rotor frequency.

Furthermore, the rolling-element faults signatures appear in the stator current spectrum at the following frequencies [24]:

$$f_{bear}(Hz) = |f_s \pm m \cdot f_v| \quad \text{with} \quad m = 1, 2, 3 \ldots \tag{5}$$

where f_s is the supply frequency and f_v is the fault characteristic frequency corresponding to either f_o, f_i, f_{cage} or $f_{ball.}$

Also, the stator current is composed of several harmonics due to different phenomena. The most important are:

a. Supply frequency: f_s
b. The odd order harmonics due to [26–29]:
   - The supply pollution (Time harmonics): $(2k + 1) f_s$
   - The Non-sinusoidal distribution of windings (Space harmonics): $f_{SH} = (6n \pm 1)f_s$.
   - The magnetic saturation represented by the third harmonic in low frequency band.
   - The unbalance voltage.
   - The static eccentricity.
   - The inter-turn short-circuits in the stator represented also by the third harmonic in the low frequency band.
c. Rotor Slot Harmonic frequency due to the Non-sinusoidal distribution of windings illustrated by the following expression:

$$f_{HPER} = f_s\left(m \cdot \frac{N_{br}}{p}(1 - s) \pm \nu\right) \tag{6}$$

d. Eccentricity harmonics since even new motors had a mixed eccentricity:

$$f_{ecc} = f_s \cdot \left(1 \pm \frac{1 - s}{p}\right) \tag{7}$$

e. Harmonics due to the load variation.
f. And harmonics due to the possible presence of faults.

Finally, it should be noted that in the case of even a new motor, the rotor cage is imbalanced due to manufacturing tolerances and impurities during molding. This imbalance is characterized by the following equation:

$$f_{BB} = f_s \cdot (1 \pm 2ks) \tag{8}$$

Note that p represents the number of poles pairs, N_{br} the number of rotor bars, s is the induction motor slip, $k = 1, 2, 3\ldots$ and $\nu = 1, 3, 5\ldots$

In other words, the temporal version of the stator current is a sum of cosine (or sine) expressed as follows [20]:

$$i_s(t) = \sum_{i=1}^{N_H} I_i \cos\left(2\pi f_i t + \varphi_i\right) + w(t) \tag{9}$$

where I_i, f_i, φ_i are respectively, the amplitude, the frequency and the initial phase of the i^{th} cosine, N_H harmonic number and w(t) is the measurement noise.

In its numeric version, the stator current of Eq. (9) can be rewritten as the sum of $2.N_H$ complex exponentials:

$$i_s(n) = \sum_{i=1}^{2N_H} \frac{I_i}{2}.e^{j(2\pi \frac{f_i}{f_{sf}} n + \varphi_i)} + w(n) \tag{10}$$

with $n = 0, 1, 2 \ldots N-1$ and where N is the number of samples and f_{sf} is the sampling frequency.

3 Auto-regressive Model

It should be known that *a priori* signal analysis (classical spectral analysis) is required to determine the type of modeling to choose [30]. Indeed,

- If the signal spectrum is flat then the Moving Average (MA) model is appropriate.
- Contrariwise, if the spectrum is composed of frequency peaks, as is the case for the stator current, then the Auto-Regressive (AR) model is chosen.

Based on the fact that the stator current spectrum is composed of several harmonics (or frequency peaks), we choose to use the AR model.

3.1 AR Modeling Principle

Generally speaking, we can say that the AR is an all-pole filter whose input is a white noise with zero mean and variance equal to σ_w^2. The AR model can be defined either by a difference equation:

$$e(n) = i_s(n) - \hat{i}_s(n) = i_s(n) + \sum_{k=1}^{L} \hat{a}_k i_s(n-k) \tag{11}$$

Or by the following transfer function:

$$H(z) = \frac{1}{1 + \sum_{k=1}^{L} \hat{a}_k z^{-k}} \tag{12}$$

where $z^{-k} = e^{-j.2.\pi.\frac{f_k}{f_{sf}}}$, L represent the model order and $e(n)$ is the prediction error modeled by a white noise.

The coefficients of this filter ($\hat{a}_k$) are determined by minimizing the prediction error $e(n)$, which means that the filter output is the closest to the modeled signal.

The *AR* process PSD with L model order of the time series data mentioned in Eq. (12) gives us the following equation:

$$PSD_{AR}(f) = \frac{\sigma_w^2}{\left|1 + \sum_{k=1}^{L} \hat{a}_k e^{-j2\pi\frac{f_k}{f_{sf}}}\right|^2} \tag{13}$$

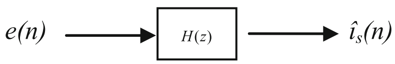

AR modeling of a random process

There are several methods for estimating the AR coefficients. These include: Yule-Walker, Burg, modified covariance and covariance [30]. The method used in this paper, chosen for its computation speed is the Yule-Walker, which uses the Levinson-Durbin algorithm (recursion on the autocorrelation matrix) to find the AR coefficients.

3.2 Estimation of the AR Model Order (L)

The estimation of AR model's order is very important for the reliability of the results, because it is this order that determines the number of searched harmonics. For that, several criteria exist for the estimation of the model order; the most relevant criteria are [19]:

- *AIC*: Akaike Information Criterion.
- *FPE*: Final Prediction Error.
- *MDL*: Minimum Description Length.
- *CAT*: Criterion Auto-Regressive Transfer.

However, these criteria only give an approximation of the model order which can cause in several cases, errors in modeling. Indeed, if the model order is underestimated, then there will be a loss of information from which the risk that the fault signature does not appear. Contrariwise, if the order is overestimated, the resulting spectrum will include more frequencies (also called false alarms) and at worst, a phenomenon called separate spectrum where each harmonic is divided into two separate peaks, hence the need for an optimal choice of the model order.

To deal with this problem, we propose in the next section to perform the processing over a defined frequency band which will allow us to choose the model order. Indeed, everything depends on the choice of the limited frequency band since the harmonic of the fault appears on a well-defined frequency band.

4 Improvements of the Auto-regressive Approach

4.1 Processing Over a Limited Frequency Band

The major disadvantage of the AR approach is the computation time which is very important and that increases with the number of samples and the number of searched harmonic. But knowing that the signature of each type of fault is localized within a specific frequency band of the stator current spectrum, the idea that we propose for solving this problem is to analyze only the frequency band where the signature of the searched harmonic is likely to appear. This solution will reduce the length of the signal on which we shall work and consequently reduce the computation time. Thus, the proposed algorithm is based on the application of AR modeling only over a frequency band defined by a low cutoff frequency f_l and a high cutoff frequency f_h [20].

The cutoff frequencies in this band will be selected on the spectrum width $[0, f_{sf}/2]$, depending on the type of the studied fault. With this solution, the processing will be done on $2.N.f_p/f_{sf}$ samples where $f_p = f_h - f_l$ but not on the N starting samples, reducing the computation time.

4.2 The Proposed Root-AR Approach

The second improvement that we propose in this paper is related to the identification of the searched harmonics by AR modeling. Indeed, according to Eq. (13) the maxima of the function L represent the searched harmonics. In other words, the Root-AR approach calculates the solutions of the following equation on N points [20]:

$$1 + \sum_{k=1}^{N} \hat{a}_k z^{-k} = 0 \tag{14}$$

The L solutions that are on (or near) the unit circle represent the searched harmonics. The corresponding frequencies to the different components of the analyzed signal will therefore be calculated by the following relationship:

$$f_k = \frac{f_{sf}}{2.\pi} . \arg(z^k) \tag{15}$$

Unfortunately in reality, this is not too simple as the location is not easy in the presence of noisy signals, because the corresponding poles at searched harmonics are no longer located on the unit circle (Fig. 2), but mixed with other solutions in the function.

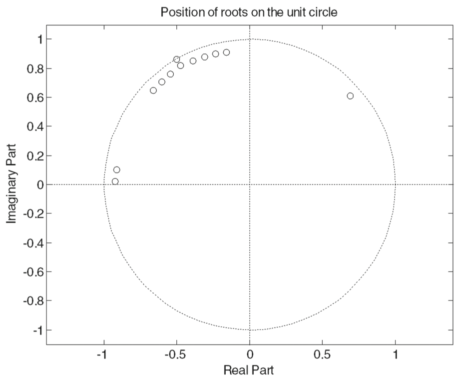

Fig. 2. Position of roots (solutions) on the unit circle.

5 Simulation Tests

The main goal of these simulations is to demonstrate the impact of the solutions proposed in this paper on improving the AR modeling. Therefore, we will first simulate, the case where the induction motor is healthy and the value of the mechanical rotor frequency is equal to f_r = *24* Hz for a motor slip of *s* = *4%*. This slip value corresponds to nominal operation of our motor. In these conditions, the stator current can be simulated as the sum of several sinusoids representing the fundamental, the eccentricity and the rotor slot harmonic. In these circumstances and based on the simulated motor parameters given in Appendix A and the Eqs. (6) and (7), the model of the stator current described in [6] and given by:

$$i_s(t) = 10\sin(2\pi 50t) + 0{,}1\sin(2\pi 26t) + 0{,}1\sin(2\pi 74t) \\ + 0{,}05\sin(2\pi 622t) + w(t) \tag{16}$$

$w(t)$ is the random white noise. This noise is added to the signal using the Signal to Noise Ratio (SNR) defined as:

$$SNR = 10\log_{10}\frac{P_s}{P_w} \tag{17}$$

where P_s and P_w respectively the powers of signal and noise.

To simulate a moderately noisy signal, we choose the SNR equal to 50 dB. The simulation time is 5 s and the sampling frequency is 1500 Hz corresponding to a frequency resolution of 0.20 Hz and a number N of 7500 samples. Stator current spectral analysis using the estimation of the PSD based on the periodogram algorithm is shown in Fig. 3.

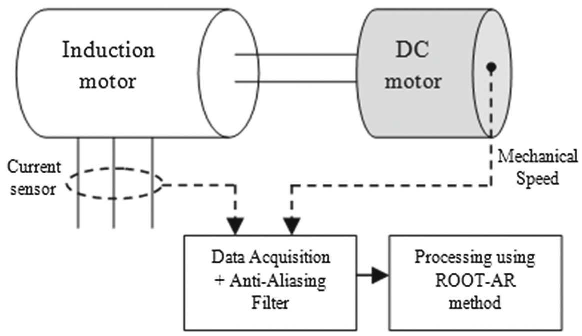

Bloc-Diagram of the proposed method

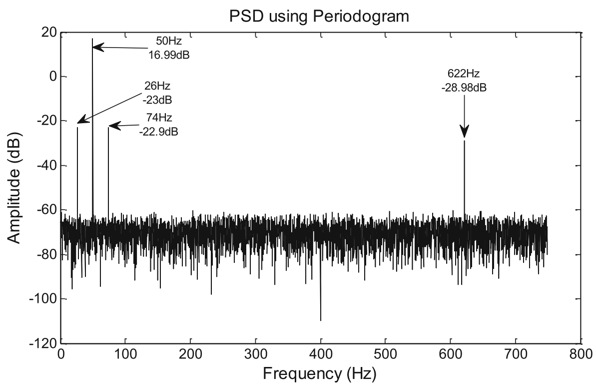

Fig. 3. Estimation of the stator current PSD using periodogram (SNR = 50 dB)

We can see on this spectrum the location of different simulated harmonics (f_s = *50* Hz, f_{ecc} = *26 and 74* Hz, f_{HPER} = *622* Hz) for a moderately noisy signal. Furthermore, Fig. 4 shows the results obtained by the estimation of the PSD based on Root-AR algorithm. Note that for this test and for these results, we took a model order L equal to 8 as long as we have N_H = *04* sinusoids.

With Fig. 4, we notice especially the clarity of the representation by the suggested technique where all the searched frequencies are well displayed.

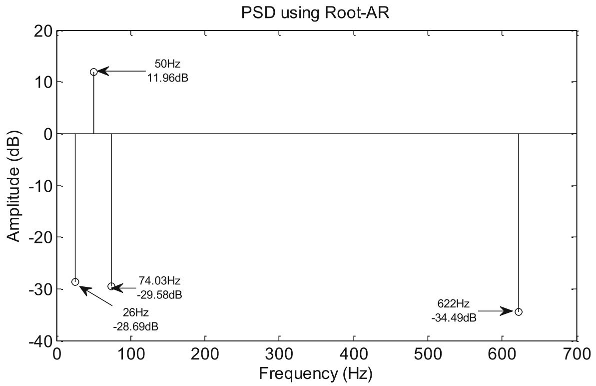

Fig. 4. Estimation of the stator current PSD using Root-AR (SNR = 50 dB)

5.1 Case of the Outer Race's Fault

We introduce now the outer race's fault. If this fault exists, then its theoretical frequency signature is calculated using Eqs. (1) and (5), based on the parameters of a real rolling-element bearing given in Appendix B in the aim of approaching the real case investigated in this paper. This frequency is given in Table 1.

Table 1. Theoretical frequency of bearing faults

Fault type	Theoretical frequency (*k = 1)*
Outer race	*36,02* Hz

Under these conditions, the expression of the stator current becomes:

$$i_s(t) = 10\sin(2\pi 50t) + 0{,}1\sin(2\pi 26t) + 0{,}1\sin(2\pi 74t) \\ + 0{,}05\sin(2\pi 622t) + 0{,}1\sin(2\pi 36,02t) + w(t) \tag{18}$$

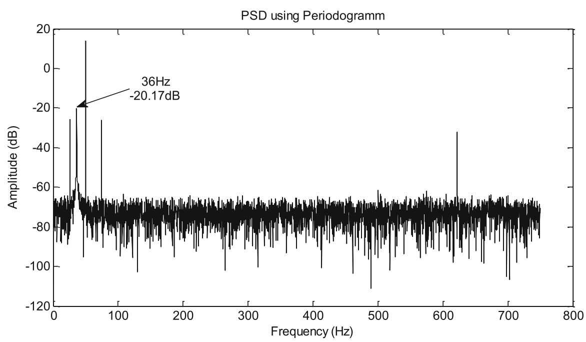

Fig. 5. Estimation of PSD by periodogram in the case of bearing faults

Figure 5 shows the estimation of the stator current PSD by periodogram for SNR = 50 dB (moderately noisy signal). We note that all simulated frequencies are identified in the spectrum.

Again, we note the clarity and readability that gives the proposed approach (Root-AR) compared to the conventional method in the identification of all searched harmonics, as shown in Fig. 6.

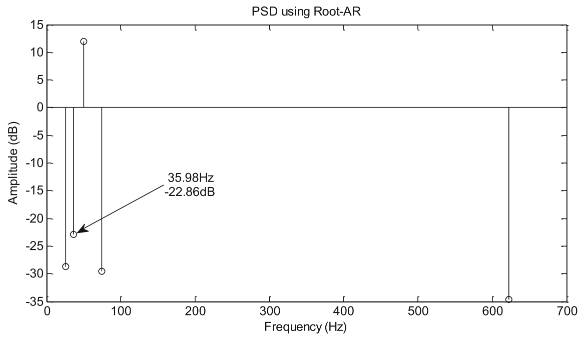

Fig. 6. Estimation of PSD by Root-AR in the case of bearing faults

However as previously mentioned, the main disadvantage of the AR modeling is the computation time. Indeed, looking at Table 2, we see the difference between the computation time required for the conventional method of Periodogram and that obtained by Root-AR. Note that the processing was performed on 7500 samples and $L = 10$ using a PC with an Intel i5-core processor and a 6 GB RAM.

Table 2. Estimation of computation time

PSD	Periodogram	Root-AR (without solution)
Computation time	0,041 s	13,09 s

Unfortunately, this problem will be even important in the case of real signals because their size can easily exceed 100000 samples.

To solve this problem, we propose in the next sub-section to perform the processing on a limited frequency band where fault-related frequencies may appear.

5.2 Effect of Processing on a Limited Frequency Band

Based on Table 1, it can be said that the frequency signatures of both faults studied in this paper can appear only on the frequency band [20 Hz–90 Hz]. The application of processing on this band will allow us to reduce the number of samples of the signal to be processed and therefore we reduce the computation time.

In this aim, Figs. 7 and 8 show, respectively, the estimation of the PSD by periodogram and that using the Root-AR algorithm. We note that the signatures of both faults are more readable without making successive zooms to show them.

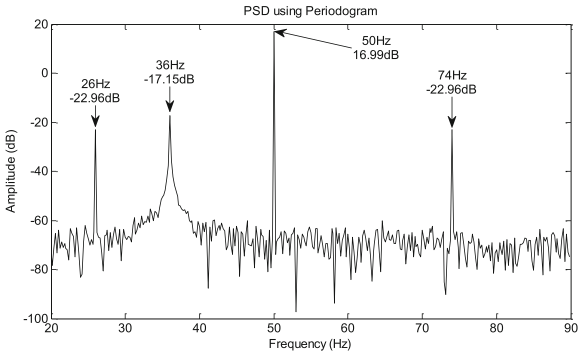

Fig. 7. Estimation of PSD by Periodogram over a limited frequency band.

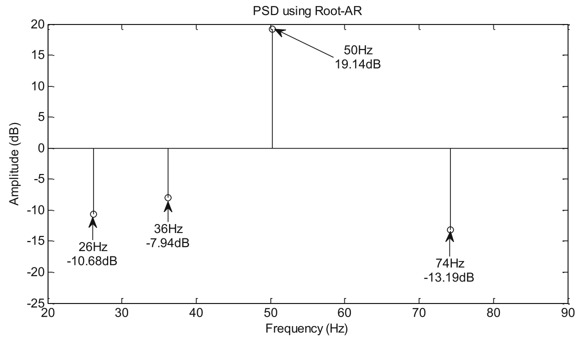

Fig. 8. Estimation of PSD by Root-AR over a limited frequency band.

In addition, using this solution, we note that the computation time of Root-AR was significantly reduced without affecting the desired results as shown in Table 3 below.

Table 3. Estimation of computation time when using a limited frequency band

Method	Periodogram	Root-AR (with solution)
Computation time (s)	0,042	0,33

Based on simulation results, we can observe the effectiveness of the Root-AR approach introduced in this paper for the diagnosis of the outer race fault. In the next section, an experimental study will verify the merits of the Root-AR method.

6 Experimental Results of Bearing Fault Diagnosis Using Root-AR Approach

The motor used in these tests is a three-phase squirrel-cage induction motor coupled to a DC generator used as a load. The parameters of the induction motor are given in Appendix A. Furthermore, the effectiveness of the ROOT-AR method, like all classic or recent diagnosis methods using spectral analysis of vibration or electrical quantities, require prior knowledge of the dimensions of the investigated bearing, to determine the frequency band where the fault signature is likely to appear. The bearing dimensions are given in Appendix B.

We consider in this paper the case of the outer race fault. This fault is artificially created, as is shown in Fig. 9.

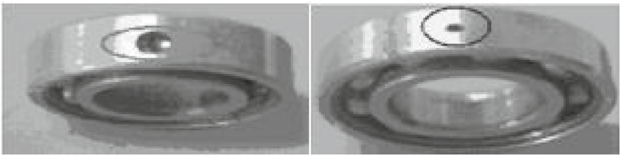

a. 6mm diameter fault. b. 3mm diameter fault.

Fig. 9. Artificial bearing fault (outer race fault)

The measurement system contains three current Hall effect sensors, an implemented anti-aliasing filter (for our tests, we chose a 400 Hz cutoff frequency), a tachometer for measuring the mechanical rotor speed and an acquisition card. Then, a computer is used for the processing of the acquired signals. This system is shown in Fig. 10.

Fig. 10. Experimental setup.

All acquisitions were made at the rated speed (for a torque estimated at 20 Nm) over a period of 40 s with a sampling frequency of 1.5 kHz, which lead to a frequency resolution equal to 0.025 Hz. The different modes of motor operating used to validate our diagnosis approach are:

– Motor operating with healthy bearings.
– Motor with faulty outer race “6 mm hole diameter”.
– Motor with faulty outer race “3 mm hole diameter”.

6.1 Tests with Healthy Motor

First, we’ll analyze the stator current in the case where both rolling-element bearings have no apparent fault. This analysis will be considered as a reference for further tests.

In addition, we call “healthy motor” in this paper, a motor that does not present any visually apparent faults in rotor, stator or bearings. This does not exclude the existence of imperfections related to either its manufacturing phase or to the existence of scratches associated with its use.

Moreover, in the case of outer race fault, the failure will appear in a well defined frequency band. Indeed, the theoretical frequency signature is calculated in Table 1.

Therefore, we choose the frequency band, which provides information on whether or not there are an outer race fault, around [30 Hz–60 Hz]. Indeed, this frequency band shows any harmonics of bearing in addition to the fundamental frequency (50 Hz). Therefore, the search for fault signature will be performed on this frequency band.

In these conditions, Fig. 11 shows the stator current PSD using the periodogram in the case of healthy motor. This figure shows the presence of two harmonics of very low amplitudes around the fundamental at 45.58 Hz and 54.33 Hz. Figure 12 shows the Stator current PSD using the improved approach of AR modeling, called Root-AR. This figure shows the presence of another frequency around 59 Hz more precisely at 59.48 Hz besides both harmonics obtained by the conventional method.

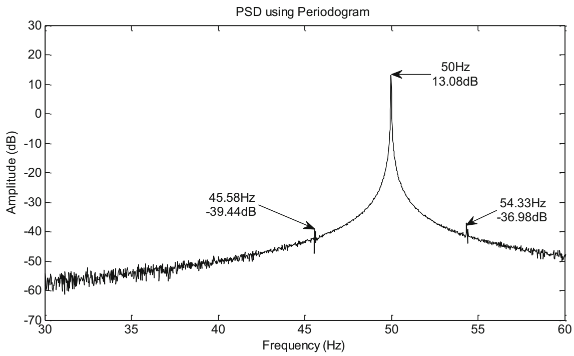

Fig. 11. Estimation of the stator current PSD using periodogram (healthy motor)

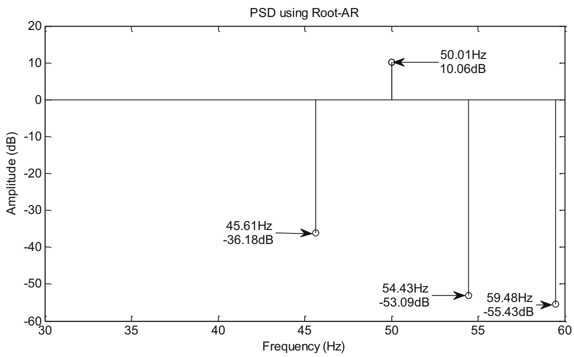

Fig. 12. Estimation of the stator current PSD using Root-AR (healthy motor)

We assume that these harmonics are caused by an imbalance rotor circuit and not to a change in load as all our tests are performed at a fixed charge. Indeed, even while new motor has an imbalance in the rotor circuit due to its manufacturing phase. To demonstrate these statements, we consider the Eq. (8). Knowing that the measured mechanical rotational speed is 1430 rpm for a slip of 4.6%, while under these conditions, the theoretical frequency signature of an imbalance rotor cage is given in the following Table 4.

Table 4. Frequency signatures of a rotor fault in the frequency band of [40 Hz, 60 Hz] (Case of a motor slip of 4.6%)

	Lower Sideband		*Upper Sideband*	
$f_b = (1 \pm 2ks)f_s$	$k = 2$	$k = 1$	$k = 1$	$k = 2$
Theoretical frequencies (Hz)	40.8	45.4	54.6	**59.2**

This frequency (in bold) is only obtained with the proposed method.

This table shows that the theoretically frequency signatures of a rotor imbalance should appear at the frequencies of 45.4 Hz and 54.6 Hz for k = 1 and the frequencies of 40.8 Hz and 59.2 Hz for a multiplicity of k = 2.

Experimentally, we obtained 59.48 Hz with the proposed method. We can therefore say that this harmonic represents the multiplicity of the rotor imbalance. Note that this slight difference is certainly due to measurement errors on the mechanical speed. These results show the power of the proposed method to detect the harmonic multiplicity 2, something that the conventional method does not do. In addition, the non-appearance of the frequency corresponding to k = 2 in the Lower Sideband is due to the selected N_H. In fact, if we increase this parameter, we can easily detect this frequency but at the expense of the emergence of false alarms.

6.2 Tests with an Outer Race Fault of 6 mm Diameter

Thereafter, a test is conducted under an outer race fault (with a hole of 6 mm diameter). Stator current PSD using the periodogram and Root-AR approaches are represented, respectively, by Figs. 13 and 14.

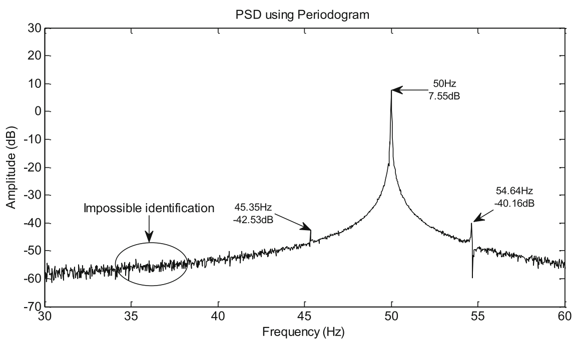

Fig. 13. Estimation of the stator current PSD using periodogram (6 mm diameter fault)

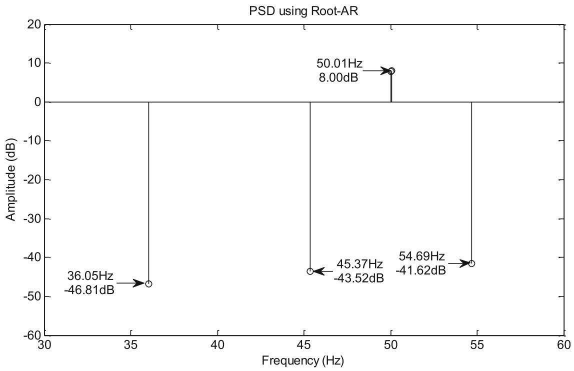

Fig. 14. Estimation of the stator current PSD using Root-AR (6 mm diameter fault)

Only the PSD spectrum using Root-AR shows the fault by the mean of a frequency at the theoretical frequency of outer race fault while the PSD by periodogram does not show clearly the fault.

6.3 Tests with an Outer Race Fault of 3 mm Diameter

Finally, another test is performed using the same fault with a smaller diameter of the outer race fault with a 3 mm hole. This fault will be used to illustrate the case of an incipient fault. This test also helps to demonstrate the behavior of each method with the evolution of the fault. This is illustrated in Figs. 15 and 16.

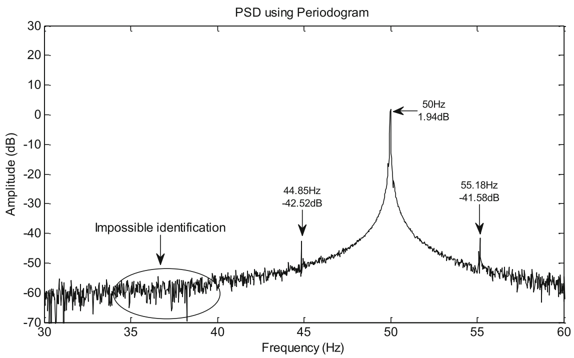

Fig. 15. Estimation of the stator current PSD using periodogram (3 mm diameter fault)

We notice that the frequency signature of the outer race fault on the spectrum using Root-AR approach changes in amplitude due to fault severity, while the identification of the outer race fault on PSD by periodogram remains impossible. For the Root-AR approach, we assume that the harmonics observed around 30 Hz are false alarms.

Therefore, Table 5 illustrates the evolution of the outer race harmonic's amplitude following the fault severity using the Root-AR approach:

Table 5. Amplitude changes following fault severity

Fault type	6 mm hole diameter	3 mm hole diameter
Amplitude (dB)	−46.81	−56.20

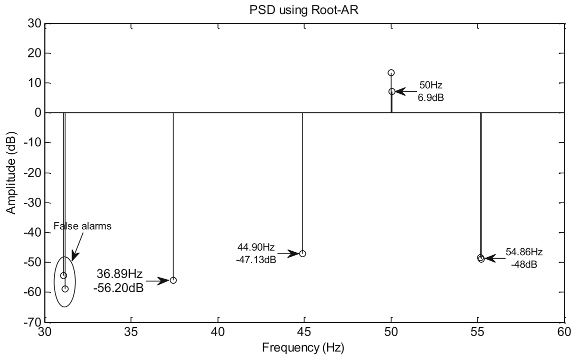

Fig. 16. Estimation of the stator current PSD using Root-AR (3 mm diameter fault)

In addition, several harmonics appear on the spectrum the Root-AR approach with very low amplitudes (less than −50 dB). We assume that these harmonics are false alarms.

Note that the main reason for the emergence of false alarms is due to an overestimation of the harmonic number N_H used in AR modeling. This overestimation may have negative effects on the reliability of diagnosis especially if this false signature appears at the same frequency position than that of another type of fault. For this reason, a check of the estimated frequencies is required. Thus, to avoid confusion between false signatures due to an overestimation of N_H and the other frequency signatures of different faults, we propose to apply this method not on a single frequency band, but on several bands where the fault signature may appear depending on the multiplicity k or m (see Eq. 5 and 8).

However, it may be noticed that in addition to the efficient identification provided by the Root-AR approach, a further improvement is made in the computation time by performing the processing over the limited frequency band around the theoretical fault signature. Indeed, the main disadvantage of high resolution signal processing techniques is the computation time. Using the Root-AR approach, we get to have a competitive computation time compared to the conventional technique by periodogram as shown in Table 6.

Table 6. Estimation of computation time

Method	Periodogram	Root-AR
Computation time (s)	0.09	0.11

7 Conclusion

In this paper, a diagnosis method is proposed based on the auto-regressive modeling of stator current. Two improvements are made to the AR modeling. Indeed, an improved algorithm of modeling AR called *Root-AR*, is developed in order to have a better identification of the searched harmonics. Then we choose to perform processing over a limited frequency band around these harmonics. Thereby, we reduced the number of samples and therefore, reduced the computation time which is a major disadvantage of the AR modeling.

Through simulation tests and experimental results, we could verify the effectiveness of the Root-AR approach against the conventional method of the periodogram.

Furthermore, we can mention another advantage of using this method in real cases in addition to the good resolution and clarity of the spectrum of the proposed method. Indeed, in the presence of several faults at the same time, the conventional method gives a large spectral preview, while the user has to search the fault signatures by making successive zooms on the frequency zones data. Otherwise, with the proposed method, we only have to define several frequency bands to be analyzed according to the searched fault and the multiplicity of appearance of its signature.

Appendix A. Induction Motor Parameters

Rated power	3 kW
Supply frequency	50 Hz
Rated voltage	380 V
Rated current	7 A
Rated speed	1440 rev/min
Number of rotor bars	28
Number of poles pairs	2

Appendix B. Geometric Parameters of Rolling-Element Bearing "Reference ZZ-6025 Coupling Opposite Side"

Ball diameter D_b	7.835 mm
Cage diameter D_c	38.5 mm
Number of balls N_b	9
Contact angle β	0

References

1. Toliyat, H.A., Nandi, S., Choi, S., Meshgin-Kelm, H.: Electric Machines: Modeling, Condition Monitoring and Fault Diagnosis. Taylor & Francis Group Eds, New York (2013)
2. Bonnett, A.H., Yung, C.: Increased efficiency versus increased reliability. Ind. Appl. Mag. IEEE **14**, 29–36 (2008)
3. Immovilli, F., Bellini, A., Rubini, R., Tassoni, C.: Diagnosis of bearing faults in induction machines by vibration or current signals: a critical comparison. IEEE Trans. Ind. Appl. **46**, 1350–1360 (2010)
4. Seshadrinath, J., Singh, B., Panigrahi, B.K.: Vibration analysis based interturn fault diagnosis in induction machines. IEEE Trans. Ind. Inform. **10**(1), 340–350 (2014)
5. Zarei, J., Tajeddini, A., Karimi, H.R.: Vibration analysis for bearing fault detection and classification using an intelligent filter. J. Mechatron. **24**, 151–157 (2014)
6. Aïmer, A.F., Boudinar, A.H., Bendiabdellah, A.: Use of the short time Fourier transform for induction motor broken bars detection. Int. Rev. Model. Simul. **16**(6), 1879–1883 (2013)
7. Jung, J.H., Lee, J.J., Kwon, B.H.: Online diagnosis of induction motors using MCSA. IEEE Trans. Ind. Electron. **53**, 1842–1853 (2006)
8. Mehala, N., Dahiya, R.: Detection of bearing faults of induction motor using Park's vector approach. Int. J. Eng. Technol. **2**(4), 263–266 (2010)
9. Silva, J.L.H., Cardoso, A.J.M.: Bearing failures diagnosis in three-phase induction motors by extended Park's vector approach. In: 31st Annual Conference of IEEE on Industrial Electronics Society, IECON 2005 (2005)
10. El Bouchikhi, E., Choqueuse, V., Benbouzid, M.E.H.: Current frequency spectral subtraction and its contribution to induction machines' bearings condition monitoring. IEEE Trans. Energy Convers. **28**(1), 135–144 (2012)
11. Gong, X., Qiao, W.: Bearing fault detection for direct-drive wind turbines via stator current spectrum analysis. In: Proceedings of IEEE Energy Conversion Congress and Exposition (ECCE) (2011)
12. El Bouchikhi, E., Choqueuse, V., Benbouzid, M.E.H.: Induction machine faults detection using stator current parametric spectral estimation. In: Mechanical Systems and Signal Processing, pp. 447–464. Elsevier (2014)
13. Ibrahim, A., Badaoui, M.E., Guillet, F., Bonnardot, F.: A new bearing fault detection method in induction machines based on instantaneous power factor. IEEE Trans. Ind. Electron. **55**(12), 4252–4259 (2008)
14. Dzwonkowski, A., Swędrowski, L.: Uncertainty analysis of measuring system for instantaneous power research. Metrol. Measur. Syst. **19**(3), 573–582 (2012)
15. Zagirnyak, M., Mamchur, D., Kalinov, A.: Comparison of induction motor diagnostic methods based on spectra analysis of current and instantaneous power signals. Przegląd Elektrotechniczny **88**(12b), 221–224 (2012)
16. Amirat, Y., Choqueuse, V., Benbouzid, M.E.H., Turri, S.: Hilbert Transform based bearing failure detection in DFIG-based wind turbines. Int. Rev. Electr. Eng. **6**(3), 1249–1256 (2011)
17. Espinosa, A.G., Rosero, J.A., Cusido, J., Romeral, L., Ortega, J.A.: Fault detection by means of Hilbert–Huang Transform of the stator current in a PMSM with demagnetization. IEEE Trans. Energy Convers. **25**(2), 312–318 (2010)
18. Khezzar, A., Kaikaa, M.Y., Oumaamar, M., Boucherma, M., Razik, H.: On the use of slot harmonics as a potential indicator of rotor bar breakage in the induction machine. IEEE Trans. Ind. Electron. **56**(11), 4592–4605 (2009)
19. Stoica, P., Selen, Y.: Model-order selection: a review of information criterion rules. IEEE Signal Process. Mag. **21**(4), 36–47 (2004)

20. Boudinar, A.H., Benouzza, N., Bendiabdellah, A., Khodja, M.: Induction motor bearing fault analysis using root-MUSIC method. IEEE Trans. Ind. Appl. **52**(5), 3851–3860 (2016)
21. Kia, S.H., Henao, H., Capolino, G.-A.: A high resolution frequency estimation method for three-phase induction machine fault detection. IEEE Trans. Ind. Electron. **54**(4), 2305–2314 (2007)
22. Kim, Y.-H., Youn, Y.-W., Hwang, D.-H., Sun, J.-H., Kang, D.-S.: High-resolution parameter estimation method to identify broken rotor bar faults in induction motors. IEEE Trans. Ind. Electron. **60**(9), 4103–4117 (2013)
23. Sahraoui, M., Cardoso, A.J.M., Ghoggal, A.: The use of a modified Prony method to track the broken rotor bar characteristic frequencies and amplitudes in three-phase induction motors. IEEE Trans. Ind. Appl. **51**(3), 455–460 (2015)
24. Munoz, A.R.: Using an autoregressive model in the detection of abnormal characteristics of squirrel cage induction motors. Electric Power Systems Research (2000)
25. Blödt, M., Granjon, P., Raison, B., Rostaing, G.: Models for bearing damage detection in induction motors using stator current monitoring. IEEE Trans. Ind. Electron. **55**, 1813–1823 (2008)
26. Samaga, R.L., Vittal, K.P., Vikas, J.: Effect of unbalance in voltage supply on the detection of mixed air gap eccentricity in an induction motor by Motor Current Signature Analysis. In: IEEE PES Innovative Smart Grid Technologies—India (2011)
27. Li, X., Nandi, S.: Performance analysis of a 3-phase induction machine with inclined static eccentricity. In: IEEE International Conference on Electric Machines and Drives, pp. 1606–1613 (2005)
28. Nandi, S.: A Detailed model of induction machines with saturation extendable for fault analysis. IEEE Trans. Ind. Appl. **40**(5), 1302–1309 (2004)
29. Joksimovic, G.M., Penman, J.: The detection of inter-turn short circuits in the stator windings of operating motors. IEEE Trans. Ind. Electron. **47**(5), 1078–1084 (2000)
30. Manolakis, D.G., Ingle, V.K., Kogon, S.M.: Statistical and Adaptive Signal Processing: Spectral Estimation, Signal Modelling, Adaptive Filtering, and Array Processing. Artech House Inc., Norwood (2005)

Induction Motor's Bearing Fault Diagnosis Using an Improved Short Time Fourier Transform

Ahmed Hamida Boudinar(✉), Ameur Fethi Aimer, Mohamed El Amine Khodja, and Noureddine Benouzza

Department of Electrical Engineering, Diagnosis Group, LDEE Laboratory, University of Sciences and Technology of Oran, Oran, Algeria
boud_ah@yahoo.fr, fethi.aimer@yahoo.fr, khodjamea@gmail.com, benouza@yahoo.com

Abstract. Induction motor diagnosis using the Power Spectral Density estimation or PSD, based on the Fourier Transform calculation, is not recommended for the processing of non stationary signals (case of variable speed applications). In fact, under these conditions, the analysis with this approach is no more reliable. To resolve this, we use in this paper, the Short Time Fourier Transform (STFT), to obtain information on changes of the frequencies over time. Furthermore, we propose the use of a new approach called Maxima's Location Algorithm (MLA) which will be associated to the STFT analysis to show only harmonics with useful information on existing faults. This approach will be used in the diagnosis of bearing faults of a PWM inverter-fed induction motor operating at variable speed. Experimental results show the merits of the proposed approach on the reliability of the bearing fault detection.

Keywords: Induction motor · Bearing faults diagnosis
Time-Frequency analysis · STFT · MLA

1 Introduction

The induction motor is the most common electric machine in the industry. Its main advantage is the absence of sliding electrical contacts, which leads to a simple and robust structure easy to build with a low cost. However, various faults can appear on the induction motor making the fault detection procedure necessary to prevent the interruption of the industrial process. A statistical study carried out on several medium and high power range induction motors [1], showed that the bearing faults account for 69% of all failures. Furthermore, most of the bearing faults act on the geometric shape of the rolling elements by surface ripples, cracks in the two races (inner and outer) or damage on the bearing cage. Another statistical study conducted by the General Electric Company has shown that over 39% of the bearing faults occur on both inner and outer races [2].

Several researches investigated vibration analysis for bearing faults diagnosis [3–5]. Unfortunately, its main drawback is the vibration sensor's location which must be

M. Chadli et al. (Eds.): ICEECA 2017, LNEE 522, pp. 411–426, 2019.
https://doi.org/10.1007/978-3-319-97816-1_31

placed in a specific position of the machine. Another technique is also used increasingly in recent years, based on the motor current signature analysis (MCSA). Indeed, several studies [6, 7] showed that the stator current bring information on almost all electrical and mechanical faults that may occur in the induction motor.

To analyze the stator current for extracting useful information on the existence or not of these faults, several studies [8–11] use the non-parametric method based on the estimation of the Power Spectral Density (PSD) by Periodogram. However, this method has several drawbacks which are essentially due to frequency resolution problem. Indeed, the estimation of the PSD introduces a smoothing effect and a side effect associated to the selected weighting window [11]. This is reflected in the appearance of side lobes in the stator current spectrum, which reduces the level of analysis. In this context, authors in [12] provides a study on different weighting windows, showing the effectiveness of the use of Hanning window in improving the frequency resolution and to decrease both smoothing effect and side effect in some fault cases. Unfortunately, this choice is not always valid for certain operating modes such as diagnosing rotor faults at very low load, because the fault signature is embedded in the fundamental. For this, many researchers have focused their works in recent years on the use of the Hilbert method to avoid the fundamental effect on the current spectrum analysis and avoid the problem of the choice of the weighting window [13, 14]. The Hilbert method is certainly suitable for diagnosis of rotor faults, but it is not very effective for other types of faults.

Moreover, all these methods are inadequate in the case of a load change. Indeed, for this operating mode, the signals become non-stationary and therefore require the use of other methods such as time-frequency methods and time-scale methods. For the time-frequency methods, the most used approach is the Short Time Fourier Transform (STFT) [15, 16]. This method allows the monitoring of useful information of the signal depending on speed change for example. However, its main disadvantage is its low time-frequency resolution. In the same family, another method based on the Wigner-Ville Distribution (WVD) [17, 18] improves the time-frequency resolution to the detriment of the rise of interference terms or cross terms around the frequencies of the signal, mainly due to the noise embedded in the signal. Unfortunately, this procedure causes a shifting of frequencies. In other hand, time-scale methods are also used in the analysis of non-stationary signals, the best known method is undoubtedly that based on wavelet transform [19–22]. Of course, this method is very effective in the case of change of speed or load, but its major drawback is the complexity of interpreting the resulting spectra and the long computation time, in addition to the importance of the choice of the used wavelet.

Therefore, we choose to use in this paper, the Short Time Fourier Transform (STFT), giving additional information on changes of the frequencies over time for the analysis of the stator current signal. Furthermore, in order to improve the reliability and efficiency of the plot of the obtained results, we propose to apply the STFT approach only on a limited frequency band where the searched fault is likely to appear. In addition, we propose the use of a new approach called Maxima's Location Algorithm (MLA) which will be associated with this calculation to show only harmonics with useful information on faults. This will allow us to have a better representation of the frequency signatures in the resulting Time-Frequency spectrum of the stator current by following also the changes of frequencies over time. This approach will be used in the diagnosis of bearing faults of a PWM inverter-fed induction motor operating at variable speed. In this aim, several experimental tests in transient state are achieved in order to illustrate the merits of the association of the STFT/MLA approaches and validate our proposition.

2 Frequency Signatures of Bearing Faults

The rolling-element bearings act as an electromechanical interface between the stator and the rotor. In addition, they represent the holding element from the shaft of the machine to ensure a proper rotation of the rotor. The bearings are constituted by two races, the inner race and the outer race, balls and the cage which provide equidistance between the balls as is shown in Fig. 1 [23]. Failures may affect the bearing on both races, on the ball or on the cage. Several studies have shown that the failure of each bearing element is manifested by a vibration frequency characterizing the fault type [24].

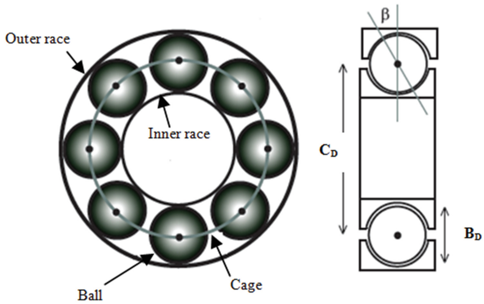

Fig. 1. Geometry of a rolling-element bearing.

- Characteristic frequency of the outer race fault

$$f_o = \frac{N_b}{2} f_r \left(1 - \frac{B_D}{C_D} \cos\beta\right) \tag{1}$$

- Characteristic frequency of the inner race fault

$$f_i = \frac{N_b}{2} f_r \left(1 + \frac{B_D}{C_D} \cos\beta\right) \tag{2}$$

- Characteristic frequency of the ball fault

$$f_{ball} = \frac{C_D}{B_D} f_r \left(1 - \frac{B_D^2}{C_D^2} \cos^2\beta\right) \tag{3}$$

- Characteristic frequency of the cage fault

$$f_{cage} = \frac{1}{2} f_r \left(1 - \frac{B_D}{C_D} \cos \beta \right) \tag{4}$$

Where N_b is the number of bearing balls, B_D and C_D respectively, are the ball and the cage diameter, β is the contact angle and f_r the mechanical rotor frequency.

Furthermore, the bearing faults signatures appear in the stator current spectrum at the following frequencies [24]:

$$f_{bear}(Hz) = |f_s \pm m \cdot f_v| \text{ with } m = 1, 2, 3\ldots \tag{5}$$

where f_s is the supply frequency and f_v is the fault characteristic frequency corresponding to either f_o, f_i, f_{cage} or $f_{ball.}$

3 Time-Frequency Analysis

The Fourier transform of stator current is expressed by the following equation:

$$FT_{i_s}(f) = \int_{-\infty}^{\infty} i_s(t) e^{-j2\pi ft} dt \tag{6}$$

We define the power spectral density or PSD as the square modulus of the Fourier transform, which is independent of the signal phase. Therefore, any information on the frequency changes with time variation is lost in the PSD. The idea of the STFT is to introduce the local frequency concept so that the Fourier transform is applied to the signal through a sliding window over which the signal is considered as stationary, as shown in Fig. 2.

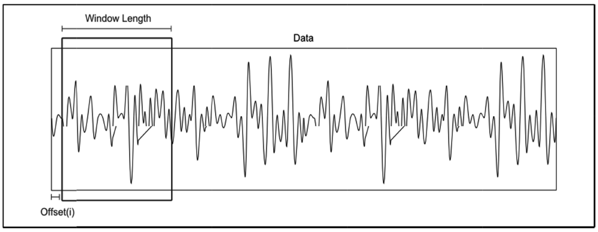

Fig. 2. The sliding window concept.

This transform represents the results in a time-frequency plane composed of spectral characteristics over time. The Short Time Fourier Transform or STFT is defined by:

$$STFT_{i_s}(t,f) = \int_{-\infty}^{+\infty} i_s(\tau)h(\tau - t)^* e^{-j2\pi f\tau} d\tau \tag{7}$$

The STFT is constituted by the FT of $i_s(\tau)h^*(\tau - t)$ obtained by weighting $i_s(\tau)$ by the window $h^*(\tau - t)$ which is a short time analysis window localized around t and that shifts by varying the time. Join to $h(\tau)$, the family of functions depending on two parameters t and f, defined by [15]:

$$h_{t,f}(\tau) = h(\tau - t)e^{j2\pi f\tau},\ (t,f) \in \Re^2 \tag{8}$$

The numbers $STFT_{i_s}(t,f)$ are commonly called projections of $i_s(\tau)$ on the function system $h_{t,f}$. If h is the rectangle window of T support, the STFT consists in taking the FT of a sequence of signals equal to i_s on the support and zero elsewhere. We begin by the discrete-time signal $[i_{sn} = i_s(nT)]$, $T > 0$. Let $h_n = h(nT)$ and N the number of samples in the analysis window. Finally, we introduce a discretization of the frequency variable f. The STFT is then defined by the entire numbers $Is_{k,n}$ calculated as follows:

$$Is_{k,n} = \sum_{n=0}^{N-1} i_{s_{n+k}} h_n^* e^{-j2\pi\frac{n}{N}},\ k \in \mathrm{Z}, n = 1, 2, \ldots \tag{9}$$

4 Heisenberg-Gabor Uncertainty Principle

The uncertainty principle, also called time-frequency inequality, is based on the uncertainty relationships established by Werner Heisenberg in quantum mechanics. The analogy with the work of Heisenberg for the Fourier transform was made by Dennis Gabor in 1946. Let us consider the finite energy signal x(t), centered in time and frequency around zero. Gabor defines the duration Δt and the spectral band Δf as follows [15]:

$$\Delta t = \frac{1}{E_x}\int_{-\infty}^{+\infty} t^2|x(t)|^2 dt \tag{10}$$

$$\Delta f = \frac{1}{E_x}\int_{-\infty}^{+\infty} f^2|X(f)|^2 df \tag{11}$$

Where E_x is the energy of the signal given by the Parceval relationship:

$$E_x = \int_{-\infty}^{+\infty} |x(t)|^2 dt = \int_{-\infty}^{+\infty} |X(f)|^2 df \tag{12}$$

Therefore, the time-frequency inequality is defined by [11]:

$$\Delta t \cdot \Delta f \geq \frac{1}{4\pi} \tag{13}$$

It expresses the fact that the duration-band product of a signal is lower bounded for a Δt duration and a Δf spectral band. In other words, a great accuracy in frequency localization leads to a low accuracy in time localization and vice versa. The STFT is subject to the uncertainty principle due to the use of Fourier transform. This issue requires the search for the best time-frequency compromise suitable to the case considered in determining the correct window width. Gaussian window has the best time-frequency localization. Indeed, it verifies the following equality:

$$\Delta t \cdot \Delta f = \frac{1}{4\pi} \tag{14}$$

Finally, the choice of the window is important because it represents another compromise (comparable to the time-frequency compromise) between the main lobe width and the amplitude of the sideband in the frequency domain.

5 Stator Current STFT Improvements

The Short Time Fourier Transform (STFT) as any time-frequency representation is subject to the computation time problem. In addition and due to the Heisenberg-Gabor inequality, the STFT has a low time-frequency resolution. For these problems, we bring in this paper some improvements to the STFT as follows, in order to obtain a better identification of bearings faults using the STFT.

5.1 Processing Over a Limited Frequency Band

The major drawback of the time-frequency approaches is the computation time which is very important and that increases with the number of samples and the number of searched harmonic. But knowing that the signature of each type of fault is localized within a specific frequency band of the stator current spectrum, the idea that we propose for solving this problem is to analyze only the frequency band where the signature of the searched harmonic is likely to appear. This solution will reduce the length of the signal on which we shall work and consequently reduce the computation time. Thus, the proposed algorithm is based on the application of the processing only over a given frequency band defined by a low cutoff frequency f_l and a high cutoff frequency f_h. The cutoff frequencies in this band will be selected on the spectrum width $[0, f_{sf}/2]$, (f_{sf} being the sampling frequency) depending on the type of the studied fault.

With this solution, the processing will be done on $2.N.f_p/f_{sf}$ samples where $f_p = f_h - f_l$ but not on the N starting samples, reducing the computation time [24].

5.2 Maxima's Location Algorithm

To improve the readability of the time-frequency stator current spectrum, we associate with the STFT a Maxima's Location Algorithm on a defined frequency band. Indeed, the algorithm locates the maximum harmonic numerically in the selected frequency band corresponding to the harmonic characterizing the bearing fault [25].

6 Experimental Validation

The motor used in these experimental tests is a three phase squirrel cage induction motor fed by a three-phase inverter and coupled to a DC generator used as a load. The induction motor characteristics are: 3 kW, 1410 rpm, 4 poles. The measurement set consists of three Effect Hall current sensors and an acquisition card. The entire set is connected to a computer for viewing, processing the measured signals and for generating the signals necessary for the control of the inverter. These control signals are obtained using a Space Vector PWM through the DSPACE 1104, as illustrated in Fig. 3.

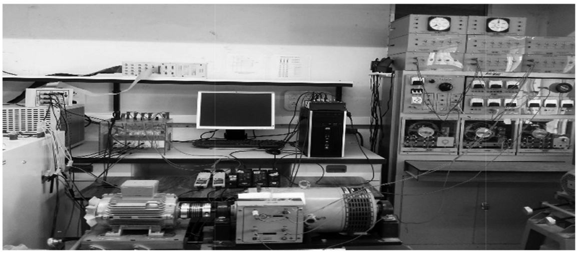

Fig. 3. Experimental setup description.

In addition, a tachometer is used for measuring the real mechanical speed of our motor. All acquisitions were performed with an acquisition time of 40 s. with a sampling frequency of 3 kHz, which lead to a frequency resolution of 0.025 Hz.

The bearing studied in this paper is a rolling-element bearing with 6205-ZZ reference; the geometrical parameters of this bearing are given in the appendix. In this context, an outer race fault is created artificially in order to have the same situations as real cases. Indeed, a scratch of 2 mm width and 2 mm deep is created in the outer race. Hence, Fig. 4 illustrates the outer race fault created in the bearing used in our experimental tests.

The different operating modes performed to validate the diagnosis procedure using the proposed approach are:

Fig. 4. Artificial bearing fault (outer race fault).

- Motor operating with a healthy bearing fed with and without inverter for a supply frequency of 50 Hz;
- Motor operating with a healthy bearing fed by inverter for a supply frequency of 30 Hz;
- Motor operating with an outer race fault fed with and without inverter for a supply frequency of 50 Hz;
- Motor operating with an outer race fault fed by inverter for a supply frequency of 30 Hz;
- Motor operating with an outer race fault fed by inverter for a supply frequency variation from 30 Hz to 50 Hz.

Knowing that the measured signals are random type, several acquisitions were made for each operating mode in order to have a more reliable analysis. Theoretically, the outer race fault signature for both supply frequencies 50 Hz and 30 Hz (for $m = 1$) is determined from Eqs. (1) and (5). This fault signature is given in Table 1.

Table 1. Bearing fault's theoretical frequencies

Supply frequency	50 Hz	30 Hz
Theoretical frequency (m = 1)	37.16 Hz	22.29 Hz

6.1 Motor Operating with a Healthy Bearing Fed with and Without Inverter for a Supply Frequency of 50 Hz

In this first operating mode, we analyze the stator current in case of healthy bearings with no apparent fault when the induction motor is fed directly from the mains and by a PWM inverter. Figure 5a shows the spectrum of the stator current when the motor is supplied directly from the mains. It is clear that the spectrum in this case represents only the fundamental and two harmonics around the fundamental. Both harmonics represent the signature of an unbalanced rotor circuit because some air bubbles may remain during the operation of molding the rotor cage for any motor, even for new motors. Note that there is no harmonic on the frequency band which may contain the outer race signature.

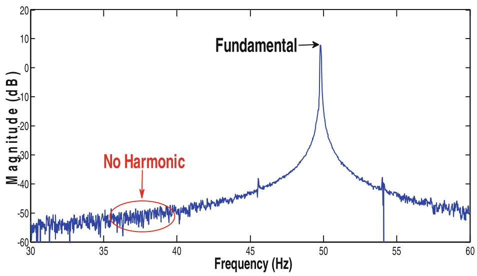

(a) Without inverter

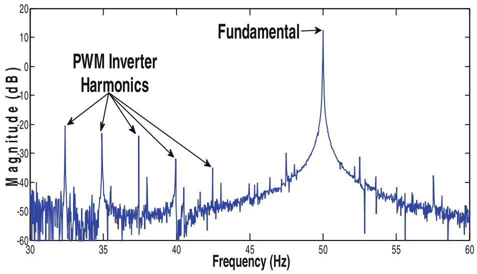

(b) With inverter

Fig. 5. Stator current spectrum for a supply frequency of 50 Hz. (Healthy bearing case)

Figure 5b illustrates the stator current spectrum when the motor is fed by a PWM inverter with a supply frequency of 50 Hz. From this spectrum and beside the fundamental harmonic and the imbalance signature of the rotor cage, the spectrum contains more harmonics compared to Fig. 5a. The origin of these additional harmonics is related to the PWM inverter. This demonstrates the high rate of harmonic pollution introduced by the PWM inverter. The presence of harmonics will certainly have a negative effect on fault diagnosis. Indeed, the existence of these harmonics leads to a difficult fault detection, especially if the fault signature is close to these harmonics and if their signatures have very low amplitude as in the case of bearing faults.

6.2 Motor Operating with a Healthy Bearing Fed by Inverter for a Supply Frequency of 30 Hz

This test is performed to demonstrate the effect of the supply frequency variation in the stator current spectrum. To this end, Fig. 6 illustrates the spectrum of stator current of a healthy motor when the motor is fed by a PWM inverter at a supply frequency of 30 Hz. In this spectrum, we can note the existence of the fundamental at the frequency of 30 Hz and the frequency signature of the rotor cage imbalance from either side of the fundamental. Also, we note the existence of harmonics associated with the PWM inverter as shown in Fig. 5b, which makes the bearing fault detection difficult even impossible with this supply frequency.

6.3 Motor Operating with an Outer Race Fault Fed with and Without Inverter for a Supply Frequency of 50 Hz

The aim of this test is to illustrate the difficulty of bearing fault detection when the motor is fed by a PWM inverter. Indeed, Fig. 7 shows the stator current spectrum in the presence of an outer race fault when the motor is supplied directly from the mains (Fig. 7a), and when the motor is supplied by a PWM inverter (Fig. 7b).

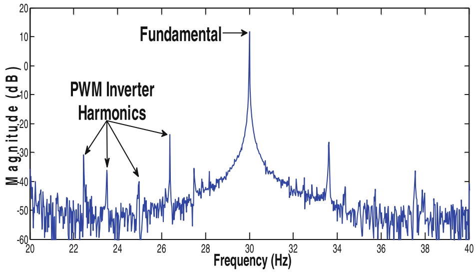

Fig. 6. Stator current spectrum for a supply frequency of 30 Hz with inverter. (Healthy bearing case)

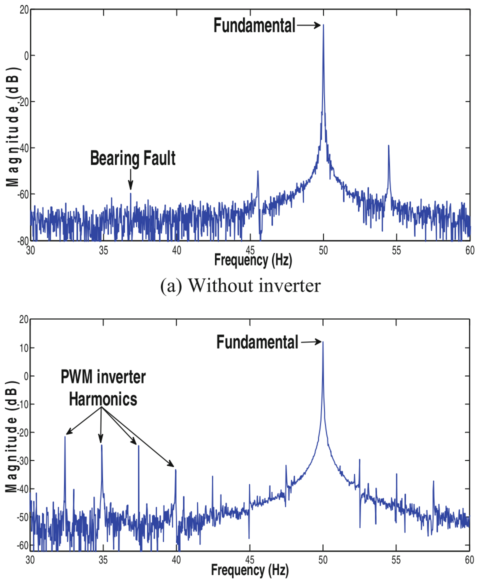

(a) Without inverter

(b) With inverter

Fig. 7. Stator current spectrum for a supply frequency of 50 Hz. (Outer race fault case)

We can notice in these figures the existence of the fundamental frequency and the rotor cage imbalance signature. In addition, we are barely able to detect the outer race fault signature in Fig. 7a because it is slightly higher compared to the other harmonics, while it is impossible to detect the fault signature in Fig. 7b because it is embedded in the harmonics generated by the PWM inverter, which again shows that the bearing fault detection is more difficult even impossible when the motor is fed by a PWM inverter.

6.4 Motor Operating with an Outer Race Fault Fed by Inverter for a Supply Frequency of 30 Hz

The purpose of this test is to show the effect of the inverter in the presence of a bearing failure when the motor is operating at a 30 Hz supply frequency. Therefore, Fig. 8 illustrates the spectrum of the stator current in this case.

It may be noted that the outer race fault signature is impossible to detect because of the harmonics generated by the inverter. Moreover, only the fundamental frequency and rotor cage imbalance signature are detectable on this spectrum. These findings are the same as those observed in Fig. 7b.

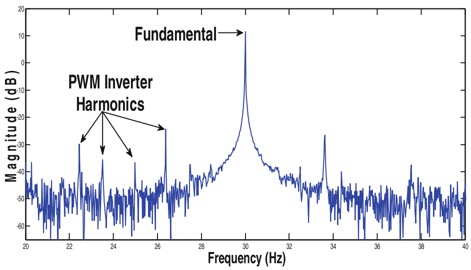

Fig. 8. Stator current spectrum for a supply frequency of 30 Hz with inverter. (Outer race fault case)

To validate the proposed STFT/MLA approach, we apply in the case where the motor is fed by a PWM inverter with a 50 Hz and 30 Hz supply frequencies. Under these conditions, Fig. 9 illustrates the analysis of the stator current using this new approach in the presence of an outer race fault with a supply frequency of 50 Hz (Fig. 9a) and a supply frequency of 30 Hz (Fig. 9b). From these two figures, we clearly notice the fundamental frequency and the rotor cage imbalance signature. Note that the difference between the fundamental frequency and the rotor cage imbalance signature is about 2.7 Hz for a supply frequency of 50 Hz and approximately 1.7 Hz for a supply frequency of 30 Hz. Moreover, there is a slight fluctuation on the rotor cage imbalance for fundamental frequency of 50 Hz, due to a slight change in the motor slip during these tests.

Also we note that the proposed approach allows the detection of the outer race fault signature at 37.4 Hz for a 50 Hz supply frequency and at 21.7 Hz for a 30 Hz supply frequency. These signatures correspond to the fault theoretical signatures seen in Table 1 with a slight difference. This difference may be explained by the measurement error in the speed measurement, the frequency resolution or the change of the motor slip during these tests. These results clearly show the effectiveness of the approach proposed in fault detection and are a validation of the proposed approach in a steady state operating mode (case of stationary signals).

6.5 Motor Operating with an Outer Race Fault Fed by Inverter for a Supply Frequency Variation from 30 Hz to 50 Hz

The purpose of this test is to show the ability and the efficiency of the proposed approach compared to the conventional method in the detection of bearing failures signatures when the frequency changes over time. For this aim, Fig. 10 illustrates the stator current spectrum when the supply frequency varies from 30 Hz to 50 Hz.

This spectrum indicates the existence of two major frequencies observed at 30 Hz and 50 Hz. In this case, we note that it is impossible to detect the rotor cage imbalance and the outer race fault signatures. In addition, this spectrum can not indicate the supply frequency with which we began our tests and that with which we ended. This is the major drawback of this method of analysis of the PSD estimation using Periodogram.

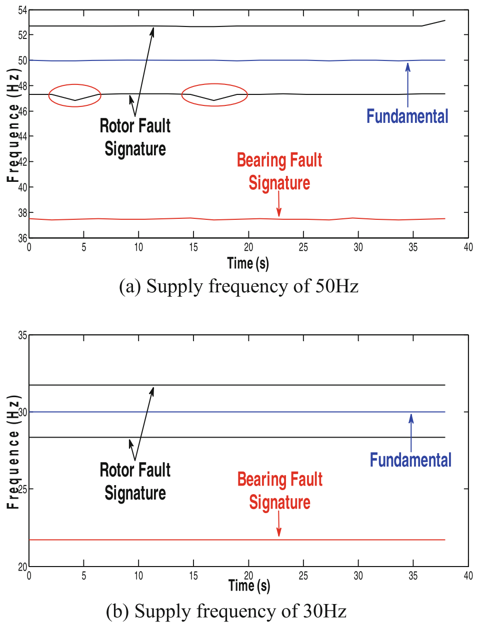

Fig. 9. Stator current Time-Frequency spectrum using the STFT/MLA approach with outer race fault.

Figure 11 shows the time-frequency representation of the stator current obtained the proposed approach of the STFT/MLA association. From this figure, we can validate the ability of the proposed approach in the detection of: the fundamental frequency, the rotor cage imbalance signature and the outer race fault signature. But especially to see their evolution in time.

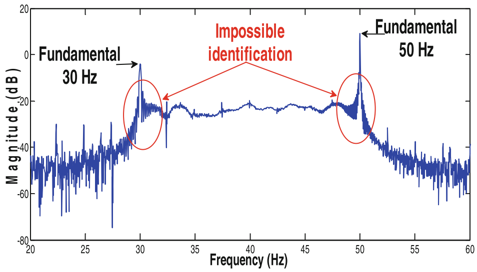

Fig. 10. Stator current spectrum with outer race fault for a supply frequency variation from 30 Hz to 50 Hz

Thus, according to Fig. 11, we see that the supply frequency used at the beginning of the tests is 30 Hz at about 5 s. At this time, a continuous variation of the supply frequency is carried out until 15 s. And from that moment until the end of the tests, the supply frequency is set to 50 Hz. This finding is similar to the signatures behaviour of rotor cage unbalance and the outer race fault. Therefore, no information is lost after the application of the proposed STFT/MLA association unlike the conventional periodogram technique. We can thus see that all failure signatures follow the variation of the supply frequency over time. These results clearly show and validate the capacity and effectiveness of the proposed approach. We note also the improvement of the readability of the time-frequency spectrum using the proposed approach.

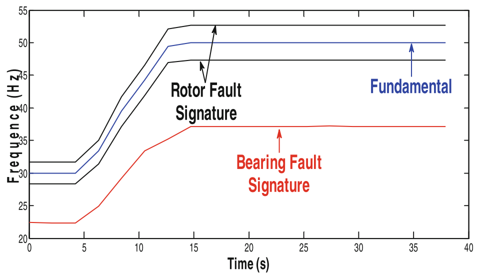

Fig. 11. Stator current Time-Frequency spectrum using the STFT/MLA approach with outer race fault for a supply frequency variation from 30 Hz to 50 Hz

7 Conclusion

The proposed approach in this paper is based on the combination of the time-frequency analysis using the STFT associated to the MLA algorithm for the detection of induction motor bearing faults when the motor is fed by a variable supply frequency through a PWM inverter. The results show the reliability and effectiveness of the proposed solution. Indeed, according to the different plots obtained, we see clearly and precisely the variation of the supply frequency delivered by the PWM inverter. This can therefore tell us about the evolution of the motor speed in time. In addition, this approach also allows us to monitor the fault signatures following the change of the motor speed. This information is of course not possible to detect with the conventional method of the PSD estimation by periodogram.

Appendix. Geometric parameters of rolling-element bearing "Reference zz-6025 coupling opposite side"

Ball diameter D_b	7.835 mm
Cage diameter D_c	38.5 mm
Number of balls N_b	9
Contact angle β	0

References

1. Bonnett, A.H., Yung, C.: Increased efficiency versus increased reliability. Ind. Appl. Mag. IEEE **14**, 29–36 (2008)
2. Boudinar, A.H., Bendiabdellah, A., Benouzza, N., Ferradj, M.: Improved stator current spectral analysis technique for bearing faults diagnosis. In: 16th International Power Electronics and Motion Control Conference and Exposition, Antalya, Turkey, 21–24 September 2014
3. Immovilli, F., Bellini, A., Rubini, R., Tassoni, C.: Diagnosis of bearing faults in induction machines by vibration or current signals: a critical comparison. IEEE Trans. Ind. Appl. **46**, 1350–1360 (2010)
4. Garcia-Perez, A., Romero-Troncoso, R., Cabal-Yepez, E., Osornio-Rios, R.A.: The application of high-resolution spectral analysis for identifying multiple combined faults in induction motors. IEEE Trans. Ind. Electron. **58**, 2002–2011 (2011)
5. Concari, C., Franceschini, G., Tassoni, C.: Differential diagnosis based on multivariable monitoring to assess induction machine rotor conditions. IEEE Trans. Ind. Electron. **55**, 4156–4167 (2008)
6. Aïmer, A.F., Boudinar, A.H., Bendiabdellah, A.: Use of the short time fourier transform for induction motor broken bars detection. In: International Review on Modelling and Simulations, vol. 16, 6th edn., December 2013
7. Jung, J.H., Lee, J.J., Kwon, B.H.: Online diagnosis of induction motors using MCSA. IEEE Trans. Ind. Electron. **53**, 1842–1853 (2006)

8. Mehala, N., Dahiya, R.: Detection of bearing faults of induction motor using park's vector approach. Int. J. Eng. Technol. **2**(4), 263–266 (2010)
9. El Bouchikhi, E., Choqueuse, V., Benbouzid, M.E.H.: Current frequency spectral subtraction and its contribution to induction machines' bearings condition monitoring. IEEE Trans. Energy Convers. **28**(1), 135–144 (2012)
10. Gong, X., Qiao, W.: Bearing fault detection for direct-drive wind turbines via stator current spectrum analysis. In: Proceedings of IEEE Energy Conversion Congress and Exposition (ECCE) (2011)
11. El Bouchikhi, E., Choqueuse, V., Benbouzid, M.E.H.: Induction machine faults detection using stator current parametric spectral estimation. In: Mechanical Systems and Signal Processing, pp. 447–464. Elsevier (2014)
12. Aïmer, A.F., Boudinar, A.H., Bendiabdellah, A., Mokhtar, C.: Effet du fenêtrage sur la résolution de la DSP et son apport dans le diagnostic des défauts rotoriques du moteur asynchrone. In: Proceedings of International Conference on Industrial Engineering and Manufacturing, Batna, 09–10 May 2010, Algeria
13. Amirat, Y., Choqueuse, V., Benbouzid, M.E.H., Turri, S.: Hilbert transform based bearing failure detection in DFIG-based wind turbines. Int. Rev. Electr. Eng. **6**(3), 1249–1256 (2011)
14. Espinosa, A.G., Rosero, A., Cusido, J., Romeral, L., Ortega, J.A.: Fault detection by means of Hilbert–Huang transform of the stator current in a PMSM with demagnetization. IEEE Trans. Energy Convers **25**(2), June 2010
15. Aïmer, A.F., Boudinar, A.H., Benouzza, N., Bendiabdellah, A.: Simulation and experimental study of induction motor broken rotor bars fault diagnosis using stator current spectrogram. In: Proceedings of IEEE 3rd International Conference on Control, Engineering & Information Technology (CEIT), Tlemcen, Algeria, 25–27 May 2015
16. El Ahmar, E., Choqueuse, V., Benbouzid, M.E.H., Amirat, Y., El Assad, J.: Advanced signal processing techniques for fault detection and diagnosis in a wind turbine induction generator drive train: a comparative study. In: Proceedings of IEEE Energy Conversion Congress and Exposition (ECCE), September 2010, Atlanta, United States, pp. 3576–3581 (2010)
17. Climente-Alarcon, V., Antonino-Daviu, J.A., Riera-Guasp, M., Vlcek, M.: Induction motor diagnosis by advanced notch FIR filters and the Wigner-Ville distribution. IEEE Trans. Ind. Electron. **61**(8), 4217–4227 (2014)
18. Henao, H., et al.: Trends in fault diagnosis for electric machines: a review of diagnostic methods. IEEE Ind. Electron. Mag. **8**(2), 31–42 (2014)
19. Yan, R., Gao, R.X., Chen, X.: Wavelets for fault diagnosis of rotary machines: a review with applications. Signal Processing. Elsevier (2014)
20. Llinares, J.P., Antonino-Daviu, J.A., Riera-Guasp, M., Pineda-Sanchez, M., Climente-Alarcon, V.: Induction motor diagnosis based on a transient current analytic wavelet transform via frequency B-splines. IEEE Trans. Ind. Electron. **58**(5), 530–1544 (2011)
21. Bouzida, A., Touhami, O., Ibtiouen, R., Belouchrani, A., Fadel, M., Rezzoug, A.: Fault diagnosis in industrial induction machines through discrete wavelet transform. IEEE Trans. Ind. Electron. **58**(9), 4385–4395 (2011)
22. Gaeid, K.S., Ping, H.W.: Wavelet fault diagnosis and tolerant of induction motor: a review. Int. J. Phys. Sci. **6**(3), 358–376 (2011)
23. Blödt, M., Granjon, P., Raison, B., Rostaing, G.: Models for bearing damage detection in induction motors using stator current monitoring. IEEE Trans. Ind. Electron. **55**, 1813–1823 (2008)

24. Boudinar, A.H., Benouzza, N., Bendiabdellah, A., Khodja, M.: Induction motor bearing fault analysis using root-MUSIC method. IEEE Trans. Ind. Appl. **52**(5), 3851–3860 (2016)
25. Bendiabdellah, A., Boudinar, A.H., Benouzza, N., Khodja, M.: The enhancements of broken bar fault detection in induction motors. In: Proceedings of International Aegean Conference on Electrical Machines & Power Electronics (ACEMP), International Conference on Optimization of Electrical & Electronic Equipment (OPTIM), International Symposium on Advanced Electromechanical Motion Systems (ELECTROMOTION), 02–04 September 2015, Side, Turkey

Signal and Communications (SC)

Adapted LBP Based Fast Image Mosaicing Algorithm for UAV Images

Abdelhai Lati[1(✉)], Mahmoud Belhocine[2], and Noura Achour[1]

[1] Laboratoire de Robotique Parallélisme et Systèmes Embarqués (LRPSE), Université de Sciences et Technologie de Houari Boumedian (USTHB), BP 32, El Alia, Bab Ezzouar, 16111 Algiers, Algeria
{alati,nachour}@usthb.dz

[2] Centre du Développement des Technologies Avancées CDTA, Cité 20 Août 1956, Baba Hassen, 16303 Algiers, Algeria
mbelhocine@cdta.dz

Abstract. UAV images are widely used in many applications, however, there are some problems with these images, e.g. the Field Of View (FOV) of these images is smaller than those of traditional aerial images, and also; the resolution of them is less than those of aerial ones. As a solution for these problems, these images with small views can be mosaiced together in order to increase the visual field and the image resolution. The most important part of image mosaicing algorithm is to find out correspondence points between the split images. Different approaches were proposed for features matching task, but most of them takes a long calculation time and give a lot of false associations. Since the Local Binary Patterns Descriptors (LBPDs) provide good and robust description for the detected key-points in two overlapped images, fast and good features matching can be obtained using the measured Hamming distance between two LBPDs. But LBP approach depends on interpolation technique; which leads to false matching results, therefore, in our proposed algorithm, we will develop Adapted LBPDs in order to overcome drawback of LBP technique.

Keywords: UAV · Image mosaicing · Harris · A LBPDs

1 Introduction

Since many years and even before the age of digital computers, image mosaicing was known. Previously, all images that were made from hilltops or balloons, were manually pieced together, but after the invention and development of airplane technology, and due to the limited flying heights of the first airplanes and the need for large photo maps, professionals were forced to create image mosaics from overlapping photographs [1]. The research on image mosaic technology is widely common in many research fields such as; aerial mapping, space exploration, remote sensing image processing, medical image analysis and other fields, that is why it has become the focus of computer graphics research in recent years.

M. Chadli et al. (Eds.): ICEECA 2017, LNEE 522, pp. 429–442, 2019.
https://doi.org/10.1007/978-3-319-97816-1_32

An Image Mosaic is a synthetic composition generated from a sequence of images and it can be obtained by understanding geometric relationships between images. The geometric relations are the coordinate systems that relates the different image coordinate systems [2].

Constructing image mosaics is an active area of research in the field of computer vision, image processing, and computer graphics. Since many years, image mosaics were used for various applications, and the most traditional application was and still until now; the construction of large aerial and satellite photographs from collections of overlapped images [3].

There exist more recent modern applications for image mosaicing including; scene stabilization, change detection, video compression. The good performance of an image mosaicing algorithm depends primarily on the performance of the used techniques for features detection and matching. The features represent the world as a set of spatially located pixels. When using this kind of representation, the main advantage is that the representation is compact, and therefore suitable for operating in large environments. For that, we are going to study the most important approaches to detect and match invariant and distinctive features from overlapped images.

Our contributions in this paper is to find a solution for areal images because of distortion, illumination conditions and visual field, also we suggest to use classical features detector with modern binary descriptors (LBPDs) and adapt the LBP technique in order to use it in the features matching stage. In this paper we will discuss some works performed in the domain of image mosaicing (Sect. 2); then we will state in (Sect. 3) the necessary stages needed to create a mosaiced image, and we will introduce the general framework of LBP technique (Sect. 4). Our image mosaicing algorithm will be presented in Sect. 5. The obtained results will be presented in Sect. 6. Finally, we will end with some conclusions (Sect. 7).

2 Related Work

In the literature [4], a novel and fast strategy was proposed for registering and mosaicing UAV data (aerial images). Firstly, the total number of the pyramid octaves in scale space was reduced to speed up the matching process; sequentially, RANSAC (Random Sample Consensus) issued to eliminate the mismatching tie points. Then, bundle adjustment was introduced to solve all of the camera geometrical calibration parameters jointly. Finally, the best seam line searching strategy based on dynamic schedule was applied to solve the dodging problem arose by aero plane's side-looking.

In [5], the goal of this research was to estimate the homography matrices that can precisely register UAV images onto the Google satellite map with less distortion. It may perform image registration between consecutive UAV images by using the scale invariant feature transform (SIFT) techniques. In contrast, for UAV-to-Google image registration, it was a great challenging task due to quality mismatch.

The PhD project of NEMRA Abdelkrim which was done in Cranfield University in 2010 [6] presents robust solutions to technical problems of airborne three-dimensional (3D) Visual Simultaneous Localization And Mapping (VSLAM). These solutions were developed based on a stereovision system available onboard Unmanned Aerial Vehicles (UAVs). The proposed airborne VSLAM enables unmanned aerial vehicles to construct a reliable map of an unknown environment and localize themselves within this map without any user intervention.

3 Construction of Image Mosaic

3.1 Features Detection

The concept of features has been widely used in order to solve many problems in computer vision domain such as image registration, and visual tracking. The main advantage of features detection is selecting special parts in the image and doing the desired analysis on them. The most desired features are points, because their coordinates can be directly used to determine the parameters of a transformation function that registers the images [7, 8]. In some images it may not be possible to detect point features; however, lines or regions may be detected. In such situations points are derived from the lines and regions. For example, both intersections of corresponding line pairs produce corresponding points. These types of primitives are the most desired features, because they can be easily visible and can be detected using simple detectors.

3.2 Features Matching

Once the interest points have been found,, the overlapping images can be identified by establishing the correspondences (matching) between all image pairs. The matching is to find for each point of an image, its correspondent in the other image knowing that the image points are projections of the real 3D points of the same scene. Several matching methods were proposed in the literature. Mainly, there are known methods based on correlation comparison criteria, there are other methods based on a comparison between the features descriptors (Descriptor based matching) and other methods based on tracking points of interest (Optical flow) [9].

3.3 Image Transformation

There are many situations in computer vision where estimating a one of the image transformations may be required. In our case, for image mosaicing; we need a transformation model to project two overlapped image on each other to create an image mosaic, therefore; the projective transformation (homography) is the most suitable model for our purpose.

The estimation of the homography between two views is a key step in many applications involving multiple view geometry. The homography exists between two views between projections of points on a 3D plane [6].

3.4 Image Warping

Image warping is the act of distorting a source image into a destination image according to a mapping between source image I(x, y) and destination image I′(x, y). The mapping is usually specified by the function I′(x, y) = T(I(x, y)).

Images aligned after undergoing geometric corrections most likely require further processing to eliminate remaining distortions and discontinuities. Alignment of images may be imperfect due to registration errors resulting from incompatible model an assumption. Image warping stage can be divided into two approaches which are image re-projection then image blending.

4 Adapted Local Binary Patterns Descriptors

4.1 Local Binary Patterns

Local Binary Patterns (LBP) algorithm is a binary system description which expresses the relationship of size of a gray image pixel point and its neighborhood pixels points; it was originally used to describe image texture information. Nowadays, research workers put forward a lot of improved LBP algorithm which has been applied in features matching; face recognition, etc. because of its simple computation complexity and partial scale, rotation, and illumination invariance [10].

4.2 Adapted LBP Features Descriptors

The original LBP operator labels the pixels of an image with decimal numbers, called Local Binary Patterns or LBP codes, which encode the local structure around each pixel. So, to describe pixel points, it should be compared with its N neighbors, however; if we want to take N greater than 8 in circular way around the pixel; some interpolations need to be done [11], this may lead to some errors, thus, in our method we propose to adapt LBPDs and avoid these interpolations. Creating the ALBP descriptors is summarized below:

(1) For the nearest 8 neighborhoods, the gray values of their pixel points should be compared with the gray value of the central pixel point. According to the comparison sign value, binarization can be done to those 8 neighborhood pixel points, i.e. If a pixel point's gray value is greater than the central pixel point's, the gray value will be set to 1, and if a pixel point's gray value is less than the central pixel point's, the gray value will be set to 0.
(2) For the second nearest 8 neighborhoods, such that the distance between old neighbor pixels and new neighbor pixels is one pixel we repeat all procedures done in step 1.
(3) For the third, fourth …, Nth nearest 8 neighborhoods, such that the distance between old neighbor pixels and new neighbor pixels is one pixel, we repeat step 1.
(4) We concatenate the obtained all eight binarized vector obtained from step (1, 2, and 3) to get N*8 binary vector.
(5) After the binarization, the obtained binarized gray values of the eight neighborhood pixel points should be multiplied by weight matrix as shown in (Fig. 1).

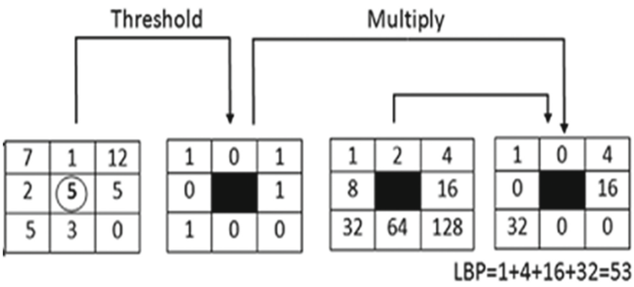

Fig. 1. The steps to create LBP feature descriptor (P = 8, R = 1).

(6) The decimal numeral after adding the eight values up is LBP = 1 + 2 + 4 + 16 = 23. And the binary vector is LBP = (10110010).

A local neighborhood is defined as a set of sampling points evenly spaced on a circle which is centered at the pixel to be labeled, and to deal with the sampling points that do not fall within the pixels, we proposed taking always eight pixels that do not need to be interpolated using bilinear interpolation, thus allowing for any radius and large number of sampling points in the neighborhood [11–13].

Figure 2 shows how to take at each step only eight neighbor pixels with exact pixel values instead of taking all neighbor pixels and interpolating values of some pixels.

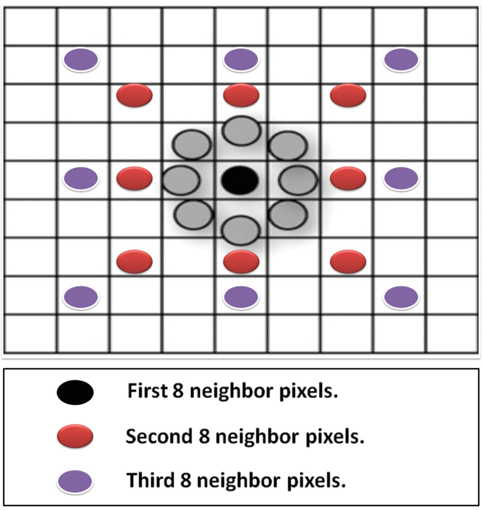

Fig. 2. LBPDs for different values of points (P) and radius (R).

For any radius and any number of sampling points in the neighborhood, the local binary patterns code for a pixel located at coordinate (x_c, y_c) can be defined in Eq. (1) as:

$$LBP_{N,R}(x,y) = \sum_{p=0}^{N-1} S(g_p - g_c)2^p$$
$$\{S = 1 \; if \; g_p \succ g_c \quad and \quad S = 0 \; if \; g_p \prec g_c \tag{1}$$

Where:

$\boldsymbol{g_c}$ is the central pixel.
$\boldsymbol{g_p}$ is the neighbor pixel.
$\boldsymbol{P}$ is the order of surrounding pixel.

4.3 Efficient Distance Matching for ALBP Descriptors

Given binary vectors for all features in the overlapped images, we can efficiently compare them. Unlike standard feature descriptors which undergo a large variety in descriptive power. For two feature points, $\mathrm{p_{ij}}$ and $\mathrm{p_{i'j'}}$ from images i and i′ respectively, we can compute the matching distance as defined in Eq. (2) [11]:

$$d_S(p_{ij}, p_{i'j'}) = d_{ham}(\widehat{h}_{ij}, \widehat{h}_{i'j'}) \tag{2}$$

Where:

$d_{ham}(a, b)$ is the Hamming distance between the two binary vectors a and b $(\widehat{h}_{ij}, \widehat{h}_{i'j'})$.

If two features are compared, small distance value context between them is a sign of good match ability. Although in the ideal case the binary vectors of the matched features should be completely coinciding, some relaxation should be made to avoid mismatching due the noise in the binary vectors. For that, we define features to have a potential to be matched if their matching distance is smaller than a threshold $\mathrm{t_{ham}}$.

5 A LBP Based Image Mosaicing Algorithm

Indeed, there are several algorithms and architectures that can be adopted for image mosaicing. For algorithms design, instead of using Harris corner detector, SIFTS or SURF detectors/descriptors can be used. The simplicity of the algorithm is one of the main things that we have focused on. So we have chosen a simple corner detector (Harris). The following diagram (Fig. 3) shows the basic followed stages in order to build our system of image mosaicing.

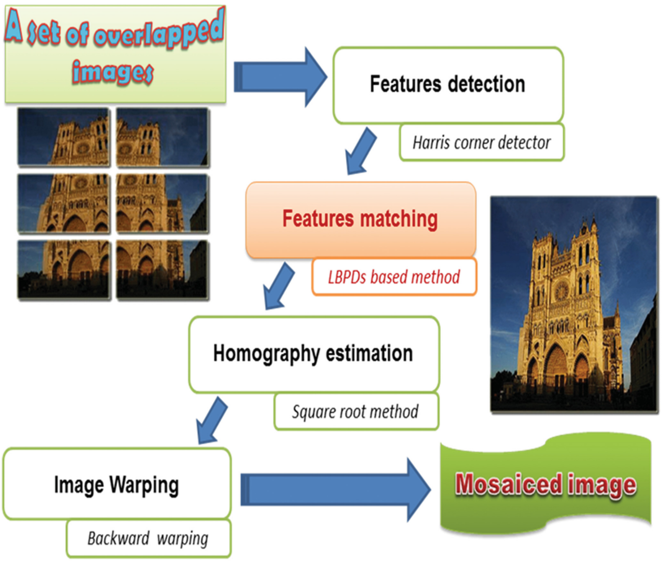

Fig. 3. The main stages of image mosaic construction.

5.1 Features Detection

5.1.1 Harris Corner Detector

Harris corner detector has been proposed by Harris C and Stephens MJ in 1988, It is based on the local auto correlation function of a signal [14, 15]. The corners image features are discrete, reliable and meaningful, therefore; they were involved in several computer vision application since a long time. The basic idea of this detector is the necessity of easily recognizing the point by looking at intensity values within a small window and by shifting the window in any direction; we should have a large change in appearance.

5.1.2 Algorithm of Harris Corner Detector

The algorithm behind the Harris Corner Detector is as follows:

1. Computing derivatives Ix and Iy for the image, where Ix and Iy are partial derivatives of I(x, y). Computing partial derivatives Ix (x, y), Iy(x, y) by finite differences:

$$\mathrm{Ix}(x,\ y) \approx \mathrm{I}(x + 1,\ y) - \mathrm{I}(x,\ y) \text{ and } \mathrm{Iy}(x,\ y) \approx \mathrm{I}(x,\ y + 1) - \mathrm{I}(x,\ y)$$

2. Constructing cornerness map.
   (a) Computing autocorrelation matrix for each pixel:

$$M = \begin{pmatrix} A & C \\ C & B \end{pmatrix} \tag{3}$$

$$A = \left(\sum_i \frac{\partial I_i}{\partial x}\right)^2 \quad B = \left(\sum_i \frac{\partial I_i}{\partial y}\right)^2 \quad C = \left(\sum_i \frac{\partial I_i}{\partial x}\frac{\partial I_i}{\partial y}\right)$$

For all $\boldsymbol{i}_s$ in the window.

(b) Computing cornerness measure MSc:

$$MSc(x, y) = \det(M) - k(trace(M))^2 \tag{4}$$

or

$$MSc(x, y) = \frac{\det(M)}{trace(M)} \tag{5}$$

Where:

- K is a constant (usually 0.04)
- $\det(M) = \lambda_1\lambda_2 = AB - C^2$
- $trace(M) = \lambda_1 + \lambda_2 = A + B$

3. Constructing threshold cornerness map:
   - if MSc(x, y) < threshold then MSc(x, y) = 0
     Where MSc(x, y) is the cornerness measure of the pixel (x, y).

5.2 Features Matching

5.2.1 ALBP Based Features Matching

From the description of Local Binary Descriptors (LBDs), it is clear that they involve only simple arithmetic operations. Furthermore, the distance between two LBDs is measured using the Hamming distance, which is a simple bitwise exclusive or (XOR) instruction [16]. Hence, computation and matching of LBDs can be implemented efficiently. Since they also provide good matching performances, LBDs are getting more and more popular over SIFT and SURF: combined with FAST or Harris for the keypoint detection, they provide a fast and efficient feature extraction and matching.

In our case, we have concatenated a set of 8 bits LPBDs in order to get longer ALPBDs with more information, these ALPBDs help for removing most of false associations.

5.2.2 Outliers Rejection

With the used features matching technique, we have verified the bidirectional condition; as shown in Fig. 4; in order to remove the pairs of false matching.

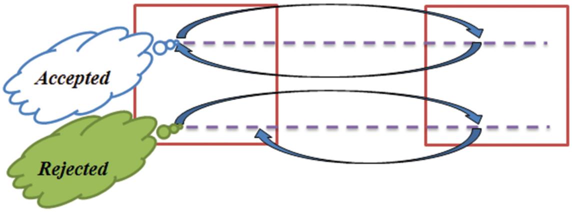

Fig. 4. Bidirectional condition for correct matching.

5.3 Image Transformation

5.3.1 Homography Estimation

Various methods for computing a planar homography between image pairs have been proposed, but they generally fall into two broad categories: first, direct correlation methods compute the homography by maximizing photometric consistency over the whole image. Second, feature based methods compute the homography from a sparsely distributed set of point-to-point correspondences.

Almost exclusively, the results presented in this paper were generated using feature based registration methods. Feature based techniques have many significant advantages over their direct correlation counterparts in terms of computation speed, and the scope that they offer for the application of robust statistical methods for outlier rejection [9]. The planar homography has 8 degrees of freedom. Each point correspondence generates 2 linear equations for the elements of H and hence 4 correspondences are enough to solve for the homography directly.

If more than 4 points are available, a least-squares solution can be found by linear methods. From the definition of H, we have:

$$\begin{pmatrix} x' \\ y' \\ 1 \end{pmatrix} = \begin{bmatrix} h_{11} & h_{12} & h_{13} \\ h_{21} & h_{22} & h_{23} \\ h_{31} & h_{32} & h_{33} \end{bmatrix} \begin{pmatrix} x \\ y \\ 1 \end{pmatrix} \tag{6}$$

Where = is equality up to scale. Each inhomogeneous, 2D point correspondence generates two linear equations in the elements of H.

$$\begin{aligned} x'(h_{31}x + h_{32}y + h_{33}) - h_{11}x - h_{12}y - h_{13} = 0 \\ y'(h_{31}x + h_{32}y + h_{33}) - h_{21}x - h_{22}y - h_{23} = 0 \end{aligned} \tag{7}$$

Hence, N points generate $2N$ linear equations, which may be arranged in a “design matrix” as follows:

$$AH = 0 \tag{8}$$

The solution for H is the one-dimensional kernel of A, which may obtained from the SVD. For N > 4 points, this equation will not have an exact solution. In this case, a solution may be obtained which minimizes the *algebraic residuals*, $r = AH$, in a least-squares sense, by taking the singular vector corresponding to the smallest singular value.

5.4 Image Warping

5.4.1 Backward Image Warping

After homography estimation for each scene, we have used this transformation matrix to warp images. First, we have determined bounds of the new combined image and where the corners of left image would fall in the coordinate frame of the right image. This was done by multiplying transformation matrix on the corner point coordinates. Then we have attempted to lookup colors for any of these positions we got from the left image as given by this equation:

$$x = H^{-1} * x' \tag{9}$$

Inverse transformation has been used to compute coordinates in left image's reference frame for all points in that range. Interpolation technique has been needed to lookup all colors in these positions from the left image.

6 Results, Analysis and Discussions

In our work, we have tested our image mosaicing algorithms on real UAV images; we have used the points based feature for both features detection and matching processes (Figs. 5, 6). Figure 3 shows the main steps of image mosaic construction from multiple overlapped images. Matlab is a powerful software platform which can be used for the development of several applications. In our case, due to the provided image processing predefined functions with Matlab toolbox; Matlab software is suitable for the development of complex image processing algorithms such as image mosaicing algorithm. To test the proposed image mosaicing algorithms, we have used Matlab running on a computer that disposes 4 GB of RAM, CPU of Intel i7 generation and Intel graphic card. We tested our image mosaicing approaches on the images of Aerial Robotics Data sets [17], and we have compared our obtained results as shown in Table 1.

Fig. 5. The two aerial overlapped images captured by UAV

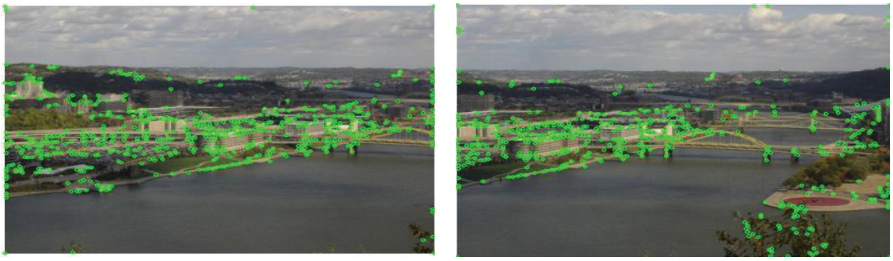

Fig. 6. Features detection using Harris corner detector.

In this paper, we have developed an image mosaicing algorithm which can create large image mosaics from a set of overlapped aerial images. First, the entire previous image which had feature matches with the new image was taken into account during the homography estimation by utilizing Local Binary Patterns (LBP) matching method. Second, bidirectional technique was used to remove the obtained false associations among the matched features. Third, the parameters of homography matrix were estimated using Least Square Theorem (LST). Finally, backward warping with an interpolation technique were used to align and blend the overlapped images (Figs. 7, 8 and 9).

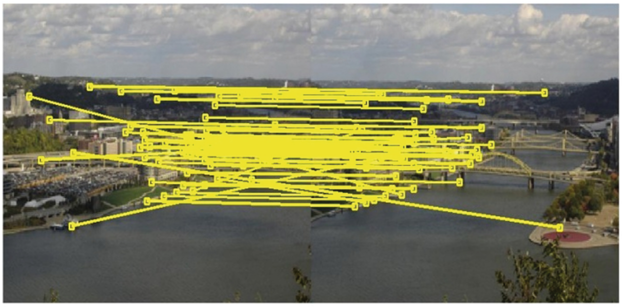

Fig. 7. Features matching using LBPDs based method.

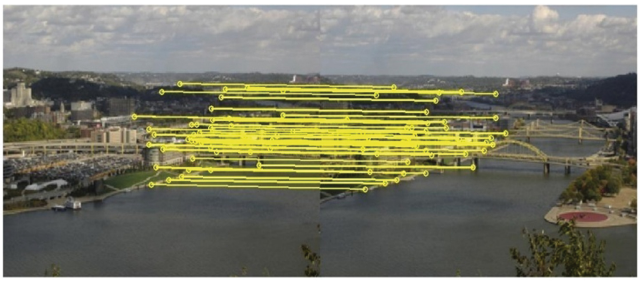

Fig. 8. Features matching using CLBPDs and bidirectional condition.

Fig. 9. The obtained image mosaic.

The following table summarizes the comparison of our simulation results and compares it to other results obtained by using the same simulation platform and tool.

As we can notice from the above table CLBPDs provides more correct associations with less computation time.

Table 1. The obtained simulation results.

Matching by	Matched features		Time
	Good matching	Wrong matching	
Correlation criteria	7	975	10.6785 s
SIFT/SURF descriptors	23	5	0.1570 s
ALBP descriptors	56	3	0.4991 s

7 Conclusions and Future Work

After applying our proposed algorithm on different sequence of images, we have achieved high mosaicing accuracy, and the execution time has been improved when comparing it with sequential execution on the images.

Our method was also compared visually and numerically with recent state-of-the-art algorithm in the literature. Performance evaluations in terms of computation time show success of our algorithm. In [18], after using SIFT point detector for extracting images salient elements, the BRIEF descriptor was used to describe and match key-points. The matching result, which was obtained from [18] shows that, to get 19 correct associations between two overlapped images, it takes about 1.9165 s, however, in our algorithm, 56 correct associations can be got in 0.4991 s. This big difference in calculation time is due to the simplicity of calculation by using LBP Descriptors; contrary to SIFT/BRIEF descriptors.

Despite many successful applications on image mosaicing, there are still some restrictions in automatic mosaicing which have a lasting impact on the output time and quality. The most important one is that well-doing the four different steps of mosaicing are time-consuming, that is the more time each step consume, the more quality it performs, so that it is much troublesome to balance time efficiency and quality over each step. Our algorithm tries to minimize the time of matching process

As future works, we recommend using other type of areal images, as IR images; also we plan to develop our algorithm for doing image mosaicing for more than two images (a set of overlapped images).

References

1. Bheda, D., Joshi, M., Agrawal, V.: A study on features extraction techniques for image mosaicing. Int. J. Innov. Res. Comput. Commun. Eng. **2**(3), 3432–3437 (2014)
2. Joshil, H., Sinha, K.: A survey on image mosaicing techniques. Int. J. Adv. Res. Comput. Eng. Technol. **2**(2), 365–369 (2013). ISSN 2278-1323
3. Shum, H.-Y., Szeliski, R.: Panoramic image mosaics. In: Proceedings of the 24th Annual Conference on Computer Graphics and Interactive Techniques (SIGGRAPH'1997), New York, USA, pp 251–258 (1997)
4. Li, M., Li, D., Fan D.: A study on automatic UAV image mosaic method for paroxysmal disaster. International Archives of the Photo grammetry, Remote Sensing and Spatial Information Sciences, Melbourne, Australia (2012)
5. Chou, C.-C., Huang, S.-M., Huang, C.-C.: Image registration among UAV image sequence and Google satellite image under quality mismatch. In: The 12th International Conference on ITS Telecommunication, pp. 311–315 (2012)
6. Nemra, A.: Robust airborne 3D visual simultaneous localisation and mapping. Ph.D. Thesis. Cranfield University (2010)
7. Azzari, P., Stefano, L.D., Mattoccia, S.: Mosaicking an evaluation methodology for image mosaicing algorithms. In: Advanced Concepts for Intelligent Vision Systems. Lecture Notes in Computer Science, vol. 5259, pp. 89–100 (2008)
8. Goshtasby, A.A.: 2-D and 3-D Image Registration for Medical, Remote Sensing, and Industrial Applications. Wiley, Hoboken (2005)
9. Capel, D., Zisserman, A.: Automated mosaicing with super-resolution zoom. Robotics Research Group, Department of Engineering Science. University of Oxford Oxford OX1 3PJ, UK (1998)
10. Ning, S., Zhenhai, J., Cairong, Z.: Gender classification based on local binary pattern. J. Huazhong Univ. Sci. Technol. **35**, 177–181 (2007). (in Chinese)
11. Ojala, T., Pietikäinen, M., Maenpaa, T.: Multiresolution gray-scale and rotation invariant texture classification with local binary patterns. IEEE Trans. Pattern Anal. Mach. Intell. **24**(7), 971–987 (2002)
12. Jin, H., Liu, Q., Lu, H., Tong, X.: Face detection using improved LBP under Bayesian framework. In: Proceedings of the 3rd International Conference on Image and Graphics, (ICIG), Hong Kong, China, pp. 306–309 (2004)
13. Hafiane, A., Seetharaman, G., Zavidovique, B.: Median binary pattern for textures classification. In: Proceedings of the 4th International Conference (ICIAR), Montreal, Canada. Lecture Notes in Computer Science, vol. 4633, pp. 387–398 (2007)
14. Lee, J.-N., KwakA, K.-C.: Trends analysis of image processing in unmanned aerial vehicle. Int. J. Comput. Electr. Autom. Control Inf. Eng. **8**(2), 271–274 (2014)
15. Carnie, R., Walker, R., Corke, P.: Image processing algorithms for UAV "Sense and Avoid". In: International Conference on ICRA, pp. 2848–2853 (2006)

16. Zhou, Z.: FPGA implementation of computer vision algorithm. A thesis submitted in partial satisfaction of the requirement for the degree of Master of Science in Electrical Engineering. University of California (Riverside) (2014)
17. AerialRobotics Dataset. ftp://www.aerialrobotics.eu/
18. Kekec, T., Yildirim, A., Unel, M.: A new approach to real-time mosaicing of aerial images. Elsevier J. Robot. Auton. Syst. (2016)

A Novel Segmentation Algorithm Based on Level Set Approach with Intensity Inhomogeneity: Application to Medical Images

Messaouda Larbi[1(✉)], Zoubeida Messali[2], Tarek Fortaki[1], and Ahmed Bouridane[3]

[1] Department of Science and Technology, University of Batna, Batna, Algeria
larbi_messaouda@yahoo.fr

[2] Department of Science and Technology, Laboratoire de Génie Electrique LGE, M'sila, University of Bordj Bou Arreridj, Bordj Bou Arreridj, Algeria
zoubeidamessali@yahoo.fr

[3] Department of Computer Science and Digital Technologies, Engineering and Environment, Northumbria, University at Newcastle, Newcastle upon Tyne, UK
ahmed.bouridane@northumbria.ac.uk

Abstract. Most image segmentation techniques are based on the intensity homogeneity. Intensity inhomogeneity frequently occurs in real word image like medical images. This type of images fails to provide accurate segmentation result; this is challenging issue. In this paper, we present a robust region-based method for image segmentation, which is able to deal with intensity inhomogeneities in the images. This method derives a local intensity clustering property of the image based on the model of images with intensity inhomogeneities, and then defines a local clustering criterion function in the neighborhood of each point. In a level set formulation, this criterion defines energy in terms of the level set function and a bias field. The level set functions represent a partition of the image domain whereas a bias field accounts for the intensity inhomogeneity of the image. Therefore by minimizing this energy, our proposed method is able to simultaneously segment the image and estimate he bias field, and the estimated bias field can be used for intensity inhomogeneity correction. Finally, experiments on some medical images have demonstrated the efficiency and robustness of the presented model.

Keywords: Image segmentation · Level set methods · Intensity inhomogeneity Medical images

1 Introduction

Image segmentation is a technique for partitioning an image into uniform and non-overlapping regions based on some similar measure [1]. It has been used in the fields including computer vision, medical images, image analysis and so on. Different segmentation methods have been developed for extraction of organ contours in medical images because it is assumed that contours and the shape of an organ form a very good means to study it. However, in the medical domain, the segmentation of images is

M. Chadli et al. (Eds.): ICEECA 2017, LNEE 522, pp. 443–451, 2019.
https://doi.org/10.1007/978-3-319-97816-1_33

complicated. The segmentation approaches differ from one modality of medical images, to another. In other words, the process for segmentation should be carried out, according to a modality of acquisition (scanners, radiography, Magnetic Resonance Images). Active contour models ACM (snakes or deformable models) have been widely used in image processing and computer vision applications [2, 3]. They have become a well-established tool in the segmentation stage [1, 2]. The original Active contour models ACM proposed by Kass et al. [4] is one of the most successful methods. The basic concept, is to move explicit parametric curves to extract objects in images. The level set method later proposed by Osher and Sethian [5] implicitly represents the curve by the zero level of a high dimensional function. This method can be categorized into partial differential equation (PDE). Recently, region-based level set methods [6–9] have been proposed and applied to image segmentation field by incorporating region-based information into the energy functional. Unlike edge-based level set methods using image gradient, region-based methods usually utilize the global region information to stabilize their responses to local variations (such as weak boundaries and noise). Thus, they can obtain a better performance of segmentation than edge-based level set methods, especially for images with weak object boundaries and noise. Among the region-based methods, Chan-Vese model [6] is a representative and popular one. CV model has achieved good performance in image segmentation task due to its ability of obtaining a larger convergence range and handling topological changes naturally. However, it still has the intrinsic limitation, i.e., it generally works for images with intensity homogeneity. The reason is due to that the intensities in each region are assumed to maintain constant. Thus, it often leads to poor segmentation results for images with intensity inhomogeneity due to wrong movement of evolving curves guided by global image information.

In this paper, we present a level set method for image segmentation with intensity inhomogeneity. By exploiting the local image region statistics, we define a mapping from the original image domain to another domain in which intensity probability model is more robust to noise while suppressing the intensity overlapping to some extent. the present method can be applied to simultaneous tissue segmentation and bias correction for medical images.

The paper is structured as follows: In Sect. 2, we briefly review the problem of intensity inhomogeneity. The proposed model of image segmentation, is presented in Sect. 3. Results and discussions of implementation issues of the considered methods are presented in Sect. 4. The main conclusion of this work is given in Sect. 5.

2 Intensity Inhomogeneity

Intensity inhomogeneity (IIH) (also termed as the intensity nonuniformity, the bias field, or the gain field in the literature) usually refers to the slow, nonanatomic intensity variations of the same tissue over the image domain. It can be due to imaging instrumentation (such as radio-frequency nonuniformity, static field inhomogeneity, etc.) or the patient movement [10–12]. This artifact is particularly severe in MR images captured by surface coils.

Let $\boldsymbol{x}$ denote the measured intensity and x' the true intensity. Then the most popular model in describing the IIH effect is:

$$\boldsymbol{x} = \boldsymbol{\alpha x}' + \boldsymbol{\varepsilon} \tag{1}$$

Where $\boldsymbol{\alpha}$ denotes the IIH effect and $\boldsymbol{\varepsilon}$ the noise.

To simplify the computation, one often ignores the noise and takes the logarithmic transform of intensity:

$$y_i = \log x_i = logx_i' + log\alpha_i = y_i' + \beta_i \tag{2}$$

In general, the presence of IIH can significantly reduce the accuracy of image segmentation and registration, hence decreasing the reliability of subsequent quantitative measurement. A number of techniques have been proposed to deal with this issue. In general, if a map of the IIH in the image domain is known or can be estimated, then it is simple to correct the IIH by division in (1) or subtraction in the log-domain (2). One can obtain the IIH map from measurement in vivo [13–15], typically of a uniform phantom, which often requires extra measurement (and increases the scanning time) or needs additional hardware which may not be readily available in some clinical departments. Also there are theoretical modeling approaches [16–19] to approximate the IIH map. However, due to the complexity that causes the IIH, it is difficult to model the IIH under a variety of imaging conditions. In particular, the object-induced IIH is hard to be accounted for by phantom study or theoretical modeling.

More often, the IIH map is derived retrospectively from the image data alone. A number of research efforts have been put in this direction and many techniques have been proposed. Popular mathematical models for IIH description can be classified as follows:

- Low-frequency model, which assumes the IIH to constitute low-frequency components in frequency domain and the IIH map can be recovered by lowpass filtering;
- Hypersurface model, which fits the IIH map by a smooth functional, whose parameters are usually obtained using regression;
- Statistical model, which assumes the IIH to be a random variable or a random process and the IIH map can be derived through statistical estimation;

3 Proposed Method: Statistical Model of Intensity Inhomogeniety (SMII)

3.1 Bias Field Formulation

Let $\mathbf{B}(\mathbf{x}) : \boldsymbol{\Omega} \to \boldsymbol{IR}$ be an unknown bias field, $\mathbf{J}(\mathbf{x}) : \boldsymbol{\Omega} \to \boldsymbol{IR}$ be the true signal to be restored, and $\boldsymbol{N}(\boldsymbol{x}) : \boldsymbol{\Omega} \to \boldsymbol{IR}$ be additive Gaussian noise with zero-mean. As illustrated by Fig. 1, we consider the following model of intensity inhomogeneity [20, 21]:

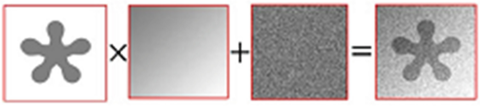

Fig. 1. Illustration of the image model of intensity inhomogeneity. Left to right: the true signal J (x), the bias field function B(x), the noise N(x), and the observed image I(x).

$$\boldsymbol{I}(x) = \boldsymbol{B}(x)\boldsymbol{J}(x) + \boldsymbol{N}(x) \tag{3}$$

The generally accepted assumption on the bias field is that it is smooth (or slowly varying). Ideally, the intensity J in each tissue should take a specific value C_i of the physical property being measured (e.g. the proton density for MR images).

In general, we assume that the true image J and the bias field b have the following properties:

- **(P1)** The bias field b is slowly varying in the entire image domain.
- **(P2)** The true image intensities J are approximately a constant within each class of tissue, i.e. $J(x) \approx C_i$ for $x \in \Omega_i$, with $\{\Omega\}_{i=1}^{N}$ being a partition of Ω.

3.2 Local Intensity Clustering Property

Region-based image segmentation methods typically depend on a specific region descriptor of the intensities in each region to be segmented. For image corrupted due to intensity inhomogeneity, it is difficult to give a region descriptor. This also leads to one more problem of overlap between the distributions of the intensities in the $\Omega_1, \Omega_2, \ldots\ldots\Omega_N$. regions. Hence the task of efficient segmentation based on the pixel intensities is incoherent. However, the property of local intensities is simple, which can be effectively used in the formulation of the level set method for image segmentation with simultaneous estimation of the bias field.

3.3 Energy Formulation

The local intensity clustering property explained above exemplifies that the intensities in the neighborhood can be classified into $\boldsymbol{N}$ clusters, with centres $\boldsymbol{m_i} \approx \boldsymbol{b}(\boldsymbol{y})\boldsymbol{c_i}, \boldsymbol{i} = 1, \ldots., \boldsymbol{N}$. This allows us to apply the standard K-means clustering to classify these local intensities. Specifically, for the intensities $\boldsymbol{I}(\boldsymbol{X})$ the neighborhood $\boldsymbol{O_y}$, the K-means algorithm is an iterative process to minimize the clustering criterion [22], which can be written in a continuous form as:

$$\boldsymbol{F_y} = \sum\nolimits_{i=1}^{N} \int_{\boldsymbol{O_y}} |\boldsymbol{I}(\boldsymbol{x}) - \boldsymbol{m_i}|^2 \boldsymbol{u_i}(\boldsymbol{x})\boldsymbol{dx} \tag{4}$$

Where;

$\boldsymbol{m_i}$ is the cluster center of the i-th cluster,

u_i is the membership function of the region $\boldsymbol{\Omega_i}$ to be determined, i.e. $\boldsymbol{u_i}(\boldsymbol{x}) = 1$ for $\boldsymbol{x} \in \boldsymbol{\Omega_i}$ and $\boldsymbol{u_i}(\boldsymbol{x}) = 0$ for $x \notin \Omega_i$

In view of the clustering criterion in (3) and the approximation of the cluster center by $m_i \approx b(y)\, c_i$, we define a clustering criterion for classifying the intensities in O_y as:

$$\boldsymbol{\varepsilon_y} = \sum\nolimits_{i=1}^{N} \int_{\boldsymbol{\Omega_i} \cap \boldsymbol{O_y}} \boldsymbol{K}(\boldsymbol{y}-\boldsymbol{x})|\boldsymbol{I}(\boldsymbol{x}) - \boldsymbol{b}(\boldsymbol{y})\boldsymbol{C_i}|^2 \boldsymbol{dx} \tag{5}$$

Where;

$k(\boldsymbol{y}-\boldsymbol{x})$ is introduced as a nonnegative window function, also called kernel function, such that $k(\boldsymbol{y}-\boldsymbol{x}) = 0$ for $x \notin O_y$. With the window function, the clustering criterion function ε_y can be rewritten as:

$$\varepsilon_y = \sum\nolimits_{i=1}^{N} \int_{\Omega_i} K(y-x)|I(x) - b(y)C_i|^2 dx \tag{6}$$

The local clustering criterion function $\boldsymbol{\varepsilon_y}$ evaluates the classification of the intensities in the neighborhood o_y given by the partition $\left\{O_y \cap \Omega_i\right\}_{i=1}^{N}$ of o_y. The smaller the value of ε_y, the better the classification. Naturally, we define the optimal partition $\{\Omega_i\}_{i=1}^{N}$ of the entire domain Ω as the one such that the local clustering criterion function ε_y is Minimized for all y in Ω. Therefore, we need to jointly minimize ε_y for all y in Ω. This can be achieved by minimizing the integral of ε_y with respect to y over the image domain Ω. Therefore, we define an energy $\varepsilon \triangleq \int \varepsilon_y dy$, i.e.,

$$\varepsilon \triangleq \int \left(\sum\nolimits_{i=1}^{N} \int_{\Omega_i} K(y-x)|I(x) - b(y)C_i|^2 dx \right) dy \tag{7}$$

The choice of the kernel function K is flexible, it is preferable to use a weighting function K(x − y) such that larger weights are assigned to the data $I(y)$ for y closer to the center x of the neighborhood o_x. In this paper, the weighting function K is chosen as a truncated Gaussian kernel:

$$K(u) = \begin{cases} \dfrac{1}{a}\, e^{-|u|^2/2\sigma^2} & for\,|u| \le \rho \\ 0 & else \end{cases} \tag{8}$$

Where:
$a\psi$ is a constant
σ is the standard deviation (or the scale parameter) of the Gaussian function,
ρ is the radius of the neighborhood O_y.

4 Experimental Results

In this section we discuss the performances of the considered segmentation method (SMII).

4.1 Data Sets

We have used three data sets of medical images with different modalities. These images present Brain MRI image obtained from [24], Arms_Xray image obtained from [23], and computed tomography (CT) image of a tumor in a liver obtained from [24]. Note that the discussed algorithms are implemented in Matlab 2016. b on 2.79-GHz Intel Pentium IV PC.

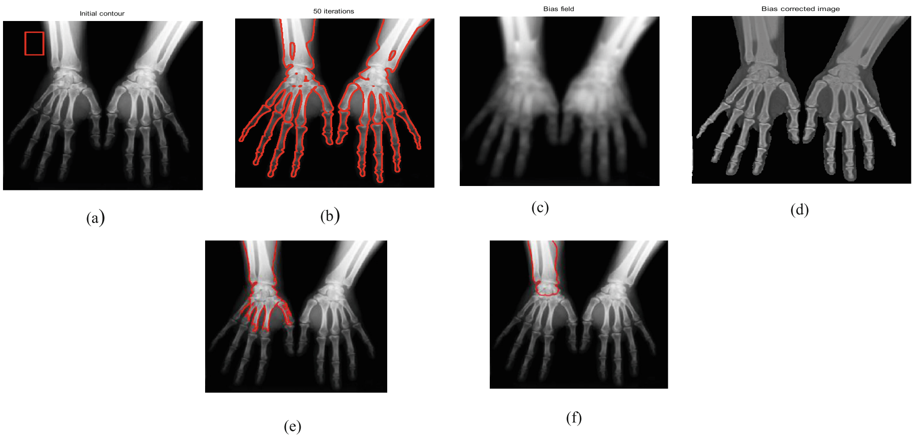

Fig. 2. Applications of the present segmentation method (SMII) to an X-ray image. (a) Original image and initial contour (Red line); (b) Segmentation result (Red lines); (c) Computed bias field; (d) Bias corrected image (e) Shi Method (Red lines); (f) Chan&Vese Method (Red lines);

This method is robust to the initialization of the constants $c = (c_1, \ldots\ldots\ldots, c_N)$, the bias field b, and the level set functions. For automatic applications, the constants $c_1, \ldots\ldots\ldots, c_N$ can be initialized as $N\psi$ equally spaced numbers between the minimum and maximum intensities of the original image, and the bias field $b\psi$ is initialized as $b\psi = 1$. The level set functions can be automatically generated or manually initialized by the users. The number of phases $N\psi$ depends on the number of tissue types in the images, which is usually known in practice.

Figure 2 shows the result of the presented method for an X-ray image. Intensity inhomogeneity is obvious in this image. We use this example to show the desirable capability of this method in joint segmentation and bias correction. The bias corrected image is given by the quotient I/b. It is worth noting that presented method allows for flexible initialization of the level set function. The initial contour can be inside, outside, or cross the object boundaries. This can be seen from the results in Fig. 2 and those for a computed tomography (CT) image of a tumor in a liver shown in Fig. 3. The initial contours used to generate the initial level set functions are shown in Fig. 3(a), and the corresponding segmentation results are shown in Fig. 3(b).

Figure 4 shows the result for a MR brain image, which has obvious intensity inhomogeneity. The segmentation result and the computed bias field and are simultaneously obtained, shown in Fig. 4(b) and 4(c), respectively. The bias corrected image is shown in Fig. 4(d). We easily conclude, from the obtained results that the best results are achieved by Proposed Method (SMII)

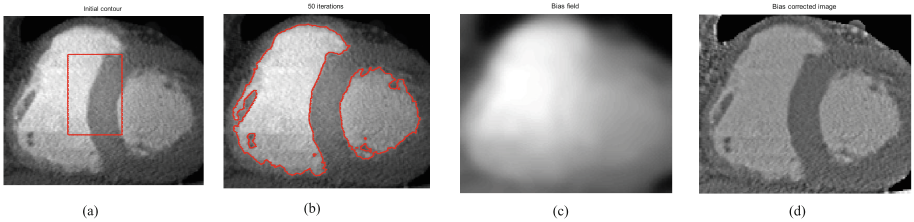

Fig. 3. Applications of SMII method to CT image (a) Original image and initial contour (Red line); (b) Segmentation result (Red lines); (c) Computed bias field; (d) Bias corrected image

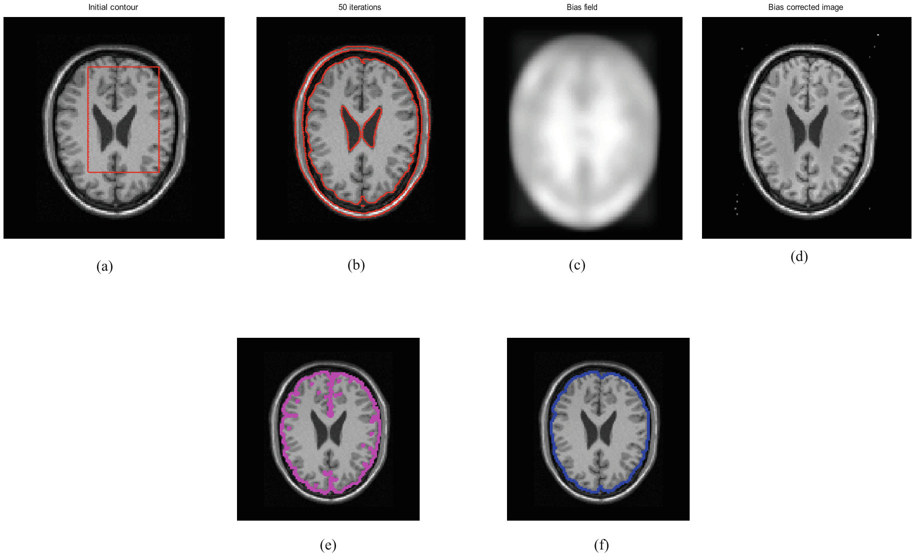

Fig. 4. Applications of SMII method to a MR image. (a) Original image and initial contour (Red line); (b) Segmentation result (Red lines); (c) Computed bias field; (d) Bias corrected image (e) Shi Method (Purple lines); (f) Chan&Vese Method (blue line)

5 Conclusion

In this paper, a variational level set framework for segmentation and bias correction of images with intensity inhomogeneities is presented. A local clustering criterion function for the intensities in a neighborhood of each point is established based on the local intensity clustering property, from a generally accepted model of images with intensity inhomogeneities. The energy of the level set functions represents a partition of the image domain and a bias field that accounts for the intensity inhomogeneity. Segmentation and bias field estimation are therefore jointly performed by minimizing the energy functional. This model efficiently utilizes the local image information and therefore able to simultaneously segment and bias correct the images with intensity inhomogeneity. Experimental results prove that the probability of image (pixels) varies for both the images and is concentrated for certain pixel values, indicating refinement of the image. Lastly reduction in value of variance for individual pixel indicates less deviation of intensity value to that of mean value for the cluster of pixel in a given neighbourhood.

References

1. Guo, D., Ming, X.: Color clustering and learning for image segmentation based on neural networks. IEEE Trans. Neural Netw. **16**(4), 925–936 (2005)
2. Li, C., Xu, C., Gui, C., Fox, M D.: Level set evolution without re-initialization: a new variational formulation. In: Proceedings of IEEE Conference Computer Vision and Pattern Recognition, vol. 1, pp. 430–436 (2005)
3. Caselles, V., Kimmel, R., Sapiro, G.: Geodesic active contours. Int. J. Comput. Vision **22**(1), 61–79 (1997)
4. Kass, M., Witkin, A., Terzopoulos, D.: Snakes: active contour models. Int. J. Comput. Vision **1**(4), 321–331 (1988)
5. Osher, S., Sethian, J.A.: Fronts propagating with curvature-dependent speed: algorithms based on Hamilton-Jacobi formulations. J. Comput. Phys. **79**(1), 12–49 (1988)
6. Chan, T.F., Vese, L.A.: Active contours without edges. IEEE Trans. Image Process. **10**(2), 266–277 (2001)
7. Tsai, A.Y., Willsky, A.S.: Curve evolution implementation of the Mumford-Shah functional for image segmentation, denoising, interpolation, and magnification. IEEE Trans. Image Process. **10**(8), 1169–1186 (2001)
8. Paragios, N., Deriche, R.: Geodesic active regions and level set methods for supervised texture segmentation. Int. J. Comput. Vis. **46**(4), 223–247 (2002)
9. Gao, S., Bui, T.D.: Image segmentation and selective smoothing by using Mumford-Shah model. IEEE Trans. Image Process. **14**(10), 1537–1549 (2005)
10. Glover, G.H., Hayes, C.E., Pelc, N.J.: Comparison of linear and circular polarization for magnetic resonance imaging. J. Magn. Reson. **64**(2), 255–270 (1985)
11. Harvey, I., Tofts, P.S., Morris, J.K., Wicks, D.A.G., Ron, M.A.: Sources of T1 variance in normal human white matter. Magn. Reson. Imaging **9**(1), 53–59 (1991)
12. Simmons, A., Tofts, P.S., Barker, G.J., Arridge, S.R.: Sources of intensity nonuniformity in spin echo images at 1.5T. Magn. Reson. Med. **32**(1), 121–128 (1994)

13. Narayana, P.A., Brey, W.W., Kulkarni, M.V., Sievenpiper, C.L.: Compensation for surface coil sensitivity variation in magnetic resonance imaging. Magn. Reson. Imaging **6**(3), 271–274 (1988)
14. Brey, W.W., Narayana, P.A.: Correction for intensity falloff in surface coil magnetic resonance imaging. Med. Phys. **15**(2), 241–245 (1988)
15. Stollberger, R., Wach, P.: Imaging of the active b1 field in vivo. Magn. Reson. Med. **35**(2), 246–251 (1996)
16. McVeigh, E.R., Bronskill, M.J., Henkelman, R.M.: Phase and sensitivity of receiver coils in magnetic resonance imaging. Med. Phys. **13**(6), 806–814 (1986)
17. Roemer, P.B., Edelstein, W.A., Hayes, C.E., Souza, S.P., Mueller, O.M.: The NMR phased array. Magn. Reson. Med. **16**(2), 192–225 (1990)
18. Noll, D.C., Meyer, C.H., Pauly, J.M., Nishimura, D.G., Macovski, A.: A homogeneity correction method for magnetic resonance imaging with time-varying gradients. IEEE Trans. Med. Imaging **10**(4), 629–637 (1991)
19. Hayes, C.E., Hattes, N., Roemer, P.B.: Volume imaging with MR phased arrays. Magn. Reson. Med. **18**(2), 309–319 (1991)
20. Li, C., et al.: A level set method for image segmentation in the presence of intensity inhomogeneities with application to MRI. IEEE Trans. Image Process. **20**(7), 2007–2016 (2011)
21. Zhang, K., Liu, Q., Song, H., Li, X.: A variational approach to simultaneous image segmentation and bias correction. IEEE Trans. Cybern. **45**, 1426–1437 (2014)
22. Theodoridis, S., Koutroumbas, K.: Pattern Recognition. Academic, New York (2003)
23. Arms XRay.png: borrowed (NIH). http://rsbweb.nih.gov/ij/index.html
24. Brain MRI.png: borrowed. http://www.itk.org/(Kitware)

TEQ Equalization in Presence of CFO for MC-CDMA System

Ramadhan Masmoudi(✉) and Ahmed Bouzidi Djebbar

Telecommunications and Digital Signal Processing Laboratory, Djillali Liabès University of Sidi Bel Abbès, BP 89, 22000 Sidi Bel Abbes, Algeria
masmoudi1987@hotmail.fr, ahbou_djebbar@yahoo.fr

Abstract. Recently, many blind and non-blind methods that equalize the channel in the time domain to remove Inter Block Interference (IBI) don't consider the presence of the Carrier Frequency Offset (CFO) or assume that the CFO is estimated perfectly. In this paper we consider an Multi-Carrier Code Division Multi Access (MC-CDMA) system with presence of CFO and we develop a semi blind approach to jointly estimated the CFO and the Time domain Equalizer (TEQ) based on the zero and non-zero pilots inserted in the transmitted symbol, in addition to reduce the complexity of our derived algorithms we adopted an adaptive standard Least Minimum Square (LMS) algorithm related to the proposed batch algorithms. The simulations results obtained demonstrated the effectiveness of our algorithms when compared with the blind once.

Keywords: BLind (BL) · CFO · MC-CDMA · TEQ · Semi Blind (SB)

1 Introduction

To improve the performance of transmission, equalization technique must be used to reduce the IBI. In literature, we find three categories of equalization methods: Non-blind (or training), Blind and Semi-Blind. In comparison to training based equalization algorithms, blind an semi blind methods represent an appropriate alternative since they don't require the channel knowledge or training sequence

Generally, the number of active (used) spreading codes per cell is less than the available codes for spreading (used and unused codes). The codes are orthogonal to each other. Based on this property, blind time domain equalization was proposed for MC-CDMA systems in [1–4]. This method is later extended to a blind channel shortening in [5], by using the orthogonality between the spreading codes in the frequency domain.

The CFO problem, which suffers the MC transmission, is due to the difference between transmitter and receiver oscillator's frequencies on the one hand and secondly to the Doppler shift. Without compensation of the CFO, transmission performance degrades. We find in the literature several methods that treat the problem of joint estimation of CFO and TEQ [1–9].

Based on the orthogonality between pilot and used spreading codes, joint estimation of CFO and TEQ method are proposed in this paper. Pilot spreading codes are

M. Chadli et al. (Eds.): ICEECA 2017, LNEE 522, pp. 452–463, 2019.
https://doi.org/10.1007/978-3-319-97816-1_34

divided in two types: zeros and non-zeros. The zeros pilots are used to estimate CFO while the non-zeros pilots are designed for TEQ equalization. It is shown in [2] that the increasing in the number of Orthogonal Frequency Division Multiplexing (OFDM) block ameliorate the performance quality of equalization and BER in the absence of CFO (or perfect knowledge of CFO), however in the presence of CFO the equalization performance and BER is significantly degraded when the number of OFDM block is sufficiently large.

The remainder of this paper is organized as follows. In Sect. 2, the discrete model of MC-CDMA system with presence of CFO is described. Section 3 presents the proposed semi blind approach, which includes both CFO estimation and TEQ channel equalization based on the zeros and the non-zeros pilots, respectively. Section 4 presents the adaptive algorithms corresponds to the proposed block processing ones. A brief discussion of the computational complexity is given in Sect. 5. Simulations results are presented in Sects. 6 and 7 concludes the paper.

Notation: Hermitian, transpose and complex conjugate superscripts are denoted by $(.)^{\mathcal{H}}$,$(.)^{\mathrm{T}}$ and $(.)^{*}$ respectively. $\mathrm{diag}(\mathbf{x})$ will stand for diagonal matrix with $\mathbf{x}$ on its main diagonal. The Euclidean norm is presented by $\|\ .\ \|$. We will use I_N to denote the $N \times N$ identity matrix [1].

2 Discrete Baseband Model of MC-CDMA System with Presence of CFO

Figure 1 represents the discrete baseband model of MC-CDMA system for N_d users. The length of cyclic prefix is denoted by P. The vector $h(n), n \in \{0, L-1\}$, represents the taps of the discrete chip-rate sampled channel.

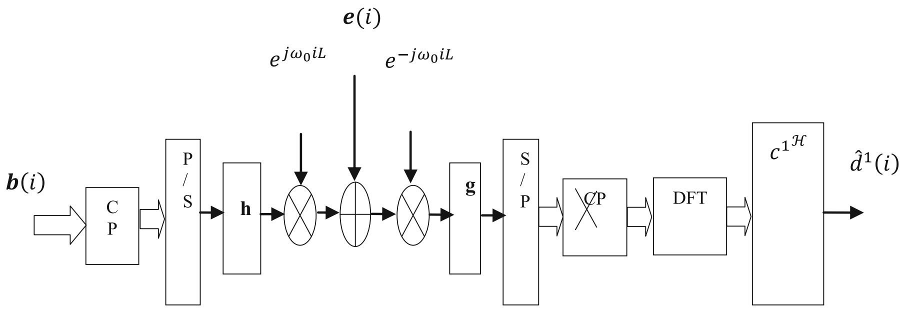

Fig. 1. Baseband model of MC-CDMA systems

The $m-th$ MC-CDMA user spreads its $i-th$ symbol $d^m(i)$ with a symbol-aperiodic spreading sequence of length N $\boldsymbol{c}^m(i) = [c^m(i,1),\ldots,c^m(i,N)]^T$. $\boldsymbol{c}^m(i,k) = w^m(k)a(i,k)\quad k \in \{1,\ldots,N\}$ represents the aperiodic spreading sequence. $\boldsymbol{w}^m = [w^m(1),\ldots,w^m(N)]^T$ is a periodic Walsh–Hadamard spreading sequence. $\boldsymbol{a}(i,k)$ is a cell-specific unit magnitude complex scrambling sequence [2].

Each block contains information-bearing symbols and pilot symbols (zero and non-zero pilots). Indeed, N_d active users employ the code c_d to spread the information-bearing symbols. $N_{\bar{p}}$ non-active users employ the code $c_{\bar{p}}$ to spread the non zero pilots, and $N_{\bar{\bar{p}}}$ null users employ $c_{\bar{\bar{p}}}$ as spreading code. The $i-th$ MC-CDMA symbols, shown in Fig. 2, can be written as follows:

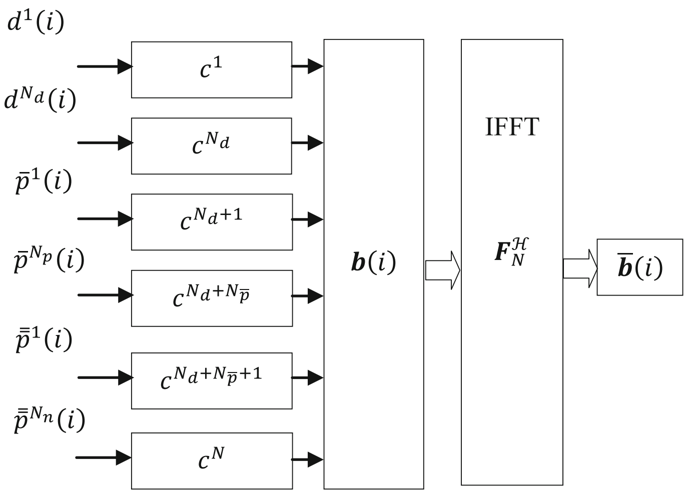

Fig. 2. Structure of MC-CDMA symbol

$$\boldsymbol{b}(i) = c_d(i)\boldsymbol{d}(i) + \boldsymbol{c}_{\bar{p}}(i)\bar{\boldsymbol{p}}(i) + \boldsymbol{c}_{\bar{\bar{p}}}(i)\bar{\bar{\boldsymbol{p}}}(i) \tag{1}$$

Where the matrices $\boldsymbol{c}_d(i)$, $\boldsymbol{c}_{\bar{p}}(i)$, $\boldsymbol{c}_{\bar{\bar{p}}}(i)$,of sizes $N \times N_d$, $N \times N_{\bar{p}}$, and $N \times N_{\bar{\bar{p}}}$, represents matrices of spreading codes of data, non-zero pilots, and zero pilots, respectively, and are mutually orthogonal. Spreading codes matrices, the data and pilot vectors are defined as follow:

$$\boldsymbol{c}_d(i) = \left[c^1(i), c^2(i), \ldots, c^{N_d}(i)\right]$$

$$\boldsymbol{c}_{\bar{p}}(i) = \left[c^{N_d+1}(i), \ldots, c^{N_d+N_{\bar{p}}}(i)\right]$$

$$\boldsymbol{c}_{\bar{\bar{p}}}(i) = \left[c^{N_d+N_{\bar{p}}+1}(i), \ldots, c^N(i)\right]$$

$$\boldsymbol{d}(i) = [d_1(i), d_2(i), \ldots, d_{N_d}(i)]$$

$$\bar{\boldsymbol{p}}(i) = \left[\bar{p}_1(i), \bar{p}_2(i), \ldots, \bar{p}_{N_{\bar{p}}}(i)\right]$$

$$\bar{\bar{\boldsymbol{p}}}(i) = [0, \ldots, 0]$$

We call each user corresponding to a zero symbol a null user or excess user.

Dependence of the code spreading matrices $\boldsymbol{c}_d(i)$, $\boldsymbol{c}_{\bar{p}}(i)$, and $\boldsymbol{c}_{\bar{\bar{p}}}(i)$ on the block index i implies that the spreading codes are changing from block to block, due to the scrambling sequence $\boldsymbol{a}(i,k)$.

For OFDM transmission, the $(N \times 1)$ vector $\boldsymbol{b}^m(i)$ is left multiplied by the $(N \times N)$ inverse DFT (IDFT) matrix $\boldsymbol{F}_N^{\mathcal{H}}$, which implements the $N-$points IDFT of $\boldsymbol{b}^m(i)$. Hence the transmitted $(N \times 1)$ vector of chip samples is given by

$$\boldsymbol{u}(i) = \boldsymbol{F}_N^{\mathcal{H}} \boldsymbol{b}^m(i) \tag{2}$$

The Cyclic Prefix (CP) matrix $\boldsymbol{T}_{CP} \triangleq \left[\left[0_{P\times(N-P)}, \boldsymbol{I}_P\right]^T, \boldsymbol{I}_N\right]^T$ is added to remove the dispersive effect of channel, with $P \geq L$.

The transmitted vector of length $Q = P + N$ is given by:

$$\boldsymbol{v}^m(i) = \boldsymbol{T}_{CP} \overline{\boldsymbol{b}}^m(i) \tag{3}$$

Therefore, in the presence of CFO the received signal is given by [2]:

$$\boldsymbol{x}(i) = [\boldsymbol{x}(iQ+1), \ldots, \boldsymbol{x}(iQ+Q)]^T$$

$$= e^{j\omega_0 iQ} \boldsymbol{D}_Q(\omega_0) (\boldsymbol{H}^{(0)} \sum\nolimits_{m=1}^{N_d} \boldsymbol{T}_{CP} \boldsymbol{F}_N^{\mathcal{H}} \overline{\boldsymbol{b}}^m(i)$$

$$+ \boldsymbol{H}^{(1)} \sum\nolimits_{m=1}^{N_d} \boldsymbol{T}_{CP} \boldsymbol{F}_N^{\mathcal{H}} \boldsymbol{b}^m(i-1)) + \boldsymbol{e}(i) \tag{4}$$

Where $\boldsymbol{D}_Q(\omega_0) = \mathrm{diag}\left\{1, e^{j\omega_0}, \ldots, e^{j\omega_0(Q-1)}\right\}$.

ω_0 represents the candidate value of CFO, N_b is the number of OFDM symbols, $\boldsymbol{e}(i)$ is an AWG noise vector and the $(Q \times Q)$ Toeplitz matrices $\boldsymbol{H}^{(0)}$ and $\boldsymbol{H}^{(1)}$ are defined in [2]

Based on orthogonality between pilot (zeros or non-zeros) and used codes, we derive CFO and TEQ estimates.

3 Pilot Design to Jointly Estimate Carrier Frequency Offset and TEQ Equalizer

3.1 Semi Blind TEQ Solution

The semi-blind equalizer is obtained by solving the least squares minimization problem [2]

$$\hat{\boldsymbol{g}} = \arg\min_{g} \frac{1}{N_b} \sum_{i=0}^{N_b-1} \left\| \left(\boldsymbol{g}^H \boldsymbol{X}(i) \boldsymbol{D}(-\omega) \right)^T - \tilde{\boldsymbol{c}}_d(i) \boldsymbol{d}(i) - \tilde{\boldsymbol{c}}_{\bar{p}}(i) \bar{\boldsymbol{p}}(i) \right\|^2 \tag{5}$$

Where

$$\boldsymbol{X}(i) = [\boldsymbol{x}(iQ + P + 1), \ldots, \boldsymbol{x}((i+1)Q)]^T$$

$$\boldsymbol{x}(n) = \left[x\left(n + \frac{d-1}{2}\right), \ldots, x\left(n - \frac{d-1}{2}\right) \right]^T$$

$$\tilde{\boldsymbol{c}}_d(i) = \boldsymbol{F}_N^{\mathcal{H}} \boldsymbol{c}_d(i)$$

$$\tilde{\boldsymbol{c}}_{\bar{p}}(i) = \boldsymbol{F}_N^{\mathcal{H}} \boldsymbol{c}_{\bar{p}}(i).$$

In the perfect case when CFO is known, i.e. $\omega = \omega_0$, the solution for $\boldsymbol{g}$ can be written as:

$$\hat{g} = \bar{\Gamma}^{-1} \bar{\boldsymbol{\Upsilon}} \tag{6}$$

Where

$$\bar{\boldsymbol{\Gamma}} = \frac{1}{N_b} \frac{1}{N} \sum_{i=0}^{N_b-1} \boldsymbol{X}(i) \boldsymbol{D}(-\omega) \left(\boldsymbol{R}_{\tilde{C}_d}^{\perp}(i) \right)^T \boldsymbol{D}(\omega) (\boldsymbol{X}(i))^{\mathcal{H}} \tag{7}$$

$$\bar{\boldsymbol{\Upsilon}} = \frac{1}{N_b} \frac{1}{N} \sum_{i=0}^{N_b-1} \boldsymbol{X}(i) \boldsymbol{D}(-\omega) \tilde{\boldsymbol{c}}_{\bar{p}}^*(i) \bar{p}^*(i) \tag{8}$$

$$\boldsymbol{R}_{\tilde{C}_d}^{\perp}(i) = \boldsymbol{I}_N - \tilde{\boldsymbol{c}}_d(i) \tilde{\boldsymbol{c}}_d^{\mathcal{H}}(i) \tag{9}$$

This solution is efficient in the absence of CFO, as shown in [2]. However the presence of CFO complicates the resolving problem. The reason for which, we must appropriately estimate the CFO. The following subsection considers the CFO estimation method.

3.2 Semi Blind CFO Estimation

Based on the orthogonality between the non-used (null user) spreading codes in one hand and the used codes (including data bearing and pilot training symbols) in the other hand, it is easy to verify that:$\boldsymbol{c}_{\bar{\bar{p}}}^{\mathcal{H}}(i) \boldsymbol{c}_{\bar{p}}(i) = \boldsymbol{c}_{\bar{\bar{p}}}^{\mathcal{H}}(i) \boldsymbol{c}_d(i) = 0$, and equivalently $\boldsymbol{c}_{\bar{\bar{p}}}^{\mathcal{H}}(i) \boldsymbol{c}_{\bar{\bar{p}}}(i) = \boldsymbol{I}_{N_p}$.

If we consider the knowledge of equalizer $\boldsymbol{g}$, the CFO estimation can be obtained by minimizing the following cost function

$$\hat{\omega} = \arg\min_{\omega} \frac{1}{N_b} \sum\nolimits_{i=0}^{N_b-1} \left\| \boldsymbol{g}^H \boldsymbol{X}(i) \boldsymbol{D}(-\omega) \tilde{\boldsymbol{c}}_{\bar{\bar{p}}}(i)^2 \right\| \tag{10}$$

Where $\tilde{\boldsymbol{c}}_{\bar{\bar{p}}}(i) = \boldsymbol{F}_N \boldsymbol{c}_{\bar{\bar{p}}}^{\mathcal{H}}(i)$.

As shown in the above cost function, the estimation of CFO is coupled with the Time domain equalization, it requires a perfect knowledge of TEQ equalizer $\boldsymbol{g}$, which in turn very sensitive to CFO value, here we assume a small value of CFO to ensuring a good initialization as in [4].

4 Adaptive Algorithms

CFO and TEQ must be updated adaptively according to time variation of channel. In this subsection, we employ a stochastic gradient method, as adaptive algorithm, due to its simplicity.

4.1 Adaptive CFO Estimation

The standard gradient LMS algorithm used for CFO estimation is defined as [1]

$$\omega_{n+1} = \omega_n - \mu \left. \frac{\partial J(\omega)}{\partial \omega} \right|_{\omega = \omega_n} \tag{11}$$

Where ω_n is the estimate of ω at the n^{th} iteration and μ is a step-size parameter. The derivation of the cost function $J(\omega)$ with respect to ω is

$$\frac{\partial J(\omega)}{\partial \omega} = \frac{j}{N_b} \sum_{i=0}^{N_b-1} \boldsymbol{g}^H \boldsymbol{X}(i) \boldsymbol{D}(-\omega) \tilde{\boldsymbol{c}}_{\bar{\bar{p}}}(i) \tilde{\boldsymbol{c}}_{\bar{\bar{p}}}^{\mathcal{H}}(i) \boldsymbol{A}_N \boldsymbol{D}(\omega) \boldsymbol{X}^{\mathcal{H}}(i) \boldsymbol{g}$$

$$- \boldsymbol{g}^{\mathcal{H}} \boldsymbol{X}(i) \boldsymbol{A}_N \boldsymbol{D}(-\omega) \tilde{\boldsymbol{c}}_{\bar{\bar{p}}}(i) \tilde{\boldsymbol{c}}_{\bar{\bar{\boldsymbol{p}}}}^{\mathcal{H}}(i) \boldsymbol{D}(\omega) \boldsymbol{X}^{\mathcal{H}}(i) \boldsymbol{g} \tag{12}$$

Where $\boldsymbol{A}_N$ represent a N by N diagonal matrix, $\boldsymbol{A}_N = \mathrm{diag}(0, 1, 2, \ldots, N-1)$.

The equalizer vector g is estimated adaptively based on the stochastic algorithm derived in the next subsection.

4.2 Adaptive TEQ Equalization

The steepest gradient-descent algorithm for the semi blind TEQ equalization is defined as [10]

$$\boldsymbol{g}[k+1] = \boldsymbol{g}[k] - \mu \nabla_{\boldsymbol{g}}(\xi(\boldsymbol{g})) \tag{13}$$

Where μ denotes the step size and ∇_g denotes the gradient with respect to $\boldsymbol{g}$. The gradient is calculated as follows

$$\nabla_g(\xi(g)) = \boldsymbol{g}^T \boldsymbol{X}^*(i)\boldsymbol{D}(\omega)\boldsymbol{R}^{\perp}_{\tilde{C}_d}(i)\boldsymbol{D}(-\omega)\boldsymbol{X}^T(i) - \bar{\boldsymbol{p}}^{\mathcal{H}}(i)\boldsymbol{c}^{\mathcal{H}}_{\bar{p}}(i)\boldsymbol{D}(-\omega)\boldsymbol{X}^T(i) \tag{14}$$

Here, we use the CFO value based on the above adaptive methods, the equalizer vector $\boldsymbol{g}[k]$ are updated each time one MC-CDMA block is received, where $[k]$ implies the $k-th$ iteration.

The adaptive rule of equalization is summarized as follows

Step 1: Initialize the equalizer vector at $k = 0$, $\boldsymbol{g}[0] = [00\ldots1\ldots00]^T$.

Step 2: Compute the gradient $\nabla_g(\xi(\boldsymbol{g}))$ as in Eq. (14).

Step 3: Update the equalizer weight vector according to Eq. (13).

Step 4: Normalize the updated equalizer as follows $\boldsymbol{g}[k+1] = \frac{\boldsymbol{g}[k+1]}{\|\boldsymbol{g}[k+1]\|}$.

Step 5: Reiterate steps 2, 3, and 4, for $k = 2, 3, 4, \ldots$, until obtaining the convergence.

5 Computational Complexity

In terms of computational complexity, the batch method for equalization needs $\mathcal{O}\big(N_b\big(dN^2\big(1+N_p\big)+N\big)\big)$ multiplications to compute $\bar{\boldsymbol{\Gamma}}$ and $\bar{\boldsymbol{\Upsilon}}$ plus one division $\mathcal{O}$(d), while computing $\boldsymbol{g}[k+1]$ requires $\mathcal{O}\big(\big(dN^2\big(1+N_p\big)+N\big)\big)$ multiplications due to computation of the gradient $\nabla_g(\xi(\boldsymbol{g}))$. However, the batch CFO estimation algorithm requires $\mathcal{O}\big(N_\omega N_b N_p(dN^2+1)\big)$ multiplications, where N_ω denote the number of samples over an interval of interest. For example, if we consider un interval between -0.5 and 0.5, with step size $\Delta = 10^{-3}$, then the cost function need a search aver $N_\omega = \frac{1}{\Delta} = 1000$ samples which is very expensive if it compared with adaptive methods which requires approximately $\mathcal{O}\big(N_b N_p(dN^3+1)\big)$ multiplications.

6 Numerical Results

In our simulations we consider: multipath Rayleigh fading channels of length $L = 4$, a CP of length $P = 5$, $N = 32$. The results are averaged over N_m = 200 Monte Carlo realizations.

The SNR used in simulation is defined by:

$$SNR = 10\log_{10}\left(\frac{\sum_{l=0}^{L-1} E\|h_l\|^2}{\sigma_v^2}\frac{N_d}{N}\right) \tag{15}$$

The Normalized Mean Square Error (NMSE) is used as performance measure. For CFO estimation, the NMSE is defined by:

$$NMSE_{CFO} = \frac{1}{N_m}\sum_{j=1}^{N_m}\frac{\|\hat{\omega}(j)-\omega_0\|^2}{\left\|\left(\frac{2\pi}{N}\right)\right\|^2} \tag{16}$$

While the MSE between the estimated and the ideal Effective Channel Impulse Response (ECIR) is defined by:

$$MSE_g = \frac{1}{N_m(L-1)} \sum\nolimits_{p=1}^{N_m} \hat{\boldsymbol{h}}_{eff}(p) - \boldsymbol{h}_{eff}^2 \tag{17}$$

Where the index p refers to the $p-th$ simulation run and N_m denotes the number of Monte Carlo simulation runs.

$\hat{\boldsymbol{h}}_{eff}$ represents the estimated ECIR, $\hat{\boldsymbol{h}}_{eff} = \hat{\boldsymbol{g}} * \boldsymbol{h}$. The perfect case of ECIR is set to all zeros with a single unity entry near the center $\boldsymbol{h}_{eff} = [000\ldots1\ldots000]^T$.

In the noisy case, it is seen from Fig. 3. That the equalizer $\hat{g}$ forces the CIR to be close to zero in all coefficients except for one tape (Zero Forcing, ZF TEQ equalization).

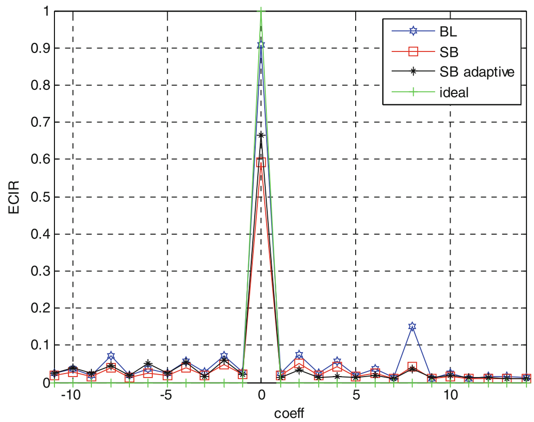

Fig. 3. Effective Channel Impulse Response versus coefficients

In Fig. 4, we show the MSE estimation performance of ECIR for both our method and the blind method proposed in [4] versus SNR. We assume the number of pilots $N_p = 4$ and the length of the equalizer $d = 23$ in all examples. From the results, it is seen that our methods benefit from the additional information offered by the pilot symbols to outperform the blind ones over all range of SNR.

Next, the NMSE defined earlier are used to measure the accuracy of CFO estimation. Figure 5 shows the NMSE of CFO when the jointly batch and adaptive semi blind method is plotted beside the blind ones. The true CFO value is chosen to be fixed at $\omega_0 = 2 \times 10^{-3}$. The results show that semi blind methods are generally better than the blind ones, and that the adaptive algorithms for both blind and semi criterion are almost approaching the batch algorithms.

In Fig. 6 we plot the Bit Error Rate (BER) performance evolution of both blind and semi blind techniques for TEQ equalization as the block number increases. We assume a number of pilot symbol $N_{\bar{p}} = 2$, and $SNR = 15\,dB$ in this example. As expected, the

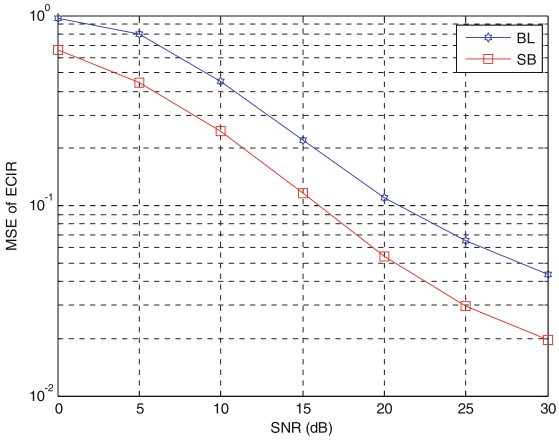

Fig. 4. MSE of ECIR versus SNR (dB)

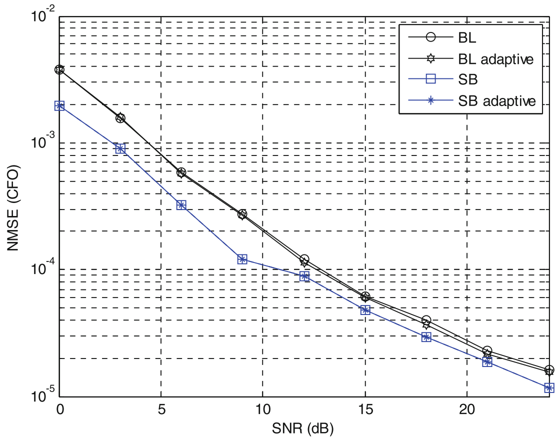

Fig. 5. NMSE of CFO versus SNR (dB)

BER performance of the both methods are improved with the increase of N_b in the absence of CFO as in [1], but in the presence of CFO the performance is significantly degraded, this phenomenon due to the residual error caused by CFO which is depends on the block index i. For illustration, to compensate the effect of CFO, the received signal is multiplied by $e^{-j\hat{\omega}iQ}\boldsymbol{D}_Q(-\hat{\omega})$ as follows:

$$\boldsymbol{y}(i) = e^{-j\hat{\omega}iQ}\boldsymbol{D}_Q(-\hat{\omega})\boldsymbol{x}(i)$$

$$= e^{j\theta}\boldsymbol{D}_Q(\omega_0 - \hat{\omega})(\boldsymbol{H}^{(0)} \sum\nolimits_{m=1}^{M} \boldsymbol{T}_{CP}\boldsymbol{F}_N^{\mathcal{H}}\boldsymbol{b}^m(i)$$

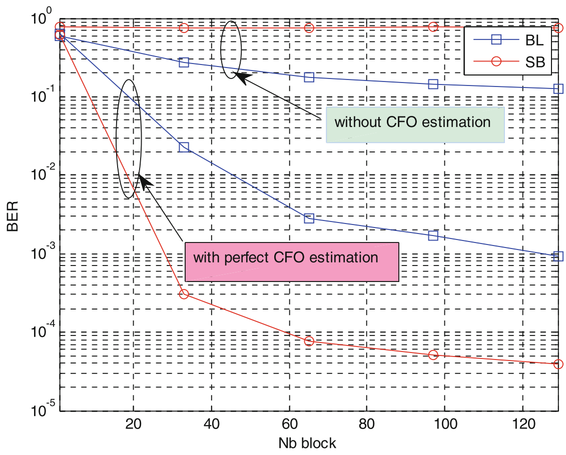

Fig. 6. BER versus number of block N_b

$$+\boldsymbol{H}^{(1)}\sum_{m=1}^{M}\boldsymbol{T}_{CP}\boldsymbol{F}_N^{\mathcal{H}}\boldsymbol{b}^m(i-1))+\tilde{\boldsymbol{e}}(i) \tag{18}$$

Where

$\theta = iQ(\omega_0 - \hat{\omega})$ is the CFO estimation error and $\tilde{\boldsymbol{e}}(i) = e^{-j\hat{\omega}iQ}\boldsymbol{D}_Q(-\hat{\omega})\boldsymbol{e}(i)$ is an AWGN noise with the same statistical properties as $\boldsymbol{e}(i)$. For example, if the NMSE of the CFO is around 10^{-6}, then $\hat{\omega} - \omega_0 = \frac{2\pi}{N}10^{-3}$. For $i = 100$, the CFO estimation error will approximately produce a phase shift equal to $e^{j100\times Q\times\frac{2\pi}{N}10^{-3}}$. From Eq. (18) it is clear that the increasing in the number of N_b produces the phase distortion which degrades the performance of the channel equalization, and also the BER performance over time. This phenomenon disappear in the perfect case when $\omega_0 - \hat{\omega} = 0$.

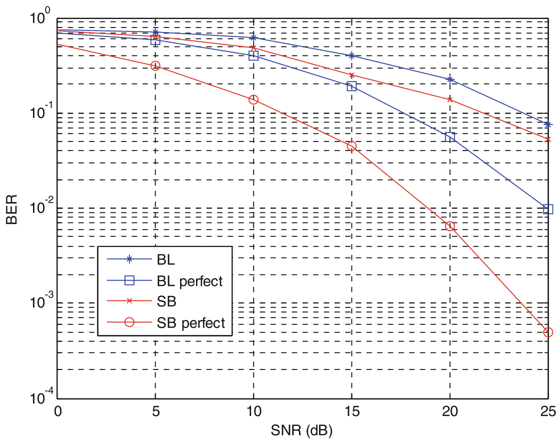

Fig. 7. BER versus SNR (dB)

In Fig. 7, we compare the BER performance between the blind and semi blind methods versus SNR; we select a small number of blocks $N_b = 10$ to avoid (or minimize) the effect of the phase rotation phenomenon. The obtained results confirmed the previous observations that the MC systems are very sensitive to the CFO, especially when the number of block is sufficiently large, and that the semi blind methods are better than the blind ones.

7 Conclusion

In this paper, we have developed a joint semi blind CFO estimation and TEQ equalization method for MC-CDMA systems. The proposed method is based on the orthogonality between the user's coed in one hand and in the pilot codes in other hand. Two types of pilots are proposed, zero and non zero pilots, the first ones is used to estimate the CFO while the second types is used for TEQ equalization, moreover we derived the adaptive algorithms related to the proposed methods in order to reduce the computational complexity.

The results obtained demonstrate that, the MC-CDMA is very sensitive to the CFO especially when the number of MC-CDMA block is sufficiently large, this degradation due to the phase rotation caused by the residual CFO estimation. It is also demonstrated that semi blind method outperformed the blind ones in the case of small number of MC-CDMA block.

References

1. Masmoudi, R., Djebbar, A.B., Dayoub, I.: Low complexity joint blind equalization and CFO estimation for MC-CDMA system. Wirel. Pers. Commun. **89**(4), 315–331 (2016). https://doi.org/10.1007/s11277-016-3545-9
2. Djebbar, A.B., Abed-Meraim, K., Djebbari, A.: Blind and semi-blind equalization of downlink MC-CDMA system exploiting guard interval redundancy and excess codes. IEEE Trans. Commun. **57**(1), 156–163 (2009)
3. Djebbar, A.B., Abed-Meraim, K., Djebbari, A.: Semi-blind equalization of downlink MC-CDMA systems. In: 2007 IEEE International Conference on Signal Processing and Communications ICSPC 2007, Dubai, pp. 460–463 (2007)
4. Djebbar, A.B., Abed-Meraim, K., Djebbari, A.: Blind channel equalization and carrier frequency offset estimation for MC-CDMA systems using guard interval redundancy and excess codes. Int. J. Electron. Commun. (AEÜ) **63**, 220–225 (2009)
5. Miyajima, T., Kotake, M.: Blind channel shortening for MC-CDMA systems by restoring the orthogonality of spreading codes. IEEE Trans. Commun. **63**(3), 938–948 (2015)
6. Thiagarajan, L.B., Attallah, S., Meraim, K.A., Liang, Y.C., Fu, H.: Non-data-aided joint carrier frequency offset and channel estimator for uplink MC-CDMA systems. IEEE Trans. Signal Process. **56**(9), 4398–4408 (2008)
7. Jang, J., Lee, K.B.: Effects of frequency offset on MC/CDMA system performance. IEEE Commun. Lett. **3**(7), 196–198 (1999)

8. Tomba, L., Krzymien, W.A.: Sensitivity of the MC-CDMA access scheme to carrier phase noise and frequency offset. IEEE Trans. Veh. Technol. **48**(5), 1657–1665 (1999)
9. Miyajima, T., Kuwana, R.: Joint channel shortening and carrier frequency offset estimation based on carrier nulling criterion in downlink OFDMA systems. IEICE Trans. Fundam. Electron. Commun. Comput. Sci. **96**(5), 1014–1016 (2013)
10. Martin, R.K.: Joint blind adaptive carrier frequency offset estimation and channel shortening. IEEE Trans. Signal Process. **54**(11), 4197–4203 (2006)

Two-Channel Acoustic Noise Reduction by New Backward Normalized Decorrelation Algorithm

Rédha Bendoumia(✉), Mohamed Djendi, and Abderrazek Guessoum

Signal Processing and Image Laboratory (LATSI),
University of Blida 1, Route of Soumaa, B.P. 270, 09000 Blida, Algeria
r.bendoumia@yahoo.fr, m_djendi@yahoo.fr,
guessouma@hotmail.com

Abstract. Recently, most adaptive filtering algorithms have been implemented on two-channel forward-and-backward blind source separation structures for noise reduction. The backward structure shows a good performance compared with forward structure in term of speech quality. The backward structure is often used to separate speech form noise and therefore reduce the acoustic noise components at processing output. In this paper, we propose new configuration of backward symmetric adaptive decorrelation algorithm using a normalized step-sizes parameters. To validate the good performances of our proposed algorithm, intensive experiments are done using objective criteria for two-channel acoustic noise reduction. The obtained results show good performances of proposed algorithm in comparison with other ones.

Keywords: Backward structure · Noise reduction · Normalized step-size SAD algorithm · System mismatch

1 Introduction

In practice, the deficiency of speech processing algorithms results a speech signal commonly infected by noise [1]. According to the application, the objective of the acoustic noise reduction algorithms is to decrease the acoustic noise to make the speech comprehensible and to improve its quality. Many algorithms have been proposed to resolve this problem, such as minimum-mean square error (MMSE) estimator [1], spectral subtraction (SS) [2], and Wiener filter based algorithms [3]. We also find several techniques that are using fullband-and-subband approaches in noise reduction applications [4, 5]. These algorithms are widely used to identify long impulse responses and/or suffer from slow convergence. However, adaptive filtering algorithms have been largely studied for use in the identification of linear systems which can be characterized by their impulse responses.

In the last decade, several family kinds of algorithm have been combined with two-channel blind source separation (BSS) structures in fullband and subband forms using fixed and variables step-sizes [6–13]. All these forms and techniques have been intensively explored for different types of applications and areas, for examples, mono, stereo

M. Chadli et al. (Eds.): ICEECA 2017, LNEE 522, pp. 464–478, 2019.
https://doi.org/10.1007/978-3-319-97816-1_35

and multi-sensors acoustic noise and echo cancellations, audio systems for speech enhancement…etc. [6–15]. These promising applications and combination of these algorithms and structures permit the extraction of a desired source signal from a mixture of several observed signals without *a priori* information of the sources or of the mixture structures. In the literature, we find two BSS structures that have been intensively studied which are the Forward and Backward forms [7, 9].

In this paper, we focus our interest on the backward BSS structure. Furthermore, we consider determined convolutive linear mixtures of speech and noise signals, which takes into account the reverberation in echoic ambient. For example in [7], they have proposed the forward and backward symmetric adaptive decorrelation (SAD) algorithms for signal separation, when the decorrelation criterion is computed between the two estimated output signals (speech and noise). These algorithms are very important solutions that are used to separate speech and noise signals. We note that, the backward SAD algorithm shows a good performance compared with forward SAD algorithm in term of quality of the enhanced speech signal. But, in two-channel backward decorrelation algorithm [7, 10], they have used the very small step-sizes values that are depends on the input signal power of each adaptive filter. In this paper, we propose a modified two-channel backward symmetric adaptive decorrelation algorithm (BND) by inserting two normalized step-sizes parameters of adaptive filters for avoid the small values of step-sizes. We propose to normalize these step-sizes by input signal power of each adaptive filter. This modified BND algorithm is proposed for acoustic noise reduction and speech enhancement.

This paper is presented as follows: in Sect. 2, the mixing model and two forward and backward BSS structures are presented. In Sect. 3, we describe the backward SAD algorithm and its formulation. Section 4 is reserved to present the proposed backward normalized SAD algorithm. The simulation results are presented in Sect. 5 and finally the conclusion of this paper is presented in Sect. 6

2 Description of Two-Channel Mixing Process and Separating System

In this section, we present the two-channel convolutive mixing model that is considered as the problem in this study. This model is shown in Fig. 1. In the next, we will present the two-channel forward and backward BSS structures.

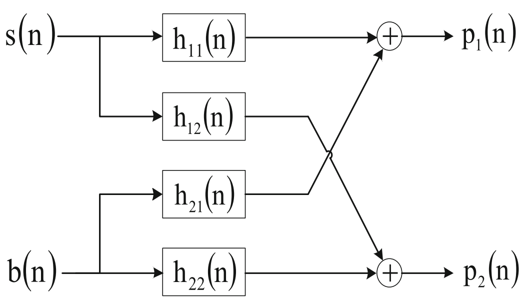

Fig. 1. Two-channel convolutive mixing model

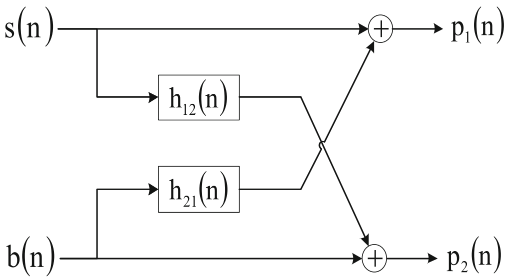

Fig. 2. Simplified two-channel convolutive mixing model

In the model presented in Fig. 1, we consider a first source of speech signal s(n) and a second source of the noise b(n). At the output of this model, we observe two convolutive mixture signals of these two point sources with impulse responses $h_{11}(n)$, $h_{22}(n)$, $h_{12}(n)$ and $h_{21}(n)$. The observed signals are given by the following equation

$$p_1(n) = s(n) * h_{11}(n) + b(n) * h_{21}(n) \tag{1}$$

$$p_2(n) = b(n) * h_{22}(n) + s(n) * h_{12}(n) \tag{2}$$

where (*) represents the convolution operation, $h_{11}(n)$ and $h_{22}(n)$ are assumed to be identity; which represents the direct acoustic path of each direct channel separately ($h_{11}(n) = h_{22}(n) = \delta(n)$) and $h_{12}(n)$ and $h_{21}(n)$ represents the cross-coupling effects between the channels [6–13].

In this paper, the convolutive mixture model that we consider is described in Fig. 2 [6–13]. In this case, Eqs. (1) and (2) of the mixture model can be rewritten as follows:

$$p_1(n) = s(n) + b(n) * h_{21}(n) \tag{3}$$

$$p_2(n) = b(n) + s(n) * h_{12}(n) \tag{4}$$

Firstly, we will present the two-channel forward BSS (FBSS) structure and its formulations (Fig. 3).

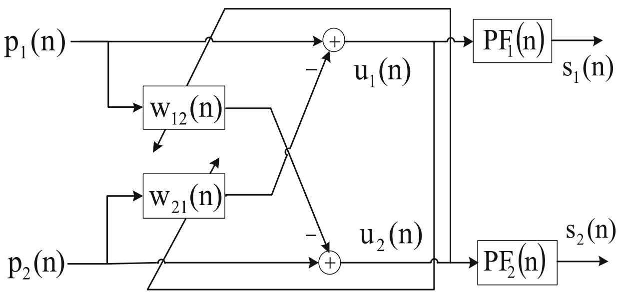

Fig. 3. Two-channel forward BSS structure

In the forward structure, the estimated speech signal $u_1(n)$ is estimated by subtracting the first mixture signal $p_1(n)$ from the output signal of adaptive filter $w_{21}(n)$. However, the second output $u_2(n)$ is obtained by subtracting the mixture $p_2(n)$ from the output signal of adaptive filter $w_{12}(n)$.

The two outputs signals of this FBSS structure are given by the following relations:

$$u_1(n) = p_1(n) - p_2(n) * w_{21}(n) \tag{5}$$

$$u_2(n) = p_2(n) - p_1(n) * w_{12}(n) \tag{6}$$

By inserting the two relations (3) and (4) in (5) and (6), After convergence and with optimal solutions, $w_{12,opt}(n) = h_{12}(n)$ and $w_{21,opt}(n) = h_{21}(n)$, the output signals $u_1(n)$ and $u_2(n)$ can be rewritten as follows:

$$u_1(n) = s(n) * (\delta(n) - h_{12}(n) * w_{21}(n)) \tag{7}$$

$$u_2(n) = b(n) * (\delta(n) - h_{21}(n) * w_{12}(n)) \tag{8}$$

In FBSS structure, we observe the disadvantage of distorting the output signals. It was shown theoretically that the correction of distortions is possible thanks to the equalization of the output signals by post-filtering PFs [7, 9, 10], therefore, we can use the two post-filtering $PF_1(n)$ and $PF_2(n)$ in output of this structure to compensate this distortion. These PFs are ideally given by:

$$PF_1(n) = PF_2(n) = \frac{1}{\delta(n) - h_{12}(n) * h_{21}(n)} \tag{9}$$

The two-channel backward BSS structure (BBSS) is presented in Fig. 4. This BBSS structure is used to estimate the source signals $s(n)$ and $b(n)$ from only observation signals that are unknown linear mixtures of unobserved source signals.

The output speech signal $v_1(n)$ is estimated by subtracting the first mixture signal $p_1(n)$ from the output signal of filters $w_{21}(n)$. However, the second output $v_2(n)$ (which can be the noise) is obtained by subtracting the mixture $p_2(n)$ from the output of adaptive filter $w_{12}(n)$. The relations between the output estimated signals and the noisy signals are given by the following equations:

$$v_1(n) = p_1(n) - w_{21}(n) * v_2(n) \tag{10}$$

$$v_2(n) = p_2(n) - w_{12}(n) * v_1(n) \tag{11}$$

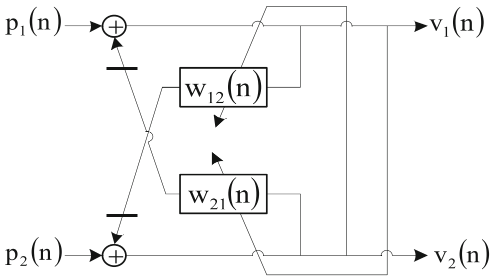

Fig. 4. Two-channel backward BSS structure

By inserting relations (3) and (4) in relations (10) and (11) with the optimal solutions of the adaptive filters is obtained by updating the adaptive filter $w_{21}(n)$ when noise is detected in $p_2(n)$, and the adaptive filter $w_{12}(n)$ is updated when speech is detected in $p_2(n)$. After the convergence and with the optimal solutions ($w_{12,opt}(n) = h_{12}(n)$ and $w_{21,opt}(n) = h_{21}(n)$). Under these conditions the output signals relations of the BBSS structure are obtained,

$$v_1(n) = s(n) \tag{12}$$

$$v_2(n) = b(n) \tag{13}$$

From these two last relations and according to the specific control of the adaptive filters $w_{12}(n)$ and $w_{21}(n)$, we get the original speech signal $s(n)$ at the output $v_1(n)$ and the noise component $b(n)$ at the output $v_2(n)$ without any temporal or spectral distortions. This is the most important advantage of the backward structure compared with its direct version (forward). Basing on the last advantage, in the next we will focus our interest on two-channel backward BSS algorithm.

3 Basic Backward Symmetric Adaptive Decorrelation Algorithm (BSAD)

The basic symmetric adaptive decorrelation (SAD) algorithm combined with backward BSS structure, is firstly proposed in [7, 10]. We assume the generating signals $s(n)$ and $b(n)$ to be zero mean and statistically independent. This implies that they are uncorrelated, i.e. $E[s(n)b(n-l)] = 0,\ \forall l$. Only this latter is required for the backward SAD algorithm (BSAD) to work. The description of BSAD algorithm is presented in Fig. 5.

The performance criterion of this BSAD algorithm is to minimize the energy of the estimated output signals $v_1(n)$ and $v_2(n)$, i.e. $E\left[v_1^2(n)\right]$ and $E\left[v_2^2(n)\right]$ respectively. For the two adaptive filters $w_{12}(n)$ and $w_{21}(n)$. $E\left[v_1^2(n)\right]$ and $E\left[v_2^2(n)\right]$ are quadratic error surface with a single optimum solutions. It has been proven [7, 10] that quadratic error minimization is completely equivalent with the decorrelation between estimated output signals $v_1(n)$ and $v_2(n)$, with the noise reference presents on the observation $p_2(n)$ and

$p_1(n)$ respectively over the span of adaptive filters $w_{12}(n)$ and $w_{21}(n)$: $C_{v_1v_2}(l) = E[v_1(n)v_2(n-l)]$ and $C_{v_2v_1}(l) = E[v_2(n)v_1(n-l)]$.

The basic formulas of the BSAD algorithm is obtained when we put $C_{v_1v_2}(l) = 0$ and $C_{v_2v_1}(l) = 0$.

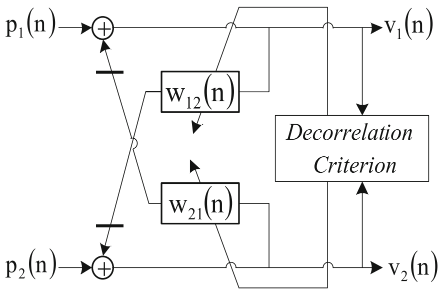

Fig. 5. A description of basic BSAD algorithm.

The exact update relations of adaptive filters $w_{12}(n)$ and $w_{21}(n)$ by the BD algorithm are given as follows [7, 10]:

$$\mathbf{w}_{12}(n) = \mathbf{w}_{12}(n-1) + \lambda_{12}\, v_2(n)\, \mathbf{v}_1(n) \tag{14}$$

$$\mathbf{w}_{21}(n) = \mathbf{w}_{21}(n-1) + \lambda_{21}\, v_1(n)\, \mathbf{v}_2(n) \tag{15}$$

with $\mathbf{v}_1(n) = [v_1(n), v_1(n-1), \ldots, v_1(n-L+1)]^T$ and $\mathbf{v}_2(n) = [v_2(n), v_2(n-1), \ldots, v_2(n-L+1)]^T$.

The two step-sizes, λ_{12} and λ_{21} represents the control parameters of BSAD algorithm which control the convergence direction of the two adaptive filters $w_{12}(n)$ and $w_{21}(n)$ respectively. They are chosen according to the relations $0 < \lambda_{12} < 2/\sigma_1^2$ and $0 < \lambda_{21} < 2/\sigma_2^2$, where σ_1^2 and σ_2^2 represents respectively the variance of the two input signals $v_1(n)$ and $v_2(n)$ [7, 10].

4 Proposed Backward Normalized Decorrelation Algorithms (BND)

In this paper, we will focus our interest on the two-channel backward SAD algorithm by proposing normalized step-sizes version that is presented in this subsection. In the output of BSAD algorithm presented in Fig. 4, we can define respectively the estimated speech signal $v_1(n)$, and it *a posteriori* error signal $e_1(n)$ in the backward structure as

$$v_1(n) = p_1(n) - \mathbf{w}_{21}^T(n-1)\mathbf{v}_2(n), \tag{16}$$

$$e_1(n) = p_1(n) - \mathbf{w}_{21}^T(n)\mathbf{v}_2(n). \tag{17}$$

When the update formulas of the adaptive filter $w_{21}(n)$ by the BSAD algorithm is given as follow:

$$\mathbf{w}_{21}(n) = \mathbf{w}_{21}(n-1) + \lambda_{21}\, v_1(n)\, \mathbf{v}_2(n) \tag{18}$$

Using (16), and inserting (18) into (17), we obtain,

$$e_1(n) = v_1(n) + \mathbf{w}_{21}^T(n-1)\mathbf{v}_2(n) - \mathbf{v}_2^T(n)\left[\mathbf{w}_{21}(n-1) + \lambda_{21} v_1(n)\mathbf{v}_2(n)\right] \tag{19}$$

Only, in noise-present segments (silence periods of speech), $e_1(n) = 0$, we obtain

$$v_1(n)\left[1 - \lambda_{21}\mathbf{v}_2^T(n)\mathbf{v}_2(n)\right] = 0 \tag{20}$$

Basing on (20) and assuming that $v_1(n) \neq 0 \rightarrow \left(1 - \lambda_{21}\mathbf{v}_2^T(n)\mathbf{v}_2(n) = 0\right)$, the step-size λ_{21} is given by

$$\lambda_{21} = \frac{1}{\mathbf{v}_2^T(n)\mathbf{v}_2(n)} \tag{21}$$

By using the same development steps but in symmetric filter $\mathbf{w}_{12}(n)$ of backward structure, the step-size λ_{12} is defined as

$$\lambda_{12} = \frac{1}{\mathbf{v}_1^T(n)\mathbf{v}_1(n)} \tag{22}$$

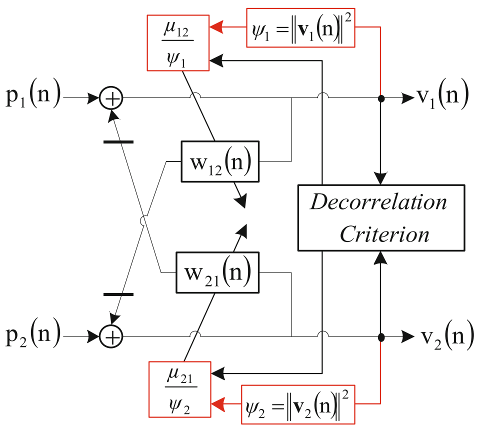

Fig. 6. A description of proposed BND algorithm.

By inserting [(22) into (14), (21) into (15)] and incorporating respectively the new normalized step-sizes, denoted: μ_{12} and μ_{21}, the two update formulas of $\mathbf{w}_{12}(n)$ and $\mathbf{w}_{21}(\mathrm{n})$ in the proposed normalized decorrelation algorithm are given by

$$\mathbf{w}_{12}(\mathrm{n}) = \mathbf{w}_{12}(\mathrm{n}-1) + \mu_{12}\,\frac{\mathrm{v}_2(n)\,\mathbf{v}_1(n)}{\mathbf{v}_1^{\mathrm{T}}(\mathrm{n})\mathbf{v}_1(\mathrm{n}) + \xi_{\mathrm{BND}}} \tag{23}$$

$$\mathbf{w}_{21}(\mathrm{n}) = \mathbf{w}_{21}(\mathrm{n}-1) + \mu_{21}\,\frac{\mathrm{v}_1(\mathrm{n})\,\mathbf{v}_2(n)}{\mathbf{v}_2^{\mathrm{T}}(\mathrm{n})\mathbf{v}_2(\mathrm{n}) + \xi_{\mathrm{BND}}} \tag{24}$$

In the modified BND algorithm presented in Fig. 6, we have proposed to normalize the two step-sizes μ_{12} and μ_{21} respectively by the input signals energy $\left\{\mathbf{v}_1^{\mathrm{T}}(\mathrm{n})\mathbf{v}_1(\mathrm{n})\right\}$ and $\left\{\mathbf{v}_2^{\mathrm{T}}(\mathrm{n})\,\mathbf{v}_2(\mathrm{n})\right\}$ of adaptive filters $\mathbf{w}_{12}(\mathrm{n})$ and $\mathbf{w}_{21}(\mathrm{n})$. The step-sizes μ_{12} and μ_{21} take their values between 0 and 2 to guarantee convergence of $\mathbf{w}_{12}(\mathrm{n})$ and $\mathbf{w}_{21}(\mathrm{n})$. The proposed BND algorithm is summarized in Table 1.

Table 1. Proposed BND algorithm

Parameters and variables

$\mathbf{w}_{12}(\mathrm{n})$ and $\mathbf{w}_{21}(\mathrm{n})$: adaptive filters

L : Adaptive filter length,

ξ_{BND} : Small positive constant,

Two step-sizes, $0 < \mu_{21} < 2$, $0 < \mu_{12} < 2$

$\mathbf{v}_1(\mathrm{n}) = [\mathrm{v}_1(\mathrm{n}),\ \mathrm{v}_1(\mathrm{n}\text{-}1),\ \ldots,\ \mathrm{v}_1(\mathrm{n}\text{-}\mathrm{L}+1)]^{\mathrm{T}}$

$\mathbf{v}_2(\mathrm{n}) = [\mathrm{v}_2(\mathrm{n}),\ \mathrm{v}_2(\mathrm{n}\text{-}1),\ \ldots,\ \mathrm{v}_2(\mathrm{n}\text{-}\mathrm{L}+1)]^{\mathrm{T}}$

Computation

for n=0,1, 2,3, . . .

$\mathrm{v}_1(\mathrm{n}) = \mathrm{p}_1(\mathrm{n}) - \mathbf{w}_{21}^{\mathrm{T}}(\mathrm{n}-1)\ \mathbf{v}_2(\mathrm{n}),$

$\mathrm{v}_2(\mathrm{n}) = \mathrm{p}_2(\mathrm{n}) - \mathbf{w}_{12}^{\mathrm{T}}(\mathrm{n}-1)\ \mathbf{v}_1(\mathrm{n}),$

Tap-weight adaptation:

$$\mathbf{w}_{12}(\mathrm{n}) = \mathbf{w}_{12}(\mathrm{n}-1) + \mu_{12}\,\frac{\mathrm{v}_2(\mathrm{n})\mathbf{v}_1(\mathrm{n})}{\mathbf{v}_1^{\mathrm{T}}(\mathrm{n})\mathbf{v}_1(\mathrm{n}) + \xi_{\mathrm{BND}}}$$

$$\mathbf{w}_{21}(\mathrm{n}) = \mathbf{w}_{21}(\mathrm{n}-1) + \mu_{21}\,\frac{\mathrm{v}_1(\mathrm{n})\mathbf{v}_2(\mathrm{n})}{\mathbf{v}_2^{\mathrm{T}}(\mathrm{n})\mathbf{v}_2(\mathrm{n}) + \xi_{\mathrm{BND}}}$$

end

5 Analysis of Simulation Results

In this section, the simulations results of proposed BND algorithm are presented, using the following criteria:

(i) Temporal evolution of the first output signals by basic BSAD and proposed BND algorithms.

(ii) System mismatch to describe the convergence rate of the cross-coupling adaptive filters. This SM criterion is evaluated according to the following expression:

$$\mathrm{SM(n)}_{\mathrm{dB}} = 20\ \log_{10}\left[\frac{\|\mathbf{h}_{21}(\mathrm{n}) - \mathbf{w}_{21}(\mathrm{n})\|}{\|\mathbf{h}_{21}(\mathrm{n})\|}\right] \tag{25}$$

(iii) Segmental SNR between the enhanced speech signal and its original version. The Segmental SNR criterion is given by the following relation

$$(\mathrm{SegSNR}_{\lambda})_{\mathrm{dB}} = 10\ \log_{10}\left(\frac{\sum_{i=0}^{U-1}|s(i)|^2}{\sum_{i=0}^{U-1}|s(i) - u_1(i)|^2}\mathrm{VAD}_{\lambda}\right) \tag{26}$$

U is number of sample needed to obtain average values of the output SNR. The $\{\mathrm{VAD}_{\lambda}\}$ is a voice activity detector used to calculate the SNR in presence speech.

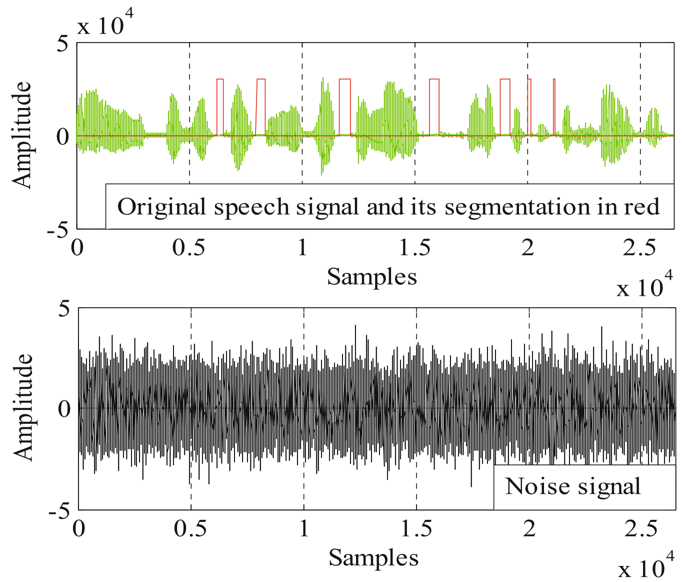

Fig. 7. Original speech signal s(n) and noise signal b(n).

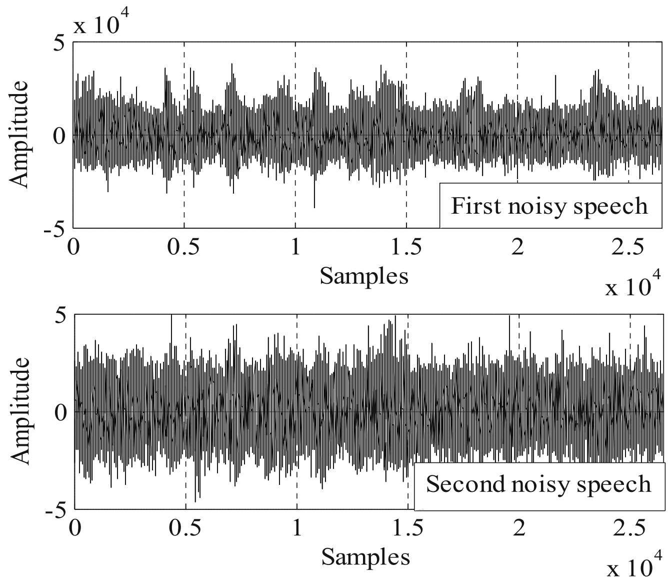

Fig. 8. Two noisy speech signals, $p_1(n)$ and $p_2(n)$.

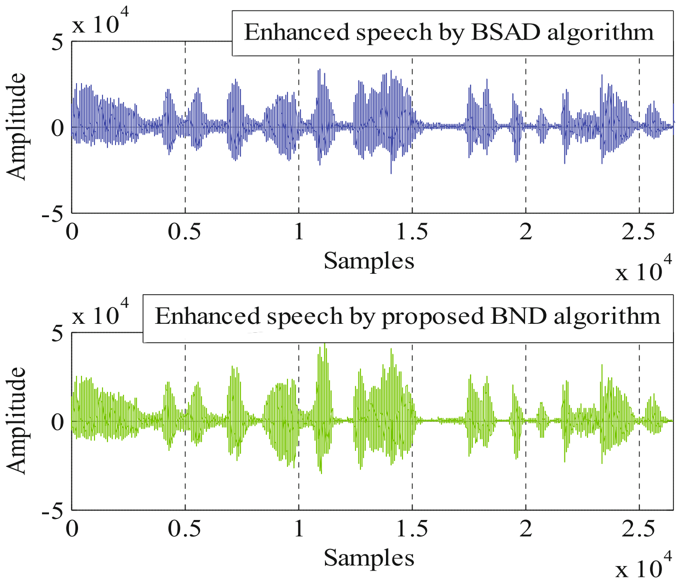

Fig. 9. Enhanced speech signal by BSAD and BND algorithms

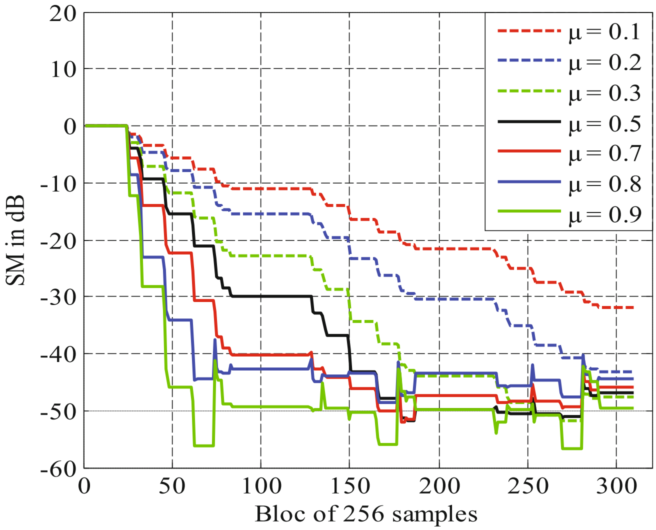

Fig. 10. Effect of step sizes values on BND algorithm.

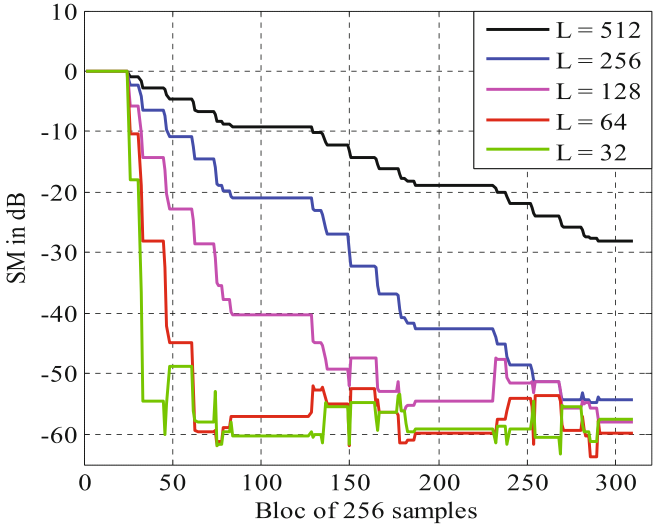

Fig. 11. Effect of adaptive filters length on BND algorithm.

We have used the mixing model of Fig. 2 to generate the noisy observations $p_1(n)$ and $p_2(n)$. The impulse responses $h_{12}(n)$ and $h_{21}(n)$ are generated by random sequences according to exponentially functions with the length of two reel filters is L = 256. In All simulations, we select the input signal-to-noise ratio to be equal to $SNR_1 = SNR_2 = -6$ dB. The source signals are, s(n) is speech signal and b(n) is USASI noise (United-state of America-Standard-Institute), and sampling frequency, 8 kHz. These two signals are presented in Fig. 7. The mixing signals $p_1(n)$ and $p_2(n)$ are show in Fig. 8. We note that the step-sizes of classical BSAD equal 0.009 and proposed BND algorithm equal 0.9.

The estimated speech signals $u_1(n)$ obtained by the classical BSAD and proposed BND algorithms are presented in Fig. 9. As we see from the last figure, and after convergence of the two algorithms (BSAD and BND algorithms). It can be easily seen that the proposed algorithm enhance the speech signal at the output and significantly reduces the acoustic noise components.

For more details about the behavior of proposed algorithm, intensive simulations are carried out with the SM criterion. In Figs. 10 and 11, we present the effect of the step-sizes values and adaptive filter length on the convergence rate of BND algorithm.

Basing on Fig. 10, we note that the convergence rate of the proposed BND algorithm increase/decrease proportionally with step-sizes values. According to Fig. and 11, we note that the convergence rate is very fast when the adaptive filters length is small. We have done others comparative simulations in very noise situations between the classical BSAD and proposed BND algorithms, by using the SM and Segmental SNR criteria. The parameters values are presented in Table 2.

Table 2. Parameters values of algorithms

Algorithms	Parameters values	
Basic BSAD	$\lambda_{12} = \lambda_{21} = 0.007$	L = 128 Input SNR = −6 dB Speech signal: 8 k Hz USASI noise
Proposed BND	$\mu_{12} = \mu_{21} = 0.7$ $\xi_{BND} = 10^{-6}$	

According to Fig. 12, we conclude the efficiency of proposed BND algorithm and their superiority in convergence speed and SM values performance compared with their classical version (SM level is −43 dB for BSAD and −50 dB for BND).

Basing on the output SegSNR results presented in Fig. 13, we can say that the proposed BND algorithm is a good performance of SNR loss that is observed with the classical BSAD algorithm. This improvement of the output SNR can be estimated by 8 dB in very noisy condition (input SNR = −6 dB).

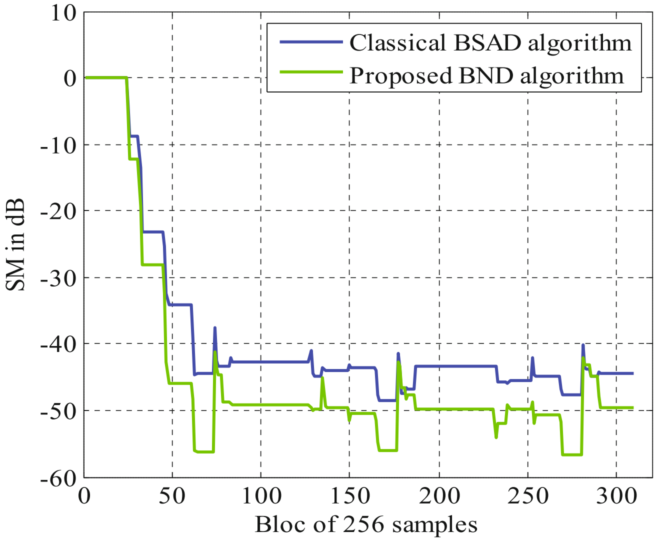

Fig. 12. Evaluation of SM criterion

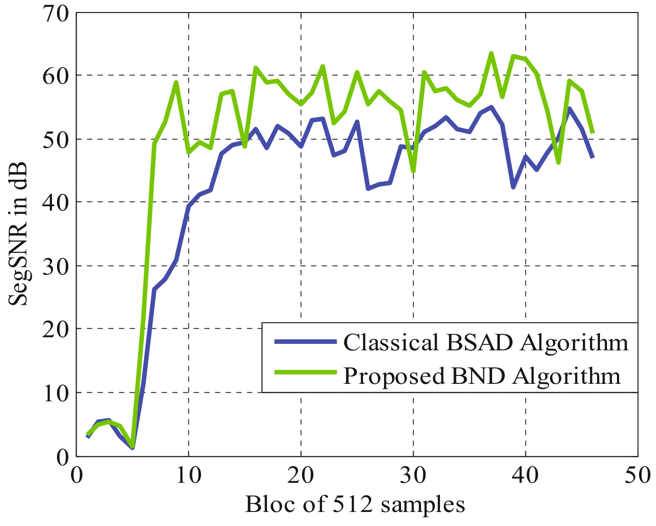

Fig. 13. Evaluation of Segmental SNR

6 Conclusion

The backward symmetric adaptive decorrelation algorithm used two very small step-sizes values. We note that the drawback of this algorithm is presented by variations of the input signals of two cross-adaptive filters. In this study, we have proposed a modified backward SAD algorithm based on normalized step-sizes by the power of input signals. Basing on the simulation results presented in this paper, the proposed BND algorithm has shown a good performance in term of convergence rate and speech quality compared with basic BSAD. We note that the BND is very efficient algorithm for noise reduction and speech enhancement

References

1. Ephraim, Y., Malah, D.: Speech enhancement using a minimum mean-square error log-spectral amplitude estimator. IEEE Trans. Acoust. Speech Signal Process. **33**(2), 443–445 (1985)
2. Boll, S.F.: Suppression of acoustic noise in speech using spectral subtraction. IEEE Trans. Acoust. Speech Signal Process. **27**(2), 113–120 (1979)
3. P. Scalart, J. Filho: Speech enhancement based on a priori signal to noise estimation. In: Proceedings of the International Conference on Acoustics, Speech, and Signal Processing, pp. 629–632 (1996)
4. Gilloire, A., Vetterli, M.: Adaptive filtering in subbands with critical sampling: analysis, experiments, and application to acoustic echo cancellation. IEEE Trans. Signal Process. **40**, 1862–1875 (1992)
5. Lee, K.A., Gan, W.S.: Improving convergence of the NLMS algorithm using constrained subband updates. IEEE Signal Process. Lett. **11**(9), 736–739 (2004)
6. Gabrea M (2003) Double affine projection algorithm-based speech enhancement algorithm. In: Proceedings of the IEEE on ICASSP, Montréal, Canada, April 2003, vol. 1, pp. 904–907
7. Van Gerven, S., Van Compernolle, D.: Signal separation by symmetric adaptive decorrelation: stability, convergence, and uniqueness. IEEE Trans. Signal Process. **43**(7), 1602–1612 (1995)
8. Djendi, M., Bendoumia, R.: A new adaptive filtering subband algorithm for two-channel acoustic noise reduction and speech enhancement. Comput. Elect. Eng. **39**(8), 2531–2550 (2013)
9. Bendoumia, R., Djendi, M.: Two-channel variable-step-size forward-and-backward adaptive algorithms for acoustic noise reduction and speech enhancement. Signal Process. **108**, 226–244 (2015)
10. van Gerven, S., van Compernolle, D.: Feedforward and feedback in symmetric adaptive noise canceller: stability analysis in a simplified case. In: Proceedings of the European Signal Processing Conference, Brussels, Belgium, August 1992, pp. 1081–1084
11. Djendi, M., Bendoumia, R.: A new efficient two-channel backward algorithm for speech intelligibility enhancement: a subband approach. Appl. Acous. **76**, 209–222 (2014)
12. Bendoumia, R., Djendi, M.: Variable step-sizes new efficient two-channel backward algorithm for speech intelligibility enhancement: a subband approach. Appl. Acoust. **76**, 209–222 (2014)

13. Djendi, M., Bendoumia, R.: Improved subband-forward algorithm for acoustic noise reduction and speech quality enhancement. App. Soft Comput. **42**, 132–143 (2016)
14. Alkindi, M.J., Dunlop, J.: Improved Adaptive noise cancellation in the presence of signal leakage on the noise reference channel. Signal Process. **17**, 241–250 (1989)
15. Pradhan, S.S., Reddy, V.E.: A new approach to subband adaptive filtering. IEEE Trans. Signal Process. **47**, 655–664 (1999)

A Variable Step Size-Forward Blind Source Separation Algorithm for Speech Enhancement

Meriem Zoulikha(✉), Mohamed Djendi, and Abderezzak Guessoum

Signal Processing and Imaging Laboratory (LATSI),
University of Blida 1, Route de Soumaa, B.P. 270, 09000 Blida, Algeria
m_zoulikha@hotmail.fr, m_djendi@yahoo.fr,
abderguessoum@yahoo.com

Abstract. This paper addresses the problem of speech enhancement in a moving car through a blind source separation (BSS) scheme involving two spaced microphones. The forward and backward BSS structures are extensively used in the literature to reduce the acoustic noise in many applications. These structures use manual activity detector (MVAD) system to control the adaptation of the separating adaptive filters. In this paper, we propose new structure called VSS-FBSS, which allows adapting the original FBSS structure, by an automatic voice activity detector (AVAD) system. This new structure is controlled automatically by an AVAD system based on the use of the FBSS structure to estimate the optimal values of the separating filters step-sizes. The performance of the proposed structure is compared to the classical FBSS structure performance where a MVAD is used. This comparison is evaluated in terms of the output signal-to-noise ratio (SNR), cepstral distance (CD) and system mismatch (SM) criteria under various environments. Experimental results have shown the good behavior of the proposed structure.

Keywords: Speech enhancement · Adaptive algorithm · LMS
Forward · Backward · BSS

1 Introduction

Noise exists in our daily life. According to the research, if human stays in the noisy environment for a long time, he may suffer from hearing loss physiologically; people have paid more and more attention to this negative impact. So the reduce and clear up of noise has attracted researches' attention for a long time [1]. In literature, a several approaches have been proposed for noise reduction based on speech enhancement techniques [2]. Two structures, conceptually simple allowing to carry out the noise reduction by sources separation. They are respectively called backward (BBSS) [3] and forward (FBSS) [4] structures. In this paper, we focus our interest on the FBSS structure employed to enhance the speech signal from a convolutive mixture. The classical FBSS structure need a VAD system to allow extracting and separating speech and noise from the mixing signal components. Usually, a MVAD system is used and which gives a perfect segmentation; the latter is not practical due to the lack of a-priori input signals information. To overcome this drawback, we need to detect the VAD

M. Chadli et al. (Eds.): ICEECA 2017, LNEE 522, pp. 479–487, 2019.
https://doi.org/10.1007/978-3-319-97816-1_36

automatically. Several techniques of automatic voice activity detector (AVAD) systems have been proposed recently in speaker localization applications [5]. In this paper, new FBSS structure which is controlled by an AVAD system is proposed. This proposed AVAD system is based on the signal SNR estimation which allows us to estimate automatically the step-sizes values of the FBSS structure. This paper is organized as follows: after the introduction which is presented in Sect. 1, we present in Sect. 2, the classical FBSS structure. The proposed structure (VSS-FBSS) and its principle are described in Sect. 3. Lastly, we show the simulation results of this new structure (VSS-FBSS).

2 Classical FBSS

Both yellow and green block diagram of Fig. 1 represent the classical FBSS structure. The FBSS has two microphones: the primary microphone to obtain the desired speech contaminated by noise, and the reference microphone to obtain the noise contaminated by useful signal. The signals obtained from both microphones called noisy observations; the latter are mixed by a convolution operation [4–6]. In Fig. 1 (green block), s(n) and b(n) are two sources of speech and noise respectively. $h_{21}(n)$ is the impulse response of the 1st channel from the noise source to the primary microphone and $h_{12}(n)$ is the impulse response of the 2nd channel from the signal source to the reference microphone.

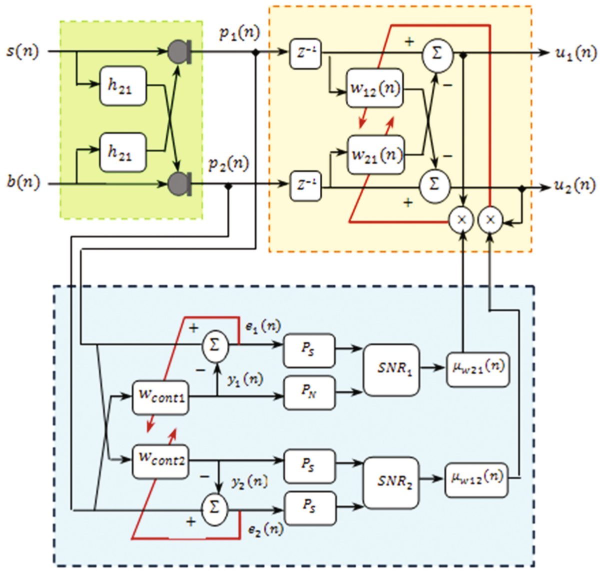

Fig. 1. Principal schema of the proposed VSS-FBSS structure.

The convolutive mixing observations ($p_1(n)$ and $p_2(n)$) can be written as:

$$p_1(n) = s(n) + h_{21}(n)^* b(n) \tag{1}$$

$$p_2(n) = b(n) + h_{12}(n)^* s(n) \tag{2}$$

The output signals $u_1(n)$ and $u_2(n)$ of the FBSS structure are given by:

$$u_1(n) = p_1(n) - u_2(n)^* w_{21}(n) \tag{3}$$

$$u_2(n) = p_2(n) - u_1(n)^* w_{12}(n) \tag{4}$$

Inserting relations (1) and (2) in (3) and (4) respectively, we get the following outputs signals:

$$u_1(n) = b(n)^*[h_{21}(n) - w_{21}(n)] + s(n)^*[\delta(n) - h_{12}(n)^* w_{21}(n)] \tag{5}$$

$$u_2(n) = s(n)^*[h_{12}(n) - w_{12}(n)] + b(n)^*[\delta(n) - h_{21}(n)^* w_{12}(n)] \tag{6}$$

If we set the optimal solution to the separating adaptive filters ($w_{21}^{opt}(n) = h_{21}(n)$ and $w_{12}^{opt}(n) = h_{12}(n)$), then the outputs relation became:

$$u_1(n) = s(n)^*[\delta(n) - h_{12}(n)^* h_{21}(n)] \tag{7}$$

$$u_2(n) = b(n)^*[\delta(n) - h_{21}(n)^* h_{12}(n)] \tag{8}$$

We note that the coefficients of both separation filters $w_{12}(n)$ and $w_{21}(n)$ are adapted from the NLMS (Normalized Least Mean Square) algorithm. The adaptation relations of both adaptive filter $w_{12}(n)$ and $w_{21}(n)$ are given by the following expressions:

$$w_{12}(n) = w_{12}(n-1) + \mu_{12} \frac{u_2(n)\ m_1(n)}{m_1^T(n)\ m_1(n)} \tag{9}$$

$$w_{21}(n) = w_{21}(n-1) + \mu_{21} \frac{u_1(n)\ m_2(n)}{m_2^T(n)\ m_2(n)} \tag{10}$$

where $m_1(n) = [p_1(n), p_1(n-1), \ldots, p_1(n-L+1)]^T$ and $m_2(n) = [p_2(n), p_2(n-1), \ldots, p_2(n-L+1)]^T$ are two vectors that contains the noisy observation sample $p_1(n)$ and $p_2(n)$ respectively. The two parameters μ_{12} and μ_{21} are the fixed step sizes of both adaptive filters $w_{12}(n)$ and $w_{21}(n)$ respectively, which must be chosen between 0 and 2 to achieve convergence of adaptive filters [6]. We can notice that the FBSS structure, which has been described previously, use an optimal assumption ($w_{21}^{opt}(n) = h_{21}(n)$ and $w_{12}^{opt}(n) = h_{12}(n)$). This optimal solution is got in practice thanks to the adaptation control of both adaptive filters ($w_{21}(n)$ and $w_{12}(n)$). This adaptation is often a MVAD system. This manual adaptation is controlled as follows: the adaptive filter $w_{21}(n)$ is adapted only during the noise presence periods, while the filter $w_{12}(n)$ is adapted only during the voice activity presence periods.

3 Proposed Structure (VSS-FBSS)

In order to separate the convolutive mixture components presented in Fig. 1 (green block), the FBSS structure (Fig. 1 (yellow block)), is classically used. The use of a MVAD system in the FBSS structure operation gives a perfect segmentation which is not the case in practice, because there is no a priori information on the input signals. For this purpose, we need to detect the VAD automatically. In this paper we propose new AVAD based on estimated signal-to-noise ratios (SNRs) from a FBSS structure (Fig. 1 (blue block)) to control the step-sizes values $\mu_{w12}(n)$ and $\mu_{w21}(n)$ that are used by the two cross-adaptive filters $w_{12}(n)$ and $w_{21}(n)$ respectively. The new proposed (VSS-FBSS) structure corresponds to FBSS structure with variable step sizes which acts as a VAD system. The VSS-FBSS structure comprises four adaptive filters, namely, the main adaptive filter ($w_{21}(n)$, $w_{12}(n)$) and the sub adaptive filters ($w_{cont1}(n)$, $w_{cont2}(n)$). The main role of these sub adaptive filters is to provide an estimation of signal to noise ratios (SNRs) measured on both noisy observation signals. These two estimated SNRs are then used to control the step sizes of the main adaptive filters ($w_{21}(n)$, $w_{12}(n)$). Coefficients in the main and sub adaptive filters are updated by NLMS algorithm [7].

3.1 SNRs Estimation by Sub Adaptive Filters

The output $y_1(n)$ of the sub adaptive filter $w_{cont1}(n)$ and the error $e_1(n)$ are used to estimate the SNR_1 at the primary path. In fact, under the filter $w_{cont1}(n)$ convergence hypothesis, the error $e_1(n)$ and the estimated signal $y_1(n)$ correspond to signal and noise components of the noisy observation signal $p_1(n)$ respectively. The step size of the main filter $w_{21}(n)$ is then controlled from the estimated SNR_1 carried out on signals present on the sub filter $w_{cont1}(n)$ output. Similarly, the sub filter $w_{cont2}(n)$ estimates the SNR_2 on the second noisy observation path $p_2(n)$. The estimation of useful signal (respectively of noise) is then obtained by measuring the average power of $y_2(n)$ (respectively of $e_2(n)$). The estimated (SNR_1, SNR_2) at the primary and reference paths respectively are given by the following relations:

$$SNR_1(n) = 10*\log_{10}\left\{\frac{P_S(n)}{P_N(n)}\right\} \tag{11}$$

$$SNR_2(n) = 10*\log_{10}\left\{\frac{Q_S(n)}{Q_N(n)}\right\} \tag{12}$$

where $P_S(n)$ and $P_N(n)$ correspond to the average power of speech and noise respectively at the primary path. Similarly, $Q_S(n)$ and $Q_N(n)$ represent the estimated average power of speech and noise at the reference path.

These powers are estimated from signals available at the outputs of both sub adaptive filters ($w_{cont1}(n)$ and $w_{cont2}(n)$) by the following equations:

$$P_S(n) = \sum_{j=0}^{M-1} e_1^2(n-j) \quad \text{and} \quad P_N(n) = \sum_{j=0}^{M-1} y_1^2(n-j) \tag{13}$$

$$Q_S(n) = \sum_{j=0}^{M-1} y_2^2(n-j) \quad \text{and} \quad Q_N(n) = \sum_{j=0}^{M-1} e_2^2(n-j) \tag{14}$$

3.2 Principal of Step Sizes Control

When $SNR_1(n)$ at the primary path's input $p_1(n)$ is large; the step size value $\mu_{w21}(n)$ of the filter $w_{21}(n)$ should be set to a small value. On the other side, when $SNR_1(n)$ is small the step size $\mu_{w21}(n)$ takes large value. A similar rule applies to step size $\mu_{w12}(n)$ for coefficients adaptation of the main filter $w_{12}(n)$ and this in function of estimated $SNR_2(n)$ evolution at the reference path's input $p_2(n)$. The variable step sizes $\mu_{w21}(n)$ and $\mu_{w12}(n)$ are controlled by the estimated $SNR_1(n)$ and $SNR_2(n)$ as in the following equations:

$$\mu_{w21}(n) = \begin{cases} \mu_{1min} & SNR_1(n) > SNR_{1max} \\ \mu_{1max} & SNR_1(n) < SNR_{2min} \\ f\,(SNR_1(n)) & \text{else} \end{cases} \tag{15}$$

$$\mu_{w12}(n) = \begin{cases} \mu_{2min} & SNR_2(n) < SNR_{2min} \\ \mu_{2max} & SNR_2(n) > SNR_{2max} \\ g\,(SNR_2(n)) & \text{else} \end{cases} \tag{16}$$

$\mu_{1max}, \mu_{2max}, \mu_{1min}, \mu_{2min}$ are the maximum and the minimum step sizes for $\mu_{w21}(n)$ and $\mu_{w12}(n)$. f(.) and g(.) are function of $SNR_1(n)$ and $SNR_2(n)$, respectively. f(.) should be a decreasing function because a small step size is suitable for a large SNR. On the other hand, it is desirable that g(.) is an increasing function.

4 Simulation Results

This section, we analyze the behavior of the proposed structure that has been presented in the previous sections. Also we compare our VSS-FBSS structure with its classical version (FBSS). We have used the specific model proposed in [8] which yields simulated impulse responses $h_{12}(n)$ and $h_{21}(n)$ [the sampling frequency $f_s = 16$ kHz, the corresponding reverberation time is 30.8 ms, and the size of the impulse responses is L = 64]. The useful signal is chosen from standardized database (AURORA) and the disturbed signal is stationary white noise. The original speech signal, the noisy observation $p_1(n)$ and the output signal $u_1(n)$ of the proposed VSS-FBSS structure are shown with their spectrogram in Fig. 2. We can observe from Fig. 2, that the available signal at the processing output $u_1(n)$ is completely denoised and very close to the original speech signal. We note that this result is achieved through the use of AVAD system as indicated before. The latter is used to control the adaptation of the main filters ($w_{21}(n)$, $w_{12}(n)$), this segmentation technique is based on the step sizes ($\mu_{w21}(n)$, $\mu_{w12}(n)$) variation in function of the estimated SNR on each observation paths.

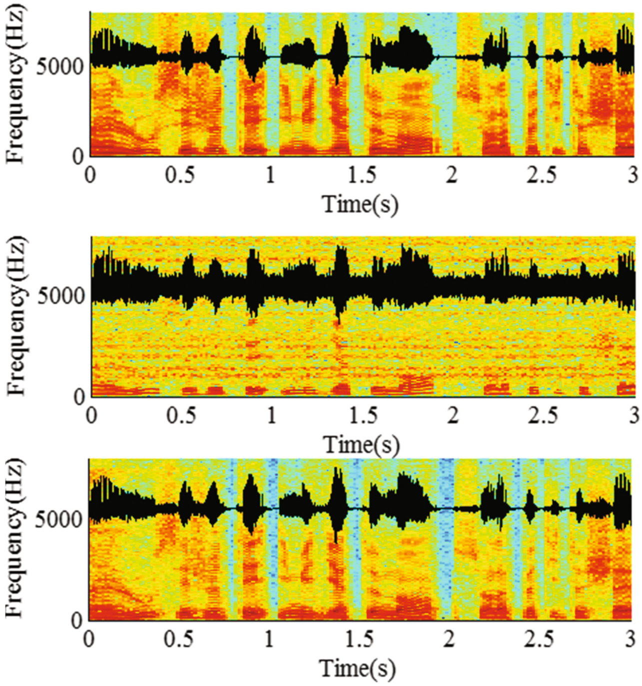

Fig. 2. Speech signal (top), the noisy observation (middle) and the output signal (bottom) obtained with the proposed VSS-FBSS structure.

In Fig. 3 we present the estimated SNR_1 evolution at the primary input $p_1(n)$ and the variable step size $\mu_{w21}(n)$ of the main filter $w_{21}(n)$. According to this figure, we notice that when the estimated SNR_1 at the primary path $p_1(n)$ is large, the step size $\mu_{w21}(n)$ of the main filter $w_{21}(n)$ takes small values. On the other hand, the step size $\mu_{w12}(n)$ is large when the speech signal is absent.

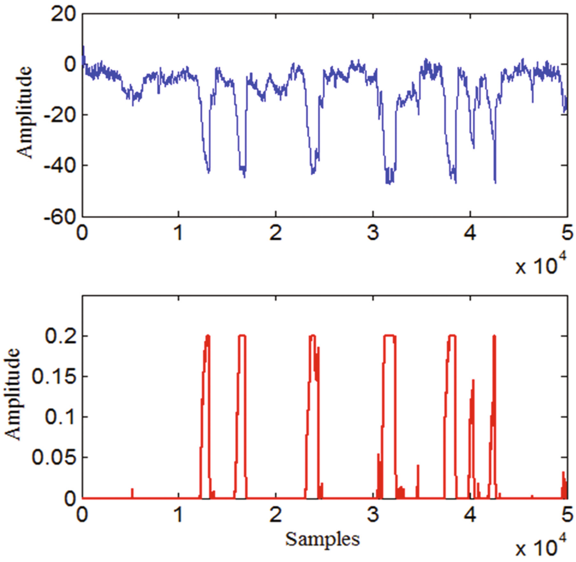

Fig. 3. Time evolution of the SNR and step-sizes. Estimated SNR_1 of the primary signal (in blue) and the step size $\mu_{w21}(n)$ of the filter $w_{21}(n)$ (in red).

A comparison in terms of the averaged cepstral distance (CD) between the original speech signal and those obtained at the output of the proposed structure (VSS-FBSS) and the classical version (FBSS) (see Fig. 4). Note that the classical structure (FBSS) used a MVAD in its operation and the proposed structure (VSS-FBSS) used an AVAD which corresponds to the step size $\mu_{w21}(n)$ evolution. From Fig. 4 (top), we can see that the CD average values are −7.86 dB and −7.80 dB for the VSS-FBSS and FBSS structures respectively. These results are very close and also show the good behavior of the proposed structure (VSS-FBSS). In Fig. 4 (middle), we have evaluated the SNR criterion for both structures (VSS-FBSS and FBSS). The mean value of the SNR of the VSS-FBSS structure is about 50.32 dB and 50.21 dB for the FBSS structure. It means that there is a very low gain between both structures. This shows that the proposed structure provides almost the same performance as the classical version. In order to complete the analysis of the proposed structure behavior, we present in the Fig. 4 (bottom) the system mismatch evolution measured on the adaptive filter coefficients $w_{21}(n)$ for both structures (VSS-FBSS and FBSS). From the result of this figure, we note that the convergence speed is almost the same for the proposed and the classical structures. This once again demonstrates the good behavior of the new VSS-FBSS structure.

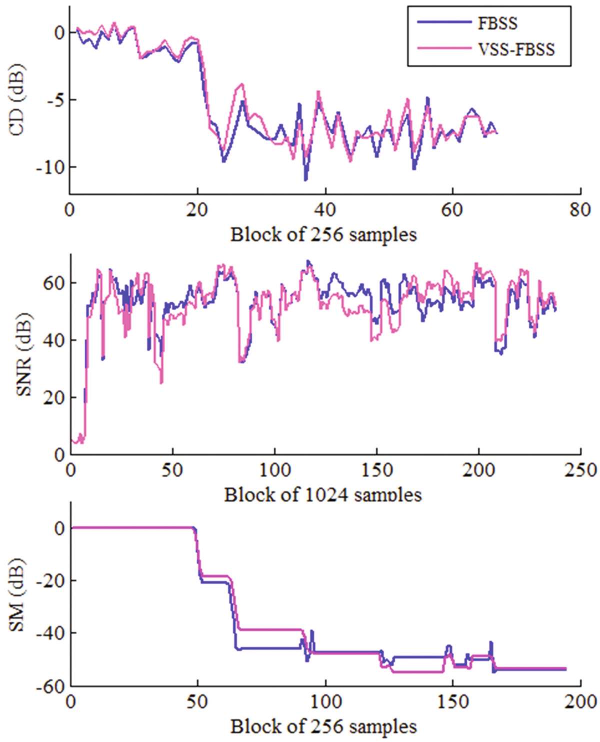

Fig. 4. Comparison of cepstral distance (CD), the Output SNR evaluation and system mismatch (SM) obtained by FBSS structure (in blue) and proposed VSS-FBSS structure (in magenta).

5 Conclusion

In this paper, we have proposed new structure called VSS-FBSS which allows extracting the speech signal from very noisy observed signals. This proposed method is mainly composed by two great parts which are the main structure and the step-sizes control structure. In this proposed structure, both the main and the control step-sizes structures are forward-type. In the proposed structure, the estimated SNRs of the primary and reference paths are used to control the step-sizes values of the main structure. Intensive simulations are carried out to validate the performance of the new proposed structure. The output signals time evolution, the system mismatch, the CD and the output SNR criteria are used to show the good performance of this proposed structure in noise reduction and speech enhancement application. Finally, we can say that the proposed structure (VSS-FBSS) is good alternative solution for this type of application (i.e. noise reduction and speech enhancement application).

References

1. Wang, Y.-N., Liao, H.-H., Lee, T.-S.: Applied variable step size algorithm to dual-adaptive noise canceller. In: Proceedings of the 7th WSEAS International Conference on Multimedia Systems and Signal Processing, Hangzhou, China, 15–17 April 2007
2. Ikeda, S., Sugiyama, A.: An adaptive noise canceller with low signal-distortion in the present of crosstalk. IEICE Trans. Fundam. **82-A**(8), 1517–1525 (1999)
3. Al-Kindi, M.J., Dunlop, J.: Improved adaptive noise cancellation in the presence of signal leakage on the noise reference channel. Sign. Process. **17**(3), 241–250 (1989)
4. Van Gerven, S., Van Compernolle, D.: Signal separation by symmetric adaptive decorrelation: stability, convergence, and uniqueness. IEEE Trans. Sign. Proc. **74**(3), 1602–1612 (1995)
5. Mak, M.W., Yu, H.B.: A study of voice activity detection techniques for NIST speaker recognition evaluations. Comput. Speech Lang. **28**(1), 295–313 (2014)
6. Djendi, M., Gilloire, A., Scalart, P.: Noise cancellation using two closely spaced microphones: experimental study with a specific model and two adaptive algorithms. In: Proceedings of International Conference on Acoustics Adaptive Algorithms, Proceedings of International Conference on Acoustics Speech, Signal Process (ICASSP), vol. 3, pp. 744–747, May 2006
7. Goodwin, G.C., Sin, K.S.: Adaptive Filtering, Prediction and Control. Prentice-Hall, Englewood Cliffs (1985). Info Sys Sci
8. Djendi, M.: Advanced techniques for two-microphone noise reduction in mobile communications. Ph.D. dissertation (in French), University of Rennes1, France 2010, n°19012010

Comparative Study Between the WDM System and the DWDM in an Optical Transmission Link at 40 Gb/s

Cheikh Kherici(✉) and Malika Kandouci

Laboratory of Electronic Photonic and Optoelectronic (LEPO),
University of Sidi Bel-Abbes, 22000 Sidi Bel-Abbes, Algeria
khericic@yahoo.fr, maikand04@gmail.com

Abstract. The WDM multiplexing is explained by the fact that always transmit multiple signals of different colors (or channels) at the same time while avoiding the costs of civil engineering about the stacking of the repeater-regenerators.

The WDM allows to multiply by 16 the capacity of the fiber at the same modulation speed, but each signal has a distinct wavelength, but the DWDM (Dense WDM) makes it possible to multiply by 160 the wavelengths [1]. In this paper we will elaborate a detailed comparative study to extract the performances using the different simulations based on a software system. This paper takes into account the different modulations of the signal in transmission (RZ, NRZ … etc.), the number of channels and the impact of the nonlinear effects on the multiplexing.

Keywords: WDM · Simulation · Eye diagram · NRZ · RZ · Multiplexing DWDM · Quality factor · Demultiplexing · Channel · Nonlinear effects Comparison

1 Introduction

In theory the capacity of optical fibers allows the establishment of transmission systems at very high bit rates. However, the electronic processing of data, at the transmission and the reception, enforces limitations in terms of bit rates due to electronic components. The increase in the number of users and the quality of information exchanged in the optical fiber networks has pushed to the development of solutions to increase networks capacity. Multiplexing technical have been developed, each for transmit N signals with D bit rates on the same channel, which is equivalent to the transmission of an overall signals with bit rate N × D [2].

These multiplexing technical must respect the necessary condition to be able to reproduce the data specific to each user after transmission without creating interference between the different users. For this, the WDM and other techniques such as DWDM, CWDM …, are suitable for optical fiber transmission links.

M. Chadli et al. (Eds.): ICEECA 2017, LNEE 522, pp. 488–498, 2019.
https://doi.org/10.1007/978-3-319-97816-1_37

2 The Wavelength Division Multiplexing (WDM)

The wavelength division multiplexing consists of transmitting several frequencies at different wavelengths on the same transmission medium with a channel spacing (frequency) greater than or equal to 0.8 nm (100 GHz), it can transmit 4 to 16 signals with D bit rates on the same channel. If this interval is less than or equal to 0.8 nm, then we are talking about DWDM multiplexing (Dense WDM). A few experiments were even carried out at intervals of 0.4 and 0.2 nm where 160 channels can be used in an optical fiber (Fig. 1).

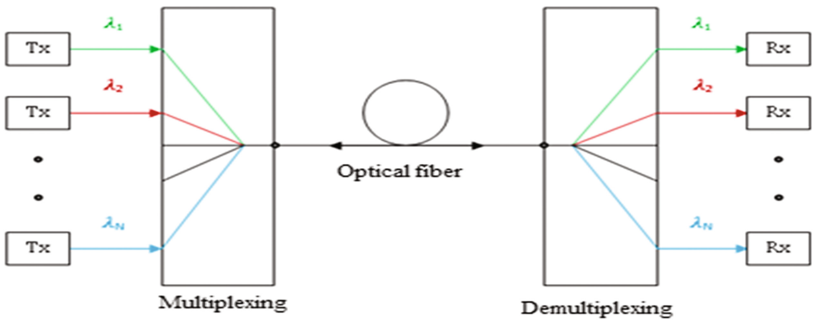

Fig. 1. The WDM system.

2.1 NRZ Modulation for WDM System at 40 Gb/s (8 Channels)

2.1.1 With Nonlinear Effects

The Fig. 2 shows the impact of nonlinear effects on the optical spectrum of the output link, this deformation of the spectrum is due to the self-phase modulation (SPM) (Fig. 3) [3].

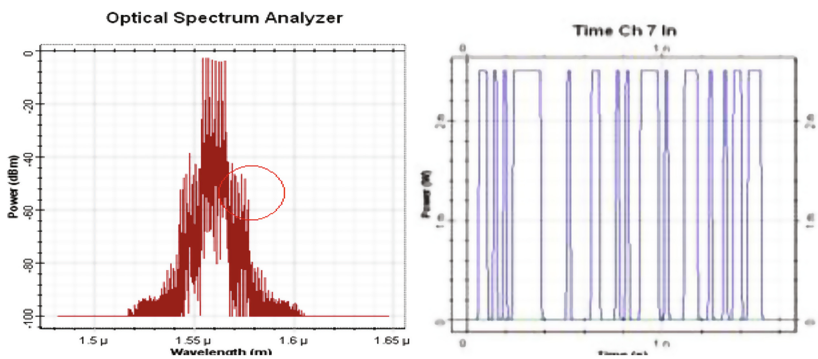

Fig. 2. The optical spectrum and the output signal for Ch7 with nonlinear effects.

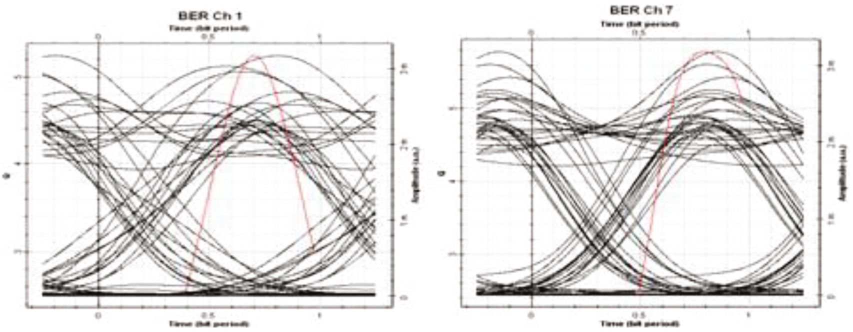

Fig. 3. Eye diagram of the Ch1 & Ch7 with nonlinear effects.

2.1.2 Without Nonlinear Effects

See Figs. 4 and 5.

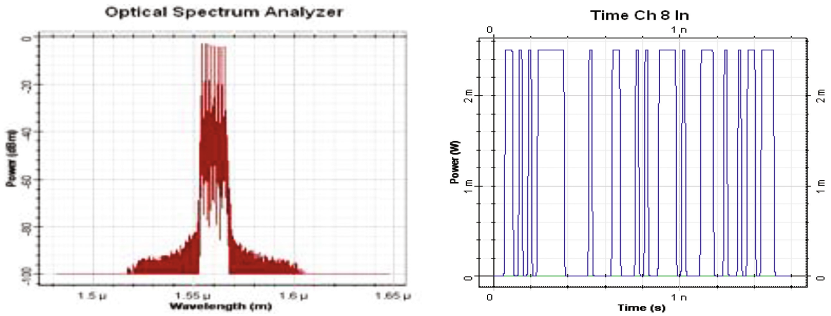

Fig. 4. The optical spectrum and the output signal for Ch8 without nonlinear effects.

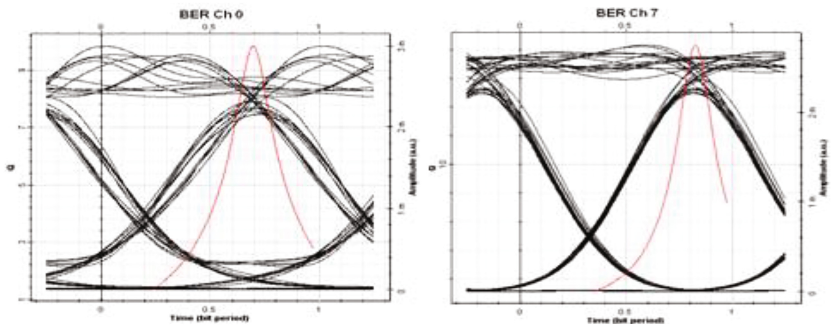

Fig. 5. Eye diagram of the Ch0 & Ch7 without nonlinear effects.

2.1.3 Comparison Between the NRZ with N.E and NRZ Without N.E

See Table 1 and Figs. 6, 7.

Table 1. Comparison.

Channel	1	2	3	4	5	6	7	8
Q without N.E	9.8	5.6	7.1	8.6	13.2	24	18	18.3
Q with N.E	5.2	5.2	5.8	6	6	5.2	5.8	5.8

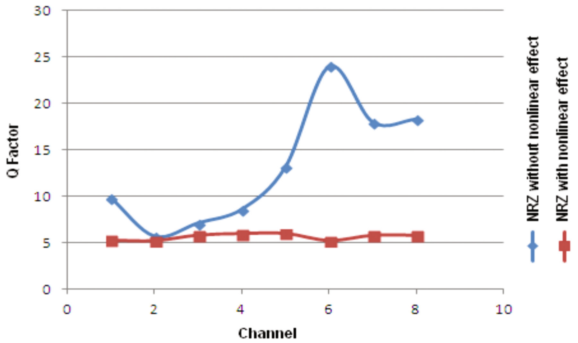

Fig. 6. Nonlinear effects impact on the Q factor (NRZ modulation).

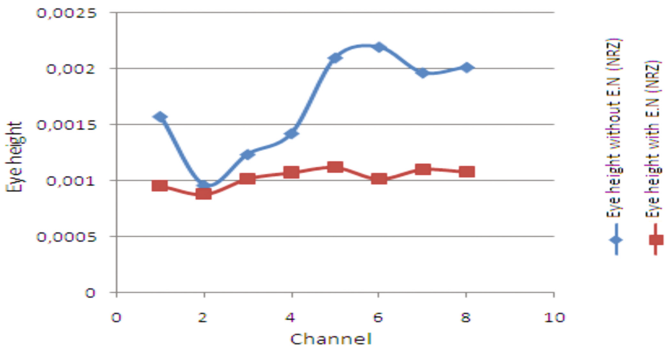

Fig. 7. Nonlinear effects impact on the Eye opening (NRZ modulation).

2.2 RZ Modulation for WDM System at 40 Gb/s (8 Channels)

2.2.1 With Nonlinear Effects

See Fig. 8.

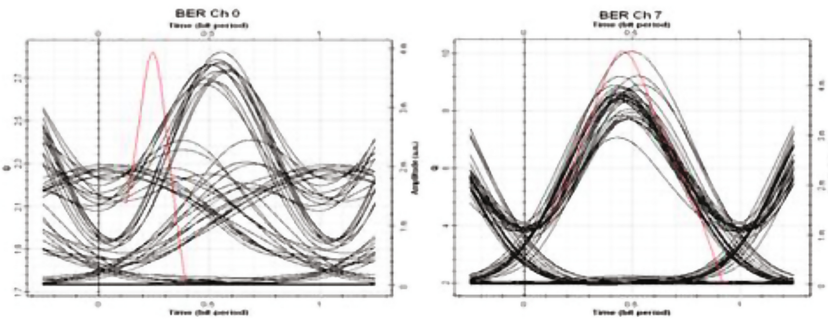

Fig. 8. Eye diagram of the Ch0 & Ch7 with nonlinear effects.

2.2.2 Without Nonlinear Effects

See Fig. 9.

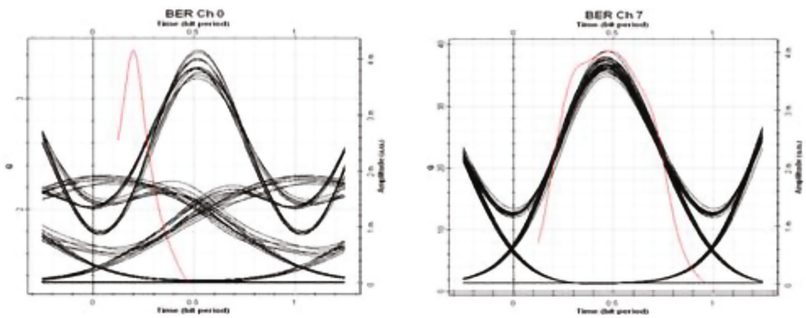

Fig. 9. Eye diagram of the Ch0 & Ch7 without nonlinear effects.

2.2.3 Comparison Between the RZ with N.E and RZ without N.E

The Table 2 shows the impact of nonlinear effects on the Q factor is significant in the RZ modulation (channel 8 of the 8 channels WDM system) with a decrease value of 29 per Signal without nonlinear effects. This observation shows that the RZ modulation is sensitive to nonlinear effects compared to the NRZ modulation (Figs. 10, 11) [3].

Table 2. Comparison.

Channel	1	2	3	4	5	6	7	8
Q without N.E	3.4	5	8	10.7	15.8	30.2	32.6	38.9
Q with N.E	2.8	3.9	5.3	5.4	6.7	7.8	8.1	10.1

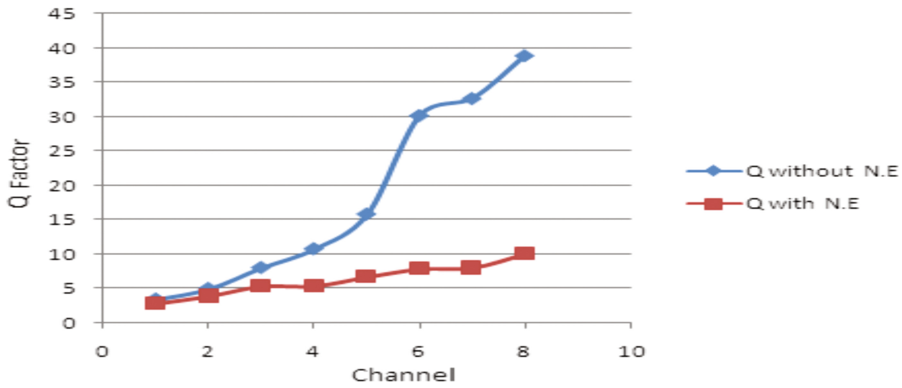

Fig. 10. Nonlinear effects impact on the Q factor (RZ modulation).

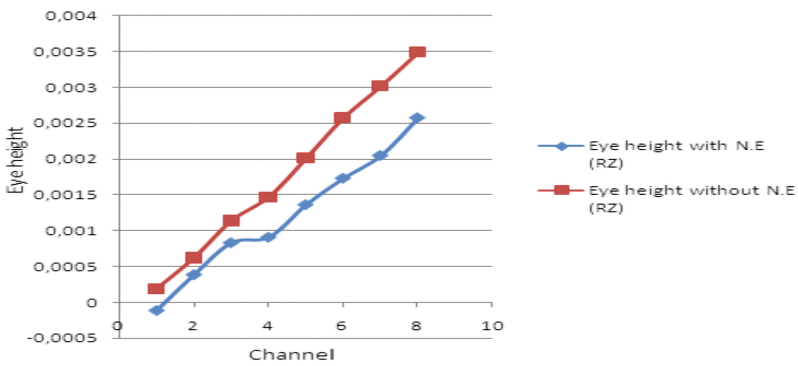

Fig. 11. Nonlinear effects impact on the Eye opening (RZ modulation).

2.3 NRZ Modulation for WDM System at 40 Gb/s (16 Channels)

2.3.1 With Nonlinear Effects

See Fig. 12.

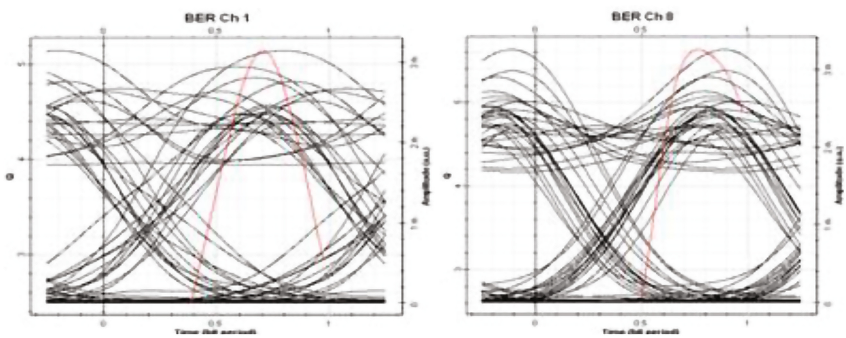

Fig. 12. Eye diagram of the Ch1 & Ch8 with nonlinear effects.

2.4 RZ Modulation for WDM System at 40 Gb/s (16 Channels)

2.4.1 With Nonlinear Effects

See Fig. 13.

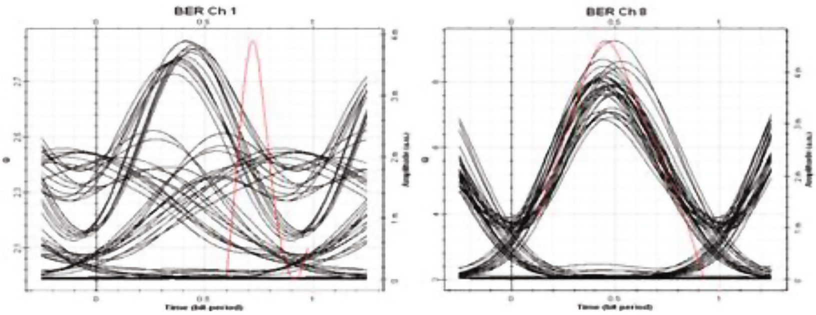

Fig. 13. Eye diagram of the Ch1 & Ch8 with nonlinear effects.

2.4.2 Comparison Between the WDM 8 Channels and the WDM 16 Channels (NRZ & RZ with N.E)

Our simulations, when we analyzed the 8 channels and 16 channels WDM system using RZ and NRZ modulation techniques, the results showed that the RZ modulation was the more suitable for the WDM system. The results of Q factor we obtained agreed well, and suggested that RZ modulation was the superior technique when dealing with small WDM systems. Independently of the fact that the NRZ is more affected by the nonlinear effects in this system. This demonstrates once again that NRZ modulation (compared to RZ modulation) is not efficient when the number of channels in the system is less than 16 channels (Table 3).

Table 3. Comparison.

Channel	8 Channels system	16 Channels system
Q Ch8 with N.E (NRZ)	6	5.63
Q Ch8 with N.E (RZ)	10.1	9.26

2.5 NRZ Modulation for DWDM System at 40 Gb/s (32 Channels)

2.5.1 With Nonlinear Effects

See Fig. 14.

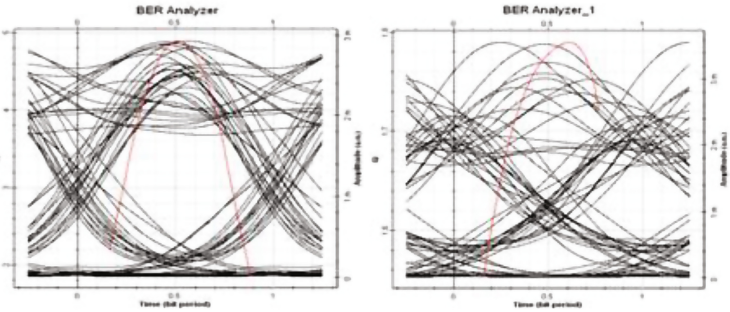

Fig. 14. Eye diagram of the Ch1 & Ch8 with nonlinear effects.

2.6 RZ Modulation for DWDM System at 40 Gb/s (32 Channels)

2.6.1 With Nonlinear Effects

See Fig. 15.

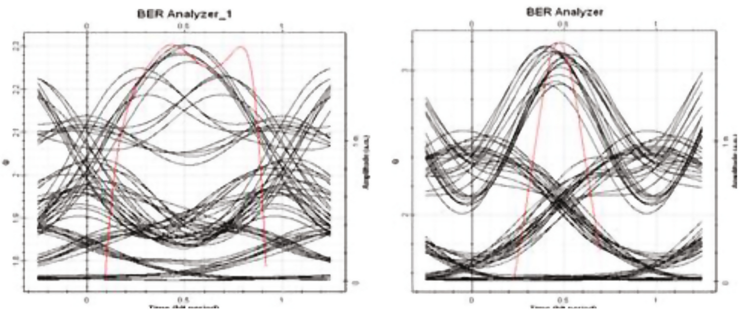

Fig. 15. Eye diagram of the Ch1 & Ch8 with nonlinear effects.

2.6.2 Comparison Between the WDM 8 Channels, WDM 16 Channels and the DWDM 32 Channels (NRZ & RZ with N.E)

We found that the Q factor in RZ modulation decreased with the increase of the number of channels compared to the NRZ modulation: the results we obtained agreed well, and suggested that NRZ modulation was the superior technique when dealing with large WDM systems (32 channels DWDM system) (Table 4) [4].

Table 4. Comparison.

Channel	8 Channels system	16 Channels system	32 Channels system
Q Ch8 with N.E (NRZ)	6	5.63	4.9
Q Ch8 with N.E (RZ)	10.1	9.26	3.19

So we're going to tip to the 64 channels DWDM system to make this ascertainment.

2.7 NRZ Modulation for DWDM System at 40 Gb/s (64 Channels)

2.7.1 With Nonlinear Effects

See Fig. 16.

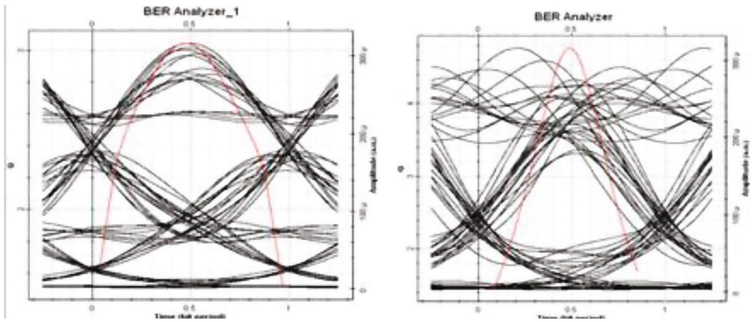

Fig. 16. Eye diagram of the Ch1 & Ch8 with nonlinear effects.

2.8 RZ Modulation for DWDM System at 40 Gb/s (64 Channels)

2.8.1 With Nonlinear Effects

See Fig. 17.

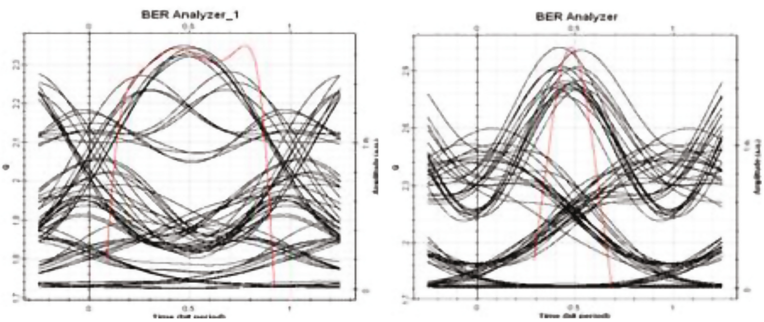

Fig. 17. Eye diagram of the Ch1 & Ch8 with nonlinear effects.

2.8.2 Comparison Between the WDM 8 Channels, WDM 16 Channels, DWDM 32 Channels and DWDM 64 Channels (NRZ & RZ with N.E)

See Table 5 and Fig. 18.

Table 5. Comparison.

Channel	8 Channels system	16 Channels system	32 Channels system	64 Channels system
Q Ch8 with N.E (NRZ)	6	5.63	4.9	4.76
Q Ch8 with N.E (RZ)	10.1	9.26	3.19	3.02

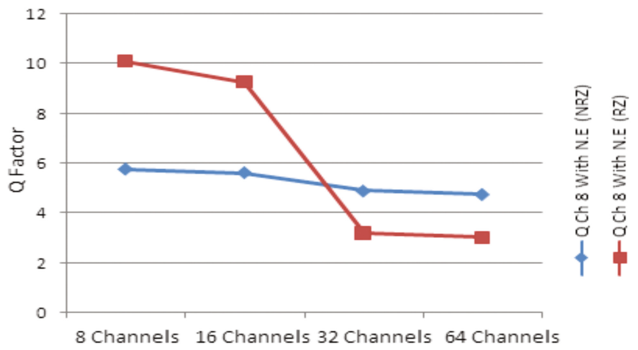

Fig. 18. Nonlinear effects impact on the Q factor NRZ and RZ modulation (8, 16, 32 & 64 channels).

3 Conclusion

Our simulations suggest that there are many critical factors that limit the performance of the WDM and DWDM system, including nonlinear effects. The analysis of an 8 channels system using RZ and NRZ modulation techniques shows that RZ modulation was the most suitable technique for the WDM system. Eye Closure penalty curves compared to the number of channels confirms that RZ modulation was the superior technique for the 8 channels system. We then expanded our 16 channels system, where we obtained results that were well correlated with those of the 8 channels system, but in the 32 and 64 channels system (the DWDM system), the results NRZ modulation was the most appropriate technique for the DWDM system. We have plotted the Q factors of quality with respect to the 32 and 64 channels system and we found that the Q factors of the RZ modulation decreased much more rapidly than those of the NRZ modulation: this confirms that the RZ modulation is more bad as NRZ when the number of channels in the system is greater than 16 channels [5].

References

1. ITU-T Recommendation G.694.1, spectral grids for WDM applications: DWDM wavelength grid
2. Tianlin, D.: Fiber-Optic Communications and Fiber Optic Information Network. Tsinghua University Press, Beijing (2005). 9
3. Furst, C., et al.: Performance limits of nonlinear RZ and NRZ coded transmission at 10 and 40 Gb/s on different fibers. In: OFC 2000 2, WM31-302 (2000)
4. Miyamoto, Y., Yonenaga, K., Hirano, A., Tomizawa, M.: Nx40-Gbit/s DWDM transport system using novel return-to-zero formats with modulation bandwidth reduction. IEICE Trans. Commun. **E85-B**, 374–385 (2002)
5. Hayee, M.I., Willner, A.E.: NRZ versus RZ in 10-40-Gb/s dispersion managed WDM transmission systems. IEEE Photon. Technol. Lett. **11**, 991–993 (1999)

Initialization of LMS and CMA Adaptive Beamforming Algorithms with SMI for Smart Antenna System

Naceur Aounallah[1(✉)] and Merahi Bouziani[2]

[1] Department of Electronic and Telecommunications, Kasdi Merbah University, 30000 Ouargla, Algeria
aounallah.na@univ-ouargla.dz
[2] Electronic Department, Djillali Liabès University, 22000 Sidi Bel Abbes, Algeria
bouzi_mera@hotmail.com

Abstract. In this paper, an initialization of two different major adaptive beamforming algorithms which are the non-blind LMS (Least Mean Squares) and the blind CMA (Constant Modulus Algorithm) is described. The idea is to use SMI (Sample Matrix Inversion) method to determine the initial weights, for use them in the computational operation of each one of the both algorithms. This idea aims also to improve their convergence speed. We choose the use of the LMS non-blind algorithm and the CMA blind algorithm because they are simples to implement, and not computationally intensives. From the simulation results, we observed that, in general, the initialized LMS, or the initialized CMA, with SMI performs more robustly than the LMS or the CMA conventional algorithms.

Keywords: Smart antenna · Adaptive array signal processing
Least Mean Squares (LMS) · Sample Matrix Inversion (SMI)
Constant Modulus Algorithm (CMA)

1 Introduction

Smart antennas and their array processing play an important role in many diverse application fields, such as radar, sonar, and modern cellular mobile communications [1, 2], among others, in acoustics, astronomy, seismology, and medical imaging [3, 4]. This new kind of antennas seems to be a promising way to increase the capacity of wireless communication systems and to optimize the radio-electric spectrum as well as possible. The basic idea is to exploit the spatial dimension mainly using multi-element antenna systems in emission and/or reception. In addition, the area of smart antennas is highly interdisciplinary, including electromagnetic tools, microwave, antennas design and signal processing. In other words, electromagnetism is crucial to develop wireless communications and digital signal processing is important to make these communications smarts.

The adaptive antenna technology is designed to optimize the beam pattern and to achieve optimal performance. This kind of antenna uses sophisticated signal processing algorithms to distinguish continually between desired signals and interference signals

M. Chadli et al. (Eds.): ICEECA 2017, LNEE 522, pp. 499–509, 2019.
https://doi.org/10.1007/978-3-319-97816-1_38

through the calculation of their direction of arrival. The adaptive approach continuously updates the beam pattern by changing the location of the desired signal (the main beams) and the interference signal (the nulls).

There are two basic adaptive approaches [5, 6]: 1. Block Adaptation, where a temporal block of data is used to estimate the optimum array weights and 2. Continuous Adaptation, in which the weights are adjusted as the data is sampled such that the weight vector converges to the optimum solution. Therefore, many researchers focused on the development of adaptive beamforming algorithms in wireless communication systems to determine the optimal weight vectors of array antenna elements dynamically, based upon certain criteria like minimizing the variance, maximizing the signal to interference ratio, minimizing the mean square error, …etc.

Among these algorithms, temporal updating algorithms such as Least Mean Square (LMS) and Constant Modulus Algorithm (CMA) which determine the optimum weight vectors sample by sample in time domain can take a long time to converge. To overcome this problem, block adaptation approach such as Sample Matrix Inversion (SMI) is employed [7]. However, adaptive block approach is unsuitable for continuous transmission because of its discontinuity in updating the weight vectors.

The remainder of this paper is organized as follows. We provide a brief description of a system model for adaptive beamforming in Sect. 2. Section 3 describes the non-blind LMS algorithm and the blind CMA algorithm and shows how to initialize them with the SMI algorithm. The simulation results are presented in Sect. 4. Finally, Sect. 5 gives our conclusions.

2 System Model

We consider a wireless communication scenario in which K narrow band user signals impinge on a uniform linear array (ULA) comprised N identical isotropic antenna elements ($N > K$). Let λ denote the wavelength and $d = \lambda/2$ be the inter-element distance of the ULA. Assuming that the k^{th} user signal impinges on the array with direction of arrival θ_k.

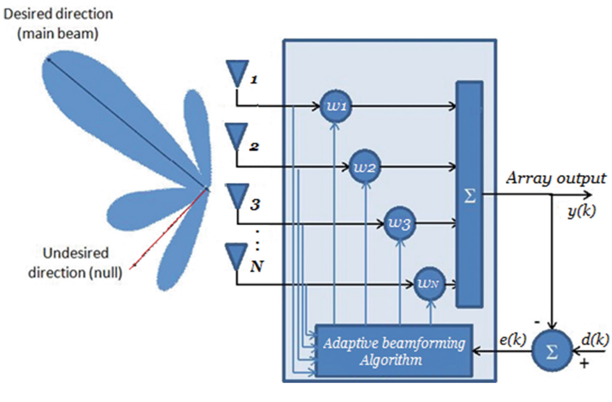

Fig. 1. Adaptive signal processing system

The structure of adaptive beamforming processing system is shown in Fig. 1. The $N \times 1$ observation vector $x(k)$ at time k can be modelled as:

$$\begin{aligned} x(k) &= A(\theta)s(k) + \sum_{n=1}^{N} i_n(k) + n(k) \\ &= A(\theta)s(k) + v(k) \end{aligned} \tag{1}$$

Where $x(k) = \left[x_1(k)\ x_2(k)\ \ldots\ x_N(k)\right]^T$ is the complex vector of array observations, $s(k) = \left[s_1(k), s_2(k), \ldots s_K(k)\right]^T$ denote the waveforms of the desired signal, $A(\theta) = \left[a_1(\theta), a_2(\theta), \ldots, a_N(\theta)\right]^T$ is the matrix of steering vectors, it contains information about the angles of arrival, $i_n(k)$ and $n(k)$ are the n^{th} interferer and the additive white Gaussian noise (AWGN) components, respectively. $v(k)$ includes the interference and noise.

Generally, the signal received from each element (x_n) is multiplied with a adjustable weight ω_n^*, and the beamformer aims to produce a weighted sum of the array output $y(k)$ at each time-instant, is given by:

$$y(k) = \sum_{n=1}^{N} \omega_n^* x_n = \omega^H x(k) \tag{2}$$

Where $\omega = \left[\omega_1, \omega_2, \ldots, \omega_N\right]^T$ is an $N \times 1$ complex vector of beamformer weights, $(.)^*$ is the conjugate operation, and $(.)^T$ and $(.)^H$ stand for the transpose and Hermitian transpose, respectively.

The beamformer output $y(k)$ is subtracted from a desired signal $d(k)$ to generate an error $e(k) = d(k) - y(k)$ which is used to control the weight vector. In particular, ω is adjusted in order to minimize the Mean Square Error (MSE) between the array output and the training sequence:

$$\begin{aligned} MSE &= \mathrm{E}\left\{|e(k)|^2\right\} = \mathrm{E}\left\{\left|\omega^H x(k) - d(k)\right|^2\right\} \\ &= \mathrm{E}\left\{|d(k)|^2\right\} - 2\omega^H r_{xd} + \omega^H R_{xx}\omega \end{aligned} \tag{3}$$

Where: $r_{xd} = E\{x(k)d^*(k)\}$ and $R_{xx} = E\left\{x(k)x^H(k)\right\}$ denote the cross-correlation between the reference signal and the array signal vector, and the spatial autocorrelation matrix respectively, and $E\{\cdot\}$ denotes the statistical expectation.

3 Adaptive Beamforming Algorithms

In this section, the mathematical formulation of the concerned adaptive beamforming techniques will be presented, and one will see how the beamformer which is based on adaptive algorithms can calculate the weighting coefficients.

3.1 Sample Matrix Inversion Algorithm

This algorithm based on block adaptation uses Minimum Mean Squared Error (MMSE) criterion to obtain the optimal array weight vector and it is probably used most often when rapid convergence is required. It is a question of inversing directly the covariance matrix to obtain optimal weightings and that also makes possible the increasing of the convergence speed. So, it is useful to use it if the signal rapidly changed. Since we do not have the true auto-correlation matrix and cross-correlation vector, this algorithm replaces both of them by their corresponding estimations (time averaging) to obtain the Wiener-Hopf solution [8]:

$$\omega_{opt} = R_{xx}^{-1} r_{dx} \tag{4}$$

The matrix R_{xx} and r_{dx} are estimated in a finite time interval:

$$R_{xx} = E\left[x(k).x^H(k)\right] = \frac{1}{K}\sum_{k=1}^{K} x(k).x^H(k) \tag{5}$$

$$r_{dx} = E\left[d^*(k)x(k)\right] = \frac{1}{K}\sum_{k=1}^{K} d^*(k).x^H(k) \tag{6}$$

With $d(k)$ is the desired signal (of reference), and K is the number of observation.

The non-blind SMI algorithm is a method per block requires a reference signal, and the weight vectors are periodically calculated. The weight with k^{th} block length K can be easily defined as follows [9]:

$$\omega_{SMI}(k) = R_{xx}^{-1}(k) r_{dx}(k) \tag{7}$$

Typically it is a rule of thumb to allow the block size, $K > 2\ N$. This means the number of samples that must be greater than or equal to twice the number of elements in the adaptive array [10].

For the dynamic block size SMI method, the MSE for each element can be determined by:

$$MSE = e = \hat{R}_{xx}\omega - \hat{r}_{xd} \tag{8}$$

3.2 Least Mean Square Algorithm

Least mean square (LMS) antenna array recursively derives the optimum weight coefficients temporal sample by sample in order to minimize mean square error (MSE) between reference signal and array outputs [11]. This calculation is made under the maximum inclination method using a value in a moment of input signal by updating weight matrix ω, in case which direction of arrival (DOA) and signal powers are unchanged. At initial period, a reference signal is required for convergence [12].

This algorithm uses a steepest decent method and computes the weight vector recursively using the following equations [13, 14]:

$$\omega(k+1) = \omega(k) + \mu x(k)e^{*}(k) \tag{9}$$

$$e(k) = d(k) - y(k) \tag{10}$$

$$y(k) = \omega^{H}(k)x(k) \tag{11}$$

Where $\omega(k)$ is the antenna weight, $x(k)$ is the input vector of the antenna signals, and $e(k)$ is the error signal between the desired response $d(k)$ and the weighted antenna output $y(k)$.

If the gain constant (called also step size) μ is chosen such that 0 < μ < 2/P (where P is the sum of powers of each antenna input signal), the algorithm guarantees the convergence of the antenna weights.

3.3 LMS Algorithm with SMI Initialization

The drawback of the standard LMS algorithm is its slow convergence due to its arbitrary weight initialization that can require more iteration to converge to optimum value. However, if we use the SMI, which is a block-data adaptive algorithm and it is the fastest algorithm for estimating the optimum weight vector, as initialization for the LMS, this latter uses the weight optimum computed and estimated by the SMI algorithm which is not any arbitrary value as an initial weights for its update equation. This technique leads the LMS algorithm to take only little time to converge.

To summarize, the principal steps to be followed for the initialization of the LMS with the SMI are:

- Step 1) Initialize $\omega(0)$, by using SMI only for first few samples.
- Step 2) Compute the output signal $y(k)$ which is $y(k) = \omega^{H}(k)x(k)$ and let $k = 1$.
- Step 3) Compute the error signal using the desired signal ($e(k) = d(k) - y(k)$).
- Step 4) Update the weight vectors using the following equation: $\omega(k+1) = \omega(k) + \mu x(k)e^{*}(k)$.
- Step 5) Compute the final output signal.
- Step 6) If $k = K$, stop. Otherwise, set $k = k + 1$, and go to step 3.

3.4 Constant Modulus Algorithm

The Constant Modulus Algorithm (CMA) was developed first by Godard [15] and later independently by Treichler and Agee [16] and was initially designed for PSK signals. The CMA belongs to the blind adaptive beamforming category which requires no pilot or training signal sequence to make an optimum beam to the intended direction. Its principle consists of preventing the deviation of the squared modulus of the outputs at the receiver from a constant. The main advantages of CMA, among others, are its simplicity, robustness, and the fact that it can be applied even for non-constant modulus communication signals [17]. In addition, the CMA is suited for all signals with a constant complex envelope like FM-, PM-, or FSK-modulation.

Generally, this algorithm is implemented as an iterative process where the development of its updating equation is similar to the case of the Least Mean Square (LMS) popular algorithm, utilizing the step size to reach convergence and to obtain the optimal weights for a particular angle of arrival. The updated value of the CMA weight vector at iteration time k can be obtained by the following recursive equation [18]:

$$\omega(k+1) = \omega(k) + 2\mu x(k)e^*(k) \tag{12}$$

Where $\omega(k)$ represents the previous weight, $\omega(k+1)$ is the current weight, and $x(k)$ is the input signal. μ is the step size parameter used to control the convergence rate, if $0 < \mu < 1/\lambda_{max}$, with λ_{max} denotes the maximum eigenvalue of covariance matrix R_{xx}, the algorithm is stable and ω converges to the optimum weight vector.

The error for this blind algorithm is computed from the actual received signal, not a training sequence as in the case of non-blind algorithm. The error equation has the following form:

$$e(k) = \frac{y(k)}{|y(k)| - y(k)} \tag{13}$$

Where $y(k)$ is the output signal.

3.5 CMA Algorithm with SMI Initialization

The idea to use an initialization of CMA with SMI is to overcome the problems in the convergence property of the blind operation. In fact, they are two major drawbacks, firstly the convergence time of the CMA algorithm is slow, and secondly the reliability or the convergence performance in certain cases. When the interfering signal is stronger than the desired signal, the algorithm tends to come up with the wrong solution by capturing the interfering signal which has the stronger power.

To summarize, the following principal steps are involved to compute optimal weights for the initialization of the CMA with the SMI:

- Step 1) Initialize $\omega(0)$, by using SMI only for first few samples.
- Step 2) Compute the output signal $y(k)$; $(y(k) = \omega^H(k)x(k))$ and let $k = 1$.
- Step 3) Compute the error signal from the output signal $(e(k) = \frac{y(k)}{|y(k)| - y(k)})$.
- Step 4) Update the weight vectors using the following equation: $\omega(k+1) = \omega(k) + 2\mu x(k)e^*(k)$.
- Step 5) Compute the final output signal.
- Step 6) If $k = K$, stop. Otherwise, set $k = k + 1$, and go to step 3.

4 Simulations and Results

In this section, we evaluate the performances of the initialized LMS, and the initialized CMA, beamforming algorithms and compare them with their existing standard versions LMS, and CMA respectively. The simulated array is assumed to be an 8-elements ULA with half wave length inter-element spacing, the non-directional noise is assumed to be as spatially white Gaussian noise of variance $\sigma^2 = 0.001$, we consider that two signals of the desired users impinge on the array from $\theta = -25°$ and $\theta = +30°$ and one interfering signal is incoming from $\theta = 10°$, signals are modulated using minimum shift keying (MSK) constant envelope method, and the step-size parameter is 0.03 for the LMS and the CMA algorithms.

The radiated energy by an array antenna is irregularly distributed in space. It is concentrated in certain directions by forming more or less important beams. Figure 2 below represents the array beam-patterns obtained with the LMS and the Initialized-LMS algorithms. Both of adaptive beam-forming algorithms are able to calculate the optimum weight vectors that can adapt the radiation pattern of the array antenna to steer main beam to the desired signals (30°, and −25°) and null in direction of interfering source (10°).

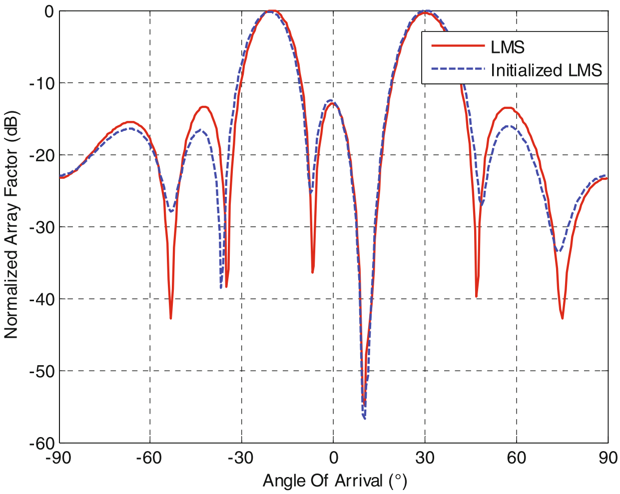

Fig. 2. Normalized array factor plots obtained with the LMS and the initialized-LMS algorithms

The results shown in Fig. 3 demonstrate that the ability to reproduce the desired response signal is much better by the application of the Initialized-LMS than by the application of the LMS algorithm. The LMS algorithm uses several iterations to update weight vectors before achieving an optimal convergence whereas the initialized-LMS thanks to SMI initialization can produce a weighted output signal very similar to the desired output signal from the initial iterations.

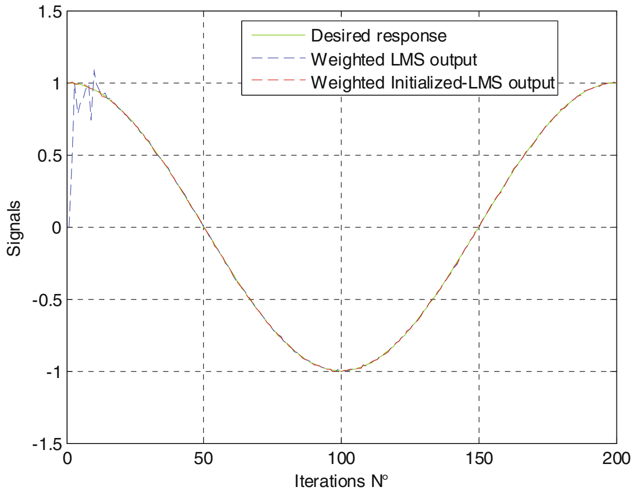

Fig. 3. Comparison of desired response, LMS output signal, and Initialized-LMS output signal

Figure 4 shows fast convergence of Initialized-LMS algorithm in comparison with conventional LMS algorithm. The Initialized-LMS algorithm has the potential to achieve the very fast convergence rate, it converges from the first iterations for which conventional LMS algorithm takes almost 12 iterations in simulated scenario. Therefore, we can conclude that Initialized-LMS algorithm has better performance and is more robust than the conventional LMS algorithm.

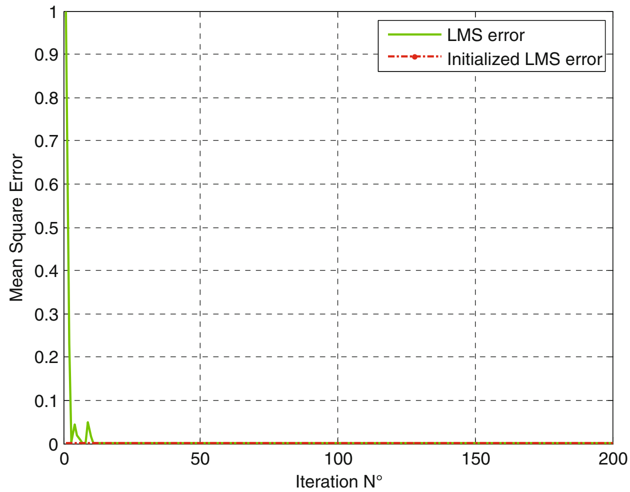

Fig. 4. Comparison of mean square error plots for the LMS and the initialized-LMS algorithms

To observe the advantage of the Initialized-CMA algorithm, the comparisons with the conventional CMA algorithm are made. These are shown in Figs. 5, 6 and 7.

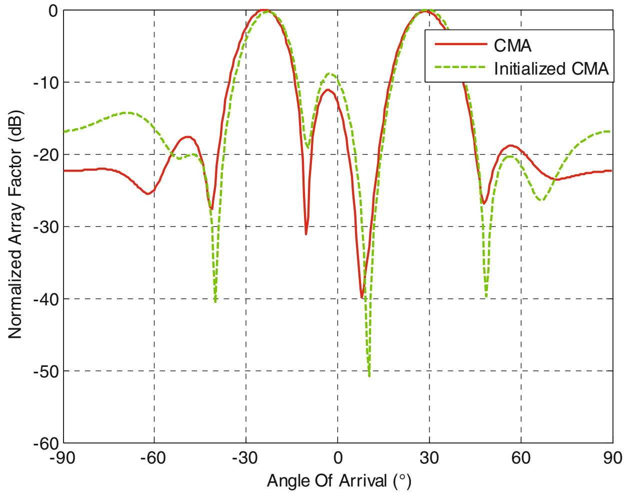

Fig. 5. Normalized array factor plots obtained with the CMA and the initialized-CMA algorithms

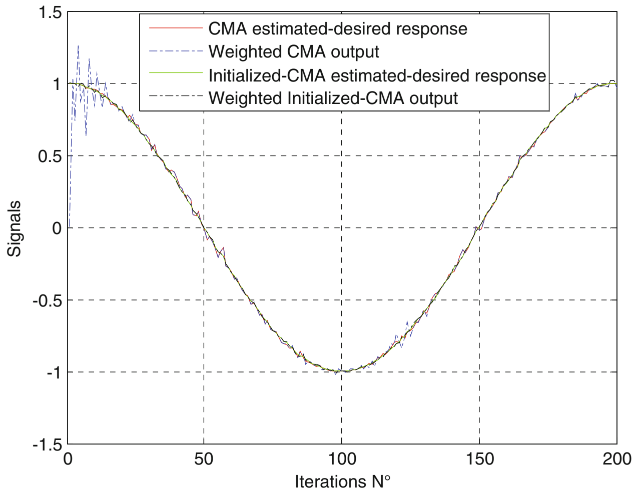

Fig. 6. Comparison of estimated-desired responses and weighted output signals

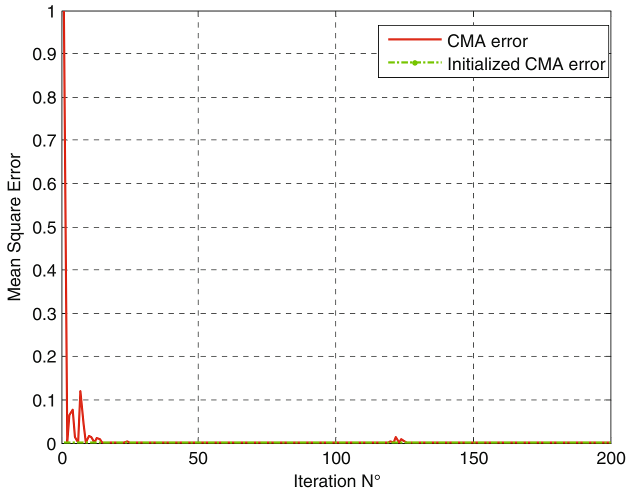

Fig. 7. Comparison of mean square error plots for the CMA and the initialized-CMA algorithms

Figure 5 shows the array beampatterns of the CMA and the Initialized-CMA algorithms. It is clear that for the two algorithms, the main beams are steered in the direction of arrival of the desired signals (at −25° and 30°) and null is formed along the direction of the interferer at 10°. However, the initialized-CMA algorithm provides better robustness and has a higher resolution as compared with the standard CMA.

The graphs illustrated in Fig. 6 leads us to note, in short, two important comments: 1. The weighted initialized-CMA output is much important than the weighted CMA output because it acquires and tracks its estimated desired response since the initial iterations, and 2. The desired responses of the CMA and the Initialized-CMA are estimated signals resulting from a blind algorithm. However, the estimated desired response curve of the Initialized-CMA seems finer than that of the CMA algorithm and that means more stability.

As can be seen from Fig. 7, the Initialized-CMA algorithm can achieve faster convergence than the CMA algorithm. Likewise, the CMA algorithm starts to converge from almost the 15th iteration whereas in the Initialized-CMA algorithm it starts to converge from the initial iteration.

Finally, our latest figures clearly demonstrate that in our simulation example, the initialized-CMA is shown to consistently enjoy a significantly improved performance as compared with the standard CMA.

5 Conclusion

In this paper, two adaptive beamforming algorithms have been investigated and initialized with another one. This later which is the SMI has been used because of its fast convergence which aim is to seek for producing improved convergence properties. On one hand, the LMS non-blind adaptive beamforming algorithm has been employed to update the weights of adaptive antenna array but its slow convergence presents a drawback for this adaptive processing system. However, the best solution of this problem is to initialize the LMS with the SMI algorithm which can help to find the optimum weight vectors within a short time. On the other hand, the CMA is a method that has been widely known as blind adaptive beamforming algorithm because it requires no knowledge about the signal except that the transmitted signal waveform has a constant envelope. Its two major problems in convergence properties (reliability and slowness) can be solved by initializing it with the major non-blind adaptive algorithm SMI.

References

1. Srar, J.A., Chung, K.S., Mansour, A.: A new LLMS algorithm for antenna array beamforming. In: Wireless Communications and Networking Conference (WCNC). IEEE, pp. 1–5 (2010)
2. Hema, S., Jha, R.M.: Trends in adaptive array processing. Int. J. Antennas Propag. (2012). https://doi.org/10.1155/2012/361768
3. Congfeng, L.: Robust beamforming and DOA estimation. In: Salih, S. (ed.) Fourier Transform Applications, Source: InTech (2012). ISBN: 978-953-51-0518-3
4. Song, X., Wang, J., Li, Q., Wang, H.: Robust least squares constant modulus algorithm to signal steering vector mismatches. Wirel. Pers. Commun. **68**(1), 79–94 (2013)
5. Veen, V., Barry, D., Buckley, K.M.: Beamforming: a versatile approach to spatial filtering. ASSP Mag. IEEE **5**(2), 4–24 (1988)
6. Saxena, P., Kothari, A.G.: Performance analysis of adaptive beamforming algorithms for smart antennas. IERI Procedia **10**, 131–137 (2014)
7. Islam, M.T., Abdul, Z.A.: Rashid, MI-NLMS adaptive beamforming algorithm for smart antenna system applications. J. Zhejiang Univ. Sci. A **7**(10), 1709–1716 (2006)
8. Reed, I.S., Mallett, J.D., Brennan, L.E.: Rapid convergence rate in adaptive arrays. IEEE Trans. Aerosp. Electron. Syst. **10**(6), 853–863 (1974)
9. Gross, F.B.: Smart Antennas for Wireless Communications with MATLAB. McGraw-Hill, New York (2005)
10. Zhigang, R., Paul, P., Theodore, S.R., Jeffrey, H.R.: Despread–respread multi-target constant modulus array for CDMA systems. IEEE Commun. Lett. **1**(4), 114–116 (1997)
11. Balanis, C.A.: Antenna Theory: Analysis and Design, 2nd edn. Wiley, New York (1997)
12. Watanabe, K., Yoshii, I., Kohno, R.: An adaptive array antenna using combined DFT And LMS algorithms. In: Proceedings of IEEE, pp. 1417–1421 (1998)
13. Godara, L.C.: Smart Antennas. CRC Press LLC, Boca Raton (2004)
14. Das, S.: Smart antenna design for wireless communication using adaptive beam-forming approach. In: TENCON. IEEE Region 10 Conference, pp. 1–5 (2008). https://doi.org/10.1109/TENCON.2008.4766732
15. Godard, D.N.: Self-recovering equalization and carrier tracking in two dimensional data communication systems. IEEE Trans. Commun. (1980)
16. Treichler, J.R., Agee, B.G.: A new approach to multipath correction of constant modulus signals. IEEE Trans. Acoust. Speech Signal Process. ASSP **31**(2), 459–472 (1983)
17. Aissa, I., Iferroujene, R., Boudjellal, A., Abed-Meraim, K., Belouchrani, A.: Constant modulus algorithms using hyperbolic Givens rotations. Signal Process. **104**, 412–423 (2014)
18. Shynk, J.J., Gooch, R.P.: The constant modulus array for cochannel signal copy and direction finding. IEEE Trans. Signal Process. **44**(3), 652–660 (1996)

Compressive Sensing Based and PNLMS-Type Sparse Adaptive Filtering Algorithms for the Identification of Long Acoustic Impulse Responses

Ayoub Tedjani(✉) and Ahmed Benallal

Signal Processing and Image Laboratory (LATSI), Department of Electronics, University of Blida 1, Blida, Algeria
superayoub001@gmail.com, a_benallal@hotmail.com

Abstract. Cost-effective adaptive system identification is a challenging problem in speech processing especially when the acoustic impulse response is "long". In this paper, an overview of three of the mostly-used recent sparse adaptive filtering algorithms is presented; and their performances in the context of system identification are studied and compared. The algorithms of interest include the proportionate normalized least mean square (PNLMS), its sparseness-controlled (SC) upgrade (SC-PNLMS) as well as the so-called variable-step-size zero-attractor NLMS (VSS-ZA-NLMS) which is based on the compressive sensing (CS) framework. Series of simulations were carried out both in synthetic and real different-sparseness long acoustic impulse responses with stationary and non-stationary inputs in order to effectively analyze, evaluate and compare the strengths and the weaknesses of these algorithms in terms of convergence speed, steady-state performance and computational complexity.

Keywords: Adaptive filtering · Sparse algorithms
Long acoustic impulse responses · System identification · Compressive sensing
Speech · NLMS · Steady-state performance · Complexity

1 Introduction

An impulse (IR) response is called "sparse" if it has only a small percentage of its components with a significant magnitude (active taps) while the rest are zeros or very small (inactive taps) [1]. For example, in a network impulse response, only about 8–12 ms in a 64 or 128 ms time duration are active and the others are zeros (or inactive). The inactive part accounts for bulk delay due to network loading, encoding … etc. [2]. Another example is the acoustic echo generated due to coupling between microphone and loudspeaker in hands free mobile telephony, where the sparseness (or sparsity) of the acoustic channel impulse response varies with the loudspeaker-microphone distance [3].

The normalized least mean square (NLMS) algorithm and its different classical versions used for conventional system identification do not use the a priori knowledge

M. Chadli et al. (Eds.): ICEECA 2017, LNEE 522, pp. 510–525, 2019.
https://doi.org/10.1007/978-3-319-97816-1_39

of the sparseness of the system. Consequently, they perform poorly both in terms of steady state excess mean square error (MSE) and convergence speed. Recently, several alternate algorithms have been proposed to exploit the sparse nature of the system impulse response and achieve better performance. The most famous amongst them is the proportionate-NLMS (PNLMS) algorithm [4] and its various versions.

Each coefficient, in the PNLMS algorithm, is updated independently with a step-size that varies proportionally with respect to the magnitude of the particular coefficient estimate of the system, resulting in fast “initial” convergence for sparse systems. However, the rate of convergence slows down afterwards considerably, sometimes slower than the NLMS algorithm. In [5, 6], an attempt had been made to overcome this limitation by imposing a “sparseness measure” on the PNLMS algorithm resulting in the so-called sparseness-controlled PNLMS (SC-PNLMS) algorithm.

In a separate side, the subject of sparse adaptive filtering algorithms has known a renewed dynamism in the last few years. This was due to the emergence of the framework of compressive sensing (CS), where a linear superposition of a small number of stored signals (called “atoms”) is used to construct a “sparse representation” of the signal. Unlike the usual basis in vector space, the atoms are drawn from an “overcomplete” dictionary and thus the representation of the signal using atoms is not unique [7].

Motivated by CS methods, a sparsity-aware NLMS algorithm was proposed in [8], namely, the zero-attracting NLMS (ZA-NLMS). This has been achieved by introducing a sparsity constraint (the ℓ_1-norm) into the convex quadratic cost function of the NLMS algorithm. The results presented in [8] showed that the ZA-NLMS algorithm behaves better than the standard NLMS in both transient and steady state performance for highly sparse systems but, for less-sparse systems, its performance degrades. Furthermore, the conventional invariable step-size (ISS) ZA-NLMS has been upgraded to a variable step-size (VSS) version resulting in a more improved-performance algorithm named the VSS-ZA-NLMS [9].

It should be addressed that most of the aforementioned studies on sparse adaptive filtering algorithms assume white Gaussian inputs and used simple impulse responses with relatively small number of taps (8, 16 and 64 taps). However, in this paper, we used different synthetic and real different-sparsity acoustic impulse responses (AIRs) that have larger sizes (256, 1024, 2048 & 8192 taps) with different-nature inputs (stationary and non-stationary). These relatively long AIRs are used in order to approach and simulate more effectively the real acoustic applications.

The objective of this work is to present, analyze and compare three mostly-known and recent NLMS-based algorithms (i.e. PNLMS, SC-PNLMS and VSS-ZA-NLMS) in order to outline their capabilities and performances in the context of “long” AIRs identification.

2 Classical Normalized Least Mean Square Acoustic Echo Cancellation

Figure 1 shows a loudspeaker-room-microphone system (LRMS) describing a typical acoustic echo cancellation (AEC) system, with an echo canceller employing an adaptive filter. An adaptive acoustic echo canceller assumed with finite impulse response (FIR) model configuration has the coefficients,

$$\hat{\mathbf{h}}(n) = \left[\hat{h}_0(n), \hat{h}_1(n), \ldots, \hat{h}_{L-1}(n)\right]^T \tag{1}$$

where L is the length of the adaptive filter assumed equal to length of the unknown room impulse response $\mathbf{h}$.

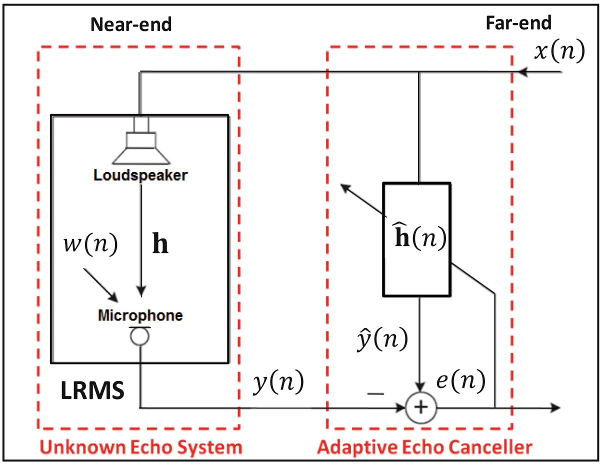

Fig. 1. Adaptive system for acoustic echo cancellation in a loudspeaker-room-microphone system (LRMS)

The microphone in the near-end room receives the desired signal (the output of the LRMS) that is given by,

$$y(n) = \mathbf{h}^T\mathbf{x}(n) + w(n) \tag{2}$$

where $\mathbf{x}(n) = [x(n), x(n-1), \ldots, x(n-L+1)]^T$ is a vector containing L samples of the input signal and $w(n)$ is a stationary, zero-mean and independent noise that is uncorrelated with any other signal [10]. The previous estimation of the impulse response $\hat{\mathbf{h}}^T(n-1)$ is used to compute the a priori error signal $e(n)$ at each iteration, as in,

$$e(n) = y(n) - \hat{\mathbf{h}}^T(n-1)\mathbf{x}(n) \tag{3}$$

Since the objective of an echo canceller is to estimate the unknown system **h** as closely as possible, $e(n)$ must come significantly smaller at each iteration, as the filter coefficients converge to the unknown true impulse response **h** [11].

The coefficients update equation of the NLMS algorithm [12] is given by,

$$\hat{\mathbf{h}}(n) = \hat{\mathbf{h}}(n-1) + \mu \frac{\mathbf{x}(n)e(n)}{\mathbf{x}^T(n).\mathbf{x}(n) + \delta_{NLMS}} \tag{4}$$

where δ_{NLMS} is a regularization parameter used to prevent division by zero and stabilizes the solution [12]. We take $\delta_{NLMS} = cst.\sigma_x^2$ [13, 14]. σ_x^2 is the variance of the input signal and cst is a positive constant. The NLMS algorithm is convergent in the mean square if its step size μ (dimensionless) satisfies that $(0 < \mu < 2)$, [3].

In case of the conventional "invariable step-size (ISS)" NLMS (or ISS-NLMS), the step-size governs the rate of convergence and the steady-state excess MSE. To meet the conflicting requirements of fast convergence and low misadjusment (good estimation accuracy), the step-size needs to be controlled. In [15], a variable step-size NLMS (VSS-NLMS) algorithm is proposed with a variable step-size,

$$\mu(n) = \mu_{max} \frac{\boldsymbol{p}^T(n)\boldsymbol{p}(n)}{\boldsymbol{p}^T(n)\boldsymbol{p}(n) + C} \tag{5}$$

where C is a positive constant parameter proportionate to the order of $(1/\mathrm{SNR})$, where SNR is the input signal-to-noise ratio, and μ_{max} is the maximal step-size [9].

According to (5), the range of the variable step size is given by $\mu(n) \in \left(0, \mu_{max}\right)$. To ensure the stability of the adaptive algorithm, the maximal step-size μ_{max} is usually set to be less than 2 [15]. $\boldsymbol{p}(n)$ is approximated as follows,

$$\boldsymbol{p}(n) = \beta \boldsymbol{p}(n-1) + (1-\beta) \frac{\mathbf{x}(n)e(n)}{\mathbf{x}^T(n)\mathbf{x}(n) + C} \tag{6}$$

where $\beta \in [0, 1)$ is the smoothing factor to control the value of the VSS and the estimation error [9].

3 The Studied Sparse Adaptive Filtering Algorithms

In this section, we present the mathematical details of the sparse NLMS-based algorithms of interest.

3.1 The Proportionate NLMS (PNLMS) Algorithm

The PNLMS algorithm assigns higher step-sizes for coefficients with higher magnitude using a control matrix **Q** and the rest of terms are carried over from NLMS [4], as in,

$$\hat{\mathbf{h}}(n) = \hat{\mathbf{h}}(n-1) + \mu \frac{\mathbf{Q}(n-1)\mathbf{x}(n)e(n)}{\mathbf{x}^T(n)\mathbf{Q}(n-1)\mathbf{x}(n) + \delta_{PNLMS}} \tag{7}$$

where δ_{PNLMS} is the regularization parameter for PNLMS. It is usually taken as $\delta_{PNLMS} = \delta_{NLMS}/L$, [5, 14] and the diagonal matrix

$$\mathbf{Q}(n-1) = \mathrm{diag}\left\{ q_0(n-1) \ \cdots \ q_{L-1}(n-1) \right\} \tag{8}$$

The elements of the control matrix can be expressed as

$$q_l(n-1) = \frac{\kappa_l(n-1)}{\frac{1}{L}\sum_{i=0}^{L-1} \kappa_i(n-1)} \tag{9}$$

where

$$\kappa_l(n-1) = max\left\{ \kappa_{min}(n), \left|\hat{h}_l(n-1)\right| \right\} \tag{10}$$

and

$$\kappa_{min}(n-1) = \rho \times max\left\{ \gamma, \left|\hat{h}_0(n-1)\right|, \cdots, \left|\hat{h}_{L-1}(n-1)\right| \right\} \tag{11}$$

with $0 \leq l \leq L-1$ being the tap-indices. The parameters γ and ρ are positive numbers with typical values $\gamma = 0.01$ and $\rho \in \left[1/L, 5/L\right]$, [16]. The parameter γ prevents the coefficients $\hat{h}_l(n-1)$ from stalling during the initialization stage where $\hat{\mathbf{h}}(0) = 0_{L\times 1}$ while, ρ prevents individual filter coefficients from stalling when their magnitudes are much smaller than the magnitude of the largest coefficient [5, 14, 16]. In addition, it can be seen that for $q_l = 1, \forall l$, PNLMS is equivalent to NLMS [5].

3.2 Sparseness Measure

The degree of sparseness can be qualitatively referred to as a range of “strongly dispersive” to “strongly sparse” [17]. The sparseness of an impulse response of length L can be quantified by the sparseness measure [18, 19],

$$\xi(\mathbf{h}) = \frac{L}{L-\sqrt{L}}\left\{ 1 - \frac{\|\mathbf{h}\|_1}{\sqrt{L}\|\mathbf{h}\|_2} \right\} \tag{12}$$

where $\|\mathbf{h}\|_1$ and $\|\mathbf{h}\|_2$ are the ℓ_1-norm and the ℓ_2-norm respectively. That is,

$$\|\mathbf{h}\|_1 = \sum_{i=0}^{L-1} |h_i| \tag{13}$$

$$\|\mathbf{h}\|_2 = \sqrt{\sum_{i=0}^{L-1} h_i^2} = \sqrt{\mathbf{h}^T\mathbf{h}} \tag{14}$$

By considering impulse responses with various degrees of sparseness, it can be shown that $0 \leq \xi(\mathbf{h}) \leq 1$.

Direct use $\xi(\mathbf{h})$ is not feasible since $\mathbf{h}$ is unknown during adaptation. Therefore, $\hat{\xi}(n)$ is employed to estimate the sparseness of an impulse response at each sample iteration [5, 6]. That is,

$$\hat{\xi}(n) = \frac{L}{L - \sqrt{L}}\left\{1 - \frac{\left\|\hat{\mathbf{h}}(n-1)\right\|_1}{\sqrt{L}\left\|\hat{\mathbf{h}}(n-1)\right\|_2}\right\}, n \geq L \tag{15}$$

which uses the estimation of the impulse response at the iteration ($\hat{\mathbf{h}}(n-1)$), instead of the unknown impulse response $\mathbf{h}$.

3.3 The SC-PNLMS Algorithm

Results presented in [6] showed that a higher value of ρ will reduce the degree of proportionality due to the $\mathbf{Q}$ matrix meaning that all filter coefficients are updated at a more uniform rate. This gives a good convergence performance of the PNLMS algorithm when the AIR is dispersive. On the other hand, a lower value of ρ will increase the influence of the $\mathbf{Q}$ matrix, hence, giving a good convergence performance for a sparse AIR.

In order to overcome the problem of slow convergence in dispersive AIRs, the PNLMS algorithm needs to have step-size control elements $q_l(n)$ robust to sparseness variations of the impulse response. To achieve a high ρ when $\hat{\xi}(n)$ is small (dispersive system), several choices can be employed. A very-used choice is the exponential-function form [6] as

$$\rho(n) = e^{-\lambda\hat{\xi}(n)}, \lambda \in \mathbb{R}^+ \tag{16}$$

Replacing ρ by $\rho(n)$ in the PNLMS update equation gives the sparseness-controlled PNLMS algorithm (SC-PNLMS). Tests discussed in [6] showed that $\lambda = 6$ gives a good compromise of convergence performance in dispersive and sparse systems. Moreover, the range of $4 \leq \lambda \leq 6$ could be considered as a good choice for the application of AEC.

In addition, it can be noted that when $n = 0$, $\left\|\hat{\mathbf{h}}(0)\right\|_2 = 0$ and hence, to prevent division by a small number or zero, $\hat{\xi}(n)$ can be computed for $n \geq L$ in SC-PNLMS. When $n < L$, we can set $\rho(n) = \rho = 5/L$, [13].

3.4 The Zero-Attracting NLMS (ZA-NLMS) Algorithm

The use of CS methods permitted to introduce a sparsity constraint (the ℓ_1-norm) into the convex quadratic cost function of the NLMS algorithm, resulting in a sparsity-aware LMS algorithm called the "zero-attracting" NLMS (ZA-NLMS) which obeys the following [7] updating scheme,

$$\left\{\begin{matrix} new \\ parameter \\ estimate \end{matrix}\right\} = \underbrace{\underbrace{\left\{\begin{matrix} old \\ parameter + \\ estimate \end{matrix}\right\}\{step\text{-}size\}\left\{\begin{matrix} new \\ information \end{matrix}\right\}}_{NLMS} + \left\{\begin{matrix} zero \\ attraction \\ term \end{matrix}\right\}}_{Sparse\ NLMS}$$

where the new information term is the error vector between the outputs of the filter and the desired signal vector. The zero-attraction (ZA) term (or zero attractor) is a norm-related regularization function which applies an attraction to zero on small parameters [7].

The corresponding updated equation [20] of the ZA-NLMS algorithm is,

$$\hat{\mathbf{h}}(n) = \hat{\mathbf{h}}(n-1) + \mu \frac{\mathbf{x}(n)e(n)}{\mathbf{x}^T(n)\mathbf{x}(n) + \delta_{NLMS}} - \rho_{ZA}.\mathrm{sgn}\left(\hat{\mathbf{h}}(n-1)\right) \tag{17}$$

where ρ_{ZA} is referred to as the "zero-attraction controller" or the "regularization step-size" in the adaptive filtering context. It controls the strength of the zero-attractor. Usually the regularization step-size is fine-tuned offline (via exhaustive simulations) or in an ad–hoc manner [7].

In [20], a systematic approach is used. It expresses ρ_{ZA} in terms of the noise level and the input signal power E_0 is set equal to unity (i.e. $E_0 = 1$), which makes the noise power $\sigma_n^2 = 10^{-\mathrm{SNR}/10}$, where SNR $(10\log_{10}(E_0/\sigma_n^2))$ is the input signal-to-noise ratio. Note that sgn(.) is a component-wise signum function defined as

$$\mathrm{sgn}(h) = \begin{cases} 1, & h > 0 \\ 0, & h = 0 \\ -1, & h < 0 \end{cases} \tag{18}$$

Observing (17), its second term attracts small-value filter coefficients to zero in high probability. In other words, most of the small-value filter coefficients can be replaced by zero. This will speed up the convergence and mitigate the noise on zero positions as well.

3.5 The VSS-ZA-NLMS Algorithm

Recently, by jointly taking advantage of system sparsity and VSS-NLMS, an improved adaptive sparse channel estimation algorithm had been proposed in [9] named as the variable step-size zero-attracting NLMS (VSS-ZA-NLMS). Its update equation is expressed as,

$$\hat{\mathbf{h}}(n) = \hat{\mathbf{h}}(n-1) + \mu(n) \frac{\mathbf{x}(n)e(n)}{\mathbf{x}^T(n)\mathbf{x}(n) + \delta_{NLMS}} - \rho_{ZA}.\mathrm{sgn}\left(\hat{\mathbf{h}}(n-1)\right) \tag{19}$$

where $\mu(n)$ is calculated as explained in Sect. 2.

In case of small step-sizes, good estimation accuracy is achieved while high convergence speed is obtained for large step-sizes. Analysis presented in [9] showed that the value of the VSS $\mu(n)$ will increase if the estimation error decreases and vice versa. In view of that, as the updating error decreases, VSS-ZA-NLMS reduces its step-size adaptively to ensure the algorithm stability as well as to achieve better steady-state estimation performance [9].

3.6 Computational Complexity Analysis

The computational complexity of an algorithm is a very important criterion that should be examined since it has a direct relationship with the hardware implementation and the operating time of the system. Although many factors contribute to the complexity of an algorithm, the relative complexities of NLMS, PNLMS, SC-PNLMS and VSS-ZA-NLMS in terms of the total number of additions, multiplications and divisions per iteration are assessed in Table 1, [21].

Table 1. Complexity of algorithms of interest in terms of: addition, multiplication and division

Algorithm	Addition	Multiplication	Division
NLMS	$2L+3$	$2L+5$	1
PNLMS	$3L+1$	$6L+4$	2
SC-PNLMS	$5L+2$	$7L+6$	3
VSS-ZA-NLMS	$5L+6$	$5L+11$	3

4 Simulation, Results and Discussion

In this section, we present some simulation results to demonstrate the performance of the algorithms of our study. They are first tested for synthetic systems where the degree of sparseness is controlled more easily. Then, we further for real systems.

4.1 Synthetic Generation of Sparse AIRs

The method proposed in [5] provides a means of generating synthetic impulse responses (Synthetic IRs) with different degrees of sparsity using random sequences.

4.2 Computer-Simulations Setup

All simulations were performed in floating-point representation using MATLAB® software. We used two different types of input signals, sampled at 16 kHz, and filtered by different-sparsity synthetic and real impulse responses to obtain the desired signals. Firstly, we used two different-sparsity synthetic acoustic impulse responses generated using the approach described in the previous subsection (see Figs. 2 and 3). Then, we used two acoustic real impulse responses in different sparsity levels; one is measured in a car enclosure where the other is measured in a real audio-conference (denoted ACN) room.

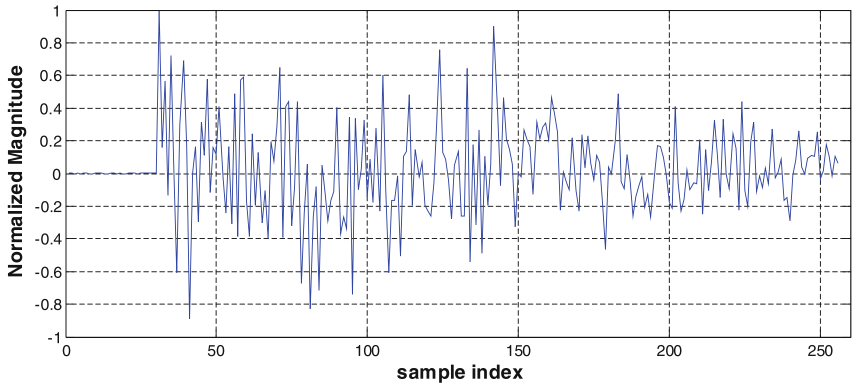

Fig. 2. Synthetic impulse response with length $L = 256$, the bulk delay length $L_p = 30$, $\psi = 160$ and $\xi = 0.3028$ (non-sparse or dispersive).

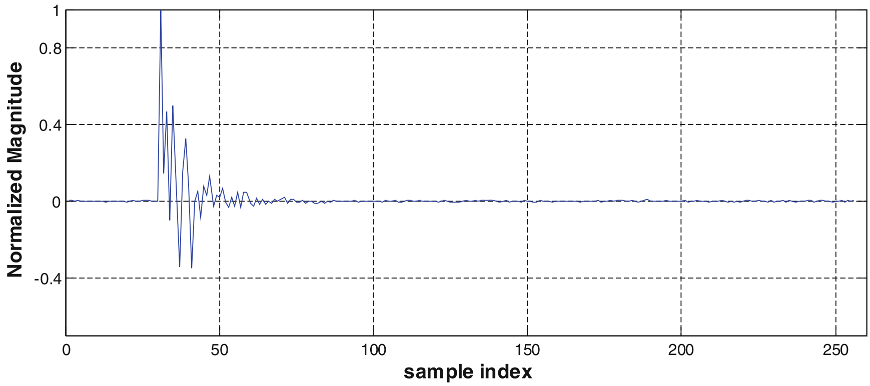

Fig. 3. Synthetic impulse response with length $L = 256$, the bulk delay length $L_p = 30$, $\psi = 10$ and $\xi = 0.8296$ (very sparse).

In order to use our two real systems in different sparsity levels, the car system is used truncated at the first 256 taps to give $\xi = 0.5138$ (less sparse), then with all of its 1024 taps which gives $\xi = 0.7410$ (more sparse) where the “very-long” ACN system is used truncated at the first 2048 taps so as to obtain $\xi = 0.3673$ (less sparse) and with all of its 8192 taps which obtains $\xi = 0.6199$ (more sparse), see Figs. 4 and 5.

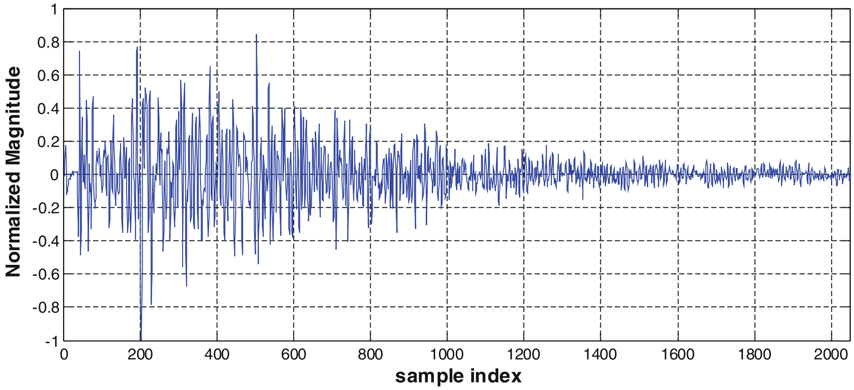

Fig. 4. ACN impulse response with $L = 2048$ and $\xi = 0.3673$ (less sparse).

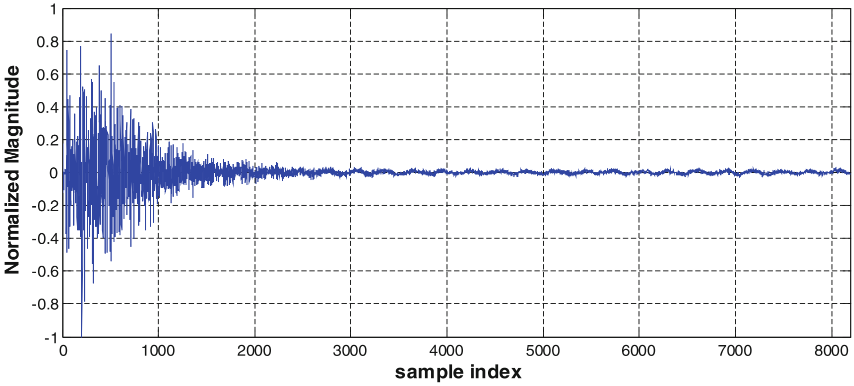

Fig. 5. ACN impulse response with $L = 8192$ and $\xi = 0.6199$ (more sparse).

Concerning inputs, the first one used is a stationary zero-mean correlated noise, with a spectrum equivalent to the average spectrum of speech. It is usually called USASI (USA Standards Institute, now ANSI) noise in the field of acoustic echo cancellation. Its spectral dynamic range is 29 dB. Since in real situations the input signal is non-stationary, the second used input is a long speech signal that was obtained by concatenation of a man voice and a woman voice in the same sequence (see Fig. 6). The estimated spectral dynamic range for this signal is 40 dB.

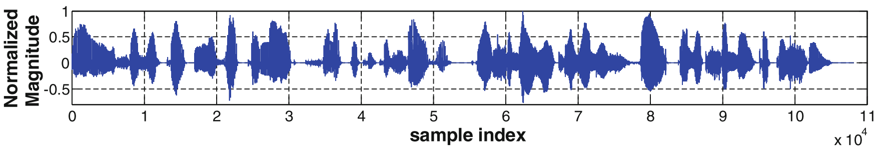

Fig. 6. The used SPEECH input signal with length of 108208 samples.

As a performance measure in our simulations, we used the time-average normalized mean square error (NMSE) learning curve for the stationary input signal (USASI-noise) (denoted as NMSE) [10] defined as

$$\mathrm{NMSE(dB)} = 10\log_{10}\left(\frac{\langle e^2(n)\rangle}{\langle y^2(n)\rangle}\right) \tag{20}$$

where $\langle . \rangle$ the symbol denotes a time averaging (over blocks of 256 samples), and y(n) is the desired signal. For the speech input signal (non-stationary), we preferred to use the time-average MSE (over blocks of 256 samples) [10] defined as,

$$\mathrm{MSE(dB)} = 10\log_{10}\left(\langle e^2(n)\rangle\right) \tag{21}$$

4.3 Performance Comparison and Discussion

We started our comparisons using USASI-noise input with two synthetic impulse responses. Then, we tested the convergence & "re-convergence" using two real car systems with a "jump" (abrupt change) at $n = 63744$, see Figs. 7 and 8. After that, the case of non-stationary speech input is tested (see Figs. 9 and 10).

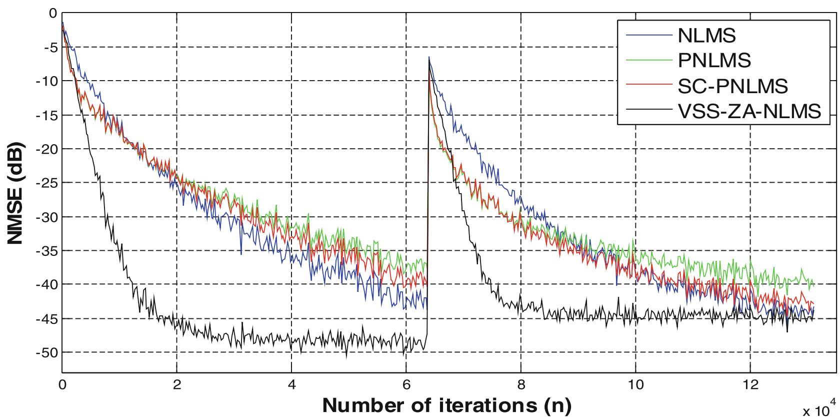

Fig. 7. USASI-noise input. Car system with $L = 256$ and $\xi = 0.5138$ (less sparse). NLMS ($\mu = 0.3$), PNLMS ($\mu = 0.3$), SC-PNLMS ($\mu = 0.3$, $\lambda = 6.0$) and VSS-ZA-NLMS ($\rho_{ZA} = 0.003\ \sigma_n^2$, $\mu_{max} = 1.0$ and $C = 10^{-7}$). Output with SNR = 50 dB. An abrupt change of the impulse response is applied at n = 63744.

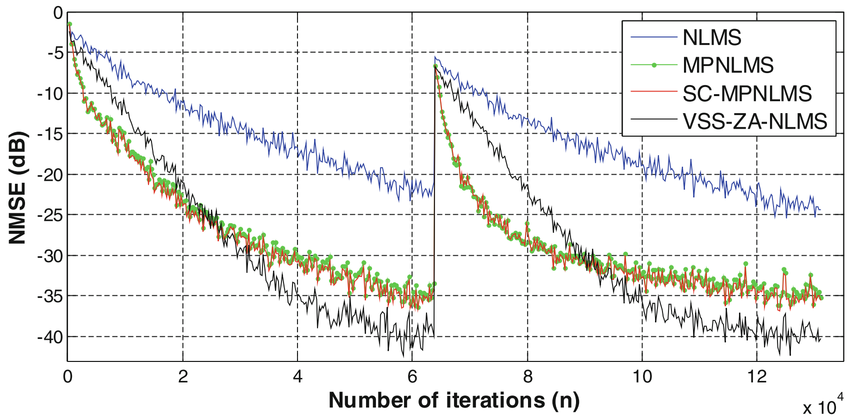

Fig. 8. USASI-noise input. Car system with $L = 1024$ and $\xi = 0.7410$ (more sparse). NLMS ($\mu = 0.3$), PNLMS ($\mu = 0.3$), SC-PNLMS ($\mu = 0.3$, $\lambda = 6.0$) and VSS-ZA-NLMS ($\rho_{ZA} = 0.003\,\sigma_n^2$, $\mu_{max} = 1.0$ and $C = 10^{-7}$). Output with SNR = 50 dB. An abrupt change of the impulse response is applied at n = 63744.

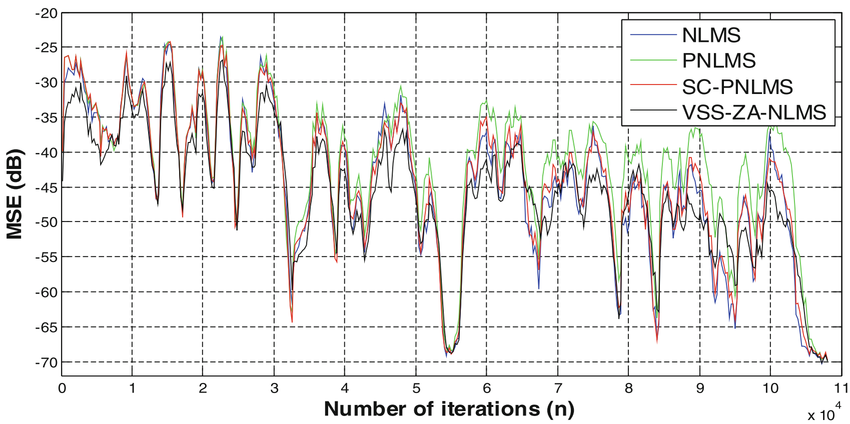

Fig. 9. Speech input. ACN system with $L = 2048$ and $\xi = 0.3673$ (less sparse). NLMS ($\mu = 0.3$), PNLMS ($\mu = 0.3$), SC-PNLMS ($\mu = 0.3$, $\lambda = 6.0$) and VSS-ZA-NLMS ($\rho_{ZA} = 0.003\,\sigma_n^2$, $\mu_{max} = 1.0$ and $C = 10^{-7}$). Output with SNR = 50 dB.

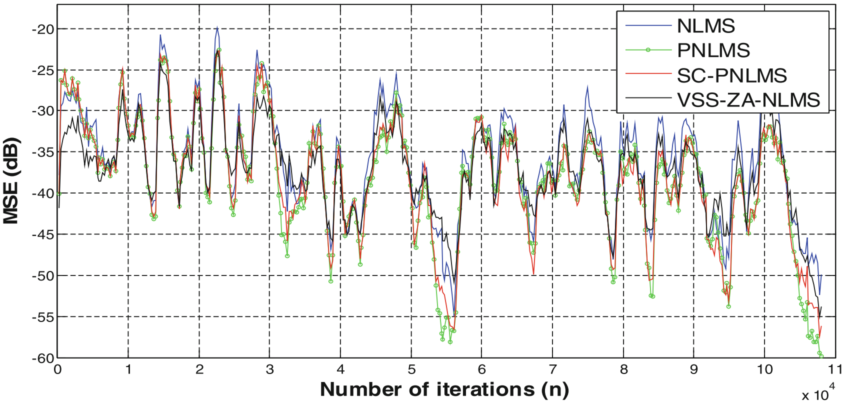

Fig. 10. Speech input. ACN system with $L = 8192$ and $\xi = 0.6199$ (more sparse). NLMS ($\mu =$ 0.3), PNLMS ($\mu = 0.3$), SC-PNLMS ($\mu = 0.3$, $\lambda = 6.0$) and VSS-ZA-NLMS ($\rho_{ZA} = 0.003\ \sigma_n^2$, μ_{max} = 1.0 and $C = 10^{-7}$). Output with SNR = 50 dB.

From these figures, we can notice that the SC-PNLMS algorithm outperforms the PNLMS algorithm especially for less-sparse and dispersive systems with a performance very close to NLMS but slightly worse. However, for sparse cases, SC-PNLMS and PNLMS become very similar and behave better than NLMS in terms of convergence rate and estimation accuracy.

For stationary inputs, the VSS-ZA-NLMS algorithm has the best overall convergence-speed and steady-state performance particularly in less-sparse and dispersive systems where PNLMS and SC-PNLMS have, most of the time, faster initial convergence (or re-convergence) speed which reduces later to be slower than the convergence speed of VSS-ZA-NLMS.

For speech input (non-stationary), PNLMS and SC-PNLMS are more favorable in highly-sparse systems where VSS-ZA-NLMS has superior performance for less-sparse and dispersive systems.

4.4 Summary

The main achieved results from the previous simulations in stationary and non-stationary cases are summarized in Tables 2 and 3 respectively. The value 5 is given for the best algorithm performance (it could be the fastest convergence speed, the most precise estimation accuracy, or the lowest computational complexity) where the value 1 is assigned for the worst (it could be the slowest convergence speed, the least precise estimation accuracy, or the highest computational complexity). The values in between indicate the closeness either to the best (e.g. 4) or to the worst (e.g. 2).

1. *Stationary-input case.*

Table 2. Recapitulation of the main obtained results (stationary input).

Stationary	Dispersive and less sparse IR		Strongly sparse systems IR		Computational complexity
Algorithm	Speed of convergence	Estimation accuracy	Speed of convergence	Estimation accuracy	
NLMS	4	5	1	2	5
PNLMS	1	1	4	4	4
SC-PNLMS	3	3	4	4	2
VSS-ZA-NLMS	5	5	3	5	3

2. *Speech-input (non-stationary) case.*

Table 3. Recapitulation of the main obtained results (non-stationary input; speech).

Speech	Dispersive and less sparse IR		Strongly sparse systems IR		Computational complexity
Algorithm	Speed of convergence	Estimation accuracy	Speed of convergence	Estimation accuracy	
NLMS	4	4	2	2	5
PNLMS	1	1	4	3	4
SC-PNLMS	2	2	4	3	2
VSS-ZA-NLMS	5	5	3	3	3

5 Conclusion

This paper addresses the problem of identifying "long" acoustic impulse responses using sparse adaptive filtering algorithms. It focuses on the study and comparison of three well-known and recent adaptive filtering NLMS-based algorithms drawn from different frameworks and tested for sparse and non-sparse AIRs, emphasizing on the achievement of fast convergence rate and good accuracy with relatively low computational complexity.

Each of the discussed algorithms has its advantages and its limitations. Depending on system nature, application design requirements and user objectives, some algorithms are more favorable than others. The trade-off between the convergence speed and the steady state MSE is an important issue in the context of system identification and AEC. This issue can be balanced by choosing the suitable algorithm with the appropriate parameters for the adaptive filtering process. If two algorithms perform similarly for a particular application, then, the one with less complexity cost is the most preferable.

References

1. Radecki, J., Zilic, Z., Radecka, K.: Echo cancellation in IP networks. In: Proceedings of the 45th Midwest Symposium on Circuits and Systems, Tulsa, Okla, USA, vol. 2, pp. 219–222 (2002)
2. Krishna, V.V., Rayala, J., Slade, B.: Algorithmic and implementation aspects of echo cancellation in packet voice networks. In: Proceedings Thirty-Sixth Asilomar Conference on Signals, Systems and Computers, vol. 2, pp. 1252–1257 (2002)
3. Hänsler, E., Schmidt, G. (eds.): Topics in Acoustic Echo and Noise Control: Selected Methods for the Cancellation of Acoustical Echoes, the Reduction of Background Noise, and Speech Processing. Springer Science & Business Media, Heidelberg (2006)
4. Duttweiler, D.L.: Proportionate normalized least-mean-squares adaptation in echo cancelers. IEEE Trans. Speech Audio Process. **8**(5), 508–518 (2000)
5. Khong, A.W.H., Naylor, P.A.: Efficient use of sparse adaptive filters. In: Proceedings of Fortieth Asilomar Conference on Signals, Systems and Computers, pp. 1375–1379 (2006)
6. Loganathan, P., Khong, A.W.H., Naylor, P.A.: A class of sparseness-controlled algorithms for echo cancellation. IEEE Trans. Audio Speech Lang. Process. **17**(8), 1591–1601 (2009)
7. Carmi, A.Y., Mihaylova, L., Godsill, S.J. (eds.): Compressed Sensing & Sparse Filtering. Springer, Berlin (2014)
8. Chen, Y., Gu, Y., Hero, A.O.: Regularized Least-Mean-Square Algorithms. arXiv preprint arXiv:1012.5066 [stat.ME], pp. 1–9 (2010)
9. Gui, G., Peng, W., Xu, L., Liuand, B., Adachi, F.: Variable-step-size based sparse adaptive filtering algorithm for channel estimation in broadband wireless communication systems. EURASIP J. Wirel. Commun. Netw. **2014**(1), 1–7 (2014)
10. Benallal, A., Arezki, M.: A fast convergence normalized least-mean-square type algorithm for adaptive filtering. Int. J. Adapt. Control Signal Process. **28**(10), 1073–1080 (2014)
11. Loganathan, P.: Sparseness-controlled adaptive algorithms for supervised and unsupervised system identification. Ph.D. dissertation, Department of Electrical and Electronic Engineering, Imperial College, London (2011)
12. Benesty, J., Gänsler, T., Morgan, D.R., Sondhi, M.M., Gay, S.L.: Advances in Network and Acoustic Echo Cancellation, pp. 31–54. Springer, Berlin (2001)
13. Benesty, J., Gay, S.L.: An improved PNLMS algorithm. In: Proceedings of the IEEE International Conference on Acoustic, Speech and Signal Processing (ICASSP), Orlando, FL, USA, pp. 1881–1884 (2002)
14. Huang, Y., Benesty, J., Chen, J.: Acoustic MIMO Signal Processing, Chap. 4, pp. 59–84. Springer, New York (2006)
15. Shin, H.C., Sayed, A.H., Song, W.J.: Variable step-size NLMS and affine projection algorithms. IEEE Signal Process. Lett. **11**(2), 132–135 (2004)
16. Xu, L., Ju, Y.: Improving convergence of the MPNLMS algorithm for echo cancellation. In: 3rd International Conference on Advanced Computer Control (ICACC), pp. 198–201 (2011)
17. Naylor, P.A., Cui, J., Brookes, M.: Adaptive algorithms for sparse echo cancellation. Signal Process. **86**(6), 1182–1192 (2006)
18. Hoyer, P.O.: Non-negative matrix factorization with sparseness constraints. J. Mach. Learn. Res. **5**, 1457–1469 (2004)

19. Benesty, J., Huang, Y.A., Chen, J., Naylor, P.A.: Adaptive algorithms for the identification of sparse impulse responses. In: Hänsler, E., Schmidt, G. (eds.) Selected Methods for Acoustic Echo and Noise Control, Chap. 5, pp. 125–153. Springer, Heidelberg (2006)
20. Gui, G., Adachi, F.: Improved least mean square algorithm with application to adaptive sparse channel estimation. EURASIP J. Wirel. Commun. Netw. **2013**(1), 1–18 (2013)
21. Tedjani, A.: Study of sparse adaptive algorithms for the identification of acoustic impulse responses. Magister thesis, Dept. of Electronics, University of Blida 1, Algeria (2016)

A New Robust Blind Source Separation Algorithm for Speech Enhancement

Mohamed Djendi(✉) and Meriem Zoulikha

Signal Processing and Imaging Laboratory (LATSI), University of Blida 1, Route de Soumaa B.P. 270, 09000 Blida, Algeria
m_djendi@yahoo.fr, m_zoulikha@hotmail.fr

Abstract. This paper addresses the problem of speech enhancement and acoustic noise reduction by adaptive filtering algorithms in a moving car through blind source separation (BSS) structures. In this paper we propose a new robust forward blind source separation (RFBSS) algorithm that does not need voice activity detection (VAD) systems, and allows getting efficient speech enhancement performances with low complexity. The proposed RFBSS algorithm is compared with recent and classical speech enhancement algorithms in different noisy conditions. This comparison is evaluated in terms of Cepstral distance (CD), the system mismatch (SM) and the Segmental signal-to-noise ratio (SegSNR) criteria. The obtained results show the efficiency of the proposed algorithm and its superiority in comparison with competitive algorithms in speech enhancement applications.

1 Introduction

It is well known that the BSS is a powerful technique for acoustic noise reduction and speech enhancement in many situation such as in a car configuration involving loosely spaced microphones and short impulse responses. Most speech enhancement algorithms which are based on the BSS structure use either a manual VAD system (MVAD) system, or an integrated bloc which realizes automatic VAD (AVAD) to control the adaptation of the cross-filters. Recently, a particular attention has been made to both forward and backward BSS (i.e. FBSS and BBSS) structures applied to enhance corrupted speech signals and to cancel the acoustic noise components.

Several works have dealt with these two structures [1, 2]. However, all of these techniques used a MVAD system that makes them inoperative in practice. The only work that proposed a VAD system with this FBSS and BBSS structure is given in [3]. In this paper, we focus our interest on the BBSS structure and propose a new robust adaptive algorithm that enhances the speech signal and reduces the acoustic noise without need of any VAD system. The solution given in this paper is algorithmic and not structural as it is given in [2]. The organization of this paper is as follows: in Sect. 2, we present the principle of BSS. The Model description of FBSS is detailed in Sect. 3. The proposed robust forward BSS (RFBSS) algorithm is presented in Sect. 4. However, in Sect. 5, we show the simulation results of the proposed RFBSS algorithm and its performances in comparison with competitive and recent techniques. Finally, we conclude our work in Sect. 6.

M. Chadli et al. (Eds.): ICEECA 2017, LNEE 522, pp. 526–536, 2019.
https://doi.org/10.1007/978-3-319-97816-1_40

2 Blind Source Separation (BSS)

In real environment such as in cars, the recorded signals by two microphones are a linear combination between the speech s(n) and the noise b(n) components. The latter depends on the microphone's positions, acoustic characteristics of the car's interior, the sources themselves, etc. [4]. Therefore, the main problem is to find, with the least a priori knowledge, useful signals which have been mixed. In order to overcome this problem, the BSS structure of [4] is used frequently to extract the sources signal from the only knowledge of noisy signals. In this paper, we focus on the convolutive noisy signals and the FBSS structure. The principle of the FBSS is shown in Fig. 1 (mixing, and separation signals processes).

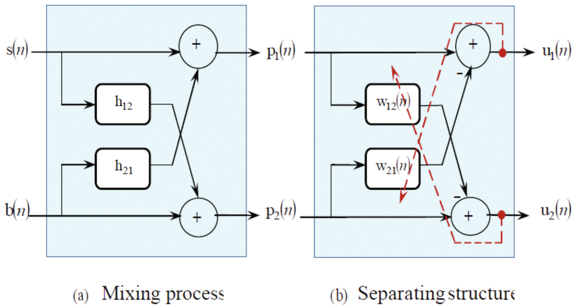

Fig. 1. Mixing process (a), and separating FBSS structure.

3 Model Description of FBSS Structure

In order to separate the noisy observation components from the given structure (Fig. 1a), we used the FBSS which is shown in Fig. 1b [5, 6]. The noisy signals $p_1(n)$ and $p_2(n)$ of the FBSS are:

$$p_1(n) = s(n) + h_{21}(n) * b(n), \tag{1}$$

$$p_2(n) = b(n) + h_{12}(n) * s(n). \tag{2}$$

where $s(n)$ and $b(n)$ are two sources of speech and noise, respectively; $h_{12}(n)$ and h_{21}(n) represent the cross-coupling effects between the two-channels. The symbol (*) represents the linear convolution operator. For this model, both adaptive filters $w_{12}(n)$ and $w_{21}(n)$ are used to identify the cross-talk path $h_{21}(n)$ and h_{21}(n), respectively. The output signals, $u_1(n)$ and $u_2(n)$, of the FBSS structure are:

$$u_1(n) = p_1(n) - p_2(n) * w_{21}(n), \tag{3}$$

$$u_2(n) = p_2(n) - p_1(n) * w_{12}(n). \tag{4}$$

where $w_{12}(n)$ and $w_{21}(n)$ are the cross-adaptive filters. If we do further development of the above relations, we obtain:

$$u_1(n) = b(n) * [h_{21}(n) - w_{21}(n)] + s(n) * [\delta(n) - h_{12}(n) * w_{21}(n)], \tag{5}$$

$$u_2(n) = s(n) * [h_{12}(n) - w_{12}(n)] + b(n) * [\delta(n) - h_{21}(n) * w_{12}(n)]. \tag{6}$$

The optimal assumption for both adaptive filters $w_{12}(n)$ and $w_{21}(n)$ means that:

$$w_{12}^{opt} = h_{12}, \text{ and } w_{21}^{opt} = h_{21} \tag{7}$$

Then the two outputs of the FBSS structure are given by:

$$u_1(n) = s(n) * [\delta(n) - h_{12}(n) * h_{21}(n)], \tag{8}$$

$$u_2(n) = b(n) * [\delta(n) - h_{21}(n) * h_{12}(n)]. \tag{9}$$

The two cross-filters $w_{12}(n)$ and $w_{21}(n)$ are adjusted adaptively by several algorithms. The first used algorithm is the Forward symmetric adaptive decorrelating (FSAD) algorithm [4]. This algorithm propagates the following relations:

$$\mathbf{w}_{21}(n+1) = \mathbf{w}_{21}(n) + \mu_{21}(u_1(n)\mathbf{u}_2(n-m)), \tag{10}$$

$$\mathbf{w}_{12}(n+1) = \mathbf{w}_{12}(n) + \mu_{12}(u_2(n)\mathbf{u}_1(n-m)). \tag{11}$$

where: $\mathbf{u}_1(n) = [u_1(n),.., u_1(n - M+1)]$ and $\mathbf{u}_2(n) = [u_2(n),.., u_2(n - M+1)]$ are the coefficients vectors of the last M samples of the outputs $u_1(n)$ and $u_2(n)$ respectively. The two step-sizes, μ_{12} and μ_{21} are both control parameters of the FSAD algorithm, which adjusts the convergence direction of the adaptive filters $w_{12}(n)$ and $w_{21}(n)$, respectively. They are chosen according to the relations $0 < \mu_{12} < 2/\sigma^2$ and $0 < \mu_{21} < 2/\sigma^2$, where σ^2 and σ^2 represent the variances of the input signals $p_1(n)$ and $p_2(n)$, respectively.

A. *Control of the FBSS structure by a VAD system*

The optimal assumption of relation (7) is obtained by using a VAD system. The VAD system combined with the FBSS structure are schematized in Fig. 2. The VAD system is useful in the estimation of noise components in observations. In fact, according to a known process of the state of art, the filter $w_{21}(n)$ is updated only during the noise-only periods and the filter $w_{12}(n)$ is updated during voice activity periods. This principle is well used in the symmetric adaptive decorrelating (SAD) algorithm combined with the FBSS structures [7].

The use of a MVAD system in the FBSS structure gives a perfect segmentation which is not the case in practice, because there is no *a priori* information on the input signals. For this purpose, we need to detect the VAD automaticly. Two algorithms called VSS-BBSS and VSS-FBSS have been already proposed in [3] that use AVAD.

Both of these proposed AVAD algorithms, for the forward and backward structures, are based on structural techniques that allow controlling adequately the step-sizes

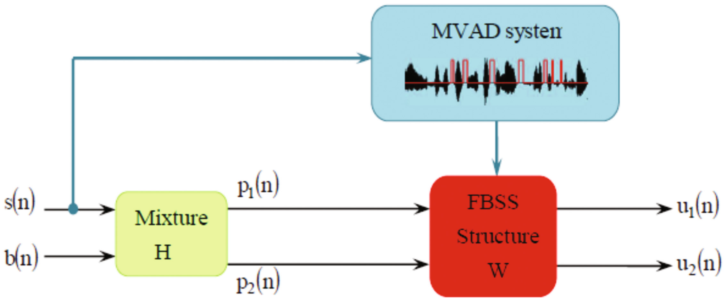

Fig. 2. Control of the FBSS structure a manual VAD (MVAD) system.

of the cross-filters. Hereafter, a new algorithm that allows to get the same behavior as these two proposed algorithms with low complexity is proposed in this paper.

4 Proposed Robust FBSS (RFBSS) Algorithm

In the formulation of the proposed RFBSS algorithm, we use the Newton's procedure of [8] that is often used in the fast adaptive filtering algorithms derivation. If we apply this principle of Newton's recursion [8] to the filter of relation (10), we obtain:

$$\mathbf{w}_{21}(n+1) = \mathbf{w}_{21}(n) + \mu_{21}[\mathbf{A}(n)]^{-1}[\mathbf{P}_{\mathrm{p1p2}} - \mathbf{R}_{\mathrm{p2}}(n)\mathbf{w}_{21}(n)]^{T}, \tag{12}$$

where $\mathbf{A}(n) = [\varepsilon(n)\mathbf{I} + \mathbf{R}_{\mathrm{p2}}]$, and $\mathbf{P}_{\mathrm{p1p2}}$ represents the cross correlation vector between the noisy signals $\mathrm{p}_1(n)$ and $\mathrm{p}_2(n)$, i.e. $\mathrm{P}_{\mathrm{p1p2}} = \mathrm{E}[\mathrm{p}_1(n)\ \mathrm{p}_2(n)]$; and R_{p2} is the auto-correlation of the vector $\mathrm{p}_2(\mathrm{n})$, i.e. $\mathbf{R}_{\mathrm{p2}} = E[\mathbf{p}_2(n)\ \mathbf{p}^{\mathrm{T}}\ (n)]$. I is $\mathrm{N} \times \mathrm{N}$ identity matrix; $\varepsilon(n)$ is a small regularization factor; and μ_{21} is an iteration-dependent step-size. In the case of dual least mean square (LMS) algorithm, we replace $\mathrm{P}_{\mathrm{p1p2}}$ and R_{p2} by their instantaneous approximation, i.e. $\mathbf{P}_{\mathrm{p1p2}} = [\mathbf{p}_1(n)\ \mathbf{p}_2(n)]$, and $\mathbf{R}_{\mathrm{p2}} = [\mathbf{p}_2(n)\ \mathbf{p}_2^{\mathrm{T}}(n)]$.

In this paper, we propose to replace the small regularization parameter $\varepsilon(\mathrm{n})$ in (12) by an averaged mean value of the power of the FBSS first output $\mathrm{u}_{1\mathrm{L}}(\mathrm{n})$ and introduce two parameters α and γ in this relation. The new relation of the cross-filter update of $\mathrm{w}_{21}(\mathrm{n})$ is given as

$$\mathbf{A}(n) = [\alpha\|\mathbf{u}_{1\mathrm{L}}(n)\|^2\mathbf{I} + \gamma\,\mathbf{P}_2(n)\mathbf{P}^{\mathrm{T}}(n)]^{-1}. \tag{13}$$

The vector $\mathrm{u}_{1\mathrm{L}}(\mathrm{n})$ is composed by the last L estimated values by relation (3), i.e. $\mathbf{u}_{1\mathrm{L}}(\mathrm{n}) = [\mathbf{u}_{1,0}(n),\ \mathbf{u}_{1,1}(n),\ \ldots,\ \mathbf{u}_{1,\mathrm{L}-1}(n)]$. The squared norm of the output $\|\mathbf{u}_{1\mathrm{L}}(n)\|^2$ relation (13) is computed as follows:

$$\|\mathbf{u}_{1\mathrm{L}}(n)\|^2 = \Sigma^{l-1}|\mathrm{u}_1(n-i)|^2. \tag{14}$$

In order to simplify the writing of relation (13), we applied the matrix inverse lemma [8] and after some simplification and rearrangement, we get the final relation of **A**(n):

$$\mathbf{A}(n) = \frac{1}{\alpha||\mathbf{u}_{1L}(n)||^2\,\mathbf{I} + \gamma||\mathbf{P}_2(n)||^2}. \tag{15}$$

In order to get the final update relation of the cross-filter $w_{21}(n)$, we insert (15) into (12) and we put $\gamma = 1 - \alpha$. Finally, As the FBSS structure is symmetric and uses two cross-adaptive filters $w_{12}(n)$ and $w_{21}(n)$ to cancel the acoustic noise components from the noisy observations, we extrapolate the analysis from (12) to (15) to derive the same formulation of the cross-filter $w_{12}(n)$:

$$\mathbf{w}_{12}(n+1) = \mathbf{w}_{12}(n) + \mu_{12}u_2(n)\mathbf{P}_1(n)\mathbf{B}(n), \tag{16}$$

$$\mathbf{B}(n) = \frac{1}{\alpha||\mathbf{u}_{2L}(n)||^2\,\mathbf{I} + \gamma||\mathbf{P}_1(n)||^2}. \tag{17}$$

$$||\mathbf{u}_{2L}(n)||^2 = \Sigma^{l-1}|u_2(n-i)|^2. \tag{18}$$

where α and γ are positive constants. The parameters α, γ, and then $\mu_{ij,}$ $\{i = j\} = 1, 2$, of the proposed algorithm are chosen to achieve the best tradeoff between convergence speed and low final mean square error (MSE).

5 Analysis of Simulation Results

In this section, we compare the performance of our pro- posed RFBSS algorithm with the forward symetric adaptive decorrelating (FSAD) [7], and variable step-size FBSS (VSS- BSS) [3] algorithms. this comparsion is done in terms of CD, SegSNR and SM creteria as explained in the abstract.

A. *Simulation of impulse responses and noisy signals*

In the adopted convolutive mixture of Fig. 1a, we use a speech signal (French male speaker) s(n) and a USASI noise (United state of America Standard Institute, now (ANSI)) b(n) to generate the noisy observations, these two source signal are taken from the AURORA database. This mixing model use a simulated impulse responses that are generated by the specific model proposed in [9], which takes into account the effect of the distance between microphones. The latter gives simulated impulse responses $h_{12}(n)$ and $h_{21}(n)$ [the sampling frequency is Fs = 16 kHz; the length of the impulse responses is L = 256].

In the noisy process of Fig. 1a, we use the impulse re- sponses $h_{12}(n)$ and $h_{21}(n)$ that model the cross-coupling effects between the two channels to generate the noisy signals $p_1(n)$ and $p_2(n)$ which are calculated by relations (1) and (2) respectively. The input signal-to-noise-ratio (SNR) is selected to be $SNR_1 = 6$ dB and $SNR_2 = -6$ dB at the first and second microphones, respectively. The original speech signal, USASI noise, and the noisy signals are represented in Fig. 3.

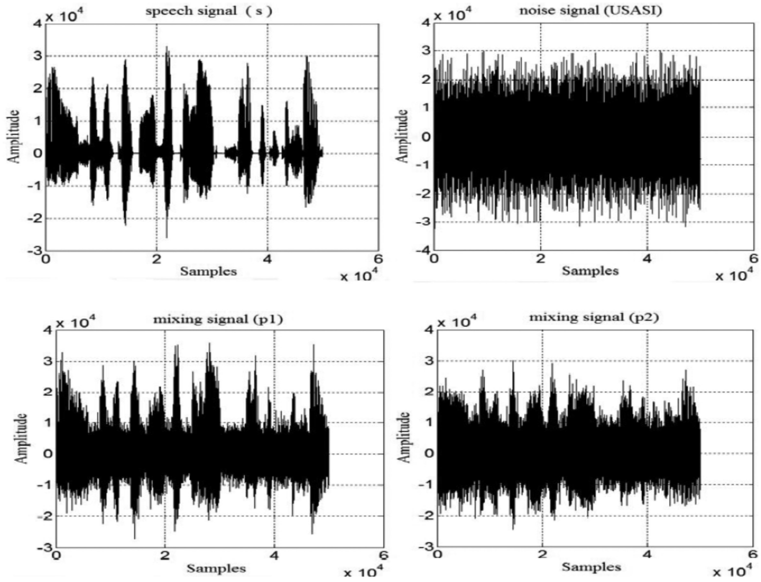

Fig. 3. Source signals (top) and noisy signals (bottom) SNR_1 = 0 dB and SNR_2 = 0 dB.

B. ***Simulation results***

In this study, we focus only on the first output of the proposed RFBSS algorithm in which the speech signal s(n) is restored. The performance of the proposed RFBSS algorithm is performed in a comparison with both FSAD and VSS- FBSS algorithms. We recall that the FSAD algorithm use a MVAD to control both of the adaptive filters $w_{12}(n)$ and $w_{21}(n)$, however, the VSS-FBSS uses a block that performs an AVAD system.

It is worth noting that both of these versions use the NLMS algorithm for the adaptive filters coefficients adaptation. To do this comparison, we use the following objective criteria [10, 11]: (i) Temporal evolution description of the output signals, (ii) Cepstral distance (CD) to quantify the distortion at the output of the proposed algorithm, (iii) System mismatch (SM) to describe the convergence rate of the cross-coupling adaptive filter $w_{21}(n)$ used in the proposed algorithm, (vi) Segmental SNR (SegSNR) between the enhanced speech signal at the output and the original version to objectively evaluate the noise reduction performance of the proposed algorithm.

The control parameters of the FSAD, VSS-FBSS and the proposed RFBSS algorithms are summarized in Table 1. We note that these parameters are used in all the simulations that are presented in this paper.

From, we can observe that the three algorithms share the adaptive filters length parameter which is selected to be equal to $L_{w12} = L_{w21}$ = 256. The other parameters are

Table 1. Simulations parameters of each algorithm: FSAD, VSS-FBSS and the proposed RFBSS. The paremeters L, Α and Γ are the adaptive filters length, the smoothed coefficients 1, and 2, respectively. μ12, and μ21 are step-sizes.

Algorithms	Parameters
FSAD [10]	$L = 256$, $\mu_{12} = \mu_{21} = 0.4$
VSS-FBSS [1]	$L = 256$, $\mu_{21} = 0.4$, $\mu_{12} = 0.001$
Proposed RFBSS [In this paper]	$L = 256$, $\mu_{21} = 0.01$, $\mu_{12} = 0.1$, $\alpha = 0.98$, $\gamma = 1 - \alpha$

chosen to achieve the best convergence speed performance possible. The parameters α and γ are specific for the new proposed RFBSS algorithm, and they are appropriately chosen to achieve the best trade-off between rate of convergence and low final mean square error. All the presented simulations are carried out with speech signal and noise components sampled at 16 kHz and coded on 16 bits.

(1) Evaluation of the enhanced speech signals: In Fig. 4, we show the output signals obtained with the three algorithms, i.e. the proposed RFBSS, FSAD and VSS-FBSS. In this Fig. 4, we show the temporal evolution of the different signals used in simulation (original speech signal and the output signal of each method). For each algorithm, the spectrogram of the signal available at the output of treatment is depicted in the same Fig. 4. From Fig. 4, available signals on the processed outputs from these three algorithms are visually denoised, also we can observe, from the spectrogram representation, that the proposed RFBSS output signal is the closer one to the original speech signal.

(2) Evaluation of the Cepstral distance (CD): we evaluate the CD evolution of the speech signals obtained by the FSAD, VSS-FBSS and the proposed RFBSS algorithms. The CD evaluation is done only with speech presence segment. We have evaluated the CD criterion for three inputs SNRs, i.e. $SNR_1 = SNR_2 = -6$ dB, 0 dB and 6 dB. In the noisy signals, we have used four types of noise, (i.e. white noise, USASI noise, Babble noise and Street noise). Figure 5 shows the obtained results of the CD values by the proposed RFBSS, FSAD and VSS-FBSS algorithms.

From this Fig. 5, we can observe the virtue of the proposed algorithm (RFBSS) over the other ones (FSAD and VSS-FBSS). It is also noted that the classical FSAD and VSS-FBSS algorithms provide almost the same performance.

It is worth noting that this new RFBSS algorithm does not need any VAD system either a MVAD, as in the case of the original FBSS structure, or an integrated block which realizes AVAD, like in the VSS-FBSS algorithm [1]. In this new RFBSS algorithm, the adaptation process of the cross-filters $w_{21}(n)$ and $w_{12}(n)$ is done automatically thanks to variable gradient part of the cross-filters $w_{21}(n)$ and $w_{12}(n)$ which are given by (20) and (21) respectively.

In the case where the speech signal energy is superior than that of the noise, the filter $w_{21}(n)$ is frozen i.e. there is no adaptation, so the noise is not removed in this period. On the other hand, when the noise energy (noisy signal) is much important than

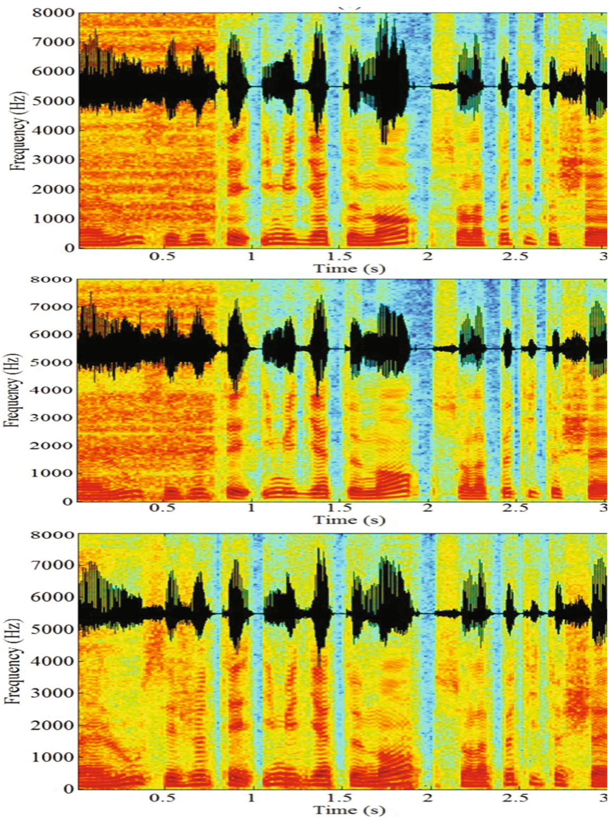

Fig. 4. Time evolution and spectrogram of the output speech signals $u_1(n)$ obtained by the following algorithms: (Top) FSAD algorithm, (Middle) VSS- FBSS algorithm, and (Bottom) the proposed RFBSS algorithm.

that of the speech signal, the cross-filter $w_{21}(n)$ is adapted and the speech signal is well denoised. More the noise signal is canceled, the estimated speech signal is enhanced. This is one of the most important advantage of this new (RFBSS) automatic algorithm (improvement of quality) without using and need of any type of segmentation.

Clearly, the first step-size μ_{21} is inversely adjusted by both energy of $u_1(n)$ and $p_2(n)$ signals. However, the first step-size μ_{12} is control by both energy of the signals $u_2(n)$ and $p_1(n)$. From these relations, we can easily note that the gradient part of the both cross-filters $w_{21}(n)$ and $w_{12}(n)$ are frozen when the energy of the output $u_1(n)$ and $u_2(n)$ are close to those of the noisy signals, i.e. $p_2(n)$ and $p_1(n)$, respectively; thus in the other case both cross-filters $w_{21}(n)$ and $w_{12}(n)$ will be updated and this is what happen in the permanent regime. In conclusion, when the FBSS output energies are small, the cross-filters $w_{21}(n)$ and $w_{12}(n)$ of this algorithm are adjusted, therefore the coefficients automatically begin to adapt. Thus, in the other case, the cross-filters are frozen and no adaptation is done, so the noise is not removed in this period.

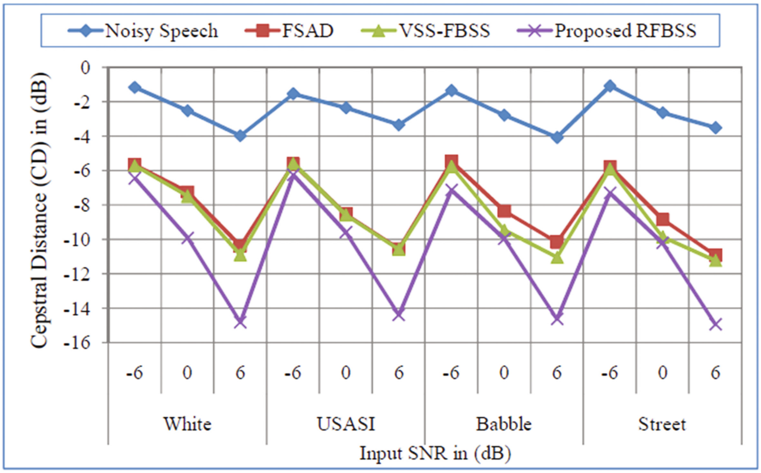

Fig. 5. Overall Cepstral Distance (CD) evaluation. Simulated algorithms are: (1) FSAD algorithm, (2) VSS-FBSS algorithm and (3) the proposed RFBSS algorithm. The algorithm parameter values are given in Table 1.

(3) System mismatch (SM) criterion evaluation: The obtained results of the SM criterion by the proposed RFBSS, FSAD and VSS-FBSS algorithms are reported in Fig. 6. In this Fig. 6, the temporal SM evolution of the adaptive filter coefficients $w_{21}(n)$ is shown. Analysis of Fig. 6 shows that the proposed RFBSS algorithm shows the best performance in comparison with both FSAD and VSS-FBSS algorithms.

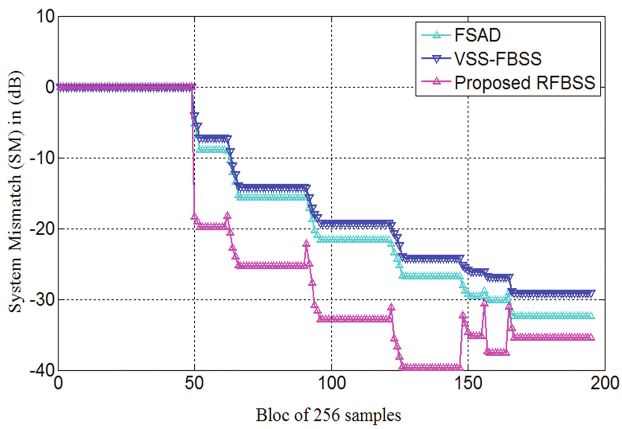

Fig. 6. The system mismatch comparison between three structures: the RFBSS (in pink), the FSAD (in cyan) and the VSS-FBSS (in blue).

(4) Segmental SNR (SegSNR) criterion evaluation: In order to complete the previous performance comparison, the obtained results of the SegSNR applied to the output speech signals of the three algorithms (proposed RFBSS, FSAD and VSS-FBSS), are shown in Fig. 7. It is worth reminding that the output segmental SNR criterion is evaluated between the original speech signal and its enhanced versions for each algorithm.

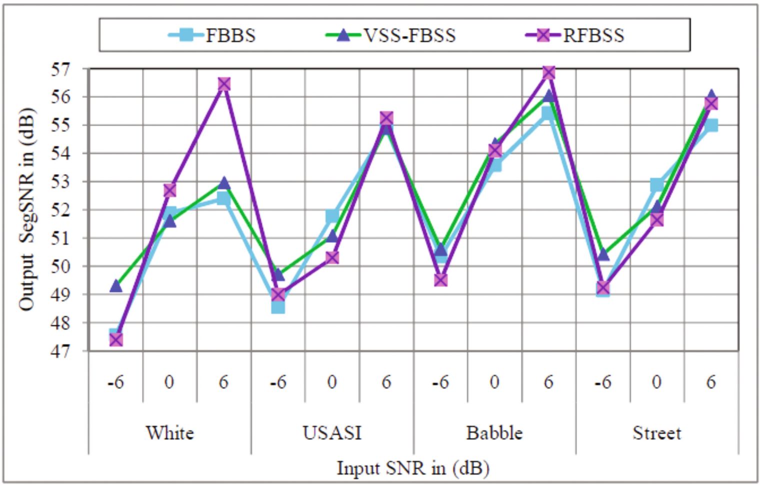

Fig. 7. The SegSNR values evaluation of the proposed RFBSS, FSAD, and VSS-FBSS algorithms.

In this simulation, we use the same noise types as in subsection 2 and evaluate the SegSNR for the input SNRs, −6 dB, 0 dB and +6 dB. Figure 7 compares the performance based on the SegSNR criterion obtained with each algorithm for different inputs SNRs.

On the same Fig. 7, the output SNR values of the noisy speech signal are compared with the other ones. According to these results, it is clear that the proposed RFBSS algorithm have almost the same segmental SNR values with classical and variable FBSS structures (i.e. FSAD and VSS-FBSS, respectively). We conclude that the segmental SNR criterion proves the good characteristic of the proposed RFBSS algorithm to reduce the noise components at the output without using any segmentation to control the adaptation of the adaptive filters.

6 Conclusions

In this paper, we have proposed a new robust FBSS algorithm (denoted RFBSS), which is used for acoustic noise reduction and speech quality enhancement application. This new algorithm is proposed to avoid mathematically the use of a MVAD system which is inherent for adaptation, control, and fast converging the FBSS cross-filters.

The proposed RFBSS algorithm does not need VAD system, and it is automatically controlled by variable step-sizes that is dependent on mixed normalization of both data and error vectors. For the validation of the proposed RFBSS algorithm performances, we have carried out several experiments based on the objective criteria (SM, CD, and SegSNR) in various environments of convolutive noisy observations (highly and slightly noisy observations). In comparison with conventional FSAD and the improved VSS-FBSS algorithms, the proposed RFBSS algorithm has demonstrated consistently superior performances both in CD and SM criteria. From these results, we conclude that the proposed RFBSS algorithm can be a good alternative for the application of acoustic noise reduction and speech enhancement.

References

1. Buchner, H., Aichner, R., Kellermann, W.: A generalization of blind source separation algorithms for convolutive mixtures based on secondorder statistics. IEEE Trans. Speech Audio Process. **13**(1), 120–134 (2005)
2. Al-Kindi, M.J., Dunlop, J.: Improved adaptive noise cancellation in the presence of signal leakage on the noise reference channel. Signal Process. **17**(3), 241–250 (1989)
3. Djendi, M., Zoulikha, M.: New automatic forward and backward blind sources separation algorithms for noise reduction and speech enhancement. Comput. Electr. Eng. **40**, 2072–2088 (2014)
4. Van Gerven, S., Van Compernolle, D.: Feedforward and feedback in symmetric adaptive noise canceller: stability analysis in a simplified case. In: European Signal Processing Conference on Brussels. Belgium, pp. 1081–1084, August 1992
5. Darazirar, I., Djendi, M.: A two-sensor Gauss-Seidel fast affine projection algorithm for speech enhancement and acoustic noise reduction. Appl. Acoust. **96**, 39–52 (2015)
6. Djendi, M., Bendoumia, R.: A new adaptive filtering subband algorithm for two-channel acoustic noise reduction and speech enhancement. Comput. Electr. Eng. **39**(8), 2531–2550 (2013)
7. Van Gerven, S., Van Compernolle, D.: Signal separation by symmetric adaptive decorrelation: stability, convergence, and uniqueness. IEEE Trans. Signal Proc. **74**(3), 1602–1612 (1995)
8. Sayed, A.H.: Fundamentals of Adaptive Filtering. Wiley, New York (2003)
9. Djendi, M., Scalart, P., Gilloire, A.: Noise cancellation using two closely spaced microphones: experimental study with a specific model and two adaptive algorithms. In: Proceedings of the IEEE, vol. 3, pp. 744–747. ICASSP, May 2006
10. ITU-T: Methods for subjective determination of transmission quality. Recommendation P.800. International Telecommunications Union (ITU-T) (1996)
11. Hu, Y., Loizou, P.C.: Subjective comparison and evaluation of speech enhancement algorithms. Speech Commun. **49**, 588–601 (2007)

Writer Retrieval Using Histogram Of Templates Features and SVM

Mohamed Lamine Bouibed(✉), Hassiba Nemmour, and Youcef Chibani

Laboratoire des Systèmes Intelligents et Communicants (LISIC),
University of Sciences and Technology Houari Boumediene (USTHB), 16111 Beb Ezzouar,
Algiers, Algeria
{mbouibed,hnemmour,ychibani}@usthb.dz

Abstract. In this work, we present a new protocol for a novel biometric scenario that is called writer retrieval. Precisely, we propose to use the Histogram Of Templates (HOT) to generate features from handwritten text images. Then, the retrieval task is achieved by SVM classifier trained according to a writer independent strategy. Experiments are conducted on the CVL database which contains 310 writers (1604 documents written in English and German). The results obtained in terms of overall accuracy highlight the effectiveness of the proposed system.

Keywords: Dichotomy transformation · HOT · SVM · Writer retrieval

1 Introduction

Various fields such as forensic science, paleography or pattern recognition, involve authentication of authorship of handwritten documents. Such application is commonly known as "writer retrieval", which consists of finding from a set of handwritten documents all those written by a specific writer. The challenge is to recognize not the content of documents but the style of the writer because in most cases documents do not contain the same text. Needless to say, that interest in the writer recovery scenario increases with the ever-increasing amount of handwritten documents available in digital format. In fact, this technique allows historians to chase the rare documents of famous individuals.

Compared to other handwriting recognition applications such character recognition or signature verification, writer retrieval is a recent research topic. One of the earliest works on writer retrieval has been proposed by Atanasiu et al. [1], conducted on IAM handwriting dataset report a precision about 100% when 70% of the database documents are considered in ranking. This performance is reduced to 70% when considering only 10% of documents. In [2] authors employ SIFT to generate features that are clustered using a GMM which is used as a vocabulary.

Inspired by the writer-identification protocol proposed in [3], presently, we propose a new automatic system "writer retrieval". Precisely, a dissimilarity framework is employed for training the retrieval system that is based on SVM classifier. For feature generation, we investigate the applicability of the histogram of templates (HOT) that is

M. Chadli et al. (Eds.): ICEECA 2017, LNEE 522, pp. 537–544, 2019.
https://doi.org/10.1007/978-3-319-97816-1_41

locally computed over textural images extracted from handwritten texts. Experiments are carried out using a CVL data set which contains 1604 documents from 310 writers.

The paper is structured as follow: Sect. 2 describes the proposed system by explaining the dissimilarity framework and how features are calculated. We introduce also in this section the different steps that constitute the retrieval system. Section 3 presents the experimental analysis. Finally, Sect. 4 gives the conclusion and indicates some perspectives of this work.

2 Proposed System

Giving a large dataset of handwritten documents, a writer retrieval system seeks all documents that are written by the same person. As shown in Fig. 1, our proposed system is composed of several steps:

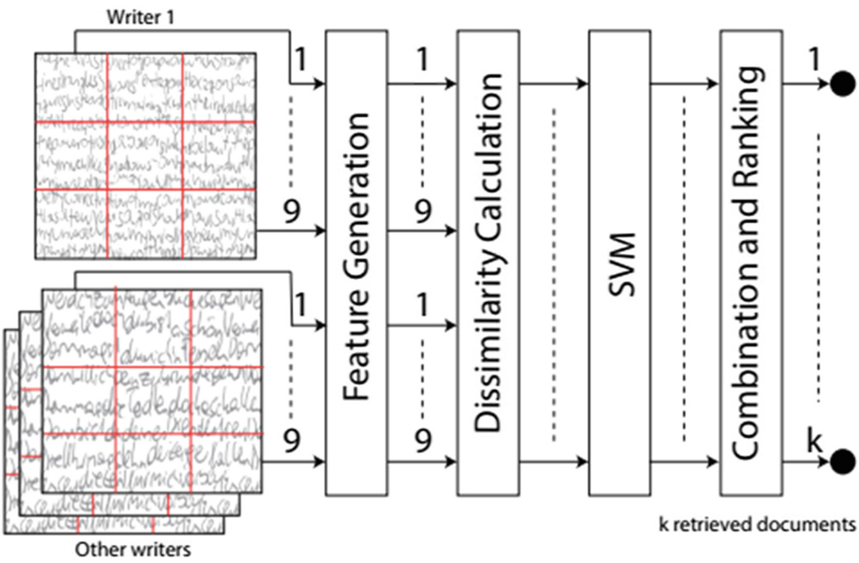

Fig. 1. Proposed system of writer retrieval

1. Build textural images
2. Divide textural images into several cells to allow a local calculation of features.
3. Feature generation using Histogram Of Templates (HOT).
4. Dissimilarity calculation.
5. Develop SVM decision to achieve the retrieval task.

2.1 Textural Images

To highlight the writing style of each individual, we extract only a text from a document. This is done by using projection histograms that help to remove small components such as periods, commas, strokes, interlines and inter-word spaces (Fig. 2).

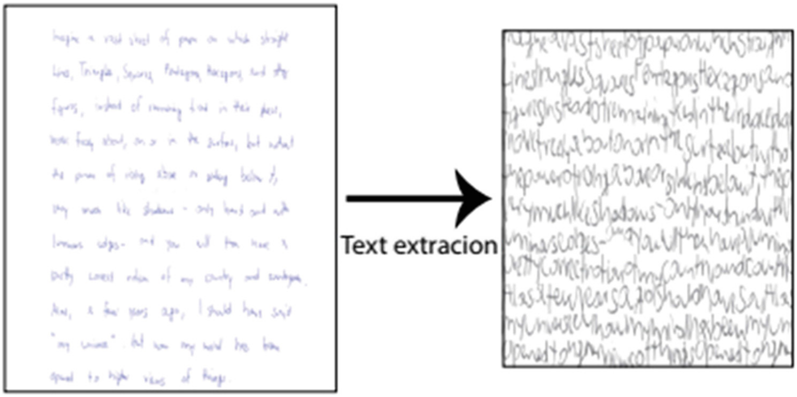

Fig. 2. Textural image extraction from a handwritten document

Projection histograms were introduced in 1956 in a hard-ware OCR system by Glauberman [4]. The horizontal and vertical histograms are calculated as shown in the Eqs. 1 and 2 below:

$$H_X(k1) = \sum\nolimits_{i=1}^{l} I(i, k1) \tag{1}$$

$$H_Y(k2) = \sum\nolimits_{J=1}^{C} I(k2, j) \tag{2}$$

Where ***(l, c)*** are the size of the document image and I is the pixel value. It should be noted that the local minimums of the vertical histogram correspond to the interline, while those of the vertical histogram correspond to the inter-word and inter-characters spaces.

2.2 Histogram of Templates (HOT)

This Descriptor was first introduced for human detection in [5]. It employs a set of 20 templates to describe segment orientations by comparing positional relationship between a pixel and its neighborhood references. Presently, HOT is proposed to highlight local orientations in textural images. Specifically, HOT can be calculated by considering the pixel and gradient information, it compares the intensity or the gradient value of a pixel neighborhood with several templates (see Fig. 3) to find the template that fits the segment orientation. Precisely, as described in Eqs. 3 and 4, the central pixel fits a given template if its intensity (or gradient value) is higher than those of its neighbors in the considered template.

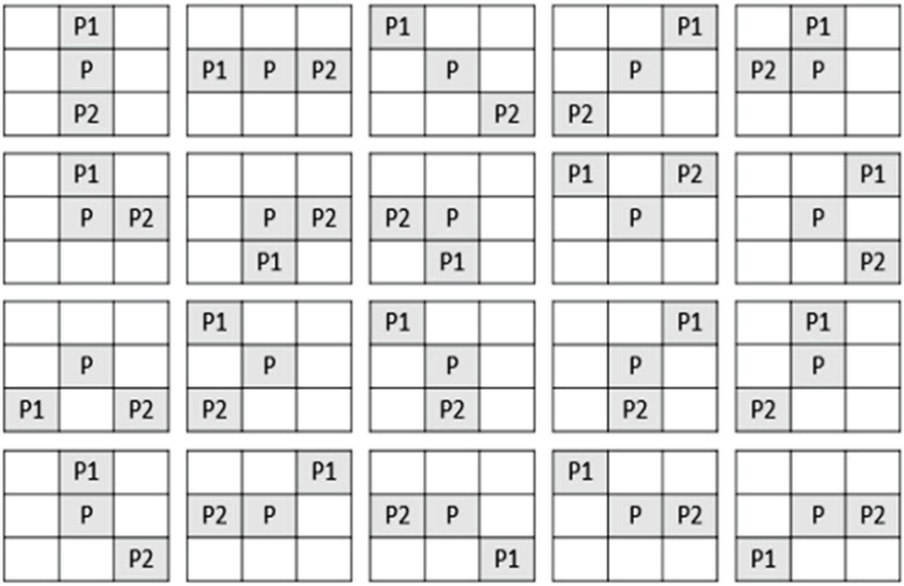

Fig. 3. Templates employed in HOT calculation from [5].

$$I(P) > I(P1)\,\&\&\,I(P) > I(P2) \tag{3}$$

For each template, if the gradient magnitude Mag(P) of a pixel P is greater than the gradient magnitude of the two adjacent pixels, P matches this template (see Eq. 4).

$$Mag(P) > Mag(P1)\ \&\&\ Mag(P) > Mag(P2) \tag{4}$$

I: the gray level value.
Mag: gradient magnitude

The histogram has 20 bins and each bin corresponds to one template. The value of each bin is the amount of pixels that meet the template in a given cells. The final feature vector is obtained by concatenating intensity and gradient histograms.

2.3 Dissimilarity Calculation

To retrieve all documents that belong to the same writer, we reduced the multi-class problem into 2-class problem by using the dissimilarity framework introduced in [6] which is based on a dichotomy transformation. It provides two classes that are independent of the number of writers: the within class (+) and the between class (−). The Fig. 4 illustrates briefly the dichotomy transformation of 4 writers {w1, …w4} to form vectors (Z1; Z2) called dissimilarity feature. Suppose two vectors A and B their dissimilarity is calculated as follow (see Eq. 5):

$$Z_I = \left|A_I - B_I\right| \tag{5}$$

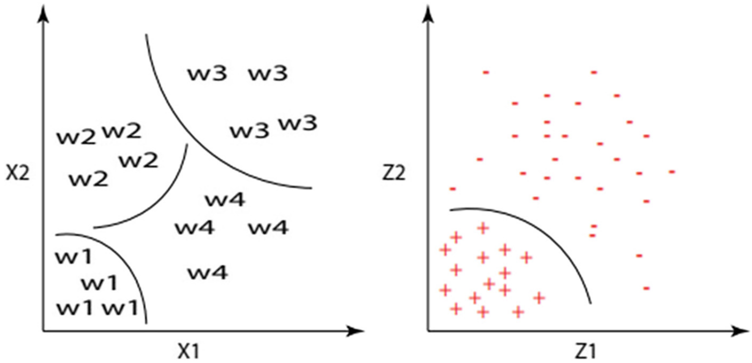

Fig. 4. Dichotomy transformation: (a) samples in the feature space and (b) samples in the dissimilarity space where (+) stand for the vectors associated to the within class and (−) stands for the vectors associated to the between class from [3].

Figure 5 shows the calculation of dissimilarities in the positive class using two textural images of the same writer. These images are partitioned into 9 cells to allow local calculation of HOT.

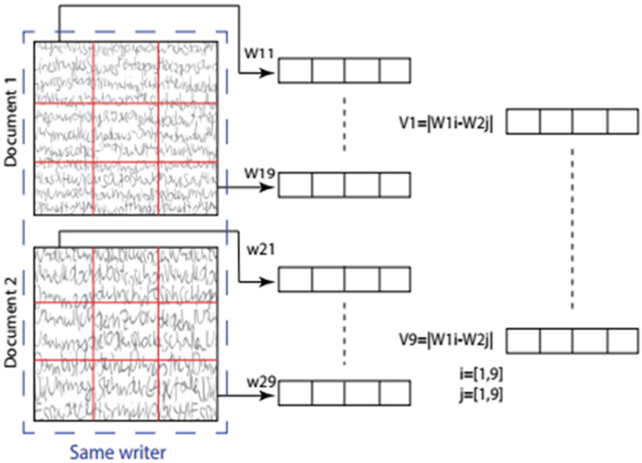

Fig. 5. Dissimilarity calculation of the positive class for one writer.

For the negative class, dissimilarities are calculated by considering the distance between the feature vector of each cell in a textural image with feature vectors of 9 other cells that are randomly extracted from images of 9 other writers see Fig. 6.

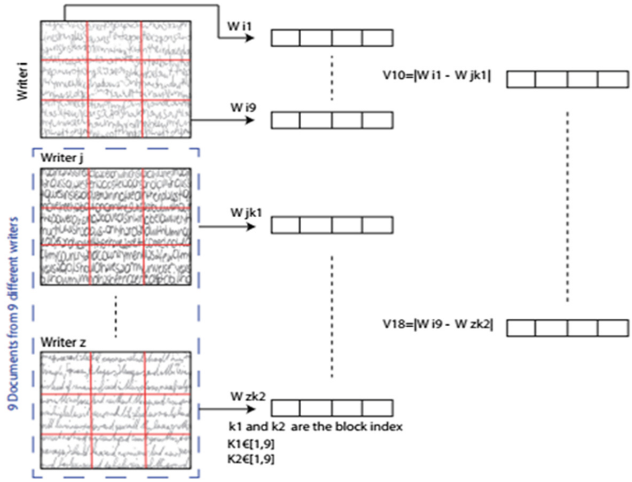

Fig. 6. Dissimilarity calculation of the negative class for one writer.

2.4 SVM-Based Writer Retrieval

In this work, we use a SVM classifier to achieve the retrieving task. The training aims to find the optimal hyperplane separating two classes from a set of training examples [7]. In our case the optimal plane must separate the two classes (the positive and the negative one). Commonly, data are mapped into a dot product space via a kernel function, such that:

$$f(z) = \sin\left(\sum_{j=1}^{S_v} \alpha_j y_j K\left(z, z_j\right) + b\right) \tag{6}$$

Sv is the number of support vectors that represent training data for which, $0 \leq \alpha j \leq C$. The bias b is a scalar while C is the cost parameter.

3 Experimentation and Result

For performance assessment of our "writer retrieval" system we use the CVL-Database[1], which contains handwritten documents of 310 writers. Each writer is represented by 7 or 5 different handwritten texts (1 in German and 6 in English script) [8]. As introduced in [2], the retrieval criterion considers the percentage of correct documents in the top N from the ranking. In addition, we evaluate the soft precision at the TOP N. For the training stage 100 writers are used, the remaining of the database is considered as test data (210 writers). From each writer the system must retrieve his all others documents to satisfies the hard criterion or at least one of those documents when using the soft criterion. The test considers the dissimilarity features between 9 blocks of the

[1] hwww.caa.tuwien.ac.at.

questioned document and all other blocks of all documents available in the data-set. Hence, 81 dissimilarities are introduced to the SVM for each document, where the SVM provides 81 answers. In fact, we compute between those 81 answers using the maximum of the averages values to get out the final SVM decision. Finally, the ranking step determine the retrieved documents. First, we performed a test on a closed system which means a system where only the writers who participated in the learning phase will be tested via other documents. Secondly, we make a test using the writers who did not participated at all in the conception of the system. The obtained Result are illustrated in the Tables 1 and 2 below:

Table 1. Retrieval result using the retrieval criterion

Precision (%)	TOP-2	TOP-3	TOP-4
Closed system	93,00	86,00	81,33
Opened system	70,00	65,50	63,00

Table 2. Retrieval result using the soft criterion

Precision (%)	TOP-2	TOP-3	TOP-4
Closed system	100,0	100,0	100,0
Opened system	90,47	92,38	94,36

From this table we can remark that a highest precision (93%) is obtained when using a closed system Which is very logical because these writers participated in the learning phase. Also, the opened system shows an acceptable performance about 70% of precision. therefor the system is able to retrieve writers even when they are not used in the learning phase.

This result shows the high performance that allows 100% of soft precision using a closed system against 94.36% when using opened system on the TOP-4.

4 Conclusion

In this paper we present a new independent protocol for “Writer Retrieval” based on a Dichotomy transformation. We also show the performance of the descriptor HOT which consider the pixel and the gradient information. Experimental analysis was performed on the CVL database. Results show that local features present mixed result, on opened system the precision of 70% is obtained, against 93% when using a closed system. Those result encourage us to make more research to improve the performance of our system. therefore, we are interested in considering more robust descriptors and also combination features.

References

1. Atanasiu, V., Likforman-sulem, L., Vincent, N.: Writer retrieval—exploration of a novel biometric scenario using perceptual features derived from script orientation. In: 11th Intl. Conf. on Document Analysis and Recognition, Beijing, China, 18–21 September 2011, pp. 628–632 (2011)
2. Bertolini, D., Oliveira, L.S., Justino, E., Sabourin, R.: Texture-based descriptors for writer identification and verification. Expert Syst. Appl. **40**(6), 2069–2080 (2013)
3. Burges, C.J.: A tutorial on support vector machines for pattern recognition. Data Min. Knowl. Disc. **2**(2), 121–167 (1998)
4. Fiel, S., Sablatnig, R.: Writer identification and writer retrieval using the fisher vector on visual vocabularies. In: Proceedings of the International Conference on Document Analysis and Recognition, ICDAR, pp. 545–549 (2013)
5. Glauberman, M.: Character recognition for business machines. Electronic (1956)
6. Hanusiak, R.K., Oliveira, L.S., Justino, E., Sabourin, R.: Writer verification using texture-based features. Int. J. Doc. Anal. Recogn. **15**(3), 213–226 (2012)
7. Kleber, F., Fiel, S., Diem, M., Sablatnig, R.: CVL-database: an off-line database for writer retrieval, writer identification and word spotting. In: Proceedings of the International Conference on Document Analysis and Recognition, ICDAR pp. 560–564 (2013)
8. Tang, S., Goto, S.: Histogram of template for human detection. In: Proceedings of the IEEE International Conference on Acoustics, Speech and Signal Processing, ICASSP, pp. 2186–2189 (2010)

Performance Analysis of Cell Averaging Based on Lookup Tables Detector of Distributed Targets in Weibull Clutter

Nabila Nouar(✉) and Atef Farrouki

Laboratoire SISCOM, Département d'électronique,
Faculté de sciences et technologies,
Université des Frères Mentouri Constantine 1, Constantine, Algeria
nabila_nouar@yahoo.com, farroukiatef@yahoo.fr

Abstract. In this paper, we analyze the performances of the Cell Averaging based on Lookup Tables (CA-LT) detector of distributed targets embedded in Weibull clutter. The target is spread over a number of cells, and its total energy is computed as the weighted sum of the energies reflected from each cell. The clutter level estimate is multiplied by the threshold factor, which is selected after estimating the actual parameters using the Moments estimation method (MOM). The total target energy is compared to the resulting product to decide the presence of the target.

Different couples of clutter parameters and numbers of reference cells are considered in order to assess the performances of the (MOM) method within the (CA-LT) scheme. The Constant False Alarm Rate (CFAR) property of (CA-LT) is also analyzed with regards to the clutter parameters.

Keywords: Lookup Tables · CFAR detection · Weibull distribution
Parameters estimation · Distributed targets

1 Introduction

In radar literature, the target is better described as a reflection from few points according to the Multiple Dominant Scatterers (MDS) concept [1], which corresponds to the High Resolution Radar (HRR) systems. In fact, the target energy is spread over the "primary cells" according to an energy model. Under this assumption, many detection schemes have been designed to detect "range spread targets" [1–5].

In [6], the authors proposed a new detection approach to detect distributed targets embedded in K-distributed clutter with unknown parameters. The latter is based on Lookup Tables containing threshold factors that maintain a Constant Probability of False Alarm (Pfa), and online estimation of the clutter parameters. The estimated parameters are then compared to the parameters in the Lookup Tables in order to select the suitable threshold factor. The performances of the (CA-LT) have been analyzed for different couples of clutter parameters and MDS models, and have been compared to the performances of the Logarithmic Cell Averaging detector (CAL) [7]. Results have shown that increasing the radar resolution enhances the detection performances, and that the (CA-LT) outperforms the CAL.

M. Chadli et al. (Eds.): ICEECA 2017, LNEE 522, pp. 545–555, 2019.
https://doi.org/10.1007/978-3-319-97816-1_42

Motivated by the working principle of the (CA-LT), the authors proposed the Greatest Of based on Lookup Tables (GO-LT), and the Smallest Of based on Lookup Tables (SO-LT) detectors to detect distributed targets embedded in compound Gaussian clutter, with Inverse Gamma texture [8]. The performances of (GO-LT) and (SO-LT) have been analyzed for different MDS models and have been compared to the (CA-LT). Simulations indicated that all detectors exhibit the best performance with the uniform target model.

In [9], the Multiple pulse Cell Averaging based on Lookup Tables (M-pulse CA-LT) detector have been proposed to detect distributed targets embedded in K-distributed clutter, using non coherent integration of multiple pulses. A pulse-to pulse estimation of clutter parameters is associated to the (M-pulse CA-LT) detector in order to estimate the per-pulse shape and scale parameters, and an average of these estimates is computed and compared to the values in the Lookup Tables to select the suitable threshold factor. The binary hypothesis test of the (M-pulse CA-LT) have been derived with regards to the expression of the target total energy. The performances of (M-pulse CA-LT) have been analyzed for different MDS models, couples of clutter parameters, and numbers of integrated pulses.

Performances of (M-pulse CA-LT) have also been compared to those of the (OS-GLRT), formerly proposed in [10]. Simulation results have shown that both detectors exhibit the best performance when the target is uniformly distributed on the primary cells. It has also been shown through simulations that the proposed approach ensures the Constant False Alarm Rate (CFAR) property.

On the other hand, bi-parametric distributions, such as the K-distribution [11], Weibull [12], Lognormal [13] are more adequate for modeling sea clutter returns. Moreover, clutter parameters are not a priori known in real radar applications. Hence, in this work, we focus on the Moments method (MOM) [14].

In this work, we analyze the performances of the (CA-LT) detector considering distributed targets embedded in Weibull clutter. As well established in [6], the (CA-LT) structure is associated to the Moments approach (MOM) [14] to estimate the shape and the scale parameters. These estimates are compared to the pre-computed values in the Lookup Tables to select the suitable threshold factor. The main purpose of this study is to assess the performances of the Moments approach within the proposed scheme. Hence, we present values of estimated shape and scale parameters and analyze the impact of the number of reference cells on the accuracy of the parameters estimation, and on the (CA-LT) performances.

2 The (CA-LT) Detector

The (CA-LT) detector is designed to detect distributed targets using Lookup Tables (LT), and online estimation of clutter parameters [6]. The main concept of this detector is to ensure the CFAR property with regards to the unknown clutter parameters. Les clutter samples X_i i = 1,…N are modeled as vector of Weibull Independent and Identically distributed (IID) random variables, and the target is spread over Np primary cells, surrounded by N reference cells (Fig. 1). The Weibull distribution is specified by the shape and the scale parameters, referred to as: β and α respectively. Its Probability Density Function (PDF) is given by [12]:

$$f_X(x) = \frac{\beta}{\alpha}\left(\frac{x}{\alpha}\right)^{\beta-1} exp\left[-\left(\frac{x}{\alpha}\right)^{\beta}\right] \tag{1}$$

The target total energy Δ, and the clutter level estimate, namely, Z_{CA-LT} are respectively given by [6]:

$$\Delta = \sum\nolimits_{k=1}^{Np} a_k X_0^k \tag{2}$$

$$Z_{CA-LT} = \sum\nolimits_{i=1}^{N} X_i \tag{3}$$

a_k is a multiplicative factor representing the amount energy proportion of the kth range location.

The threshold factors T maintaining a Constant Probability of False Alarm (Pfa) are offline computed and stored in Lookup Tables for different couples of clutter parameters (α, β). Then, the Moments (MOM) Weibull parameters estimation technique [14] is associated to the (CA-LT) structure, to estimate is the shape and the scale parameters referred to as: $\hat{\beta}$ and $\hat{\alpha}$ respectively.

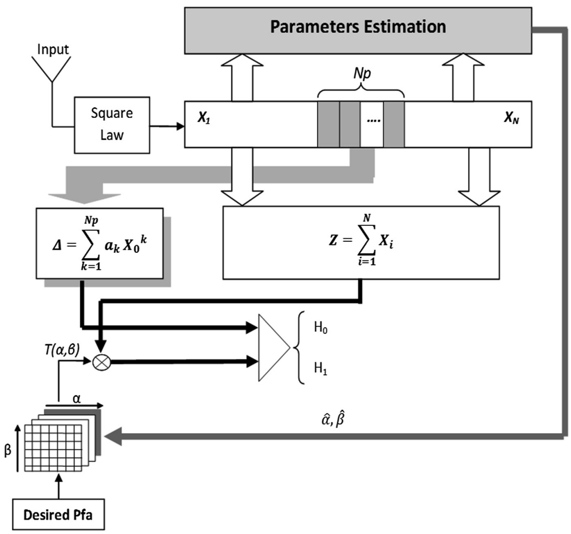

Fig. 1. Detection scheme of the (CA-LT) detector

The scale parameter α can be estimated as follows [14]

$$\hat{\alpha} = \hat{\mu}/\Gamma\left(1 + \frac{1}{\hat{\beta}}\right) \tag{4}$$

The shape parameter β can be estimated using the following function [15]

$$\frac{\hat{\mu}^2}{\hat{\mu}^2 + \hat{\sigma}^2} = \frac{\Gamma\left(1 + \frac{1}{\beta}\right)\Gamma\left(1 + \frac{1}{\beta}\right)}{\Gamma\left(1 + \frac{2}{\beta}\right)} \tag{5}$$

where $\Gamma(.)$ is the Gamma function, $\hat{\mu}$ and $\hat{\sigma}$ are computed using the clutter samples X_i as follows [14]

$$\hat{\mu} = E(X) = \frac{1}{N}\sum_{i=1}^{N} X_i \tag{6}$$

$$\hat{\sigma} = E\left(X^2\right) - (E(X))^2 \tag{7}$$

The couple ($\hat{\alpha}$, $\hat{\beta}$) is compared to the parameters in the Lookup Tables to select the suitable threshold factor T(α, β), which is multiplied by the clutter level estimate Z_{CA-LT}. The obtained product is compared to the distributed total energy Δ. The binary hypothesis test of the (CA-LT) for detecting distributed targets is given by [6]:

$$\sum_{k=1}^{Np} a_k X_0^k \underset{H_0}{\overset{H_1}{\gtrless}} T(v, \mu) Z_{CA-LT} \tag{8}$$

where H_0 and H_1 refer to the null and the alternative hypothesis respectively.

3 Simulations Results

Detection performances of the (CA-LT) are analyzed for different couples of parameters (α, β), considering a uniformly distributed target on Np = 5 primary cells. We also consider a Pfa of 10-3. We use Monte Carlo simulations with 100/Pfa independent trials. The signal to clutter ratio (SCR) in the case of Weibull distribution is given by:

$$SCR = 10log_{10}\left(\frac{2\sigma^2}{\left(\frac{\Gamma\left(1+\frac{1}{\beta}\right)\Gamma\left(1+\frac{1}{\beta}\right)}{\Gamma\left(1+\frac{2}{\beta}\right)}\right)}\right) \tag{9}$$

σ represents the parameter of a Rayleigh fluctuating target.

3.1 Lookup Tables

Tables 1, 2 and 3 refer to the Lookup Tables of (CA-LT) for different couples of clutter parameters (α, β), assuming Np = 5, a Pfa of 10-3 and N = 16,32 and 64 respectively. We observe that the threshold factor T is not affected by the scale parameter α. However, it decreases for higher values of the shape parameter β. Moreover, by comparing the Tables, we observe that the threshold value decreases when the number of reference cells N increases.

Table 1. Threshold factor of CA-LT detector, N = 16

β	α				
	1	3	6	8	10
1	0.2550	0.2550	0.2550	0.2550	0.2550
1.5	0.1684	0.1684	0.1684	0.1684	0.1684
2	0.1340	0.1340	0.1340	0.1340	0.1340
3	0.1055	0.1055	0.1055	0.1055	0.1055
4	0.0942	0.0942	0.0942	0.0942	0.0942
6	0.0822	0.0822	0.0822	0.0822	0.0822
8	0.0775	0.0775	0.0775	0.0775	0.0775
10	0.0743	0.0743	0.0743	0.0743	0.0743

Table 2. Threshold factor of CA-LT detector, N = 32

β	α				
	1	3	6	8	10
1	0.1064	0.1064	0.1064	0.1064	0.1064
1.5	0.0750	0.0750	0.0750	0.0750	0.0750
2	0.0610	0.0610	0.0610	0.0610	0.0610
3	0.0500	0.0500	0.0500	0.0500	0.0500
4	0.0459	0.0459	0.0459	0.0459	0.0459
6	0.0400	0.0400	0.0400	0.0400	0.0400
8	0.0378	0.0378	0.0378	0.0378	0.0378
10	0.0364	0.0364	0.0364	0.0364	0.0364

Table 3. Threshold factor of CA-LT detector, N = 64

β	α				
	1	3	6	8	10
1	0.0506	0.0506	0.0506	0.0506	0.0506
1.5	0.0354	0.0354	0.0354	0.0354	0.0354
2	0.0295	0.0295	0.0295	0.0295	0.0295
3	0.0242	0.0242	0.0242	0.0242	0.0242
4	0.0219	0.0219	0.0219	0.0219	0.0219
6	0.0197	0.0197	0.0197	0.0197	0.0197
8	0.0186	0.0186	0.0186	0.0186	0.0186
10	0.0180	0.0180	0.0180	0.0180	0.0180

3.2 MOM Estimation Results

In this part, we assess the performances of the MOM approach within the (CA-LT) detector. We present different tables containing estimated shape and scale parameters values ($\hat{\alpha}$, $\hat{\beta}$) for different couples of parameters (α, β), and analyze the effect of the number of reference cells N on the quality of estimation.

Tables 4 and 5 refer to the estimated values of the shape and the scale parameters, namely, $\hat{\beta}$ and $\hat{\alpha}$ respectively. Assuming N = 16 reference cells, we observe that the MOM method ensures good estimates for both parameters. Also, Tables 6 and 7 refer to the estimated values $\hat{\alpha}$ and $\hat{\beta}$ assuming N = 32 reference cells, the obtained values indicate that the estimated values are close to the real values of the parameters, and the MOM method presents better results than the cased of N = 16.

Finally, and in order to assess the effect of the number of reference cells on the quality of estimation, we computed the MOM method assuming N = 64 cells. By comparing the results, which are summarized in Tables 8 and 9 for $\hat{\alpha}$ and $\hat{\beta}$ respectively to the previous results, we observe that the best results are obtained with N = 64 cells. We conclude that better estimation is obtained with higher numbers of reference cells N, since it guarantees a more accurate selection of threshold factor, when associated to a Lookup Tables based detector. This result is in accordance with the chosen number of N in the CA-LT in [6].

Table 4. Estimated scale parameter α, N = 16

β	α						
	1.0	1.5	2.0	3.0	3.5	4.0	5.0
1.0	0.9108	1.8115	1.8663	3.1951	4.3081	5.8008	6.2396
1.5	1.5536	1.6002	1.5972	2.6082	3.5309	4.4823	5.4213
2.0	0.7245	1.9425	2.3537	2.9043	3.226	4.0587	5.4292
2.5	1.0168	1.9422	2.3376	2.7116	3.4895	3.3730	5.7459
3.0	1.1966	1.7211	2.1304	3.3694	2.8541	5.7053	4.7103
3.5	1.3438	1.7887	2.4053	2.7955	3.6260	3.1629	4.3330
4.0	1.2086	1.2325	2.1288	3.3175	5.1392	5.7860	6.0189
4.5	0.9745	1.9355	1.8996	2.681	3.8986	4.6742	4.893
5.0	1.2703	1.6717	2.3817	3.7825	2.8694	4.0614	4.6373

Table 5. Estimated shape parameter β, N = 16

β	α						
	1.0	1.5	2.0	3.0	3.5	4.0	5.0
1.0	0.8371	1.3227	0.9319	1.0302	1.0499	0.9742	1.0612
1.5	2.3679	1.3695	1.3692	1.4317	1.5624	1.3893	1.5343
2.0	1.8545	1.6094	1.7758	2.0711	2.1014	1.8989	2.0841
2.5	2.2685	1.4630	2.5513	2.3758	2.3709	2.2072	2.3959
3.0	3.5589	2.4641	2.6168	2.8080	3.0630	2.8760	2.8390
3.5	4.7518	3.6603	3.4571	3.4196	3.4525	3.0646	3.5881
4.0	3.7642	2.8605	3.7149	3.6358	4.4846	4.1677	3.9545
4.5	5.8626	4.1820	5.2583	4.4055	4.6986	4.5759	4.6043
5.0	4.2503	5.3255	5.4349	4.8969	4.6149	5.0073	4.9171

Table 6. Estimated scale parameter α, N = 32

β	α						
	1.0	1.5	2.0	3.0	3.5	4.0	5.0
1.0	1.0385	1.5747	2.1790	3.3900	3.2229	3.9871	5.2396
1.5	1.1008	1.4629	1.9267	3.0767	3.168	4.4773	5.1214
2.0	1.1066	1.4903	1.9492	2.8837	3.3881	4.0807	4.7183
2.5	0.985	1.6375	2.4490	2.797	3.7706	4.8576	5.2456
3.0	1.138	1.2180	2.5014	3.5513	3.8564	4.0007	5.9285
3.5	1.3827	1.5999	1.8169	3.2579	3.6266	4.1872	5.1003
4.0	0.9934	1.8044	1.6787	2.9393	3.9439	3.905	6.5232
4.5	1.0616	1.4638	2.0612	2.8316	3.8190	3.8699	4.9782
5.0	1.2724	1.6873	2.7330	3.2205	3.3196	3.8778	4.5010

Table 7. Estimated shape parameter β, N = 32

β	α						
	1.0	1.5	2.0	3.0	3.5	4.0	5.0
1.0	1.1494	1.0089	1.0232	0.9890	0.9447	1.0347	0.951
1.5	1.2479	1.3931	1.8176	1.5956	1.5881	1.3934	1.4428
2.0	1.9448	2.0924	2.0079	2.0154	1.9418	1.9535	2.0579
2.5	2.4899	2.3234	2.4874	2.4612	2.4425	2.4190	2.5310
3.0	4.3014	2.7613	3.3757	3.2832	2.9696	2.8017	3.0402
3.5	3.6919	3.5774	3.4629	3.6294	3.6128	3.5292	3.731
4.0	4.7081	4.931	3.7821	4.0947	4.2684	4.0952	4.0708
4.5	2.6738	4.0234	4.8508	4.2577	4.6352	4.4965	4.4097
5.0	4.6539	5.069	5.4764	5.0138	5.1810	5.3465	4.9490

Table 8. Estimated scale parameter α, N = 64

β	α						
	1.0	1.5	2.0	3.0	3.5	4.0	5.0
1.0	1.1042	1.5248	1.9846	3.1155	3.1504	4.4097	5.1716
1.5	1.0850	1.5389	1.9884	3.3171	4.2072	4.2892	4.8936
2.0	1.1159	1.4993	1.9293	2.6570	3.0242	4.2854	5.1349
2.5	1.0334	1.4388	1.8802	3.3685	3.8377	3.4699	5.0350
3.0	0.7620	1.5426	2.0953	3.0326	3.7888	3.4444	4.9467
3.5	1.0124	1.4963	1.7780	2.6402	3.0247	3.7521	4.6642
4.0	1.2712	1.2331	1.7346	2.8816	3.5281	4.5885	4.4611
4.5	0.8676	1.488	2.0671	3.092	3.3999	4.3460	5.0899
5.0	0.9413	1.3921	1.9371	2.4842	4.2956	4.0572	6.3609

Table 9. Estimated shape parameter β, N = 64

β	α						
	1.0	1.5	2.0	3.0	3.5	4.0	5.0
1.0	0.9753	1.0839	1.0214	0.9791	1.0149	1.0192	0.9591
1.5	1.4892	1.5797	1.6435	1.4964	1.445	1.4441	1.5011
2.0	1.9467	1.8231	1.8626	2.0019	1.9820	1.8918	2.0231
2.5	2.6431	2.6682	2.1715	2.4809	2.4193	2.5655	2.5797
3.0	2.8735	2.92	3.5288	2.9938	3.0757	2.9003	3.0197
3.5	3.4119	3.4988	3.3347	3.5159	3.5224	3.3935	3.6573
4.0	3.4578	3.6853	3.6925	3.6282	4.1048	4.1185	4.0343
4.5	4.2115	4.2162	4.4177	4.4403	4.4737	4.4219	4.4594
5.0	5.5616	4.6875	4.8124	4.8676	5.0401	5.2635	5.0043

3.3 Detection Performances of CA-LT

In order to analyze the effect of the online estimation of the clutter parameters on the detection performances of (CA-LT), we plot its Pd against SCR for different couples (α, β) for different N.

In Fig. 2, we present detection performances of (CA-LT) assuming different couples of clutter parameters, namely (α, β) = (1, 1), (1, 2) and (1, 10) assuming N = 16 and N = 64 reference cells. We observe that CA-LT exhibits the best performance with the couple (1, 1), and it is degraded as the parameter β decreases, which is the case of β = 10.

We also observe that increasing the number of reference cells enhances the detection performances.

Another important property is the Constant False Alarm Rate CFAR) property. As presented in Fig. 3, the Pfa of the (CA-LT) does not depend on the value of α, and it is maintained to 10-3 for any given number of reference cells.

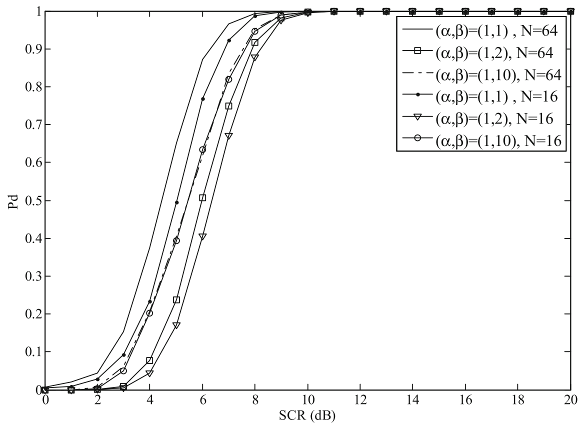

Fig. 2. Pd of (CA-LT) for different couples of clutter parameters (α, β)

Moreover, the Pfa of (CA-LT) is plotted for different values of β. As illustrated in Fig. 4, the best result is obtained with N = 64, which is expected since the effective parameters estimation allows a more accurate indexation of Lookup Tables, and selection of suitable threshold factor. For, N = 16 and N = 32, the Pfa is still close to the nominal Pfa (10-3) which is in accordance with the results presented above with regards to the accuracy of the estimation. We conclude that the proposed Lookup Tables approach guarantees the CFAR property with regards to both clutter parameters (α, β).

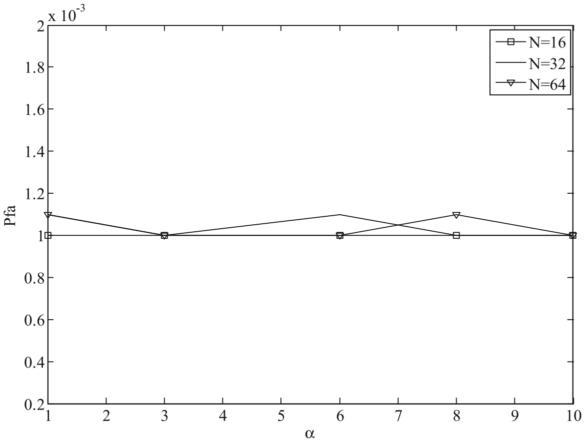

Fig. 3. Pfa of (CA-LT) for different values of α

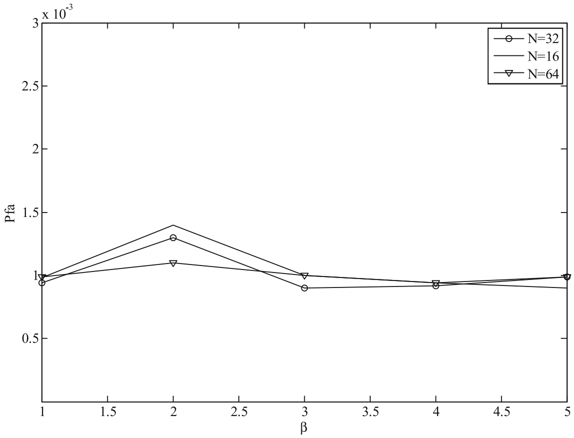

Fig. 4. Pfa of (CA-LT) for different values of β

4 Conclusion

In this paper, we analyzed the performances of the (CA-LT) detector considering range spread targets embedded in Weibull clutter with unknown parameters. First, expression of binary hypothesis tests of (CA-LT) when range spread targets are consider is presented. Then, the performances of the Moments (MOM) method, which is associated to the detectors structure, are assessed for different couples of clutter parameters and for different numbers of reference cells.

Simulation results are carried out for different couples of clutter parameters using Monte Carlo method. Results have shown that the proposed approach is significantly dependent on the number of reference cells used in the estimation, since it affects the correct indexation of Lookup Tables at the detection stage.

It has also been shown by means of simulations that the(CA-LT) detector is CFAR with regards to both the shape and the scale parameters (α, β).

References

1. Conte, E., De Maio, A.: GLRT-based adaptive detection algorithms for range-spread targets. IEEE Trans. Sign. Process. **49**(7), 1336–1348 (2001)
2. Conte, E., De Maio, A., Ricci, G.: CFAR detection of distributed targets in non-Gaussian disturbance. IEEE Trans. Aerosp. Electron. Syst. **38**(2), 612–621 (2002)
3. Gerlach, K.: Spatially distributed target detection in non-Gaussian clutter. IEEE Trans. Aerosp. Electron. Syst. **35**(3), 926–934 (1999)
4. Alfano, G., De Maio, A., Farina, A.: Model-based adaptive detection of range-spread targets. IEE Proc. Radar Sonar Navig. **151**(1), 2–10 (2004)
5. Wang, L., Chen, X.: Detection of range spread target with coherent integration. In: Proceedings IET International Radar Conference, Xi'an, China, pp. 1–4 (2013)

6. Nouar, N., Farrouki A.: CFAR detection of spatially distributed targets in K-distributed clutter with unknown parameters. In: Proceedings 22nd European Signal Processing Conference (EUSIPCO 2014), Lisbon, Portugal, pp. 1731–1735 (2014)
7. Bucciarelli, T., Lombardo, P., Tamburrini, S.: Optimum CFAR detection against compound Gaussian clutter with partially correlated texture. IEE Proc. Radar Sonar Navig. **148**(4), 95–104 (2001)
8. Nouar, N. Farrouki, A.: Detection of distributed targets embedded in homogeneous compound Gaussian clutter with inverse Gamma texture. In: 2017 Seminar on Detection systems Architectures and Technologies (DAT), Alger, Algeria (2017)
9. Nouar, N., Farrouki, A.: Lookup tables-based detection of range spread targets in compound Gaussian environment with multiple-pulse non-coherent integration. Sign. Image Video Process. **11**(61), 1–8 (2017)
10. He, Y., Jian, T., Su, F., Qu, C., Gu, X.: Novel range spread target detectors in non-Gaussian clutter. IEEE Trans. Aerosp. Electron. Syst. **46**(3), 1312–1328 (2010)
11. Guan, J., He, Y., Peng, Y.N.: CFAR detection in k-distributed clutter. In: Proceedings of ICSP (1998)
12. Guida, M., et al.: Biparametric linear estimation for CFAR against Weibull clutter. IEEE Trans. Aerosp. Electron. Syst. **AES-28**(1), 138–152 (1992)
13. Guida, M., et al.: Biparametric linear estimation for CFAR for lognormal clutter. IEEE Trans. Aerosp. Electron. Syst. **AES-29**(3), 798–809 (1993)
14. Al-Fawzan, M.: Methods for Estimating the Parameters of Weibull Distribution. King Abdulaziz City for Science and Technology, Riyadh (2000)

Assess the Effects of Wind on Forest Parameters Inversion by Using Pol-InSAR Applications

Sofiane Tahraoui(✉) and Mounira Ouarzeddine

LTIR, Faculty of Electronics and Computer Science, USTHB, BP No. 32 El Alia, Bab Ezzouar, Algiers, Algeria
Sofiane.tahraoui@gmail.com, m.ouarzeddine@yahoo.fr

Abstract. A most critical factor that should be taken into consideration for a successful implementation of Pol-InSAR parameter inversion is the temporal baseline decorrelation, which are caused by changes within the scene occurring in the time between acquisitions, especially in the case of repeat-pass space-borne measurements.

Temporal decorrelation bias the volume decorrelation contribution and reduce the reliability of estimated parameters. This paper try to examines and quantify its effect with experimental methods over simulated forests data.

Keywords: PolInSAR · Polarimetric SAR interferometry · Inversion RVoG · Temporal baseline

1 Introduction

The study of the vegetation in the context of diffusion modeling allows to relate the observation to physical parameters of the medium.

A reliable forest parameter estimation depends on the ability to separate volume from other scattering contributions and from physical phenomenal that can affect the decorrelation.

The high sensitivity of the interferometric coherence behavior to the polarization state [1, 2], and to the change occurring within the scene, persuade us to consider the temporal changes which appear in stochastic form [3, 4], and cannot be modeled with the required accuracy.

The amount of temporal decorrelation depends in one side, on the natural processes occurring in the time between the interferometric acquisitions, such wind, moisture content change, and anthropogenic pressure (e.g. **population growth**), and in another side on the radar parameters (frequency, baseline..).

These aforementioned facts, leading to assess the impact of the estimated temporal decorrelation levels on the performance of Pol-InSAR inversion techniques.

M. Chadli et al. (Eds.): ICEECA 2017, LNEE 522, pp. 556–564, 2019.
https://doi.org/10.1007/978-3-319-97816-1_43

In the first section of this paper, a brief review of the basic concepts of **PolInSAR** (polarimetric SAR interferometry) is given, followed by second section in which we attempt to describe the estimated temporal decorrelation behavior caused by two principal factor, namely the wind and the moisture content change within the scene, and finally some conclusions are drawn.

2 Basic Notions

2.1 The Interferometric Coherence

The Interferometric coherence measures the correlation between the radar signals corresponding to complex SAR images viewed from close angles.

The strong reliance of the interferometric coherence behavior to the polarization state can be exploited in inversion methods for estimation of forest parameters [5].

The complete information measured by the SAR system can be represented in form of three 3×3 complex matrices $[T_{11}]$, $[T_{12}]$, and $[T_{22}]$ formed using the outer products of scattering vector from each antenna $\vec{k}_{p1}$, and $\vec{k}_{p2}$ represented in Pauli basis as:

$$\begin{aligned}[\boldsymbol{T}_{11}] &= \left\langle \vec{k}_{p1}\vec{k}_{p1}^{*} \right\rangle \\ [\boldsymbol{T}_{22}] &= \left\langle \vec{k}_{p2}\vec{k}_{p2}^{*} \right\rangle \\ [\boldsymbol{T}_{12}] &= \left\langle \vec{k}_{p1}\vec{k}_{p2}^{*} \right\rangle \end{aligned} \tag{1}$$

$[\boldsymbol{T}_{11}]$, and $[\boldsymbol{T}_{22}]$ are hermitian coherency matrices that describe the polarimetric properties for each acquisition separately, however, and $[\boldsymbol{T}_{12}]$ is a non-hermitian complex matrix which contains the interferometric phase information [6].

By introducing two unity complex vectors $\vec{\omega}_1$, and $\vec{\omega}_2$ which may be interpreted as generalized scattering mechanisms, we are able to generate two complex scalar images Im_1 and Im_2 by projecting the scattering vectors $\vec{k}_{p1}$, and $\vec{k}_{p2}$ into this vectors, as:

$$Im_1 = \vec{\omega}_1^{*T}\vec{k}_{p1} \quad Im_1 = \vec{\omega}_2^{*T}\vec{k}_{p2} \tag{2}$$

The interferogram related to the scattering mechanisms $\vec{\omega}_1$, and $\vec{\omega}_2$, is then given by:

$$Im_1.Im_1 = (\vec{\omega}_1^{*T}\vec{k}_{p1})\left(\vec{\omega}_2^{*T}\vec{k}_{p2}\right)^{*T} = \vec{\omega}_1^{*T}[\boldsymbol{T}_{12}]\vec{\omega}_2 \tag{3}$$

And the corresponding interferometric phase follow as:

$$\phi = \arg(Im_1.Im_1) = \arg(\vec{\omega}_1^{*T}[\boldsymbol{T}_{12}]\vec{\omega}_2) \tag{4}$$

Finally, a general expression for the complex interferometric coherence for an arbitrary choice of scattering mechanisms $\vec{\omega}_1$, and $\vec{\omega}_2$, may be derived:

$$\tilde{\gamma} = \frac{\left\langle \vec{\omega}_1^{*T} [\boldsymbol{T}_{12}] \vec{\omega}_2 \right\rangle}{\sqrt{\left\langle \vec{\omega}_1^{*T} [\boldsymbol{T}_{11}] \vec{\omega}_1 \vec{\omega}_2^{*T} [\boldsymbol{T}_{22}] \vec{\omega}_2 \right\rangle}} = \gamma e^{j\phi} \tag{5}$$

where γ is the amplitude of the complex coherence $\tilde{\gamma}$, and ϕ is the interferogram phase.

3 The Sensitivity of the Coherence to the Polarization

The inversion of physical parameters of the volume, is based on the behavior of interferometric coherence, since this latter is very sensitive to the change of polarization states of the electromagnetic field [7].

In practice, and in order to develop the model, some assumptions has been proposed in [7–9] for simplifying Eq. (5) as follows:

- The polarimetric information acquired from the two interferometric antennas are the same, then $[\boldsymbol{T}_{11}] = [\boldsymbol{T}_{22}]$.
- The two acquisitions are realized in similar conditions, so the projection vectors for the two observations are equal.

So the interferometric coherence formula (5) can be expressed simpler as:

$$\tilde{\gamma} \approx \frac{\left\langle \vec{\omega}_1^{*T} [\boldsymbol{T}_{12}] \vec{\omega}_2 \right\rangle}{\left\langle \vec{\omega}_1^{*T} [\boldsymbol{T}_{11}] \vec{\omega}_1 \right\rangle} \tag{6}$$

This last coherence formula has the same phase as (5) but less magnitude. In the following we use (6) to indicate the complex coherence under the two conditions stated above.

4 Temporal Baseline Effect on Parameter Inversion

4.1 Coherence Interpretation

The complex interferometric coherence $\tilde{\gamma}$ is an important tools used in **Pol-InSAR** application for parameter estimation at different polarizations. As we aforementioned, its depends on instrument and acquisition parameters as well as on dielectric and structural parameters of scatterers. Thus, it could be composed into different decorrelation contributions [10] therefore it can be rewritten as:

$$\tilde{\gamma} = \tilde{\gamma}_{tmp} \tilde{\gamma}_{SNR} \tilde{\gamma}_{sct} \tag{7}$$

where is the decorrelation $\tilde{\gamma}_{sct}$ (or $\tilde{\gamma}_{vol}$ in our case) reflects the phase stability of the scatterer (i.e. volume) under the different incidence angles induced by the interferometric baseline, $\tilde{\gamma}_{tmp}$ is the temporal decorrelation caused by change occurring in time within the scene between acquisitions, and $\tilde{\gamma}_{SNR}$ comprises decorrelation effects induced by the non-ideal SAR system and preprocessing including contributions induced by additive noise.

Volume decorrelation $\tilde{\gamma}_{sct}$ is directly linked to the vertical distribution of scatterers F(z) through a (normalized) Fourier transformation relationship [3, 8]. A widely and successfully used model for F(z) is the **R**andom **V**olume **o**ver an impenetrable **G**round. It is a two layer model, composed by a vegetation layer (canopy + trucks) and a ground component.

4.2 The Volume De-correlation Model

The vegetation layer is modelled as a layer of given thickness containing randomly oriented particles characterized by scattering amplitude per unit volume. The volume decorrelation caused by the vegetation layer only can be described as [9]:

$$\tilde{\gamma}_{sct} = \tilde{\gamma}_{vol} = \frac{\int_0^{h_v} e^{\frac{2\sigma_z z}{\cos\theta} + jk_z z} dz}{\int_0^{h_v} e^{\frac{2\sigma_z z}{\cos\theta}}} e^{jk_z z_0} \tag{8}$$

where θ is the incidence angle, σ is a mean extinction coefficient [7, 9], and k_z is the effective vertical sensitivity factor which relates changes in terrain elevation (vegetation height) to changes in interferometric phase. As such, it represents one of the essential parameters for PolInSAR forest height inversion. k_z is directly linked to the system parameter as:

$$k_z = \frac{4\pi}{\lambda \sin\theta} \Delta\theta = \frac{4\pi}{\lambda R \sin\theta} \mathrm{B}_\perp \tag{9}$$

where λ is the radar wavelength, and $\Delta\theta$ denotes the incidence angle difference between the two interferometric antennas, $\mathrm{B}_\perp$ is the perpendicular component of the spatial baseline, and R the slant range distance.

In other way, if we suppose have two scatterers S_v and S_g received by two antennas, master "m" and slave "s". The interferometric coherence made through the coherent summation of their coherences:

$$\tilde{\gamma} \approx \frac{\left\langle \left(S_{v_m} + S_{g_m}\right)\left(S_{v_s} + S_{g_s}\right)^* \right\rangle}{|S_v|^2 + |S_g|^2} \approx \frac{\left\langle \left(S_{v_m} S_{v_s}\right)\left(S_{g_m} S_{g_s}\right) \right\rangle}{|S_v|^2 + |S_g|^2} \tag{10}$$

Under the assumption that the contributions S_v and S_v are not correlated:

$$\left\langle S_{v_k} . S_{g_l} \right\rangle = 0 \tag{11}$$

The interferometric coherence of the sum of the two contributions can be expressed in terms of interferometric coherence of these pure contributions $\tilde{\gamma}_v$ and $\tilde{\gamma}_g$ [7]:

$$\begin{aligned} \tilde{\gamma} &= e^{j\phi_0} \frac{\tilde{\gamma}_v + m(w)}{1 + m(w)} \\ &= e^{j\phi_0} \left[\tilde{\gamma}_v + \frac{m(w)}{1 + m(w)} (1 - \tilde{\gamma}_v) \right] \end{aligned} \tag{12}$$

where m(w) is the power ratio of these two contributions at polarisation w:

$$m = \frac{|\tilde{\gamma}_v|^2}{|\tilde{\gamma}_g|^2} \tag{13}$$

One can fairly notice that (12) exhibit a straight line equation form, and the position of the interferometric coherences $\tilde{\gamma}_w$ on this segment, depends on $\mu = \frac{m(w)}{1 + m(w)}$.

The estimation problem can be resolved as follows:

- **linear regression of $\tilde{\gamma}_w$ in the complex plane**
  In Realistic case, and due to temporal decorrelation effect, the interferometric coherence are distributed in a non-aligned manner. To remedy this problem, we resort to minimizing the mean-square distance between the coherence loci and an unknown line.
- **Ground phase ϕ_0 determination**
  The backscattered energy of the bare surfaces is predominantly present in the co-polar channels, and the HV channel contains essentially the contribution of canopy. The interferometric coherence of ground, which is assumed equal to 1 ($\tilde{\gamma}_g = e^{j\phi_0}$) is then localized in the intersection of the regression line and trigonometric circle farthest from the interferometric coherence associated to HV channel in the complex plane, because this channel is characterized by the lowest ratio μ among all polarimetric channels.
- **$\tilde{\gamma}_v$ estimation**
  We make the assumption that the pure contribution of the canopy is measured for at least one state of polarization. The interferometric coherence assumed to be that from canopy, $\tilde{\gamma}_v$ will logically be the highest phase centre relative to the ground, and which therefore satisfy the condition $\max_w(\arg(\tilde{\gamma}_w) - \phi_0)$. From the complex value of $\tilde{\gamma}_v$ we can deduce the height h_v and the mean extinction coefficient σ of waves in the canopy by the relation given in Eq. (8).

However this model does not account for volume decorrelation which reduce in general the correlation between the acquired images and lead to erroneous and/or biased parameter estimates.

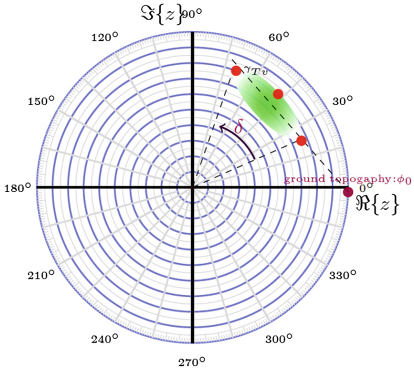

Fig. 1. Coherence loci in **RVoG** model.

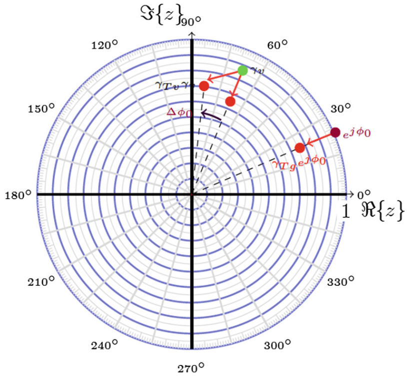

Fig. 2. Effect of temporal decorrelation over Coherence loci in **RVoG** models.

5 Experimental Evaluation of $\tilde{\gamma}_{tmp}$

In repeat-pass Pol-InSAR system, temporal decorrelation cannot be neglected. It affects in general both the volume layer and the underlying ground layer, in order to consider those effect, [1] propose to rewrite (12) as:

$$\begin{aligned}\tilde{\gamma} &= e^{j\phi_0}\frac{\tilde{\gamma}_v\tilde{\gamma}_{tv} + m(w)\tilde{\gamma}_{tg}}{1+m(w)} \\ &= e^{j\phi_0}\left[\tilde{\gamma}_v\tilde{\gamma}_{tv} + \frac{m(w)\tilde{\gamma}_{tg}}{1+m(w)}(1-\tilde{\gamma}_v\tilde{\gamma}_{tv})\right]\end{aligned} \tag{14}$$

$\tilde{\gamma}_{tg}$ represents the scalar correlation coefficient describing the temporal decorrelation of the underlying surface scatterers, and $\tilde{\gamma}_{tv}$ denotes the complex correlation coefficient describing the temporal decorrelation of the volume layer. Thus, we got two additional unknown parameters introduced by temporal baseline, which makes the problem insoluble using a quad-polarization single baseline acquisition (three complex coherences). One solution consist on using the experimental quantification of each effects apart (Fig. 1).

This effect on the ground layer can arise from surface changes between the two acquisitions, this result in complex plane by a shift in position of the volume coherence ward the centre, but the phase centre remains unchanged as Fig. 2 show.

On the other hand, its effect on volume is more complex and critical due to its susceptibility to wind which is nonstationary spatiotemporally even on very short time and small spatial-scales. Thus, in this case, temporal decorrelation reduces the amplitude of volume decorrelation and changes the effective phase centre depending on the temporal structure function. In case of a constant temporal decorrelation function, temporal decorrelation in volume becomes a scalar value as shown in Fig. 2.

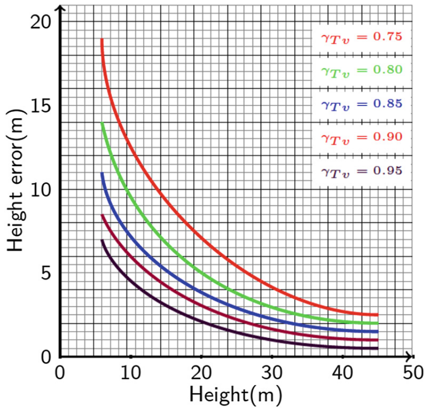

Fig. 3. Height bias (overestimation) induced by different levels of temporal baseline as a function of forest heights assuming a constant vertical wavenumber.

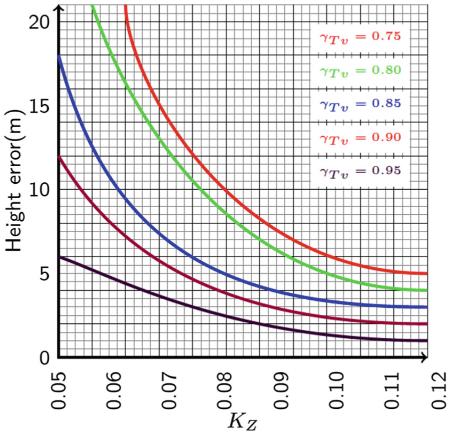

Fig. 4. Height bias (overestimation) induced by different levels of temporal baseline as a function of wavenumber for a constant forest heights h = 20 m.

When the temporal gap between the two acquisition is short enough, we can assume that the ground properties still unchanged, and the dielectric properties of the volume does not change. Thus, the most common temporal decorrelation in forests is due to the motion in volume layer caused by the wind. In this case, the model with temporal decorrelation contributions mentioned in (14) can be simplified as:

$$\tilde{\gamma} = e^{j\phi_0} \frac{\tilde{\gamma}_v \tilde{\gamma}_{tv} + m(w)}{1 + m(w)} \tag{15}$$

The coherence contaminated by temporal decorrelation leads to overestimating of forest height.

Figure 3 shows the height bias obtained by inverting (15) for different levels of $\tilde{\gamma}_{tv}$ as a function of forest height assuming a constant effective vertical wavenumber.

One can clearly see that the estimation biases are higher for low heights and that the height error are greater for high temporal decorrelation $\tilde{\gamma}_{tv}$. It can be also noticed, that even for low temporal decorrelation levels the height bias becomes critical for low forest heights.

In Fig. 4, the Height bias induced by different levels of temporal decorrelation as a function of vertical wavenumber k_z (assuming a constant forest height h = 20 m). By observing the curves, we can notice that the error become less critical by increasing the wavenumber values.

By reference to (9), a valuable option to reduce the impact of this bias arise, wish is to increase the vertical wavenumber by increasing the spatial baseline or the used radar frequency [11]. This last solution is ruled by trade-off, because the frequency control resolution and penetration depth. *i.e.* more the frequency is high, less is the penetration depth which prevent the ground access [12], so the remained solution is the baseline length.

6 Conclusion

In this paper, a critical natural parameters that can affect the inversion process are analysed, namely the temporal decorrelation. These parameter can be divided into two classes, namely long baseline in which the media are affected by dielectric change caused by moisture content change with climate, growth cycle,… and short temporal baseline class in which ground is assumed to be not affected, but wind induced movement of unstable scatterers within canopy layer and subsequently decreases the coherence.

Temporal decorrelation is always present (whatever the time interval between acquisitions) for repeat-pass and introduces a height bias. The problem of inversion will be not possible when temporal baseline became too long, because of the additional number of unknowns.

When dealing with a constant forest height. A solution can be applied in order to reduce the error rate caused by temporal baseline effect, is by increasing the wavenumber values by varying some of the system parameters (i.e. radar frequency, angle of view).

References

1. Cloude, S.R., Papathanassiou, K.P.: Three-stage inversion process for polarimetric SAR interferometry. IEE Proc. Radar Sonar Navig. **150**, 125–134 (2003). https://doi.org/10.1049/ip-rsn:20030449
2. Tahraoui, S., Ouarzeddine, M., Souissi, B.: Interferometric coherence optimization: a comparative study. In: 2013 Eighth International Conference on Broadband and Wireless Computing, Communication and Applications (BWCCA). Presented at the 2013 Eighth International Conference on Broadband and Wireless Computing, Communication and Applications (BWCCA), pp. 427–431 (2013). https://doi.org/10.1109/BWCCA.2013.75
3. Forkuo, E.K., Frimpong, A.: Analysis of forest cover change detection. Int. J. Remote Sens. Appl. **2**, 82–92 (2012)
4. Sun, H., Zeng, T., Yang, J.: The impact of residual motion deviations on forest height inversion by SAR remote sensing. In: Geoscience and Remote Sensing Symposium (IGARSS), 2012 IEEE International, Presented at the Geoscience and Remote Sensing Symposium (IGARSS), pp. 6503–6506 (2012). https://doi.org/10.1109/IGARSS.2012.6352750
5. Lavalle, M., Khun, K.: Three-baseline InSAR estimation of forest height. IEEE Geosci. Remote Sens. Lett. **11**, 1737–1741 (2014). https://doi.org/10.1109/LGRS.2014.2307583

6. Papathanassiou, K.P., Cloude, S.R.: Single-baseline polarimetric SAR interferometry. IEEE Trans. Geosci. Remote Sens. **39**, 2352–2363 (2001). https://doi.org/10.1109/36.964971
7. Garestier, F. Evaluation du potentiel de la technique PolInSAR pour l'estimation des paramètres physiques de la végétation en conditions satellitaires (Phd Thesis). Université Sciences et Technologies - Bordeaux I (2006)
8. Lavalle, M., Hensley, S.: Extraction of structural and dynamic properties of forests from polarimetric-interferometric SAR data affected by temporal decorrelation. IEEE Trans. Geosci. Remote Sens. **53**, 4752–4767 (2015). https://doi.org/10.1109/TGRS.2015.2409066
9. Treuhaft, R.N., Cloude, S.R.: The structure of oriented vegetation from polarimetric interferometry. IEEE Trans. Geosci. Remote Sens. **37**, 2620–2624 (1999). https://doi.org/10.1109/36.789657
10. Martinez, J.M., Floury, N., Toan, T.L., Beaudoin, A., Hallikainen, M.T., Makynen, M.: Measurements and modeling of vertical backscatter distribution in forest canopy. IEEE Trans. Geosci. Remote Sens. **38**, 710–719 (2000). https://doi.org/10.1109/36.842000
11. Kugler, F., Lee, S.-K., Papathanassiou, K.P.: Estimation of forest vertical structure parameter by means of multi-baseline Pol-InSAR. In: 2009 IEEE International, Geoscience and Remote Sensing Symposium, IGARSS 2009, pp. IV-721–IV-724 (2009). https://doi.org/10.1109/IGARSS.2009.5417478
12. Kugler, F., Koudogbo, F.N., Papathanassiou, K.P., Gutjahr, K.: Frequency Effects in Pol-InSAR Forest Height Estimation - Conference papers - VDE Publishing House (2006)

A Novel SIW Corrugated Travelling Wave Antennas Array for Microwave Imaging

Mehadji Abri(✉), Benzerga Fellah, and Hadjira Badaoui

STIC Laboratory, Department of Telecommunication, Faculty of Technology, University of Tlemcen, Tlemcen, Algeria
abrim200@yahoo.fr, fellahttl@yahoo.fr, elnbh@yahoo.fr

Abstract. Communication systems require antennas with compact size, low cost and losses, high gain and high efficiency. In order to realize a satisfactory antenna, these requirements are needed to design a compact structure with longitudinal radiation pattern. This antipodal antenna is combined with a waveguide integrated into the substrate (Integrated Waveguide SIW substrate) to operate in the C-band frequency. We analyze the behavior of the antenna arrays for different profiles in order to clearly demonstrate the role played by the exponential factor. The antipodal vivaldi antenna will be studied and simulated by the CST Micro Wave Studio simulator.

Keywords: Antipodal antenna arrays · Vivaldi antenna · SIW technology CST microwave studio

1 Introduction

The innovations continues to improve day by day and in particularly in the field of telecommunications which are in a period of globalization. The field of telecommunications is in perpetual evolution. Its main areas of investigation are mainly motivated by an increasing need for data throughput, but is constrained by an increasingly busy spectrum of frequencies. Antennas are omnipresent in our daily lives. The performance race as the improvement of the characteristics of so-called Vivaldi antipodal antennas and the modern needs of telecommunications (increased throughput) because the antenna is an indispensable part of any wireless device. They are an engine for the development of so-called Ultra Large Band (ULB) technologies, which have many advantages and are used in a wide range of civil and military applications. Indeed, power transmission lines at millimeter frequencies are the waveguides, appreciated for its low losses of dissipation as well as for its electrical performances. They are the origin of the design of a large number of microwave devices such as filters, transformers, adapters and polarizers, often applied in space telecommunications, antennas and airborne radar systems. However, they are cumbersome, costly to manufacture and their integration with other planar circuits having a low quality factor. On the other hand, technological developments in telecommunications and microwaves have for several years tended towards the miniaturization of circuits, a reduction in costs, masses and losses in the devices. Thus, SIW circuits present a new technology of replacement and at present

M. Chadli et al. (Eds.): ICEECA 2017, LNEE 522, pp. 565–574, 2019.
https://doi.org/10.1007/978-3-319-97816-1_44

subject of many topics of research with direct applications [1–5]. It is in this context that the design and study of the Vivaldi antipodal antenna behavior in SIW technology adapted to ULB systems are important because they must respond to each of the challenges raised [6–17]. Thus, the antenna must exhibit an optimum efficiency and constant characteristics over a very wide frequency band but keep a limited cost. In addition, of course, there are the problems of integration and therefore the need to design a minimal footprint structure without, however, degrading its performance.

The objective set in this paper is to participate in this research effort to master this new SIW technology in order to design a Vivaldi antipodal antenna (Ultra Large Band (ULB) with longitudinal radiation with good gain, presented in the S bands frequency in SIW Technology for communication systems or network structure is of compact size and low cost, exhibiting high gain, low losses and high efficiency.

Our goal is to explore the possibility of designing new very broadband antenna arrays with a Vivaldi antipodal antenna in SIW technology, compact and agile in radiation. The choice of the radiating element differs depending on the networking and the required performance of radiation.

2 Proposed Antenna Geometry

A new Vivaldi antipodal antenna structure has been proposed consisting of two antipodal exponential sections which form a fine aperture.

Along the outer edges of the regular antenna of the comb-like undulations are cut into the upper part of metalized and lower layers. These last two layers will be separated by a "substrate" dielectric of a certain thickness and of course the whole will be powered by a SIW guide in order to have a directional and high gain antenna. As illustrated in the following Fig. 1.

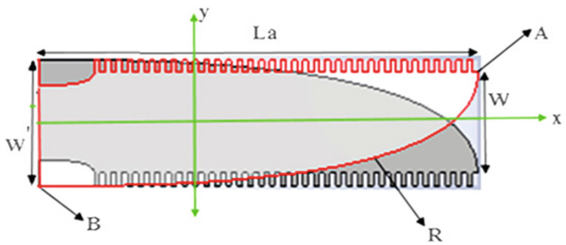

Fig. 1. The AVA antenna structure.

The choice of the dielectric substrate plays an important role in design and simulation. The substrate parameters are: $\varepsilon_r = 4.3$, h = 1.54 mm and tg$\partial = 0.018$. The design parameters were studied only with regard to the shape and size of the antenna and not the parameters of the substrate. The SIW waveguide is used to power the AVA, which is the feeding technique that ensures minimum loss. The characteristic of SIW loss is an order of magnitude better than microstrip. Using the standard waveguide equations, the SIW operates in the band C frequency range [4–8 GHz], the cut-off frequency of the

SIW circuit *fc* = 5 GHz for the TE_{10} mode with the previous parameters. To ensure a perfect connection between the SIW and coaxial probe port of 50 Ω to have a better adaptation, the AVA taper as shown in Fig. 2 is characterized by W_1 = 3 mm and W_2 = 18.8 mm and L_1 = 18 mm and L_2 = 2 mm and m = 2 mm are the parameters used for the simulation operating in the C [4–8 GHz] band. The antipodal Vivaldi antenna is characterized by certain parameters which will facilitate the design task and make it more organized to have good results. The parameters required for antenna design are as follows:

The antenna input width, labeled “W”, “W” antenna output, “La” means antenna length, substrate thickness “h” and a spacing denoted “n” between the undulations. The corrugation width “s”.

The antenna geometry SIW parameters associated as well as typing and the substrate used were determined we arrive at the final structure of an antipodal Vivaldi antenna based on the SIW technology presented in the following figure.

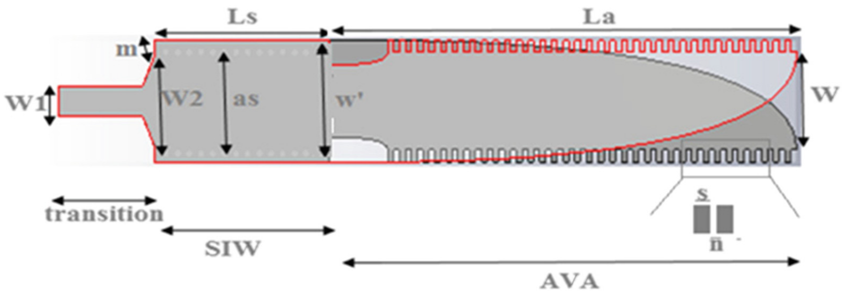

Fig. 2. AVA settings.

In our work, we begin by making a parametric study of the antipodal Vivaldi antenna by seeing the influence of the profile; of the SIW parameters and the antenna parameters on the variations of the reflection coefficient S11 as a function of the frequency, and then the antenna proper is designed. The antenna AVA is operational in the C-band [4–8 GHz].

3 Parametric Study

We keep the same parameters and characteristics of the substrate used in the basic structure.

To ensure the proper transition between the power supply line and the radiating element two essential factors will be studied: “W1”, “L1” and “W” antenna opening to have a directional antenna. We varied the “W1” in the interval 2 to 6 mm with a pitch of 0.5 and we obtained 5 mm as an optimized value. Then L1 in the interval 1 to 10 mm and the best value was 2 mm. And finally, we study the influence of the antenna length La in the range 10 to 18 mm. We find that the optimized value is 18 mm. The value of

La varies automatically W the antenna aperture also varies, they are inversely proportional. Figure 3 shows the good variations for the reflection coefficient S11 as a function of the frequency under the simulation tool CST.

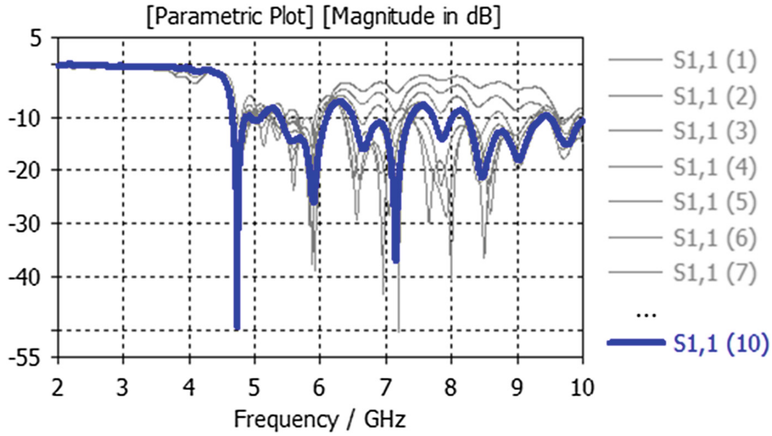

Fig. 3. Reflection coefficient S_{11} as a function of frequency.

The best result after this parametric study is the graph plotted in blue which shows that the structure is perfectly adapted; we see several peaks lower than −20 dB, a very wide bandwidth from 4.9 GHz to 9 GHz. It is the optimal structure.

4 Optimized AVA Antenna

The previous section on the Vivaldi antipodal antenna in SIW technology highlighted the role of the critical parameters on the different antenna characteristics; we can deduce an optimized AVA antenna with SIW technology in the operating frequency band [4–8 GHz], with adaptation levels that remain below −10 dB. The following parameters of the optimized antipodal Vivaldi antenna: La = 80 mm, W = 19.8 mm, W′ = 21.8 mm, n = 2, s = 2 mm. After this optimization we get the Vivaldi antipodal antenna in SIW technology optimized as shown in the Fig. 4 below:

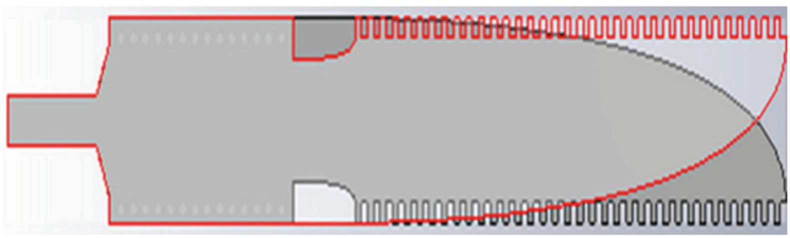

Fig. 4. View of the AVA antenna face under CST.

The plots of the reflection coefficients S11 measured in decibels as a function of the frequencies GHz are illustrated in Fig. 5.

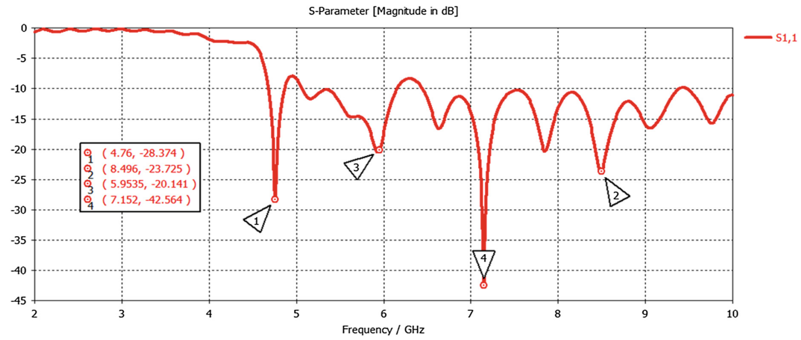

Fig. 5. Simulation result of the reflection coefficient S_{11} of the optimized structure.

The simulation result obtained for the variations of the reflection coefficient S11 as a function of the frequency with the optimized values of the various parameters. At frequency 4.76 GHz the S11 reached the value −28.374 dB, −23.725 dB for a frequency 8.496 GHz and a third peak equal to −20.141 dB for frequency 5.954 GHz, there are also other lower peaks of −10 dB, it proves to have that we have a very wide band from 4.77 to 8 GHz with excellent adaptation and high radiant power.

Respectively, the figures illustrate the distribution of the electric field in the antenna for the frequency 7.15 GHz.

Figure 6 shows the phenomenon of distribution of the electric field for the TE_{10} guided mode in the SIW guide and the antipodal Vivaldi antenna. We notice that the field is well located by two rows of metal vias for the SIW guide and well delimited by the exponential shape and the undulations of the walls of the antenna AVA, it means that the structure radiates perfectly. We present respectively in Fig. 7 the radiation pattern for the frequency 7.152 GHz.

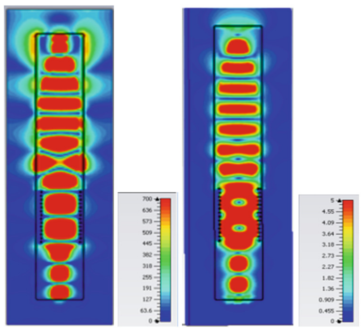

Fig. 6. Electric field distribution in the AVA for different instances.

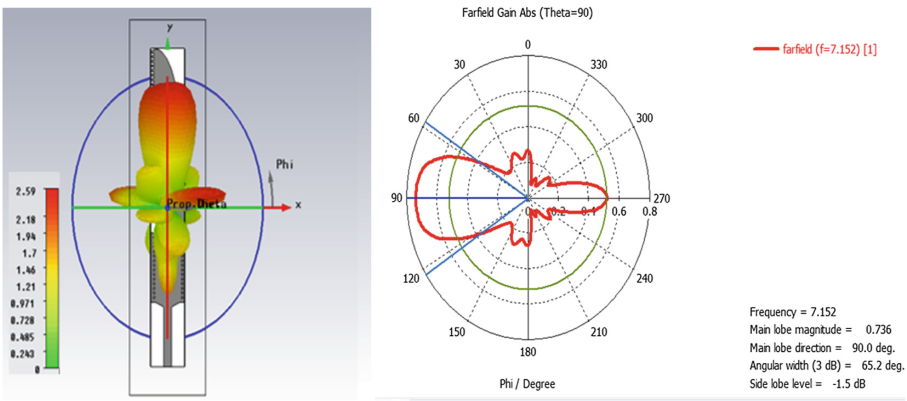

Fig. 7. Antenna radiation patters of the AVA antenna.

According to Fig. 7, we observe that the simulated gain for the 7.152 GHz frequency is 0.776 dBi, the maximum directivity is 2.59 dB with an aperture angle of 3 dB of 65.2° and the angle of the main lobe direction 90°. The main lobe is of the order of −1.5 dB. It is then pointed out that the antipodal Vivaldi antenna has longitudinal directional radiation in the chosen frequency. Directional radiation is highly recommended in microwave Imaging, communication and detection.

5 1 × 4 AVA Antennas Array

For this application, we keep the same parameters of the structure but we approach the radiating elements to see the influence of the spacing between the antennas on the network radiation diagram. We will try to design an array consisting of four Vivaldi antipodal antennas operating at the interval [4–8 GHz] at the base of SIW technology in Y configuration. The array is powered by a 50 Ω microstrip line operating in the C-band simulated under the CST environment. The power is distributed to different antennas via a power divider which has an input and 4 radiating elements at the output. The radiating elements are positioned periodically to avoid inter-element coupling. The plot of reflection coefficients S_{11} for the 1 × 4 antenna array in the frequency band 4 to 8 GHz is depicted in the Fig. 8.

Figure 9 shows that there are three resonant frequencies in the frequency range from 4 to 7 GHz. A good adaptation is observed at the frequency 6.684 GHz. The reflected powers are −22.077 dB and both remain below −10 dB. We can therefore evaluate the radiation performance of this array.

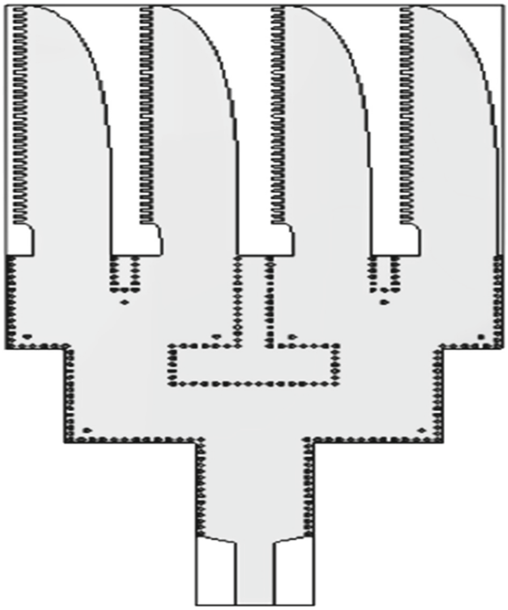

Fig. 8. Front view the 1 × 4 AVA antennas array.

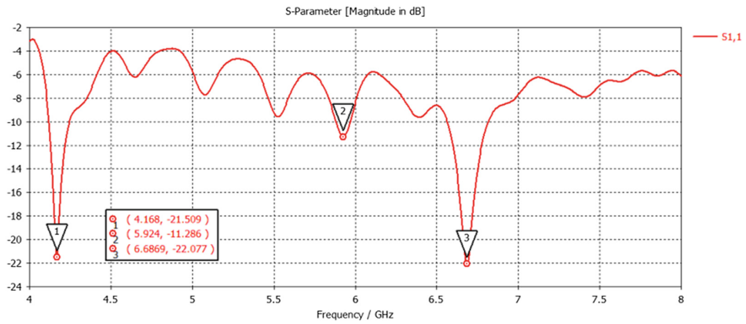

Fig. 9. Reflection coefficient S_{11} of the 1 × 4 AVA antennas array.

We illustrate in Fig. 10, the distribution of the electric field in contour on the 1 × 4 AVA antennas array in SIW for $f = 5.92$ GHz.

The figure below shows the radiation pattern in 3D and 2D patterns. Figure 11 illustrates the radiation pattern for the frequency 6.536 GHz. The maximum directivity is 7.95 dB and the aperture angle (3 dB) = 28.6°. The increase in directivity and the decrease in the angle of aperture are clearly visible on these results.

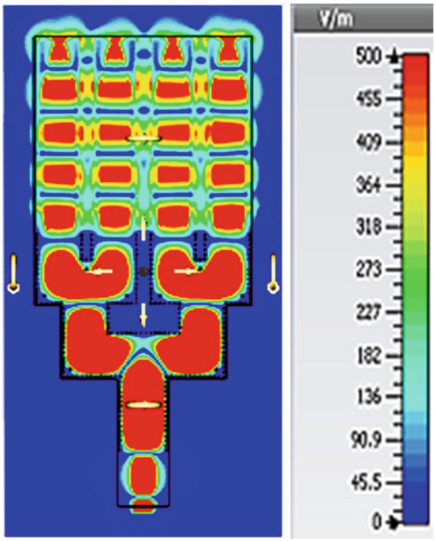

Fig. 10. E-field distribution under CST for $f = 5.92$ GHz.

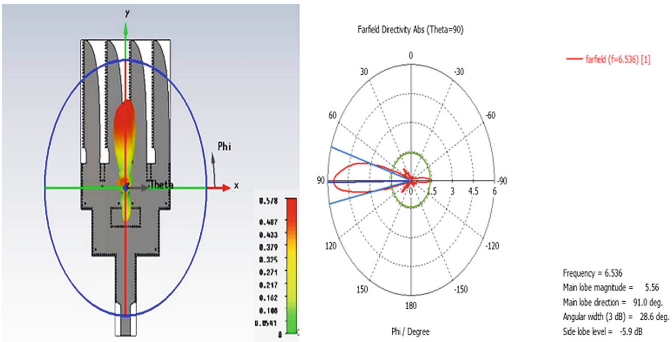

Fig. 11. Radiation patterns for 1 × 4 AVA antennas array at the frequency $f = 6.53$ GHz.

It can also be seen from Fig. 11 that the array radiates in the direction normal to the longitudinal axis and the radiation is more directional with very weak secondary lobes. This structure is highly recommended for directional longitudinal radiation for short-range detection and microwave imaging.

6 Conclusion

At the beginning of our study, we presented an antenna belonging to two different categories of ULB antennas, the Vivaldi antipodal antenna and two 1 × 4 AVA antenna arrays. This study made it possible to demonstrate the role of the critical parameters of these two antennas on their performances and thus to design antennas operating in the frequency band [4–8 GHz]. For the antenna Vivaldi antipodal, among the most important factors for these antennas is the exponential profile. By using the optimized AVA antenna with a SIW power divider operating in the C band at the first time, a configuration of an AVA 1×4 antennas array was made. The results obtained are very interesting with regard to bandwidth and adaptation and show the value of using Vivaldi antennas for communications applications and in the medical field and imaging and radar detection.

References

1. Rabah, M.A., Abri, M., Tao, J., Vuong, T.H.: Substrate integrated waveguide design using the two dimentionnal finite element method. Prog. Electromagnet. Res. M **35**, 21–30 (2014)
2. Doucha, S., Abri, M.: New design of leaky wave antenna based on SIW technology for beam steering. Int. J. Comput. Networks Commun. IJCNC **5**, 73–82 (2013)
3. Rabah, M.A., Abri, M., Badaoui, H.A., Tao, J., Vuong, T.-H.: Compact miniaturized half-mode waveguide/high pass-filter design based on SIW technology screens transmit-IEEE C-band signals. Microwave Opt. Technol. Lett. **58**(2) (2016)
4. Fellah, B., Abri, M., Badaoui, H.A.: Optimized bends and corporate 1×4 and 1×8 SIW power dividers junctions analysis for V band applications using a rigorous finite element method. Arab. J. Sci. Eng., 1–9 (2015)
5. Diaz, E., Belenguer, A., Esteban, H., Monerris-Belda, O., Boria, V.: A novel transition from microstrip to a substrate integrated waveguide with higher characteristic impedance. In: IEEE MTT-S International Microwave Symposium Digest, pp. 1–4 (2013)
6. Fellah, B., Mehadji, A.: Design of antipodal linearly tapered slot antennas (ALTSA) arrays in SIW technology for UWB imaging. In: The Second International Conference on Electrical Engineering and Control Applications, CEECA 2014 Constantine, Algeria, 18–20 November 2014
7. Puskely, J., Mikulášek, T.: Compact wideband vivaldi antenna array for microwave imaging applications. In: 7th European Conference on Antennas and Propagation (EuCAP), pp. 1519–1522 (2013)
8. Doucha, S., Abri, M., Badaoui, H.A.: Leaky wave antenna design based on SIW technology for millimeter wave applications. WSEAS Trans. Commun. **14**, 108–112 (2015)
9. Rabah, M.A., Abri, M., Tao, J.W.: A numerically study of a new SIW waveguide using the CST microwave studio for C-band applications. In: The Third International Conference on Image and Signal Processing and Their Applications, Mostaganem, Algeria 2, 3 et 4 Décembre 2012
10. Rabah, M.A., Abri, M., Tao, J.W.: A performance propagation Study's of a SIW waveguide technology for Ka-band applications. In: International Conference on Systems and Processing Information, 12–14 May 2013, Guelma, Algeria (2013)
11. Doucha, S., Abri, M.: Simulation d'un Nouveau Guide d'Ondes Intégré au Substrat Opérant dans la Bande [3.4–4.2 GHz]. In: International Conference on Electrical Engineering, CIGE 2013, 17–19 Novembre 2013, Bechar, Algeria (2013)
12. Rabah, M.A., Abri, M., Tao, J.W.: Half mode waveguide design based on SIW technology. In: International Congress on Telecommunication and Application 2014, University of A. MIRA Bejaia, Algeria, 23–24 April 2014
13. Doucha, S., Mehadji, A.: A leaky wave antenna based on SIW technology for ka band applications. In: The Second International Conference on Electrical Engineering and Control Applications, ICEECA 2014 Constantine, Algeria, 18–20 November 2014

14. Rabah, M.A., Abri, M., Tao, J.W.: Study and miniaturization of the SIW technology. In: 2eme Conférence Internationale Sur les Nouvelles Technologies et la Communication (ICNTC 2015), Chlef, Algérie, 03–04 Mars 2015
15. Benzerga, F., Mehadji, A.: Design of millimeter substrate integrated wave guide MSIW analysis by the quick finite element method (QFEM). In: International Conference on Advanced Communication Systems and Signal Processing, ICOSIP 2015, 8–9 November, Tlemcen, Algeria (2015)
16. Fellah, B., Mehadji, A., Badaoui, H.A., Tao, J.W., Vuong, T.-H.: 1 × 2 SIW power dividers modeling using a rigorous finite element method for V-band applications. In: 9th Jordanian International Electrical and Electronics Engineering Conference (JIEEEC), 12–14 October, Jordan
17. Rabah, M.A., Abri, M., Badaoui, H.A., Tao, J., Vuong, T.-H.: Half-mode substrate integrated waveguide (Hmsiw) for X-band applications. In: 10 th Research World International Conference, Beijing, China, 13th February 2016

Correction to: Total Harmonic Distortion Performance in PV Systems Using Fuzzy Logic Controller

Ahmed Ali, Bhekisipho Twala, Tshilidzi Marwala,
and Ilyes Boulkaibet

Correction to:
Chapter "Total Harmonic Distortion Performance in PV Systems Using Fuzzy Logic Controller" in:
M. Chadli et al. (Eds.): *Advanced Control Engineering Methods in Electrical Engineering Systems*, LNEE 522,
https://doi.org/10.1007/978-3-319-97816-1_25

The original version of the chapter was inadvertently published with incorrect fourth author "Ilyes Boulkabet", which should be corrected to read as "Ilyes Boulkaibet" in chapter "Total Harmonic Distortion Performance in PV Systems Using Fuzzy Logic Controller". The correction chapter and the book have been now updated with the change.

The updated online version of this chapter can be found at
https://doi.org/10.1007/978-3-319-97816-1_25

M. Chadli et al. (Eds.): ICEECA 2017, LNEE 522, p. E1, 2019.
https://doi.org/10.1007/978-3-319-97816-1_45

Author Index

M. Chadli et al. (Eds.): ICEECA 2017, LNEE 522, pp. 575–576, 2019.
https://doi.org/10.1007/978-3-319-97816-1